applied
sciences

Special Issue

Organo-Fluorine Chemical Science

Inventing the Fluorine Future

2012

Helmut Martin Hügel (Ed.)

MDPI

OPEN ACCESS

Summary

Dear Colleagues,

The unique properties imparted on molecules by fluorine substitution, continues to be the subject of intense research as the products have widespread application in all areas of science. Incorporation of fluorine can productively and unpredictably modulate several properties that interest medicinal chemists. Selected drugs for the treatment of high cholesterol such as Lipitor® by Pfizer, Crestor® by AstraZeneca, Zetia® by Merck/Schering-Plough and Lescol® by Novartis all of which contain one or more fluorine atoms that increase metabolic stability, rank amongst the highest selling prescription drugs ever developed. Without doubt every current drug discovery and development program includes and evaluates fluorine-containing drug candidates. A one step ^{18}F-labeling of peptides that contain a specific arene group has emerged that is rapid and simple to perform for ^{18}F PET (positron emission tomography) an *in vivo* imaging technology for medical use has potential wide application. The synthesis of many pharmaceuticals and agrochemicals with fluorine atoms or groups is closely dependent on the development of new chemical methodologies by organic and industrial chemists. Monofluoroalkenes are known as nonisomerable, nonhydrolyzable stable bioisosteres of amide bonds and recently published highly enantio- and diastereoselective organocatalytic monofluorovinylations reactions have led to the isolation of monofluorovinylated products. A practical methodology for the enatioselective a-fluorination of ketene enolates has been optimized by the utilization of a three-component catalysis system provides an array of a-fluorocarboxylic acid derivatives. A generally useful coupling protocol for copper-catalyzed $1H-$perfluoroalkane arylation by aryl iodides allows ready access to a range of perfluoroalkyl substituted aromatic compounds. Tetrafluoroethylene (TFE) is the organofluorine feedstock for the production of poly-(tetrafluoroethylene)polymers that have many applications. The transformation of TFE to a,b,b,-trifluorostyrenes via palladium-catalyzed coupling and arylzincs has been achieved in excellent yields and paves the way to new fluorine-polymers. The deployment of a fluorine substituted conjugated polymer in photovoltaic cells exhibited medium band gap yields above 7% attributed in part to the increased hole mobility of the fluorinated polymer. Organo-fluorine chemistry has had an enormous global impact on science and society, the fluorine fever continues to flourish and grow and we are delighted that experts in this field have agreed to contribute their research achievements to this special issue.

Dr. Helmut Martin Hügel
Guest Editor

Table of Contents

Article

Nanoimprint Resist Material Containing Ultraviolet Reactive Fluorine Surfactant for Defect Reduction in Lithographic Fabrication

Satoshi Takei [1,2,]* and Atsushi Sekiguchi [1]

[1]   Department of Mechanical Systems Engineering, Toyama Prefectural University, Imizu, Toyama 939-0398, Japan

[2]   Department of Materials Engineering Science, Osaka University, Toyonaka, Osaka 560-8531, Japan

*   Author to whom correspondence should be addressed; E-Mail: takeis@pu-toyama.ac.jp; Tel.: +81-766-56-7500; Fax: +81-766-56-6131.

Abstract: The generated resist based defects on the template in addition to the presence of particles and contaminants is critical for ultraviolet curing of nanoimprint lithographic fabrication. This procedure is proven to be suitable for advanced resist material design under the process conditions. Nanoimprint resist material containing an ultraviolet reactive fluorine surfactant was developed to modify the fundamental surface interactions between resists and the template for defect reduction in nanoimprint patterning replication. The developed acrylate type nanoimprint resist material containing 4,4,5,5,6,6,7,7,8,8,9,9,10,10,11,11,11-heptadecafluoro-2-hydroxyundecyl acrylate as an ultraviolet reactive fluorine surfactant, indicated excellent patterning dimensional accuracy by minimizing surface free energy, and having the effect of improving the generated resist based defect numbers on the template, with a 500 nm contact hole and 2 μm line patterns, in the replication of 20 nanoimprint process cycles. This desirable concept using an ultraviolet reactive fluorine surfactant with an acrylate group in the acrylate type nanoimprint resist material is one of the most promising processes ready to be incorporated into mass fabrication in the next generation of electronic devices.

Keywords: ultraviolet reactive fluorine surfactant; nanoimprint lithography; resist; defect reduction; surface free energy

1. Introduction

Heading towards mass fabrication for the next nano electronic devices, ultraviolet (UV) curing nanoimprint lithography is one option for the pattern generation of electronic circuits on wafers. In UV curing nanoimprint lithography, the mold of quartz or polymer is used as the template. The fluorinated alkyl silane as a fluorinated self assembled monolayer was coated on the template with one of the surface modification techniques in UV curing nanoimprint lithography. UV curing nanoimprint resist materials are dispensed as droplets on underlayer materials, and then are set with the template with low pressure. The nanoimprint resist materials fill the template and are then solidified by brief UV irradiation, forming the desired pattern. These processes are repeated across the wafer, similar to the step and repeat lithography process.

UV curing nanoimprint lithography is a promising method recently used for next generation device manufacturing because it is of low production cost, high throughput and can be carried out at room temperature. In addition, UV curing nanoimprint lithography takes advantage of the synergetic effects of micro- to nano-sized patterns on various flexible substrates, three-dimensional patterns, direct patterns of metal, and develop-less patterning applications such as magnetic memory structures, organic light-emitting diodes, optical sensor devices, hybrid-laser system, biosensor devices, and biomedical nanospectrometer devices.

UV curing nanoimprint lithography offers the opportunity to relax the very complex mask patterns by avoiding much of the sub-resolution assist features required for ArF lithography at a comparable design rule. In addition, in order to solve the cost issues using mass fabrication methods nanoimprint lithography was investigated in nanoelectronic devices [1]. In advanced electronic device applications using nanoimprint lithography, a UV curing glucose-based resist material from biomass was studied for environmental applicability with 65 nm dense line patterning [2]. A UV sensitive hard mask underlayer material with terminal methacrylate groups has been developed, in order to improve the generated resist peeling and contamination problem, when the template was removed from the resist after UV irradiation [3]. The formulation of advanced resist materials design of fluorinated silicon-based resist materials in the step and flash nano imprint lithography for the next generation was reported [4]. The thermal nanoimprint lithography for Au electrodeposition was demonstrated [5]. The shrinkage behaviors and elimination time of bubbles for different cavity sizes and resist thicknesses were investigated [6]. The direct patterning of low-dielectric constant (low-k) materials via nanoimprint lithography was evaluated [7].

However, the UV curing nanoimprint lithography in the mass fabrication of the next generation device manufacturing, faces a challenge because of the various kinds of defects, particles, and contaminants positioned between the nanoimprint resist material and the template Examples of which are resist peeling, dislocations, voids, and impurities. The defect inspections which focused on two key defect types of random non-fill defects occurring during the nanoimprint resist filling process together with repeater defects caused by interactions with particles on the substrate, were summarized [8]. The new proposed nanoimprint resist material design and the nano imprinting processing conditions were investigated to decrease the resist based defect number on the template, when the template was removed from the resist material after pressing the template into the resist

material [9]. Figure 1 shows the classic optical images of a dirty-template causing the generated resist based defects on the template in the repeatability of nanoimprint process cycles.

Figure 1. Optical images of the generated resist based defects on the template in nanoimprint lithography.
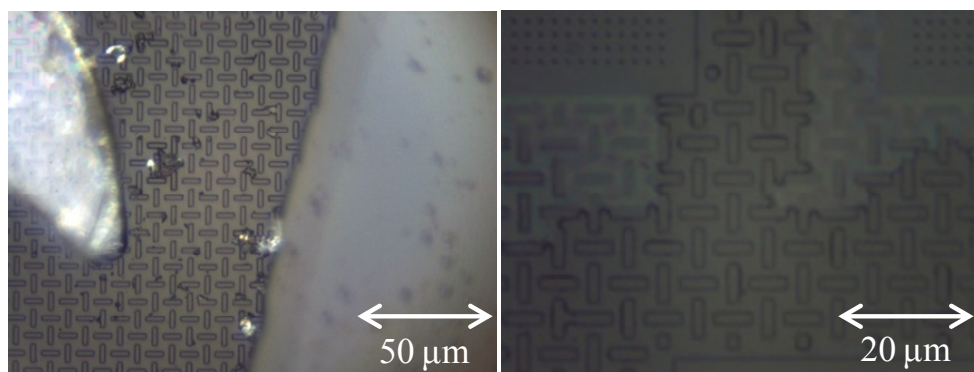
UV curing nanoimprint lithography requires the clean separation of a template from a nanoimprint resist material, and the force required to create this separation must be minimized to decrease the generated resist based defect number on the template. This problem of nanoimprint resist material on the template is critical for mass fabrication using UV curing nanoimprint lithography, when the template is removed from the nanoimprint resist material after pressing the template into the nanoimprint resist material.

Therefore, the nanoimprint resist material containing a UV reactive fluorine surfactant was investigated to modify the fundamental surface interactions between nanoimprint resist material and template for defect reduction in nanoimprint patterning dimensional accuracy, by replication of imprint process cycles. The effect of reducing the defect numbers on the template with a 500 nm contact hole and 2 μm line patterns in the replication of nanoimprint process cycles was demonstrated and is discussed in terms of minimizing the surface free energy of nanoimprint resist material.

2. Experimental Procedure

2.1. UV Curing Nanoimprint Lithography

It is essentially a stamping process, the nanoimprint lithography mechanically deforms a nanoimprint medium using a three-dimensional template with the desired pattern. The nanoimprint medium is then hardened to produce a negative of the template pattern. UV curing nanoimprint lithography was focused on in this study as the next generation process of choice for the mass fabrication of next generation device manufacturing. Figure 2 shows a schematic of the UV curing nanoimprint lithographic process cycles. The cycles were as follows: (1) The underlayer material TPU-UL (Toyama Prefectural University) is spin-coated on a substrate [9], and then the underlayer-coated substrate is prebaked at 200 °C for 2 min. The nanoimprint resist material containing a UV reactive fluorine surfactant was dispensed onto the underlayer-coated substrate. Total volume of nanoimprint resist material was 0.15 mL; (2) The template was pressed onto this nanoimprint resist material. The nanoimprint resist material filled thetemplate. To examine the effect of improving the issue of the

generated resist based defects on thetemplate in the replication of nanoimprint process cycles, the transparent quartz template with a 500 nm contact hole and 2 μm line patterns was prepared. The imprinting force was 17.4 N, and the template was pressed for 2 min; (3) Once the nanoimprint resist material completely filled the template patterns, it was exposed to UV irradiation through the template, activating a UV curing reaction to solidify the molded nanoimprint resist material. The UV irradiation was performed at an energy density of 3.48 J/cm^2; (4) Finally, the template was separated from the polymerized nanoimprint resist material. The cycles were repeated across the wafer, similar to the step-and-repeat lithography processes. The UV curing nanoimprint lithography is repeatable, and the durable template is necessary. This is because the generated resist based defects limit the effectiveness of pattern transfer in nanoimprint process cycles. The template was cleaned before each test of the different nanoimprint resist material, and the optical microscope images on the template were examined every time.

Figure 2. Schematic of process cycles in UV curing nanoimprint lithography: (**1**) deposition of resist droplets; (**2**) spreading of resist by nanoimprinting; (**3**) UV irradiation; and (**4**) template release.
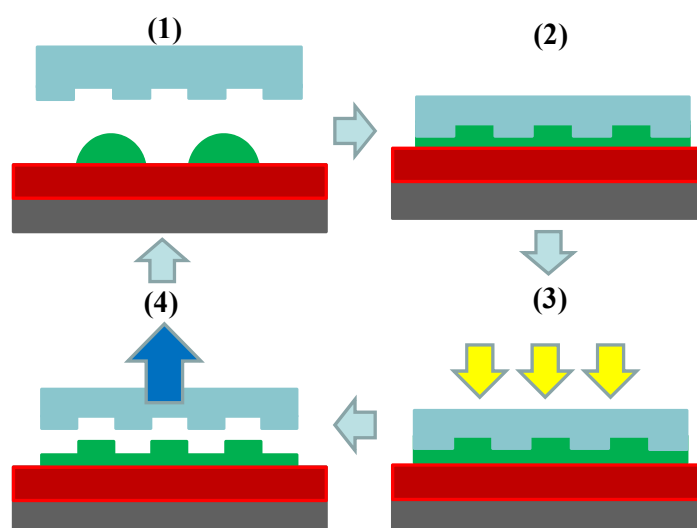
In order to obtain a better understanding of defect reduction on the template in nanoimprint patterning replication, the effect of an ultraviolet reactive fluorine surfactant, reacted with the main components in nanoimprint resist material, was evaluated using the above process cycles of UV curing nanoimprint lithography in this study.

2.2. Nanoimprint Resist Material Containing a UV Reactive Fluorine Surfactant

The properties of nanoimprint resist material include low viscosity, low vapor pressure, high sensitivity in UV irradiation, minimal film volumetric shrinkage during UV curing process, suitable mechanical strength, and suitable thermal stability. The low viscosity of the nanoimprint resist material is necessary to enable the dispense technique and the low pressure capillary fill process in UV curing nanoimprint lithography. The low vapor pressure of the nanoimprint resist material allows a smaller droplet size to be used in the dispense process, which increases the drop pattern resolution and volume

control, and improves the overall process throughput. The high sensitivity to UV irradiation was related to a fast UV curing rate, which enables an ambient temperature imprint process and improves the overall throughput in mass fabrication. The low film volumetric shrinkage of the nanoimprint resist material in the UV curing reaction is necessary to maintain both patterning dimensional accuracy and lithographic resolution in UV curing nanoimprint lithography, in order to prevent pattern distortions and crack formations during the UV curing reactions. The nanoimprint resist material needs to have suitable mechanical strength and thermal stability, to survive the environmental stress during the nanoimprint and etch processes.

The chemical structures of the developed nanoimprint resist material containing a UV reactive fluorine surfactant are shown in Figure 3. Heptadecafluoro-2-hydroxyundecyl acrylate as a UV reactive fluorine surfactant was blended with tricylodecane dimethanol diacrylate as a bulk polymerizable organic monomer, dipentaerythritol polyacrylate-based composition as a UV crosslinker, and 2-hydroxy-2-methyl-1-phenylpropane-1-one as a photoinitiator. The bulk polymerizable organic monomers had low viscosity and can be rapidly polymerized. The UV crosslinker had the suitable mechanical strength and the thermal stability of the polymerized nanoimprint resist. The liquid photoinitiator needed to have a UV curing reaction. The nanoimprint resist materials are often formulated from the above process requirements with additional modifications tailored for the specific application. Table 1 shows the formulation of the prepared nanoimprint resist materials at three different weight ratios of heptadecafluoro-2-hydroxyundecyl acrylate; 9.0 wt% (sample name: TPULR9), 4.5 wt% (TPULR4.5), and 0 wt% (TPULR0). The resulting nanoimprint resist materials were filtered through an ultrahigh-molecular-weight polyethylene membrane filter having an average pore size of 50 nm.

Figure 3. Chemical structures of the nanoimprint resist material containing a UV reactive fluorine surfactant: (**a**) heptadecafluoro-2-hydroxyundecyl acrylate; (**b**) tricylodecane dimethanol diacrylate; (**c**) dipentaerythritol polyacrylate-based composition; and (**d**) 2-hydroxy-2-methyl-1-phenylpropane-1-one.

Table 1. Formulation of the developed nanoimprint resist materials TPULR9, TPULR4.5, and TPULR0.

Resist material	Heptadecafluoro-2-hydroxyundecyl acrylate	Tricylodecane dimethanol diacrylate	Di-pentaerythritol polyacrylate	2-Hydroxy-2-methyl-1-phenyl-propane-1-one
TPULR0	0 wt%	47 wt%	47 wt%	6.0 wt%
TPULR4.5	4.5	45	45	5.5
TPULR9	9	43	43	5

The spin-on underlayer material with terminal methacrylate groups was developed to improve the dirty-template-causing resist pattern peeling and defect on the template due to stronger adhesion between the resist material and the underlayer, compared with that between the template and resist material [3]. The underlayer was then named as TPU-UL.

2.3. Solvent Resistance of Nanoimprint Resist Materials

In order to induce the anti-adhesion of the nanoimprint resist material to the template, the resistances of the above nanoimprint resist materials to the solvents were evaluated. In this procedure, the solutions of the above-mentioned solvent-diluted nanoimprint resist materials TPULR9, TPULR4.5, and TPULR0 were spun onto the prepared underlayer material TPU-UL at 2,500 rpm for 60 s and then UV-polymerized. UV polymerization was carried out by using a metal halide lamp system (Sun Energy, broad band targeted for the 365 nm peak, irradiation intensity: 58 mW/cm^2, irradiation time: 40 s). The thicknesses of TPULR9, TPULR4.5, and TPULR0 were then measured using a thin film measurement system. Ethyl lactate was dispensed on the coated resist materials, and then kept for 120 s, followed by spin drying at 5,000 rpm for 60 s. The thickness of each resist layer was then re-measured. The amount of stripping was determined as the difference between the initial and final thicknesses of the resist layers.

2.4. Surface Free Energy of Nanoimprint Resist Materials

The surface free energy of nanoimprint resist materials is essential to prevent the generated resist based defects on the template when the template is removed from the nanoimprint resist material after pressing the template into the nanoimprint resist material. The surface free energies of TPULR9, TPULR4.5, and TPULR0 were calculated using the reported surface free energy components of water, n-hexadecane, and diiodomethane, together with the experimental contact angles of water, n-hexadecane, and diiodomethane on TPULR9, TPULR4.5, and TPULR0 layers. The following Equations (1), (2), and (3) were used, proposed by Owens [10] who extended the Fowkes concept [11].

$$\gamma_L(1 + \cos\theta) = 2\left(\gamma_S^d \cdot \gamma_L^d\right)^{1/2} + 2\left(\gamma_S^p \cdot \gamma_L^p\right)^{1/2} + 2\left(\gamma_S^h \cdot \gamma_L^h\right)^{1/2} \tag{1}$$

$$\gamma_S = \gamma_S^d + \gamma_S^p + \gamma_S^h \tag{2}$$

$$\gamma_L = \gamma_L^d + \gamma_L^p + \gamma_L^h \tag{3}$$

In the criterion, γ_L is surface free energy, γ_L^d is the dispersive component, γ_L^p is the polar component, and γ_L^h is the hydrogen-bonded component of the liquid solvent. γ_S is surface free energy of the solid nanoimprint resist materials, γ_S^d is the dispersive component, γ_S^p is the polar component, and γ_S^h is the hydrogen-bonded component.

In the contact angle measurement process, which enables the determination of the surface free energy, three types of solvents, water, n-hexadecane, and diiodomethane, were selected, and the surface free energy components were reported as shown in Table 2 [12].

Table 2. Surface free energy components of water, n-hexadecane, and diiodomethane: γ_L surface free energy, γ_L^d dispersive component, γ_L^p polar component, and γ_L^h hydrogen-bonded component.

Liquid	γ_L	γ_L^d	γ_L^p	γ_L^h
Water	72.8	29.1	1.3	42.4
n-Hexadecane	27.6	27.6	0.0	0.0
Diiodomethane	50.8	46.8	4.0	0.0

TPULR9, TPULR4.5, and TPULR0 were spin-coated onto the underlayer material TPU-UL at 2,500 rpm for 60 s and then UV-polymerized. The contact angles of water, n-hexadecane, and diiodomethane on TPULR9, TPULR4.5, and TPULR0 layers were measured using a dynamic contact angle analyzer DropMaster500Z (Kyowa Interface Science) as follows (analysis method: θ/2 method, drop amount: 1.0 μL, measurement time after droping: 1.0 s).

2.5. Film Volumetric Shrinkage During UV Curing Process

Minimal film volumetric shrinkage during the UV curing process is one of the important criteria for developing the nanoimprint resist material. The amount of volumetric shrinkage was determined as the difference between the initial and final thicknesses in the UV curing process. TPULR9, TPULR4.5, and TPULR0 were spun onto the prepared underlayer material TPU-UL at 2,500 rpm for 60 s and then baked on a hotplate at 90 °C for 30 s. The thickness was then measured. UV polymerization was carried out by using a metal halide lamp system (Sun Energy, broad band targeted for the 365 nm peak, irradiation intensity: 58 mW/cm^2, irradiation time: 40 s). The thickness was re-measured after the UV curing process.

3. Results and Discussion

3.1. Solvent Resistance of Nanoimprint Resist Materials

TPULR9, TPULR4.5, and TPULR0 must have the UV polymerizable property and solvent resistance in order to achieve the excellent patterning dimensional accuracy. The evaluation of solvent resistance using ethyl lactate showed no detectable changes in film thickness, indicating that TPULR9, TPULR4.5, and TPULR0 do not significantly interact. It was obvious that TPULR9, TPULR4.5, and TPULR0 were polymerized on the basis of their solvent resistance.

3.2. Effect of Surface Free Energy of Nanoimprint Resist Materials Containing a UV Reactive Fluorine Surfactant on Defect Reduction in Nanoimprint Patterning Replication

Table 3 shows the calculated surface free energy components of TPULR9, TPULR4.5, and TPULR0 with different concentrations of UV reactive fluorine surfactant.

Table 3. Surface free energy components of TPULR9, TPULR4.5, and TPULR0.

Resist material	γ_S	γ_S^d	γ_S^p	γ_S^h
TPULR0	47	27	12	8.1
TPULR4.5	20	16	3.6	0.1
TPULR9	22	21	0.5	0.0
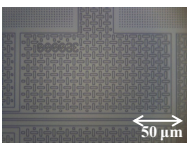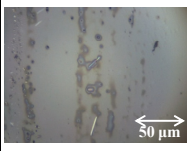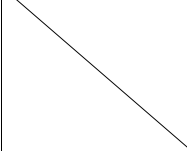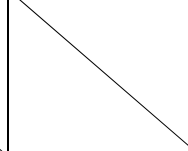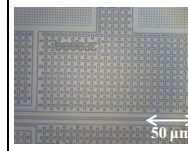
The surface free energy of TPULR9, TPULR4.5, and TPULR0 were determined as 22, 20 and 47, respectively. TPULR4.5 and TPULR9 containing 4,4,5,5,6,6,7,7,8,8,9,9,10,10,11,11,11-heptadecafluoro-2-hydroxyundecyl acrylate showed a better range of surface free energy than TPULR0. This was because the surface free energy in the nanoimprint resist materials was considered to be related to the rounding of sharp corners due to the surface free energy after the template was released from the surface of the nanoimprinted resist material on the template. Therefore, the reduction of the surface free energy in TPULR4.5 and TPULR9 was expected to lead to stronger anti-adhesion. The surface free energy and the components were related to the concentration of 4,4,5,5,6,6,7,7,8,8,9,9,10,10,11,11,11-heptadecafluoro-2-hydroxyundecyl acrylate as shown in Table 1.

The surface free energy and the components decreased generally as the concentration of the prepared UV reactive fluorine surfactant in the resist material increased. In the material combination of the developed resist TPULR4.5 and TPULR9 on underlayer TPU-UL, it was not possible to find the significant difference of surface energy value between 4.5 wt% and 9 wt%, as the concentration of the UV reactive fluorine surfactant increases more than 4.5 wt%. In order to investigate the cause of the observed relationship between surface energy value and materials, the influences such as UV cross-link reaction ratio, the surface energy value of the underlayer, phase separation, and micro-morphology were considered. The optimized concentration was found to be 4.5 wt%, in order to develop the new nanoimprint resist with great repeatability and durability of the nanoimprint processes. Therefore, TPULR4.5 was used in this study being acceptable for the evaluation of repeatability and durability of nanoimprint processes.
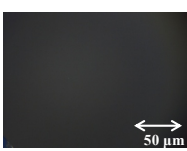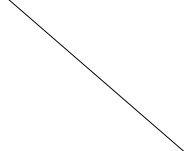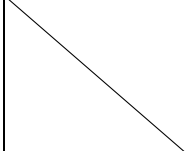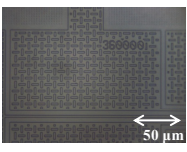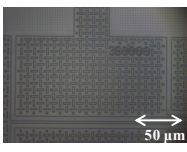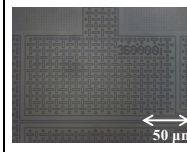
3.3. UV Curing Nanoimprint Lithography

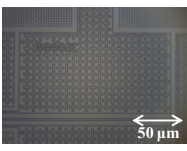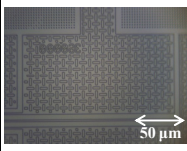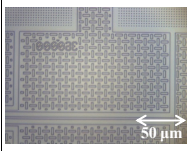The repeatable properties of producing lines and trenches with a 500 nm contact hole and 2 μm line patterns on the surface of TPU-UL were evaluated, to observe the effect of reducing the defect numbers on the template in the replication of nanoimprint process cycles. The same template was used to imprint TPULR4.5 and TPULR0 over 20 times. Figure 4 shows the optical microscope images of the template with a 500 nm contact hole and 2 μm line patterns in TPULR4.5 containing 4,4,5,5,6,6,7,7,8,8,9,9,10,10,11,11,11-heptadecafluoro-2-hydroxyundecyl acrylate as a UV reactive fluorine surfactant and TPULR0.

Figure 4. Optical microscope images of (**a**) template and (**b**) nanoimprint resist material on underlayer with 500 nm contact hole and 2 μm line patterns.

(**a**)

(**b**)

The resist patterns of the referenced TPULR0 without a UV reactive fluorine surfactant were non-imprinted after one imprint and almost part of the resist patterns was observed on the template. The template separation failure was considered to be due to the fact that the adhesion between TPULR0 and template was stronger compared with that between TPULR0 and the underlayer material TPU-UL, in the case of no approach to use a coated fluorinated self assembled monolayer on the surface of template.

On the other hand, no noticeable changes on the template with a non-coated fluorinated self assembled monolayer after 20 nanoimprint process cycles were achieved by using the developed TPULR4.5 on TPU-UL. TPULR4.5 on TPU-UL indicated excellent patterning dimensional accuracy in the replication of 20 nanoimprint process cycles. Anti-adhesion was found between the template and TPULR4.5 containing a UV reactive fluorine surfactant. The nanoimprint lithography over 20 nanoimprint process cycle times can be expected to give good repeatability and durability. The surfactant 4,4,5,5,6,6,7,7,8,8,9,9,10,10,11,11,11-heptadecafluoro-2-hydroxyundecyl acrylate as a template release component included in TPULR4.5 was confirmed to be effective for the reduction of contamination and defect of nanoimprint resist material on the template,and thus as a clean separation technology for mass-production using UV curing nanoimprint lithography. It was also believed that

this approach to use the developed nanoimprint resist materials containing UV reactive fluorine surfactants, produced high fidelity replication by defect reduction, with a single polymeric material as a disposable nanoimprint template instead of quartz or silica templates.

The common surface modification technique in nanoimprint lithography applied a fluorinated self assembled monolayer on the template. The fluorinated self assembled monolayer reacts with the free silanol groups on the surface of the quartz template in a condensation reaction to form a single layer of fluorinated alkyl chains. The treatment using a fluorinated self assembled monolayer is found to degrade after repeated nanoimprints, suggesting a breakdown or erosion of the fluorinated monolayer [13,14]. The used template surface in this study was not treated with a common fluorinated self assembled monolayer. Future study to reduce the defects generated from de-molding is expected; in addition to use of a common fluorinated self assembled monolayer on the template.

3.4. Film Volumetric Shrinkage during UV Curing Process

The experimental film volumetric shrinkages during the UV curing process in TPULR9, TPULR4.5, and TPULR0 were 9.2, 9.0 and 8.9%, respectively. The film volumetric shrinkages of the different nanoimprint resist materials have been investigated in the previous study [13]. The film volumetric shrinkages of mr-UVCur06 (Micro Resist Technology) with a liquid UV curing polymer system of low viscosity and high curing rate as a commercial nanoimprint material, and a second acrylate type resist consisting of n-butyl acrylate (27 wt%), isobornyl acrylate (50 wt%), ethylene glycol diacrylate (20 wt%), and 2-hydroxy-2-methyl-1-phenyl-1-propanone (3 wt%) were 8.3 and 9.0%, respectively.

It was found that TPULR9, TPULR4.5, and TPULR0 had good shrinkage of film thickness, compared with the referenced resist materials. The bulky structure in tricylodecane dimethanol diacrylate was considered to be effective for minimizing film shrinkage.

4. Conclusions

The developed nanoimprint resist material containing a UV reactive fluorine surfactant as a template release component was successfully applied in UV curing nanoimprint lithography. The development of the nanoimprint resist material and the associated lithography enabled the patterning of a 500 nm contact hole and 2 μm lines on the underlayer over 20 nanoimprint process cycles. The optimized formulation and the surface free energy components of the nanoimprint resist material were considered to lead to the high anti-adhesion between template and the nanoimprint resist material. It was also shown that the nanoimprint process cycles could be performed using the same template, without the use of a fluorinated self assembled monolayer on the template as a common surface modification technique.

References

1. Willson, C.G. A decade of step and flash imprint lithography. *J. Photopolym. Sci. Technol.* **2009**, *22*, 147–153.
2. Takei, S. Development of ultraviolet crosslinking glucose-based resist materials for advanced electronic device applications using nanoimprint lithography. *Jpn. J. Appl. Phys.* **2011**, *50*, 01BA02:1–01BA02:4.
3. Takei, S.; Ogawa, T.; Deschner, R.; Hanabata, M.; Willson, C.G. Advanced step and flash nano imprint lithography using ultraviolet sensitive hard mask underlayer material. *Micro Nano Lett.* **2010**, *5*, 117–120.
4. Takei, S. Ultraviolet nano imprint lithography using fluorinated silicon-based resist materials. *Appl. Phys. Express* **2010**, *3*, 025203:1–025203:3.
5. Nagase, K.; Kubo, S.; Nakagawa, M. Resist properties of thin poly(methyl methacrylate) and polystyrene films patterned by thermal nanoimprint lithography for Au electrodeposition. *Jpn. J. Appl. Phys.* **2010**, *49*, 075201:1–075201:5.
6. Youn, S.W.; Hiroshima, H.; Takahashi, M.; Maeda, R. Size dependence of quick cavity filling behavior in ultraviolet nanoimprint lithography using pentafluoropropane gas. *Jpn. J. Appl. Phys.* **2010**, *49*, 06GL06:1–06GL06:4.
7. Okada, M.; Nakayama, T.; Kang, Y.; Haruyama, Y.; Kanda, K.; Matsui, S. Direct patterning on sol–gel low-k porous silica by thermal nanoimprinting. *Jpn. J. Appl. Phys.* **2010**, *49*, 06GL08:1–06GL08:3.
8. Singh, L.; Luo, K.; Ye, Z.; Xu, F. Haase, G.; Curran, D.; LaBrake, D.; Resnick, D.; Sreenivasan, S.V. Defect reduction of high-density full-field patterns in jet and flash imprint lithography. *J. Micro/Nanolithogr. MEMS MOEMS* **2011**, *10*, doi:10.1117/1.3625635.
9. Takei, S.; Ogawa, T.; Willson, C.G. Study of fluorinated silicon-based resist material and photoreactive underlayer for defect reduction in step and flash nanoimprint lithography. *Micro Nano Lett.* **2011**, *6*, 442–424.
10. Owens, D.K.; Wendt, R.C. Estimation of the surface free energy of polymers. *J. Appl. Polym. Sci.* **1969**, *13*, 1741–1747.
11. Fowkes, F.M. Additivity of intermolecular forces at interfaces. I. determination of the contribution to surface and interfacial tensions of dispersion forces in various liquids. *J. Phys. Chem.* **1963**, *67*, 2538–2541.
12. Shouro, D.; Ito, K.; Takata, T. Study on molecular structure in the surface of polyethylene terephthalate fiber for the industrial use. *Sen'i Gakkaishi* **2005**, *61*, 177–182.
13. Takei, S. Step and flash nano imprint lithography of 80 nm dense line pattern using trehalose derivative resist material. *Appl. Phys. Express* **2010**, *3*, 025202:1–025202:3.
14. Wang, Q.; Hiroshima, H. Effects of environmental gas in UV nanoimprint on the characteristics of UV-curable resin. *Jpn. J. Appl. Phys.* **2010**, *49*, 06GL04:1–06GL04:5.

Review

Enhancement of Brillouin Scattering Signal in Perfluorinated Graded-Index Polymer Optical Fibers

Yosuke Mizuno * and Kentaro Nakamura

Precision and Intelligence Laboratory, Tokyo Institute of Technology, 4259 Nagatsuta, Midori-ku, Yokohama 226-8503, Japan; E-Mail: knakamur@sonic.pi.titech.ac.jp

* Author to whom correspondence should be addressed; E-Mail: ymizuno@sonic.pi.titech.ac.jp; Tel.: +81-45-924-5052; Fax: +81-45-924-5091.

Abstract: Perfluorinated graded-index polymer optical fibers (PFGI-POFs), fabricated by replacing the hydrogen atoms of standard polymethyl methacrylate-based POFs with fluorine atoms, have been extensively studied due to their relatively low propagation loss even at telecommunication wavelength. Recently, Brillouin scattering, which is one of the most significant nonlinear effects in optical fibers, has been successfully observed in PFGI-POFs at 1.55-μm wavelength. The Brillouin Stokes signal was, however, not large enough for practical applications or for detailed investigations of the Brillouin properties. In this paper, we review our recent work on Stokes signal enhancement. First, we induce stimulated Brillouin scattering based on the so-called pump-probe technique, and discuss its applicability to temperature sensors. Then, we investigate the influence of the core diameter and length of PFGI-POFs on Stokes signal, and observe the Brillouin linewidth narrowing effect. We believe our work is an important technological step toward the implementation of practical Brillouin-based devices and systems including distributed strain and temperature sensors.

Keywords: Brillouin scattering; Brillouin gain spectrum; perfluorinated graded-index polymer optical fiber; pump-probe technique; fiber-optic sensing; distributed temperature sensing; nonlinear optics

1. Introduction

Polymer optical fibers (POFs) [1,2] have attracted considerable attention for the past several decades due to their extremely easy and cost-effective connection, high safety, and high flexibility [3] compared to conventional glass fibers. Therefore, in spite of their propagation loss being higher than that of silica glass fibers, POFs have been made use of in medium-range communication applications such as home networks and automobiles [4] as well as in high-strain monitoring applications [3,5].

On the other hand, Brillouin scattering in optical fibers [6,7], one of the most significant nonlinear processes, has been extensively studied, and a great number of useful applications have been reported so far, such as optical amplification [7], lasing [7,8], optical comb generation [8], microwave signal processing [9], slow light generation [10], phase conjugation [11], tunable delay [12], optical storage [13], core alignment of butt-coupling [14], and strain/temperature sensing [15–18]. For the purpose of improving the performance of these applications, Brillouin scattering has been investigated not only in silica single-mode fibers (SMFs) but also in some specialty fibers. They include, for example, silica multimode fibers (MMFs) [14], tellurite glass fibers [19,20], chalcogenide glass fibers [21,22], bismuth-oxide glass fibers [23,24], and photonic crystal fibers (PCFs) [25,26].

Recently, we have succeeded in observing spontaneous Brillouin scattering (SpBS) in POFs, for the first time to the best of our knowledge, at the telecommunication wavelength of 1.55 μm [27,28], which will offer many advantages of POFs to the conventional Brillouin application fields. The POFs used in the experiment were cyclic transparent optical polymer (CYTOP)-based perfluorinated graded-index (PFGI-) POFs, which are fabricated by replacing the hydrogen atoms of standard polymethyl methacrylate (PMMA)-based POFs with fluorine atoms. Their detailed structure and fabrication method are well summarized in [29]. Their Brillouin gain coefficient was estimated to be approximately 3.09×10^{-11} m/W, which was almost the same as that of silica SMFs, indicating that Brillouin scattering in PFGI-POFs can be applied to a variety of practical devices and systems in the same way as Brillouin scattering in silica SMFs. We have also investigated the dependences of the Brillouin frequency shift (BFS) on strain and temperature in a PFGI-POF at 1.55 μm, and found that SpBS in PFGI-POFs can be potentially utilized to develop high-accuracy temperature sensors with reduced strain sensitivity [30]. Small Brillouin Stokes signal was, however, a major problem to be solved for practical future applications as well as for detailed investigations of the Brillouin gain spectrum (BGS).

In this review, we summarize two methods to enhance the Brillouin Stokes signal. First, stimulated Brillouin scattering (SBS) is induced using the so-called pump-probe technique [31], and its applicability to temperature sensors is discussed. Second, the influence of the core diameter and length of the PFGI-POFs is investigated [32], which will be a good guideline for designing PFGI-POF structures suitable for future applications.

2. Brillouin Scattering in Optical Fibers

When a light beam is injected into a fiber under test (FUT), it interacts with acoustic phonons, generating backscattered light called Stokes light. This phenomenon is called SpBS. Since the phonons decay exponentially, the backscattered Brillouin light spectrum, known as BGS, takes the shape of

Lorentzian function with the bandwidth of several tens of MHz. If the power of the pump light is higher than the Brillouin threshold power P_{th}, the Stokes light caused by SpBS acts as a seed of stimulated scattering, and there occurs a transition from SpBS to SBS. As a result, the power of the Stokes light is drastically enhanced. P_{th} is given as [7]

$$P_{th} = \frac{21\, b\, A_{eff}}{K\, g_B\, L_{eff}}$$

(1)

where b is the correction factor for multimode fibers [33], which can be treated as 2 when the numerical aperture (NA) is ~0.2; A_{eff} is the effective cross-sectional area, which is approximately in proportion to the core diameter for multimode fibers [34,35]; K is the polarization coefficient, which is 1, if polarization is maintained and 0.667 otherwise; g_B is the Brillouin gain coefficient; and L_{eff} is the effective fiber length defined as

$$L_{eff} = \left[1 - \exp\left(-\alpha L\right)\right] \big/ \alpha$$

(2)

where α is the propagation loss and L is the fiber length.

Both in SpBS and in SBS, the frequency where the peak power is obtained in the BGS is downshifted by several GHz from the incident light frequency, and the amount of this frequency shift is called BFS. In optical fibers, the BFS v_B is given by [7]

$$v_B = \frac{2n\, v_A}{\lambda_p}$$

(3)

where n is the refractive index, v_A is the acoustic velocity in the fiber, λ_p is the wavelength of the incident pump light. If tensile strain is applied or temperature is changed in a standard silica SMF, the BFS moves to higher frequency in proportion to the applied strain (+580 MHz/%) [36] and the temperature change (+1.18 MHz/K) [37]. In some specialty fibers, such as tellurite glass fibers, it is known that the BFS moves to lower frequency with increasing applied strain (−230 MHz/%) [20] and temperature (−1.14 MHz/K) [24]. In both cases, we can derive the strain amplitude and temperature change by measuring the BFS in the fiber.

3. Spontaneous Brillouin Scattering in PFGI-POFs

A standard POF composed of PMMA [1,2] is optimally designed for light transmission at 650 nm, with propagation loss of ~200 dB/km. Its loss at telecommunication wavelength is, however, so high ($\gg 1 \times 10^5$ dB/km) that the Brillouin signal cannot be detected. In the meantime, in order to observe Brillouin scattering in a PMMA-based POF at 650 nm, we are required to prepare all the necessary optical devices at this wavelength, which are not easy from the viewpoint of availability and cost. Therefore, instead of PMMA-based POFs, we used PFGI-POFs with lower loss (~250 dB/km) even at 1.55 μm, which is the optimal wavelength for long distance data transmission in silica optical fibers.

Up to now, the spontaneous Brillouin scattering properties in a PFGI-POF with 120-μm core diameter have been investigated at 1.55 μm [27]. The BFS and the Brillouin linewidth were 2.83 GHz and 105 MHz, respectively. Using these values, the Brillouin gain coefficient was calculated to be 3.09×10^{-11} m/W, which is almost the same as that of standard silica SMFs and higher than that of silica

GI-MMFs. Here, we should bear in mind that the actual Brillouin gain coefficient may be higher than this value due to the multimode nature of the PFGI-POF. The Brillouin threshold power of a 100-m PFGI-POF was estimated to be as high as 24 W, and the Stokes signal was not sufficiently large to be applied to practical devices and systems.

The BFS dependences on strain and temperature in a 5-m PFGI-POF have also been investigated at 1.55 μm [30]. They showed negative dependences with coefficients of −121.8 MHz/% and −4.09 MHz/K, respectively, which are −0.2 and −3.5 times as large as those in silica fibers. These BFS dependences were found to originate from the dependences of the Young's modulus on strain and temperature. Thus, Brillouin scattering in PFGI-POFs has a big potential for high-accuracy temperature sensing with reduced strain sensitivity.

4. Enhancement of Brillouin Stokes Signal (I): Induction of Stimulated Scattering

In this Section, we describe the observation of SBS in a PFGI-POF with 120-μm core diameter at 1.55 μm with pump-probe technique [31]. The BGS is detected with extremely high S/N ratio, even with a 1-m PFGI-POF, scrambled polarization state, and no averaging. We also investigate the BGS dependences on probe power and temperature, and confirm that SBS in a PFGI-POF measured with this technique can be utilized to develop high-accuracy temperature sensors as well.

4.1. Motivation and Principle

The Brillouin scattering in PFGI-POFs observed in the previous experimental setup [27,28] was not stimulated but spontaneous, because the Brillouin threshold of PFGI-POFs was estimated to be as high as 24 W, as already described in Section 3. Consequently, the power of the reflected Stokes light was so low that we had to face the following four problems: (1) a PFGI-POF longer than several meters was required, (2) the polarization state had to be optimized, (3) averaging of the spectral data had to be conducted several tens of times, and (4) signal-to-noise (S/N) ratio of the BGS was quite low, even when (1), (2), and (3) were cleared. In order to implement practical Brillouin sensors and other systems using PFGI-POFs, these problems need to be resolved.

One solution is to employ so-called pump-probe technique. As described in Section 2, when the pump power is higher than the Brillouin threshold, a transition from SpBS to SBS occurs, leading to drastic enhancement of the Stokes light. On the other hand, when probe light at the same frequency as the Stokes light is also injected into the other end of the FUT, SBS is induced even when the power of the pump light is much lower than the Brillouin threshold, because the probe light itself acts as a seed of stimulated scattering [38]. This technique, called pump-probe technique, has been used to develop Brillouin systems with high S/N ratio [17].

4.2. Experimental Setup

The FUT used in the experiment was a 1-m PFGI-POF (Asahi Glass Co., Ltd., 2009) with a core diameter of 120 μm, NA of 0.185, a core refractive index of ~1.35, and propagation loss of ~250 dB/km at 1.55 μm (manufacturer's specifications). The experimental setup is schematically shown in Figure 1, which is similar to that of Brillouin optical correlation-domain analysis (BOCDA) [16,17].

The light beam from a 1550-nm three-electrode laser diode (LD) was divided into two. One was used as the pump light, after being chopped with an intensity modulator (IM) for lock-in detection and being amplified with an erbium-doped fiber amplifier (EDFA). The other was used as the probe light, after passing two EDFAs, a single-sideband modulator (SSBM), and a polarization scrambler (PSCR). The SSBM was employed with a microwave generator (MG) and a proper DC bias control to suppress the carrier (pump) and the anti-Stokes component of the two first-order sidebands and to maintain a stable frequency downshift from the pump light. This frequency downshift was swept from 2.5 GHz to 3.5 GHz with a period of 300 ms to obtain the BGS of the PFGI-POF, which is observed approximately at 2.8 GHz. The suppression ratio of the other frequency components was kept higher than 25 dB, as shown in Figure 2.

Figure 1. Experimental setup for observing stimulated Brillouin scattering (SBS) in perfluorinated graded-index polymer optical fibers (PFGI-POFs) with pump-probe technique: LD, laser diode; EDFA, erbium-doped fiber amplifier; FG, function generator; FUT, fiber under test; IM, intensity modulator; ISO, isolator; LI-A, lock-in amplifier; MG, microwave generator; OSC, oscilloscope; PD, photo-detector; POF, polymer optical fiber; PSCR: polarization scrambler; SSBM, single-sideband modulator; VOA, variable optical attenuator.
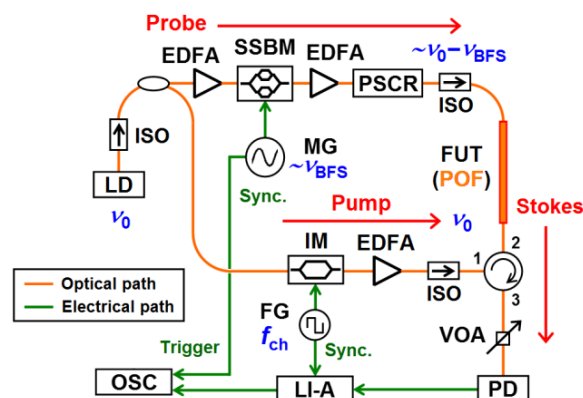
Figure 2. Measured optical spectrum of the SSBM output when the frequency of the MG was set to 2.83 GHz.
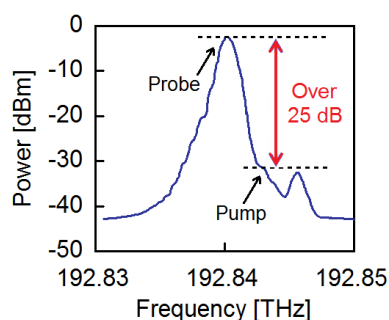
The PSCR, which can modulate the polarization state at 1 MHz, was inserted to suppress the polarization-dependent fluctuations of the signal. The PFGI-POF and the silica SMFs were butt-coupled [27] with the gaps filled with index matching oil ($n = 1.46$) to minimize the Fresnel reflection. The Stokes

light was adjusted in power with a variable optical attenuator (VOA), and converted to an electrical signal with a 125-MHz photo-detector (PD). After passing a lock-in amplifier (LI-A) with a chopping frequency of 5.018 MHz and a time constant of 10 ms, the electrical signal was observed as a BGS with an oscilloscope (OSC) synchronized with the frequency sweep of the SSBM.

4.3. Experimental Results

Figure 3 shows the measured BGS without averaging when the pump power and the probe power were 23 dBm and 22 dBm, respectively. The power was normalized so that the peak power was 1.0. Although the PFGI-POF length was only 1 m and the polarization state was scrambled, the BGS was observed with much higher S/N ratio than that previously reported [30]. The BFS was 2.86 GHz, which is slightly higher than the previously reported value of 2.83 GHz [27]. This discrepancy seems to originate from the difference in temperature and the time constant of the LI-A which is not short enough. The 3-dB bandwidth of the BGS measured in this experiment was about 160 MHz, but further research is needed on the bandwidth because it is also dependent on the time constant of the LI-A (Note that, when the time constant was shorter than 10 ms, the BGS was distorted).

Figure 3. BGS in PFGI-POF observed without averaging.
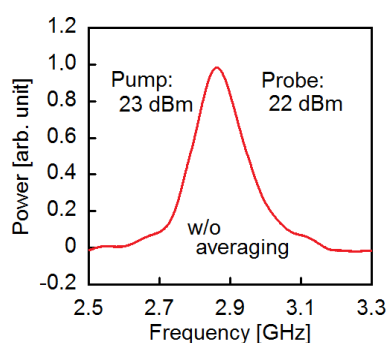
Figure 4 shows the dependence of the BGS on probe power when the pump power was fixed at 23 dBm. The probe power was reduced from 22 dBm down to 6 dBm, and averaging was conducted 30 times for the observable readout when the Stokes power was very low. As the probe power decreased, the Stokes power also decreased, which proves that this BGS is caused by the interaction between the pump light and the probe light, *i.e.*, SBS.

Figure 4. Dependence of BGS on probe power in PFGI-POF.
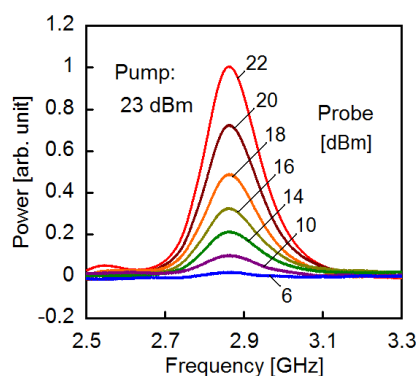
The dependence of the BGS on temperature was also measured as shown in Figure 5(a). The pump power and the probe power were 23 dBm and 22 dBm, respectively, and averaging was conducted 30 times. The temperature was set to 20, 40, and 60 ℃. With the increasing temperature, the BGS shifted toward lower frequency. The temperature dependence of the BFS is shown in Figure 5(b). The slope of −4.05 MHz/K is in good agreement with the previous report [30], which confirms that the BGS in a PFGI-POF observed with the pump-probe technique can be applied to high-accuracy temperature sensing.

Figure 5. Dependence of (**a**) BGS and (**b**) BFS on temperature in PFGI-POF.

(**a**)   (**b**)
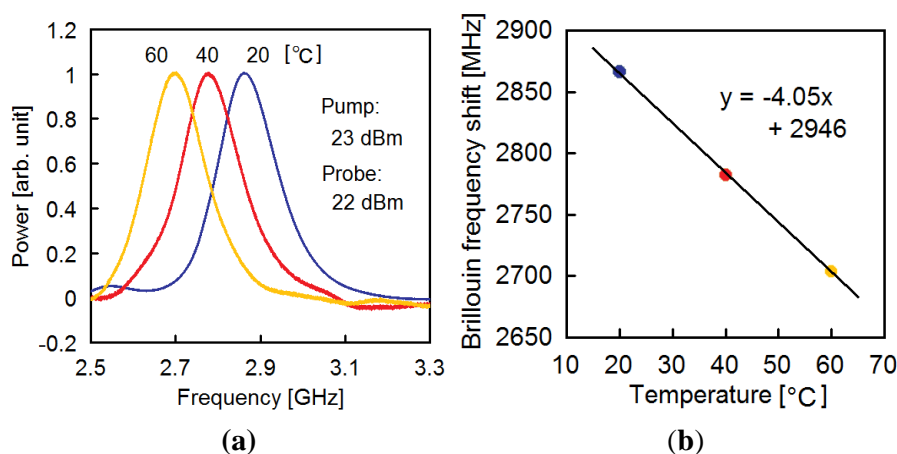
4.4. Summary

The SBS in a PFGI-POF was successfully observed at 1.55 μm with pump-probe technique. We detected the BGS with extremely high S/N ratio, even with a 1-m PFGI-POF, scrambled polarization state, and no averaging. We also investigated the BGS dependence on probe power, which proved that the measured BGS was caused not by SpBS but by SBS. Besides, we measured the BGS dependence on temperature, showing that BGS in a PFGI-POF observed with this technique can be applied to temperature sensing with high accuracy. We are sure that use of SBS with large Stokes signal will be indispensable in developing Brillouin-based distributed temperature/strain sensing systems using PFGI-POFs.

5. Enhancement of Brillouin Stokes Signal (II): Influence of Core Diameter and Fiber Length

In this Section, we describe the characterization on the BGS in PFGI-POFs with 62.5-μm core diameter [32]. First, using 5-m PFGI-POFs, we show that extremely high Stokes power can be obtained compared to that of a PFGI-POF with 120-μm core, and estimate the Brillouin threshold power to be 53.3 W. Then, we experimentally show that using a PFGI-POF longer than ~50 m is not an effective way to enhance the Stokes signal. We also theoretically predict that it is difficult to decrease the Brillouin threshold power of PFGI-POFs at 1.55-μm wavelength down to that of km-order-long silica SMFs even when their core diameter is sufficiently reduced to satisfy the single-mode condition. Finally, we investigate the Brillouin linewidth as a function of pump power, and confirm the linewidth narrowing effect.

5.1. Motivation

As described in Section 3, the power of the SpBS Stokes light generated in the PFGI-POFs with 120-μm core diameter was quite low, and it needs to be enhanced for detailed investigations of the BGS [39] including the linewidth narrowing effect. Since the BGS observed with the pump-probe technique described in Section 4 is easily influenced by the time constant of lock-in detection, detailed evaluation of its linewidth was not feasible. Another approach to enhance the Stokes signal is to make use of PFGI-POFs with core diameters smaller than 120 μm. Although PFGI-POFs with 62.5-μm core diameter have become commercially available very recently (Sekisui Chemical Co., Ltd., 2011), no study has been reported on their Brillouin scattering properties. Therefore, in this Section, we characterize the BGS in PFGI-POFs with 62.5-μm core diameter.

5.2. Experimental Setup

Irrespective of the length and the core diameter, PFGI-POFs used in the experiment had NA of 0.185, a core refractive index of ~1.35, and propagation loss of ~250 dB/km at 1.55 μm. The experimental setup was basically the same as that previously reported in [27], where the BGS can be observed with high resolution by heterodyne detection. A distributed-feedback laser diode (DFB-LD) at 1,547 nm was used as a light source. One end of the PFGI-POF to be measured was optically butt-coupled to the silica SMF, and the other end was kept open.

5.3. Effects of Small Core Diameters

Figure 6 shows the measured BGS of a 5-m PFGI-POF with 62.5-μm core at pump power P_{in} of 5, 10, 15, and 20 dBm. The polarization state optimized for P_{in} of 20 dBm was employed for all the measurements. The center frequency of the BGS, *i.e.*, the BFS, was approximately 2.81 GHz, which is slightly lower than previously-reported value of 2.83 GHz [27] due to the difference in room temperature [30]. Even when P_{in} was as low as 5 dBm, small but clear BGS was observed.

Figure 6. BGS dependence on pump power P_{in}.
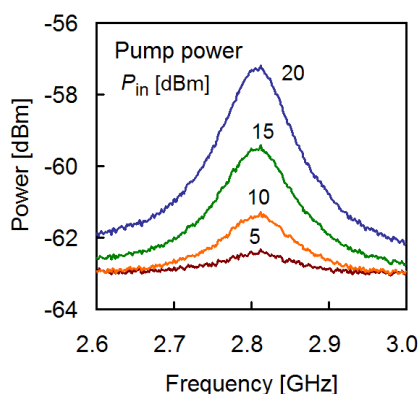
Figure 7 shows the P_{in} dependences of the relative Stokes power, when 5-m PFGI-POFs with core diameters of 62.5 μm and 120 μm (Asahi Glass Co., Ltd., 2009) were employed. The reference power was set to about −63 dBm, which is the Stokes power when P_{in} is sufficiently low. The dependence

curve of the PFGI-POF with 62.5-μm core was about 10 dB lower in pump power than that with 120-μm core, which indicates that, even at the same pump power, we can largely enhance the Stokes signal by using a PFGI-POF with a smaller core diameter.

Figure 7. Relative Stokes power as a function of pump power; comparison between PFGI-POFs with 62.5-μm and 120-μm core diameters.
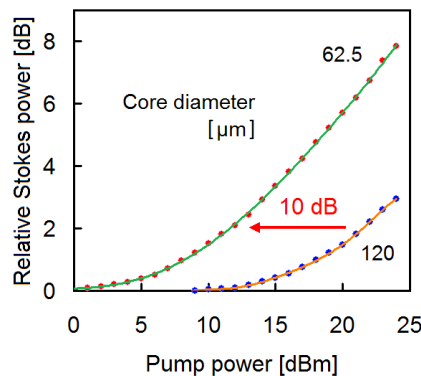
One of the reasons for the 10-dB curve shift is the difference in Brillouin threshold power P_{th}. By substituting into Equations (1) and (2) the values of $b = 2$ [33], $K = 0.667$ [7], $g_B = 3.09 \times 10^{-11}$ m/W [27], $\alpha = 0.056$ /m (= 250 dB/km), and $L = 5$ m, P_{th} of the PFGI-POF with 120-μm core ($A_{eff} = 209$ μm^2 [40]) was calculated to be 97.7 W. On the other hand, P_{th} of the PFGI-POF with 62.5-μm core ($A_{eff} = 108.9$ μm^2) was calculated to be 53.3 W, which is lower than 97.7 W by 2.63 dB. Thus, the curve shift observed in Figure 7 can be partially explained by the difference in P_{th}, but its amount of 10 dB is much larger than the calculated value.

Another reason for the curve shift is the improvement of optical coupling efficiency at the butt coupling when the Stokes light generated in the PFGI-POF propagates back and is injected into the SMF. Although, due to the unstable core alignment and the rough surface of the PFGI-POF, it is difficult to measure the coupling loss accurately, we confirmed that the loss with the PFGI-POF with 62.5-μm core was several dB lower than that with 120-μm core. This fact, along with the difference in internal structure designed by different manufacturers, moderately explains the 10-dB curve shift.

5.4. Effects of Long Fiber Length

According to Equations (1) and (2), to employ long PFGI-POFs is another way to reduce P_{th} and to enhance the Stokes signal. Figure 8 shows the measured BGS of 80-m and 200-m PFGI-POFs with 62.5-μm core at P_{in} of 5, 10, 15, and 20 dBm. Much larger Stokes signals (~7 dB higher at P_{in} of 20 dBm) than those of the 5-m PFGI-POF shown in Figure 6 were observed.

There was, however, almost no difference between the BGS of the 80-m PFGI-POF and that of the 200-m PFGI-POF, only with a slight discrepancy of the BFS caused by the room-temperature difference. This means that the incident light is considerably attenuated after propagation for 80 m in the PFGI-POF. In order to estimate this effect quantitatively, the effective PFGI-POF length L_{eff} was plotted as a function of actual length L as shown in Figure 9, where L_{eff} gradually approaches 18 m

(P_{th} ~ 13 W) with the increasing L. Thus, we proved that employing a PFGI-POF longer than ~50 m is not an effective way to enhance the Stokes signal at 1.55 μm.

Figure 8. BGS dependence on pump power P_{in}; comparison between 80-m PFGI-POF (solid line) and 200-m PFGI-POF (dotted line).
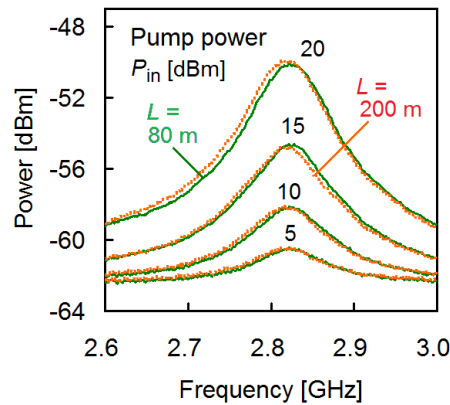
Figure 9. Calculated effective fiber length *vs.* fiber length.
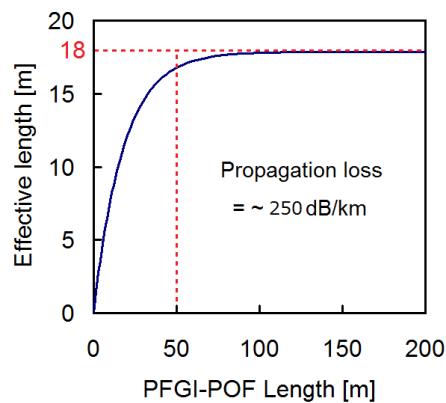
According to Equations (1) and (2), as the core diameter decreases, the Brillouin threshold P_{th} also becomes lower. When P_{in} is higher than P_{th}, SBS is induced and consequently the Stokes signal is exponentially enhanced [7]. Here, under the rough assumption that the multimode nature, NA, refractive index, and loss do not change with core diameters, we calculated P_{th} of a 50-m PFGI-POF with 10-μm core diameter (hypothetical; A_{eff} = 17.4 μm^2) to be 2.22 W (= 33.5 dBm). This value is more than one order magnitude higher than the pump power of several tens to hundreds of mW commonly used in BGS characterization in silica SMFs [39]. Even when the PFGI-POF is treated as an SMF (*i.e.*, b = 1 [7] but A_{eff} becomes larger [35] in Equation (1)), this difference cannot be compensated. Thus, it seems to be difficult to reduce P_{th} of PFGI-POFs down to the same level of that of long silica SMFs by decreasing the core diameter, which is due to the limited effective length of 18 m associated with the high propagation loss at 1.55 μm.

5.5. Brillouin Linewidth Narrowing Effect

Although the Brillouin linewidth of a PFGI-POF has been reported to be 105 MHz at P_{in} of 20 dBm in [27], detailed investigations were difficult because the Stokes power was extremely low. Here, by making use of the enhanced Stokes power, we investigated the Brillouin linewidth dependence on P_{in}.

Figure 10(a) shows the measured BGS of the 200-m PFGI-POF with 62.5-μm core at P_{in} of 14.5, 17.5, and 23.5 dBm, where the Stokes power is normalized so that the maximum power is 0 dB. Figure 10(b) shows the Brillouin linewidth dependence on P_{in}. From these figures, we can see that, with the increasing P_{in}, the 3-dB linewidth of the BGS decreases, but that its slope gradually becomes small. This behavior agrees well with the experiment and theory of the linewidth narrowing effect in silica-based SMFs [39].

Figure 10. (**a**) Normalized BGS at pump power of 14.5, 17.5, and 23.5 dBm. (**b**) Brillouin linewidth *vs.* pump power.
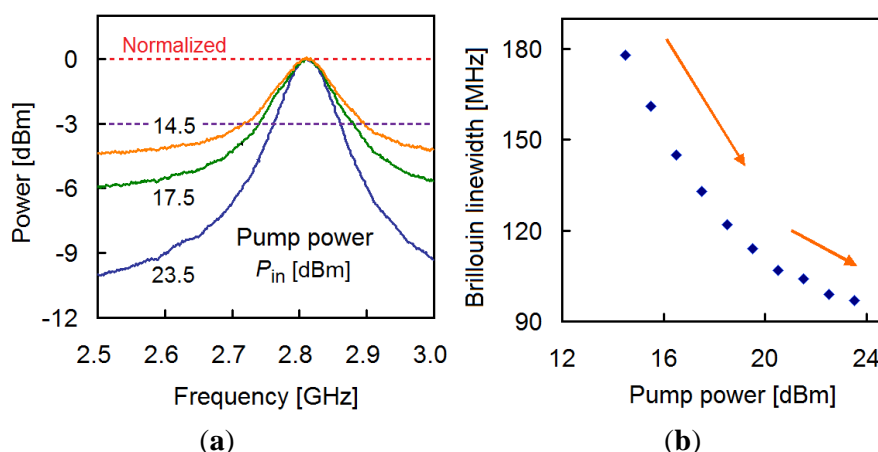
5.6. Summary

The BGS properties of PFGI-POFs with 62.5-μm core diameter were investigated. The Stokes power was extremely high compared to that of a PFGI-POF with 120-μm core, and the Brillouin threshold power for 5-m PFGI-POF was estimated to be 53.3 W. It was also shown that employing a PFGI-POF longer than ~50 m is not an effective way to enhance the Stokes signal. In addition, it was theoretically found that it is difficult to reduce the Brillouin threshold power of PFGI-POFs at 1.55-μm wavelength below that of long silica SMFs even if their core diameter is sufficiently decreased to satisfy the single-mode condition. Finally, the Brillouin linewidth narrowing effect was confirmed. These results will be a good guideline for developing practical Brillouin systems using PFGI-POFs as well as for designing new PFGI-POF structures for Brillouin applications in future.

6. Conclusions

We reviewed two methods of enhancing the Brillouin Stokes signal in PFGI-POFs for future practical applications as well as for detailed investigations of the BGS.

In the first half of this paper, using an experimental setup similar to BOCDA system [16,17] based on the pump-probe technique, SBS in a PFGI-POF with 120-μm core diameter was, for the first time, observed at 1.55 μm. The BGS was detected with extremely high S/N ratio, even with a 1-m PFGI-POF, scrambled polarization state, and no averaging. We also investigated the BGS dependences on probe power and temperature, and confirmed that SBS in a PFGI-POF measured with this technique can also be utilized to develop high-accuracy temperature sensors.

In the latter half, the influence of the core diameter and fiber length on the Stokes signal was investigated by use of PFGI-POFs with 62.5-μm core diameter. First, using 5-m PFGI-POFs, we showed that extremely high Stokes power can be obtained compared to that of a PFGI-POF with 120-μm core, and estimated the Brillouin threshold power to be 53.3 W. Then, we experimentally showed that using a PFGI-POF longer than ~50 m is not an effective way to enhance the Stokes signal. We also theoretically predicted that it is difficult to decrease the Brillouin threshold power of PFGI-POFs at 1.55-μm wavelength down to that of km-order-long silica SMFs even when their core diameter is sufficiently reduced to satisfy the single-mode condition. Finally, we investigated the Brillouin linewidth as a function of pump power, and confirmed the linewidth narrowing effect.

Thus, the Brillouin Stokes signal has been drastically enhanced. It is also natural to predict that the Stokes signal will be further enhanced if we induce SBS by pump-probe technique using PFGI-POFs with 62.5-μm core diameter or less. Therefore, we are sure that the first demonstration of distributed temperature sensing based on Brillouin scattering in PFGI-POFs will be possibly carried out in the near future, based on optical correlation-, time-, or frequency-domain technology. We believe our work to be a significant technological step toward the implementation of such sensing systems and other POF-Brillouin devices.

Acknowledgements

References

1. Kuzyk, M.G. *Polymer Fiber Optics: Materials, Physics, and Applications*, 1st ed.; CRC Press: Boca Raton, FL, USA, 2006.
2. Koike, Y.; Ishigure, T.; Nihei, E. High-bandwidth graded-index polymer optical fiber. *J. Lightwave Technol.* **1995**, *13*, 1475-1489.
3. Husdi, I.R.; Nakamura, K.; Ueha, S. Sensing characteristics of plastic optical fibres measured by optical time-domain reflectometry. *Meas. Sci. Technol.* **2004**, *15*, 1553-1559.
4. Mollers, I.; Jager, D.; Gaudino, R.; Nocivelli, A.; Kragl, H.; Ziemann, O.; Weber, N.; Koonen, T.; Lezzi, C.; Bluschke, A.; *et al.* Plastic optical fiber technology for reliable home networking—Overview and results of the EU project POF-ALL. *IEEE Commun. Mag.* **2009**, *47*, 58-68.

5. Liehr, S.; Lenke, P.; Wendt, M.; Krebber, K.; Seeger, M.; Thiele, E.; Metschies, H.; Gebreselassie, B.; Munich, J.C. Polymer optical fiber sensors for distributed strain measurement and application in structural health monitoring. *IEEE Sens. J.* **2009**, *9*, 1330-1338.

6. Ippen, E.P.; Stolen, R.H. Stimulated Brillouin scattering in optical fibers. *Appl. Phys. Lett.* **1972**, *21*, 539-541.

7. Agrawal, G.P. *Nonlinear Fiber Optics*, 4th ed.; Academic Press: San Diego, CA, USA, 1995; pp. 329-367.

8. Cowle, G.J.; Yu, D.; Chieng, Y.T. Brillouin/erbium fiber lasers. *J. Lightwave Technol.* **1997**, *15*, 1198-1204.

9. Norcia, S.; Tonda-Goldstein, S.; Dolfi, D.; Huignard, J.P. Efficient single-mode Brillouin fiber laser for low-noise optical carrier reduction of microwave signals. *Opt. Lett.* **2003**, *28*, 1888-1890.

10. Song, K.Y.; Herraez, M.G.; Thevenaz, L. Observation of pulse delaying and advancement in optical fibers using stimulated Brillouin scattering. *Opt. Express* **2005**, *13*, 82-88.

11. Kuzin, E.A.; Petrov, M.P.; Davydenko, B.E. Phase conjugation in an optical fibre. *Opt. Quantum Electon.* **1985**, *17*, 393-397.

12. Zou, W.; He, Z.; Hotate, K. Tunable fiber-optic delay line based on stimulated Brillouin scattering. *Appl. Phys. Express* **2010**, *3*, doi:10.1143/APEX.3.012501.

13. Zhu, Z.; Gauthier, D.J.; Boyd, R.W. Stored light in an optical fiber via stimulated Brillouin scattering. *Science* **2007**, *318*, 1748-1750.

14. Mizuno, Y.; Nakamura, K. Core alignment of butt-coupling between single-mode and multi-mode optical fibers by monitoring Brillouin scattering signal. *J. Lightwave Technol.* **2011**, *29*, 2616-2620.

15. Horiguchi, T.; Tateda, M. BOTDA—Nondestructive measurement of single-mode optical fiber attenuation characteristics using Brillouin interaction: Theory. *J. Lightwave Technol.* **1989**, *7*, 1170-1176.

16. Hotate, K.; Hasegawa, T. Measurement of Brillouin gain spectrum distribution along an optical fiber using a correlation-based technique—Proposal, experiment and simulation. *IEICE Trans. Electron.* **2000**, *E83-C*, 405-412.

17. Song, K.Y.; Hotate, K. Enlargement of measurement range in a Brillouin optical correlation domain analysis system using double lock-in amplifiers and a single-sideband modulator. *IEEE Photon. Technol. Lett.* **2006**, *18*, 499-501.

18. Mizuno, Y.; Zou, W.; He, Z.; Hotate, K. Proposal of Brillouin optical correlation-domain reflectometry (BOCDR). *Opt. Express* **2008**, *16*, 12148-12153.

19. Abedin, K.S. Stimulated Brillouin scattering in single-mode tellurite glass fiber. *Opt. Express* **2006**, *14*, 11766-11772.

20. Mizuno, Y.; He, Z.; Hotate, K. Distributed strain measurement using a tellurite glass fiber with Brillouin optical correlation-domain reflectometry. *Opt. Commun.* **2010**, *283*, 2438-2441.

21. Abedin, K.S. Observation of strong stimulated Brillouin scattering in single-mode As_2Se_3 chalcogenide fiber. *Opt. Express* **2005**, *13*, 10266-10271.

22. Song, K.Y.; Abedin, K.S.; Hotate, K.; Herraez, M.G.; Thevenaz, L. Highly efficient Brillouin slow and fast light using As_2Se_3 chalcogenide fiber. *Opt. Express* **2006**, *14*, 5860-5865.

23. Lee, J.H.; Tanemura, T.; Kikuchi, K.; Nagashima, T.; Hasegawa, T.; Ohara, S.; Sugimoto, N. Experimental comparison of a Kerr nonlinearity figure of merit including the stimulated Brillouin scattering threshold for state-of-the-art nonlinear optical fibers. *Opt. Lett.* **2005**, *30*, 1698-1700.

24. Mizuno, Y.; He, Z.; Hotate, K. Dependence of the Brillouin frequency shift on temperature in a tellurite glass fiber and a bismuth-oxide highly-nonlinear fiber. *Appl. Phys. Express* **2009**, *2*, 112402:1-112402:3.

25. Lee, J.H.; Yusoff, Z.; Belardi, W.; Ibsen, M.; Monro, T.M.; Richardson, D.J. Investigation of Brillouin effects in small-core holey optical fiber: Lasing and scattering. *Opt. Lett.* **2002**, *27*, 927-929.

26. Beugnot, J.C.; Sylvestre, T.; Alasia, D.; Maillotte, H.; Laude, V.; Monteville, A.; Provino, L.; Traynor, N.; Mafang, S.F.; Thevenaz, L. Complete experimental characterization of stimulated Brillouin scattering in photonic crystal fiber. *Opt. Express* **2007**, *15*, 15517-15522.

27. Mizuno, Y.; Nakamura, K. Experimental study of Brillouin scattering in perfluorinated polymer optical fiber at telecommunication wavelength. *Appl. Phys. Lett.* **2010**, *97*, doi:10.1063/1.3463038.

28. Mizuno, Y.; Nakamura, K. Brillouin scattering in polymer optical fibers: Fundamental properties and potential use in sensors. *Polymers* **2011**, *3*, 886-898.

29. Lethien, C.; Loyez, C.; Vilcot, J.-P.; Rolland, N.; Rolland, P.A. Exploit the bandwidth capacities of the perfluorinated graded index polymer optical fiber for multi-services distribution. *Polymers* **2011**, *3*, 1006-1028.

30. Mizuno, Y.; Nakamura, K. Potential of Brillouin scattering in polymer optical fiber for strain-insensitive high-accuracy temperature sensing. *Opt. Lett.* **2010**, *35*, 3985-3987.

31. Mizuno, Y.; Kishi, M.; Hotate, K.; Ishigure, T.; Nakamura, K. Observation of stimulated Brillouin scattering in polymer optical fiber with pump-probe technique. *Opt. Lett.* **2011**, *36*, 2378-2380.

32. Mizuno, Y.; Ishigure, T.; Nakamura, K. Brillouin gain spectrum characterization in perfluorinated graded-index polymer optical fiber with 62.5-μm core diameter. *IEEE Photon. Technol. Lett.* **2011**, *23*, 1863-1865.

33. Tei, K.; Tsuruoka, Y.; Uchiyama, T.; Fujioka, T. Critical power of stimulated Brillouin scattering in multimode optical fibers. *Jpn. J. Appl. Phys.* **2001**, *40*, 3191-3194.

34. Marcuse, D. Loss analysis of single-mode fiber splices. *Bell Sys. Tech. J.* **1977**, *56*, 703–718.

35. Mocofanescu, A.; Wang, L.; Jain, R.; Shaw, K.D.; Gavrielides, A.; Peterson, P.; Sharma, M.P. SBS threshold for single mode and multimode GRIN fibers in an all fiber configuration. *Opt. Express* **2005**, *13*, 2019-2024.

36. Horiguchi, T.; Kurashima, T.; Tateda, M. Tensile strain dependence of Brillouin frequency shift in silica optical fibers. *IEEE Photon. Technol. Lett.* **1989**, *1*, 107-109.

37. Kurashima, T.; Horiguchi, T.; Tateda, M. Thermal effects on the Brillouin frequency shift in jacketed optical silica fibers. *Appl. Opt.* **1990**, *29*, 2219-2222.

38. Shibata, N.; Azuma, Y.; Horiguchi, T.; Tateda, M. Identification of longitudinal acoustic mode guided in the core region of a single-mode optical fiber by Brillouin gain spectra measurements. *Opt. Lett.* **1988**, *13*, 595-597.

39. Yeniay, A.; Delavaux, J.M.; Toulouse, J. Spontaneous and stimulated Brillouin scattering gain spectra in optical fibers. *J. Lightwave Technol.* **2002**, *20*, 1425-1432.

Appl. Sci. **2012**, *2*

40. Dossou, M.; Szriftgiser, P.; Goffin, A. Theoretical study of stimulated Brillouin scattering (SBS) in polymer optical fibres. In *13th Annual Symposium IEEE/LEOS Benelux Chapter*, Enschede, The Netherlands, 2008; volume 13, 175-178.

Article

Novel Fluorinated Indanone, Tetralone and Naphthone Derivatives: Synthesis and Unique Structural Features

Joseph C. Sloop [1,]*****, **Paul D. Boyle** [2], **Augustus W. Fountain** [3], **Cristina Gomez** [4], **James L. Jackson** [5], **William F. Pearman** [4], **Robert D. Schmidt** [2] **and Jonathan Weyand** [4]

[1] School of Science and Technology, Georgia Gwinnett College, 1000 University Center Lane, Lawrenceville, GA 30043, USA

[2] Department of Chemistry, North Carolina State University, P.O. Box 8204, Raleigh, NC 27695, USA; E-Mails: boyle@ncsu.edu (P.D.B.); rdschmid@ncsu.edu (R.D.S.)

[3] Edgewood Chemical and Biological Center, 5183 Blackhawk Road, Aberdeen Proving Ground, MD 21010, USA; E-Mail: augustus.w.fountain@us.army.mil

[4] Department of Chemistry and Life Science, United States Military Academy, 646 Swift Road, West Point, NY 10996, USA; E-Mail: cristina.c.gomez@us.army.mil (C.G.); William.Pearman@usma.edu (W.F.P.); jon.weyand@us.army.mil (J.W.)

[5] US Army Corps of Engineers, 101 West Oglethorpe Avenue, Savannah, GA 31401, USA; E-Mail: James.L.Jackson@usace.army.mil

***** Author to whom correspondence should be addressed; E-Mail: jsloop@ggc.edu; Tel.: +1-678-407-5022; Fax: +1-678-407-5938.

Abstract: Several fluorinated and trifluoromethylated indanone, tetralone and naphthone derivatives have been prepared via Claisen condensations and selective fluorinations in yields ranging from 22–60%. In addition, we report the synthesis of new, selectively fluorinated bindones in yields ranging from 72–92%. Of particular interest is the fluorination and trifluoroacetylation regiochemistry observed in these fluorinated products. We also note unusual transformations including a novel one pot, dual trifluoroacetylation, trifluoroacetylnaphthone synthesis via a deacetylation as well as an acetyl-trifluoroacetyl group exchange. Solid-state structural features exhibited by these compounds were investigated using crystallographic methods. Crystallographic results, supported by spectroscopic data, show that trifluoroacetylated ketones prefer a chelated cis-enol form whereas fluorinated bindone products exist primarily as the cross-conjugated triketo form.

1. Introduction

Molecules which have medicinal, industrial and herbicidal properties are of continued interest to the pharmaceutical, chemical and agrochemical communities. For example, indanone derivatives have anticoagulant properties and are used in elaborating latent fingerprints, bindone variants comprise components of near infrared dyes while certain tetralones and naphthones, ketones similar in structure to those shown in Figure 1, have demonstrated bioactive properties [1–6]. Since bioactivity is known to be enhanced in many classes of fluorinated molecules [3,7], it is desirous to prepare fluorine-containing molecules with similar architecture and gain a better understanding of their structure-property relationships.

Figure 1. Medicinally and industrially important ketones.

indanones	**bindones**	**tetralones**	**naphthones**
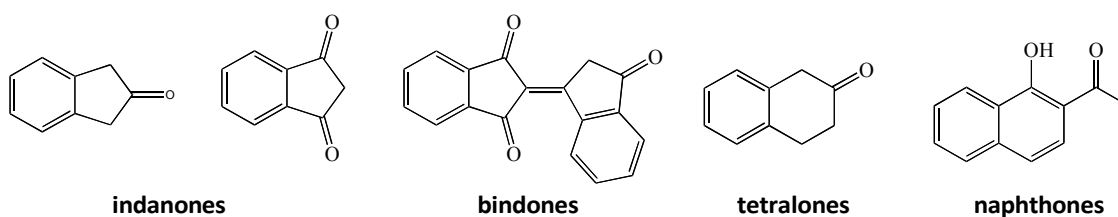
Previously, we reported the preparation and structure-property relationships of acyclic fluorinated and trifluoromethylated *β*-diketones, precursors to a variety of heterocyclic molecules [8–10]. While the syntheses and properties of these molecules have been investigated thoroughly, the preparation and study of selectively fluorinated, cyclic ketones containing the structural features of the molecules depicted in Figure 1 remains relatively limited [11].

The molecules of interest in this study, shown in Scheme 1, provide this sort of molecular architecture. This paper addresses the design and synthetic approach to prepare these novel molecules, the interesting synthetic results and the unique solid-state structural features that differentiate these molecules.

Scheme 1. Synthesis of fluorinated ketones.
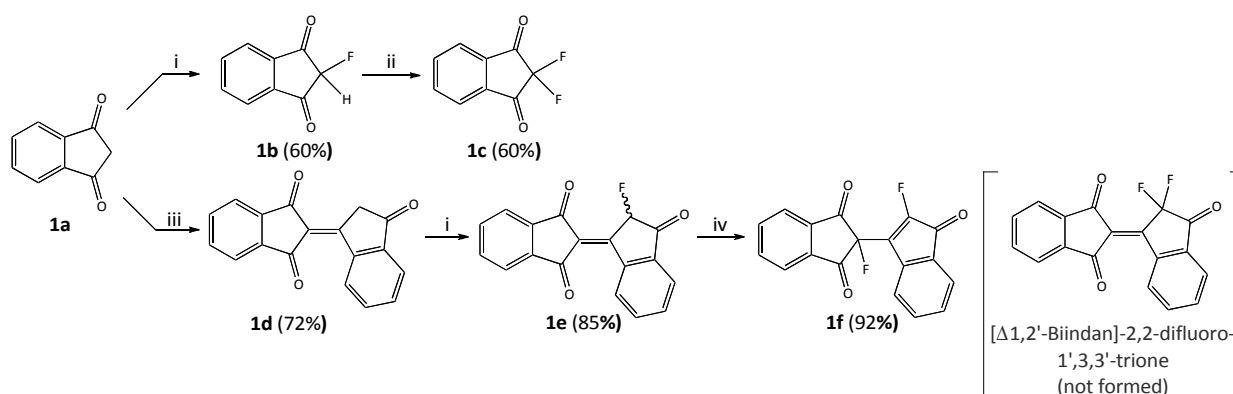
Scheme 1. *Cont.*
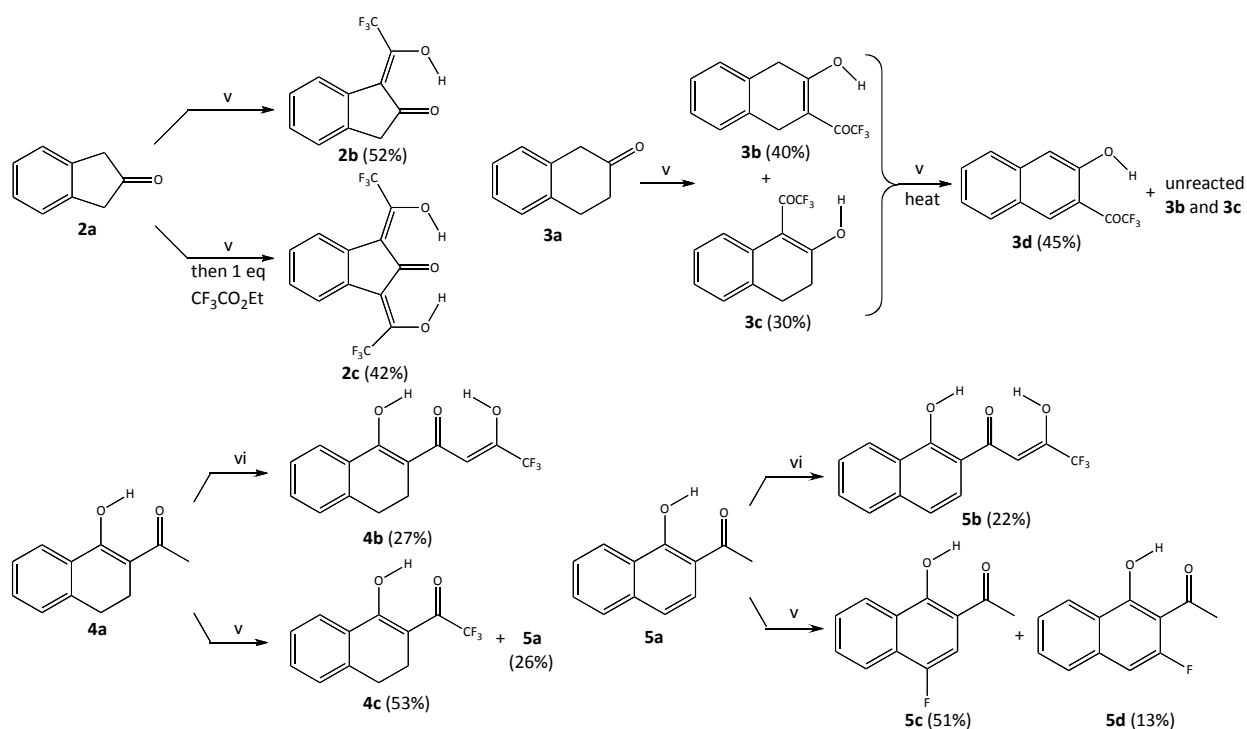
Conditions: i. 1.1 eq Selectfluor®, MeCN, reflux, 10 h; ii. 1.5 eq Selectfluor®, MeCN, RT, 18–30 h; iii. H$_2$SO$_4$, MeOH, reflux, 24 h; iv. 1.1 eq Selectfluor®, MeCN, reflux, 16 h; v. CF$_3$CO$_2$Et, NaOMe, Et$_2$O, rt, 18 h; vi. (1) 3.0 eq LDA, Et$_2$O, 0 °C; (2) 2 eq CF$_3$CO$_2$Et, 0 °C→rt, 24 h; (3) 2 eq CF$_3$CO$_2$Et.

2. Experimental Section

2.1. Chemicals

All chemicals were obtained from the Aldrich Chemical Company, Eastman Kodak, or Fisher Chemical Company. All solvents (spectrophotometric grade) and starting materials were checked for purity by mass spectrometry prior to use.

2.2. Instrumentation

Melting points were obtained on a Mel-Temp melting point apparatus and are uncorrected. NMR data were collected using a Varian VXR-200 spectrometer with a broad band probe operating at 200.0 MHz for ^{1}H, 188.2 MHz for ^{19}F and 50.3 MHz for ^{13}C, and/or a Brüker Avance 300 spectrometer operating at 300.0 MHz for ^{1}H, 282.0 MHz for ^{19}F and 75.4 MHz for [13]C. Unless otherwise noted, CDCl$_3$ was used as the solvent and internal standard for ^{1}H and ^{13}C NMR experiments while CFCl$_3$ served as the internal standard for ^{19}F NMR experiments. All X-ray measurements were made on a Bruker-Nonius X8 Apex2 diffractometer. See the appendix for complete crystallographic experimental details.

2.3. General Procedure for the Preparation of Trifluoromethyl-β–Diketones and Triketones [12]

A 100 mL round bottom flask equipped with a magnetic stirrer is charged with 50 mL diethyl ether and 60 mmol of sodium methoxide is added slowly. Then, 1eq (60 mmol) of trifluoromethyl ethyl acetate is added dropwise slowly while stirring. After 5 minutes, 1eq (60 mmol) of the ketone is added dropwise and stirred overnight at room temperature under a calcium chloride drying tube. The resulting solution is evaporated to dryness under reduced pressure and the solid residue dissolved in 30 mL 3*M* sulfuric acid. This solution is extracted with ether, and the organic layer dried over Na_2SO_4. The solvent is evaporated under reduced pressure and the crude diketone purified by radial chromatography.

2.4. General Procedure for the Preparation of Selectively Fluorinated Ketones [10,13]

A 100 mL round bottom flask equipped with a magnetic stirrer is charged with 40 mL CH_3CN and the ketone (1 eq: 1–10 mmol). Then, Selectfluor® (1–3 eq (3–30 mmol)) dissolved in 30 mL CH_3CN is added slowly while stirring. The solution is either allowed to stir at room temperature or refluxed as required. Times range from 10–30 h. The resulting solution is evaporated to dryness under reduced pressure and the solid residue taken up in distilled water. This solution is extracted with CH_2Cl_2, and the organic layer dried over Na_2SO_4. The solvent is evaporated under reduced pressure and the crude fluorinated ketone purified by radial chromatography.

2-fluoro-1,3-indanedione (**1b**). This compound was obtained in 60% yield as pale yellow crystals (EtOH), m.p. 97–99 °C lit [14] (m.p. 96–98 °C). NMR: ^{1}H: δ 5.4 (d, $^1J_{H-F}$ = 51.0 Hz, 1H), 7.65–8.22 (m, 4H). ^{13}C: δ 90.1 (d, $^1J_{C-F}$ = 211.2 Hz, CF), 125.3, 138.9, 141.9, 193.5 (d, $^2J_{C-F}$ = 24.0 Hz, C-CF). ^{19}F: δ −207.3 (d, $^1J_{F-H}$ = 51.1 Hz, 1F). HRMS (ESI+) Calcd. for $C_9H_5FO_2$: 164.02740. Found: 164.027580.

2,2-difluoro-1,3-indanedione (**1c**). This compound was obtained in 60% yield from fluorination of **1b** as described in the general procedure above as yellowish-brown crystals (EtOH), m.p. 116–117 °C, lit [15] (m.p. 117–118 °C). NMR: ^{1}H: δ 8.0–8.15 (m, 4H). ^{13}C: δ 104.0 (t, $^1J_{C-F}$ = 264 Hz, CF_2), 128.8, 138.2, 139.3 (t, $^3J_{C-F}$ = 4.3 Hz), 185.8(t, $^2J_{C-F}$ = 24.0Hz, $C-CF_2$). ^{19}F: δ −125.9 (s, 2F).

[Δ1,2'-Biindan]-1',3,3'-trione (**1d**). This compound was obtained in 72% yield as orange crystals (EtOH), m.p. 207–209 °C, lit [16] (m.p. 205–208 °C). NMR: ^{1}H: δ 4.17 (s, 2H), 7.74–8.04 (m, 8H), 9.50 (d, J = 7.8 Hz, 1H). ^{13}C: δ 43.4, 123.0, 123.4, 123.5, 125.8, 131.7, 134.2, 135.3, 135.4, 140.4, 141.2, 141.6, 145.9, 155.4, 189.5, 191.0, 201.2.

[Δ1,2'-Biindan]-2-fluoro-1',3,3'-trione (**1e**). This compound was obtained was obtained in 85% yield from fluorination of **1d** as described in the general procedure above as orange crystals (EtOH), m.p. 165–168 °C (dec). NMR: ^{1}H: δ 6.45 (d, $^1J_{H-F}$ = 46.1 Hz, 1H), 7.75–8.20 (m, 7H), 9.50 (d, J = 7.7 Hz, 1H). ^{13}C: δ 70.8 (d, $^1J_{C-F}$ = 194 Hz, CF), 125.4, 126.6, 129.3, 130.1, 132.0, 137.7, 138.5, 166.3, 189.3, 191.2, 204.1 (d, $^2J_{C-F}$ = 24 Hz, C-CF). ^{19}F: δ −182.4 (d, $^1J_{F-H}$ = 46.0 Hz, 1F). Analysis calcd for $C_{18}H_9FO_3$: C, 73.97, H, 3.10. Found: C, 74.06, H, 3.21.

2-fluoro-2-(2'-fluoro-3'-oxoindenyl)-1,3-indanedione (**1f**). This compound was obtained in 92% yield from fluorination of **1e** as described in the general procedure above as yellow crystals (EtOH), m.p. 126–129 °C. NMR: ^{1}H: 7.8–8.25 (7H, m), 9.53 (1H, d, J = 6.9 Hz). ^{13}C: δ 89.9, 125.1, 126.3, 129.5, 130.0, 132.2, 137.1, 138.0 (d, $^1J_{C-F}$ = 254 Hz, CF), 166.1, 185.9, 189.1. ^{19}F: δ −137.3 (s, 1F),

−176.7 (s, 1F). HRMS (ESI+) calcd for $C_{18}H_8F_2O_3$: 310.04415. Found: 310.04415.

1-trifluoroacetyl-2-indanone (**2b**). This compound was obtained in 52% yield as a brown oil. NMR: ^{1}H: δ 3.73 (2H, s), 7.29 (2H, m), 7.60 (2H, m), 14.19 (1H, bs), ^{13}C: δ 40.9, 111.5, 120.4 (CF$_3$, q, ^{1}J$_{C-F}$ = 277 Hz), 122.9, 123.0, 124.9, 127.7, 128.1, 128.8, 129.6, 154.5 (C-CF$_3$, q, ^{2}J$_{C-F}$ = 37 Hz), 203.0. ^{19}F: −68.59 (s, 3F). Analysis calcd for $C_{11}H_7F_3O_2$: C, 57.90, H, 3.09. Found: C, 58.04, H, 3.02.

1,3-ditrifluoroacetyl-2-indanone (**2c**). To 30 mL dry Et$_2$O in a round bottom flask equipped with a magnetic stirrer is added sodium methoxide (0.449 g, 8.32 mmol) all at once. Then, trifluoromethyl ethyl acetate (0.903 mL, 7.57 mmol) is added dropwise slowly while stirring. After 5 minutes, 2-indanone (1.00 g, 7.57 mmol) dissolved in 20 mL dry Et$_2$O is added dropwise and stirred overnight at room temperature under a calcium chloride drying tube. After 24 h, another equivalent of trifluoromethyl ethyl acetate is added dropwise and stirred overnight at room temperature under a calcium chloride drying tube. The reaction mixture is acidifed with 30 mL 3*M* sulfuric acid. The organic layer was separated, washed with deionized water, and the organic layer dried over Na$_2$SO$_4$. The solvent was evaporated under reduced pressure, providing a yellow solid, which when recrystallized, yielded yellow crystals (cyclohexane), in 42% yield, m.p. 111–113 °C. NMR: ^{1}H: δ 7.34 (2H, m), 7.65 (2H, m), 13.50 (2H, bs). ^{13}C: δ 111.5, 118.4 (CF$_3$, q, ^{1}J$_{C-F}$ = 273 Hz), 119.6, 122.9, 126.7, 128.4, 128.9, 130.2, 168.5 (C-CF$_3$, q, ^{2}J$_{C-F}$ = 35 Hz), 177.0. ^{19}F: −68.53 (s, 3F). HRMS (ESI+) calcd for $C_{13}H_6F_6O_3$: 324.02211, found: 324.02158.

3-trifluoroacetyl-2-tetralone (**3b**) and 1-trifluoroacetyl-2-tetralone (**3c**). These compounds were obtained as a 4:3 mixture of **3b**:**3c**. Radial chromatography (100% CH$_2$Cl$_2$–50/50 CH$_2$Cl$_2$/MeOH) afforded two product fractions. Fraction 1: **3b** as orange crystals (hexane), in 40% yield, m.p. 123–126 °C. NMR: ^{1}H: δ, 3.76 (2H, s), 3.81 (2H, s), 7.25–8.05 (4H, m), 15.01 (1H, bs). ^{13}C: δ 27.8, 38.3, 103.7, 117.5 (CF$_3$, q, ^{1}J$_{C-F}$ = 281 Hz), 127.1, 127.3, 127.8, 127.9, 130.5, 133.4, 157.3, 174.8 (C-CF$_3$, q, ^{2}J$_{C-F}$ = 35 Hz), 191.0. ^{19}F (C$_6$F$_6$ ext. std.): δ−70.62 (s, 3F). HRMS (ESI+) calcd for $C_{12}H_9F_3O_2$: 242.04470, found: 242.04436. Fraction 2: **3c** (30%) as an orange solid, m.p. 88–91 °C. **3c**: NMR: ^{1}H: δ 2.72 (2H, t, ^{2}J = 1.9 Hz), 3.01 (2H, t, ^{2}J = 1.9 Hz), 7.25 (4H, m), 14.98 (1H, bs). ^{13}C: δ 25.0, 30.3, 102.9, 118.6 (CF$_3$, q, ^{1}J$_{C-F}$ = 282 Hz), 126.6, 126.9, 127.3, 128.1, 130.2, 133.8, 158.1, 175.4 (C-CF$_3$, q, ^{2}J$_{C-F}$ = 35 Hz), 189.1. ^{19}F (C$_6$F$_6$ ext. std.): δ−67.70 (s, 3F). HRMS (ESI+) calcd for $C_{12}H_9F_3O_2$: 242.04470, found: 242.04442.

3-trifluoroacetyl-2-naphthol (**3d**). A round bottom flask equipped with a magnetic stirrer containing 30 mL dry Et$_2$O is charged with 1 equivalent NaOCH$_3$. Then, 1 equivalent ethyl trifluoroacetate is added dropwise slowly and stirred for 15 min. To this solution is added a 4:3 mixture of compounds **3b**:**3c** dissolved in 20 mL Et$_2$O. The reaction mixture is stirred overnight at room temperature under a calcium chloride drying tube. The solvent is removed under reduced pressure while heating at 60 °C for 20 min. The solid residue is acidified with 30 mL 3*M* sulfuric acid and extracted with 3–15 mL portions of Et$_2$O. The organic layers were combined, washed with deionized water, and the organic layer dried over Na$_2$SO$_4$. The solvent was evaporated under reduced pressure, providing a orange solid, which when subjected to radial chromatography, gave a fraction which upon recrystallization, yielded pale, orange crystals (CH$_2$Cl$_2$), **3d**, in 45% yield, m.p. 80–83 °C. An additional fraction was collected which contained unreacted **3b** and **3c**. **3d**: NMR: ^{1}H: δ, 7.25–8.05 (6H, m), 14.83 (1H, bs). ^{13}C: δ 119.3 (CF$_3$, q, ^{1}J$_{C-F}$ = 284 Hz), 124.9, 125.4, 126.9, 129.9, 130.1, 130.4, 131.4, 135.1, 139.1, 157.3, 184.6 (C-CF$_3$, q, ^{2}J$_{C-F}$ = 35 Hz). ^{19}F (C$_6$F$_6$ ext. std.): δ −74.25 (s, 3F). Analysis calcd for $C_{12}H_7F_3O_2$:

C, 60.01, H, 2.94. Found: C, 60.13, H, 2.88.

4,4,4-trifluoro-1-(1-oxotetrahydronaphthyl)-1,3-butanedione (**4b**) [17]. A 100 mL round bottom flask is charged with 50 mL dry Et_2O, 5 mL dry diisopropylamine, equipped with a magnetic stir bar and placed under N_2 at 0 °C. To this is added LDA (6.0 mL, 0.0120 mol) and stirred for fifteen minutes. Then, a solution of **4a** (0.752 g, 0.004 mol) in 15 mL dry Et_2O is added dropwise slowly via syringe. After 8 h, ethyl trifluoroacetate (0.96 mL, 0.008 mol) is delivered dropwise slowly via syringe, the reaction mixture is stirred overnight and allowed to warm to rt. A third equivalent of ethyl trifluoroacetate (0.004 mol) is added after 24 hours and the solution is left to stir again overnight. The reaction mixture is acidifed with 30 mL 3*M* sulfuric acid. The organic layer was separated, washed with deionized water, and the organic layer dried over Na_2SO_4. The solvent was evaporated under reduced pressure, and subjected to radial chromatography. After recrystallization from cyclohexane, **4b** was obtained as reddish-brown crystals in 27% yield, mp 133–135 °C. **4b**: NMR: ^{1}H: δ 2.85 (2H, t, 7.6 Hz), 2.93 (2H, t, 7.6 Hz), 6.76 (s, 1H), 7.37–7.77 (4H, m), 15.68 (2H, bs). ^{13}C: δ 20.9, 22.7, 104.6, 118.4 (CF_3, q, $^1J_{C-F}$ = 270 Hz), 125.9, 126.8, 127.3, 127.4, 128.2, 128.5, 128.6, 129.9, 133.9, 142.8, 177.0 (C-CF_3, q, $^2J_{C-F}$ = 36 Hz), 182.2. ^{19}F (C_6F_6 ext. std.): δ −72.04 (s, 3F). Analysis calcd for $C_{14}H_{11}F_3O_3$: C, 59.16, H, 3.90. Found: C, 58.99, H, 4.01.

2-trifluoroacetyl-1-tetralone (**4c**). This compound was obtained as off-white crystals, **4c**, in 53% yield, m.p. 50–52 °C lit [18] (m.p. 51–52 °C). **4c**: NMR: ^{1}H: δ 2.75 (2H, t, 9.0 Hz), 2.88 (2H, t, 9.0 Hz), 7.16–7.87 (4H, m), 15.62 (1H, bs). ^{13}C: δ 21.0, 27.8, 38.3, 103.7, 117.5 (CF_3, q, $^1J_{C-F}$ = 285 Hz), 127.1, 127.3, 127.8, 127.9, 130.5, 133.4, 157.3, 174.8 (C-CF_3, q, $^2J_{C-F}$ = 35 Hz), 185.0. ^{19}F (C_6F_6 ext. std.): δ −70.61 (s, 3F). HRMS (ESI+) calcd for $C_{12}H_9F_3O_2$: 242.04470, found: 242.04436.

4,4,4-trifluoro-1-(1-hydroxynaphthyl)-1,3-butanedione (**5b**) [17]. A 100 mL RBF equipped with a magnetic stir bar is charged with 50 mL dry Et_2O, 5 mL dry diisopropylamine (DIPA) and placed under N_2 at 0 °C. To this is added LDA (6.0 mL, 0.0120 mol) and stirred for fifteen minutes. Then, a solution of **5a** (0.740 g, 0.004 mol) in 15 mL dry Et_2O is added dropwise slowly via syringe. After 8 h, ethyl trifluoroacetate (0.96 mL, 0.008 mol) is delivered dropwise slowly via syringe and the reaction mixture is stirred overnight and allowed to warm to rt. After 24 h, another equivalent of ethyl trifluoroacetate (0.46 mL, 0.004 mol) is added all at once. The reaction is stirred for an additional 24 h. The reaction mixture is acidifed with 30 mL 3*M* sulfuric acid. The organic layer was separated, washed with deionized water, and the organic layer dried over Na_2SO_4. The solvent was evaporated under reduced pressure, and subjected to radial chromatography. After recrystallization (cyclohexane) **5b** was obtained as brown crystals, in 22% yield, m.p. 154–157 °C. **5b**: NMR: ^{1}H: δ 6.90 (s, 1H), 7.51–8.50 (6H, m), 14.44 (1H, bs), 15.70 (1H, bs). ^{13}C: δ 111.9, 115.7 (CF_3, q, $^1J_{C-F}$ = 271 Hz), 127.1, 127.3, 127.8, 127.9, 130.5, 133.4, 157.3, 174.8 (C-CF_3, q, $^2J_{C-F}$ = 35 Hz), 185.0. ^{19}F (C_6F_6 ext. std.): δ −71.60 (s, 3F). Analysis calcd for $C_{14}H_9F_3O_3$: C, 59.59, H, 3.21. Found: C, 59.86, H, 3.16.

2-acetyl-4-fluoro-1-naphthol (**5c**) and 2-acetyl-3-fluoro-1-naphthol (**5d**). These compounds were obtained as a 5:1 mixture of **5c**:**5d**. Radial chromatography (100% CH_2Cl_2–50/50 CH_2Cl_2/MeOH) afforded **5c** as brown crystals (51%, m.p. 93–95 °C) and **5d** as a tan solid (13%, m.p. 88–91 °C). **5c**: NMR: ^{1}H: δ 2.71 (3H, s), 7.31–8.48 (5H, m), 14.01 (1H, bs). ^{13}C: δ 26.9, 113.1, 118.3, 124.9, 126.0, 127.4, 130.1, 137.4, 150.5 (Ar-F, d, $^1J_{C-F}$ = 243 Hz), 162.4, 204.2. ^{19}F (C_6F_6 ext. std.): δ −134.0 (s, 1F). Analysis calcd for $C_{12}H_9FO_2$: C, 70.59, H, 4.44. Found: C, 70.77, H, 4.31. **5d**: NMR: ^{1}H: δ 2.63 (3H, s), 7.40–8.00 (5H, m), 13.82 (1H, bs). ^{13}C: δ 27.6, 111.3, 120.3, 124.6, 125.1, 126.9, 128.6, 130.2,

130.3, 155.5 (Ar-F, d, $^1J_{C\text{-}F}$ = 244 Hz), 158.7, 203.4. ^{19}F (C_6F_6 ext. std.): δ −134.2 (s, 1F). Analysis calcd for $C_{12}H_9FO_2$: C, 70.59, H, 4.44. Found: C, 70.44, H, 4.49.

3. Results and Discussion

3.1. Synthesis

Compounds **1a-5a** are commercially available and were used without further purification. Compounds **1b** and **1c** have been previously described, but were prepared according to a different method [14,15]. Compound **1d** is known and was synthesized via a previously described method [12,16]. The remaining compounds were prepared using a modified Claisen condensation or direct fluorination with Selectfluor® [10,12,13,18,19]. See Scheme 1.

Recent work by our group showed that regioselective monofluorination and geminal difluorination of acyclic β-diketones could be effected with Selectfluor$^®$ under mild conditions without the necessity of specialized glassware or safety precautions [10,14,15]. The current synthetic investigation sought to take advantage of this earlier work by probing Selectfluor$^®$'s efficiency and effectiveness in the mono- and difluorination of 1,3-indanedione and bindone. Our efforts revealed some unexpected findings. The monofluorination of **1a** proceeded with little difficulty to give 2-fluoro-1,3-indanedione (**1b**) in the diketonic form (as evidenced by a doublet signal ($J_{F\text{-}H}$ = 51.1 Hz) in the ^{19}F NMR at −207.3 ppm), albeit in slightly lower yield compared to fluorination achieved with 5% F_2 in N_2[10]. Diketone **1b** was also successfully fluorinated (as evidenced by a singlet signal in the ^{19}F NMR at −125.9 ppm), delivering the geminally difluorinated product **1c** in good overall yield.

We then examined whether bindone, the aldol self-condensation product of 1,3-indanedione, would react similarly to treatment with Selectfluor$^®$. As expected, monofluorination was achieved in high yield to give **1e** as an enantiomeric triketone pair (^{19}F NMR: −182.4 ppm, $J_{F\text{-}H}$ = 46.0 Hz), but the site of fluorination was the α-carbon adjacent to the isolated ketone rather than fluorination between the 1,3-diketone residue. Subsequent fluorination of **1e** likewise yielded interesting results. Particularly noteworthy were the fluorination regioselectivity and alkene rearrangement observed during the formation of triketone **1f**. We expected an outcome similar to the fluorination of **1b**, but the occurrence of two distinct signals in the ^{19}F NMR at −137.3 ppm and −176.7 ppm ruled out geminal difluorination. Evidently, the alkene in **1e** retains sufficient nucleophilic nature to permit electrophilic fluorination between the β-dicarbonyl residue. This addition, coupled with a concomitant E1-like elimination leads to **1f**, rather than formation of [Δ1,2'-Biindan]-2,2-difluoro-1',3,3'-trione, shown in Scheme 1.

While preparing **2b** and **2c**, the previously undescribed one-pot, twin trifluoroacetylation of 2-indanone gave the dual exocyclic enol **2c** in moderate yield (confirmed by the presence of a single ^{19}F NMR resonance at −68.5 ppm) and no **2c'**, Figure 2. In this case, the ethoxide base present following the condensation apparently deprotonates the unsubstituted benzylic α-hydrogen (H_3) rather than the more acidic α-hydrogen H_1.

There are several possible explanations for the formation of **2c** and the failure to obtain **2c'**. The most plausible scenario involves initial formation of **2c'**. Given the basic reaction conditions, however, we surmise that upon attachment of the second $COCF_3$ group, **2c'** may undergo nucleophilic acyl substitution by ethoxide, reverting **2c'** back to enolate **A**. A second possibility for the failure to obtain

2c' may be larger steric demands in the transition state leading to enolate **A** formation relative to that leading to enolate **B**. Finally, a base-promoted tautomerization from enolate **A** to enolate **B** could occur before formation of **2c'**, ultimately leading to **2c**.

Figure 2. Formation of 1,3-ditrifluoroacetyl-2-indanone (**2c**).
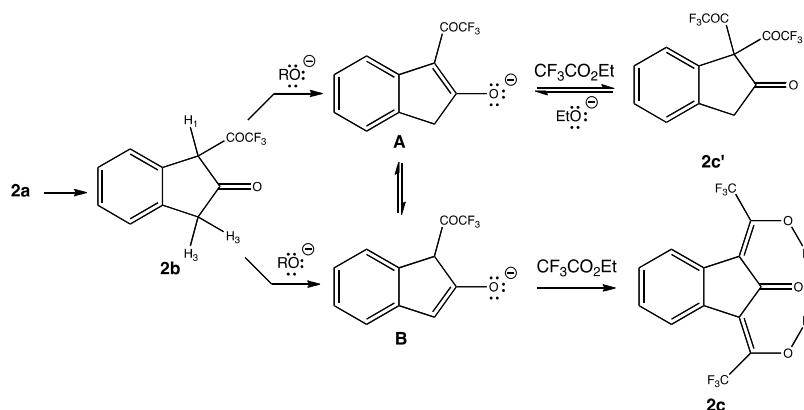
We then attempted a similar strategy with *β*-tetralone (**3a**) to ascertain whether this ditrifluoroacetylation methodology could be generalized to other ketones with two acidic *α*-hydrogen sets. Sequential treatment of **3a** with two equivalents of ethyl trifluoroacetate followed by neutralization at room temperature led to a mixture of the 3- and 1-trifluoroacetyl-2-tetralone endocyclic enols **3b** and **3c**, respectively; the formation of 1,3-ditrifluoroacetyl-2-tetralone was not observed. Assignment of the endocyclic enolic structures was based on the observation of a single ^{19}F NMR resonance at −70.6 ppm for **3b** and −67.7 ppm for **3c**. When the reaction workup conditions were modified by subjecting the enols **3b** and **3c** to an additional equivalent of base and ethyl trifluoroacetate followed by *in vacuo* removal of solvent at elevated temperature, we were surprised to find that aromatization occurred to give the trifluoroacetylated naphthol **3d** in moderate overall yield. Figure 3 depicts a plausible route to naphthol **3d**. We surmise that deprotonation of the less sterically hindered *α*-hydrogen enroute to **3b** occurs rather than abstraction of the more acidic, benzylic *α*-hydrogen. Detrifluoroacetylation of triketone **I** followed by tautomerization of diketone **II** under acidic workup provides naphthol **3d**.

Figure 3. Formation of 3-trifluoroacetyl-2-tetralone (**3b**) and 3-trifluoroacetyl-2-naphthol (**3d**).
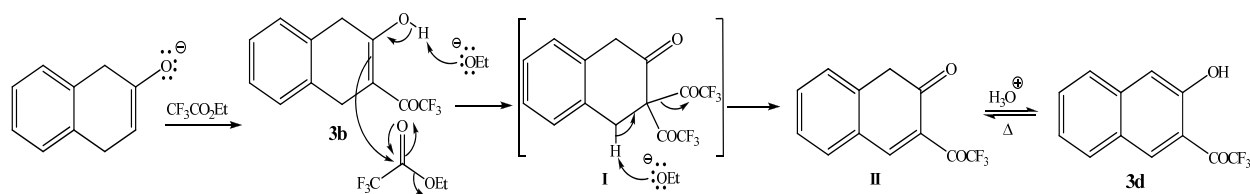
Application of Light and Hauser's method to **4a** and **5a** produced the cross-conjugated, dienolic 1,3,5-triketones **4b** and **5b** in modest yields [17]. Assignment of the enolic structures was based on a combination of resonances found in their NMR spectra—(**4b**) ^{1}H: an alkene proton signal @ 6.76 ppm (1H), a broad, unresolvable singlet corresponding to the enol protons @ 15.68 ppm (2H) and ^{19}F: a

singlet @ −72.0 ppm (3F); for (**5b**) ^{1}H: an alkene proton signal @ 6.90 ppm (1H), a singlet corresponding to the phenolic enol proton @ 14.44 (1H), a broader singlet @ 15.68 ppm (1H) corresponding to the enol adjacent to the CF$_3$ group and ^{19}F: a singlet @ −71.6 ppm (3F). Addition of D$_2$O to the NMR samples of **4b** and **5b** resulted in rapid diminuation of the exchangeable enolic protons in the ^{1}H NMR. Increasing the molar ratio of ethyl trifluoroacetate:diketone to >2:1, although necessary for triketone product formation, also led to *O*-trifluoroacetylated by-products. Fortunately, these were easily separated by chromatography from the desired 1,3,5-triketones. Additionally, we found that when **4a** was subjected to standard Claisen reaction conditions, an unintended acetyl-trifluoroacetyl group exchange occurred to give 2-trifluoroacetyl-1-tetralone (**4c**) in good yield along with, to our surprise, naphthol **5a**. A process similar to the detrifluoroacetylation depicted in Figure 2 may be operating in these cases as well.

Treatment of **5a** with Selectfluor$^{®}$ demonstrated the fluorination preference of activated aromatic substrates over acetyl groups [19–21]. The fluorinated naphthols **5c** and **5d** were achieved in good overall yield and a 5:1 ratio of the *para*:*meta* isomers, respectively. Ring fluorination was confirmed by the observation of resonances in the ^{19}F NMR spectra as singlets: −134.0 ppm (1F) and −134.2 ppm (1F) for **5c** and **5d**, respectively. Preferential *para* fluorination is in accord with the *o-p* directing ability of the hydroxyl group. Use of up to 5 equivalents of Selectfluor$^{®}$ to effect fluorination at the acetyl carbon provided only the monofluorinated naphthols **5c** and **5d**.

3.2. Solid State Structural Features: X-ray Crystallography

Several of the target molecules (**1d**, **2c**, **3c** and **4c**) were examined by x-ray crystallography. Crystal data and structure refinement information for **1d** and **2c** are recorded in Figure 4 and Table 1 while Figure 5 and Table 2 contain data for **3d** and **4c**. Critical bond information is listed in Table 3. The crystallographic information files for these molecules have been uploaded to the Cambridge Crystallographic Data Center and have the following control numbers: **1d**: 854704, **2c**: 854697, **3d**: 854705 and **4c**: 854706.

Figure 4. ORTEP drawings of **1d** and **2c**. Ellipsoids are at the 50% probability level and hydrogen atoms were drawn with arbitrary radii for clarity.

1d   **2c**

Table 1. Crystal data and structure refinement for **1d** and **2c**.

Compound	**1d**	**2c**
Formula	$C_{18}H_{10}O_3$	$C_{13}H_6F_6O_3$
Formula Weight (*g*/*mol*)	274.26	324.18
Crystal Dimensions (*mm*)	$0.30 \times 0.24 \times 0.20$	$1.20 \times 0.10 \times 0.06$
Crystal Color and Habit	clear prism	yellow needle
Crystal System	orthorhombic	monoclinic
Space Group	F d d 2	P 2_1/c
Temperature, K	173	173
a, Å	18.0996(6)	
b, Å	20.9271(7)	18.6978(12)
c, Å	26.0789(8)	13.8431(9)
α,°	90.00	90.0
β,°	90.00	98.964(3)
Compound	**1d**	**2c**
γ,°	90.00	90.0
V, Å^3	9878.0(6)	1218.11(14)
Reflections to determine final unit cell	9975	9959
2θ range, °	5.0, 56.84	5.28–57.7
Z	32	4
F(000)	4544	648.71
ρ (*g*/*cm*)	1.475	1.768
λ, Å, (MoKα)	0.71070	0.71073
μ, (*cm^{-1}*)	0.101	0.18
Reflections collected	103146	26516
Unique reflections	6360	3195
R_{merge}	0.0403	0.027
Cut off Threshold Expression	>2sigma(I)	Inet > 1.0sigma(Inet)
Refinement method	full matrix least-sqs using F^2	full matrix least-sqs using F
Weighting Scheme	$1/[sigma^2 (Fo^2) + (0.0555P)^2 + 3.0465P]$ where $P = (Fo^2 + 2Fc^2)/3$	$1/(sigma^2 (F) + 0.0005F^2)$
R_1[a]	0.0342	0.038
wR_2	0.0846 [b]	0.053 [c]
R_1 (all data)	0.0400	0.046
wR_2 (all data)	0.0880	0.054
GOF	1.038 [d]	1.74 [e]

[a] $R_1 = \Sigma||F_o| - |F_c||/\Sigma F_o$; [b] $wR_2 = [\Sigma(w(F_o^2 - F_c^2)^2)/\Sigma(wF_o^4)]^{1/2}$; [c] $wR_2 = [\Sigma(w(F_o^2 - F_c^2)^2)/\Sigma(wF_o^4)]^{1/2}$; [d] $GOF = [\Sigma(w(F_o^2 - F_c^2)^2)/(\# reflns - \# params)]^{1/2}$; [e] $GOF = [\Sigma(w(F_o^2 - F_c^2)^2)/(No. reflns. No. params.)]^{1/2}$.

Figure 5. ORTEP drawings of **3d** and **4c**. Ellipsoids are at the 50% probability level and hydrogen atoms were drawn with arbitrary radii for clarity.
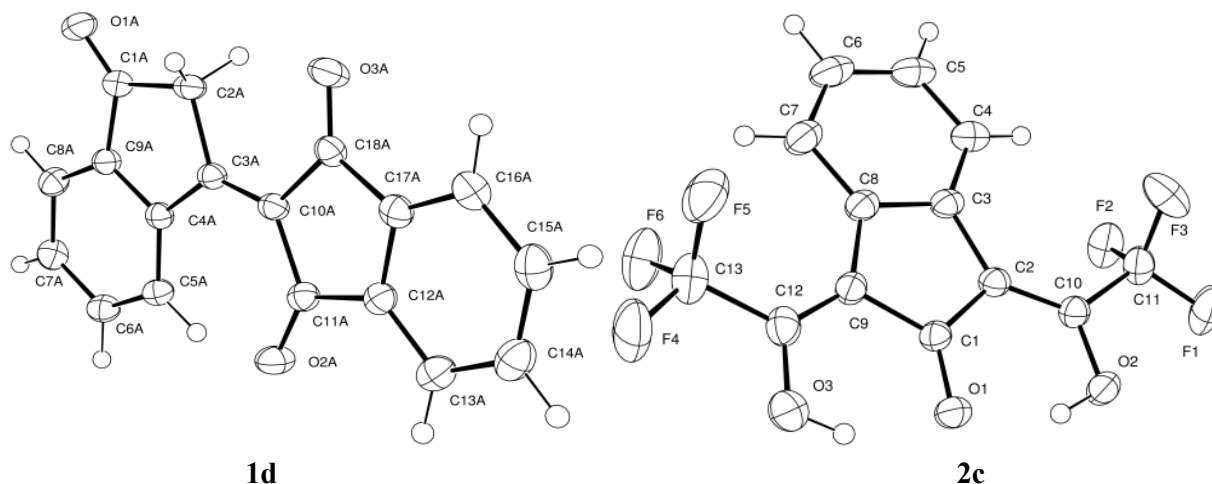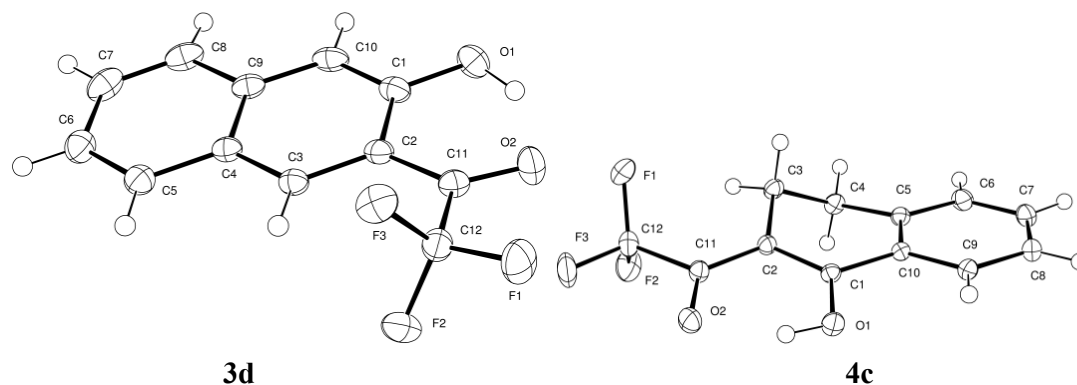

3d   **4c**

Table 2. Crystal data and structure refinement for **3d** and **4c**.

Compound	3d	4c
Formula	$C_{12}H_7F_3O_2$	$C_{12}H_9F_3O_2$
Formula Weight (*g/mol*)	240.18	242.19
crystal size (*mm*)	0.46 × 0.08 × 0.04	0.38 × 0.28 × 0.04
crystal color/shape	orange yellow needle	colourless plate
cryst syst	orthorhombic	triclinic
space group	P n a 2_1	P-1
temp, K	110	110
a, Å	13.5923(5)	7.3528(2)
b, Å	14.9695(5)	7.9165(2)
c, Å	4.8381(2)	9.7991(2)
α,°	90.00	73.0533(11)
β,°	90.00	85.3968(12)
γ,°	90.00	68.3581(11)
V, Å^3	984.41(6)	506.92(2)
Reflections to final unit cell	5859	6416
2θ range, °	5.44–52.66	5.78–71.38
Z	4	2
F(000)	488	248
ρ (*g/cm*)	1.621	1.587
λ, Å, (MoKα)	0.71070	0.71073
μ, (*cm^{-1}*)	0.147	0.143
Reflections collected	21568	20479
Unique reflections	2632	4691
R_{merge}	0.0444	0.0265
Cut off Threshold Expression	>2sigma(I)	>2sigma(I)
refinement method	full matrix least-sqs using F^2	full matrix least-sqs using F^2
Weighting Scheme	$1/[sigma^2 (Fo^2) + (0.0406P)^2 + 0.0000P]$ where $P = (Fo^2 + 2Fc^2)/3$	$1/[sigma^2 (Fo^2) + (0.0707P)^2 + 0.0436P]$ where $P = (Fo^2 + 2Fc^2)/3$
R_1[a]	0.0370	0.0382
wR_2	0.0712	0.1082

Table 2. *Cont.*

Compound	**3d**	**4c**
R_1 (all data)[b]	0.0538	0.0525
wR_2 (all data)[a]	0.0762	0.1220
GOF	1.035	1.048

[a] $R_1 = \Sigma(|F_o - F_c|)/\Sigma F_o$, $wR_2 = [\Sigma(w(F_o - F_c)^2)/\Sigma(F_o^2)]^{1/2}$, $GOF = [\Sigma(w(F_o - F_c)^2)/(\text{No. reflns.} - \text{No. params.})]^{1/2}$;

[b] $R_1 = \Sigma(||F_o| - |F_c||)/\Sigma F_o$, $wR_2 = [\Sigma(w(F_o^2 - F_c^2)^2)/\Sigma(wF_o^4)]^{1/2}$, $GOF = [\Sigma(w(F_o^2 - F_c^2)^2)/(\text{No. reflns.} - \text{No. params.})]^{1/2}$

Table 3. Selected interatomic distances and bond lengths of **1d**, **2c**, **3d** and **4c**.

	Interatomic Distances (Å)		Bond Lengths (Å)			Dihedral ∠ (°)
	O⋯O	O⋯H	O-H	C-O	C-C	
1d	NA	NA	NA	$C_{1A}-O_{1A}$ 1.2143(17)	$C_{3A}-C_{10A}$ 1.3574(19)	$O_3-C_{18}-C_{10}-C_3$ -2.4(11)
				$C_{11A}-O_{2A}$ 1.2212(17)		
				$C_{18A}-O_{3A}$ 1.2143(17)		
2c	$O_1⋯O_2$ 2.5781(13)	$O_1⋯H_2$ 1.75(2)	O_2-H_2 0.90(2)	C_1-O_1 1.2576(15)	C_1-C_2 1.4547(15)	$O_1-C_1-C_2-C_{10}$ -1.91(11)
	$O_1⋯O_3$ 2.5926(14)	$O_1⋯H_3$ 1.81(2)	O_3-H_3 0.88(2)	$C_{10}-O_2$ 1.3308(15)	C_2-C_{10} 1.3593(17)	
				$C_{12}-O_3$ 1.3242(17)	C_9-C_{12} 1.3602(17)	
3d	$O_1⋯O_2$ 2.6142(17)	$O_2⋯H$ 1.75(3)	O_1-H 0.97(3)	C_1-O_1 1.3588(19)	C_1-C_2 1.438(2)	$O_1-C_1-C_2-C_{11}$ 1.9(2)
				$C_{11}-O_2$ 1.2199(18)	C_2-C_{11} 1.459(2)	
4c	$O_1⋯O_2$ 2.5063(9)	$O_2⋯H$ 1.72(2)	O_1-H 0.855(19)	C_1-O_1 1.3215(9)	C_1-C_2 1.3895(10)	$O_1-C_1-C_2-C_{11}$ -2.04(11)
				$C_{11}-O_2$ 1.2476(10)	C_2-C_{11} 1.4193(10)	

In the case of compound **1d**, the small $O_3-C_{10}-C_{18}-C_3$ dihedral angle of −2.4° shows bindone to be nearly planar across the ring bridge in the solid state. The C-O and C_3-C_{10} bond lengths are consistent with those of typical carbonyls and alkenes, respectively and identify **1d** as a cross-conjugated triketone in the solid state. For **2c**, x-ray crystallography confirms the preference of a previously unreported structure in the solid state: a planar, exocyclic dienol shown in Figure 4. The weak intramolecular H-bonding normally observed in cyclic triketones is clearly supported for **2c** by the interatomic O⋯H-O distances of 1.75Å and 1.81Å and very short O-H bond lengths of 0.88Å and 0.90Å [11,22]. The small $O_1-C_1-C_2-C_{10}$ dihedral angle of −1.91° attests to the planar nature of the cyclopentanone residue.

Likewise, 3-trifluoroacetyl-2-naphthol (**3d**) and 2-trifluoroacetyl-1-tetralone (**4c**) show trends consistent with a single endocyclic cis-enol tautomer having weak intramolecular H-bonding, e.g.,

interatomic O···H-O distances >1.7Å, O-H bond lengths < 1.0Å and small O_1-C_1-C_2-C_{11} dihedral angles. For **3d**, the aromatic ring introduces an additional structural constraint prohibiting tautomerism to either the diketo form or any other enolic structure.

Spectral data provided in the experimental section supports the solid-state structural data presented herein [8–10,23–28]. A detailed examination of the absorption, vibrational and magnetic resonance spectroscopy of these molecules is underway to discern the keto-enol and enol-enol behavior of these di- and triketones in various solvent systems and where applicable in the solid-state and/or neat liquid. Those results, along with a comparative ab initio component, will be presented in a future communication.

Acknowledgments

References

1. Nauta, W.T., Rekker, R.F., Eds.; *Biological Activities of 1,3-Indandiones. Pharmacochemistry of 1,3-Indanediones*; Elsevier Scientific Publishing Co.: New York, NY, USA, 1981; pp. 187–269.
2. Wiesner, S.; Springer, E.; Sasson, Y.; Almog, J. Chemical development of latent fingerprints: 1,2-Indanedione has come of age. *J. For. Sci.* **2001**, *46*, 1082–1084.
3. Near-Infrared Dyes for high Technology Applications. In *Proceedings of the NATO Advanced Research Workshop on Syntheses, Optical Properties and Applications of Near Infrared (NIR) Dyes in High Technology Fields*, Daehne, S., Resch-Genger, U., Wolfbeis, O.S., Eds.; Kluwer Academic Publishers: Dordrecht, The Netherlands, 1997; Volume 52, pp. 363–364.
4. van Klink, J.W.; Larsen, L.; Perry, N.B.; Weavers, R.T.; Cook, G.M.; Bremer, P.J.; MacKenzie, A.D.; Kirikae, T. Triketones active against antibiotic-resistant bacteria: Synthesis, structure-activity relationships, and mode of action. *Bioorg. Med. Chem.* **2005**, *13*, 6651–6662.
5. An, T.Y.; Hu, L.H.; Chen, R.M.; Chen, Z.L.; Li, J.; Shen, Q. Anti-diabetes agents—1. Tetralone derivative from *Juglans regia. Chin. Chem. Lett.* **2003**, *14*, 489–490.
6. Jain, R.; Jain, S.C.; Arora, R. A new cholestane derivative of *Abutilon bidentatum* Hochst. And ist bioactivity. *Pharmazie* **1996**, *51*, 253–254.
7. Mentré, F.; Pousset, F.; Comets, E.; Plaud, B.; Diquet, B.; Montalescot, G.; Ankri, A.; Mallet, A.; Lechat. P. Population pharmacokinetic-pharmacodynamic analysis of fluindione in patients. *Clin. Pharmacol. Ther.* **1998**, *63*, 64–78.
8. Sloop, J.C.; Bumgardner, C.; Washington, G.; Loehle, W.D.; Sankar, S.; Lewis, A. Keto-Enol and Enol-Enol Tautomerism in Trifluoromethyl-$\tilde{\beta}$-Diketones, *J. Fluorine Chem.* **2006**, *127*, 780–786.
9. Sloop, J.C.; Bumgardner, C.; Washington, G.; Loehle, W.D. Synthesis of fluorinated heterocycles. *J. Fluorine Chem.* **2002**, *118*, 135–147.

10. Sloop, J.C.; Boyle, P.; Fountain, A.W.; Pearman, W.; Swann, J. Electron deficient aryl *β*-diketones: synthesis and novel tautomeric preferences. *Eur. J. Org. Chem*. **2011**, *5*, 936–941.

11. Bolvig, S.; Hansen, P.E. Deuterium-Induced Isotope Effects on ¹³C Chemical Shifts as a Probe for Tautomerism in enolic *β*-Diketones. *Mag. Res. Chem.* **1996**, *34*, 467–478.

12. Reid, J.C.; Calvin, M. Some New *β*-Diketones Containing the Trifluoromethyl Group. *J. Am. Chem. Soc.* **1950**, *72*, 2948–2952.

13. Stavber, G.; Zupan, M.; Stavber, S. Micellar-System-Mediated direct fluorination of ketones in water. *Synlett* **2009**, *4*, 589–594.

14. Sloop, J.C. *Synthesis of Fluorinated Pyrazoles and Isoxazoles. The Effect of 2-Fluoro and 2-Chloro Substituents on the Keto-Enol Equilibria of 1,3-Diketones*; DOD Technical Report, Defense Technical Information Center: Fort Belvoir, VA, USA, 18 May 1990; pp. 1–32.

15. Zajc, B.; Zupan, M. Fluorination with xenon difluoride. 27. The effect of catalyst on fluorination of 1,3-diketones and enol acetates. *J. Org. Chem.* **1982**, *47*, 573–575.

16. MSDS. Bindone. Available online: http://www.chemcas.org/chemical/msds/cas/AA_M/ AAB24557-03.asp (accessed on 20 November 2011). Mp: 205–208 °C. See Carey, F.J.; Sundberg, R.J. *Advanced Organic Chemistry, Part B: Reactions and Synthesis*, 2nd ed.; Plenum Press: New York, NY, USA, 1983; pp. 43–45.

17. Light, R.J.; Hauser, C.R. Aroylations of β-diketones at the terminal methyl group to form 1,3,5-Triketones. Cyclizations to 4-Pyrones and 4-Pyridones. *J. Org. Chem.* **1960**, *25*, 538–546.

18. Park, J.D.; Brown, H.A.; Lacher, J.R. A Study of Some Fluorine-containing *β*-Diketones. *J. Am. Chem. Soc.* **1953**, *75*, 4753–4756.

19. Sloop, J.C.; Jackson, J.; Schmidt, R. Microwave-Mediated pyrazole fluorinations using Selectfluor®. *Heteroatom Chem.* **2009**, *20*, 341–345.

20. Riofski, M.V.; John, J.P.; Zheng, M.M.; Kirshner, J.; Colby, D.A. Exploiting the facile release of trifluoroacetate for the *α*-Methylation of the sterically hindered carbonyl groups on (+)-Sclareolide and (−)-Eburnamonine. *J. Org. Chem*. **2011**, *76*, 3676–3683.

21. Kirsch, P. *Modern Fluoroorganic Chemistry: Synthesis, Reactivity, Applications*; Wiley-VCH VerlagGmbH & Co.: Darmstadt, Germany, 2004; pp. 78–79.

22. Crouse, D.J.; Hurlbut, S.L.; Wheeler, D.M. Photo Fries rearrangements of 1-naphthyl esters in the synthesis of 2-acylnaphthoquinones. *J. Org. Chem*. **1981**, *46*, 374–378.

23. Murdock, K.C. Triacylhalomethanes: 2-Halo-2-acyl-1,3-indanediones. *J. Org. Chem*. **1959**, *24*, 845–849.

24. Forsen, S.; Nilsson, M. Proton magnetic resonance studies of enolised *β*-Triketones. *Acta Chem. Scand.* **1959**, *13*, 1383–1394.

25. Hunig, S.; Hoch, H. 2-Acetyl-cyclanone und Cyclandione-(1,3), ein Vergleich. *Justus Liebigs Ann. Chem.* **1968**, *716*, 68–77.

26. Ebraheem, K.A. ¹H, ¹³C and ¹⁹F NMR Studies on the Structure of the Intramolecularly Hydrogen Bonded *cis*-Enols of 2-Trifluoroacetylcycloalkanones. *Monatsh. Chem.* **1991**, *122*, 157–163.

27. Hansen, P.E.; Ibsen, S.N.; Kristensen, T.; Bolvig, S. Deuterium and ¹⁸O Isotope Effects on ¹³C Chemical Shifts of Sterically Hindered and/or Intramolecularly Hydrogen-Bonded *o*-Hydroxy Acyl Aromatics. *Mag. Res. Chem.* **1994**, *32*, 399–408.

28. Dolbier, W.R. *Guide to Fluorine NMR for Organic Chemists*; John Wiley and Sons, Inc.: Hoboken, NJ, USA, 2009; Volume 70–81, pp. 152–158.

29. Bruker-Nonius, *SAINT version 7.34A*; Bruker-Nonius: Madison, WI, USA, 2006.
30. Bruker-Nonius, *SADABS version 2.10*; Bruker-Nonius: Madison, WI, USA, 2004.
31. Altomare, A.; Cascarano, G.; Giacovazzo, C.; Guagliardi, A.; Burla, M. C.; Polidori, G.; Camalli, M. SIR92-a program for automatic solution of crystal structures by direct methods. *J. Appl. Cryst.* **1994**, *27*, 435.
32. Bruker-AXS, *XL version 6.12*; Bruker-AXS: Madison, WI, USA.
33. Gabe, E.J.; Le Page, Y.; Charland, J.P.; Lee, F.L.; White, P.S. NCRVAX-an interactive program system for structure analysis. *J. Appl. Cryst.* **1989**, *22*, 384-387.

Appendix. X-Ray Experimental Procedures and Data

1. Compound **1d**

Experimental for $C_{18}H_{10}O_3$ (1d)

Data Collection and Processing. The sample **1d** was submitted by Joseph Sloop of the Sloop research group at Georgia Gwinnett College. The sample was mounted on a nylon loop with a small amount of NVH immersion oil. All X-ray measurements were made on a Bruker-Nonius X8 Apex2 diffractometer at a temperature of 173 K. The unit cell dimensions were determined from a symmetry constrained fit of 9975 reflections with $5.0° < 2\theta < 56.84°$. The data collection strategy was a number of ω and φ scans which collected data up to $58.24°$ (2θ). The frame integration was performed using SAINT [29]. The resulting raw data was scaled and absorption corrected using a multi-scan averaging of symmetry equivalent data using SADABS [30].

Structure Solution and Refinement. The structure was solved by direct methods using the SIR92 program [31]. All non-hydrogen atoms were obtained from the initial E-map. The hydrogen atoms were introduced at idealized positions and were allowed to refine isotropically. The structural model was fit to the data using full matrix least-squares based on F^2. The calculated structure factors included corrections for anomalous dispersion from the usual tabulation. The structure was refined using the XL program from SHELXTL [32], graphic plots were produced using the NRCVAX crystallographic program suite. Additional information and other relevant literature references can be found in the reference section of the Facility's Web page (http://www.xray.ncsu.edu).

Figure 6. ORTEP drawing of *1d molecule A* showing naming and numbering scheme. Ellipsoids are at the 50% probability level and hydrogen atoms were drawn with arbitrary radii for clarity.
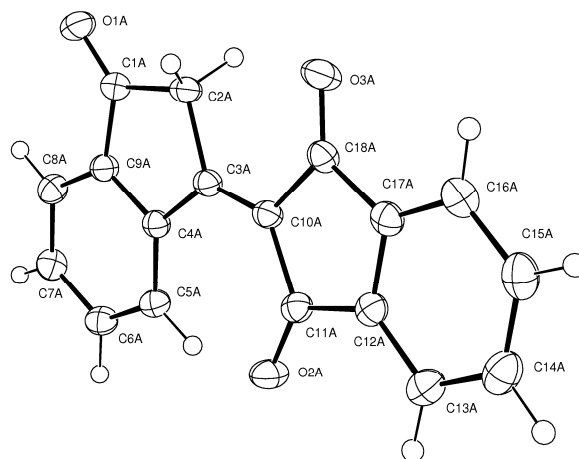
Figure 7. ORTEP drawing of *1d molecule A*. Ellipsoids are at the 50% probability level and hydrogen atoms were drawn with arbitrary radii for clarity.
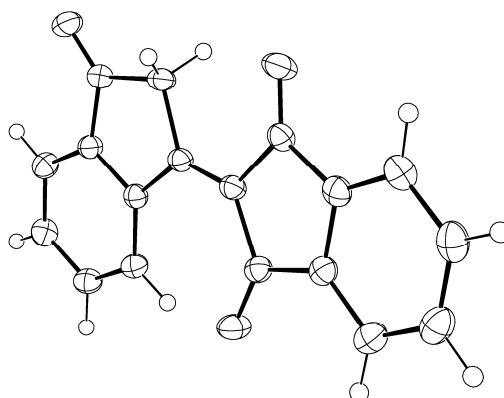
Figure 8. Stereoscopic ORTEP drawing of *1d molecule A*. Ellipsoids are at the 50% probability level and hydrogen atoms were drawn with arbitrary radii for clarity.
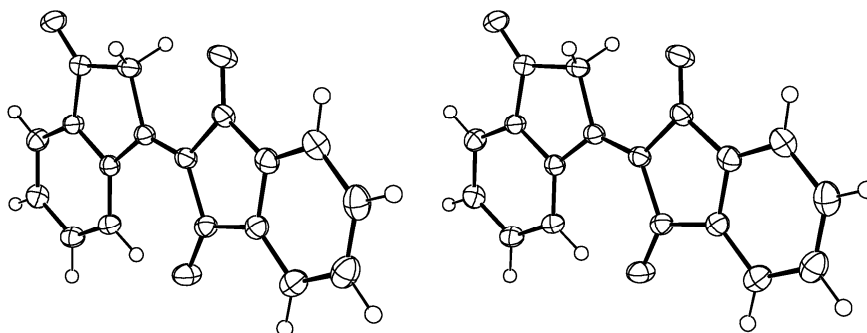
Figure 9. ORTEP drawing of *1d molecule B* showing naming and numbering scheme. Ellipsoids are at the 50% probability level and hydrogen atoms were drawn with arbitrary radii for clarity.
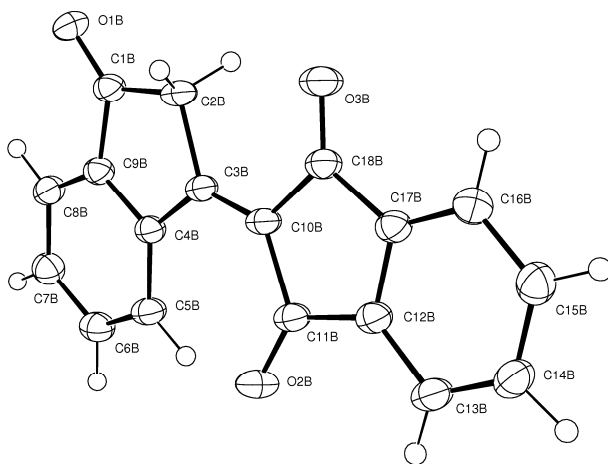
Figure 10. ORTEP drawing of *1d molecule B*. Ellipsoids are at the 50% probability level and hydrogen atoms were drawn with arbitrary radii for clarity.
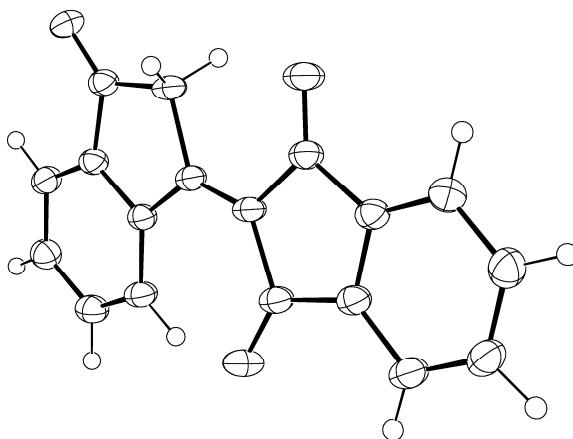
Figure 11. Stereoscopic ORTEP drawing of *1d molecule B*. Ellipsoids are at the 50% probability level and hydrogen atoms were drawn with arbitrary radii for clarity.
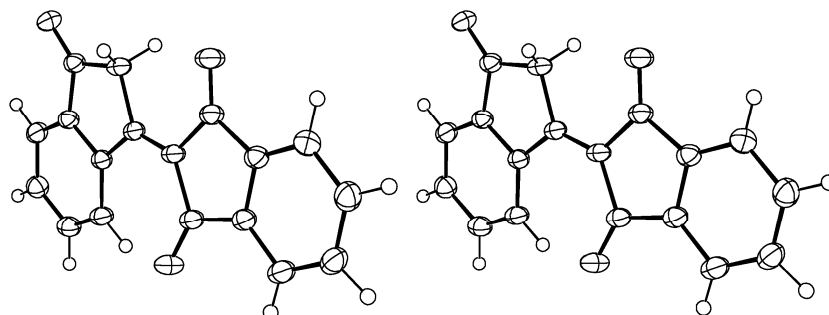
Table 4. Summary of Crystal Data for *1d*.

Formula	$C_{18}H_{10}O_3$
Formula Weight (*g*/*mol*)	274.26
Crystal Dimensions (*mm*)	$0.30 \times 0.24 \times 0.20$
Crystal Color and Habit	clear prism
Crystal System	orthorhombic
Space Group	F d d 2
Temperature, K	173
a, Å	18.0996(6)
b, Å	20.9271(7)
c, Å	26.0789(8)
α,°	90.00
β,°	90.00
γ,°	90.00
V, Å^3	9878.0(6)
Number of reflections to determine final unit cell	9975
Min and Max 2θ for cell determination, °	5.0, 56.84
Z	32
F(000)	4544
ρ (*g/cm*)	1.475
λ, Å, (MoKα)	0.71070
μ, (*cm*$^{-1}$)	0.101
Diffractometer Type	Bruker-Nonius X8 Apex2
Scan Type(s)	omega and phi scans
Max 2θ for data collection, °	58.24
Measured fraction of data	1.000
Number of reflections measured	103146
Unique reflections measured	6360
R_{merge}	0.0403
Number of reflections included in refinement	6360
Cut off Threshold Expression	>2sigma(I)
Structure refined using	full matrix least-squares using F^2
Weighting Scheme	calc w = 1/[sigma^2(Fo^2) + (0.0555P)^2 + 3.0465P] where P=(Fo^2 + 2Fc^2)/3
Number of parameters in least-squares	458
R_1	0.0342
wR_2	0.0846
R_1 (all data)	0.0400
wR_2 (all data)	0.0880
GOF	1.038
Maximum shift/error	0.000
Min & Max peak heights on final ΔF Map (*e*$^-$/Å)	−0.219, 0.216

Where:

$R_1 = \Sigma(|F_O| - |F_C|)/\Sigma F_O$

$wR_2 = [\Sigma(w(F_O^2 - F_C^2)^2)/\Sigma(w\, F_O^4)]^{1/2}$

$GOF = [\Sigma(w(F_O^2 - F_C^2)^2)/(\text{No. of reflns.} - \text{No. of params.})]^{1/2}$

Table 5. Atomic Coordinates for *1d*.

Atom	x	y	z	$U_{iso/equiv}$
O1A	0.20028(6)	0.13639(6)	0.62634(6)	0.0362(3)
O2A	0.36237(6)	0.01557(5)	0.4220	0.0310(2)
O3A	0.40033(6)	−0.02683(5)	0.59892(6)	0.0329(2)
C1A	0.23461(8)	0.12010(7)	0.58853(6)	0.0257(3)
C2A	0.29550(8)	0.07078(7)	0.58765(6)	0.0265(3)
C3A	0.31404(7)	0.06171(6)	0.53149(6)	0.0215(2)
C4A	0.27141(7)	0.10937(6)	0.50228(6)	0.0214(2)
C5A	0.27082(8)	0.12548(7)	0.45022(6)	0.0246(3)
C6A	0.22256(8)	0.17252(7)	0.43340(7)	0.0271(3)
C7A	0.17513(8)	0.20411(7)	0.46700(7)	0.0283(3)
C8A	0.17630(8)	0.19033(7)	0.51873(7)	0.0279(3)
C9A	0.22477(7)	0.14322(7)	0.53572(6)	0.0234(3)
C10A	0.36116(7)	0.01514(6)	0.51589(6)	0.0217(2)
C11A	0.38319(7)	−0.00519(6)	0.46328(6)	0.0228(3)
C12A	0.43567(7)	−0.05931(6)	0.46890(7)	0.0231(3)
C13A	0.47199(8)	−0.09342(7)	0.43109(7)	0.0289(3)
C14A	0.51888(9)	−0.14212(8)	0.44613(8)	0.0328(3)
C15A	0.52844(9)	−0.15676(8)	0.49786(8)	0.0331(3)
C16A	0.49169(8)	−0.12272(7)	0.53601(7)	0.0293(3)
C17A	0.44557(7)	−0.07332(6)	0.52064(7)	0.0242(3)
C18A	0.40165(7)	−0.02813(7)	0.55238(7)	0.0237(3)
O1B	0.14120(7)	0.04113(5)	0.35875(6)	0.0349(2)
O2B	0.25973(7)	−0.11687(6)	0.56110(5)	0.0351(2)
O3B	0.29954(7)	−0.15569(6)	0.38414(6)	0.0367(3)
C1B	0.15538(8)	0.00789(7)	0.39573(6)	0.0270(3)
C2B	0.20581(8)	−0.04922(7)	0.39627(6)	0.0267(3)
C3B	0.21160(8)	−0.06899(7)	0.45205(6)	0.0233(3)
C4B	0.16128(8)	−0.02763(7)	0.48137(7)	0.0241(3)
C5B	0.14109(8)	−0.02690(8)	0.53345(7)	0.0286(3)
C6B	0.09013(9)	0.01792(8)	0.54976(7)	0.0314(3)
C7B	0.05876(9)	0.06238(8)	0.51670(7)	0.0318(3)
C8B	0.07692(9)	0.06178(7)	0.46499(7)	0.0298(3)
C9B	0.12772(8)	0.01681(7)	0.44855(6)	0.0255(3)
C10B	0.25683(8)	−0.11716(7)	0.46724(6)	0.0245(3)
C11B	0.27541(8)	−0.14057(7)	0.52003(7)	0.0259(3)
C12B	0.32241(8)	−0.19790(7)	0.51345(7)	0.0262(3)
C13B	0.35157(9)	−0.23821(8)	0.55099(7)	0.0322(3)
C14B	0.39368(10)	−0.28954(8)	0.53526(8)	0.0352(3)
C15B	0.40794(9)	−0.30056(8)	0.48342(8)	0.0352(3)
C16B	0.37983(9)	−0.25975(7)	0.44609(7)	0.0322(3)
C17B	0.33643(8)	−0.20886(7)	0.46172(7)	0.0264(3)
C18B	0.29790(8)	−0.15934(7)	0.43065(7)	0.0269(3)
H2A1	0.2800(10)	0.0306(10)	0.6041(7)	0.038(5)
H2A2	0.3395(11)	0.0877(9)	0.6072(7)	0.037(5)

Table 5. *Cont.*

H5A	0.3041(10)	0.1074(9)	0.4261(8)	0.033(4)
H6A	0.2211(10)	0.1858(9)	0.3965(7)	0.034(5)
H7A	0.1431(11)	0.2367(9)	0.4567(7)	0.036(5)
H8A	0.1442(12)	0.2130(10)	0.5435(9)	0.045(6)
H13A	0.4637(10)	−0.0835(9)	0.3957(8)	0.036(5)
H14A	0.5436(10)	−0.1635(9)	0.4193(8)	0.035(5)
H15A	0.5585(12)	−0.1908(10)	0.5071(8)	0.044(6)
H16A	0.4962(11)	−0.1324(10)	0.5727(8)	0.041(5)
H2B1	0.2541(12)	−0.0384(10)	0.3821(9)	0.052(6)
H2B2	0.1831(10)	−0.0855(9)	0.3765(8)	0.035(5)
H5B	0.1623(10)	−0.0581(9)	0.5574(7)	0.033(5)
H6B	0.0744(12)	0.0181(10)	0.5865(9)	0.049(6)
H7B	0.0234(10)	0.0921(9)	0.5291(8)	0.035(5)
H8B	0.0572(10)	0.0917(9)	0.4398(8)	0.038(5)
H13B	0.3432(11)	−0.2287(9)	0.5847(8)	0.036(5)
H14B	0.4143(11)	−0.3227(10)	0.5586(8)	0.039(5)
H15B	0.4354(11)	−0.3383(9)	0.4722(8)	0.043(5)
H16B	0.3894(10)	−0.2680(9)	0.4103(7)	0.029(4)

Table 6. Anisotropic Displacement Parameters for *1d*.

Atom	u^{11}	u^{22}	u^{33}	u^{12}	u^{13}	u^{23}
O1A	0.0362(6)	0.0485(7)	0.0238(5)	0.0094(5)	0.0051(4)	−0.0015(5)
O2A	0.0394(6)	0.0338(6)	0.0198(5)	0.0040(4)	0.0011(4)	0.0012(4)
O3A	0.0398(6)	0.0369(6)	0.0221(5)	0.0069(5)	−0.0075(4)	−0.0029(4)
C1A	0.0256(6)	0.0301(7)	0.0215(6)	0.0000(5)	−0.0008(5)	−0.0014(5)
C2A	0.0291(7)	0.0326(7)	0.0179(6)	0.0040(6)	−0.0015(5)	−0.0015(5)
C3A	0.0217(6)	0.0238(6)	0.0191(6)	−0.0048(5)	−0.0004(4)	−0.0006(5)
C4A	0.0218(6)	0.0212(6)	0.0213(6)	−0.0030(5)	−0.0006(4)	−0.0007(5)
C5A	0.0276(7)	0.0253(7)	0.0210(6)	−0.0012(5)	0.0020(5)	0.0006(5)
C6A	0.0332(7)	0.0251(7)	0.0230(6)	−0.0029(5)	0.0008(5)	0.0032(5)
C7A	0.0299(7)	0.0245(7)	0.0306(7)	0.0028(5)	−0.0008(6)	0.0047(6)
C8A	0.0283(7)	0.0272(7)	0.0282(7)	0.0019(5)	0.0025(5)	−0.0001(6)
C9A	0.0244(6)	0.0250(6)	0.0209(6)	−0.0010(5)	0.0003(5)	−0.0001(5)
C10A	0.0227(6)	0.0235(6)	0.0190(6)	−0.0021(5)	−0.0016(5)	−0.0008(5)
C11A	0.0232(6)	0.0235(6)	0.0217(6)	−0.0034(5)	0.0019(5)	−0.0011(5)
C12A	0.0223(6)	0.0225(6)	0.0247(6)	−0.0031(5)	0.0014(5)	−0.0011(5)
C13A	0.0300(7)	0.0286(7)	0.0282(7)	−0.0032(6)	0.0055(5)	−0.0030(5)
C14A	0.0305(7)	0.0284(7)	0.0396(8)	−0.0010(6)	0.0067(6)	−0.0076(6)
C15A	0.0266(7)	0.0284(7)	0.0443(9)	0.0033(6)	−0.0025(6)	−0.0028(6)
C16A	0.0279(7)	0.0279(7)	0.0321(8)	0.0000(5)	−0.0052(6)	−0.0001(6)
C17A	0.0225(6)	0.0235(6)	0.0264(6)	−0.0046(5)	−0.0021(5)	−0.0016(5)
C18A	0.0225(6)	0.0249(7)	0.0237(6)	−0.0015(5)	−0.0034(5)	−0.0017(5)
O1B	0.0463(6)	0.0351(6)	0.0235(5)	−0.0023(5)	−0.0037(4)	0.0079(4)
O2B	0.0415(6)	0.0444(6)	0.0192(5)	0.0011(5)	−0.0023(4)	0.0013(4)
O3B	0.0480(6)	0.0425(6)	0.0196(5)	0.0073(5)	−0.0015(4)	0.0010(4)

Table 6. *Cont.*

C1B	0.0292(7)	0.0303(7)	0.0214(6)	−0.0089(5)	−0.0038(5)	0.0019(5)
C2B	0.0287(7)	0.0344(7)	0.0168(6)	−0.0024(6)	−0.0015(5)	0.0028(5)
C3B	0.0240(6)	0.0277(7)	0.0181(6)	−0.0080(5)	−0.0024(5)	0.0031(5)
C4B	0.0252(6)	0.0271(6)	0.0200(6)	−0.0078(5)	−0.0020(5)	0.0014(5)
C5B	0.0309(7)	0.0349(8)	0.0200(6)	−0.0068(6)	−0.0009(5)	0.0039(5)
C6B	0.0326(8)	0.0379(8)	0.0238(7)	−0.0048(6)	0.0018(5)	−0.0002(6)
C7B	0.0329(7)	0.0330(7)	0.0296(7)	−0.0032(6)	0.0011(6)	−0.0008(6)
C8B	0.0328(7)	0.0306(7)	0.0261(7)	−0.0037(6)	−0.0026(6)	0.0045(6)
C9B	0.0270(7)	0.0288(7)	0.0207(6)	−0.0068(5)	−0.0034(5)	0.0014(5)
C10B	0.0261(7)	0.0310(7)	0.0163(6)	−0.0071(5)	−0.0015(5)	0.0022(5)
C11B	0.0273(7)	0.0313(7)	0.0190(6)	−0.0078(5)	−0.0020(5)	0.0040(5)
C12B	0.0268(6)	0.0289(7)	0.0227(7)	−0.0089(5)	−0.0046(5)	0.0034(5)
C13B	0.0367(8)	0.0351(8)	0.0247(7)	−0.0091(6)	−0.0067(6)	0.0076(6)
C14B	0.0410(9)	0.0304(8)	0.0344(8)	−0.0063(6)	−0.0125(7)	0.0085(6)
C15B	0.0378(8)	0.0293(7)	0.0386(9)	−0.0001(6)	−0.0093(6)	0.0010(6)
C16B	0.0373(8)	0.0315(8)	0.0279(8)	−0.0012(6)	−0.0054(6)	−0.0008(6)
C17B	0.0284(7)	0.0281(7)	0.0228(6)	−0.0064(5)	−0.0043(5)	0.0020(5)
C18B	0.0301(7)	0.0304(7)	0.0203(6)	−0.0048(6)	−0.0030(5)	0.0016(5)

Table 7. Bond Lengths for *1d*.

O1A-C1A	1.2143(17)	O1B-C1B	1.2166(17)
O2A-C11A	1.2212(17)	O2B-C11B	1.2140(18)
O3A-C18A	1.2143(17)	O3B-C18B	1.2159(17)
C1A-C9A	1.4705(19)	C1B-C9B	1.4775(19)
C1A-C2A	1.510(2)	C1B-C2B	1.504(2)
C2A-C3A	1.5145(18)	C2B-C3B	1.5159(17)
C2A-H2A1	0.99(2)	C2B-H2B1	0.98(2)
C2A-H2A2	1.01(2)	C2B-H2B2	1.006(19)
C3A-C10A	1.3574(19)	C3B-C10B	1.358(2)
C3A-C4A	1.4733(19)	C3B-C4B	1.471(2)
C4A-C5A	1.3989(18)	C4B-C9B	1.4025(19)
C4A-C9A	1.4052(19)	C4B-C5B	1.4065(19)
C5A-C6A	1.387(2)	C5B-C6B	1.383(2)
C5A-H5A	0.95(2)	C5B-H5B	0.982(19)
C6A-C7A	1.394(2)	C6B-C7B	1.390(2)
C6A-H6A	1.001(19)	C6B-H6B	1.00(2)
C7A-C8A	1.380(2)	C7B-C8B	1.388(2)
C7A-H7A	0.94(2)	C7B-H7B	0.95(2)
C8A-C9A	1.392(2)	C8B-C9B	1.384(2)
C8A-H8A	0.99(2)	C8B-H8B	0.98(2)
C10A-C11A	1.4908(18)	C10B-C18B	1.497(2)
C10A-C18A	1.5043(19)	C10B-C11B	1.4995(18)
C11A-C12A	1.4855(19)	C11B-C12B	1.481(2)
C12A-C13A	1.383(2)	C12B-C17B	1.3916(19)
C12A-C17A	1.3924(19)	C12B-C13B	1.396(2)

Table 7. *Cont*

C13A-C14A	1.383(2)	C13B-C14B	1.379(3)
C13A-H13A	0.96(2)	C13B-H13B	0.91(2)
C14A-C15A	1.394(2)	C14B-C15B	1.395(2)
C14A-H14A	0.94(2)	C14B-H14B	1.00(2)
C15A-C16A	1.393(2)	C15B-C16B	1.392(2)
C15A-H15A	0.93(2)	C15B-H15B	0.98(2)
C16A-C17A	1.388(2)	C16B-C17B	1.385(2)
C16A-H16A	0.98(2)	C16B-H16B	0.965(19)
C17A-C18A	1.4870(19)	C17B-C18B	1.489(2)

Table 8. Bond Angles for *1d*.

O1A-C1A-C9A	127.32(14)	O1B-C1B-C9B	126.54(14)
O1A-C1A-C2A	125.28(13)	O1B-C1B-C2B	126.15(13)
C9A-C1A-C2A	107.40(11)	C9B-C1B-C2B	107.30(11)
C1A-C2A-C3A	105.20(11)	C1B-C2B-C3B	105.54(11)
C1A-C2A-H2A1	111.6(11)	C1B-C2B-H2B1	110.9(13)
C3A-C2A-H2A1	112.2(11)	C3B-C2B-H2B1	111.4(13)
C1A-C2A-H2A2	109.2(11)	C1B-C2B-H2B2	110.3(11)
C3A-C2A-H2A2	110.9(11)	C3B-C2B-H2B2	108.3(11)
H2A1-C2A-H2A2	107.7(16)	H2B1-C2B-H2B2	110.2(18)
C10A-C3A-C4A	131.31(12)	C10B-C3B-C4B	131.19(12)
C10A-C3A-C2A	121.27(12)	C10B-C3B-C2B	121.63(13)
C4A-C3A-C2A	107.40(11)	C4B-C3B-C2B	107.18(12)
C5A-C4A-C9A	118.44(12)	C9B-C4B-C5B	118.01(13)
C5A-C4A-C3A	131.98(13)	C9B-C4B-C3B	109.95(12)
C9A-C4A-C3A	109.58(12)	C5B-C4B-C3B	132.01(13)
C6A-C5A-C4A	118.86(13)	C6B-C5B-C4B	118.54(14)
C6A-C5A-H5A	118.3(12)	C6B-C5B-H5B	121.1(11)
C4A-C5A-H5A	122.8(12)	C4B-C5B-H5B	120.3(11)
C5A-C6A-C7A	121.72(13)	C5B-C6B-C7B	122.40(14)
C5A-C6A-H6A	121.2(11)	C5B-C6B-H6B	119.2(12)
C7A-C6A-H6A	117.1(11)	C7B-C6B-H6B	118.4(12)
C8A-C7A-C6A	120.41(14)	C8B-C7B-C6B	120.00(15)
C8A-C7A-H7A	116.4(12)	C8B-C7B-H7B	119.7(12)
C6A-C7A-H7A	123.2(12)	C6B-C7B-H7B	120.2(12)
C7A-C8A-C9A	117.96(14)	C9B-C8B-C7B	117.68(14)
C7A-C8A-H8A	121.9(13)	C9B-C8B-H8B	118.1(12)
C9A-C8A-H8A	120.2(13)	C7B-C8B-H8B	124.2(12)
C8A-C9A-C4A	122.55(13)	C8B-C9B-C4B	123.35(13)
C8A-C9A-C1A	127.40(13)	C8B-C9B-C1B	126.87(13)
C4A-C9A-C1A	110.03(12)	C4B-C9B-C1B	109.78(13)
C3A-C10A-C11A	130.45(12)	C3B-C10B-C18B	123.44(12)
C3A-C10A-C18A	123.28(12)	C3B-C10B-C11B	130.22(13)
C11A-C10A-C18A	106.27(11)	C18B-C10B-C11B	106.33(12)
O2A-C11A-C12A	123.76(13)	O2B-C11B-C12B	124.59(13)

Table 8. *Cont.*

O2A-C11A-C10A	128.89(12)	O2B-C11B-C10B	128.62(14)
C12A-C11A-C10A	107.32(11)	C12B-C11B-C10B	106.68(12)
C13A-C12A-C17A	121.39(13)	C17B-C12B-C13B	120.75(14)
C13A-C12A-C11A	128.82(13)	C17B-C12B-C11B	110.53(12)
C17A-C12A-C11A	109.79(11)	C13B-C12B-C11B	128.72(14)
C14A-C13A-C12A	118.02(15)	C14B-C13B-C12B	118.09(15)
C14A-C13A-H13A	121.9(11)	C14B-C13B-H13B	123.2(12)
C12A-C13A-H13A	120.1(11)	C12B-C13B-H13B	118.7(12)
C13A-C14A-C15A	120.83(14)	C13B-C14B-C15B	121.28(15)
C13A-C14A-H14A	115.4(12)	C13B-C14B-H14B	124.6(12)
C15A-C14A-H14A	123.7(12)	C15B-C14B-H14B	114.1(12)
C16A-C15A-C14A	121.30(15)	C16B-C15B-C14B	120.57(16)
C16A-C15A-H15A	119.2(13)	C16B-C15B-H15B	118.2(12)
C14A-C15A-H15A	119.5(13)	C14B-C15B-H15B	121.2(12)
C17A-C16A-C15A	117.51(15)	C17B-C16B-C15B	118.27(15)
C17A-C16A-H16A	119.1(12)	C17B-C16B-H16B	121.7(11)
C15A-C16A-H16A	123.4(12)	C15B-C16B-H16B	120.0(11)
C16A-C17A-C12A	120.94(13)	C16B-C17B-C12B	121.03(14)
C16A-C17A-C18A	129.38(13)	C16B-C17B-C18B	129.85(14)
C12A-C17A-C18A	109.68(11)	C12B-C17B-C18B	109.11(13)
O3A-C18A-C17A	125.54(13)	O3B-C18B-C17B	125.12(14)
O3A-C18A-C10A	127.53(13)	O3B-C18B-C10B	127.65(14)
C17A-C18A-C10A	106.93(11)	C17B-C18B-C10B	107.22(11)

Table 9. Torsion Angles for *1d*.

O1A-C1A-C2A-C3A	173.35(14)	O1B-C1B-C2B-C3B	173.77(14)
C9A-C1A-C2A-C3A	−5.93(15)	C9B-C1B-C2B-C3B	−5.04(14)
C1A-C2A-C3A-C10A	−172.45(12)	C1B-C2B-C3B-C10B	−175.90(12)
C1A-C2A-C3A-C4A	6.20(14)	C1B-C2B-C3B-C4B	4.41(14)
C10A-C3A-C4A-C5A	−6.6(2)	C10B-C3B-C4B-C9B	178.21(14)
C2A-C3A-C4A-C5A	174.97(14)	C2B-C3B-C4B-C9B	−2.13(15)
C10A-C3A-C4A-C9A	174.20(13)	C10B-C3B-C4B-C5B	−3.9(2)
C2A-C3A-C4A-C9A	−4.26(15)	C2B-C3B-C4B-C5B	175.74(14)
C9A-C4A-C5A-C6A	−2.2(2)	C9B-C4B-C5B-C6B	−0.83(19)
C3A-C4A-C5A-C6A	178.62(13)	C3B-C4B-C5B-C6B	−178.57(14)
C4A-C5A-C6A-C7A	0.3(2)	C4B-C5B-C6B-C7B	−0.5(2)
C5A-C6A-C7A-C8A	1.6(2)	C5B-C6B-C7B-C8B	1.6(2)
C6A-C7A-C8A-C9A	−1.5(2)	C6B-C7B-C8B-C9B	−1.3(2)
C7A-C8A-C9A-C4A	−0.5(2)	C7B-C8B-C9B-C4B	0.0(2)
C7A-C8A-C9A-C1A	−179.00(14)	C7B-C8B-C9B-C1B	−179.50(14)
C5A-C4A-C9A-C8A	2.4(2)	C5B-C4B-C9B-C8B	1.1(2)
C3A-C4A-C9A-C8A	−178.25(13)	C3B-C4B-C9B-C8B	179.32(13)
C5A-C4A-C9A-C1A	−178.91(12)	C5B-C4B-C9B-C1B	−179.32(12)
C3A-C4A-C9A-C1A	0.45(15)	C3B-C4B-C9B-C1B	−1.12(15)
O1A-C1A-C9A-C8A	2.9(3)	O1B-C1B-C9B-C8B	4.7(2)

Table 9. *Cont.*

C2A-C1A-C9A-C8A	−177.83(14)	C2B-C1B-C9B-C8B	−176.51(14)
O1A-C1A-C9A-C4A	−175.70(15)	O1B-C1B-C9B-C4B	−174.87(14)
C2A-C1A-C9A-C4A	3.56(15)	C2B-C1B-C9B-C4B	3.94(15)
C4A-C3A-C10A-C11A	−2.9(2)	C4B-C3B-C10B-C18B	172.57(13)
C2A-C3A-C10A-C11A	175.35(13)	C2B-C3B-C10B-C18B	−7.0(2)
C4A-C3A-C10A-C18A	178.09(13)	C4B-C3B-C10B-C11B	−6.0(2)
C2A-C3A-C10A-C18A	−3.6(2)	C2B-C3B-C10B-C11B	174.40(13)
C3A-C10A-C11A-O2A	−1.1(2)	C3B-C10B-C11B-O2B	−8.6(2)
C18A-C10A-C11A-O2A	177.98(14)	C18B-C10B-C11B-O2B	172.65(15)
C3A-C10A-C11A-C12A	−179.17(13)	C3B-C10B-C11B-C12B	175.12(14)
C18A-C10A-C11A-C12A	−0.06(14)	C18B-C10B-C11B-C12B	−3.62(14)
O2A-C11A-C12A-C13A	2.9(2)	O2B-C11B-C12B-C17B	−173.55(14)
C10A-C11A-C12A-C13A	−178.90(13)	C10B-C11B-C12B-C17B	2.91(15)
O2A-C11A-C12A-C17A	−177.23(13)	O2B-C11B-C12B-C13B	6.2(2)
C10A-C11A-C12A-C17A	0.94(15)	C10B-C11B-C12B-C13B	−177.33(14)
C17A-C12A-C13A-C14A	−0.1(2)	C17B-C12B-C13B-C14B	−0.9(2)
C11A-C12A-C13A-C14A	179.72(14)	C11B-C12B-C13B-C14B	179.39(14)
C12A-C13A-C14A-C15A	0.7(2)	C12B-C13B-C14B-C15B	1.0(2)
C13A-C14A-C15A-C16A	−0.5(2)	C13B-C14B-C15B-C16B	0.0(3)
C14A-C15A-C16A-C17A	−0.5(2)	C14B-C15B-C16B-C17B	−1.2(2)
C15A-C16A-C17A-C12A	1.1(2)	C15B-C16B-C17B-C12B	1.3(2)
C15A-C16A-C17A-C18A	−177.97(13)	C15B-C16B-C17B-C18B	−178.14(15)
C13A-C12A-C17A-C16A	−0.8(2)	C13B-C12B-C17B-C16B	−0.3(2)
C11A-C12A-C17A-C16A	179.30(13)	C11B-C12B-C17B-C16B	179.50(13)
C13A-C12A-C17A-C18A	178.41(12)	C13B-C12B-C17B-C18B	179.26(13)
C11A-C12A-C17A-C18A	−1.45(15)	C11B-C12B-C17B-C18B	−0.96(16)
C16A-C17A-C18A-O3A	1.4(2)	C16B-C17B-C18B-O3B	−0.8(2)
C12A-C17A-C18A-O3A	−177.79(14)	C12B-C17B-C18B-O3B	179.73(14)
C16A-C17A-C18A-C10A	−179.45(13)	C16B-C17B-C18B-C10B	178.11(15)
C12A-C17A-C18A-C10A	1.39(15)	C12B-C17B-C18B-C10B	−1.38(15)
C3A-C10A-C18A-O3A	−2.4(2)	C3B-C10B-C18B-O3B	3.1(2)
C11A-C10A-C18A-O3A	178.39(14)	C11B-C10B-C18B-O3B	−178.05(15)
C3A-C10A-C18A-C17A	178.42(12)	C3B-C10B-C18B-C17B	−175.76(12)
C11A-C10A-C18A-C17A	−0.77(14)	C11B-C10B-C18B-C17B	3.10(14)

2. Compound **2c**

Experimental for C$_{13}$H$_6$F$_6$O$_3$ (2c)

Data Collection and Processing. The sample **2c** was submitted by Joseph Sloop of the Sloop research group at Georgia Gwinnett College. The sample was mounted on a nylon loop with a small amount of NVH immersion oil. All X-ray measurements were made on a Bruker-Nonius X8 Apex2 diffractometer at a temperature of 173 K. The unit cell dimensions were determined from a symmetry constrained fit of 9959 reflections with 5.28° < 2θ < 57.7°. The data collection strategy was a number of ω and φ scans which collected data up to 57.74° (2θ). The frame integration was performed using

SAINT+ [29]. The resulting raw data was scaled and absorption corrected using a multi-scan averaging of symmetry equivalent data using SADABS [30].

Structure Solution and Refinement. The structure was solved by direct methods using the SIR92 program [31]. All non-hydrogen atoms were obtained from the initial E-map. The hydrogen atoms were introduced at idealized positions and were allowed to refine isotropically. The structural model was fit to the data using full matrix least-squares based on F. The calculated structure factors included corrections for anomalous dispersion from the usual tabulation. The structure was refined using the LSTSQ program from NRCVAX [33], graphic plots were produced using the NRCVAX crystallographic program suite. Additional information and other relevant literature references can be found in the reference section of the Facility's Web page (http://www.xray.ncsu.edu).

Figure 12. ORTEP drawing of *2c* showing naming and numbering scheme. Ellipsoids are at the 50%.
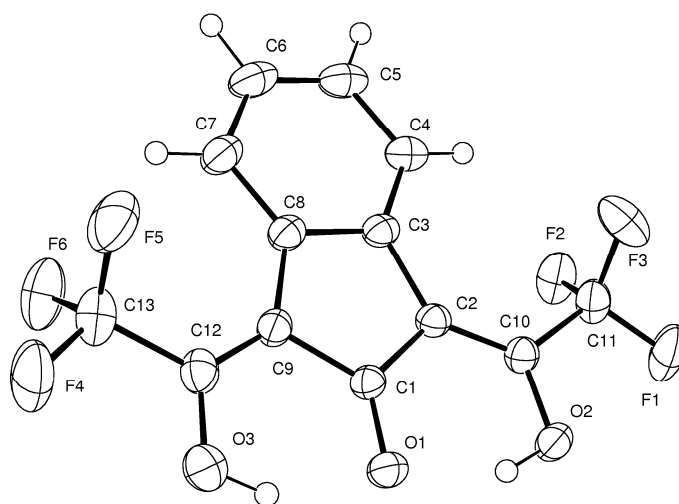

Figure 13. ORTEP drawing of *2c*. Ellipsoids are at the 50% probability level and hydrogen atoms were drawn with arbitrary radii for clarity.
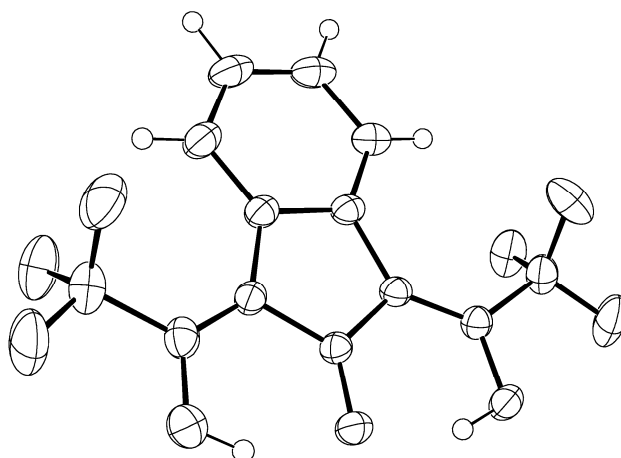
Figure 14. Stereoscopic ORTEP drawing of *2c*. Ellipsoids are at the 50% probability level and hydrogen atoms were drawn with arbitrary radii for clarity.
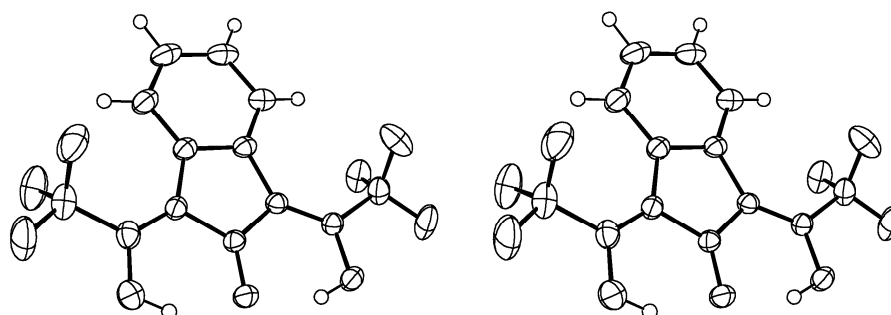

Table 10. Summary of Crystal Data for *2c*.

Formula	$C_{13}H_6F_6O_3$
Formula Weight (*g/mol*)	324.18
Crystal Dimensions (*mm*)	$1.20 \times 0.10 \times 0.06$
Crystal Color and Habit	yellow needle
Crystal System	monoclinic
Space Group	P 2_1/c
Temperature, K	173
a, Å	4.7643(3)
b, Å	18.6978(12)
c, Å	13.8431(9)
α,°	90.0
β,°	98.964(3)
γ,°	90.0
V, Å^3	1218.11(14)
Number of reflections to determine final unit cell	9959
Min and Max 2θ for cell determination, °	5.28, 57.7
Z	4
F(000)	648.71
ρ (*g/cm*)	1.768
λ, Å, (MoKα)	0.71073
μ, (*cm^{-1}*)	0.18
Diffractometer Type	Bruker-Nonius X8 Apex2
Scan Type(s)	omega and phi scans
Max 2θ for data collection, °	57.74
Measured fraction of data	0.98
Number of reflections measured	26516
Unique reflections measured	3195
R$_{merge}$	0.027
Number of reflections included in refinement	2755
Cut off Threshold Expression	Inet > 1.0 sigma(Inet)
Structure refined using	full matrix least-squares using F
Weighting Scheme	$1/(sigma^2(F) + 0.0005F^2)$

Table 10. *Cont.*

Number of parameters in least-squares	223
R_f	0.038
R_w	0.053
R_f(all data)	0.046
R_w (all data)	0.054
GOF	1.74
Maximum shift/error	0.003
Min & Max peak heights on final ΔF Map (e^-/Å)	-0.30, 0.35

Where:

$R_f = \Sigma(|F_O - F_C|) / \Sigma F_O$

$R_W = [\Sigma(w(F_O - F_C)^2) / \Sigma(F_O^2)]^{\frac{1}{2}}$

$GOF = [\Sigma(w(F_O - F_C)^2) / (\text{No. of reflns.} - \text{No. of params.})]^{\frac{1}{2}}$

Table 11. Atomic Coordinates for *2c*.

Atom	x	y	z	$U_{iso/equiv}$
O1	0.81730(18)	0.99675(5)	0.07954(6)	0.0316(4)
O2	0.77456(19)	1.10306(5)	−0.04046(7)	0.0328(5)
O3	0.8507(2)	0.90513(5)	0.22145(8)	0.0392(5)
C1	0.6645(2)	1.03312(6)	0.12739(8)	0.0244(5)
C2	0.5495(2)	1.10365(6)	0.10029(9)	0.0243(5)
C3	0.3836(2)	1.12503(7)	0.17672(8)	0.0257(5)
C4	0.2245(3)	1.18602(8)	0.18650(10)	0.0319(6)
C5	0.0812(3)	1.19205(8)	0.26621(11)	0.0377(7)
C6	0.0964(3)	1.13855(8)	0.33508(11)	0.0396(7)
C7	0.2560(3)	1.07730(8)	0.32738(10)	0.0352(6)
C8	0.4020(2)	1.07009(7)	0.24809(9)	0.0270(5)
C9	0.5808(2)	1.01187(6)	0.22025(8)	0.0263(5)
C10	0.6161(2)	1.13484(7)	0.01809(9)	0.0259(5)
C11	0.5253(3)	1.20877(7)	−0.01820(11)	0.0337(6)
C12	0.6894(3)	0.95005(7)	0.26242(9)	0.0311(6)
C13	0.6515(3)	0.92528(8)	0.36396(11)	0.0401(7)
F1	0.61454(20)	1.22376(5)	−0.10179(7)	0.0526(5)
F2	0.24328(16)	1.21541(5)	−0.03293(6)	0.0430(4)
F3	0.62851(20)	1.25846(5)	0.04657(7)	0.0526(5)
F4	0.8000(2)	0.86675(5)	0.39034(7)	0.0592(6)
F5	0.7410(2)	0.97545(6)	0.43055(6)	0.0548(5)
F6	0.38149(19)	0.91237(6)	0.37079(7)	0.0579(5)
H2	0.822(4)	1.0603(13)	−0.0133(14)	0.064(6)
H3	0.877(5)	0.9223(11)	0.1643(16)	0.072(6)
H4	0.213(3)	1.2212(8)	0.1414(11)	0.030(4)
H5	−0.019(3)	1.2318(8)	0.2728(11)	0.035(4)
H6	−0.004(4)	1.1455(9)	0.3899(12)	0.045(4)
H7	0.272(3)	1.0418(9)	0.3767(12)	0.039(4)

Table 12. Anisotropic Displacement Parameters for *2c*.

Atom	u^{11}	u^{22}	u^{33}	u^{12}	u^{13}	u^{23}
O1	0.0384(5)	0.0291(5)	0.0291(5)	0.0065(4)	0.0112(4)	0.0003(4)
O2	0.0380(5)	0.0333(5)	0.0302(5)	0.0053(4)	0.0146(4)	0.0045(4)
O3	0.0482(6)	0.0321(5)	0.0380(6)	0.0067(4)	0.0085(5)	0.0061(4)
C1	0.0264(5)	0.0255(6)	0.0214(5)	−0.0027(5)	0.0040(4)	−0.0019(4)
C2	0.0245(5)	0.0243(6)	0.0243(5)	−0.0014(5)	0.0042(4)	−0.0029(4)
C3	0.0230(5)	0.0294(6)	0.0248(6)	−0.0045(5)	0.0042(4)	−0.0063(5)
C4	0.0303(6)	0.0330(7)	0.0321(6)	0.0012(5)	0.0041(5)	−0.0072(5)
C5	0.0313(6)	0.0419(8)	0.0407(7)	0.0023(6)	0.0084(6)	−0.0160(6)
C6	0.0341(6)	0.0531(9)	0.0343(7)	−0.0067(6)	0.0139(6)	−0.0166(7)
C7	0.0358(7)	0.0441(8)	0.0275(6)	−0.0092(6)	0.0112(5)	−0.0064(6)
C8	0.0255(5)	0.0316(6)	0.0242(6)	−0.0068(5)	0.0051(4)	−0.0053(5)
C9	0.0290(5)	0.0282(6)	0.0222(6)	−0.0067(5)	0.0054(5)	−0.0015(4)
C10	0.0241(5)	0.0270(6)	0.0271(6)	−0.0010(5)	0.0051(4)	0.0005(5)
C11	0.0293(6)	0.0323(7)	0.0409(7)	0.0007(5)	0.0096(5)	0.0079(5)
C12	0.0324(6)	0.0314(7)	0.0291(6)	−0.0071(5)	0.0031(5)	0.0023(5)
C13	0.0380(7)	0.0444(8)	0.0374(7)	−0.0058(6)	0.0045(6)	0.0128(6)
F1	0.0516(5)	0.0533(6)	0.0594(6)	0.0131(4)	0.0287(5)	0.0306(5)
F2	0.0296(4)	0.0493(5)	0.0507(5)	0.0088(4)	0.0084(4)	0.0178(4)
F3	0.0538(5)	0.0258(4)	0.0750(7)	0.0008(4)	0.0006(5)	−0.0021(4)
F4	0.0650(6)	0.0577(6)	0.0569(6)	0.0082(5)	0.0154(5)	0.0322(5)
F5	0.0661(6)	0.0702(7)	0.0276(4)	−0.0148(5)	0.0057(4)	0.0044(4)
F6	0.0427(5)	0.0755(7)	0.0574(6)	−0.0133(5)	0.0133(4)	0.0236(5)

Table 13. Bond Lengths for *2c*.

O1-C1	1.2576(15)	C6-C7	1.388(2)
O2-C10	1.3308(15)	C6-H6	0.967(18)
O2-H2	0.90(2)	C7-C8	1.3944(18)
O3-C12	1.3242(17)	C7-H7	0.947(17)
O3-H3	0.88(2)	C8-C9	1.4703(18)
C1-C2	1.4547(17)	C9-C12	1.3602(18)
C1-C9	1.4590(17)	C10-C11	1.5108(18)
C2-C3	1.4714(17)	C11-F1	1.3235(16)
C2-C10	1.3593(17)	C11-F2	1.3329(15)
C3-C4	1.3876(18)	C11-F3	1.3311(17)
C3-C8	1.4186(18)	C12-C13	1.5173(19)
C4-C5	1.3893(20)	C13-F4	1.3233(18)
C4-H4	0.903(15)	C13-F5	1.3375(18)
C5-C6	1.376(2)	C13-F6	1.3267(17)
C5-H5	0.896(17)		

Table 14. Bond Angles for *2c*.

C10-O2-H2	105.8(12)	C3-C8-C9	109.21(10)
C12-O3-H3	109.1(14)	C7-C8-C9	131.18(12)
O1-C1-C2	125.45(11)	C1-C9-C8	106.17(10)
O1-C1-C9	125.23(11)	C1-C9-C12	118.14(11)
C2-C1-C9	109.30(10)	C8-C9-C12	135.54(12)

Table 14. *Cont.*

C1-C2-C3	106.48(10)	O2-C10-C2	123.15(11)
C1-C2-C10	118.51(11)	O2-C10-C11	111.48(11)
C3-C2-C10	134.99(11)	C2-C10-C11	125.36(11)
C2-C3-C4	131.02(12)	C10-C11-F1	111.72(11)
C2-C3-C8	108.80(10)	C10-C11-F2	111.45(10)
C4-C3-C8	120.17(11)	C10-C11-F3	110.99(11)
C3-C4-C5	119.18(14)	F1-C11-F2	107.46(11)
C3-C4-H4	120.4(9)	F1-C11-F3	107.80(11)
C5-C4-H4	120.4(9)	F2-C11-F3	107.21(11)
C4-C5-C6	120.80(14)	O3-C12-C9	124.23(12)
C4-C5-H5	119.0(10)	O3-C12-C13	111.34(12)
C6-C5-H5	120.2(10)	C9-C12-C13	124.39(13)
C5-C6-C7	121.13(13)	C12-C13-F4	111.87(13)
C5-C6-H6	117.8(10)	C12-C13-F5	110.68(11)
C7-C6-H6	121.0(10)	C12-C13-F6	112.22(11)
C6-C7-C8	119.11(14)	F4-C13-F5	106.89(12)
C6-C7-H7	120.5(9)	F4-C13-F6	108.20(12)
C8-C7-H7	120.3(9)	F5-C13-F6	106.69(13)
C3-C8-C7	119.60(12)		

Table 15. Torsion Angles for *2c*.

O1-C1-C2-C3	179.6(2)	C8-C3-C4-C5	−0.78(13)
O1-C1-C2-C10	−1.91(11)	C2-C3-C8-C7	−178.6(3)
C9-C1-C2-C3	−1.90(11)	C2-C3-C8-C9	0.26(11)
C9-C1-C2-C10	176.6(2)	C4-C3-C8-C7	0.88(13)
O1-C1-C9-C8	−179.4(3)	C4-C3-C8-C9	179.7(3)
O1-C1-C9-C12	4.37(11)	C3-C4-C5-C6	0.17(13)
C2-C1-C9-C8	2.04(11)	C4-C5-C6-C7	0.35(13)
C2-C1-C9-C12	−174.2(3)	C5-C6-C7-C8	−0.25(13)
C1-C2-C3-C4	−178.4(2)	C6-C7-C8-C3	−0.36(13)
C1-C2-C3-C8	1.00(11)	C6-C7-C8-C9	−178.9(3)
C10-C2-C3-C4	3.44(12)	C3-C8-C9-C1	−1.41(11)
C10-C2-C3-C8	−177.2(3)	C3-C8-C9-C12	173.8(3)
C1-C2-C10-O2	2.08(10)	C7-C8-C9-C1	177.3(3)
C1-C2-C10-C11	−177.3(2)	C7-C8-C9-C12	−7.50(13)
C3-C2-C10-O2	−179.9(2)	C1-C9-C12-O3	−4.98(11)
C3-C2-C10-C11	0.67(11)	C1-C9-C12-C13	172.4(3)
C2-C3-C4-C5	178.6(3)		

3. Compound **3d**

Experimental for C$_{12}$H$_7$F$_3$O$_2$ (3d)

Data Collection and Processing. The sample **3d** was submitted by Joseph Sloop of the Sloop research group at Georgia Gwinnett College. The sample was mounted on a nylon loop with a small

amount of NVH immersion oil. All X-ray measurements were made on a Bruker-Nonius X8 Apex2 diffractometer at a temperature of 110 K. The unit cell dimensions were determined from a symmetry constrained fit of 5859 reflections with $5.44° < 2\theta < 52.66°$. The data collection strategy was a number of ω and φ scans which collected data up to 62.92° (2θ). The frame integration was performed using SAINT [29]. The resulting raw data was scaled and absorption corrected using a multi-scan averaging of symmetry equivalent data using SADABS [30].

Structure Solution and Refinement. The structure was solved by direct methods using the SIR92 program [31]. All non-hydrogen atoms were obtained from the initial solution. The carbon bound hydrogen atoms were introduced at idealized positions while the hydroxy hydrogen atom position was obtained from a diffeence Fourier map. All hydrogen atoms were allowed to refine isotropically. The structural model was fit to the data using full matrix least-squares based on F^2. The calculated structure factors included corrections for anomalous dispersion from the usual tabulation. The space group is achiral, therefore the structure has an absolute sense to it. However, the anomalous scattering signal is weak due to the absence of any atoms heavier than F, and the absolute structure could not be definitively determined. The structure was refined using the XL program from SHELXTL [32], graphic plots were produced using the NRCVAX crystallographic program suite. Additional information and other relevant literature references can be found in the reference section of the Facility's Web page (http://www.xray.ncsu.edu).

Figure 15. ORTEP drawing of *3d* showing naming and numbering scheme. Ellipsoids are at the 50% probability level and hydrogen atoms were drawn with arbitrary radii for clarity.
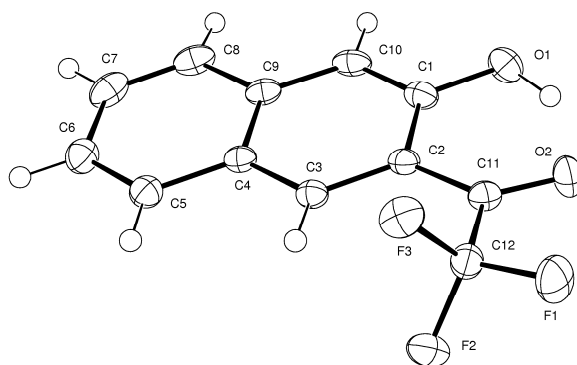
Figure 16. ORTEP drawing of *3d*. Ellipsoids are at the 50% probability level and hydrogen atoms were drawn with arbitrary radii for clarity.
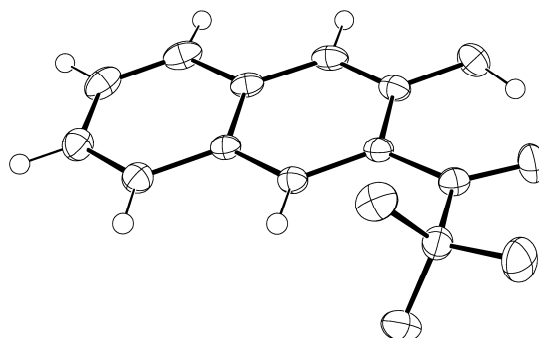
Figure 17. Stereoscopic ORTEP drawing of *3d*. Ellipsoids are at the 50% probability level and hydrogen atoms were drawn with arbitrary radii for clarity.
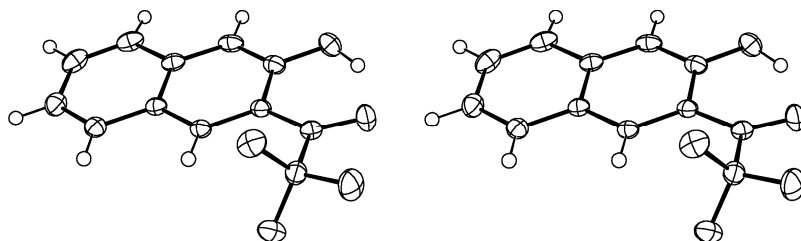
Table 16. Summary of Crystal Data for *3d*.

Formula	$C_{12}H_7F_3O_2$
Formula Weight (*g/mol*)	240.18
Crystal Dimensions (*mm*)	$0.46 \times 0.08 \times 0.04$
Crystal Color and Habit	orange yellow needle
Crystal System	orthorhombic
Space Group	P n a 2_1
Temperature, K	110
a, Å	13.5923(5)
b, Å	14.9695(5)
c, Å	4.8381(2)
α,°	90.00
β,°	90.00
γ,°	90.00
V, Å^3	984.41(6)
Number of reflections to determine final unit cell	5859
Min and Max 2θ for cell determination, °	5.44, 52.66
Z	4
F(000)	488
ρ (*g/cm*)	1.621
λ, Å, (MoKα)	0.71070
μ, (*cm^{-1}*)	0.147
Diffractometer Type	Bruker-Nonius X8 Apex2
Scan Type(s)	omega and phi scans
Max 2θ for data collection, °	62.92
Measured fraction of data	0.874
Number of reflections measured	21568
Unique reflections measured	2632
R_{merge}	0.0444
Number of reflections included in refinement	2632
Cut off Threshold Expression	>2sigma(I)
Structure refined using	full matrix least-squares using F^2
Weighting Scheme	calc w = 1/[sigma^2(Fo^2) + (0.0406P)^2 + 0.0000P] where P=(Fo^2 + 2Fc^2)/3
Number of parameters in least-squares	182

Table 16. *Cont.*

R_1	0.0370
wR_2	0.0712
R_1 (all data)	0.0538
wR_2 (all data)	0.0762
GOF	1.035
Maximum shift/error	0.000
Min & Max peak heights on final ΔF Map (e^-/Å)	−0.229, 0.183

Where:

$R_1 = \Sigma(\, |F_O| - |F_C| \,) \, / \, \Sigma F_O$

$wR_2 = [\, \Sigma(\, w(\, F_O^2 - F_C^2 \,)^2 \,) \, / \, \Sigma(w \, F_O^4 \,) \,]^{1/2}$

$GOF = [\, \Sigma(\, w(\, F_O^2 - F_C^2 \,)^2 \,) \, / \, (\text{No. of reflns.} - \text{No. of params.} \,) \,]^{1/2}$

Table 17. Atomic Coordinates for *3d*.

Atom	x	y	z	$U_{iso/equiv}$
O1	0.11391(8)	0.26937(8)	0.6424(3)	0.0315(3)
O2	0.22469(8)	0.37533(7)	0.3464(3)	0.0294(3)
C1	0.19885(11)	0.24126(10)	0.7623(4)	0.0227(3)
C2	0.29250(11)	0.27865(9)	0.6863(4)	0.0190(3)
C3	0.37673(11)	0.24539(9)	0.8101(4)	0.0193(3)
C4	0.37205(11)	0.17792(10)	1.0120(4)	0.0192(3)
C5	0.45775(12)	0.14260(10)	1.1386(4)	0.0230(3)
C6	0.45137(13)	0.07873(10)	1.3373(4)	0.0269(3)
C7	0.35837(14)	0.04578(11)	1.4184(4)	0.0300(4)
C8	0.27466(13)	0.07695(10)	1.3003(4)	0.0275(4)
C9	0.27804(11)	0.14416(10)	1.0917(4)	0.0213(3)
C10	0.19325(12)	0.17720(11)	0.9629(4)	0.0247(3)
C11	0.29517(12)	0.35023(10)	0.4818(4)	0.0217(3)
C12	0.39217(11)	0.40275(10)	0.4367(4)	0.0224(3)
F1	0.37724(7)	0.47125(6)	0.2675	0.0341(3)
F2	0.46266(6)	0.35198(6)	0.3256(3)	0.0286(2)
F3	0.42682(6)	0.43562(6)	0.6742(3)	0.0297(2)
H1	0.1301(19)	0.3131(16)	0.500(7)	0.079(9)
H3	0.4391(12)	0.2686(10)	0.766(4)	0.022(4)
H5	0.5197(14)	0.1674(10)	1.079(4)	0.033(5)
H6	0.5078(13)	0.0544(10)	1.422(4)	0.026(4)
H7	0.3543(13)	0.0040(11)	1.553(4)	0.030(5)
H8	0.2120(15)	0.0566(12)	1.334(5)	0.053(6)

Table 18. Anisotropic Displacement Parameters for *3d*.

Atom	u^{11}	u^{22}	u^{33}	u^{12}	u^{13}	u^{23}
O1	0.0164(6)	0.0433(7)	0.0347(7)	0.0007(5)	−0.0018(5)	0.0012(6)
O2	0.0251(6)	0.0319(6)	0.0312(6)	0.0036(5)	−0.0074(6)	0.0048(6)
C1	0.0174(8)	0.0271(8)	0.0236(8)	−0.0003(6)	0.0012(6)	−0.0060(7)

Table 18. *Cont.*

C2	0.0180(8)	0.0211(7)	0.0178(7)	0.0006(6)	0.0021(6)	−0.0031(6)
C3	0.0174(8)	0.0209(7)	0.0196(7)	−0.0016(6)	0.0019(6)	−0.0013(7)
C4	0.0199(8)	0.0195(7)	0.0182(7)	−0.0011(6)	0.0023(6)	−0.0032(6)
C5	0.0249(9)	0.0212(8)	0.0229(8)	0.0011(6)	0.0005(7)	−0.0006(6)
C6	0.0338(9)	0.0226(8)	0.0245(8)	0.0051(7)	−0.0020(7)	0.0001(7)
C7	0.0471(11)	0.0208(8)	0.0223(9)	−0.0038(7)	0.0034(7)	0.0020(7)
C8	0.0324(9)	0.0256(8)	0.0247(9)	−0.0107(7)	0.0084(8)	−0.0037(7)
C9	0.0249(8)	0.0193(7)	0.0198(7)	−0.0031(6)	0.0041(6)	−0.0060(6)
C10	0.0178(8)	0.0300(8)	0.0264(8)	−0.0068(7)	0.0072(7)	−0.0062(7)
C11	0.0226(9)	0.0230(8)	0.0195(8)	0.0020(6)	0.0017(6)	−0.0026(6)
C12	0.0238(8)	0.0226(8)	0.0208(7)	0.0010(6)	−0.0013(7)	0.0006(6)
F1	0.0369(6)	0.0279(5)	0.0375(6)	−0.0005(4)	−0.0013(5)	0.0126(5)
F2	0.0238(5)	0.0291(5)	0.0329(5)	0.0011(4)	0.0082(4)	−0.0003(4)
F3	0.0309(5)	0.0300(5)	0.0282(5)	−0.0080(4)	−0.0005(4)	−0.0051(4)

Table 19. Bond Lengths for *3d*.

O1-C1	1.3588(19)	C6-C7	1.412(2)
O1-H1	0.97(3)	C6-H6	0.941(18)
O2-C11	1.2199(18)	C7-C8	1.356(2)
C1-C10	1.367(2)	C7-H7	0.905(18)
C1-C2	1.438(2)	C8-C9	1.426(2)
C2-C3	1.385(2)	C8-H8	0.92(2)
C2-C11	1.459(2)	C9-C10	1.400(2)
C3-C4	1.406(2)	C10-H10	0.939(18)
C3-H3	0.941(16)	C11-C12	1.551(2)
C4-C5	1.418(2)	C12-F1	1.3278(18)
C4-C9	1.427(2)	C12-F3	1.3356(19)
C5-C6	1.359(2)	C12-F2	1.3359(18)
C5-H5	0.963(19)		

Table 20. Bond Angles for *3d*.

C1-O1-H1	108.5(16)	C8-C7-H7	119.3(12)
O1-C1-C10	118.24(14)	C6-C7-H7	119.8(12)
O1-C1-C2	121.49(14)	C7-C8-C9	120.94(15)
C10-C1-C2	120.25(14)	C7-C8-H8	126.2(13)
C3-C2-C1	118.78(13)	C9-C8-H8	112.8(13)
C3-C2-C11	122.46(13)	C10-C9-C8	122.53(15)
C1-C2-C11	118.76(13)	C10-C9-C4	119.43(15)
C2-C3-C4	121.41(13)	C8-C9-C4	118.04(15)
C2-C3-H3	121.0(10)	C1-C10-C9	121.21(15)
C4-C3-H3	117.5(10)	C1-C10-H10	116.9(11)
C3-C4-C5	122.04(13)	C9-C10-H10	121.8(11)
C3-C4-C9	118.85(13)	O2-C11-C2	124.81(14)
C5-C4-C9	119.11(14)	O2-C11-C12	115.85(13)

Table 20. *Cont.*

C6-C5-C4	121.03(15)	C2-C11-C12	119.28(13)
C6-C5-H5	122.5(11)	F1-C12-F3	107.45(12)
C4-C5-H5	116.5(11)	F1-C12-F2	107.51(13)
C5-C6-C7	119.96(16)	F3-C12-F2	107.63(12)
C5-C6-H6	121.7(10)	F1-C12-C11	110.39(12)
C7-C6-H6	118.3(10)	F3-C12-C11	111.44(13)
C8-C7-C6	120.91(16)	F2-C12-C11	112.21(12)

Table 21. Torsion Angles for *3d*.

O1-C1-C2-C3	−178.15(14)	C3-C4-C9-C8	−178.87(13)
C10-C1-C2-C3	3.2(2)	C5-C4-C9-C8	1.1(2)
O1-C1-C2-C11	1.9(2)	O1-C1-C10-C9	178.95(14)
C10-C1-C2-C11	−176.80(13)	C2-C1-C10-C9	−2.3(2)
C1-C2-C3-C4	−1.6(2)	C8-C9-C10-C1	−179.58(14)
C11-C2-C3-C4	178.34(13)	C4-C9-C10-C1	−0.1(2)
C2-C3-C4-C5	179.37(14)	C3-C2-C11-O2	171.95(15)
C2-C3-C4-C9	−0.7(2)	C1-C2-C11-O2	−8.1(2)
C3-C4-C5-C6	178.62(14)	C3-C2-C11-C12	−11.0(2)
C9-C4-C5-C6	−1.3(2)	C1-C2-C11-C12	168.99(13)
C4-C5-C6-C7	0.7(2)	O2-C11-C12-F1	4.49(18)
C5-C6-C7-C8	0.1(2)	C2-C11-C12-F1	−172.83(12)
C6-C7-C8-C9	−0.3(2)	O2-C11-C12-F3	123.80(14)
C7-C8-C9-C10	179.23(15)	C2-C11-C12-F3	−53.51(17)
C7-C8-C9-C4	−0.3(2)	O2-C11-C12-F2	−115.41(15)
C3-C4-C9-C10	1.6(2)	C2-C11-C12-F2	67.28(18)
C5-C4-C9-C10	−178.48(14)		

4. Compound **4c**

Experimental for $C_{12}H_9F_3O_2$ (4c)

Data Collection and Processing. The sample **4c** was submitted by Joseph Sloop of the Sloop research group at Georgia Gwinnett College. The sample was mounted on a nylon loop with a small amount of Paratone N oil. All X-ray measurements were made on a Bruker-Nonius Kappa Axis X8 Apex2 diffractometer at a temperature of 110 K. The unit cell dimensions were determined from a symmetry constrained fit of 6416 reflections with $5.78° < 2\theta < 71.38°$. The data collection strategy was a number of ω and φ scans which collected data up to 71.58° (2θ). The frame integration was performed using SAINT [29]. The resulting raw data was scaled and absorption corrected using a multi-scan averaging of symmetry equivalent data using SADABS [30].

Structure Solution and Refinement. The structure was solved by direct methods using the XS program [31]. All non-hydrogen atoms were obtained from the initial solution. The hydrogen atoms were located from a difference Fourier map and were allowed to refine isotropically. The structural model was fit to the data using full matrix least-squares based on F^2. The calculated structure factors included corrections for anomalous dispersion from the usual tabulation. The structure was refined

using the XL program from SHELXTL [32], graphic plots were produced using the NRCVAX crystallographic program suite. Additional information and other relevant literature references can be found in the reference section of the Facility's Web page (http://www.xray.ncsu.edu).

Figure 18. ORTEP drawing of *4c* showing naming and numbering scheme. Ellipsoids are at the 50% probability level and hydrogen atoms were drawn with arbitrary radii for clarity.
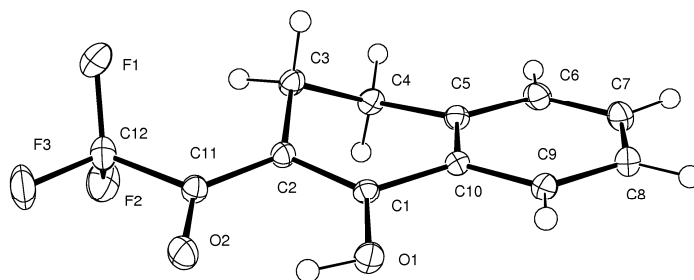
Figure 19. ORTEP drawing of *4c*. Ellipsoids are at the 50% probability level and hydrogen atoms were drawn with arbitrary radii for clarity.
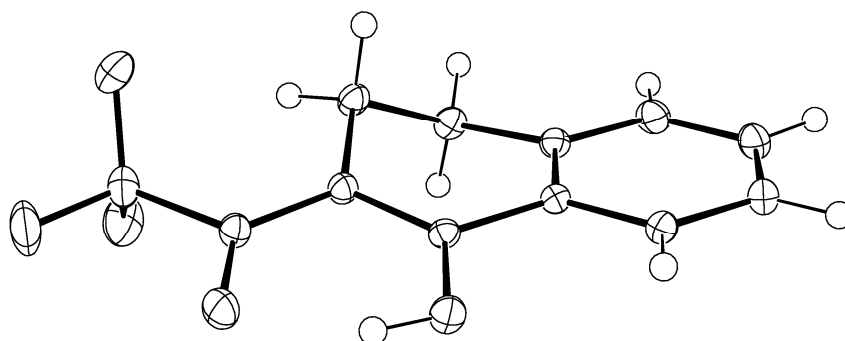
Figure 20. Stereoscopic ORTEP drawing of *4c*. Ellipsoids are at the 50% probability level and hydrogen atoms were drawn with arbitrary radii for clarity.
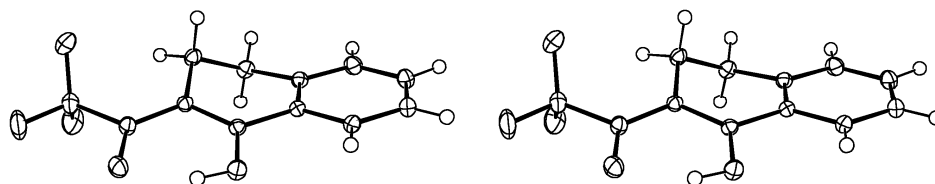
Table 22. Summary of Crystal Data for *4c*.

Formula	$C_{12}H_9F_3O_2$
Formula Weight (*g*/*mol*)	242.19
Crystal Dimensions (*mm*)	$0.38 \times 0.28 \times 0.04$
Crystal Color and Habit	colourless plate
Crystal System	triclinic
Space Group	P -1

Table 22. *Cont.*

Temperature, K	110
a, Å	7.3528(2)
b, Å	7.9165(2)
c, Å	9.7991(2)
α,°	73.0533(11)
β,°	85.3968(12)
γ,°	68.3581(11)
V, Å^3	506.92(2)
Reflections to determine final unit cell	6416
Min and Max 2θ for cell determination, °	5.78, 71.38
Z	2
F(000)	248
ρ (*g/cm*)	1.587
λ, Å, (MoK)	0.71073
μ, (cm^{-1})	0.143
Number of reflections measured	20479
Unique reflections measured	4691
R_{merge}	0.0265
Number of reflections included in refinement	4691
Cut off Threshold Expression	>2sigma(I)
Structure refined using	full matrix least-squares using F^2
Weighting Scheme	$w = 1/[\text{sigma}^2(F_o^2) + (0.0707P)^2 + 0.0436P]$ where $P = (F_o^2 + 2F_c^2)/3$
R_1	0.0382
wR_2	0.1082
R_1 (all data)	0.0525
wR_2 (all data)	0.1220
GOF	1.048

Where:

$R_1 = \Sigma(|F_o| - |F_c|) / \Sigma F_o$

$wR_2 = [\Sigma(w(F_o^2 - F_c^2)^2) / \Sigma(w F_o^4)]^{\frac{1}{2}}$

$GOF = [\Sigma(w(F_o^2 - F_c^2)^2) / (\text{No. of reflns.} - \text{No. of params.})]^{\frac{1}{2}}$

Table 23. Atomic Coordinates for *4c*.

Atom	x	y	z	$U_{iso/equiv}$
O1	0.77448(8)	0.28007(9)	0.27345(6)	0.01748(12)
O2	0.99446(9)	0.28522(9)	0.06442(6)	0.02064(13)
C1	0.92164(10)	0.26838(10)	0.34926(7)	0.01305(12)
C2	1.10003(10)	0.26974(10)	0.29126(8)	0.01358(12)
C3	1.25154(11)	0.27188(11)	0.38557(8)	0.01584(13)
C4	1.24786(11)	0.15172(11)	0.53827(8)	0.01618(13)

Table 23. *Cont.*

C5	1.04451(11)	0.19875(10)	0.59451(8)	0.01444(13)
C6	1.00916(12)	0.18008(12)	0.73914(8)	0.01899(15)
C7	0.82002(13)	0.21517(12)	0.78875(9)	0.02070(15)
C8	0.66361(12)	0.26962(12)	0.69526(9)	0.01971(15)
C9	0.69574(11)	0.28853(11)	0.55100(8)	0.01598(13)
C10	0.88579(10)	0.25358(10)	0.50052(7)	0.01326(12)
C11	1.12232(11)	0.27815(10)	0.14448(8)	0.01590(13)
C12	1.31898(12)	0.27354(12)	0.07494(9)	0.02008(15)
F1	1.37562(8)	0.40737(8)	0.09309(6)	0.02557(13)
F2	1.46211(8)	0.10631(8)	0.12997(6)	0.03004(14)
F3	1.30731(9)	0.29835(10)	−0.06471(6)	0.03180(15)
H1	0.818(3)	0.282(3)	0.190(2)	0.066(5)
H3A	1.2210(17)	0.4028(17)	0.3866(12)	0.018(3)
H3B	1.386(2)	0.2261(18)	0.3516(13)	0.026(3)
H4A	1.3333(19)	0.1700(17)	0.5989(13)	0.021(3)
H4B	1.2933(18)	0.0209(17)	0.5436(13)	0.020(3)
H6	1.120(2)	0.1395(19)	0.8020(14)	0.030(3)
H7	0.806(2)	0.204(2)	0.8859(17)	0.041(4)
H8	0.526(2)	0.304(2)	0.7231(14)	0.033(3)
H9	0.5882(18)	0.3326(17)	0.4836(13)	0.019(3)

Table 24. Anisotropic Displacement Parameters for *4c*.

Atom	u^{11}	u^{22}	u^{33}	u^{12}	u^{13}	u^{23}
O1	0.0149(2)	0.0246(3)	0.0147(2)	−0.0091(2)	−0.00183(19)	−0.0048(2)
O2	0.0229(3)	0.0269(3)	0.0145(2)	−0.0113(2)	−0.0001(2)	−0.0061(2)
C1	0.0127(3)	0.0135(3)	0.0133(3)	−0.0052(2)	−0.0005(2)	−0.0035(2)
C2	0.0129(3)	0.0155(3)	0.0131(3)	−0.0059(2)	0.0007(2)	−0.0042(2)
C3	0.0137(3)	0.0189(3)	0.0166(3)	−0.0081(2)	0.0007(2)	−0.0046(2)
C4	0.0134(3)	0.0184(3)	0.0162(3)	−0.0059(2)	−0.0019(2)	−0.0035(2)
C5	0.0151(3)	0.0148(3)	0.0143(3)	−0.0062(2)	0.0003(2)	−0.0044(2)
C6	0.0226(4)	0.0212(3)	0.0144(3)	−0.0091(3)	−0.0007(3)	−0.0051(3)
C7	0.0270(4)	0.0225(3)	0.0156(3)	−0.0115(3)	0.0055(3)	−0.0078(3)
C8	0.0210(4)	0.0215(3)	0.0203(3)	−0.0104(3)	0.0077(3)	−0.0097(3)
C9	0.0142(3)	0.0171(3)	0.0185(3)	−0.0069(2)	0.0030(2)	−0.0068(2)
C10	0.0133(3)	0.0143(3)	0.0136(3)	−0.0061(2)	0.0012(2)	−0.0047(2)
C11	0.0174(3)	0.0162(3)	0.0140(3)	−0.0067(2)	0.0021(2)	−0.0038(2)
C12	0.0204(3)	0.0226(4)	0.0166(3)	−0.0077(3)	0.0049(3)	−0.0058(3)
F1	0.0244(3)	0.0283(3)	0.0279(3)	−0.0162(2)	0.0068(2)	−0.0065(2)
F2	0.0215(3)	0.0254(3)	0.0345(3)	−0.0013(2)	0.0080(2)	−0.0070(2)
F3	0.0341(3)	0.0473(4)	0.0169(2)	−0.0181(3)	0.0108(2)	−0.0115(2)

Table 25. Bond Lengths for *4c*.

O1-C1	1.3215(9)	C5-C10	1.4016(10)
O1-H1	0.855(19)	C6-C7	1.3903(12)
O2-C11	1.2476(10)	C6-H6	0.960(14)
C1-C2	1.3895(10)	C7-C8	1.3860(12)
C1-C10	1.4626(10)	C7-H7	0.931(15)
C2-C11	1.4193(10)	C8-C9	1.3877(11)
C2-C3	1.5112(10)	C8-H8	0.984(14)
C3-C4	1.5255(11)	C9-C10	1.3992(10)
C3-H3A	0.979(12)	C9-H9	0.964(12)
C3-H3B	0.984(13)	C11-C12	1.5408(11)
C4-C5	1.5016(10)	C12-F3	1.3298(10)
C4-H4A	0.972(12)	C12-F1	1.3322(10)
C4-H4B	0.950(12)	C12-F2	1.3410(10)
C5-C6	1.3946(10)		

Table 26. Bond Angles for *4c*.

C1-O1-H1	105.2(13)	C7-C6-H6	122.1(8)
O1-C1-C2	123.08(7)	C5-C6-H6	117.4(8)
O1-C1-C10	115.65(6)	C8-C7-C6	120.54(7)
C2-C1-C10	121.28(6)	C8-C7-H7	123.4(9)
C1-C2-C11	116.88(7)	C6-C7-H7	116.1(9)
C1-C2-C3	118.29(6)	C7-C8-C9	119.86(7)
C11-C2-C3	124.76(6)	C7-C8-H8	124.2(8)
C2-C3-C4	111.06(6)	C9-C8-H8	115.9(8)
C2-C3-H3A	108.3(7)	C8-C9-C10	119.82(7)
C4-C3-H3A	108.5(7)	C8-C9-H9	121.1(7)
C2-C3-H3B	113.2(7)	C10-C9-H9	119.0(7)
C4-C3-H3B	108.2(8)	C9-C10-C5	120.59(7)
H3A-C3-H3B	107.4(10)	C9-C10-C1	120.17(7)
C5-C4-C3	112.07(6)	C5-C10-C1	119.22(6)
C5-C4-H4A	110.3(7)	O2-C11-C2	125.09(7)
C3-C4-H4A	109.1(7)	O2-C11-C12	115.47(7)
C5-C4-H4B	105.9(7)	C2-C11-C12	119.42(7)
C3-C4-H4B	111.1(7)	F3-C12-F1	107.53(7)
H4A-C4-H4B	108.2(10)	F3-C12-F2	107.30(7)
C6-C5-C10	118.70(7)	F1-C12-F2	107.24(7)
C6-C5-C4	121.98(7)	F3-C12-C11	110.83(7)
C10-C5-C4	119.24(6)	F1-C12-C11	112.56(6)
C7-C6-C5	120.50(8)	F2-C12-C11	111.13(6)

Table 27. Torsion Angles for *4c*.

O1-C1-C2-C11	−2.04(11)	C4-C5-C10-C9	176.58(7)
C10-C1-C2-C11	177.93(6)	C6-C5-C10-C1	−178.26(7)
O1-C1-C2-C3	175.03(7)	C4-C5-C10-C1	−1.57(10)

Table 27. *Cont.*

C10-C1-C2-C3	−4.99(10)	O1-C1-C10-C9	−12.24(10)
C1-C2-C3-C4	36.71(9)	C2-C1-C10-C9	167.79(7)
C11-C2-C3-C4	−146.47(7)	O1-C1-C10-C5	165.92(6)
C2-C3-C4-C5	−49.62(8)	C2-C1-C10-C5	−14.06(10)
C3-C4-C5-C6	−149.82(7)	C1-C2-C11-O2	0.34(11)
C3-C4-C5-C10	33.60(9)	C3-C2-C11-O2	−176.52(7)
C10-C5-C6-C7	0.04(11)	C1-C2-C11-C12	−178.03(6)
C4-C5-C6-C7	−176.56(7)	C3-C2-C11-C12	5.11(11)
C5-C6-C7-C8	−0.13(12)	O2-C11-C12-F3	6.60(10)
C6-C7-C8-C9	0.30(12)	C2-C11-C12-F3	−174.87(7)
C7-C8-C9-C10	−0.37(11)	O2-C11-C12-F1	127.07(8)
C8-C9-C10-C5	0.28(11)	C2-C11-C12-F1	−54.40(10)
C8-C9-C10-C1	178.41(7)	O2-C11-C12-F2	−112.62(8)
C6-C5-C10-C9	−0.11(11)	C2-C11-C12-F2	65.91(9)

applied sciences

Article

A Study of Fluorinated β-Nitrostyrenes as Antimicrobial Agents

King Lo, Hugh Cornell, Gina Nicoletti, Neale Jackson and Helmut Hügel *

Health Innovations Research Institute & School of Applied Sciences, RMIT University, Melbourne, 3001 Australia; E-Mails: s3185155@student.rmit.edu.au (K.L.); hugh.cornell@rmit.edu.au (H.C.); gina.nicoletti@rmit.edu.au (G.N.); neale.jackson@rmit.edu.au (N.J.)

* Author to whom correspondence should be addressed; E-Mail: helmut.hugel@rmit.edu.au; Tel.: +61-3-9925-2626; Fax: +61-3-9925-3747.

Abstract: The effect of variously fluorine-substituted β-methyl-β-nitrostyrenes on their antimicrobial activity was investigated. Their efficacy was determined by minimum inhibition concentration (MIC) in cultures of Gram positive and Gram negative bacteria and a fungus. Highest activity against the Gram negative bacterium, *E.coli*, was achieved with 4-fluorine-aryl substituted β-methyl-β-nitrostyrenes, while most compounds gave excellent results against gram positive bacteria. Importantly, the addition of the β-methyl group profoundly enhanced the antibacterial activity of the compounds tested. The comparative K_D values for the most potent compounds against *E.coli* were much lower than those required for the gram positive and fungus counterparts. This investigation illustrated that fluorine substituted nitropropenylarenes have enhanced antimicrobial activity suitable for antibiotic applications.

Keywords: antimicrobial agents; Henry reaction; fluoro-β-methyl-β-nitrostyrenes; MIC; partition coefficients; log P values

1. Introduction

Time is running out for antibiotics. The rising levels of antibacterial resistance, the decline in productive drug development and the reduction in the numbers of pharmaceutical companies engaging in research and development of anti-infective agents are huge public health concerns and pose problems for the effective management of microbial infections [1]. There is an urgent need to source

novel antimicrobial agents to combat human pathogens that are not susceptible to currently available antibiotics coupled with the strategic use of all available and emerging antimicrobial agents.

In 1952 Schales and Graefe [2] found that a range of substituted β-nitrostyrenes including nitropropenyl aromatic compounds were active against Gram positive and Gram negative bacteria and Denisenko *et al.* [3] who confirmed that **1** was as active as clinical antibiotics against bacteria including methicillin-resistant *Staphylococcus aureus* (MRSA) and vancomycin-resistant *enterococci* (VRE). From the work of Milhazes *et al.* in 2006, the antibacterial activity against S *aureus* American Type Culture Collection (ATCC) 29213 of some aryl-hydroxy/methoxy substituted β-nitrostyrenes was found to be improved by the addition of a β-methyl group on the nitro alkene, with a 2 to 8 fold increase in the minimum inhibitory concentrations (MIC) relative to the β-nitrostyrene [4]. Interestingly, this MIC enhancement was most pronounced for Gram positive bacteria utilizing 3-hydroxy-4-methoxy-β-methyl-β-nitrostyrene **2** (MIC 32); whereas 3,4-dihydroxy-β-methyl-β-nitrostyrene **3** (MIC 64) showed the best result against all Gram negative bacteria except for *Pseudomonas aeruginosa.*
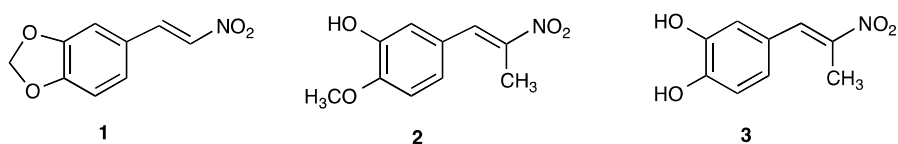
Protein-tyrosine phosphatases (PTPases) are modulators of signal transduction pathways that regulate numerous cell functions. Malfunction of PTPases has been linked to a number of oncogenic and metabolic disease states. The PTPases are also utilized by microbes and viruses for pathogenic activity. Therefore, inhibitors of PTPases have potential as therapeutic antimicrobial agents [5–7]. Park and Pei in enzyme mechanistic studies found *trans*-β-nitrostyrene derivatives to be a new class of inhibitors of protein tyrosine phosphatase PTP1B [8]. They proposed that β-nitrostyrene is a reversible inhibitor of the tyrosine phosphatases PTP1B by their interaction and formation of a covalent complex with cysteine at the catalytic site.

Scheme 1. Park and Pei [8] mechanism of PTP1B inhibition by β-nitrostyrene. Reprinted with permission from Park, J.; Pei, D. Trans- β-nitrostyrene Derivatives as Slow-Binding Inhibitors of Protein Tyrosine Phosphatases. *Biochem.* **2004**, *43*, 15014–15021. Copyright ©2004, American Chemical Society.
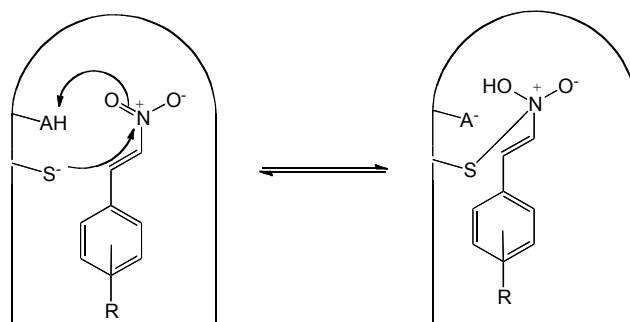
Their evidence suggested that in the absence of free thiols, nucleophilic attack by enzymic cysteine occurs on the side chain nitro group, as shown in Scheme 1. This rationale was based on the positive charge on the nitrogen atom being susceptible to nucleophilic attack, forming a reversible adduct that inhibited PTP1B. However, exactly the opposite is found in the literature. It has been reported [9] that β-nitrostyrenes reversibly add to the thiol group of cysteine and cysteine peptides under mild conditions. In contrast, sodium trimethylsilane thiolate at 185 °C for 24 h has been found to reduce nitro groups to amines [10]. The conjugate addition to β-nitroalkenes reflects the high reactivity of β-nitroalkenes as Michael acceptors [11], and it is widely recognized that nitro group olefins undergo rapid conjugate addition with thiol-type nucleophiles [12,13].

4
R = variable group

5
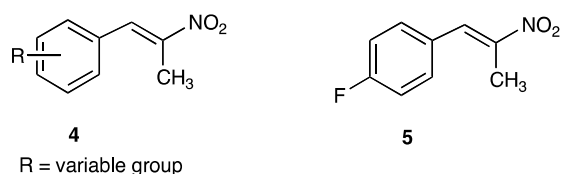
The antimicrobial activity of a range of β-methyl-β-nitrostyrene derivatives **4** against Gram positive, Gram negative bacteria and fungi were evaluated by Nicoletti *et al.* [14] who had previously found that:

(a) *E.coli* was suppressed effectively by chlorine or fluorine C_4-aryl-substituents relative to the unsubstituted or the 3-4-methylenedioxy ring compounds.

(b) *S.aureus* was suppressed effectively by a wide range of nitropropenyl arenes including β-methyl-β-nitrostyrene, the 4-fluorine and 4-chlorine substituted β-methyl-β-nitrostyrene, imidazolyl, benzothiazole and the 3,4-methylenedioxy derivatives. An important finding was that when two hydroxy groups were present on the ring in the 2- and 4- positions or the 2- or 5- positions, activity against this microorganism noticeably reduced. The fact that this also occurred with substitution by *N,N*-dimethyl and *N,N*-diethyl groups indicated that the more polar nature of these substituents was detrimental to activity. This was supported by the K_D values of the latter compounds being relatively low compared with the unsubstituted and halogenated-substituted compounds.

(c) *B.subtilis* was suppressed by a wide range of compounds in a similar fashion to *S.aureus*. The 2,4- and 2,5- dihydroxyaryl substituted compounds exhibited poor bacterial inhibition whereas the 3,4-dihydroxy derivative gave high activity.

(d) *C.albicans* was suppressed by the 3,4-dichloro, 4-chloro, 4-fluoro, derivatives. However 2,4-dihydroxy, 2,5-dihydroxy and the benzimidazole derivatives were very unreactive.

The introduction of 'fluorine functionality' into molecular architecture has proved to be invaluable for modulation of the molecular properties of medicinal compounds [15]. The substitution of hydrogen and other functional groups with fluorine can have multiple molecular impacts, including electronic, lipophilic, *H*-bonding, chemical, metabolic stability and steric factors, which can influence the pharmacodynamic and pharmacokinetic properties of pharmaceuticals [16]. When fluorine atoms or trifluoromethyl groups were introduced into either the peptidic chain or the C-terminal end of cationic pentapeptides, the antimicrobial activity always improved by diminishing the minimal inhibitory concentration (MIC) [17]. A recent report on the structure activity relationships of antitubercular

nitroimidazoles highlighted the high activity achieved by the inclusion of trifluoromethoxybenzyl substituents in the nitroimidazoles [18]. Carbon films with a high fluorine content exhibited excellent antibacterial properties against *E. coli* growth [19]. Furthermore, a simple super hydrophobic coating composed of nano-structured fluorinated silica colloids with fluoroalkoxysilane on a silane structure demonstrated that the adhesion of *Staphylococcus aureus* and *Pseudomonas aeruginosa* was reduced by 2.08 ± 0.25 and 1.76 ± 0.12 log over controls, respectively [20]. The fluorine containing 4-(substituted-2-hydroxybenzoyl) pyrazoles **6**, **7**, **8** showed promising antibacterial activity [21].
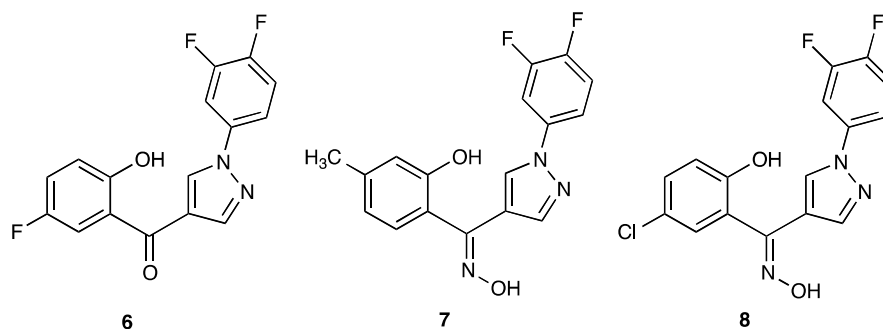
MIC_{50} (microgram/mL)			
E. coli	62.5	25	12.5
S. aureus	100	250	100

Based on the discoveries that fluorine substituted β-nitrostyrene enhanced antimicrobial activity, this investigation was undertaken to study the effects on antimicrobial activity of difluoro-, trifluoromethyl- and trifluoromethoxy- substituted β-methyl-β-nitrostyrenes and related compounds that were prepared via the Henry reaction [22]. For an antimicrobial agent to be effective, it must penetrate the bacterial cell first to reach its target enzymes, therefore the lipophilicity of the prepared compounds was determined from the octanol-water partition coefficients. The antimicrobial activities of all products were measured by minimum inhibitory concentration (MIC). Three Gram positive bacteria (*Staphylococcus aureus*, *Bacillus subtilis* and *Enterococcus faecalis*), one Gram negative bacterium (*Escherichia coli*) and a fungus (*Candida albicans*) were tested.

2. Experimental Section

2.1. Chemicals

Chemicals and solvents were typically sourced from Sigma-Aldrich Chemical Company, and were AR grade or better.

2.2. Instrumentation and Synthesis

Gas chromatography and Mass Spectroscopy (GC/MS) spectra were obtained in either electron ionization (EI) or positive/negative electrospray (ESI) modes with the Varian Saturn 2200 GC/MS/MS (ion-trap) coupled to a Varian CP-3800 GC (FactorFour—Capillary Column; Stationary Phase: VF-5ms; L(m) ID(mm) × OD (mm): 30 × 0.25 × 0.39) or Micromass Platform II ESI/MS (240 V, 10 A). Resultant ions are expressed as m/z values.

NMR spectroscopy was performed on Bruker Advance 300 MHz or Bruker Avance 300 III MHz spectrometer. Some FIDs from Bruker Advance 300 MHz were processed using Mestrec23. [1]H chemical shifts were recorded as δ values in parts per million (ppm) downfield shifts, referenced internally to the residual CHCl$_3$ singlet at 7.26 ppm. Chemical shifts are presented in multiplicity, coupling constant(s) (*J* in Hz), integration and assignments. Abbreviations: s = singlet, d = doublet, t = triplet, q = quartet, p = pentet, dd = doublet of doublet, m = multiplet. [13]C chemical shifts were ^{1}H decoupled and recorded as δ values in parts per million (ppm), referenced internally to the CHCl$_3$ triplet at 77.0 ppm. Assignments have typically been made using additional information from COSY and gCOSY spectra, DEPT, HMBC and HSQC experiments.

Flash Column Chromatography was performed using silica gel 60 Å, 0.04–0.06 mm (230–400 mesh ASTM).

Melting Points were determined on a Gallenkamp melting point apparatus, and were uncorrected.

2.2.1. Synthesis of 1-Fluoro-4-(Nitroprop-1-Enyl)Benzene **5**
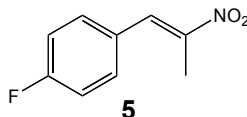
Compound **5** was prepared [23] in 30% yield, yellow crystals, mp. 65–66 °C. ^{1}H NMR (300 MHz, CDCl$_3$): δ$_H$ (ppm): 8.06 (s, 1H, H-C=C), 7.46 (dd, *J* = 3.30, 5.37 Hz, 2H, Ar-H), 7.17 (t, *J* = 8.66 Hz, 2H, Ar-H), 2.46 (s, 3H, C-H, *E*), 1.59 (s, 3H, C-H, *Z*). ^{13}C NMR (300MHz, CDCl$_3$) δ$_C$ (ppm): 165.2 (d, *J* = 252.21 Hz, 1C, C-F), 147.5 (C=C, β carbon), 132.5 (C=C, α carbon), 132.2 (Ar), 128.5 (Ar), 128.5 (Ar), 116.3 (Ar), 116.0 (Ar), 14 .0 (CH$_3$). GC/MS *m/z* (M$^+$) 181.

2.2.2. Synthesis of 4-fluoro-β-nitrostyrene **9** [4-fluoro-2-(nitroethen-1-enyl)benzene]
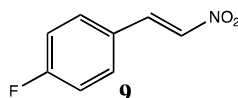
Following literature procedures [24], a stirred solution of acetic acid (33.5 mL) and ammonium acetate (4.4 g, 57.1 mmol) was added to nitromethane (10 g, 164.0 mmol) followed by 4-fluorobenzaldehyde (2.94g, 23.7mmol) and the solution was refluxed in an oil bath at 100 °C for 5.5 hr. The dark orange mixture was then cooled to room temperature and poured into water (100 mL). The pH of the solution was basified with sodium hydroxide solution (2 M), and the product was extracted with ethyl acetate (3 × 100 mL). The combined organic extracts were dried over MgSO$_4$, filtered and concentrated under high vacuum. Recrystallization from 95% ethanol removed the brown oily impurities, giving pale yellow needles, 57% yield and mp. 99–100 °C. ^{1}H NMR (300 MHz, CDCl$_3$): δ$_H$ (ppm) 7.94–7.89 (d, *J* = 13.81 Hz, 1H, αC-H), 7.52–7.44 (m 1H, βC-H), 7.52–7.44 (m, 2H, Ar-H), 7.11–7.05 (t, *J* = 8.40, 2H, Ar-H). ^{13}C NMR (300 MHz, CDCl$_3$): δ$_H$ (ppm) 164.9 (d, *J* = 255.08 Hz, C-F), 137.8 (C=C, β carbon), 136.8 (C=C, α carbon), 131.2 (Ar), 126.3 (Ar), 116.7 (Ar). GC/MS *m/z* (M$^+$) 167.

2.2.3. 1-Fluoro-2-(Nitroprop-1-Enyl)Benzene **10**
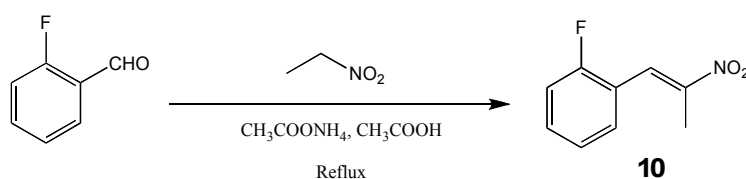
2-Fluoro-benzaldehyde (4.81 g, 38.8 mmol) was dissolved in nitroethane (4.01 g, 53.5 mmol, 20% excess), ammonium acetate (4.00 g, 52 mmol) and glacial acetic acid (5 mL) added and the mixture refluxed for 2 h in an oil bath at 100 °C. The orange mixture was then chilled and de-ionized water (6 mL) was then added. A small portion of the crude orange crystalline product obtained by filtration was taken for determination of melting point. The rest of the product was dissolved in hot ethanol (95%, 2 mL) and chilled for an hour to obtain the recrystallized product. The recrystallization procedure was repeated and light yellow crystals were obtained (2.38 g, 34% yield, mp 45–47 °C. ^{1}H NMR (300 MHz, CDCl$_3$): δ_H (ppm): 7.98 (s, 1H, H-C=C), 7.39–7.33 (t, J = 8.70 Hz, 1H, Ar-H), 7.19 (d, J = 8.67 Hz, 1H, Ar-H), 7.12 (d, J = 8.57 Hz, 1H, Ar-H), 7.04 (d, J = 8.76 Hz, 1H, Ar-H), 2.36 (s. 3H,C-H, *E*), 1.59 (s, 3H, C-H, *Z*). ^{13}C NMR (300MHz, CDCl$_3$) δ_C (ppm): 165.1 (d, J = 252.21 Hz, C-F), 147.5 (C=C, β carbon), 132.5 (C=C, α carbon), 132.2 (Ar), 132.0 (Ar), 128.7 (Ar), 116.4 (Ar), 116.2 (Ar), 14.0 (CH$_3$); GC/MS *m/z* (M$^+$) 181.

2.2.4. 1-Fluoro-3-(Nitroprop-1-Enyl)Benzene **11**
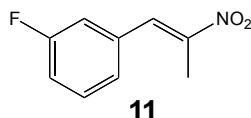
This compound was prepared [23] by reacting 3-fluorobenzaldehyde (1 g, 8.05 mmol) with ammonium acetate (0.19 g, 2.4 mmol) in nitroethane (4.98 g, 66.4 mmol), under reflux overnight (approximately 17 h) in an oil bath at 125 °C. The compound was identified by thin layer chromatography (TLC). The mixture was then concentrated under high vacuum to remove the excess nitroethane and then the yellow mixture was dissolved in chloroform (20 mL), washed with water (3 × 20 mL) and with sodium chloride solution (25%, 20mL). The mixture was dried over (MgSO$_4$) and concentrated under high vacuum. A yellow liquid was obtained (0.75 g) this being 52% of theoretical yield. ^{1}H NMR (300 MHz, CDCl$_3$): δ_H (ppm): 8.04 (s, 1H, C=C-H), 7.46–7.39 (m, 1H, Ar-H), 7.46–7.39 (m, 1H, Ar-H), 7.22–7.19 (d, J = 7.80 Hz, 1H, Ar-H), 7.13–7.09 (d, J = 9.30 Hz, 1H, Ar-H coupled with F), 2.42 (s, 3H, CH$_3$). ^{13}C NMR (300MHz, CDCl$_3$) δ_C (ppm): 164.3 (d, J = 246.79 Hz, 1C, C-F), 148.7 (C=C, β carbon), 134.6 (Ar), 132.0 (Ar), 130.6 (C=C, α carbon), 130.5 (Ar), 125.9 (Ar), 125.7 (Ar), 13.9 (CH$_3$). GC/MS *m/z* (M$^+$) 181.

2.2.5. 1,3-Difluoro-4-(Nitroprop-1-Enyl)Benzene **12**
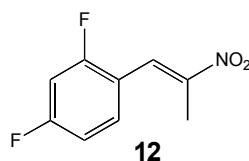
43% yield mp. 48–49 °C. ^{1}H NMR (300 MHz, CDCl$_3$): δ$_H$ (ppm): 8.06 (s, 1H, C=C-<u>H</u>), 7.45–7.35 (dd, *J* = 8.30, 8.38Hz, coupling due to two fluorine atoms were coupling with this proton. 1H, Ar-<u>H</u>); 7.04–6.96 (dd, for the proton at the middle of two fluorine atoms it should split to a quartet as two fluorine atoms were coupling with it. *J* = 8.47, 8.50 Hz. 1H Ar-<u>H</u>. The other proton at position 6 should be a triplet as there is only fluorine atom coupling with it. t, *J* = 8.48 Hz, 1H, Ar-<u>H</u>), 2.38 (s 3H, C<u>H</u>$_3$, *E*), 1.57 (s 3H, C<u>H</u>$_3$, *Z*). ^{13}C NMR (300MHz, CDCl$_3$) δ$_C$ (ppm): 163–162.3 (quartet due to two fluorine atoms coupling with the carbon. *J* = 222.02, 233.55Hz. 1C, F-<u>C</u>=C-C-F), 162.2–159 (q, *J* = 234,37 Hz. 1C, F-C=C-<u>C</u>-F), 149.5 (s, <u>C</u>=C α carbon), 134.1–131.1 (q, *J* = 234.64 Hz, 1C, F-C-C=<u>C</u>-C=C-F), 125.7–125.4 (s, C=<u>C</u>, β carbon), 117.0–116.5 (d, *J* = 9.88 Hz, 1C, F-C=<u>C</u>), 112.3–111.7 (q, *J* = 3.57, 21.68, 24.97Hz, 1C, F-C-=<u>C</u>-C-F), 104.8 – 104.4 (d, *J* = 25.80, 1C, F-C-<u>C</u>=C), 14.2–14.0 (CH$_3$). GC/MS *m/z* (M$^+$) 199.

2.2.6. 1-Trifluoromethyl-4-(Nitroprop-1-Enyl)Benzene **13**
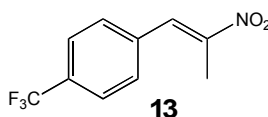
This compound was synthesized [25] using 4-trifluoromethylbenzaldehyde (1 g, 5.7 mmol) and ammonium acetate (0.38 g, 5.0 mmol) dissolved in nitroethane (20 mL, 280 mmol), heated to 100 °C and refluxed overnight. The excess nitroethane was removed under high vacuum and the yellow mixture was poured into water (20 mL) and extracted with ethyl acetate (3 × 20 mL). The combined organic extracts were washed with water (3 × 20 mL) and sodium chloride solution (25%, 20 mL) and then dried over anhydrous MgSO$_4$. The solvent was removed under high vacuum (enhanced with liquid nitrogen) to yield a yellow solid (1.16 g, 87% yield). The material was purified by washing with cold ethanol (95%) to yield **13** (0.748g, 42%), a yellow solid which had a melting point of 96–98 °C. ^{1}H NMR (300 MHz, CDCl$_3$): δ$_H$ (ppm) 8.02 (s, 1H, C=C-<u>H</u>), 7.65 (d, *J* = 8.3 Hz, 2H, Ar-<u>H</u>), 7.46 (d, *J* = 8.2 Hz, 2H, Ar-<u>H</u>), 2.37 (s, 3H, C-<u>H</u>, *E*), 1.59 (s, 3H, C-<u>H</u>, *Z*). ^{13}C NMR (300MHz, CDCl$_3$) δ$_C$ (ppm): 148.9 (s, <u>C</u>=C, β carbon), 135.6 (Ar), 132.6 (s, <u>C</u>=C, α carbon), 131.4 (s, Ar-<u>C</u>-CF$_3$), 129.8 (Ar), 128.5 (Ar), 123.7 (q. *J* = 273.6 Hz, <u>C</u>F$_3$), 13.6 (<u>C</u>H$_3$). GC/MS *m/z* (M$^+$) 231.

2.2.7. 1-Trifluoromethyl-2-(Nitroprop-1-Enyl)Benzene **14**
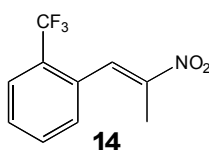
The product [25] was purified by flash column chromatography on silica gel with hexane/ethyl acetate (20/1) to obtain a yellow liquid 46% yield. ^{1}H NMR (300 MHz, CDCl$_3$): δ_H (ppm) 8.16 (s, 1H, C=C-<u>H</u>), 7.69–7.67 (d, *J* = 7.80 Hz, 1H, Ar-<u>H</u>, *trans*-compound), 7.61–7.53 (m, multiplets, overlapping of the *cis* and *trans*-compounds, 1H, Ar-<u>H</u>), 7.48–7.42 (m, 1H, Ar-<u>H</u>), 7.39–7.34 (t, *J* = 6.60 Hz, *Z*-conformer, 1H, Ar-<u>H</u>), 7.28–7.26 (d, *J* = 7.50 Hz, *Z*-conformer, 1H, Ar-<u>H</u>), 7.17–7.15 (d, *J* = 6.30 Hz, *E*-conformer, 1H, Ar-<u>H</u>), 2.31 (s, *E*-isomer, 3H, C<u>H</u>$_3$), 2.17 (s, *E*-conformer, 3H, C<u>H</u>$_3$). ^{13}C NMR 149.9 (s, 1C, <u>C</u>=C, β C), 148.9 (Ar), 132.0 (Ar), 130.2 (s, <u>C</u>=C, α carbon), 130.0 (*Z*-Ar), 129.3 (Ar), 129.0 (*E* Ar),128.4 (*Z*-Ar),127.2 (q, J = 264.5 Hz,1C, <u>C</u>F$_3$), 126.4 (*E*-Ar), 125.9 (Ar), 124.7 (Ar), 122.0 (Ar), 19.3 (s, 1C, *E*-<u>C</u>H$_3$), 13.7 (s, 1C, *Z* <u>C</u>H$_3$). GC/MS *m/z* (M$^+$) 231.

2.2.8. 1-Trifluoromethyl-3-(Nitroprop-1-Enyl)Benzene **15**

15
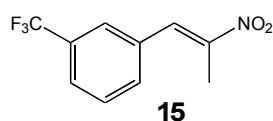
The product was purified by flash column chromatography on silica gel with hexane/ethyl acetate (20/1) to obtain a yellow liquid in yield of 46%. ^{1}H NMR (300 MHz, CDCl$_3$): δ_H (ppm) 8.07 (s, 1H, C=C-<u>H</u>), 7.44–4.38 (t, *J* = 8.66 Hz, 1H Ar-<u>H</u>), 7.27 (d, *J* = 7.91 Hz, 1H, Ar-<u>H</u>), 7.19 (d, 1H, Ar-<u>H</u>), 7.17 (s, 1H, r-<u>H</u>), 2.34 (s, 3H, C<u>H</u>$_3$). ^{13}C NMR 149.1 (s, <u>C</u>=C, β C), 133.3 (Ar), 132.8 (Ar), 131.6 (Ar), 131.2 (Ar), 130.3 (Ar), 129.5 (Ar), 126.3 (s, <u>C</u>=C, α carbon), 123.6 (q, *J* = A272.4 Hz, 1C, <u>C</u>F$_3$), 13.8 (s, <u>C</u>H$_3$). GC/MS *m/z* (M$^+$) 231.

2.2.9. 1-Trifluoromethoxy-4-(Nitroprop-1-Enyl)Benzene **16**

16
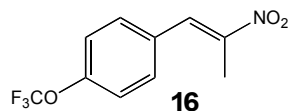
4-trifluoromethoxybenzaldehyde (1 g, 5.3 mmol), ammonium acetate (0.12 g, 1.6 mmol) and nitroethane (3.3 g, 43.3 mmol) were heated at 115 °C for 5 h. The yellow mixture was placed under high vacuum to remove excessive nitroethane and then dissolved in chloroform (10 mL), washed with water (3 × 20 mL) and washed again with saturated brine solution (25%, 2 × 20 mL). The washed mixture was then dried over MgSO$_4$, and then concentrated under high vacuum. 73% yield, yellow crystals mp 47–48 °C. ^{1}H NMR (300 MHz, CDCl$_3$): δ_H (ppm) 7.98 (s, 1H, C=C–H), 7.42 (d, *J* = 8.66 Hz, 2H, Ar-<u>H</u>), 7.24 (d, *J* = 8.29 Hz, 2H, Ar-<u>H</u>), 2.37 (s, 3H, C<u>H</u>$_3$). ^{13}C NMR 150.0 (s, O-<u>C</u> in Ar), 148.3 (s, <u>C</u>=C, β C), 131.9 (s, <u>C</u>=C, α C), 131.5 (Ar), 130.9 (Ar), 121.1 (Ar), 120.3 (q, *J* = 258.2 Hz, 1C, <u>C</u>F$_3$), 13.9 (s, <u>C</u>H$_3$).GC/MS *m/z* (M$^+$) 247.

2.2.10. 1-Trifluoromethoxy-3-(Nitroprop-1-Enyl)Benzene **17**

17
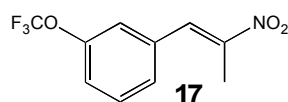
51% yield, yellow liquid. ^{1}H NMR (300 MHz, CDCl$_3$): δ$_H$ (ppm) 8.05 (s, 1H, C=C–H), 7.45–7.49 (t, *J* = 8.70 Hz, 1H, Ar-H, *trans* compound), 7.40–7.36 (t, *J* = 6.60 Hz, 1H, Ar-H, *Z*- conformer), 7.31–7.28 (d, *J* = 7.20 Hz, 1H, Ar-H, *E*-conformer), 7.19–7.17 (d, *J* = 7.80 Hz, 1H, Ar-H, *Z*-conformer), 6.49 (s, 1H, Ar-H)2.45 (s, 1H, CH$_3$, *E*-conformer), 2.38 (s, 1H, CH$_3$, *Z*-isomer). ^{13}C NMR (300 MHz, CDCl$_3$): δ$_H$ (ppm) 149.3 (s, C-OCF$_3$), 149.2 (s, C=C, β carbon), 134.4 (Ar), 131.7 (s, C=C, α carbon), 130.4 (*E*- Ar), 130.0 (Ar), 128.1 (*Z*-Ar), 126.2 (*E*-Ar), 124.1 (Ar), 122.6 (q, *J* = 258.0 Hz, 1C, OCF$_3$), 122.1 (Ar), 121.2 (*trans* Ar), 120.6 (*Z*-Ar), 19.9 (s, 1C, *Z*-CH$_3$), 13.9 (s, 1C, *E*-CH$_3$). **GC/MS** *m/z* (M$^+$) 247.

2.2.11. Minimum Inhibitory Concentrations

The strains used for biological tests were: *Staphylococcus aureus* ATCC 29213, *Bacillus subtilis* ATCC 6633, *Enterococcus faecalis* ATCC 29212, *Escherichia coli* ATCC 25922 and *Candida albicans* ATCC 10231. Stocks of all microorganisms were kept in −80 °C in MHB (Oxoid, Cambridge, UK) with 20% v/v glycerol (BDH chemicals, Poole, UK). Strains were subcultured onto Nutrient agar (NA, Oxoid) and subcultures between three and nine used to prepare inocula. Inocula were prepared by adjusting a suspension to match McF 0.5 turbidity standard (equal to ~1.5 × 10^8 bacterial cells/mL or ~1.5 × 10^6 yeast cells/mL) and subsequent dilution to the required density. Broth microdilution testing was according to the National Committee for Clinical Laboratory Standards standard methods [26,27] in MHB (Oxoid) for bacteria or Sabouraud Liquid Medium (SLM, Oxoid) for *C. albicans*. Microplate assays were performed in clear, round-bottomed, 96-well plates (Sarstedt Australia, SA, AUS) with a total volume of 200 µL per well. Standard inoculum densities were approximately 1 × 10^5 Colony Forming Units per mL (CFU/mL) for bacteria and 1 × 10^4 CFU/mL for *C. albicans*. Inoculum densities were confirmed by serial dilution plating onto NA and incubation aerobically at 37 °C for 24 h.

The test β-nitrostyrene derivatives were added to plates at two times tested concentrations in 100 µL media. Ciprofloxacin was used as an internal positive control for bacteria and miconazole for *C.albicans*. Microplates were incubated 18–24 h at 37 °C aerobically before reading wells visually for turbidity. All assays included duplicated wells and were at least twice replicated. The geometric MIC (µg/mL) for each strain was adjusted to the nearest log$_2$ dilution tested. MIC results were reported as MIC (µg/mL) for standards.

2.2.12. Octanol-Water Partition Coefficients

The lipophilicity level of each compound was determined by octanol-water partition coefficients. The buffer solution used in the determination of K$_D$ was made by mixing sodium chloride (3.78 g, 65 mmol), disodium hydrogen orthophosphate (2.14 g, 18 mmol) and sodium dihydrogen orthophosphate (0.78 g, 5.5 mmol) in 500 mL water at room temperature (~22 °C) and had a pH of 7.5. Each compound (10 mg) was dissolved in octanol (2 mL) in a stoppered test tube, followed with the addition of the buffer solution (2 mL) and the tube was shaken over 48 hours. Finally the mixtures were allowed to separate into two layers. The top layers were removed and absorbance measured after dilution 1:20, 1:50 or 1:200 to 3 mL with octanol in a 1 cm cuvette path length at 370 nm for each diluted sample. The aqueous bottom layers were removed and the absorbance measured without dilution.

K_D measurements were according to the equation:

$$K_D = \frac{[\text{Octanol}]}{\text{Water}}$$

As the absorbance of the octanol and water layers is directly proportional to the concentration in each layer, the K_D value can be calculated from the relative absorbance of each layer.

3. Results and Discussion

The preparation of the β-methyl-β-nitrostyrenes involved the Henry condensation reaction [22] of the aromatic aldehyde with nitroethane under basic conditions followed by dehydration of the resultant alcohol. The NMR analysis of the β-methyl-β-nitrostyrene fluorine derivatives indicated that the β-methyl-β-*E*-nitrostyrene conformation was predominant in most of the compounds prepared. For example, for 13 the *E/Z* ratio is 14/1.

The antibacterial activity of β-nitrostyrene derivatives and related compounds has been well known for a number of years. Their resurgence is attributed to the strong antibacterial/antifungal activity of some compounds with applications in veterinary and human medicine. It has been established from SAR studies that their lipohilicity plus the nucleophilic addition of thiol groups of some enzymes to the exocyclic double bond of these compounds are critical for the development of their antimicrobial activity. The antimicrobial efficacy of the β-nitrostyrenes was assessed by their activity against a panel of bacteria and a fungus (*Candida albicans*). The results appear as the minimum inhibitory concentration (MIC) for each compound. The partition coefficient (K_D) between octanol and water for each compound, representing its degree of lipophilicity, was also determined in order to access the extent of its interaction with the surface of the microorganism. The measured and calculated log P values are also included. Compounds with the incorporation of fluorine were of considerable interest as earlier studies had indicated an improvement of antibacterial activity [9].

The antibacterial assays shown in Table 1 indicated that the β-nitrostyrene compounds **20** and **9** displayed significantly lower activity towards all the tested bacteria relative to all the β-methyl-β-nitrostyrene analogues that were studied. This is exemplified by comparing the activity values of **20** and **21** as well as **9** and **5** that differ by at least an order of magnitude. The β-nitropropenyl side chain deviates 28° from coplanarity with the benzene ring [4] and the relative higher K_D values of the β-methyl-β-nitrostyrene compounds provides evidence that the steric effect and presence of the β-methyl group is substantial. However, the reasons for their enhanced antibacterial potency are unclear. It is also difficult to correlate the position of fluorine substitution on the benzene ring or the effect of multiple fluorine substituents with activities and K_D values of **5, 10 11** and **12**. The activity order of the four most potent antibacterial compounds **5** > **10** > **12** > **13** does not correlate with their K_D values. The data also provides evidence of the apparent tendency for fluorine functionalized β-methyl-β-nitrostyrenes to show considerable hydrophilic properties. The results also suggest that the more hydrophilic nature of the fluorine functionalized-β-methyl-β-nitrostyrenes with K_D values in the lowest range (23–132) is more effective against *E.coli.* It is interesting to note that substituent size appears to affect antibacterial activity against *E. coli.*, since for F-, the potency order is *p* > *o* > *m* and for CF$_3$-, its *p* > *m* > *o.* Of all the substances tested, compound **5** was most active against *E.coli* (27 µg/mL) and the MIC values against the other microorganisms were 6 µg/mL or less, making it also

Appl. Sci. **2012**, *2*

the most effective against the three Gram positive bacteria and *C.albicans*. We deduce from this that for many Gram negative bacteria (such as *E. coli*) that are known to have polysaccharide structures, hydrophilic compounds more readily penetrate the bacterial cell wall to inhibit bacterial enzymes. From our results, the only Log *P* value for that can be cited for an effective fluorinated compound on *E.coli* (Gram negative) is 2.00 for compound **5**. For the Gram positive bacteria, a range of Log *P* values of 1.15–2.19 apparently relate to efficacy. For the non-fluorinated compounds, optimal Log *P* values cover a wider range 1.61–3.41, and becomes wider 1.15–3.41 with the inclusion of *C.albicans*.

Table 1. Antibacterial/fungus assays of various β-*E*-nitrostyrene compounds, their MIC [μg/mL] and K_D, logP values. MIC and K_D values are the means of two determinations.

Strain	5	9	10	11	12	13	14	15	16	17	18	19	20	21
S. aureus	2	128	3	8	2	2	16	16	2	16	3	2	256	8
B. subtilis	2	256	3	16	2	2	8	8	4	8	2	2	256	16
E. faecalis	5.5	64	5	16	6	4	32	16	8	16	4	5	128	16
E. coli	27	256	42	256	45	96	512	256	512	256	256	128	256	96
C. albicans	2	32	3	8	3	4	16	8	8	8	3	4	32	6
Meas. K_D	88	73	207	23	155	68	74	213	66	132	354	247	44	133
Meas. logP	1.94	1.86	2.32	1.36	2.19	1.83	1.87	2.33	1.82	2.12	2.55	2.39	1.64	2.12
Calc. logP	2.34	2.27	2.34	2.34	3.49	3.08	3.08	3.08	3.63	3.63	1.82	1.88	2.13	2.20

The plots of the MIC–K_D for the twelve β-methyl-β-nitrostyrenes investigated for their antibacterial activities against *E. coli* and *E. faecalis* presented in Figure 1 reflect the poor correlation between the effectiveness against *E.coli* and the partition coefficients of the compounds tested (r^2 = 0.0498 for *E.coli*, r^2 = 0.1416 for *E. faecalis*). There were no correlations between MIC value and K_D value for *S. aureus*, *B. subtilis*, and *C. albicans* (graphs not shown).

Figure 1. MIC–K_D plots for (**a**) *E. coli* and (**b**) *E. faecalis*.
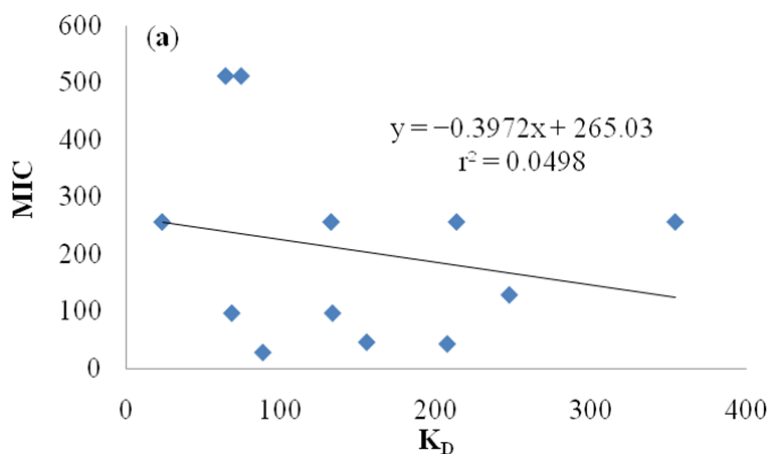
Figure 1. *Cont*.
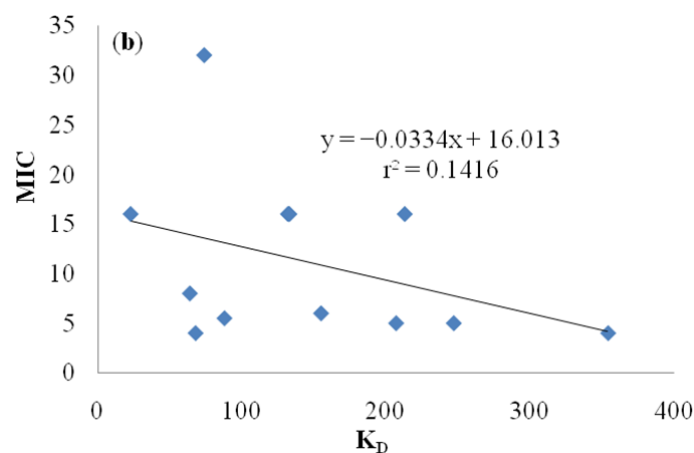
The low K_D for fluorine containing compound **5** [K_D = 88] may be accounted by the presence of fluorine atom back bonding, leading to polar resonance structures and a gain in solvation energy in a hydrophilic compared to lipophilic medium, as shown in Scheme 2. Similarly, the 2,4-difluoro substituted compound **12** results in additional fluorine back bonding resonance structures with an overall increase in polarity and solvation in the aqueous solvent, significantly lowering its partition coefficient value.

Scheme 2. Fluorine back-bonding in fluorine substituted β-methyl-β-*E*-nitrostyrene compounds.
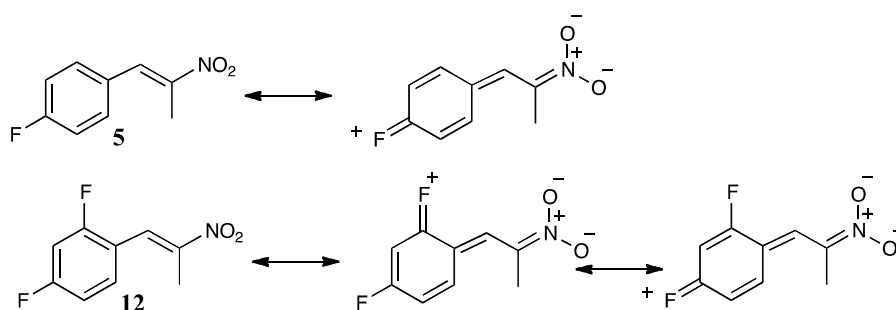
Can aromatic ring fluorine/hydrogen exchange influence membrane permeability? Generally, aromatic F/H substitution tends to increase compound lipophilicity, in direct contrast to what is observed. Alternatively, the reason for the effectiveness of fluorine substitution on the aromatic ring may be connected with the high electronegativity of fluorine, although size factors could also be important. Perhaps the electronegativity of fluorine could affect binding affinity to the binding site of the bacteria, thus causing inhibition of the enzyme. Further investigations with other fluorine-substituted compounds to determine the structural features required for the optimal anti-bacterial activity of β-methyl-β-nitrostyrene compounds are currently being carried out.

4. Conclusions

We have deployed the β-methyl-β-nitrostyrene scaffold for the development of fluorinated derivatives with enhanced antibacterial activity. While the screening of whole cells in MIC assays ensures cell

penetration and antimicrobial activity, it does not distinguish selective inhibitors from toxic compounds. In addition, the mechanism of antimicrobial action is unknown. The dependency between antimicrobial activity and lipophilicity K_D of fluorinated β-methyl-β-nitrostyrenes (FBNS) was examined for three Gram positive and one Gram negative bacteria and a fungus. The antimicrobial activity is rationalized with unspecific cytoplasmic membrane damaging effects that is near optimum at a lipophilicity (logP) of 2 (±0.5) for Gram-negative bacteria. For Gram-positive bacteria and fungus poor MIC *vs.* log K_D correlations were found. The disparity between measured and calculated log P values is also under investigation. There is, however, unequivocal literature evidence that both the β-nitrostyrenes and the β-methyl-β-nitrostyrenes are exceptional Michael acceptors. An expanded set of substituted β-methyl-β-nitrostyrene compounds will be investigated to determine the structural features required for the optimal anti-bacterial activity of β-methyl-β-nitrostyrene compounds.

Acknowledgments

References

1. Payne, D.J.; Gwynn, M.N.; Holmes, D.J.; Pompliano, D.L. Drugs for bad bugs: Confronting the challenges of antibacterial discovery. *Nat. Rev. Drug Discov.* **2007**, *6*, 29–40.
2. Schales, O.; Graefe, H.A. Arylnitroalkenes: A new group of antibacterial agents. *J. Am. Chem. Soc.* **1952**, *74*, 4486–4490.
3. Denisenko, P.P.; Sapronov, N.S.; Tarasenko, A.A. Antimicrobial and radioprotective compounds. Patent No. 20040266844, issued on 30 December 2004.
4. Milhazes, N.; Calheiros, R.; Marques, M.P.M.; Garrido, J.; Cordeiro, M.N.D.S.; Rodrigues, C.; Quinteira, S.; Novais, C.; Peixe, L.; Borges, F. β-Nitrostyrene derivatives as potential antibacterial agents: A structure-property-activity relationship study. *Bioorg. Med. Chem.* **2006**, *14*, 4078–4088.
5. Bialy, L.; Waldmann, H. Inhibitors of protein tyrosine phosphatases: Next-generation drugs? *Angew. Chem. Int. Ed.* **2005**, *44*, 3814–3839.
6. Heneberg, P. Use of protein tyrosine phosphatase inhibitors as promising targeted therapeutic drugs. *Curr. Med. Chem.* **2009**, *16*, 706–733.
7. Zhang, S.; Zhang, Z.-Y. PTP1B as a drug target: Recent developments in PTP1B inhibitor discovery. *Drug Discov. Today* **2007**, *12*, 373–381.
8. Park, J.; Pei, D. Trans-β-nitrostyrene derivatives as slow-binding inhibitors of protein tyrosine phosphatases. *Biochemistry* **2004**, *43*, 15014–15021.
9. Jung, G.; Fouad, H.; Heusel, G. 2-Nitro-1-phenylethyl: A new protecting and chiroptical reporter group for cysteine peptides. *Angew. Chem. Int. Ed.* **1975**, *14*, 817–818.
10. Hwu, J.R.; Wong, F.F.; Shiao, M.-J. Reduction of aromatic nitro compounds to aromatic amines by sodium trimethylsilanethiolate. *J. Org. Chem.* **1992**, *57*, 5254–5255.
11. Berner, O.M.; Tedeschi, L.; Enders, D. Asymmetric Michael additions to nitroalkenes. *Eur. J. Org. Chem.* **2002**, *67*, 1877–1894.

12. Baker, L.M.S.; Baker, P.R.S.; Golin-Bisello, F.; Schopfer, F.J.; Fink, M.; Woodcock, S.R.; Branchaud, B.P.; Radi, R.; Freeman, B.A. Nitro-fatty acid reaction with glutathione and cysteine: Kinetic analysis of thiol alkylation by a Michael addition reaction. *J. Biol. Chem.* **2007**, *282*, 31085–31093.

13. Bernasconi, C.F.; Schuck, D.F. Kinetics of reversible thiolate ion addition to substituted beta-nitrostyrenes in water. Radicaloid transition state or principle of nonperfect synchronization? *J. Org. Chem.* **1992**, *57*, 2365–2373.

14. Nicoletti, G.; Cornell, H.; Hügel, H.; White, K.S.; Nguyen, T.; Zalizniak, L. Synthesis and biological activity of nitropropenyl arenes. **2012**, in preparation.

15. Ojima, I. *Fluorine in Medicinal Chemistry and Chemical Biology*; Wiley-Blackwell: Chichester, UK, 2009.

16. Smart, B.E. Fluorine substituent effects (on bioactivity). *J. Fluorine Chem.* **2001**, *109*, 3–11.

17. Giménez, D.; Andreu, C.; del Olmo, M.; Varea, T.; Diaz, D.; Asensio, G. The introduction of fluorine atoms or trifluoromethyl groups in short cationic peptides enhances their antimicrobial activity. *Bioorg. Med. Chem.* **2006**, *14*, 6971–6978.

18. Cherian, J.; Choi, I.; Nayyar, A.; Manjunatha, U.H.; Mukherjee, T.; Lee, Y.S.; Boshoff, H.I.; Singh, R.; Ha, Y.H.; Goodwin, M.; *et al.* Structure-activity relationships of antitubercular nitroimidazoles. 3. Exploration of the linker and lipohilic tail of ((S)-2-nitro-6,7-dihydro-5*H*-imidazo[2,1-*b*][1,3]oxazin-6-yl)-(4-trifluoromethoxybenzyl)amine (6-amino PA-824). *J. Med. Chem.* **2011**, *54*, 5639–5659.

19. Boonyawan, D.; Sarapirom, S.; Tunma, S.; Chaiwong, C.; Rachtanapun, P.; Auras, R. Characterization and antimicrobial properties of fluorine-rich carbon films deposited on poly(lactic acid). *Surf. Coat. Technol.* **2011**, *205*, S552–S557.

20. Privett, B.J.; Youn, J.; Hong, SA.; Lee, J.; Han, J.; Shin, J.H.; Schoenfisch, M.H. Antibacterial fluorinated silica colloid superhydrophobic surfaces. *Langmuir* **2011**, *27*, 9597–9601.

21. Gadakh, A.V.; Pandit, C.; Rindhe, S.S.; Karale, B.K. Synthesis and antimicrobial activity of novel fluorine containing 4-(substituted-2-hydroxybenzoyl)-*H*-pyrazoles and pyrazolyl benzo[*d*]oxazoles. *Bioorg. Med. Chem. Lett.* **2010**, *20*, 5572–5576.

22. Luzzio, F.A. The Henry Reaction: Recent examples. *Tetrahedron* **2001**, *57*, 915–945.

23. Werbel, L.M.; Cook, P.D.; Elslager, E.F.; Hung, J.H.; Johnson, J.L.; Kesten, S.J.; McNamara, D.J.; Ortwine, D.F.; Worth, D.F. Antimalarial drugs. 60. Synthesis, antimalarial activity, and quantitative structure-activity relationships of tebuquine and a series of related 5-[(7-chloro-4-quinolinyl)amino]-3-[(alkylamino)methyl][1,1'-biphenyl]-2-ols and N-oxides. *J. Med. Chem.* **1986**, *29*, 924–39.

24. Cote, A.; Lindsay, V.N.G.; Charette, A.B. Application of the chiral bis(phosphine) monoxide ligand to catalytic enantioselective addition of dialkylzinc reagents to beta-nitroalkenes. *Org. Lett.* **2007**, *9*, 85–87.

25. Bergner, I.; Opatz, T. Modular one-pot synthesis of tetrasubstituted pyrroles from alpha-(alkylideneamino)nitriles. *J. Org. Chem.* **2007**, *72*, 7083–7090.

26. NCCLS. *Reference Method for Broth Dilution Susceptibility Testing of Yeasts*; Approved Standard 2nd ed.; National Committee for Clinical Laboratory Standards: Wayne, PA, USA, 2002; M27-A2; Volume 22:15.

27. NCCLS. National Committee for Clinical Laboratory Standards. Methods for dilution antimicrobial susceptibility tests for bacteria that grow aerobically. Document M7-A6. NCCLS, Wayne, PA, USA, 2003; Volume 22.

Article

Computational Study on the Acid Catalyzed Reactions of Fluorine-Containing 2,4-Dialkoxy-3,4-dihydro-2*H*-pyrans with Aromatic Compounds

Norio Ota [1], Yasuhiro Kamitori [2],*, Ryusuke Shirai [3], Mizuki Hatakenaka [2] and Etsuji Okada [2],*

[1] Graduate School of Science and Technology, Kobe University, Rokkodai-cho, Nada-ku, Kobe 657-8501, Japan; E-Mail: norio.ota@shionogi.co.jp

[2] Department of Chemical Science and Engineering, Graduate School of Engineering, Kobe University, Rokkodai-cho, Nada-ku, Kobe 657-8501, Japan; E-Mail: 119t453t@stu.kobe-u.ac.jp

[3] Department of Chemical Science and Engineering, Faculty of Engineering, Kobe University, Rokkodai-cho, Nada-ku, Kobe 657-8501, Japan; shirai@s-micro.com

* Authors to whom correspondence should be addressed; E-Mails: kamitori@kobe-u.ac.jp (Y.K.); okaetsu@kobe-u.ac.jp (E.O.); Tel.: +81-78-803-6163; Fax: +81-78-803-6163.

Abstract: The reaction of 2,4-diethoxy-6-trifluoromethyl-3,4-dihydro-2*H*-pyran (**1**) with aromatic compounds in refluxing acetonitrile in the presence of *p*-toluenesulfonic acid gave the mixture of 4-aryl-2-trifluoromethyl-4*H*-pyrans (**3**) and 6-aryl-1,1,1-trifluorohexa-3,5-dien-2-ones (**4**). In contrast, the same reaction carried out in trifluoroacetic acid at ambient temperature afforded 4-aryl-2-ethoxy-6-trifluoromethyl-3,4-dihydro-2*H*-pyrans (**2**) selectively. These two types of reactions giving quite different products under each condition were studied on the basis of DFT calculations. Moreover, the proposed mechanism for the reaction of 5-trifluoroacetyl-6-trifluoromethyl-3,4-dihydro-2*H*-pyran (**5**) with aromatic compounds affording butadiene derivatives (**6**) exclusively was also discussed based on the calculations and comparison with the reactivity of pyrylium intermediate (**7**).

Keywords: fluorine-containing dihydropyrans; fluorine-containing 1,3-butadienes; acid catalyzed reaction; DFT calculation

1. Introduction

In recent years, a number of researches have been reported about the development of new methodologies for syntheses of various kinds of fluorine-containing heterocycles. These compounds have put emphasis on the interest of high biological activities especially in life-science fields due to the unique character that could contribute to the exploration of new active ingredients [1–4]. In the course of our researches concerning syntheses and reactions of novel fluorine-containing heterocycles, we found that 2,4-diethoxy-6-trifluoromethyl-3,4-dihydro-2*H*-pyran (**1**) prepared in a simple step of hetero-Diels–Alder reaction of 4-ethoxy-1,1,1-trifluorobut-3-en-2-one with ethyl vinyl ether [5] reacted with aromatic compounds in trifluoroacetic acid at ambient temperature to give 4-aryl-2-ethoxy-6-trifluoromethyl-3,4-dihydro-2*H*-pyrans (**2**) as a sole product (Scheme 1) [6]. In contrast to this, it was found that the reaction of **1** with 1,3-dimethoxybenzene in refluxing acetonitrile in the presence of catalytic amounts (0.3 equiv.) of *p*-toluenesulfonic acid afforded *ca.* 1:1 mixture of the corresponding 4-aryl-2-trifluoromethyl-4*H*-pyrans (**3**) and the ring-opening product, 6-aryl-1,1,1-trifluorohexa-3,5-dien-2-ones (**4**) [6]. Similar ring-opening reaction of fluorine-containing dihydro-2*H*-pyrans giving 6-aryl-1,1,1,5,5,5-hexafluoro-3-[(*E*)-3-propylidene]pentane-2,4-diones (**6**) was also found in the reaction of 2-ethoxy-4-isobutoxy-5-trifluoroacetyl-6-trifluoromethyl-3,4-dihydro-2*H*-pyran (**5**) [7] with aromatic compounds in refluxing trifluoroacetic acid [8].

Scheme 1. Acid catalyzed reactions of 2,4-dialkoxy-3,4-dihydro-2*H*-pyrans with aromatic compounds.
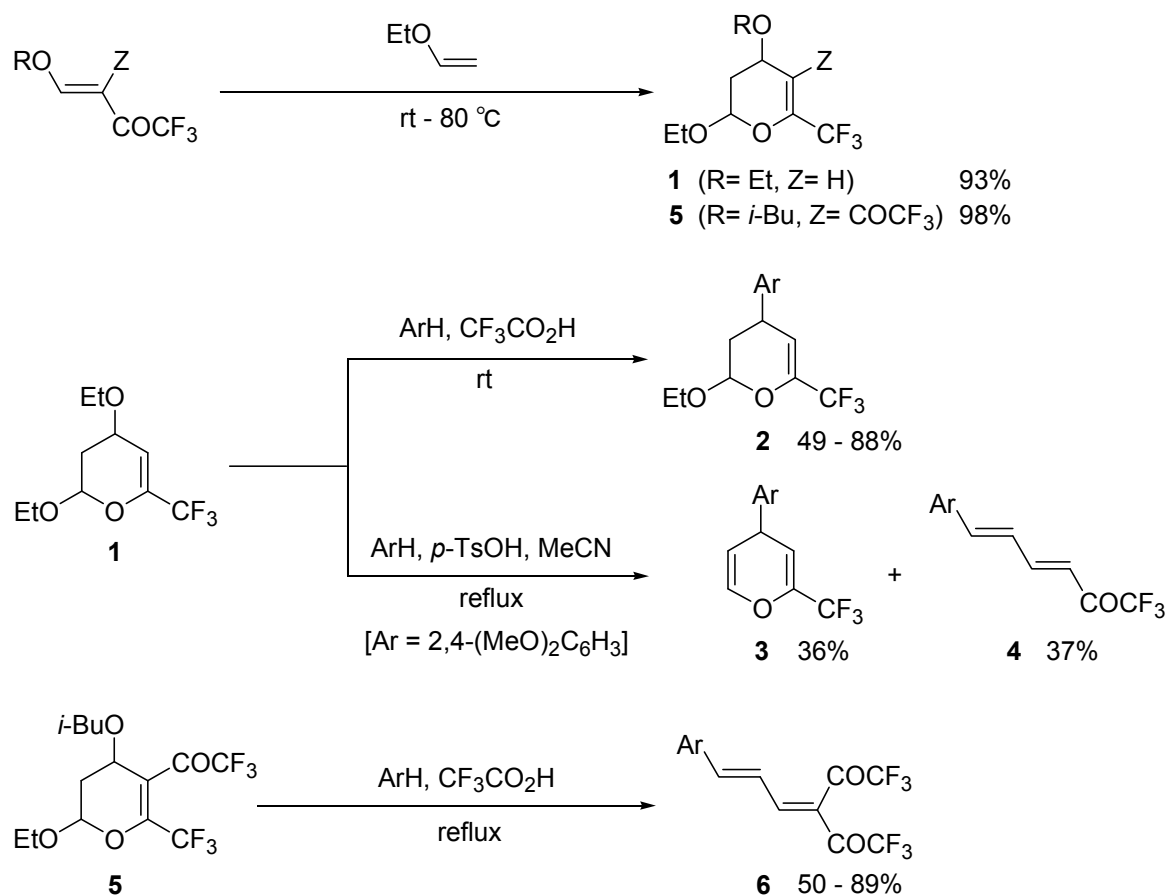
Derivatives having the skeletons of dihydropyrans (**2**), 4*H*-pyrans (**3**), and 1,3-butadienes (**4** and **6**) have a high potential use as synthetic intermediates to access a variety of heterocycles [9–15]. Hence, highly important practices for the constructions of various kinds of novel fluorine-containing heterocyclic systems would be provided by the above reactions of dihydropyrans, **1** and **5**.

As we proposed in our previous report [16], the selective formation of dihydropyrans (**2**) from **1** and of butadiene derivatives (**6**) from **5** could be explained by the kinetically controlled reactions of pyrylium (**7a**) at C-4 and the thermodynamically controlled reaction of **7b** at C-6, respectively (Figure 1). Such pyryliums (**7a**,**b**) are assumed to form easily from **1** and **5** in the strong acid, trifluoroacetic acid. Moreover, the unexpected formation of **7a** in the course of the reaction of dihydropyran (**1**) giving 4*H*-pyrans (**3**) and butadiene derivatives (**4**) is also figured out under weaker acidic conditions such as the presence of catalytic *p*-toluenesulfonic acid in refluxing acetonitrile. In this case, it is probable that **3** and **4** are directly derived from 4-cation (**8a**) and 6-cation (**9a**), respectively, which are the precursors of pyrylium (**7a**).

Figure 1. Cations **7a**,**b**, **8a**,**b**, and **9a**,**b**.

| **7a** Z= H | **8a** Z= H | **9a** Z= H |
| **7b** Z= COCF$_3$ | **8b** Z= COCF$_3$ | **9b** Z= COCF$_3$ |
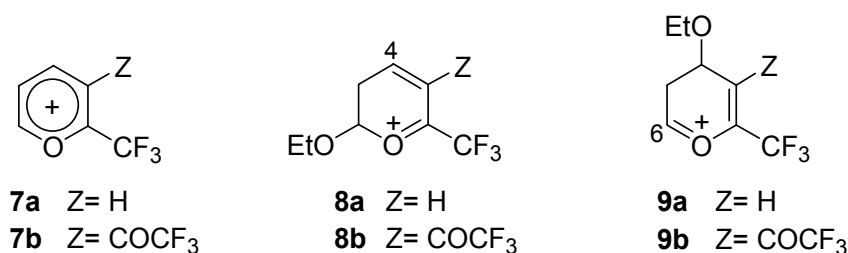
Here we wish to report our DFT calculation study for these acid catalyzed reactions of dihydropyrans, **1** and **5**, with aromatic compounds. The mechanisms giving 4*H*-pyrans (**3**) and 1,3-butadienes (**4**) from **1** in the presence of *p*-toluenesulfonic acid catalyst were elucidated by making use of benzene as a model of aromatic compounds. Additionally, the pathways via cations, **8a** and **9b**, for the reactions of **1** and **5** in trifluoroacetic acid giving dihydropyrans (**2**) and 1,3-butadienes (**6**), respectively, were also examined to support the proposed mechanisms via pyryliums [16] further.

2. Computational Method

All calculations employed in this paper were accomplished by making use of the computer programs packages PC SPARTAN 02 and PC SPARTAN 04 [17]. All calculations for geometrical optimizations were performed with the 6-31G* basis set at B3LYP level [18]. The starting geometries employed for all optimizations were resulted from molecular mechanics using SYBYL [19] force field and subsequent semi-empirical PM3 [20] optimizations. The calculations for transition state geometries and their energies were also taken with the 6-31G* basis set at B3LYP level.

3. Results and Discussion

In trifluoroacetic acid, pyryliums (**7a**,**b**) are assumed to form from **1** and **5** via 4-cations (**8a**,**b**) or 6-cations (**9a**,**b**) as illustrated in Scheme 2. As we proposed in previous report [16], the selective formation of dihydropyrans (**2**) from **1** and of butadiene derivatives (**6**) from **5** could be reasonably

explained by the kinetically controlled reaction of pyrylium (**7a**) with aromatic compounds giving the precursor, 4*H*-pyrans (**3**) and the thermodynamically controlled reaction of **7b** with aromatic compounds affording the intermediate, 2*H*-pyrans (**10**), respectively (Scheme 2).

Scheme 2. Proposed reaction paths for the acid catalyzed reactions of dihydropyrans (**1** and **5**) with aromatic compounds.
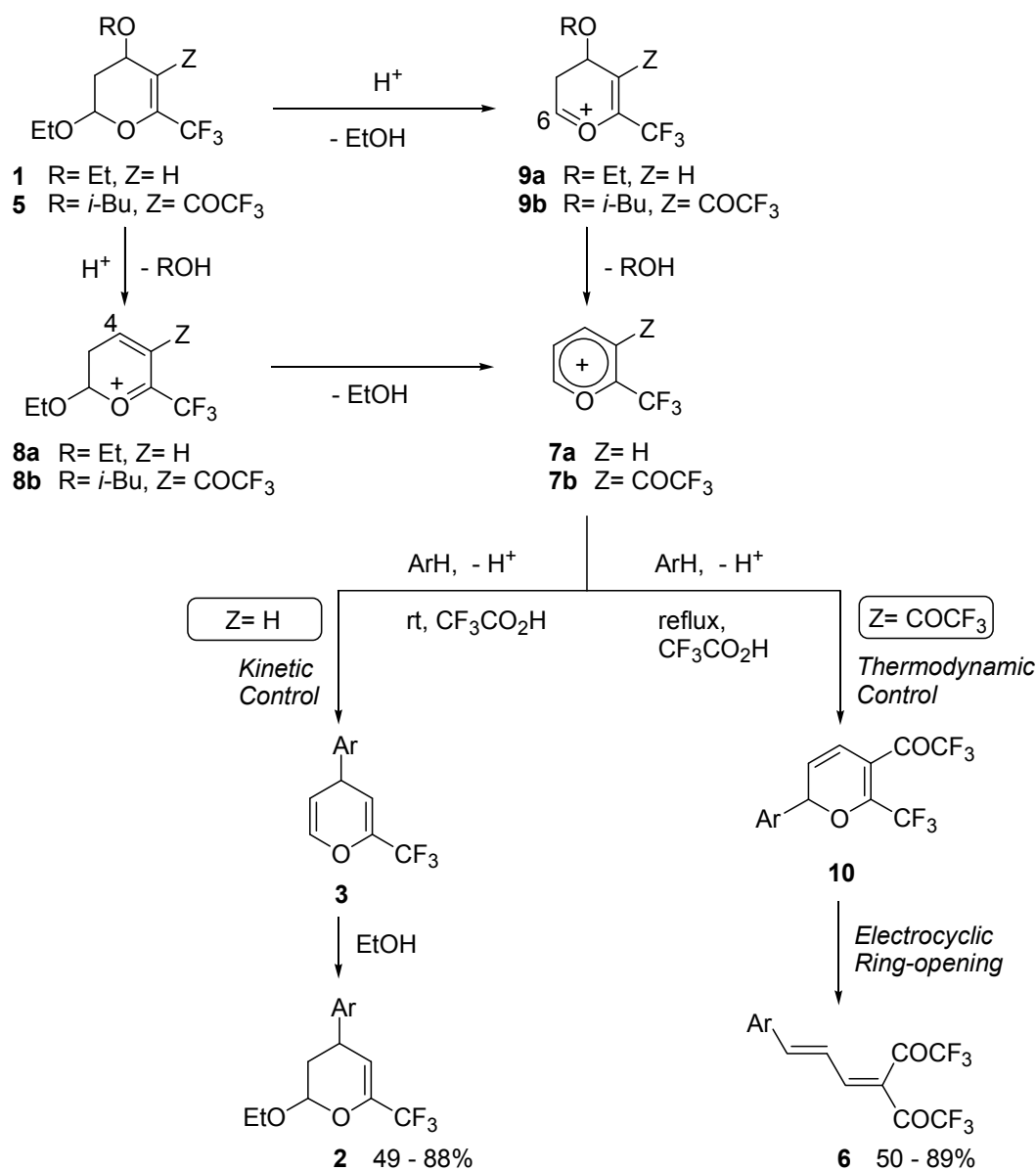
Meanwhile, the formation of pyrylium (**7a**) was hardly considered to occur in the reaction of dihydropyran (**1**) with aromatic compounds giving 4*H*-pyrans (**3**) and butadiene derivatives (**4**) under weaker acidic conditions such as the presence of catalytic *p*-toluenesulfonic acid in acetonitrile. In this case, the alternative pathways in which **3** and **4** are directly derived from 4-cation (**8a**) and 6-cation (**9a**), respectively, are possible. We figured out the optimized structures of **8a** and **9a** using RB3LYP/6-31G* as depicted in Figure 2 together with the result for dihydropyran (**2**) to confirm these reaction pathways.

The results exhibit that 4-cation (**8a**) is *ca.* 21 kcal/mol more stable than 6-cation (**9a**). This value accounts for the exclusive formation of **8a** in the presence of acid catalyst, which suggest that 1,3-butadienes (**4**) are not derived from **9a**. On the other hand, the reaction of **8a** with aromatic compounds giving **2** followed by the elimination of ethanol from **2** can afford 4*H*-pyrans (**3**). According to the energy value for **2** (Ar = Ph) and our previous calculation results for **3** (Ar = Ph) [16,21], the latter elimination process from **2** to **3** is estimated to be an endothermic step with *ca.* 27 kcal/mol, which would negatively affect the conversion of **2** to **3** even if the reaction is carried out in refluxing acetonitrile. Though the de-ethanolization on 4-cation (**8a**) giving pyrylium (**7a**) [22] is also computed to be an endothermic process, the required external energy is no more than 11.3 kcal/mol. It means this elimination reaction is presumed to proceed readily in refluxing acetonitrile. Therefore, the above results strongly suggest the formation of 1,3-butadienes (**4**) and 4*H*-pyrans (**3**) via pyrylium (**7a**). The conversion from **1** to pyrylium (**7a**) is noteworthy in spite of the conditions using only a catalytic amount of *p*-toluenesulfonic acid.

Figure 2. Optimized structures and energy values of intermediates (**8a,b**, **2**, and **11**).

	Bond lengths(Å)					
	O1-C2	C2-C3	C3-C4	C4-C5	C5-C6	O1-C6
8a	1.635	1.517	1.494	1.357	1.425	1.266
9a	1.422	1.329	1.518	1.541	1.466	1.271
2	1.441	1.523	1.548	1.509	1.335	1.368
11	1.354	1.345	1.455	1.343	1.508	1.467
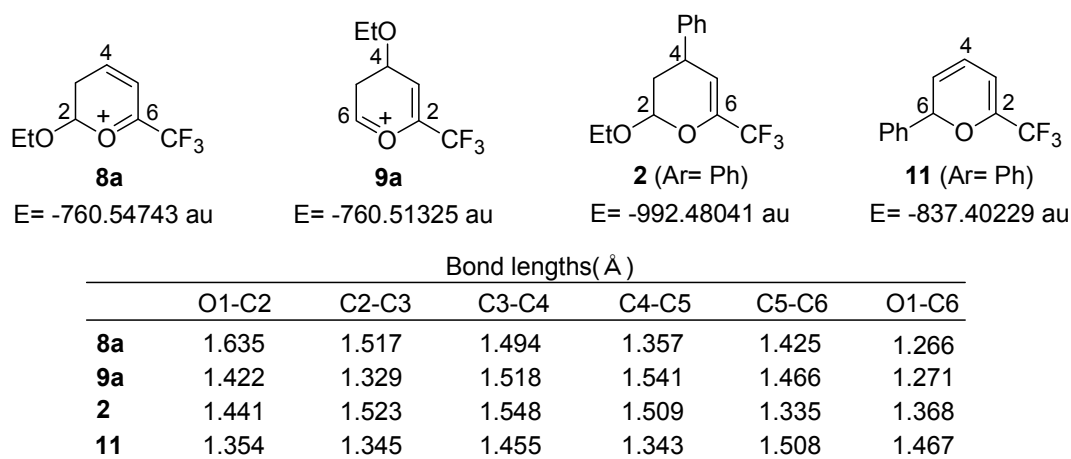
As is described in previous report [16], the kinetically controlled reaction of **7a** with aromatic compounds is predicted to proceed selectively at C-4 to give 4*H*-pyrans (**3**) because the frontier electron density (LUMO of **7a**) at C-4 is considerably larger than that at C-6 [23]. In contrast, the energy of 4*H*-pyrans (**3**) is very close to 2*H*-pyrans (**11**) [24] which are the precursors of 1,3-butadienes (**4**) shown in Figure 2 to attribute the preparation of both **3** and **11** to the thermodynamically controlled reaction of **7a** with aromatic compounds. Relatively high temperature (the temperature of refluxing acetonitrile) required for the reaction of **1** giving **3** and **4** is consistent with the thermodynamically controlled reaction of pyrylium (**7a**) with aromatic compounds.

Next, we estimated the activation energy for the ring-opening process from 2*H*-pyrans (**11**) resulted by the reaction of pyrylium (**7a**) with aromatic compounds at 6-position (Figure 3). The optimized transition state structure (**TS11**; Ar = Ph) [25] and the most stable structure of **4** (Ar = Ph) are illustrated together with their energies. The energy difference between **11** (Ar = Ph) [16] and **TS11** (Ar = Ph) is estimated to be *ca.* 15 kcal/mol, which corresponds to the activation energy of this process. The (*E,Z*)-dienes (**4'**) given by ring-opening of **11** readily isomerize to thermodynamically more stable (*E,E*)-dienes (**4**) via protonation and deprotonation processes (Figure 3). The dienes **4'**

(Ar = Ph) and **4** (Ar = Ph) are calculated to be *ca.* 8 kcal/mol and *ca.* 9 kcal/mol more stable than **11** (Ar = Ph), respectively. The above results suggest that the irreversible ring-opening of the intermediates (**11**) will easily occur at acetonitrile reflux temperature to afford **4**.

Figure 3. Ring-opening process from 2*H*-pyrans (**11**) to (*E*,*E*)-dienes (**4**).
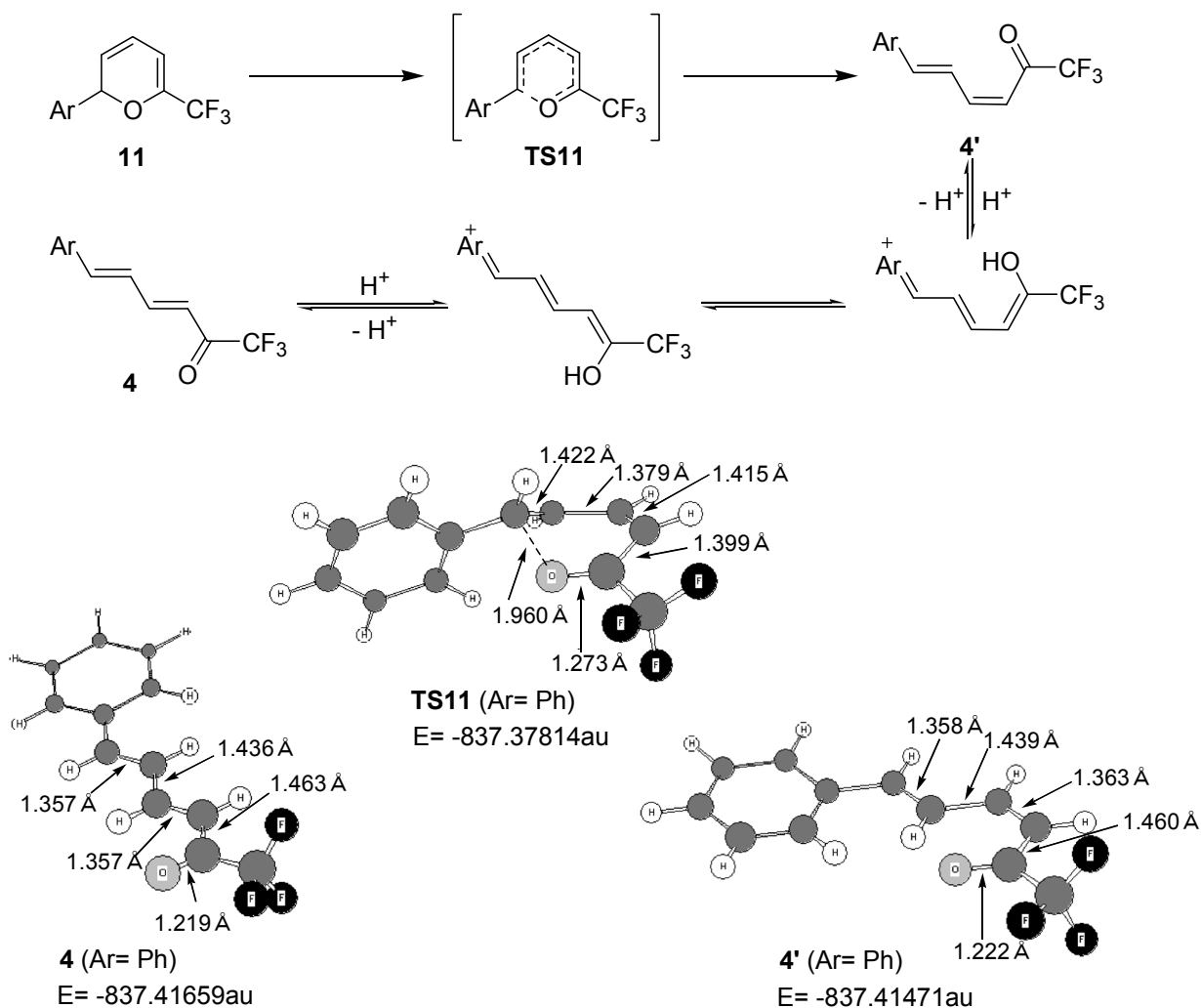
In addition, we examined the process from 4-cation (**8a**) to pyrylium (**7a**) to support the mechanism presented in our previous report [16] for the reaction of dihydropyran (**1**) with aromatic compounds in trifluoroacetic acid at ambient temperature giving dihydro-4*H*-pyrans (**2**) solely (Scheme 1). As is mentioned before, this elimination is an endothermic reaction requiring the external energy of 11.3 kcal/mol [22]. Therefore, this result predicts that the reaction of the first intermediate, 4-cation (**8a**), with aromatic compounds directly affording dihydro-4*H*-pyrans (**2**) have precedence over the course via 4*H*-pyrans (**3**) comprised of the reaction of pyrylium (**7a**) with aromatic compounds given that the dihydropyran (**1**) would undergo the reaction at ambient temperature. Even though 4*H*-pyrans (**3**) was given by the *p*-toluenesulfonic acid catalyzed reaction, the reaction of **1** carried out in trifluoroacetic acid with aromatic compounds [6] resulted in the failure of the formation of **3**. These experimental evidences provide us with compatible conclusion as to the above calculated prediction.

Finally, we examined the reaction of dihydropyran (**5**) with aromatic compounds giving butadiene derivatives (**6**) shown in Scheme 1. As for this reaction, an alternative pathway including the reaction of 6-cation (**9b**) with aromatic compounds directly affording 2*H*-pyrans (**10**) is possible in addition to the pathway via pyrylium (**7b**) illustrated in Scheme 2. To elucidate such alternative pathway, we considered as to figuring out dihydropyran (**5**), 4-cation (**8b**), and 6-cation (**9b**). The results are summarized in Figure 4.

Figure 4. Optimized structures and energy values of dihydropyran (**5**), and cations (**8b** and **9b**).

Bond lengths(Å)						
	O1-C2	C2-C3	C3-C4	C4-C5	C5-C6	O1-C6
5	1.466	1.513	1.533	1.518	1.360	1.337
8b	1.651	1.512	1.490	1.364	1.448	1.262
9b	1.424	1.332	1.541	1.538	1.466	1.271
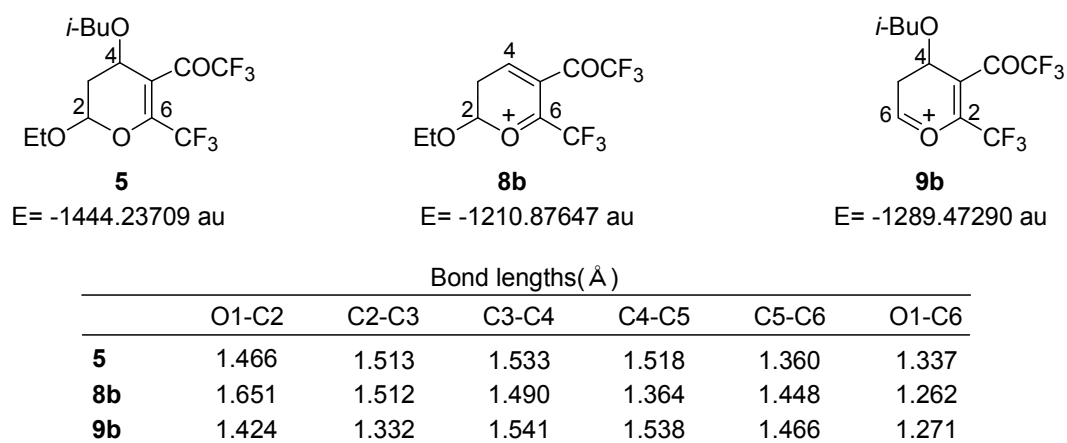
Based on the energy values for **5**, **8b**, and **9b**, the ionization process from **5** to 6-cation (**9b**) is estimated to require *ca.* 20 kcal/mol more energy [26] compared with such ionization to 4-cation (**8b**). The exclusive formation of **8b** from **5** in trifluoroacetic acid is attributed to this value. Hence, the reaction of **5** with aromatic compounds giving **6** does not proceed along the pathway via **9b**. In other words, butadiene derivatives (**6**) are assumed to be derived from pyrylium (**7b**) which formed via 4-cation (**8b**) along the pathway shown in Scheme 2 as we reported previously [16,27]. This de-alcoholization step from **8b** to **7b** is an endothermic process, however the required external energy no more than 13 kcal/mol suggests that **8b** is easily converted to **7b** in refluxing trifluoroacetic acid.

The proposed most reasonable and interesting mechanisms based on our DFT calculations for the acid catalyzed reactions of dihydropyrans (**1** and **5**) with aromatic compounds are summarized in Scheme 3.

Scheme 3. Proposed most reasonable mechanisms for the acid catalyzed reactions of dihydropyrans (**1** and **5**) with aromatic compounds.

Reaction of 1 in refluxing acetonitrile in the presence of p-toluenesulfonic acid
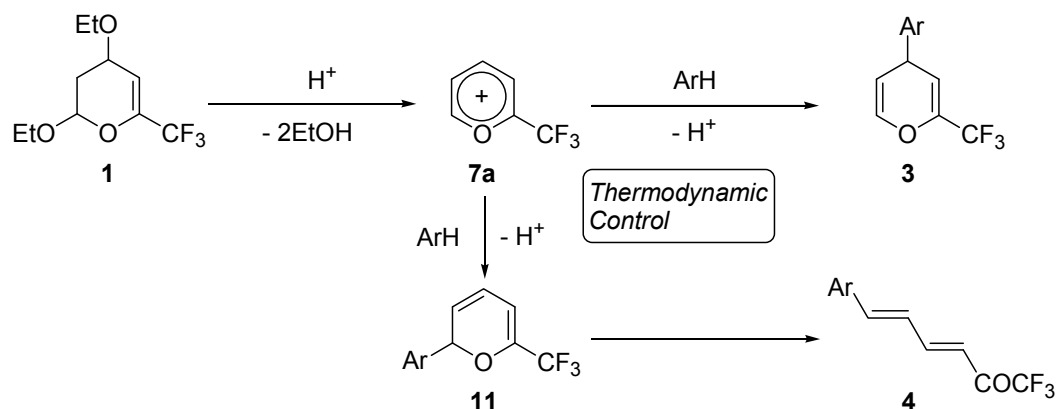
Reaction of 1 in trifluoroacetic acid at ambient temperature
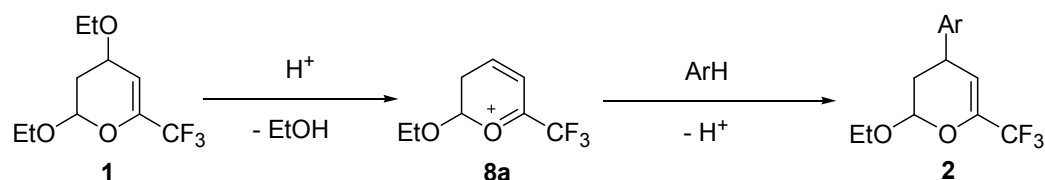
Reaction of 5 in refluxing trifluoroacetic acid
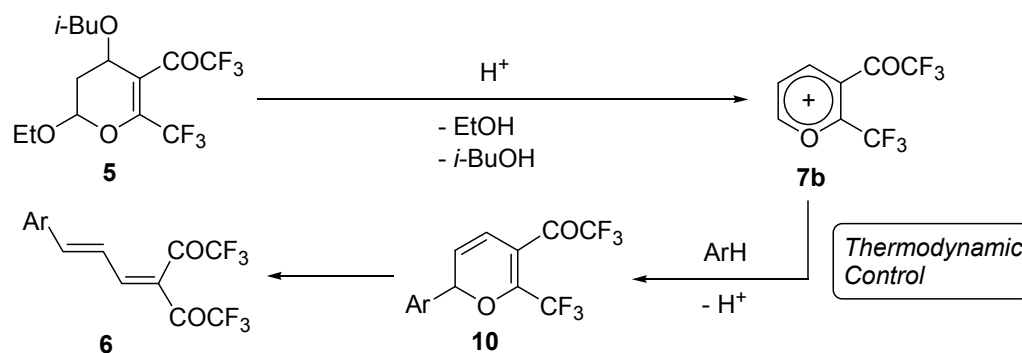
4. Conclusions

On the basis of DFT calculation results, we have achieved a comprehensive explanation regarding the mechanisms for the reactions of dihydropyran (**1**) with aromatic compounds under different acidic reaction conditions. The reaction in the presence of *p*-toluenesulfonic acid giving 4*H*-pyrans (**3**) and butadiene derivatives (**4**) proceeding in refluxing acetonitrile is reasonably explained by the thermodynamically controlled reaction of pyrylium (**7a**) with aromatic compounds. Meanwhile, the reaction in trifluoroacetic acid affording dihydropyrans (**2**) at ambient temperature can be interpreted as a result of the reaction of 4-cation (**8a**) with aromatic compounds. Our study also illustrated the selective formation of butadiene derivatives (**6**) from dihydropyran (**5**) by the reaction in refluxing trifluoroacetic acid in which the thermodynamically controlled attack of aromatic compounds to pyrylium (**7b**) was comprised.

References and Notes

1. Filler, R.; Kobayashi, Y. *Biomedicinal Aspects of Fluorine Chemistry*; Kodansha & Elsevier Biomedical: Tokyo, Japan, 1982.

2. Filler, R. *Organofluorine Chemicals and Their Industrial Applications*; Ellis Horwood: London, UK, 1979.

3. Welch, J.T. Advances in the preparation of biologically active organofluorine compounds. *Tetrahedron* **1987**, *43*, 3123–3197.

4. Filler, R.; Kobayashi, Y.; Yagupolskii, L.M. *Organofluorine Compounds in Medicinal Chemistry and Biomedical Applications*; Elsevier: Amsterdam, The Netherlands, 1993.

5. Hojo, M.; Masuda, R.; Okada, E. A facile synthesis of 2,4-dialkoxy-, 2-alkoxy-4-phenoxy-, and 2,4-diphenoxy-6-(trifluoromethyl)-3,4-dihydro-2*H*-pyrans. Hetero Diels-Alder reactions of trans-β-(trifluoroacetyl)vinyl ethers with various vinyl ethers. *Synthesis* **1989**, vol? 215–217.

6. Ota, N.; Okada, E.; Shibata, D.; Adachi, S.; Saikawa, S. A facile synthesis of 4-aryl-1,1,1-trifluorobut-3-en-2-ones via 4-aryl substituted CF_3-containing dihydropyran derivatives: A versatile method for the introduction of fluorine-containing C_4- and C_6- unit to aromatic compounds. *Heterocycles* **2010**, *80*, 515–525.

7. Hojo, M.; Masuda, R.; Okada, E. A convenient synthetic route to functionalized 5-(trifluoroacetyl)-3,4-dihydro-2*H*-pyrans: hetero-Diels-Alder reaction of β,β-bis(trifluoroacetyl) vinyl ethers with electron-rich alkenes. *Synthesis* **1990**, vol? 347–350.

8. Ota, N.; Okada, E.; Sonoda, A.; Muro, N.; Shibata, D.; Médebielle, M. One step introduction of 4,4-bis(trifluoroacetyl)-1,3-butadiene system to aromatic rings using fluorine-containing 3,4-dihydro-2*H*-pyrans. A facile synthetic method for 1,1,1,5,5,5-hexafluoro-3-[(E)-3-arylallylidene] pentane-2,4-diones. *Heterocycles* **2008**, *76*, 215–219.

9. Zanatta, N.; Fernandes, L.S.; Nachtigall, F.M.; Coelho, H.S.; Amaral, S.S.; Flores, A.F.C.; Bonacorso, H.G.; Martins, M.A.P. Highly chemoselective synthesis of 6-alkoxy-1-alkyl(aryl)-3-trifluoroacetyl-1,4,5,6-tetrahydropyridines and 1-alkyl(aryl)-6-amino-3-trifluoroacetyl-1,4,5,6-tetrahydropyridines. *Eur*. *J. Org. Chem*. **2009**, vol? 1435–1444.

10. Shimizu, M.; Oishi, A.; Taguchi, Y.; Sano, T.; Gama, Y.; Shibuya, I. Quinoline ring formation by cycloaddition of *N*-arylketenimines with enol ethers under high pressure. *Heterocycles* **2001**, *55*, 1971–1980.

11. Caramella, P.; Invernizzi, A.G.; Pastormelo, E.; Quadrelli, P.; Corsaro, A. A pericyclic cascade in the addition of diphenyl nitrile imine to pyridine. *Heterocycles* **1995**, *40*, 515–520.

12. Oinuma, H.; Dan, S.; Kakisawa, H. Stereoselective syntheses of α-isosparteine. *J. Chem. Soc. Perkin Trans*. **1990**, vol? 2593–2597.

13. Wendelin, W.; Schramm, H.-W.; Blasi-Rabassa, A. Reactions of guanidine and thiourea with α,β,γ,δ-unsaturated ketones. *Monatsh*. *Chem*. **1985**, *116*, 385-400.

14. Mohammed, F.K. Synthesis of some new benzo[b]carbazole-6,11-diones. *Egypt*. *J. Chem*. **2006**, *49*, 139–147.

15. Rubinov, D.B.; Rubinova, I.L.; Lakhvich, F.A. Synthesis of exo- and endocyclic enamino derivatives of 2-(3-arylprop-2-enoyl)cyclohexane-1,3-diones. *Russ*. *J. Org. Chem*. **2011**, *47*, 319–330.

16. Ota, N.; Kamitori, Y.; Nishiguchi, E.; Ishii, M.; Okada, E. A molecular orbital calculation study on the interesting reactivity of fluorine-containing 3,4-dihydro-2*H*-pyrans with aromatic compounds in the presence of trifluoroacetic acid. *Heterocycles* **2011**, *82*, 1337–1343.
17. Wavefunction, Inc. Irvine, CA, USA. Available online: http://www.wavefun.com (accessed on 20 February 2012).
18. Becke, A.D. Density-functional thermochemistry. III. The role of exact exchange. *J. Chem. Phys.* **1993**, *98*, 5648–5652.
19. Clark, M.; Cramer, R.D., III.; van Opdensch, N. Validation of the general purpose Tripos 5.2 force field. *J. Comput. Chem.* **1989**, *10*, 982–1012.
20. Stewart, J.J.P. Optimization of parameters for semiempirical methods. I. Method. *J. Comput. Chem.* **1989**, *10*, 209–220.
21. The previously calculated energy value (−837.40329 au: see ref. 16) was used for **3** (Ar= Ph). The energy of ethanol was calculated as −155.06425 au (this work).
22. The previously calculated energy value (−605.49511 au: see ref. 16) was used for **7a**.
23. The frontier electron densities (LUMO) at C-4 and C-6 of **7a** were calculated as 0.582 and 0.341, respectively: see ref. 16.
24. The energy deference between **3** and **11** was estimated to be less than 1 kcal/mol: see ref. 16.
25. Our calculations for vibrational frequencies of **TS11** showed only one imaginary frequency at −416.3 cm^{-1} having the vibrational mode corresponding to the bond formation and cleavage between C6 and O1.
26. The previously calculated energy value (−1055.82147 au: see ref. 16) was used for **7b**. The energy of isobutanol was calculated as −233.66241 au (this work).
27. It was predicted that the reaction of pyrylium (**7b**) with aromatic compounds occurs at C-4 under kinetically controlled conditions and that proceeds at C-6 under thermodynamically controlled conditions: see ref. 16. In addition, the steric hindrance due to trifluoroacetyl group at C-5 would prevent the attack to C-4 on **7b**.

Article

Self-Assembled Fluorinated Organogelators for Surface Modification

Anilkumar Raghavanpillai * and Vincent A. Franco

DuPont Central Research & Development, Experimental Station, Wilmington, DE 19880, USA;
E-Mail: vincent.a.franco@usa.dupont.com

* Author to whom correspondence should be addressed;
   E-Mail: anilkumar.raghavanpillai@usa.dupont.com; Tel.: +1-302-695-6846;
   Fax: +1-302-695-2112.

Abstract: A new class of alkyl- and perfluoroalkyl-containing urea and amide derivatives was synthesized from amino acid derivatives. Most of these compounds showed excellent gelation behavior in organic solvents at low concentrations. A few organogelators selected from the initial screening were used for surface modification of fibrous substrates to create hydrophobic and oleophobic composites. The hydrophobic and oleophobic behaviors of these composites were ascribed to a combination of increased surface roughness and the alkyl/fluorinated functionalities present in the gelator backbone.

Keywords: organogelator; gelation; perfluoroalkyl; urea; amide; amino acid; xerogel; nonwoven; hydrophobic; oleophobic; contact angle; surface modification

1. Introduction

Low molecular weight organogelators (LMWOGs) are gaining increased attention due to their potential applications in a variety of industrial sectors related to materials, cosmetics, health care, food and oil technology [1–9]. The design and elucidation of structure-property relationships of gelators is also a valuable area of research, in particular, establishing the relationship between the chemical structure of a gelator and its gelation properties in a given solvent [10–18]. Thermally reversible physical gels are generally formed by self-assembly of the gelator molecules in solvent, leading to the

formation of a fibrous supramolecular network with the encapsulation of solvent. This complex process of self-assembly into supramolecular structures varies based on the functionalities present in the organogelator and external factors, including solvent, temperature, and pH. Various non-covalent interactions, such as hydrogen bonding, π-π stacking, hydrophobic interactions, and metal coordination, influence the formation and stabilization of the organogelator self-assemblies [1,2,10–14,19–21]. However, the non-covalent forces influencing gelation are relatively weak compared to covalent bonds, and a combination of many of these interactions is required to form a strong intermolecular network. Each molecule of an organogelator can establish several types of physical interactions with a neighboring molecule. For example, intermolecular hydrogen bonding usually facilitates the growth of linear, elongated aggregates with solvent entrapment. Evaporation of solvent from a gel results in the formation of a dried gel (xerogel) with a fibrous or web-like morphology [21]. It is possible to alter the surface morphology of the substrate, and thus surface properties, if the gelation and subsequent evaporation of solvent are performed on a substrate. Hence, gel impregnation methodology could provide the low surface energies desired for fabricating superhydrophobic surfaces [19,21–24]. Surfaces on which the contact angle of water exceeds 150°, and shows low contact angle hysteresis, are described as superhydrophobic or ultrahydrophobic [25–27]. These surfaces repel water like a lotus leaf and are also considered 'self-cleaning', since any surface contamination is removed by water as the droplets roll across the surface [28–30]. The self-cleaning ability of these surfaces is largely due to the increased surface area created by a two-tier micro and nano roughness morphology. It is possible to incorporate nano- or microscale morphologies on any substrate via organogelator impregnation, which could be further controlled by suitable gelling solvents, as well as concentration and temperature effects. In addition, incorporation of low surface energy functionalities like fluorinated groups in the gelator framework could further lower the surface energy and provide oleophobic properties to the modified surface [31].

Urea and amide derivatives are exceptionally well-suited candidates for the design of low molecular weight gelators owing to their rigidity, strength and ability to form highly directional hydrogen bonds [32]. We recently demonstrated this concept by fabricating low surface energy surfaces via the surface modification of nonwoven substrates using partially fluorinated urea-amide gelators [33]. The general structure and examples of these urea-amide gelators reported in that study are shown Figure 1.

Figure 1. General structure and examples of partially fluorinated urea-amide gelators described in [31].

$R_H = C_8H_{17}$, $R_f = C_6F_{13}$
$R_H = C_8H_{17}$, $R_f = C_4F_9$,
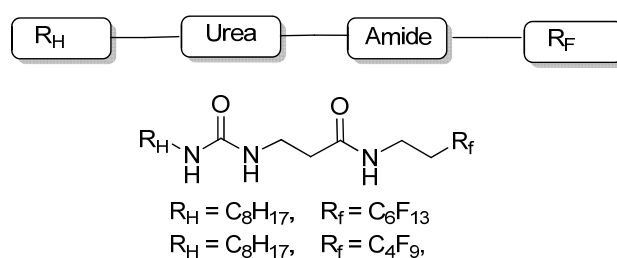
The compounds depicted in Figure 1 were prepared via amidation of the *N*-Boc protected amino acid with fluorinated amines, followed by deprotection and reaction with an alkyl isocynate. They showed excellent gelation behavior in organic solvents. Gelation in the presence of a nonwoven

substrate led to a gel-impregnated surface, which upon drying produced a composite with porous microstructure morphology. The resulting composite also showed high water and hexadecane contact angles, indicative of excellent hydrophobic and oleophobic properties. Herein, we discuss the design and synthesis of two novel classes of partially fluorinated amide and urea-amide derivatives, where the positions of the hydrocarbon and fluorocarbon tail are reversed in the molecular structure in comparison to the gelator described in Figure 1. General structures of these partially fluorinated amide and urea-amide derivatives are shown in Figure 2. This report also describes the gelation behavior as a function of structural/functional variations of these derivatives and surface modification of nonwoven substrates using them.

Figure 2. General structure of partially fluorinated amide and urea-amide derivatives described in this study.
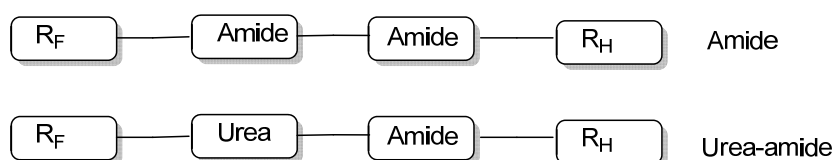
2. Experimental Section

2.1. General

All solvents and reagents, unless otherwise indicated, were purchased from commercial sources and used directly as supplied. Tyvek® polyethylene nonwoven fabric was obtained from E. I. du Pont de Nemours and Company, Wilmington, DE, and Kolon® gsm70 spun-bonded polyester fabric was obtained from Korea Vilene, Inc. ^{1}H and ^{19}F NMR spectra were recorded on a Bruker DRX 400 or 500 spectrometer. Chemical shifts are reported in ppm relative to an internal reference (CDCl$_3$, CFCl$_3$ or TMS). All melting points reported are uncorrected. Contact angle (CA) measurements for both water and hexadecane on a surface were performed according to procedures in the manufacturer's manual using a Ramé-Hart Standard Automated Goniometer Model 200 employing DROP image standard software and equipped with an automated dispensing system with a 250 μL syringe and an illuminated specimen stage assembly. 2*H*,2*H*,3*H*,3*H*-perfluorononoyl chloride, 2*H*,2*H*,3*H*,3*H*-perfluoroheptanoyl chloride, 1*H*,1*H*,2*H*,2*H*-perfluorooctyl isocyanate and 1*H*,1*H*,2*H*,2*H*-perfluorohexyl isocyanate were synthesized from the corresponding perfluoroalkylethyl iodides [34].

2.2. Synthesis of 2H,2H,3H,3H-Perfluorononoyl Chloride and 1H,1H,2H,2H-Perfluorooctyl Isocyanate

A four-neck reactor fitted with a stirrer, thermocouple, nitrogen purge, addition funnel and jacketed condenser was purged with nitrogen and charged with magnesium turnings (4.86 g, 202.5 mmol) and anhydrous ether (300 mL). To this suspension was slowly added a solution of 1*H*,1*H*,2*H*,2*H*-perfluorooctyl iodide (94.8 g, 200 mmol) in ether (100 mL) over a 2 h period. After the addition of about 10 mL of iodide, the mixture was heated to 35 °C, and when the reaction was initiated the rest of the iodide was added, keeping the temperature below 35 °C. The mixture was stirred for 2 h at room temperature (RT) and cooled to 5–10 °C. Excess dry ice (~15 g) was added in small portions with

constant stirring. After 15 min, the mixture was quenched with H_2SO_4 (25%) and the ether phase was separated. The aqueous phase was extracted with ether (2 × 100 mL). Combined ether phases were washed with NaOH solution (25%, 3 × 75 mL). The combined alkaline phases were heated at 100 °C for 10 min and neutralized using H_2SO_4 (50%) after cooling to ice temperature. The precipitate formed was filtered and washed with water to obtain 2*H*,2*H*,3*H*,3*H*-perfluorononoic acid as a white crystalline solid (56.5 g, 14.1 mmol, 72%). mp. 61–63 °C.

The 2*H*,2*H*,3*H*,3*H*-perfluorononoic acid (44.4 g, 113.2 mmol) was heated with PCl_5 (35.4 g, 169.8 mmol) at 110 °C for 3 h and the resulting mixture fractionally distilled to obtain 2*H*,2*H*,3*H*,3*H*-perfluorononoyl chloride as a colorless liquid (44.5 g, 107.5 mmol, 95%). bp. 129 °C @ 85 mm Hg.

A 3-necked flask fitted with a stirrer, an addition funnel and a condenser with N_2 purge was charged with freshly distilled 2*H*,2*H*,3*H*,3*H*-perfluorononoyl chloride (16.26 g, 39.6 mmol). Trimethylsilyl azide (TMSN$_3$, 4.57 g, 39.61 g) was added dropwise via the addition funnel, keeping the temperature about 5–10 °C. The mixture was then stirred at 10 °C for 30 min and heated at 75 °C for 1.5 h. After the reaction was complete (GC analysis), trimethylsilyl chloride was distilled off at atmospheric pressure and then the product was fractionally distilled under vacuum to produce 1*H*,1*H*,2*H*,2*H*-perfluorooctyl isocyanate as a colorless liquid (11.9 g, 30.6 mmol, 77%) bp.100–103 °C @ 30 mm Hg.

2.3. Synthesis of 2*H*,2*H*,3*H*,3*H*-*Perfluoroheptanoyl Chloride and* 1*H*,1*H*,2*H*,2*H*-*Perfluorohexyl Isocyanate*

Using a similar procedure as described above, reaction of 1*H*,1*H*,2*H*,2*H*-perfluorohexyl iodide (74.8 g, 200 mmol) with Mg (4.86 g, 202.5 mmol) and dry-ice (~15 g) produced 2*H*,2*H*,3*H*,3*H*-perfluoroheptanoic acid as a white crystalline solid (43 g, 145.7 mmol). Reaction of 2*H*,2*H*,3*H*,3*H*-perfluoroheptanoic acid (30.0 g, 102.7 mmol, mp. 44 °C) with PCl_5, followed by distillation, produced 2*H*,2*H*,3*H*,3*H*-perfluoroheptanoyl chloride as a colorless liquid (18.0 g, 61.8 mmol, 60%, bp. 27 °C @ 3 mm Hg. The 2*H*,2*H*,3*H*,3*H*-perfluoroheptanoyl chloride (4.30 g, 10.5 mmol) upon reaction with TMSN$_3$ (1.45 g, 12.6 mmol), followed by fractional distillation, produced 1*H*,1*H*,2*H*,2*H*-perfluorohexyl isocyanate as a colorless liquid (2.5 g, 6.42 mmol, 61%). bp.101–103 °C @ 50 mm Hg.

2.4. Synthesis of **1**

A mixture of dichloromethane (350 mL), *N*-Boc-β-alanine (8.50 g, 45.0 mmol), 1-[3-(dimethylamino)propyl]-3-ethylcarbodiimide hydrochloride (EDCl) (8.6 g, 45.0 mmol) and 4-(dimethylamino)pyridine (5.49 g, 45.0 mmol) were stirred for 10 min at RT, followed by addition of octylamine (5.71 g, 45.0 mmol). The mixture was stirred for 12 h at RT. The mixture was washed with 5% HCl (2 × 100 mL), saturated $NaHCO_3$ solution (1 × 100 mL) and brine (1 × 50 mL). The resulting organic layer was dried ($MgSO_4$) and concentrated to provide *N*-Boc-β-ala-octylamide (**1**) as a white crystalline solid (11.6 g, 38.6 mmol, 86%): mp. 67.5–68.4 °C; ^{1}H NMR (methanol-*d*4): δ 3.18 (t, J = 7.0 Hz, 2H), 2.90 (t, *J* = 6.5 Hz, 2H), 2.35 (t, J = 6.5 Hz, 2H), 1.51 (quintet, *J* = 7.0 Hz, 2H), 1.34 (m, 10H), 0.93 (t, distorted, *J* = 6.5 Hz, 3H):

2.5. Synthesis of **2**

A suspension of **1** (10.5 g, 35.0 mmol) in dichloromethane (40 mL) was stirred with trifluoroacetic acid (TFA) (31.9 g, 280.0 mmol) at RT for 3 h. Chloroform (100 mL) was added and the bulk of the solvents and TFA evaporated under vacuum. The resulting trifluoroacetate salt was suspended in dichloromethane (50 mL) and stirred with dropwise addition of saturated $NaHCO_3$ solution (200 mL) and the solid formed was filtered. The residue was washed several times with cold water and dried under vacuum to provide compound **2** as a white solid (6.5 g, 32.5 mmol, 93%): mp. 142–143.5 °C. ^{1}H NMR (methanol-d4): δ 3.46 (t, J = 7.2 Hz, 2H), 3.17 (t, J = 7.0 Hz, 2H), 2.58 (m, 2H), 2.40 (t, J = 6.5 Hz, 4H), 1.50 (quintet, J = 7.0 Hz, 2H), 1.34 (m, 10H), 0.93 (t, distorted, 3H): ^{19}F NMR (methanol d4): δ −82.8 (m, 3F), −115.9 (m, 2F), −123.3 (s, 2F), −124.3 (s, 2F), −125.0 (m, 2F), −127.7 (m, 2F).

2.6. Synthesis of **3**

Using a similar procedure as described for the synthesis of compound **1**, reaction of *N*-Boc-L-aspartic acid (10.0 g, 43.1 mmol) with *n*-octylamine (11.1 g, 86.2 mmol) 1-[3-(dimethylamino)propyl]-3-ethylcarbodiimide hydrochloride (EDCl) (16.5 g, 86.2 mmol) and 4-(dimethylamino)pyridine (5.25 g, 43.1 mmol) in dichloromethane (300 mL) provided *N*-Boc-L-Asp-dioctylamide **3** (18.8 g, 41.3 mmol, 92%). mp. 112–113 °C.

2.7. Synthesis of **4**

Using a similar procedure as described for the synthesis of compound **2**, reaction of **3** (18.6 g, 41.0 mmol) with trifluoroacetic acid (46.7 g, 410 mmol) in dichloromethane (50.0 mL) provided compound **4** (13.4 g, 96%) as a white solid. mp. 120.5–122 °C. ^{1}H NMR (acetone-d6) δ 7.14 (bs, 2H), 4.35 (dd, J = 8.8, 4.6 Hz, 1H), 3.18 (m, 4H), 2.66 (dd, J = 14.0, 4.0 Hz, 1H), 2.35 (dd, J = 14.0, 8.0 Hz, 1H), 1.90 (bm, 2H), 1.50 (m, 4H), 1.31 (m, 10H), 0.90 (t, J = 6.8 Hz, 3H).

2.8. Synthesis of **5a**

To a mixture of **2** (1.0 g, 5.0 mmol), dichloromethane (20 mL) and triethylamine (0.526 g, 0.52 mmol) under a N_2 purge was added 2*H*,2*H*,3*H*,3*H*-perfluorononoyl chloride (2.13 g, 5.2 mmol) and the mixture stirred for 5 h at RT. The bulk of the dichloromethane was evaporated and the solid obtained was taken in ethyl acetate (60 mL) and then washed with 2% HCl (2 × 30 mL), water (1 × 30 mL) and brine (1 × 30 mL). The resulting organic layer was dried ($MgSO_4$) and concentrated to provide **5a** as a white solid (2.46 g, 4.29 mmol, 86%): ^{1}H NMR (methanol-d4): δ 3.46 (t, J = 7.2 Hz, 2H), 3.17 (t, J = 7.0 Hz, 2H), 2.58 (m, 2H), 2.40 (t, J = 6.5 Hz, 4H), 1.50 (quintet, J = 7.0 Hz, 2H), 1.34 (m, 10H), 0.93 (t, distorted, 3H): ^{19}F NMR (methanol-d4): δ −82.8 (m, 3F), −115.9 (m, 2F), −123.3 (s, 2F), −124.3 (s, 2F), −125.0 (m, 2F), −127.7 (m, 2F).

2.9. Synthesis of **5b**

Using a similar procedure as described for the synthesis of compound **5a**, reaction of **2** (1.37 g, 6.85 mmol) with 2*H*,2*H*,3*H*,3*H*-perfluoroheptanoyl chloride (2.13 g, 6.85 mmol) and triethylamine

(0.69 g, 6.85 mmol) provided **5b** as a white solid (2.8 g, 5.90 mmol, 86%): mp. 99–102 °C; ^{1}H NMR (CDCl$_3$): δ 6.78 (bs, 1H), 5.81 (bs, 1H), 3.56 (q, *J* = 6.4 Hz, 2H), 3.25 (q, *J* = 7.2 Hz, 2H), 2.47 (m, 2H), 2.43 (t, *J* = 5.6 Hz, 4H), 1.51 (quintet, *J* = 7.0 Hz, 2H), 1.30 (m, 10H), 0.901 (t, *J* = 7.5 Hz, 3H); ^{19}F NMR (CDCl$_3$): δ −81.6 (m, 3F), −115.3 (m, 2F), −125.0 (m, 2F), −126.6 (m, 2F).

2.10. Synthesis of **5c**

Using a similar procedure as described for the synthesis of compound **5a**, reaction of **2** (1.37 g, 6.85 mmol) with pentafluorobenzoyl chloride (1.57 g, 6.85 mmol) and triethylamine (0.69 g, 6.85 mmol) provided **5c** as a white solid (2.2 g, 5.58 mmol, 82%): mp. 154–155 °C; ^{1}H NMR (methanol-d4): δ 3.65 (t, *J* = 6.8 Hz, 2H), 3.19 (t, *J* = 7.2 Hz, 2H), 2.53 (t, *J* = 5.6 Hz, 2H), 1.52 (quintet, *J* = 7.0 Hz, 2H), 1.34 (m, 10H), 0.92 (t, distorted, 3H); ^{19}F NMR (methanol-*d*4): δ −144.3 (m, 2F), −155.8 (m, 1F), −164.3 (m, 2F).

2.11. Synthesis of **6a**

Using a similar procedure as described for the synthesis of compound **5a**, reaction of **4** (1.775 g, 5.0 mmol) with 2*H*,2*H*,3*H*,3*H*-perfluorononoyl chloride (0.438 g, 2.7 mmol) provided **6a** as a white solid (2.8 g, 77%): mp. 178–180 °C; ^{1}H NMR (acetone-d6) δ 7.52 (bs, 1H), 7.17 (bs, 1H), 7.06 (bs, 1H), 4.55 (m, 1H), 3.02 (bs, 4H), 2.55-2.40 (m, 6H), 1.27 (m, 4H), 1.16 (bs, 20 H), 0.75 (bs, 6H); ^{19}F NMR (acetone-d6): δ −82.1 (s, 3F), −115.2 (s, 2F), −122.8 (s, 2F), −123.8 (s, 2F), −124.4 (s, 2F), −127.1 (s, 2F).

2.12. Synthesis of **6b**

Using a similar procedure as described for the synthesis of compound **5a**, reaction of **4** (1.77 g, 5.0 mmol) with 2*H*,2*H*,3*H*,3*H*-perfluoroheptanoyl chloride (1.55 g, 5.0 mmol) provided **6b** as a white solid (1.92 g, 61%): mp. 163.5–165.5 °C; ^{1}H NMR (DMF-d7): δ 8.80 (bs, 1H), 8.0 (bs, 1H), 7.96 (bs, 1H), 4.91 (q, *J* = 6.0 Hz, 1H), 3.32 (m, 4H), 2.87–2.70 (m, 4H), 1.63 (m, 4H), 1.45 (bs, 20 H), 0.75 (t, distorted, 6H); ^{19}F NMR (DMF-d7): δ −81.8 (m, 3F), −114.9 (m, 2F), −125.9 (m, 2F), −126.6 (m, 2F).

2.13. Synthesis of **6c**

Using a similar procedure as described for the synthesis of compound **5a**, reaction of **4** (1.77 g, 5.0 mmol) with pentafluorobenzoyl chloride (1.15 g, 5.0 mmol) provided **6c** as a white solid (1.8 g, 66%): mp. 172–183.5 °C; ^{1}H NMR (DMF-d7): δ 9.11 (d, *J* = 8.0 Hz, 1H), 7.88 (m 2H), 4.96 (q, *J* = 6.8 Hz, 1H), 3.19 (m, 4H), 2.78–2.70 (m, 2H). 1.48 (m, 4H), 1.29 (bs, 20 H), 0.89 (t, distorted, 6H); ^{19}F NMR (DMF-*d*7): δ −143.0 (m, 2F), −155.5 (t, *J* = 21.6 Hz, 1F), −163.9 (m, 2F).

2.14. Synthesis of **7a**

To a mixture of **2** (0.822 g, 4.11 mmol), dichloromethane (20 mL) and triethylamine (0.02 g, 0.2 mmol) under a N$_2$ purge was added 1*H*,1*H*,2*H*,2*H*-perfluorooctyl ioscyanate (1.75 g, 4.52 mmol), and the mixture stirred for 5 h at RT. The solid product was filtered and washed with cold hexanes (2 × 5 mL) to provide **7a** as a white solid (1.8 g, 3.05 mmol, 74%): mp. 132–136 °C; ^{1}H NMR

(methanol-d4): δ 3.46 (t, *J* = 7.2 Hz, 2H), 3.39 (t, *J* = 6.4 Hz, 2H), 2.94 (m, 2H), 2.60 (t, *J* = 6.0 Hz, 2H), 2.39 (m, 2H), 1.53 (m, 2H), 1.34 (bs, 10H), 0.92 (t, distorted, 3H); ^{19}F NMR (methanol-d4): δ −82.8 (m, 3F), −115.6 (m, 2F), −123.2 (s, 2F), −124.2 (s, 2F), −125.0 (m, 2F), −127.7 (m, 2F).

2.15. Synthesis of **7b**

Using a similar procedure as described for the synthesis of compound **7a**, reaction of **2** (0.629 g, 3.14 mmol) with 1*H*,1*H*,2*H*,2*H*-perfluorohexyl isocyanate (1.2 g, 4.15 mmol) provided **7b** (1.08 g, 67%): ^{1}H NMR (methanol-d4): δ 3.46 (t, *J* = 7.2 Hz, 2H), 3.39 (t, *J* = 6.4 Hz, 2H), 3.19 (m, 2H), 2.61 (t, *J* = 6.0 Hz, 2H), 2.39 (m, 2H), 1.53 (m, 2H), 1.34 (bs, 10H), 0.92 (t, distorted, 3H); ^{19}F NMR (methanol-*d*4): δ −83.0 (m, 3F), −115.8 (m, 2F), −126.1 (m, 2F), −127.6 (m, 2F).

2.16. Synthesis of **7c**

Using a similar procedure as described for the synthesis of compound **7a**, reaction of **2** (1.0 g, 5.0 mmol) with pentafluorophenyl isocyanate (1.04 g, 5.0 mmol) provided **7c** as a white solid (1.72 g, 84%): mp. 175–176 °C; ^{1}H NMR (methanol-d4): δ 3.48 (t, *J* = 6.8 Hz, 2H), 3.20 (t, *J* = 7.2 Hz, 2H), 2.45 (t, *J* = 5.6 Hz, 2H), 1.52 (quintet, *J* = 7.0 Hz, 2H), 1.33 (m, 10H), 0.91 (t, *J* = 7.5 Hz, 3H); ^{19}F NMR (methanol-d4): δ −149.4 (m, 2F), −162.8 (t, *J* = 20.6 Hz, 1F), −167.3 (m, 2F).

2.17. Synthesis of **8a**

Using a similar procedure as described for the synthesis of compound **7a**, reaction of **4** (0.912 g, 2.57 mmol) with 1*H*,1*H*,2*H*,2*H*-perfluorooctyl isocyanate (1.16 g, 3.0 mmol) provided **8a** as a white solid (1.1 g, 1.47 mmol, 58%): ^{1}H NMR (methanol-d4): δ 4.54 (t, *J* = 6.8 Hz, 1H), 3.46 (t, *J* = 6.8 Hz, 2H), 3.21 (m, 4H), 2.60 (m, 2H), 2.40 (m, 2H), 1.53 (m, 4H), 1.33 (bs, 20H), 0.922 (t, distorted, 6H); ^{19}F NMR (methanol-d4): δ −82.8 (m, 3F), −115.6 (s, 2F), −123.2 (s, 2F), −124.2 (s, 2F), −125.0 (s, 2F), −127.6 (m, 2F).

2.18. Synthesis of **8b**

Using a similar procedure as described for the synthesis of compound **7a**, reaction of **4** (0.79 g, 2.24 mmol) with 1*H*,1*H*,2*H*,2*H*-perfluorohexyl isocyanate (1.0 g, 3.26 mmol) provided **8b** as a white solid (1.51 g, 71%) ^{1}H NMR (methanol-d4): δ 4.54 (t, *J* = 6.8 Hz, 1H), 3.46 (t, *J* = 6.8 Hz, 2H), 3.22 (m, 4H), 2.61 (m, 2H), 2.41 (m, 2H), 1.51 (m, 4H), 1.33 (bs, 20H), 0.922 (t, distorted, 6H); ^{19}F NMR (methanol-*d*4): δ −83.0 (m, 3F), −115.8 (m, 2F), −126.0 (m, 2F), −127.6 (m, 2F).

2.19. Synthesis of **8c**

Using a similar procedure as described for the synthesis of compound **7a**, reaction of **4** (1.77 g, 5.0 mmol) with pentafluorophenyl isocyanate (1.04 g, 5.0 mmol) provided **8c** as a white solid (2.0 g, 3.45 mmol, 71%): ^{1}H NMR (DMF-d7, 100 °C): δ 8.74 (m, 1H), 7.57 (bs, 2H), 7.17 (bs, 1H), 4.74 (q, *J* = 6.8 Hz, 1H), 3.35 (m, 4H), 2.86 (dd, *J* = 15.2, 6.0 Hz, 1H), 2.78 (dd, *J* = 15.2, 6.0 Hz, 1H), 1.65 (m, 4H), 1.47 (bs, 20 H), 1.03 (t, distorted, 6H); ^{19}F NMR (DMF-d7): δ −147.8 (m, 2F), −163.2 (t, *J* = 22.0 Hz, 1F), −168.3 (m, 2F).

2.20. Synthesis of **9**

Using a similar procedure as described for the synthesis of **1**, reaction of *N*-Boc-β-alanine (8.5 g, 45.0 mmol) with *n*-octanol (5.85 g, 45.0 mmol), 1-[3-(dimethylamino)propyl]-3-ethylcarbodiimide hydrochloride (8.62 g, 45.0 mmol) and 4-(dimethylamino)pyridine (5.49 g, 45.0 mmol) in dichloromethane (350 mL) provided *n*-octyl-*N*-Boc-β-alanine (12.75 g, 42.3 mmol, 94%). Using a similar procedure as described for the synthesis of **2**, *n*-octyl-*N*-Boc-β-alanine (12.0 g, 39.87 mmol) was deprotected with trifluoroacetic acid to obtain *n*-octyl-β-alanine (6.8 g, 33.8 mmol, 85%). Reaction of *n*-octyl-β-alanine (0.573 g, 2.85 mmol) with 1*H*,1*H*,2*H*,2*H*-perfluorooctyl isocyanate (1.1 g, 2.85 mmol) provided **9** as a pale yellow oil (1.95 g, 62%): ^{1}H NMR (CDCl$_3$): δ 4.06 (t, J = 7.2 Hz, 2H), 3.53 (t, J = 6.4 Hz, 2H), 3.26 (m, 2H), 2.30 (m, 2H), 1.55 (m, 2H), 1.20 (bs, 10H), 0.81 (t, distorted, 3H); ^{19}F NMR (CDCl$_3$): δ −81.2 (m, 3F), −114.4 (m, 2F), −122.2 (s, 2F), −123.2 (m, 2F), −124.0 (m, 2F), −126.5 (m, 2F).

2.21. Synthesis of **10**

Using a similar procedure as described for the synthesis of **1**, reaction of *N*-Boc-L-aspartic acid (10.0 g, 43.1 mmol) with *n*-octanol (11.2 g, 86.2 mmol) provided *N*-Boc-dioctylaspartate as an oil (19.0 g, 41.5 mmol, 96%): ^{1}H NMR (CDCl$_3$): δ 5.49 (d, J = 8 Hz, 1H), 4. 53 (m, 1H), 4.14 (m, 2H), 4.06 (t, J = 7.2 Hz, 2H), 2.95 (dd, J = 17.2, 4.4 Hz, 1H), 2.78 (dd, J = 17.8, 5.2 Hz, 1H), 1.60 (quintet, J = 7.2 Hz, 4 H), 1.29 (bm, 10H), 1.44 (s, 9H) 0.87 t, J = 7.8 Hz, 6H).

Using a similar procedure as described for the synthesis of **2**, *N*-Boc-dioctylaspartate (19.0 g, 41.5 mmol) was deprotected using trifluoroacetic acid to obtain dioctylaspartate as a viscous oil which solidified in the freezer (12.1 g, 34.0 mmol, 82%).^{1}H NMR (CDCl$_3$): δ 4.16 (m, 4H), 3.82 (dd, J = 7.2, 5.3 Hz, 1H), 2.95 (dd, J = 17.6, 4.6 Hz, 1H), 2.71 (dd, J = 17.6, 4.5 Hz, 1H), 1.80 (bs, 2H), 1.62 (m, 4H), 1.31 (m, 10 H), 0.90 (t, J = 6.8 Hz, 6H). Using a similar procedure as described for the synthesis of **7a**, reaction of octyldiaspartate (0.629 g, 3.14 mmol) with 1*H*,1*H*,2*H*,2*H*-perfluorohexyl isocyanate (1.21 g, 4.21 mmol) provided **10** as an oil (1.12 g, 67%): 1H NMR (CDCl3): δ. 5.70 (bs, 1H), 5.39 (bs, 1H), 4.75 (m, 1H), 4.15-3.4.0 (m, 4H), 3.55 (t, J = 6.4 Hz, 2H), 2.97 (dd, J = 16.8, 4.8 Hz, 1H), 2.78 (dd, J = 16.8, 4.8 Hz, 1H), 2.34 (m, 2H), 1.60 (m, 4H), 1.26 (m, 16H), 0.93 (t, J = 6.8 Hz, 6H); 19F NMR (CDCl3): δ. −81.5 (m, 3F), −114.5 (m, 2F), −122.4 (s, 2F), −123.5 (s, 2F), −124.4 (s, 2F), −126.7 (m, 2F).

2.22. Gelation Experiments in Organic Solvents

Typically, 1–4 mg/mL of a gelator in an organic solvent in a closed vial was heated in a reactor block equipped to heat multiple vials. The vials were heated to 5–10 °C below the boiling point of the solvent until a clear solution was obtained, and then were allowed to cool to RT either by switching off the heat or by transferring the vials to a constant temperature water bath kept at 25 °C. The state of the solution was evaluated after 2–12 h. Stability of the gel was tested by inverting the vial, and gel samples for which the whole mass remains a single phase (no phase separation between solid and liquid phase) are considered stable.

2.23. Gel-Impregnation of Nonwoven Supports in Organic Solvents

Nonwoven fabrics (Tyvek® polyethylene nonwoven fabric and Kolon® spun-bonded polyester fabric (about 3.0 cm × 3.0 cm) were immersed in a suspension of amide or urea-amide gelator (1–3 mg/mL) in organic solvent kept in closed reaction flask equipped with a stir bar and temperature controller. The mixtures were heated to 5 °C below the boiling point of the solvent for 1–2 h until clear solutions formed. The flasks were then either rapidly cooled to RT by removing the oil bath or slowly cooled to RT by switching off the heat. Gel formation was usually observed in about 0.5–6 h, and the gels were allowed to age for an additional 6 h. The gelator-impregnated samples were removed and dried in a vacuum oven at RT overnight. The dried samples were weighed and used for contact angle measurements.

3. Results and Discussion

3.1. Organogelators: Design and Synthesis

Several new partially fluorinated organogelators were designed via careful manipulation of hydrogen bonding functionalities (urea and amide) and hydrophobic functionalities (fluorocarbon and hydrocarbon) in the molecule to promote gelation. Boc-protected amino acids, *N*-Boc-β-alanine and *N*-Boc-L-aspartic acid were chosen as the building blocks. First *N*-Boc-β-alanine and *N*-Boc-L-aspartic acid were transformed to the corresponding *N*-Boc-octylamides (**1** and **3**) by reacting with octylamine (Scheme 1). The resulting amides were deprotected to obtain the corresponding free amide-amine derivatives (**2** and **4**), the primary building blocks for partially fluorinated amide or urea-amide derivatives.

Scheme 1. Synthesis of 3-amino-*N*-octylpropanamide (**2**) L-asparticdioctylamide (**4**) building blocks from *N*-Boc-β-alanine and *N*-Boc-L-aspartic acid.
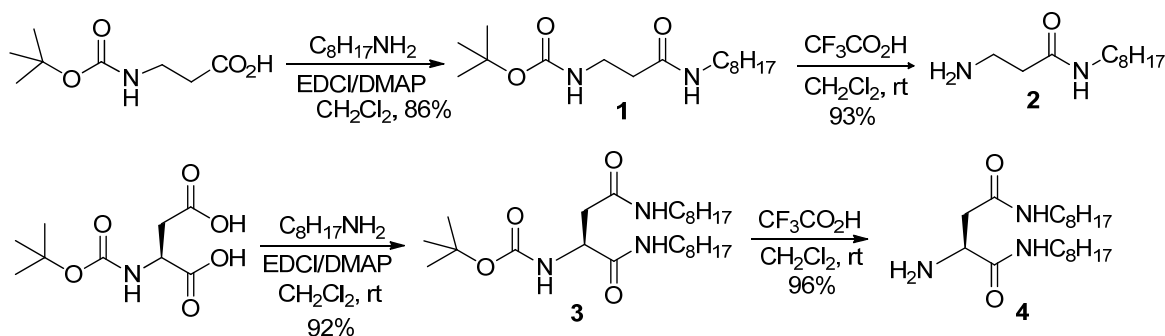
3.1.1. Partially Fluorinated-bis- and Tris-Amides

The amide-amine building blocks (**2** and **4**) were used for the preparation of partially fluorinated amide derivatives as shown in Scheme 2. Reaction of **2** with 2*H*,2*H*,3*H*,3*H*-perfluorononoyl chloride or 2*H*,2*H*,3*H*,3*H*-perfluoroheptanoylchloride provided the bis-amide derivatives **5a** or **5b**, respectively, in very good yield. Similar reaction of **2** with pentafluorobenzoyl chloride provided the bis-amide **5c**. Similarly, the reaction of **4** with corresponding fluorinated acid chlorides provided the tris-amide derivatives **6a–c** in good yield.

Scheme 2. Synthesis of amide-amine building blocks from *N*-Boc-β-alanine and *N*-Boc-L-aspartic acid.

5a: R_F = $C_6F_{13}CH_2CH_2$- 86%
5b: R_F = $C_4F_9CH_2CH_2$- 86%
5c: R_F = C_6F_5- 82%

6a: R_F = $C_6F_{13}CH_2CH_2$- 77%
6b: R_F = $C_4F_9CH_2CH_2$- 61%
6c: R_F = C_6F_5- 66%
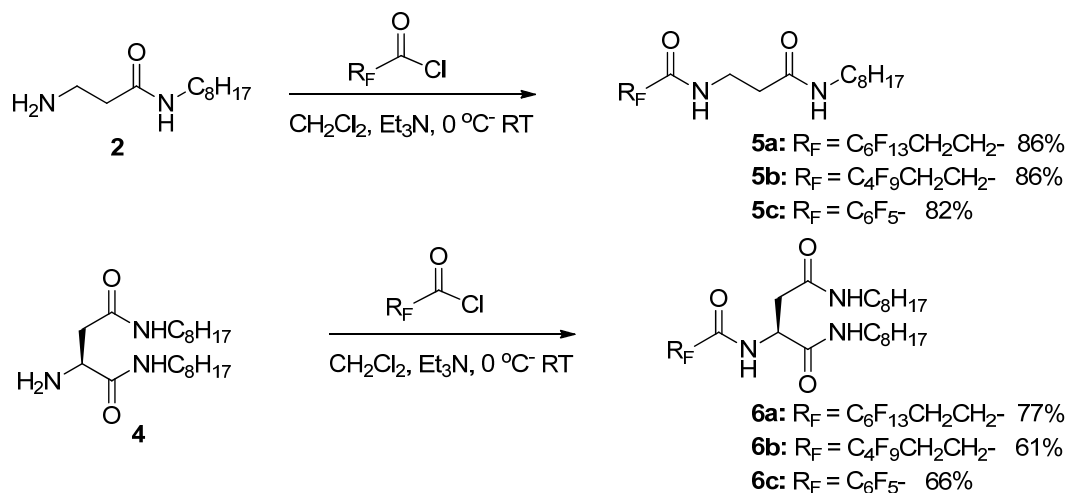
3.1.2. Partially Fluorinated Urea-Amides

The amide-amine building blocks (**2** and **4**) were also used for the preparation of partially fluorinated urea-amide derivatives, as described in Scheme 3. Compound **2**, upon reacting with 1*H*,1*H*,2*H*,2*H*-perfluorooctyl isocyanate or 1*H*,1*H*,2*H*,2*H*-perfluorohexyl isocyanate, provided the urea-amide derivatives **7a** or **7b**, respectively, in good yield. Similar reaction of **2** with pentafluorophenyl isocynante provided the bis-amide **7c** in very good yield. Similarly, the reaction of compound **4** with corresponding fluorinated isocyanates provided the urea-bis-amide derivatives **8a–c** in very good yield.

Scheme 3. Synthesis of amide-amine building blocks from *N*-Boc-β-alanine and *N*-Boc-L-aspartic acid.

7a: R_F = $C_6F_{13}CH_2CH_2$- 74%
7b: R_F = $C_4F_9CH_2CH_2$- 67%
7c: R_F = C_6F_5- 84%

8a: R_F = $C_6F_{13}CH_2CH_2$- 58%
8b: R_F = $C_4F_9CH_2CH_2$- 71%
8c: R_F = C_6F_5- 71%
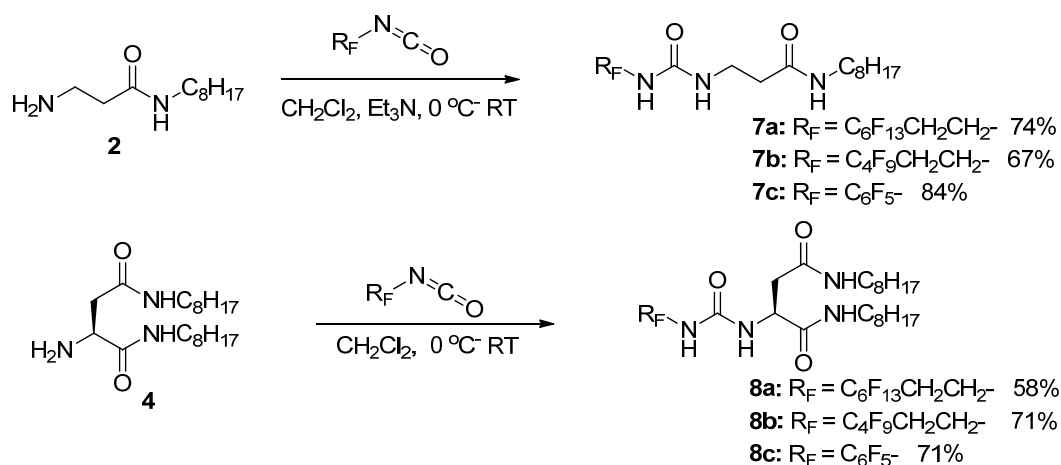
3.2. Gelation in Organic Solvents

The majority of these newly synthesized amide and urea-amide derivatives showed gelation properties in organic solvents during their work-up or isolation. A systematic study was then

performed to examine the gelation behavior of these partially fluorinated amide or urea-amide derivatives in various organic solvents. A methodology was developed where gelation was attempted with varying amounts of organogelator with a matching a solvent system. A suitable solvent system selection is based on initial solubility experiments. In general, a gelator that is too soluble in an organic solvent will stay dissolved without forming a gel, even at high concentrations. If the gelator is not soluble in an organic solvent, and partially or fully dissolves at high temperature, it may precipitate again as the temperature is lowered. Ideally, the organogelators should dissolve in a solvent at a temperature close to its boiling point and assemble into a network upon cooling, leading to a single gel phase that does not move upon shaking or inverting the vial.

In a typical screening experiment, 0.5–4 mg/mL slurries of the organogelators in various organic solvents were prepared and heated with stirring at a temperature 5 °C below the boiling point of the solvent to induce full dissolution. Gelation occurred upon cooling, as was evident by significant increase in viscosity and/or the formation of a translucent-to-opaque appearance, without the formation of precipitate. The majority of the partially fluorinated amide and urea-amide derivatives showed gelation properties in a variety of organic solvents at remarkably low concentrations, ranging from 0.5 to 4 mg/mL. The partially fluorinated amide derivative **5a** showed gelation properties in acetone (2–3 mg/mL) and *n*-butanol (3–4 mg/mL) leading to partial gels. The corresponding perfluorobutyl derivative (**5b**) showed gelation in acetone at 3–4 mg/mL and was a clear solution in *n*-butanol at various concentrations. Both **5a** and **5b** existed either as clear solutions or slurries in THF, dichloromethane, methanol and toluene at various concentrations (0.5–4 mg/mL), and did not show any signs of gelation. Compound **5c** did not gel under any conditions tested, indicating that a long-chain perfluoroalkyl group is probably needed to induce gelation of these bis-amide systems. We then examined the tris-amide systems **6a–c** for their gelation abilities at various concentrations in a variety of organic solvents. Compound **6a** gelled in acetone (2 mg/mL) and in *n*-butanol (4 mg/mL) to form opaque gels which were stable for several weeks at room temperature. Similarly, compound **6b** formed stable hazy gels in acetone at (3 mg/mL) and in dichloromethane (2 mg/mL). Compound **6c** formed gels in acetone at (1–2 mg/mL) and in methanol (2 mg/mL), indicating gelation could be induced on this tris-amide system even though it comprises a pentafluorophenyl group.

Gelation of urea-amide derivatives (**7a–c** and **8a–c**) was then attempted in a variety of organic solvents under varying concentrations. Compound **7a** gelled in THF (2 mg/mL) and acetone (2 mg/mL) forming stable gels, and partially gelled in *n*-butanol (3 mg/mL). Compound **7b** gelled in acetone and THF (3 mg/mL), leading to stable gels. The pentafluorophenyl urea-amide derivative **7c** remained as slurry or solution in many organic solvents, although partial gel formation was observed in dichloromethane (2 mg/mL). The urea-bis-amide derivatives **8a-c** showed excellent gelation properties in a variety of organic solvents. Compound **8a** gelled in both acetone and dichloromethane at 2–3 mg/mL concentrations. Compound **8a** also showed partial gelation in THF and *n*-butanol at 2–4 mg/mL concentrations. Compound **8b** gelled in dichloromethane (2 mg/mL) and acetone (3 mg/mL), leading to stable gels. Compound **8c** showed excellent gelation behavior with a variety of organic solvents (toluene, THF, acetone, dichloromethane, *n*-butanol and methanol) at concentrations ranging from 0.5–3 mg/mL, and formed stable gels in several instances. Table 1 summarizes some of the best conditions for gel formation, and the minimum concentration of gelator where stable gels were obtained.

Table 1. Gelation properties of partially fluorinated amides (**5a–c**, **6a–c**) and urea-amides (**7a–c**, **8a–c**).

Compound	Gelation Conditions		Appearance [b]
	Gelator Concentration mg/mL	Solvent	
5a	2,3	Acetone	Partial Gel
	3–4	*n*-Butanol	Partial Gel
5b	3	Acetone	Partial Gel
5c	0.5–4	Acetone, THF, CH$_2$Cl$_2$, *n*-Butanol, hexane, methanol	Clear Solution or Precipitate
6a	3 [a]	Acetone	Opaque Gel
	4 [a]	*n*-Butanol	Opaque Gel
6b	2 [a]	CH$_2$Cl$_2$	Hazy Gel
	3 [a]	Acetone	Hazy Gel
6c	2 [a]	Acetone, methanol	Opaque Gel
7a	2 [a]	THF or acetone	Opaque Gel
	3	*n*-Butanol	Partial Gel
7b	3 [a]	Acetone or THF	Opaque Gel
7c	2	CH$_2$Cl$_2$	Partial Gel
8a	2 [a]	Acetone	Opaque Gel
	3 [a]	CH$_2$Cl$_2$	Hazy Gel
	2–4	THF, *n*-butanol	Partial Gel
8b	2 [a]	CH$_2$Cl$_2$	Opaque Gel
	3 [a]	Acetone	Hazy Gel
8c	0.5 [a], 1, 2, 3	Acetone	Hazy Gel
	0.5 [a]	CH$_2$Cl$_2$	Transparent Gel
	2	THF	Opaque Gel

[a] Minimum gel concentration for stable gel formation; [b] Hazy = partially transparent, solid gel. Transparent = completely transparent, solid gel. Opaque = solid gel, not transparent. Partial gel = solid gel with some movement. Precipitate = phase- separated liquid, with solid particles.

In general, we conclude that the partially fluorinated urea-amide derivatives (**7a–c** and **8a–c**) are better gelators than the corresponding amide systems (**5a–c** and **6a–c**), possibly due to the ability of the urea moieties to form directional hydrogen bonds. In order to further understand the influence of amide groups in the gelation ability of these urea-amide systems, we synthesized the corresponding urea-ester derivatives, which in general did not show any gelation properties under the same gelation conditions as the urea-amide systems. For example, urea-ester derivatives **9** and **10** (comparable to urea-amides **7a** and **8b**) were synthesized via the esterification of *N*-Boc-β-alanine and *N*-Boc-L-aspartic acid with *n*-octanol, followed by deprotection and reaction of the amine with 1*H*,1*H*,2*H*,2*H*-perfluorooctyl isocyanate (Figure 3). Both **9** and **10** were oils and failed to gel in common organic solvents, indicating amide functionalities are desired in addition to the urea group in the backbone of these partially fluorinated compounds to obtain good gelation properties.

Figure 3. Urea-ester derivatives from *N*-Boc-β-alanine and *N*-Boc-L-aspartic acid.
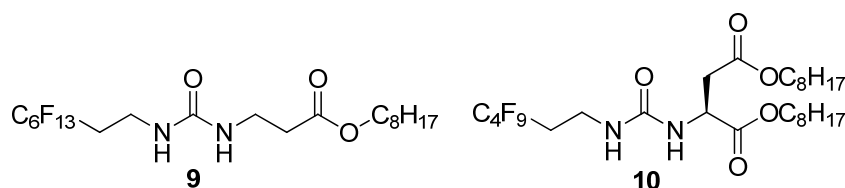
3.3. Surface Modification of Nonwoven Supports in Organic Solvents

The concept of fabricating low surface energy surfaces via surface modification of nonwoven substrates using self-assembly of partially fluorinated urea or amide gelators has been described in our earlier reports [29,31]. The gelators self-assemble into fiber-like morphologies in solution, which grow sufficiently long and become entangled with one another, forming a gel with their solvent medium. In the presence of a solid or fibrous substrate, the gelation occurs on the surface of the substrate, creating a composite with an altered surface topology. Removal of the solvent from the gel composite leaves behind a network of assembled gelator fibers on the substrate, thus producing a composite surface with high surface area and roughness, which are desirable for superior hydrophobic/oleophobic properties.

A few of the partially fluorinated amide and urea-amide gelators that showed good gelation properties were gel-impregnated on nonwoven supports (Tyvek® polyethylene nonwoven fabric and Kolon® polyester fabric) in a suitable organic solvent. The nonwoven supports were then dried in a vacuum oven at room temperature to produce a composite of xerogel coated on the substrate. These surface-modified composites were then evaluated for hydrophobic and oleophobic properties. The tris-amide gelators (**6a** and **6b**) were impregnated on the Tyvek® and Kolon® fabrics in acetone and dichloromethane, respectively, leading to the corresponding gel-impregnated composites. Similarly, the partially fluorinated urea-amide gelators (**7a** and **8c**) that showed excellent gelation behavior were gel impregnated on both Tyvek® and Kolon® fabrics in acetone, leading to the corresponding surface-modified composites. Examination of these composites by SEM showed a nanofibrous network of gelators impregnated on the fabric surface, vastly different from the micro structured surfaces of Tyvek® and Kolon® fabrics [31]. Figure 4 shows SEMs at 2,000× and 10,000× magnification of the Kolon® fabric surface-treated with gelator **7a** with an average fiber diameter of 142 nm.

Figure 4. SEMs of composite prepared by impregnation of gelator **7a** on Kolon® fabric at 2,000× (left) and 10,000× (right) magnifications.
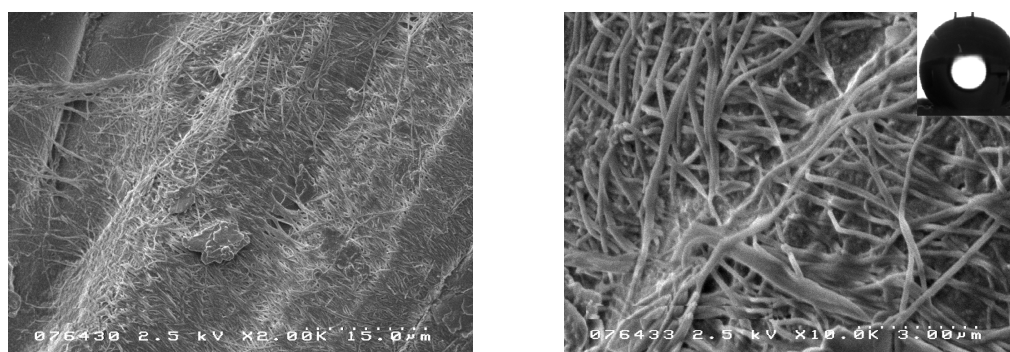
The composites produced by gel-impregnation of fluorinated organogelators were evaluated for water/oil repellency via dynamic contact angle measurement for water and hexadecane. Table 2 summarizes the results of contact angle measurements for the composites and those for untreated controls (Tyvek® and Kolon® fabrics). The results indicate that the composite materials produced by the gel impregnation of fluorinated gelators **6a**, **6b**, **7a**, **8a** and **8c** exhibit significantly higher water advancing contact angles than the untreated controls. The higher water contact angles observed for these surfaces suggest increased surface roughness in addition to the incorporation of hydrophobic alkyl or fluoroalkyl functionalities. The inset in Figure 4 shows a water droplet sitting on the Kolon® fabric surface treated with gelator **7a**, with an advancing contact angle of 140°. The effect of surface structure created by gel-impregnation is particularly important as clear solutions (no gel with solvents chosen) of urea-amide gelators dip-coated on nonwoven substrates showed relatively inferior performance (water advancing contact angle <117°). The treated composites derived from gelators **6a**, **6b** and **7a** (comprising perfluoroalkyl chains) also showed a high advancing contact angle for hexadecane, indicating excellent oil repellency. Surprisingly, the pentafluorophenyl-derived urea-amide derivative **8c**, which showed excellent gelation characteristics, also showed excellent water advancing and receding contact angles (superhydrophobic), but extremely poor oil repellency, as hexadecane penetrated into the substrate within a few seconds. This observation is consistent with the need for long-chain perfluoroalkyl groups with terminal CF_3 groups in the gelator molecule in order to provide oil repellency [35]. Surface structure created by the gelator and pentafluorophenyl groups or hydrocarbon alkyl groups in the gelator backbone are not sufficient for imparting oil repellency to the treated composites.

Table 2. Water and hexadecane contact angles of treated nonwoven composites prepared via gelation in organic solvents

Composite	Average Amount of Dry Gel Impregnated per Unit Area, g/cm²	Contact angle [†]			
		Water		Hexadecane	
		Adv CA	Rec CA	Adv CA	Rec CA
6a on Tyvek®	0.0014	141 ± 4	134 ± 1	89 ± 2	64 ± 1
6a on Kolon®	0.0027	157 ± 6	144 ± 3	94 ± 5	61 ± 3
6b on Tyvek®	0.0041	128 ± 4	112 ± 3	60 ± 2	30 ± 3
6b on Kolon®	0.0012	134 ± 1	118 ± 2	59 ± 4	29 ± 5
7a on Tyvek®	0.0015	140 ± 4	126 ± 1	84 ± 4	43± 1
7a on Kolon®	0.0030	154 ± 3	138 ± 2	87± 4	42± 2
8c on Tyvek®	0.0013	161 ± 1	148 ± 1	Absorbed in 25 s	
8c on Kolon®	0.0037	158 ± 2	145 ± 1	Absorbed in 30 s	
Untreated Tyvek®	---	108 ± 1	78 ± 1	Absorbed on contact	
Untreated Kolon®	---	115 ± 4	85 ± 4	Absorbed on contact	

[†] Average of 3 runs at different positions on each sample.

4. Conclusions

A new class of partially fluorinated amides and urea-amides useful as organogelators was synthesized from amino acid building blocks. These derivatives showed good gelation properties in a

variety of organic solvents, and in general the urea-amide derivatives were better gelators than the corresponding bis- or tris-amide derivatives. Analogous urea-ester derivatives failed to gel in any organic solvents, indicating a combination of urea and amide functionalities, or multiple amide groups, are desirable to induce gelation. Good organogelators derived from the initial screening were evaluated for surface modification of nonwoven substrates, and surface analysis indicated a gel-impregnated surface with porous microstructure morphology. Composites obtained via impregnation by gelators provided surfaces with excellent hydrophobic properties. The nonwoven surfaces impregnated with perfluoroalkyl-containing organogelators showed excellent oleophobic behavior. Superior hydrophobic and oleophobic behavior exhibited by these composites were attributed to a combination of micro-structured surface morphology created by the xerogel and the presence of fluorocarbon/hydrocarbon functionalities in the gelator backbone.

Acknowledgments

References

1. Terech, P.; Weiss, R.G. Low-molecular mass gelators of organic liquids and the properties of their gels. *Chem. Rev.* **1997**, *97*, 3133–3160.
2. Weiss, R.G., Terech, P., Eds.*Molecular Gels: Materials with Self-Assembled Fibrillar Networks*; Springer: Dordrecht, The Netherlands, 2006.
3. George M.; Weiss, R.G. Molecular organogels. Soft matter comprised of low-molecular-mass organic gelators and organic liquids. *Acc. Chem. Res.* **2006**, *39*, 489–497.
4. van Esch, J.H.; Feringa, B.L. New functional materials based on self-assembling organogels: From serendipity towards design. *Angew. Chem. Int. Ed.* **2000**, *39*, 2263–2266.
5. Srinivasan, S.; Babu, P.A.; Mahesh, S.; Ajayaghosh, A. Reversible self-assembly of entrapped fluorescent gelators in polymerized styrene gel matrix: Erasable thermal imaging via recreation of supramolecular architectures. *J. Am. Chem. Soc.* **2009**, *131*, 15122–15123.
6. Sahoo, S.; Kumar, N.; Bhattacharya, C.; Sagiri, S.S.; Jain, K.; Pal, K.; Ray, S.S.; Nayak, B. Organogels: Properties and applications in drug delivery. *Des. Monomers Polym.* **2011**, *14*, 95–108.
7. Debnath, S.; Shome, A.; Dutta, S.; Das, Prasanta, K. Dipeptide-based low-molecular-weight efficient organogelators and their application in water purification. *Chem.-A Eur. J.* **2008**, *14*, 6870–6881.
8. Smith, D.K. Molecular gels: Nanostructured soft materials. In *Organic Nanostructures*; Atwood, J.L., Steed, J.W., Eds.; Wiley-VCH: Weinheim, Germany, 2008; pp. 111–154.
9. Hughes, N.E.; Marangoni, A.G.; Wright, A.J.; Rogers, M.A.; Rush, J.W.E. Potential food applications of edible oil organogels. *Trends Food Sci. Technol.* **2009**, *20*, 470–480.
10. Fages, F.; Voegtle, F.; Zinic, M. Systematic design of amide- and urea-type gelators with tailored properties. *Top. Curr. Chem.* **2005**, *256*, 77–131.

11. Allix, F.; Curcio, P.; Pham, Q.; Pickaert, G.; Jamart-Grégoire, G. Evidence of intercolumnar π-π stacking interactions in amino-acid-based low-molecular-weight organogels. *Langmuir* **2010**, *26*, 16818–16827.

12. Song, B.; Wei, H.; Wang, Z.; Zhang, X.; Smet, M.; Dehae, W. Supramolecular nanofibers by self-organization of bola-amphiphiles through a combination of hydrogen bonding and π–π stacking interactions. *Adv. Mater.* **2007**, *19*, 416–420.

13. Suzuki, M.; Hanabusa, K. Polymer organogelators that make supramolecular organogels through physical cross-linking and self-assembly. *Chem. Soc. Rev.* **2010**, *39*, 455–463.

14. de Loos, M.; Feringa, B.L.; van Esch, J.H. Design and application of self-assembled low molecular weight hydrogels. *Eur. J. Org. Chem.* **2005**, 3615–3631.

15. Hirst, A.R.; Coates, I.A.; Boucheteau, T.R.; Miravet, J.F.; Escuder, B.; Castelletto, V.; Hamley, I.W.; Smith, D.K. Low-molecular-weight gelators: Elucidating the principles of gelation based on gelator solubility and a cooperative self-assembly model. *J. Am. Chem. Soc.* **2008**, *130*, 9113–9121.

16. Liu, J.; Ma, J.; Chen, C. Structure-property relationship of a class of efficient organogelators and their multistimuli responsiveness. *Tetrahedron* **2011**, *67*, 85–91.

17. Mohmeyer, N.; Schmidt, H. Synthesis and structure-property relationships of amphiphilic organogelators. *Chem. Eur. J.* **2007**, *13*, 4499–4509.

18. Raynal, M.; Laurent, B. Organogel formation rationalized by Hansen solubility parameters. *Chem. Commun.* **2011**, *47*, 8271–8273.

19. Srinivasan, S.; Praveen, V.K.; Philip, R.; Ajayaghosh, A. Bioinspired superhydrophobic coatings of carbon nanotubes and linear π systems based on the "bottom-up" self-assembly approach. *Angew. Chem. Int. Ed.* **2008**, *47*, 5750–5754.

20. Ren, C.L.; Xu, S.Y.; Xu, J.; Chen, H.Y.; Zeng, H.Q. Planar macrocyclic fluoropentamers as supramolecular organogelators. *Org. Lett.* **2011**, *13*, 3840–3843.

21. Hanabusa, K. Development of organogelators based on supramolecular chemistry. In *Macromolecular Nanostructured Materials*; Ueyama, N., Harada, A., Eds.; Springer Series in Materials Science: Dordrecht, The Netherlands, 2004; Volume 78, pp. 118–137.

22. Shi, C.; Huang, Z.; Kilic, S.; Xu, J.; Enick, R.M.; Beckman, E.J. Carr, A.J.; Melendez, R.E.; Hamilton, A.D. The gelation of CO_2: A sustainable route to the creation of microcellular materials. *Science* **1999**, *286*, 1540–1543.

23. Zhou, Y.; Yi; T.; Li, T.; Zhou, Z.; Li, F.; Huang, W.; Huyang, C. Morphology and wettability tunable two-dimensional superstructure assembled by hydrogen bonds and hydrophobic interactions. *Chem. Mater.* **2006**, *18*, 2974.

24. Yamanaka, M.; Sada, K.; Miyata, M.; Hanabusa, K.; Nakano, K. Construction of superhydrophobic surfaces by fibrous aggregation of perfluoroalkyl chain-containing organogelators. *Chem. Commun.* **2006**, *21*, 2248–2250.

25. Nakajima, A.; Hashimoto, K.; Watanabe, T. Some Recent studies on super-hydrophobic films. *Monateshefte Fur Chemie* **2001**, *132*, 31–41.

26. Feng, L.; Li, S.; Li, Y.; Li, H.; Zhang, L.; Zhai, J.; Yanlin, S.; Liu, B.; Jiang, L.; Zhu, D. Super-hydrophobic surfaces: from natural to artificial. *Adv. Mater.* **2002**, *14*, 1857–1864.

27. Chen, W.; Fadeev, A.Y.; Che Hsieh, M.; Oner, D.; Youngblood, J.; McCarthy, T. Ultrahydrophobic and ultralyophobic surfaces: Some comments and examples. *Langmuir* **1999**, *15*, 3395–3399.
28. Barthlott, W.; Neinhuis, C. Purity of the sacred lotus, or escape from contamination in biological surfaces. *Planta* **1997**, *202*, 1–8.
29. Nun, E.; Oles, M.; Schleich, B. Lotus-effect-surfaces. *Macromol. Symp.* **2002**, *187*, 677–682.
30. Gould, P. Smart clean surfaces. *Mater. Today* **2003**, *6*, 44–48.
31. Raghavanpillai, A.; Reinartz, S.; Hutchenson, K.W. Hydrophobic and oleophobic surface modification using fluorinated bis-urea and bis-amide gelators. *J. Fluor. Chem.* **2009**, *130*, 410–417.
32. Schoonbeek, F.S.; Van Esch, J.H.; Hulst, R.; Kellogg, R.M.; Feringa, B.L. Geminal Bis-ureas as gelators for organic solvents: Gelation properties and structural studies in solution and in the gel state. *Chem. Eur. J.* **2000**, *6*, 2633–2643.
33. Raghavanpillai, A.; Franco, V.A.; Meredith, W.E. Hydrophobic and oleophobic surface modification using gelling agents derived from amino acids. *J. Fluor. Chem.* **2012**, *135*, 187–194.
34. Jouani, A.M.; Szonyi, F.; Cambon, A. Synthesis of 2-F-alkylethyl isocyanates. *J. Fluor. Chem.* **1992**, *56*, 85–92.
35. Honda, K.; Morita, M.; Otsuka, H.; Takahara, A. Molecular aggregation structure and surface properties of poly(fluoroalkyl acrylate) thin films. *Macromolecules* **2005**, *38*, 5699–5705.

Article

Stain Resistance of Cotton Fabrics before and after Finishing with Admicellar Polymerization

Srinivas Hanumansetty [1], Jayanta Maity [1], Rod Foster [2] and Edgar A. O'Rear [1,2,*]

[1] School of Chemical, Biological and Materials Engineering and Institute of Applied Surfactant Research, University of Oklahoma, 100 E. Boyd SEC T335, Norman, OK 73019, USA; E-Mails: hanu.srinivas@ou.edu (S.H.); jayanta_june@yahoo.co.in (J.M.)

[2] Synthesized Nano Coatings, 1009 Bentbrook Pl., Norman, OK 73072, USA; E-Mail: rodfoster@yahoo.com

* Author to whom correspondence should be addressed; E-Mail: eorear@ou.edu; Tel.: +1-405-325-5811; Fax: +1-405-325-5813.

Abstract: Environmental concerns related to perfluoroctanoic acid (PFOA) led to a re-examination of the methods for imparting stain resistance and stain repellency to textiles. Non-PFOA fluoropolymer finishes have been formed on cotton knits by admicellar polymerization, a surface analogue of emulsion polymerization. Fabric samples were characterized by a drop test, contact angle measurements, SEM, elemental analysis and durability studies. Stain resistance and stain release properties were assessed by reflectance and AATCC tests with results comparing favorably with swatches from commercially available garments. Admicellar polymerization enabled the formation of durable finishes that exhibited high performance in stain resistance and stain repellency.

Keywords: admicellar polymerization; cotton; stain resistance; stain release; fluoropolymer

1. Introduction

In recent years, several technologies have been developed for modifying cotton blends and cotton as multi-functional textiles. Surface modification of cotton fabrics can impart wrinkle free finishes, self-cleaning properties, anti-microbial activity, UV protection, and flame retardancy [1,2]. Self-cleaning features include stain release and stain repellent or resistant finishes [3]. The latter of these, acts to

block the uptake of the blemishing agent. Liquids like coffee, soda, oil and water, bead up on fabric when spilled and can be wiped off without staining the fabric. In contrast, a stain release fiber coating may allow oil and aqueous staining materials to penetrate the fabric and then, when the fabric is laundered, ideally enables the stain to be easily removed.

Fluorochemical coatings dominate the stain repellency textile apparel market. Out of all existing textile chemicals, only fluorochemicals have shown the unique property to provide fabrics a sufficiently low surface energy coating able to resist penetration of both oil and water-based stains (polar and non-polar liquids). Unfortunately, fabrics modified with fluorochemicals by conventional textile finishing methods often show poor performance with laundering or wear [4].

Application of perfluorochemicals can be accomplished in a variety of ways, many of which impart hydrophobicity and/or oleophobicity to fabrics in addition to other desirable properties. Scientists at the German Textile Research Centre North West, for example, obtained a hydrophobic coating of perfluoro-4-methylpent-2-ene by photonic surface treatment with a pulsed UV-laser [1]. Similarly, pulsed plasma polymerization of monomers with long perfluoroalkyl chains by Badyal and co-workers yielded a hydrophobic thin film coating [5]. Superhydrophobic mats have been prepared with initiated chemical vapor deposition involving polymerization of perfluoroalkylethyl methacrylate [6] while Gleason and co-workers used initiated chemical vapor deposition to coat electrospun non-woven fabrics, also with superhydrophobic character [7]. In a very different approach, direct fluorination of twaron fiber with elemental fluorine not only changed the nature of the fiber surface, it also increased mechanical and thermal properties of a fiber composite [8]. Sol-gel methods have been successfully employed to impart oil/water repellency and anti-bacterial capability to cotton using fluorocarbon polymer/SiO_2 and silver nanoparticle-doped silica hybrid materials, respectively [9,10]. Lastly, nanoparticles of fluorochemical coated silica and of gold have been applied to cotton and other fabrics to create a chemically inert fiber surface with superlyophobic properties [11–16]. This broad range of approaches reflects the interest and challenges in this area.

Admicellar polymerization is an in situ polymerization reaction proceeding within surfactant aggregates formed at the interface between the substrate and a supernatant solution. The technique, a surface analogue of emulsion polymerization, has been used to form a variety of polymeric thin films on different solids such as polystyrene and poly methyl methacrylate over silica and alumina [17–20]. Recently, admicellar polymerization has been expanded into the textile area with application of finishes to impart functionality like flame retardancy, blocking of UV radiation, and water repellency [21–23]. This method is a simple, water-based process using low energy and a small amount of chemicals. Since the thickness of the film formed is typically on the order of nanometers to tens of nanometers, the fabric surfaces retain softness and feel.

In this paper we examine the use of admicellar polymerization to prepare knit type cotton fabric with stain release/stain resistant features. The fluoropolymer finishes are characterized by standard and improvised test methods and compared to commercially available stain release/stain resistant fabrics for performance and durability.

2. Experimental Section

2.1. Materials

Interlock type knit cotton fabric was purchased from Alamac American Knits (Lumberton, North Carolina, USA). The fabric was scoured and then prior to use, rinsed several times in a washing machine until it was free from surfactant. Reference samples from a commercially available, off-the-shelf stain resistant knit shirt (designated Ref. 1) and from commercially available, off-the-shelf stain resistant woven slacks (Ref. 2) were purchased from local stores for comparison purposes. Short and long chain partially fluorinated alkyl acrylates were purchased from Synquest labs Inc. (USA) while fluorosurfactants were obtained from Mason Chemicals (USA). A water soluble persulfate initiator and an acrylamide bonding agent were purchased from Sigma Aldrich (USA). All chemicals were used without further purification.

2.2. Preparation of Samples, Admicellar Polymerization

Modification of interlock knit cotton swatches was carried out in 24 mL glass vials. Reaction media consisted of fluorsurfactants at the cmc and either a short chain or long chain fluoroalkyl acrylate ester fluoromonomer (5 mM) with the corresponding respective polyacrylates designated as PA1 and PA2. Concentrations of initiator (5 mM) and bonding agent (1 mmol/g) in DI water at pH 4 were added to vials. Swatches of washed cotton fabric weighing 2.0 g were added to the vials. The reaction was carried out at 80 °C in a shaker bath at 80 rpm with an adsolubilization period of 2 h and a polymerization time of 2 h before being rinsed and dried in an oven at 80 °C. Samples were repeatedly home laundered using detergent (Tide) in a laboratory washing machine at 30 °C for 20 min and dried in conventional tumble dryer at 60 °C for 45 min to test durability of treated fabric.

2.3. Characterization of Treated Fabric

Modified cotton knits and reference samples were characterized by wetting times, static contact angle determination, SEM, elemental analysis, stain resistance and stain recovery measurements.

2.3.1. Water Repellency Tests

Two test methods were employed for assessing water repellency. The first involved a simple drop test, with 20 µL water being deposited from a pipette at a height of 1 cm. Time for absorption of water (wetting time) on a fabric surface in the drop test was determined up to maximum of 30 min, at which point the sample passed. A second method was performed according to AATCC test method 22 (spray test). This method requires larger samples that were prepared by carrying out admicellar polymerization in a Werner Mathis Labomat Type BFA 16 beaker dyeing unit.

2.3.2. Contact Angle Analysis

Contact angle is a quantitative measure of the wetting of a solid by a liquid, which can evaluate the potential for water and stain repellency. We performed static contact angle measurements using an optical tensiometer (KSV T2000) and software supplied with the instrument. A 20 µL drop of distilled,

deionized water of surface tension 72.75 mN/m was deposited on fabric by syringe from a height of 2 cm. Observations occurred over a 10 min period with replicates at five different sites on the fabric.

2.3.3. SEM Study

SEM images of modified and unmodified interlock swatches were taken using a JEOL JSM 880 after the samples were sputter coated with a thin layer of gold. Elemental analyses were carried out using ZEISS 960A SEM equipped with Oxford Link energy dispersive spectroscopy (EDS) with a thin window and using IXRF EDS 2008 software at beam energy of 5 keV. Elemental analyses provided an indication of fluorine content at the surface of the fibers.

2.3.4. Stain Recovery and Stain Resistance Tests

Stain tests were performed on untreated control and treated fabric samples and compared to results for the commercial reference samples. Standardized measurements followed AATCC test method 130, referred to as the oily stain release method, and AATCC test method 118, referred to as the oil repellency test. In AATCC test method 118, 50 µL drops of different grades of hydrocarbon oil specified in the protocol are applied to the fabric material and scored on a scale from 1 to 8. Higher values indicate the point at which ever lighter aliphatic oils penetrate the fabric in a period of 30 s or less and thus greater oil repellency. In AATCC test method 130, the fabric is placed on a blotting paper and 5 drops corn oil of 40 µL each are deposited in the center. A blotting paper is laid on top followed by a 5 lb weight for 60 s. The fabric is washed in the specified manner at 41 °C and evaluated according to the test protocol. To further assess stain resistance and recovery, we examined the effects of common staining materials like oil, mustard and ketchup by reflectance measurements of the fabric samples. Stain resistance measurements were performed after wiping with tissue paper while stain recovery evaluation was done after washing. Reflectance was determined by using an Ultrascan colorimeter (Hunter Lab) at a wavelength of 440 nm. Percentage of stain resistance and percentage of stain recovery were calculated using the formulas

$$\% \text{ of Stain Resistance} = \frac{\text{Reflectance of stain on treated fabric after wiping}}{\text{Reflectance of untreated fabric}} \times 100$$

$$\% \text{ of Stain Recovery} = \frac{\text{Reflectance after one wash - Reflectance after staining}}{\text{Reflectance before staining - Reflectance after staining}} \times 100$$

2.3.5. Tensile Strength Measurement

Dumbbell-shaped samples were punched out (using dumbbell shaped die cutter, ASTM D638) from fabric. Tensile strength measurements were performed at room temperature using computerized model testing machine (SSTM tester from United Testing Systems) at a speed of 0.5 in/min according to ASTM D1708. Four measurements for each sample were done.

3. Results and Discussion

3.1. Appearance of Thin Film

SEM images and elemental analysis of the fabric samples before and after admicellar polymerization were obtained. Figure 1(a,b) shows fibers in the untreated cotton fabric samples, the surface of fibers is smooth with striations evident in places. It is devoid of polymer aggregates and any other agglomerations over the surface.

Figure 1. Untreated fibers of interlock knit cotton.

(**a**)　　　　　　　　　　　　　　　　　(**b**)
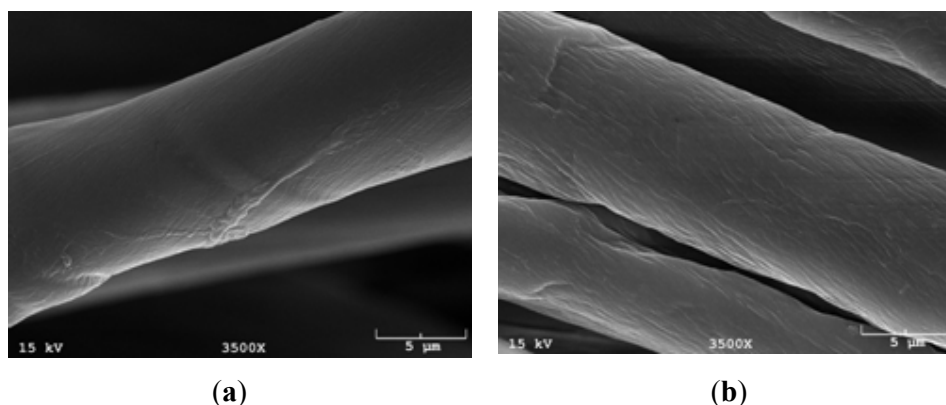
Figure 2(a,b) shows fibers of treated cotton fabric with PA1 after modification by admicellar polymerization. Compared to untreated samples shown in Figure 1, striations are not visible while a coarse, bumpy appearance indicates formation of fluoropolymer on the fiber surface. Figure 2(c,d) shows fibers in the treated cotton fabric with PA2. In this case, striations are also not visible and fluoropolymer coating can be seen on the surface of fibers. With the longer chain fluorocarbon of PA2, the coating appears to be more evenly spread as a uniform layer. It is evident in both cases that the coatings are thin.

Figure 2. Interlock knit cotton fibers treated with PA1 (a,b) and PA2(c,d).

(**a**)　　　　　　　　　　　　　　　　　(**b**)

Figure 2. *Cont.*

(**c**)   (**d**)
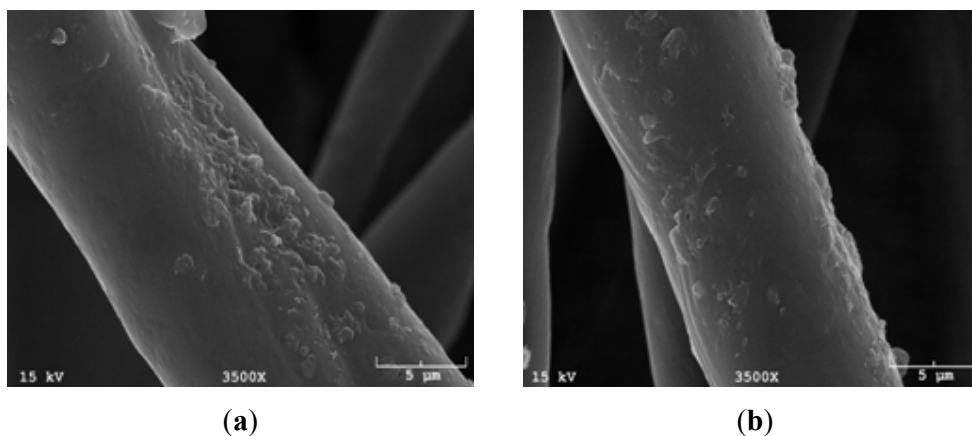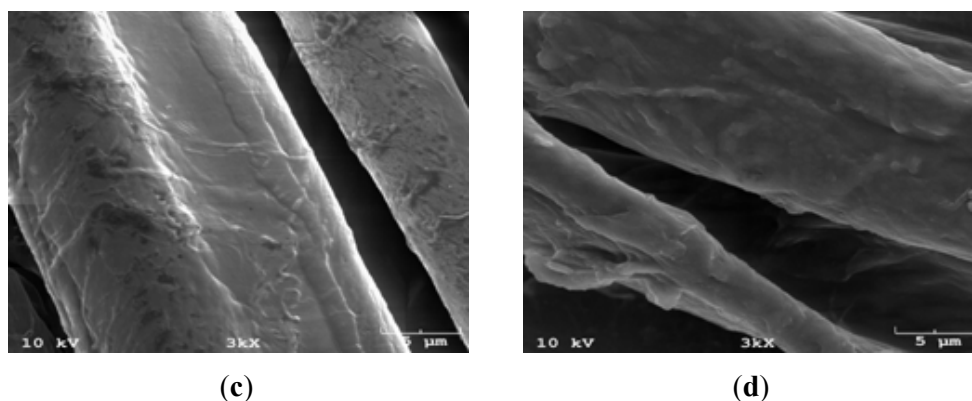
The EDS spectrum of an untreated control sample (Figure 3a) does not exhibit a significant fluorine peak with the resulting elemental analysis for carbon, nitrogen, oxygen and fluorine indicating a fluorine content of only 0.33 atomic%. Carbon and oxygen, the main constituents of the cellulose substrate, give strong peaks. In treated fabrics (Figure 3(b,c)), distinct peaks are observed for fluorine along with those for carbon and oxygen. Fluorine content in PA1 was 6.89% while in PA2 was 10.53%, consistent with the longer fluorocarbon chains of the latter. The levels of carbon and oxygen observed reflect contributions from penetration of the electron beam through the film and/or regions where the fiber surface was not covered.

Figure 3. Energy dispersive spectroscopy (EDS) spectrum of: (**a**) untreated fiber (**b**) treated fiber with PA1 (**c**) treated fiber with PA2.

(**a**)   (**b**)

(**c**)
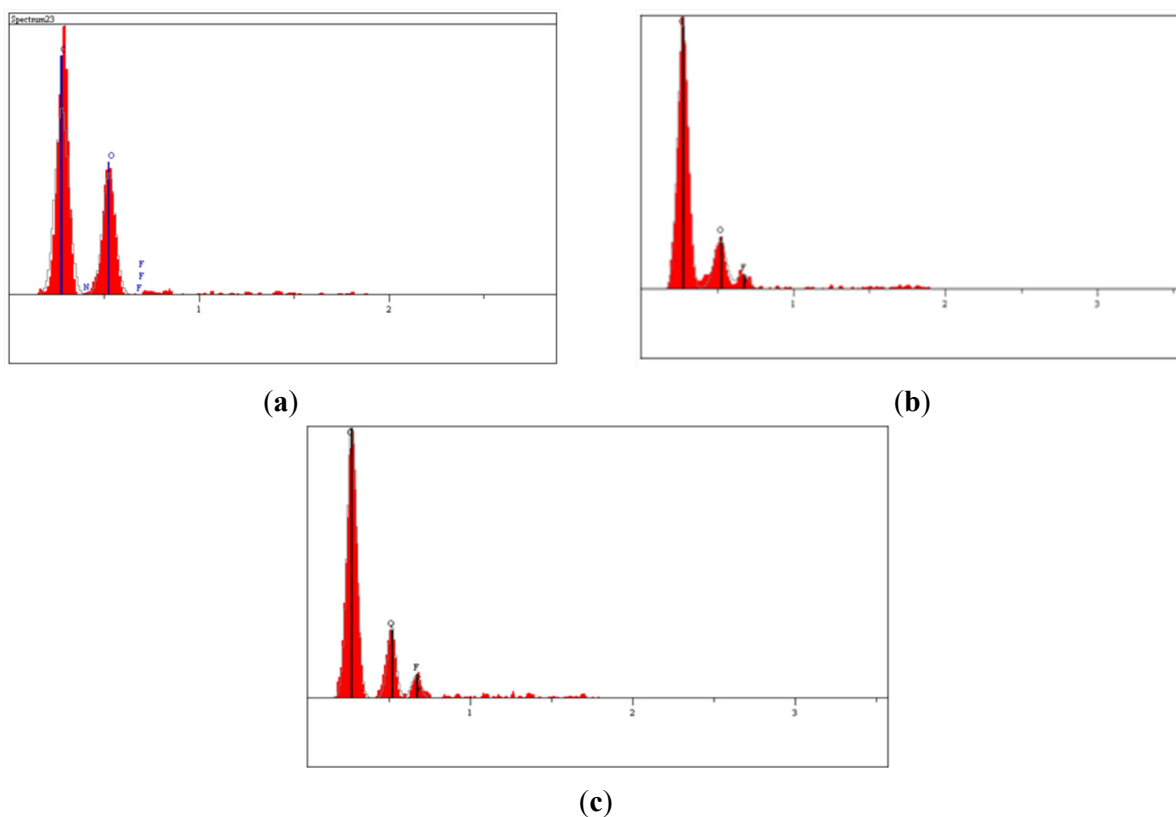
3.2. Mechanical Characterization

Figure 4 shows stress-strain relationships of untreated fabric and treated fabric with two formulations PA1 and PA2. UIF1 and UIF2 are results of untreated interlock fabric in two orthogonal directions indicating anisotropic behavior. The Young's moduli of treated fabrics PA1 and PA2 correspond to the higher modulus of the untreated interlock knit, regardless of direction. Greater stiffness of PA1 and PA2 suggest the adhesion between fibers due to formation of polymer bridges between fibers. Between PA1 and PA2, Young's modulus does not differ greatly but PA1 is somewhat stiffer than PA2. These trends mirror observations previously reported for plain and modified pique fabric [21]. Although the Young's modulus increases, these fabrics retain soft feel after modification.

Figure 4. Stress-strain plot of untreated fabric and treated fabric with formulations PA1 and PA2.
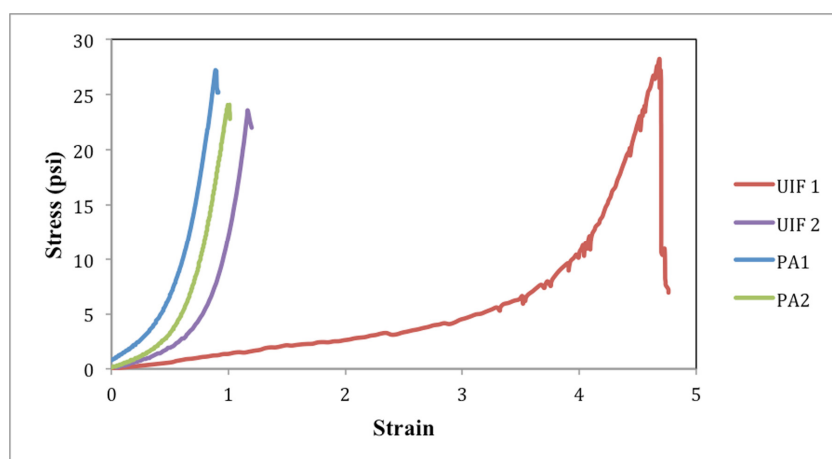
3.3. Water Repellency Tests

Evaluation of fabric hydrophobicity is difficult to assess by any one method. The drop test enables a quick and easy determination, while multiple methods of testing help us to know performance and quality of the material more precisely. To ascertain the water-repellency characteristics of the fabric, the resistance of the fabric to surface penetration by a spray and resistance to surface wetting should be measured. Tests have to be carried out in combination with each other in order to obtain a complete understanding of performance. Samples were assessed for performance using drop test, spray test and contact angle measurement.

Interlock cotton knit modified with polyacrylates PA1 and PA2 displayed drop test results greater than 30 min. In fact, superhydrophobic character was found with contact angles of 150° for PA1 and 160° for PA2. Figure 5 shows static contact angle results for the various fabric samples, all of which displayed strong hydrophobic character. With a contact angle near 160°, PA2 had the highest value observed. The remaining fabric samples have contact angles around 150° or less. Contact angles in this range result from a combination of chemical composition and surface microstructure. The microstructure includes fibers within the cotton yarns and possibly texture on the surface of the fibers due to the

presence of the fluoropolymer. The SEM and EDS data suggest that the higher fluorocarbon content explains why PA2 exhibits a higher contact angle than PA1.

Figure 5. Comparison of contact angles for treated and commercial reference samples.
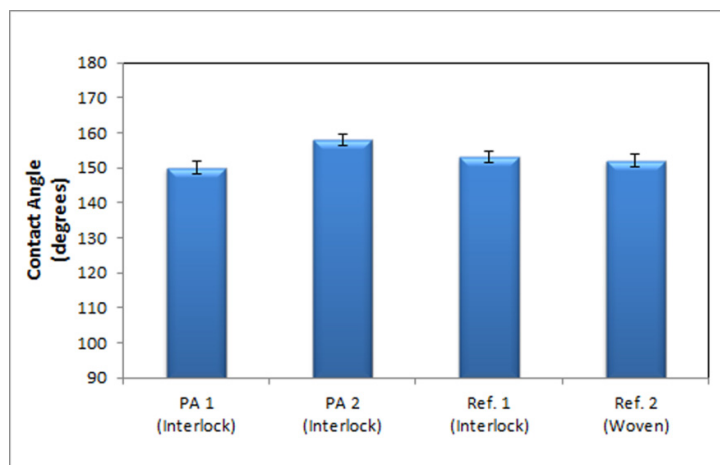
Samples were repeatedly home laundered with washing and drying steps to gauge durability characteristics. Results for the drop test with number of laundering cycles appear in Figure 6. Treated fabric with PA1 passes with as many as 20 washes while PA2 can hold its treatment up to 30 home launderings. As shown above, PA2 has greater fluorine content and, as such, would be expected to have lower solubility which might explain its ability to endure more home launderings. Findings for fabrics modified by admicellar polymerization were compared to commercial materials. The off-the-shelf knit sample (Ref. 1) fared poorly as it failed the drop test after only 5 washes. The interlock knit material PA1 with the lower fluorochemical content compared well to the woven commercial sample (Ref. 2) with both passing the drop test for 20 washes. The interlock knit PA2 surpassed them all with 30 washes.

Figure 6. Comparison of durability of treated fabrics with commercial reference samples by the drop test.
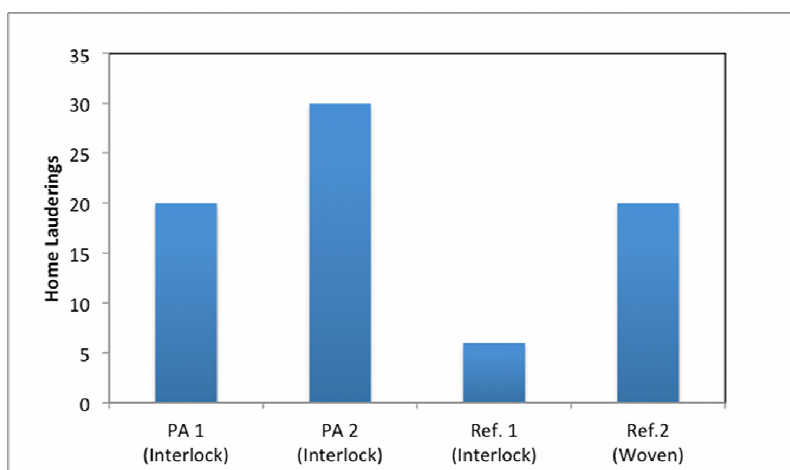
In the spray test (AATCC 22), repellency of fabric is assessed in a dynamic system by comparison to wetting patterns on a standard chart. Measurements of spray test rating were made after a series of home laundering which were discontinued once the fabric failed the drop test. From Figure 7, the interlock commercial sample (Ref. 1) is seen to exhibit a decrease in performance with each home laundering down to a rating of 60 when the drop test result was less than 30 min. The woven material (Ref. 2) performed well with a rating of 100 up to 15 home launderings where it decreased to a rating of 90. Performance of PA1 was comparable to the woven fabric. Notably, PA2 showed substantially greater durability. Trends observed among the different fabric samples by the spray test were consistent with those of the drop test.

Figure 7. Comparison of spray test of treated fabric and commercial samples.
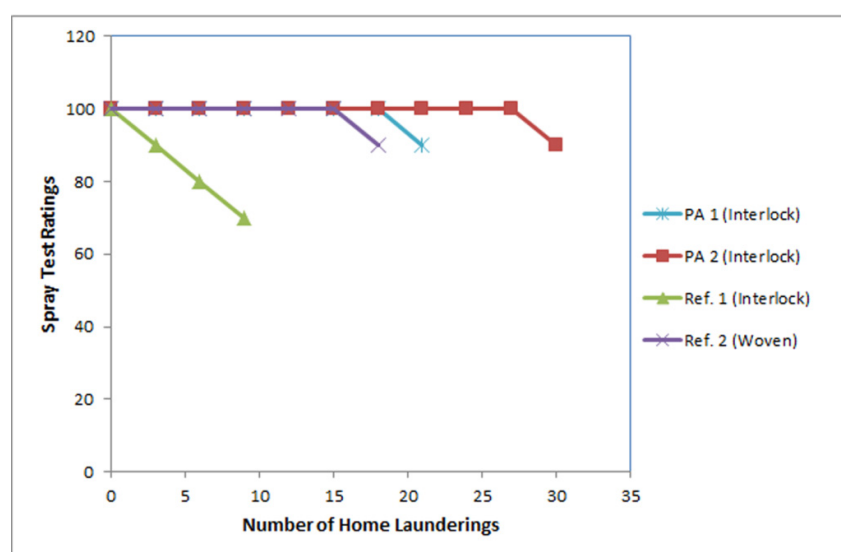
3.4. Oil Repellency

Oil test results performed according to AATCC test method 118 are reported in Figure 8. Treated fabric with PA1 did not show any oil repellency. In contrast, application of PA2 by admicellar polymerization yielded an initial oil repellency of grade 7. This value dropped to grade 5 after half a dozen home launderings and then remained at grade 5 after many cycles. In fact, it was in these oil repellency tests where the effects of the longer chain fluoroalkyl moiety in polyacrylate PA2 were most evident in its effect on oil repellency. Both off-the-shelf reference samples were rated initially at grade 5. However, interlock sample Ref. 1 degraded rapidly to ratings of 3 and 2. The performance of the woven fabric Ref. 2 paralleled that of PA2, only 2 grades lower throughout. With the exception of PA1, the oil test results for durability corresponded to findings by the water repellency tests.

Figure 8. Comparison of oil test for treated fabric with commercial reference samples.
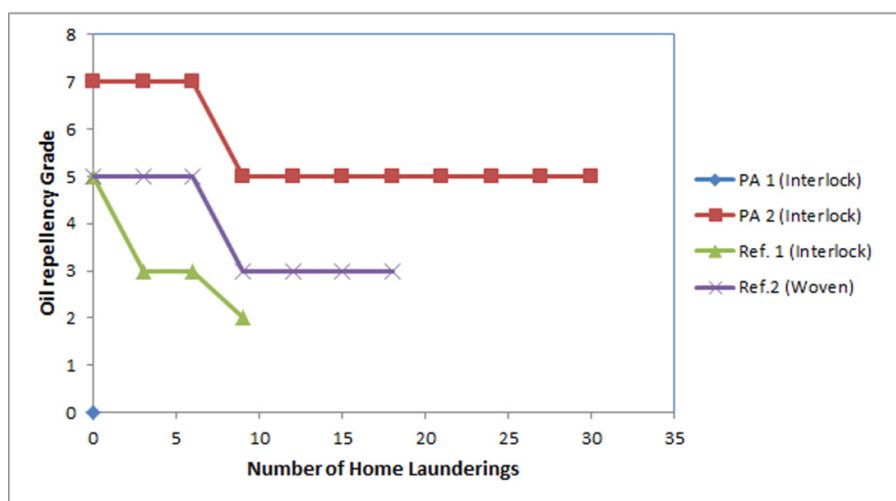
3.5. Stain Recovery and Stain Resistance

The main advantage of a stain resistant and stain recovery finish for fabric is that, when a spill occurs, it can be cleaned easily. Removal of stains during low temperature home launderings is often recommended. Assessment of performance under such conditions can be done according to standard tests, such as AATCC test 130. Results for stain release (Table 1) roughly followed the oil repellency findings except the woven commercial fabric received a lower rating than the commercial interlock fabric. At a grade of 4.5, sample PA2 received the highest rating of the group and PA1 the poorest at 1.

Table 1. Stain release grades according to AATCC test method 130.

Types of fabric	Stain release grade
Interlock (PA1)	1
Interlock (PA2)	4.5
Interlock (Ref. 1)	3
Woven (Ref. 2)	2

Fabrics were stained with oil, mustard and ketchup in additional tests. On the basis of the oil repellency and oil release results, sample PA1 was excluded from further testing. After wiping the stain with a tissue paper, stains remained visibly attached to untreated cotton, but, for treated fabric with PA2, all the stains were wiped away. To quantify this, we measured the reflectance of the fabric after wiping the stains for oil, mustard and ketchup. Figure 9 shows the stain resistance performance of treated cotton with PA2 and untreated cotton. PA2 exposed to oil showed stain resistance of 100% indicating oil can be wiped off immediately. When stains were dropped on untreated cotton, stains penetrated and contributed to lower reflectance. For treated cotton, the various agents did not penetrate and could be wiped off easily so reflectance retuned nearly to 100%.

Staining tests were also performed on the commercial reference samples and compared with PA2. Figure 10 presents reflectance measurements of stain resistance for treated and reference samples after exposure to oil, mustard and ketchup. All fabrics performed well in resisting blemishes by oil. Overall, PA2 performed comparably to the woven commercial material and outperformed the commercial knit.

The commercial interlock type fabric (Ref. 1) showed poor performance compared to the fabric modified by admicellar polymerization with only about 75% of stain resistance with mustard and about 80% with ketchup. It is a significant finding that the coated cotton knit could function at a level comparable to a fabric with a tighter weave.

Figure 9. Stain resistance for untreated and treated fabric with PA2 with different staining agents.
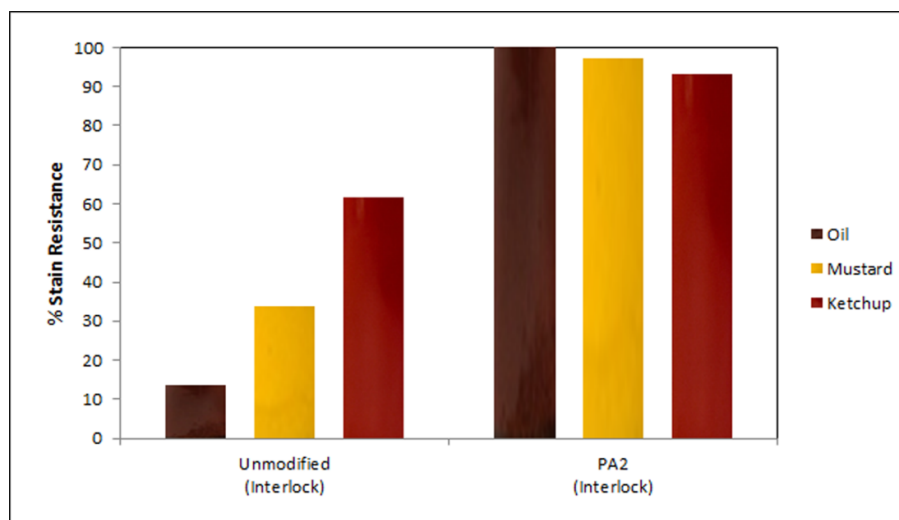
Figure 10. Stain resistance comparison for PA2 and commercial fabrics with different stains.
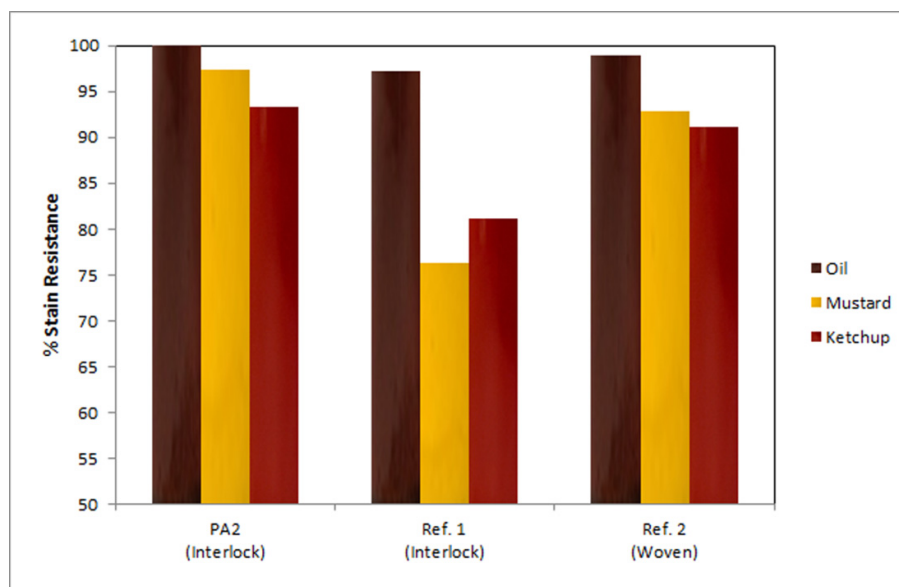
Similar experiments for stain recovery of the fabric were carried out by doing one home laundering and then assessing the level of stain recovery using reflectance measurements. Results for stain recovery are presented in Figure 11. All materials perform well in removal of oil by washing. Otherwise, stain recovery of PA2 was substantially better than the reference samples.

Figure 11. Stain recovery of treated fabric with PA2 compared to commercial reference fabrics.
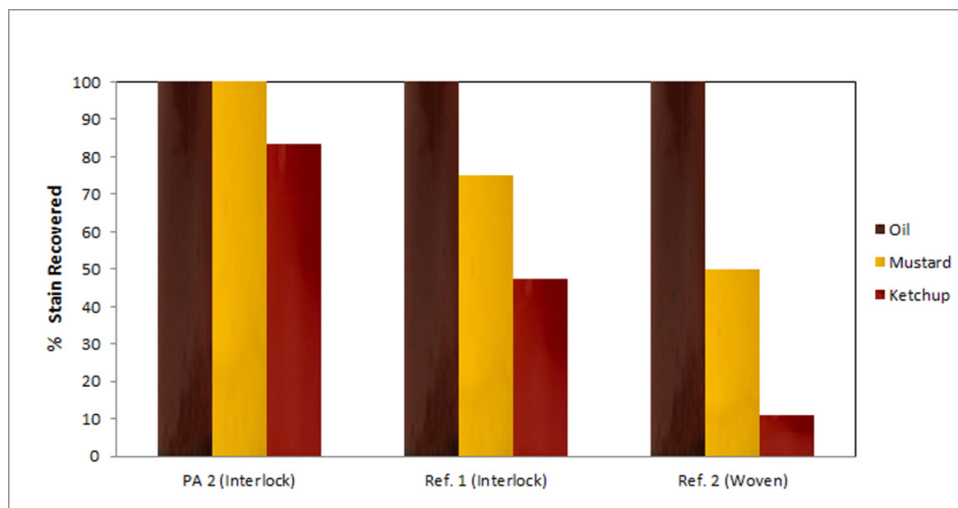
4. Conclusion

Application of fluorocarbon finishes by admicellar polymerization can yield durable cotton fabrics with excellent stain resistance and stain recovery properties. Performance of these fabrics, prepared in a laboratory, compare well to that of commercial production materials examined.

Acknowledgements

Conflict of Interest

Author Edgar O'Rear is affiliated with both The University of Oklahoma and SyntheSized Nano Coatings, Inc. The conflict of interest is under a management plan administered in accordance with the policies and procedures of the University of Oklahoma.

References

1. Holme, I. Innovative technologies for high performance textiles. *Color Technol.* **2007**, *123*, 59–73.
2. Sawhney, A.P.S.; Condon, B.; Singh, K.V.; Pang, S.S.; Li, G.; Hui, D. Modern applications of nanotechnology in textiles. *Text. Res. J.* **2008**, *78*, 731–739.
3. Vazquez, F. Silicone softeners for stain repellent and stain resistance fabric finishing. *Dyes and Chemicals* **2004**, Available online: http://www.fibre2fashion.com/industry-article/7/619/silicone-softeners-for-stain-repellent-and-stain-release-fabric-finishing6.asp (accessed on 27 January 2012).

4. Kathirvelu, S.; D'Souza, L.; Dhurai, B. Study of stain-eliminating textiles using ZnO nanoparticles. *J. Tex. I* **2010**, *101*, 520–526.

5. Badyal, J.P. Beyond the surface-cold plasmas are streamlining the surface coating. C*hem. Br.* **2001**, *37*, 45–46.

6. Bubert, H. Surface and thin film analysis. *Ullmann's Encycl. Ind. Chem.* **2011**, doi:10.1002/14356007.b06_023.pub2.

7. Ma, M.L.; Gupta, M.; Zhai, L.; Gleason, K. K.; Cohen, R. E.; Rubner, M. F.; Rutledge, G. C. Decorated electrospun fibers exhibiting superhydrophobicity. *Adv. Mater.* **2007**, *19*, 255–259.

8. Maity, J.; Jacob, C.; Das, C.K.; Singh, R.P. Direct fluorination of Twaron fiber and investigation of mechanical thermal and morphological properties of high density polyethylene and Twaron fiber composites. *J. Appl. Polym. Sci.* **2008**, *107*, 3739–3749.

9. Tarimala, S.; Kothari, N.; Abidi, N.; Hequet, E.; Fralick, J.; Dai, L.L. New approach to antibacterial treatment of cotton fabric with silver nanoparticle–doped silica using sol-gel process. *J. Appl. Polym. Sci.* **2006**, *101*, 2938–2943.

10. Yeh, J.-T.; Chen, C.-L.; Huang, K.-S. Preparation and application of fluorocarbon polymer/SiO_2 hybrid materials, part 2: Water and oil repellent processing for cotton fabrics by sol-gel method. *J. Appl. Polym. Sci.* *2007*, *103*, 3019–3024.

11. Wang, T.; Hu, X.; Dong, S. A general route to transform normal hydrophilic cloths into superhydrophobic surfaces. *Chem. Commun.* **2007**, 1849–1851.

12. Hoefnagels, H.F.; Wu, D.; de With, G.; Ming, W. Biomimetic superhydrophobic and highly oleophobic cotton textiles. *Langmuir* **2007**, *23*, 13158–13163.

13. Xue, C.H.; Jia, S.T.; Chen, H.Z.; Wang, M. Superhydrophobic cotton fabrics prepared by sol-gel coating of TiO_2 and surface hydrophobization. *Sci. Technol. Adv. Mater.* **2008**, *9*, doi:10.1088/1468-6996/9/3/035001.

14. Wang, H.; Fang, J.; Cheng, T.; Ding, J.; Qu, L.; Dai, L.; Wang, X.; Lin, T. One-step coating of fluoro-containing silica nanoparticles for universal generation of surface superhydrophobicity. *Chem. Commun.* **2008**, 877–879.

15. Leng, B.; Shao, Z.Z.; de With, G.; Ming, W. Superoleophobic cotton textiles. *Langmuir* **2009**, *25*, 2456–2460.

16. Zhao, Y.; Tang, Y.W.; Wang, X.G.; Lin, T. Superhydrophobic cotton fabric fabricated by electrostatic assembly of silica nanoparticles and its remarkable buoyancy. *Appl. Surf. Sci.* **2010**, *256*, 6736–6742.

17. Luna-Xavier, J.-L.; Guyot, A.; Bourgeat-Lami, E. Synthesis and characterization of silica/poly (methyl methacrylate) nanocomposite latex particles through emulsion polymerization using a cationic azo initiator. *J. Colloid Interface Sci.* **2002**, *250*, 82–92.

18. O'Haver, J.H.; Harwell, J.H.; O'Rear, E.A.; Snodgrass, L.J.; Waddell, W.H. *In situ* formation of polystyrene in adsorbed surfactant bilayers on precipitated silica. *Langmuir* **1994**, *10*, 2588–2593.

19. Wang, S.; Russo, T.; Qiao, G.G.; Solomon, D.H.; Shanks, R.A. Admicellar polymerization of styrene with divinyl benzene on alumina particles: The synthesis of white reinforcing fillers. *J. Mater. Sci.* **2006**, *41*, 7474–7482.

20. Karlsson, P.M.; Esbjornsson, N.B.; Holmberg, K. Admicellar polymerization of methyl methacrylate on aluminum pigments. *J. Colloid Interface Sci.* **2009**, *337*, 364–368.

21. Maity, J.; Kothary, P.; O'Rear, E.A.; Jacob, C. Preparation and comparison of hydrophobic cotton fabric obtained by direct fluorination and admicellar polymerization of fluoromonomers. *Ind. Eng. Chem. Res.* **2010**, *49*, 6075–6079.

22. Siriviriyanun, A.; O'Rear, E.A.; Yanumet, N. Improvement in the flame retardancy of cotton fabric by admicellar polymerization of 2-acryloyloxyethyl diethyl phosphate using an anionic surfactant. *J. Appl. Polym. Sci.* **2008**, *109*, 3859–3866.

23. Tragoonwichian, S.; O'Rear, E.A.; Yanumet, N. Broad ultraviolet protection by copolymerization of 2-[3-(2H-benzotriazol-2-yl)-4-hydroxyphenyl]ethyl methacrylate and 2-hydroxy-4-acryloyloxybenzophenone on cotton via admicellar polymerization. *J. Appl. Polym. Sci.* **2008**, *108*, 4004–4013.

Review

Oxyfluoride Chemistry of Layered Perovskite Compounds

Yoshihiro Tsujimoto [1,*], Kazunari Yamaura [2,3] and Eiji Takayama-Muromachi [2,3]

[1] International Center for Young Scientists (ICYS), International Center for Materials Nanoarchitechtonics (WPI-MANA), National Institute for Materials Science (NIMS)/Namiki 1-1, Tsukuba, Ibaraki 305-0044, Japan

[2] Superconducting Properties Unit, NIMS/Namiki 1-1, Tsukuba, Ibaraki 305-0044, Japan; E-Mails: yamaura.kazunari@nims.go.jp (K.Y.); muromachi.eiji@nims.go.jp (E.T.-M.)

[3] JST (Japan Science and Technol- ogy Agency), Transformative Research-Project on Iron Pnictides (TRIP)/Namiki 1-1, Tsukuba, Ibaraki 305-0044, Japan

* Author to whom correspondence should be addressed; E-Mail: TSUJIMOTO.Yoshihiro@nims.go.jp; Tel.: +81-29-851-3354; Fax: +81-29-860-4706.

Abstract: In this paper, we review recent progress and new challenges in the area of oxyfluoride perovskite, especially layered systems including Ruddlesden-Popper (RP), Dion-Jacobson (DJ) and Aurivillius (AV) type perovskite families. It is difficult to synthesize oxyfluoride perovskite using a conventional solid-state reaction because of the high chemical stability of the simple fluoride starting materials. Nevertheless, persistent efforts made by solid-state chemists have led to a major breakthrough in stabilizing such a mixed anion system. In particular, it is known that layered perovskite compounds exhibit a rich variety of O/F site occupation according to the synthesis used. We also present the synthetic strategies to further extend RP type perovskite compounds, with particular reference to newly synthesized oxyfluorides, Sr_2CoO_3F and $Sr_3Fe_2O_{5+x}F_{2-x}$ ($x \sim 0.44$).

Keywords: oxyfluoride; layered perovskite; high-pressure synthesis; low-temperature fluorination

1. Introduction

Since the discovery of a high-T_C superconducting cuprate by Bednorz and Muller [1], there has been considerable progress in the field of solid-state chemistry and physics. In particular, we have deepened the understanding of metal oxides, while making improvements and development of experimental techniques and theories. It is well known that a perovskite structure formulated as ABO_3 (*A* = large *s*-, *d*-, or *f*-block cation; *B* = smaller transition metal cation) has rich variety in structural, electronic and magnetic properties, ranging from superconductivity, through ferroelectricity, to photocatalytic activity. Figure 1(a) shows the ideal perovskite structure in which *A* cation occupies an interstitial site of an eight corner-sharing BO_6 octahedra. This type of structure can be extended to the layered perovskite intergrowth system termed the Ruddlesden-Popper (RP) phase, $A_2A'_{n-1}B_nO_{3n+1}$ (*n* = the number of perovskite block), the structures with *n* = 1 and 2 which are depicted in Figure 1(b) and (c). Each perovskite block is intervened with double rock-salt *A*O layers. Thanks to the ability of the *A* and *B* sites to adopt various metal cations, we are able to finely control the chemical compositions as well as the physical properties, as exemplified by magnetoresistive manganite [2–4] and superconducting cuprate [5,6]. While the majority of studies have concentrated on the influence of cation substitution, little effort has been made to control the structural and physical properties by manipulating the anion lattices. Considering that the anion strongly affects the crystal field and electronic state of the metal center, we can expect that substitution of anions with different bonding nature, valence state or ionic radius from oxygen in a metal oxide can enhance the original physical properties or induce new exotic phenomena. In fact, $LaTiO_2N$ [7] and $Sr_2CuO_2F_{2+\delta}$ [8] exhibit visible-light photocatalytic activity and superconductivity, respectively.

Figure 1. Structure of the ideal perovskite structure, $A_{n-1}B_nO_{3n+1}$ (*n* = 1, 2, ∞).
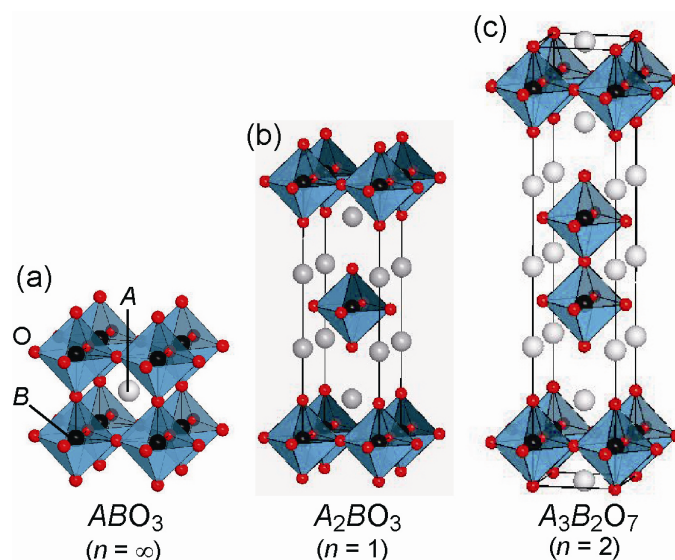
In general, it is very difficult to stabilize two kinds of hetero anions in one structure using conventional solid-state reactions, in comparison with compounds with a single anion, such as an oxide, sulfide or nitride. As for the oxyfluoride compounds, several synthetic approaches are employed to overcome the problem, namely a low-temperature reaction using fluorinating agents [8–11],

hydrothermal reaction [12] or high-pressure synthesis [13,14]. Interestingly, O/F site order and/or F contents inserted, which are closely correlated with the structural and physical properties, depend on the reaction method used. In particular, layered perovskite structures exhibit three types of anion distribution patterns; (i) regular or random anion occupation pattern in the perovskite blocks, (ii) fluorine insertion into only interstitial sites between the perovskite blocks, or (iii) fluorine occupation of both the terminal apical sites and the interstitial sites. In this paper, we first review recent progress in the oxyfluoride chemistry of perovskite-based compounds, then present a synthesis strategy to further extend layered perovskite systems.

2. Fluorine Occupation Patterns in Layered Oxyfluoride Perovskite

2.1. Regular or Random Anion Occupation Pattern in the Perovskite Blocks

Early in the study on the layered oxyfluoride perovskite, high temperature solid-state reaction, one of the easiest synthetic methods, was commonly employed. However, the variety of transition metals in the reported oxyfluoride compounds is quite limited, mainly due to the high chemical stability of the simple starting fluoride materials. To the best of our knowledge, the first example of the RP-type layered perovskite compound is K_2NbO_3F, which was reported in 1962 by Galasso and Darby [15]. As shown in Figure 2(a), the niobium oxyfluoride adopts the tetragonal structure in the space group of *I*4/*mmm* with octahedral coordination around Nb atom and O/F site disorder at the apical sites. The preferential occupation of the fluoride anion at the apical sites elongated the Nb-O/F bonds (2.0642 Å) along the *c* axis compared with those (1.9780 Å) in the *ab* plane. Subsequently, the same authors reported an isostructural iron oxyfluoride, Sr_2FeO_3F [16] and determined the crystal structure to be *I*4/*mmm*. However, Weller and his collaborators demonstrated that the exact crystal symmetry could be described as *P*4/*nmm* [17]. In contrast to K_2NbO_3F, the Fe counterpart possesses the O/F site order at the apical sites leading to a strong distortion of the FeO_5F octahedron (see Figure 2(b)). In fact, the bond length between Fe and O or F is 1.904 or 2.730 Å. Therefore, the iron metal center effectively takes a square pyramidal coordination against five O^{2-} anions. Weller *et al.* also extended the layered oxyfluoride system to Ba_2BO_3F (*B* = Sc and In) [18]. Both compounds exhibit preferential occupation by F^- anions at the apical sites, but the anion-site order/disorder in *B* = In/Sc.

In addition to the RP-type layered perovskite, Dion-Jacobson (DJ) and Aurivillius (AV) -type layered oxyfluoride phases are reported. The formulas of DJ and AV phases are expressed as $AA'_{n-1}B_nO_{3n+1}$ and $(Bi_2O_2)(A'_{n-1}B_nO_{3n+1})$, respectively. $ASrNb_2O_6F$ (*A* = Li, Na, Rb) [19] (Figure 3) and $RbLnTiNbO_6F$ (*Ln* = La, Pr, Nd) [20] were synthesized by conventional solid-state reaction. In contrast to the above RP phases, the F atoms prefer to occupy the equatorial and central apical anion sites in the double-layered perovskite block, not the terminal apical ones, because the covalency of the chemical bond between Nb and the terminal apical oxygen is incompatible with the ionicity of the Nb-F bond. On the other hand, Kobayashi *et al.* reported the reductive fluorination of DJ-$RbLaNb_2O_7$ and RP-$NaYTiO_4$ into $RbLaNb_2O_{7-x}F_x$ and $NaYTiO_{4-x}F_x$ using poly(vinylidene)fluoride (PVDF) [21]. PVDF or poly(tetrafluoroethylene) (PTFE) are effective fluorinating agents, utilized by Slater for the first time [11]. This fluorination proceeds in a topotactic manner; the framework of the precursor is maintained through the reaction. While $ASrNb_2O_6F$ and $RbLnTiNbO_6F$ with the non-magnetic *B*

cations are insulating, $RbLaNb_2O_{7-x}F_x$ possesses mixed valence states between Nb^{4+} and Nb^{5+} cations, which makes it electrically conductive.

Figure 2. Crystal structure of (**a**) K_2NbO_3F, (**b**) Sr_2FeO_3F, and (**c**) Sr_2CoO_3F. Solid line represents the unit cell.
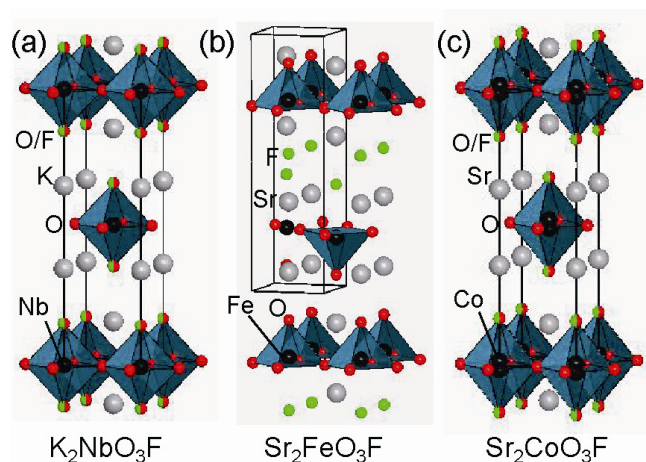
Figure 3. Crystal structure of (**a**) $RbSrNb_2O_6F$ and (**b**) $LiSrNb_2O_6F$.
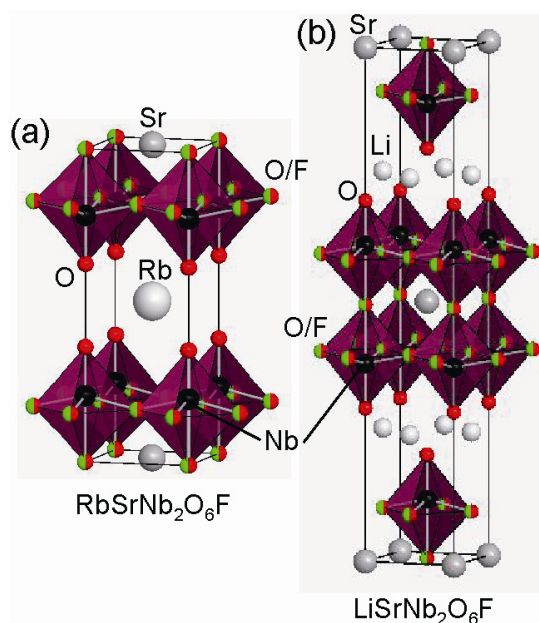
For $n = 2$ RP-type layered perovskite, $Ba_3In_2O_5F_2$ [22] and $Sr_3Fe_2O_6F_{0.68}$ [17] are known. Common to both compounds, fluorine atoms occupy the terminal apical sites. In comparison with $Ba_3In_2O_5F_2$, synthesized by conventional high-temperature reaction, $Sr_3Fe_2O_6F_{0.68}$ is obtained by a low-temperature fluorination using F_2 gas. As shown in Figure 4, the precursor $Sr_3Fe_2O_6$ has an oxygen vacancy at the central apical site, but its oxidative fluorination causes local migration of the terminal apical site to the original oxygen vacant site. Because the intercalated F atoms occupy the terminal apical sites with O, the deviation of the O-Fe-O bond angle in the plane from the ideal 180° is only 7.6°, much smaller

than the corresponding value of 15.28° in $Ba_3In_2O_5F_2$ with full fluorine occupation of the terminal apical sites.

Figure 4. Crystal structure of (**a**) $Sr_3Fe_2O_6$ and (**b**) $Sr_3Fe_2O_6F_{0.86}$. (**c**) Fluorination process of $Sr_3Fe_2O_6$ to $Sr_3Fe_2O_6F_{0.86}$, showing rearrangement of oxide and fluoride anions.
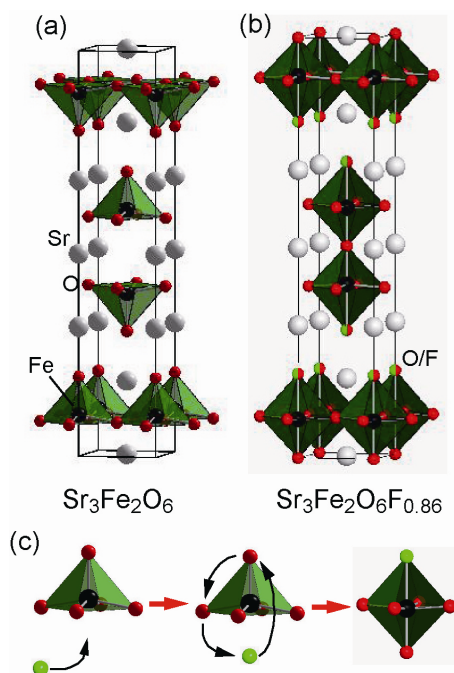
Figure 5. Crystal structure of (**a**) $Bi_2TiO_4F_2$, and (**b**) Bi_2NbO_5F.
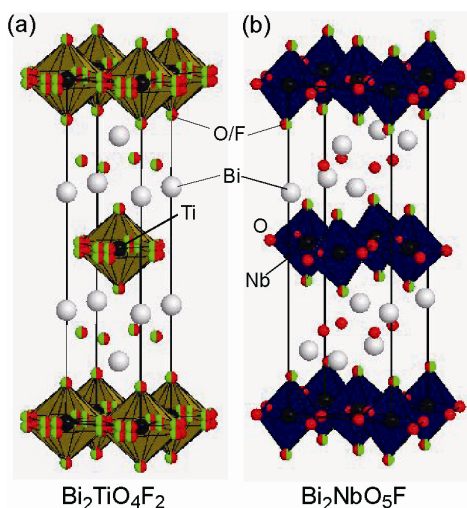
Three kinds of AV-type layered oxyfluoride perovskites, Bi_2BO_5F (*B* = Nb, Ta) and $Bi_2TiO_4F_2$ (Figure 5), were synthesized by Aurivillius [23]. Later work presented the ferroelectric phase transitions at T_C = 303, 283, and 284 K, respectively, but the relationship between the crystal structure and the ferroelectricity is still controversial. Hydrothermal synthesis yields better sample quality than conventional solid-state reaction [24]. $Bi_2TiO_4F_2$ adopts the simple body-centered tetragonal structure in the space group *I*4/*mmm* [24] while Bi_2NbO_5F is proposed to adopt *Pbca* symmetry [25]. These

centrosymmetric crystal structures contradict the requirement for the ferroelectricity. In fact, the reexamination of electrical properties in Bi_2NbO_5F demonstrated neither second-harmonic generation nor a permittivity anomaly associated with ferroelectric phase transition reported previously. It is believed from bond-valence-sum calculations that F atoms tend to occupy the equatorial sites for $Bi_2TiO_4F_2$ or the apical sites for Bi_2NbO_5F.

We would like to show a new class of anion ordered perovskite materials, $KNaNbOF_5$ and $KNaMO_2F_4$ ($M = Mo^{6+}$, W^{6+}) expressed as the general formula $ABB'(O,F)_6$ [12]. Poeppelmeier *et al.* successfully synthesized these three compounds by hydrothermal reaction. Layers of K^+ cations and cation vacancies are alternately located in the A site along the c axis, and Na^+ and B (Nb^{5+}, Mo^{6+}, W^{6+}) cations are ordered in a rock salt configuration. More interestingly, fluoride anions are located in K^+ cation layers while apical oxide anions are located in the adjacent A-site layer containing the A-site vacancies. Similar to DJ-ASrNb_2O_6F, the Nb^{5+} cation form short Nb=O bonds and one long Nb-F bond opposite the O^{2-} anion, leading to strong distortion of the Nb^{5+}-centered octahedron. This type of O/F anion order has never been seen in any other oxyfluorides. It is apparent that the cation order in both A and B sites influences the O/F anion order.

2.2. Fluorine Insertion into Only Interstitial Sites between the Perovskite Blocks

There are a few examples that involve fluorine insertion into only interstitial sites between the perovskite block layers. The RP-type layered manganese oxides, $LaSrMnO_4$ ($n = 1$) and $Ln_{1.2}Sr_{1.8}Mn_2O_7$ ($Ln = $ Pr, Nd, Sm, Eu, and Gd) ($n = 2$), accommodate fluorine in the (La/Sr)O rock-salt layers between the Mn-O perovskite blocks, followed by large expansion of the c-axis of $1 \sim 3$ Å (see Figure 6). Utilization of F_2 gas, NH_4F, CuF_2 or PVDF as a fluorination agent at low temperatures yields $LaSrMnO_4F_2$ [26,27] and $Ln_{1.2}Sr_{1.8}Mn_2O_7F_2$ [26,28] where fluorine is inserted in each perovskite block. In addition, heating these fluorinated compounds with the corresponding precursors in appropriate ratios results in a staged intercalation structure, namely $LaSrMnO_4F$ [27,29] and $La_{1.2}Sr_{1.8}Mn_2O_7F$ [27] where F is inserted between alternate rock-salt layers. It should be noted that the F sites in the rock-salt layers are different between $LaSrMnO_4F$ and $LaSrMnO_4F_2$, and $La_{1.2}Sr_{1.8}Mn_2O_7F$ and $Ln_{1.2}Sr_{1.8}Mn_2O_7F_2$; the F atoms in $LaSrMnO_4F$ and $La_{1.2}Sr_{1.8}Mn_2O_7F$ are located in the interlayer space so as to bridge between La/Sr and the apical oxygen, while the F atoms in $LaSrMnO_4F_2$ and $Ln_{1.2}Sr_{1.8}Mn_2O_7F_2$ occupy tetrahedral sites of $(La/Sr)_4$ in the rock-salt layers. In spite of the valences of Mn cations close to 4+, no long-range magnetic order is observed down to 5 K.

The $n = 2$ RP phase $Sr_3Ru_2O_7$ is also fluorinated using CuF_2 to give the oxyfluoride $Sr_3Ru_2O_7F_2$ [30]. In the fluorinated phase, fluorine is inserted in the tetrahedral sites of Sr_4 in rock-salt layers between perovskite blocks (see Figure 7). The precursor crystallizes in the tetragonal structure with $I4/mmm$, but the fluorine insertion lowers the crystal symmetry to orthorhombic symmetry (*Pbam*), which is associated with rotation and tilting of the RuO_6 octahedra. The magnetic properties also change after the fluorination reaction, from the ferromagnetic state with $T_C = 105$ K to weak ferromagnetic state with $T_N = 185$ K.

Figure 6. Crystal structure of (**a**) $La_{1.2}Sr_{1.8}Mn_2O_3F$, and (**b**) $La_{1.2}Sr_{1.8}Mn_2O_3F_2$.

$La_{1.2}Sr_{1.8}Mn_2O_3F$ $La_{1.2}Sr_{1.8}Mn_2O_3F_2$
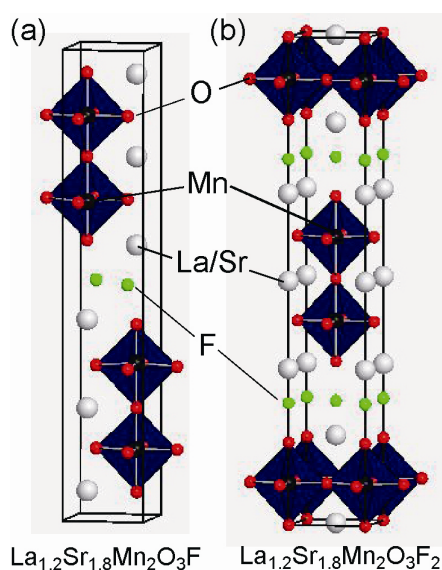
Figure 7. Crystal structure of $Sr_3Ru_2O_7F_2$.

$Sr_3Ru_2O_7F_2$
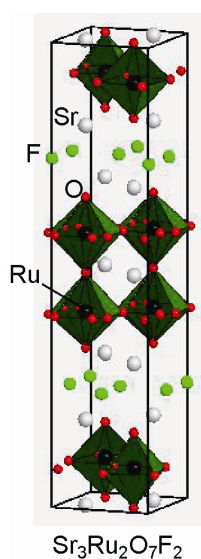
Fluorination of the RP-$Ba_{2-x}Sr_xPdO_3$ ($0 \leq x \leq 1.5$) by PVDF involves unusual oxygen displacement through anion exchange [31,32], which is different from the case of the fluorination of $Sr_3Fe_2O_6$ described above [17]. As shown in Figure 8, the structure of $Ba_{2-x}Sr_xPdO_3$ comprises corner-linked chains of PdO_4 squares along the *a*-axis, similar to the one-dimensional structure in Sr_2CuO_3. Fluorination to $Ba_{2-x}Sr_xPdO_2F_2$ involves structural conversion to *T'*-structure (isostructural with Nd_2CuO_4), namely rearrangement of the PdO_4 network from a 1-D chain to a 2-D plane. The remaining O^{2-} anions in the apical site move to the original vacant site and the two inserted F^- anions build fluorite block layer with Ba/Sr cations. Because the Pd^{2+} cation exhibits a strong preference for square lattice geometry, no additional fluorine insertion at the apical sites is allowed.

Figure 8. (**a**), (**b**), (**c**) Fluorination of A_2BO_3 to $A_2BO_2F_{2-\delta}$ (A = Sr, Ba; B = Cu, Pd). (**d**) Rearrangement of oxide and fluoride anions during fluorination reaction.
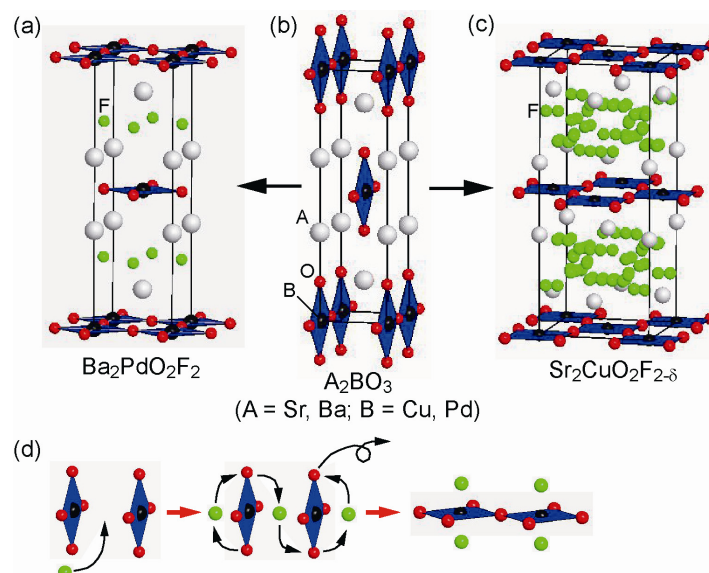
2.3. Fluorine Occupation of Both the Terminal Apical Sites and the Interstitial Sites

In most cases, low-temperature fluorination in layered perovskite structure proceeds by anion substitution at the apical sites and fluorine insertion in interstitial sites between perovskite blocks. This type of fluorination, especially in Cu oxides, has already been reviewed in detail by Greaves *et al.* and Wiley *et al.*, independently [33–35], so we will present the following four examples in this paper, namely $Sr_2CuO_2F_{2+\delta}$ [8,36], $Ba_2ZrO_3F_2 \cdot xH_2O$ [37], $Sr_2TiO_3F_2$ [38], and nitride-fluoride $Ce_2MnN_3F_{2-\delta}$ [39].

The discovery of a superconducting copper oxyfluoride $Sr_2CuO_2F_{2+\delta}$ by Greaves *et al.* triggered the search for new oxyfluoride perovskite materials by a low-temperature route [8]. Other fluorinating agents, such as NH_4F and XeF_2, were shown to be useful in later work [9,10]. This compound was initially obtained by reaction of a 1-D structure Sr_2CuO_3 with F_2 gas. As observed in $Ba_{2-x}Sr_xPdO_2F_2$ [31], the network of corner-sharing CuO_4 units drastically changes from a 1-D chain to a 2-D layer in the fluorination process (see Figure 8). However, fluorine anions partially occupy not only interstitial sites between the perovskite blocks but also the apical sites. The superconducting temperature takes a maximum value of T_C = 46 K at $\delta \sim 0.3$. Interestingly, reduction of $Sr_2CuO_2F_{2+\delta}$ in a flowing H_2/N_2 gas atmosphere yields an insulating *T'*-structure $Sr_2CuO_2F_2$ [36]; fluorine removal at the apical sites and rearrangement of the remaining F^- anions form a fluorite Sr_2F_2 layer and square planar coordinated CuO_4.

$Sr_2TiO_3F_2$ or $Ba_2ZrO_3F_2 \cdot xH_2O$ can be prepared by the reaction of n = 1RP Sr_2TiO_4 or Ba_2ZrO_4 with NH_4F, CuF_2, ZnF_2 or PVDF [37,38]. In both cases, fluorination occurs by substitution of two F^- anions for one O^{2-} anion, but the fluorine insertion manner and coordination environment around the metal center are different between these two compounds (see Figure 9). Fluoride anions in $Sr_2TiO_3F_2$ occupy both the apical sites and interstitial sites in alternate rock-salt layers. Additionally, the TiO_5F octahedron is highly distorted, probably due to O/F site order at the apical sites. In contrast, $Ba_2ZrO_3F_2 \cdot xH_2O$

possesses fluorine, located at the apical sites and in each rock-salt layer. The Zr metal center takes an octahedral coordination, with O/F anions being disordered at the apical sites.

Figure 9. Crystal structure of (**a**) $Sr_2TiO_3F_2$, (**b**) $Ba_2ZrO_3F_2 \cdot xH_2O$, and (**c**) $Ce_2MnN_3F_{2-\delta}$.
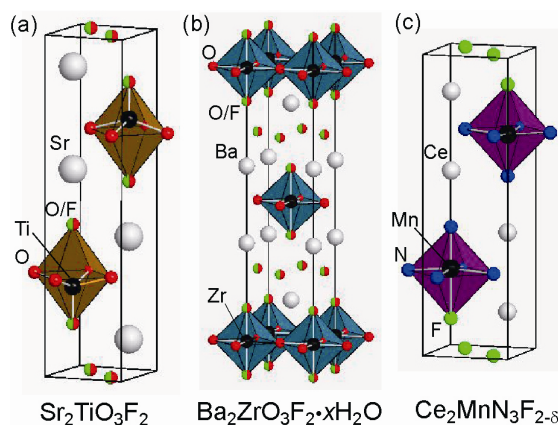
It is important to note that a RP-type layered manganese nitride Ce_2MnN_3, which is isostructural with Sr_2CuO_3, accommodates fluorine in a different way [39]. Unlike $Sr_2CuO_2F_{2+\delta}$ and $Ba_{2-x}Sr_xPdO_2F_2$, fluorination involves local migration of the original apical oxygen to the equatorial anion vacant sites, but anion substitution or oxygen removal does not take place. Moreover, additional fluorine atoms are incorporated in alternate rock-salt layers. The resultant structure resembles that of $Sr_2TiO_3F_2$ and the N/F site order results in deformation of the MnN_4F octahedron. Upon fluorination, the magnetic properties changes the Pauli paramagnetic behavior to a paramagnetic one.

3. Recent Results on New Layered Iron and Cobalt Oxyfluoride Compounds

3.1. Unusual O/F Site Disorder in Layered Cobalt Oxyfluoride

As reviewed above, a variety of fluorinating agents greatly contributes to oxyfluoride chemistry. Considering the limited variety of transition metals, however, a further search for new oxyfluoride phase is necessary in order to better understand oxyfluoride. Co is among the 3d transition metals studied to a lesser extent. In fact, only one Co-based perovskite compound has been reported: $LaSrCoFeO_5F$ [40], where O/F sites are randomly distributed as well as Fe/Co sites. High-pressure synthesis is an effective alternative approach to low-temperature fluorination, although expensive apparatus required for the reaction method is necessary. Recently, we have achieved the synthesis of the first example of RP-type layered cobalt oxyfluoride Sr_2CoO_3F, under a pressure of 6 GPa at 1,700 °C [41]. This compound adopts a simple body-centered tetragonal structure with the space group *I*4/*mmm* (Figure 2(c)). Magnetic susceptibility measurements revealed an antiferromagnetic phase transition at around 320 K, which is different from the ferromagnetic behavior in the corresponding oxide Sr_2CoO_4 [42]. Furthermore, neutron powder diffraction study characterized the $S = 2$ high-spin state at Co cations. The structural features in the cobalt oxyfluoride are also worthy of attention. The O/F anions are disordered at the apical sites, and the cobalt cation shifted from the basal plane takes a square pyramidal coordination. We noticed that the coordination environment around Co center is

unusual when compared with related oxyfluoride compounds (see Figure 2). As described above, a similar O/F site disorder is observed in Ba_2ScO_3F and K_2NbO_3F, but each B cation with d^0 electronic configuration takes octahedral coordination without shifting from the basal plane. In comparison, Sr_2FeO_3F and Ba_2InO_3F have a square-pyramidal coordinated metal center, but O/F site occupation occurs in an ordered manner. Thus, coexistence of anion disorder and square-pyramidal coordination, which has never seen in related oxyfluoride, is realized in the new cobalt oxyfluoride. It was initially assumed that square-pyramidal coordination stabilizes the O/F site ordered state, but this is not the case in Sr_2CoO_3F. Square-pyramidal coordination of Co cations is commonly seen in cobalt-based materials with d^6 high spin configuration, such as $BiCoO_3$ [43] and Sr_2CoO_3Cl [44]. The observed O/F disorder, however, is non-trivial. The role played in the unusual coordination environment around Co is probably related to the reaction condition employed: high-pressure and high-temperature synthesis. A denser environment at high pressure or entropic effects associated with high temperature are likely to stabilize the anion-disordered phase.

3.2. Highly Fluorinated Iron Oxides

Various fluorinating agents have been reported so far, for example, F_2 gas, NH_4F, XeF_2, CuF_2 and PVDF and PTFE [8–11,21]. Each fluorinating agent exhibits a distinct fluorinating power and reaction pathway. Thus, the fluorine contents in the resultant material depend on the choice, not only of the fluorinating agent, but also the anion lattice of the precursors. For example, the fluorine contents incorporated by XeF_2 in $YBa_2Cu_3O_{7-\delta}$ increase with decreasing the oxygen deficient contents [45]. The fluorination of perovskite $SrFeO_3$ using PVDF yields $SrFeO_2F$ while the reaction of brownmillerite $Sr_2Fe_2O_5$ with F_2 gas results in the formation of two cubic phases different from $SrFeO_2F$ [17,46].

On the other hand, as shown above, the $n = 2$ RP-type layered iron oxide $Sr_3Fe_2O_6$ was fluorinated with F_2 gas to give the oxyfluoride $Sr_3Fe_2O_6O_{0.87}$ [17]. This fluorination did not involve anion substitution. There are two approaches to extending the fluorine contents; a precursor with smaller oxygen concentrations is reacted with F_2 gas, or a fluorinating agent with higher reducing power is employed. According to such perspectives, we successfully synthesized a more highly fluorinated iron oxide, $Sr_3Fe_2O_{5.44}F_{1.56}$, by reaction of $Sr_3Fe_2O_{7-\delta}$ ($\delta \sim 0.25$) [47]. As is the case in $Sr_3Fe_2O_6O_{0.87}$, fluoride anions preferentially occupy the terminal apical anion sites with oxide anions, but the O/F sites are displaced from the ideal $4e$ $(0, 0, z)$ to more general sites $16m$ (x, x, z). Moreover, fluorination with PTFE results in more significant expansion of the c-axis (21.406(2) Å) and the deviation of the O-Fe-O bond angle in the plane from 180° is 15.28° nearly close to that in $Ba_3In_2O_5F_2$, reflecting the increased fluorine content in $Sr_3Fe_2O_{5.44}F_{1.56}$. And, the antiferromagnetic phase transition temperature greatly differs from below r.t. to 390 K.

Interestingly, work that is more recent has demonstrated further extended fluorination. Slater *et al.* have successfully synthesized three more fluorinated phases, $Sr_3Fe_2O_{5.28}F_{1.72}$, $Sr_3Fe_2O_4F_4$, and $Sr_3Fe_2O_3F_6$, by changing the molar ratios of $Sr_3Fe_2O_{7-\delta}$ to PVDF [48]. While $Sr_3Fe_2O_{5.28}F_{1.72}$ has structural features similar to $Sr_3Fe_2O_{5.44}F_{1.56}$, fluorine atoms in $Sr_3Fe_2O_4F_4$ occupy half interstitial sites between rock-salt layers as well as terminal and central anion sites (see Figure 10). These two compounds exhibit antiferromagnetic order at r.t. In contrast, $Sr_3Fe_2O_3F_6$, which is assumed to

correspond to complete filling of both apical sites and interstitial sites by fluorine, magnetically orders below r.t.

Figure 10. Crystal structure of (**a**) $Sr_3Fe_2O_{5.44}F_{1.56}$, and (**b**) $Sr_3Fe_2O_4F_4$.

$Sr_3Fe_2O_{5.44}F_{1.56}$ $Sr_3Fe_2O_4F_4$
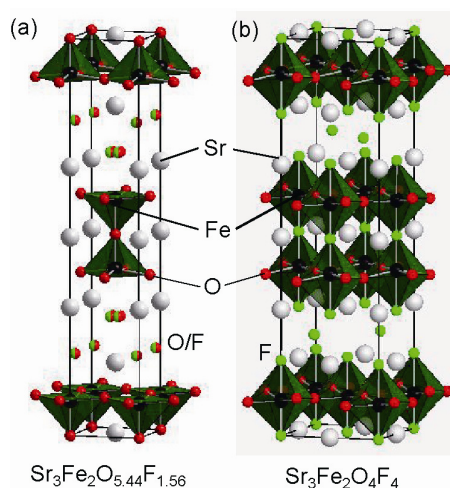
5. Conclusions

We have reviewed how layered oxyfluoride perovskite compounds have a rich variety of fluorine occupation, depending on reaction route, namely, low-temperature reaction, hydrothermal reaction, and high-pressure synthesis. Low temperature topotactic reaction is an attractive and straightforward technique to synthesize kinetically stable phases; Not only anion substitution but also fluorine insertion in interstitial sites between perovskite blocks occur, in some cases involving a rearrangement of anions around the metal center. In particular, the high capacity for fluorine insertion observed in $Sr_3Fe_2O_{7-\delta}$ is quite unusual compared with other metal oxides. High-pressure synthesis can also provide good opportunities for extending oxyfluoride chemistry. Indeed, an unusual coordination environment in Sr_2CoO_3F was realized under extreme experimental conditions. This result should contribute not only to further syntheses of new oxyfluoride compounds, but also to controlling the structural and physical properties through anion order/disordering.

Acknowledgments

References

1. Bednorz, J.G.; Müller, K.A. Possible high Tc superconductivity in the Ba-La-Cu-O. *Z. Phys. B* **1986**, *64*, 189–193.
2. Urushibara, A.; Moritomo, Y.; Arima, T.; Asamitsu, A.; kido, G.; Tokura, Y. Insulator-metal transition and giant magnetoresistance in $La_{1-x}Sr_xMnO_3$. *Phys. Rev. B* **1995**, *51*, 14103–14109.
3. Moritomo, Y.; Asamitsu, A.; Kuwahara, H.; Tokura, Y. Giant magnetoresistance of manganese oxides with a layered perovskite structure. *Nature* **1996**, *380*, 141–144.
4. Tokura, Y.; Nagaosa, N. Orbital physics in transition-metal oxides. *Science* **2000**, *288*, 462–468.
5. Cava, R.J. Oxide superconductors. *J. Am. Ceram. Soc.* **2000**, *83*, 1–28.
6. Dagotto, E. Correlated electrons in high-temperature superconductors. *Rev. Mod. Phys.* **1994**, *66*, 763–841.
7. Kasahara, A.; Nukumizu, K.; Hitoki, G.; Takata, T.; Kondo, J.N.; Hara, M.; Kobayashi, H.; Domen, K. Photoreaction on $LaTiO_2N$ under visible light irradiation. *J. Phys. Chem. A* **2002**, *106*, 6750–6753.
8. Al-Mamouri, M.; Edwards, P.P.; Greaves, C.; Slaski, M. Synthesis and superconducting properties of the strontium copper oxy-fluoride $Sr_2CuO_2F_{2+\delta}$. *Nature* **1994**, *369*, 382–384.
9. Slater, P.R.; Hodges, J.P.; Francesconi, M.G.; Edwards, P.P.; Greaves, C.; Gameson, I.; Slaski, M. An improved route to the synthesis of superconducting copper oxyfluorides $Sr_{2-x}A_xCuO_2F_{2+\delta}$ (A = Ca, Ba) using transition metal difluorides as fluorinating reagents. *Phys. C* **1995**, *253*, 16–22.
10. Ardashnikova, E.I.; Lubarsky, S.V.; Denisenko, D.I.; Shpanchenko, R.V.; Antipov, E.V.; van Tendeloo, G. A new way of synthesis and characterization of superconducting oxyfluoride $Sr_2Cu(O, F)_{4+\delta}$. *Phys. C* **1995**, *253*, 259–265.
11. Slater, P.R. Poly(vinylidene fluoride) as a reagent for the synthesis of K_2NiF_4-related inorganic oxide fluorides. *J. Fluor. Chem.* **2002**, *117*, 43–45.
12. Pinlac, R.A.; Stern, C.L.; Poeppelmeier, K.R. New layered oxide-fluoride perovskites: $KNaNbOF_5$ and $KNaMO_2F_4$ (M = Mo^{6+}, W^{6+}). *Crystals* **2011**, *1*, 3–14.
13. Troyanchuk, I.O.; Kasper, N.V.; Mantytskaya, O.S.; Shapovalova, E.F. High-pressure synthesis of some perovskite-like compounds with a mixed anion type. *Mater. Res. Bull.* **1995**, *30*, 421–425.
14. Katsumata, T.; Nakashima, M.; Umemoto, H.; Inaguma, Y. Synthesis of the novel perovskite-type oxyfluoride $PbScO_2F$ under high pressure and high temperature. *J. Solid State Chem.* **2008**, *181*, 2737–2740.
15. Galasso, F.; Darby, W. Preparation, structure, and properties of K_2NbO_3F. *J. Phys. Chem.* **1962**, *66*, 1318–1320.
16. Galasso, F.; Darby, W. Preparation and properties of Sr_2FeO_3F. *J. Phys. Chem.* **1963**, *67*, 1451–1453.
17. Case, G.S.; Hector, A.L.; Levason, W.; Needs, R.L.; Thomas, M.F.; Weller, M.T. Synthesis powder neutron diffraction structures and Mössbauer studies of some complex iron oxyfluorides: $Sr_3Fe_2O_6F_{0.87}$, Sr_2FeO_3F and $Ba_2InFeO_5F_{0.68}$. *J. Mater. Chem.* **1999**, *9*, 2821–2827.
18. Needs, R.L.; Weller, M.T.; Scheler, U.; Harris, R.K. Synthesis and structure of Ba_2InO_3X (X = F, Cl, Br) and Ba_2ScO_3F; oxide/halide ordering in K_2NiF_4-type structures. *J. Mater. Chem.* **1996**, *6*, 1219–1224.

19. Choy, J.H.; Kim, J.Y.; Kim, S.J.; Sohn, J.S. New Dion-Jacobson-type layered perovskite oxyfluorides, $ASrNb_2O_6F$ (A = Li, Na, and Rb). *Chem. Mater.* **2001**, *13*, 906–912.

20. Caruntu, G.; Spinu, L.; Wiley, J.B. New rare-earth double-layered-perovskite oxyfluorides, $RbLnTiNbO_6F$ (Ln = La, Pr, Nd). *Mater. Res. Bull.* **2002**, *37*, 133–140.

21. Kobayashi, Y.; Tian, M.; Eguchi, M.; Mallouk, T. Ion-exchangeable, electronically conducting layered perovskite oxyfluorides. *J. Am. Chem. Soc.* **2009**, *131*, 9849–9855.

22. Needs, R.L.; Weller, M.T. Structure of $Ba_3In_2O_5F_2$ by combined powder analysis; oxide/fluoride ordering in a Ruddlesden-Popper phase. *J. Chem. Soc. Dalton Trans.* **1995**, *18*, 3015–3017.

23. Aurivillius, B. The structure of Bi_2NbO_5F and isomorphous compounds. *Ark. Kemi.* **1952**, *5*, 39–47.

24. Needs, R.L.; Dann, S.E.; Weller, M.T. Cherryman, J.C.; Harris, R.K. The structure and oxide/fluoride ordering of the ferroelectrics $Bi_2TiO_4F_2$ and Bi_2NbO_5F. *J. Mater. Chem.* **2005**, *15*, 2399–2407.

25. McCabe, E.E.; Jones, I.P.; Zhang, D.; Hyatt, N.C.; Greaves, C. Crystal structure and electrical characterization of Bi_2NbO_5F: An Aurivillius oxide fluoride. *J. Mater. Chem.* **2007**, *17*, 1193–1200.

26. Greaves, C.; Kissick, J. L.; Francesconi, M.G.; Aikens, L.D. Gillie, L.J. Synthetic strategies for new inorganic oxide fluorides and oxide sulfates. *J. Mater. Chem.* **1999**, *9*, 111–116.

27. Aikens, L.D.; Gillie, L.J.; Li, R.K.; Greaves, C. Staged fluorine insertion into manganese oxides with Ruddlesden-Popper structures: $LaSrMnO_4F$ and $La_{1.2}Sr_{1.8}MnO_2O_7F$. *J. Mater. Chem.* **2002**, *12*, 264–267.

28. Sivakumar, T.; Wiley, J.B. Topotactic route for new layered perovskite oxides containing fluorine: $Ln_{1.2}Sr_{1.8}Mn_2O_7F_2$ (Ln = Pr, Nd, Sm, Eu, and Gd). *Mater. Res. Bull.* **2009**, *44*, 74–77.

29. Aikens, L.D.; Li, R.K.; Greaves, C. The synthesis and structure of a new oxide fluoride, $LaSrMnO_4F$, with stated fluorine insertion. *Chem. Commun.* **2000**, 2149–2130.

30. Li, R.K.; Greaves, V. Double-layered ruthenate $Sr_3Ru_2O_7F_2$ formed by fluorine insertion into $Sr_3Ru_2O_7$. *Phys. Rev. B* **2000**, *62*, 3811–13815.

31. Baikie, T.; Dixon, E.L.; Rooms, J.F.; Young, N.A.; Francesconi, M.G. $Ba_{2−x}Sr_xPdO_2F_2$ ($0 \leq x \leq 1.5$): The first palladium-oxide-fluoride. *Chem. Commun.* **2003**, 1580–1581.

32. Baikie, T.; Islam, M.S.; Francesconi, M.G. Defects in the new oxide-fluoride $Ba_2PdO_2F_2$: The search for fluoride needles in an oxide haystack. *J. Mater. Chem.* **2005**, *15*, 119–123.

33. Greaves, C.; Fracesconi, M.G. Fluorine insertion in inorganic materials. *Curr. Opni. Solid State Mater. Sci.* **1998**, *3*, 132–136.

34. McCabe, E.E. Greaves, C. Fluorine insertion reactions into preformed metal oxides. *J. Fluor. Chem.* **2007**, *128*, 448–458.

35. Sanjaya Ranmohotti, K.G.; Josepha, E.; Choi, J.; Zhang, J.; Wiley, J.B. Topochemical manipulation of perovskites: Low-temperature reaction strategies for directing structure and properties. *Adv. Mater.* **2011**, *23*, 442–460.

36. Kissick, J.L.; Greaves, C.; Edwards, P.P.; Cherkashenko, V.M.; Kurmaev, E.Z.; Bartkowski, S.; Neumann, M. Synthesis, structure, and XPS characterization of the stoichiometric phase $Sr_2CuO_2F_2$. *Phys. Rev. B* **1997**, *56*, 2831–2835.

37. Slater, P.R.; Gover, R.K.B. Synthesis and structure of the new oxide fluoride $Ba_2ZrO_3F_2 \cdot xH_2O$. *J. Mater. Chem.* **2001**, *11*, 2035–2038.

38. Slater, P.R.; Gover, R.K.B. Synthesis and structure of the new oxide fluoride $Sr_2TiO_3F_2$ from the low temperature fluorination of Sr_2TiO_4: An example of a staged fluorine substitution/insertion reaction. *J. Mater. Chem.* **2002**, *12*. 291–294.

39. Headspith, D.A.; Sullivan, E.; Greaves, C.; Francesconi, M.G. Synthesis and characterization of the quaternary nitride-fluoride $Ce_2MnN_3F_{2-\delta}$. *Dalton Trans.* **2009**, 9273–9279.

40. El Shinawi, H; Marco, J.F.; Berry, F.J.; Greaves, C. $LaSrCoFeO_5$, $LaSrCoFeO_5F$ and $LaSrCoFeO_{5.5}$: New La-Sr-Co-Fe perovskites. *J. Mater. Chem.* **2010**, *20*, 3253–3259.

41. Tsujimoto, Y.; Li, J.J.; Yamaura, K.; Matsushita, Y.; Katsuya, Y.; Tanaka, M.; Shirako, Y.; Akaogi, M.; Takayama-Muromachi, E. New layered cobalt oxyfluoride, Sr_2CoO_3F. *Chem. Commun.* **2011**, *47*. 3263–3265.

42. Wang, X.L.; Takayama-Muromachi, E. Magnetic and transport properties of the layered perovskite system $Sr_{2-y}Y_yCoO_4$ $(0 \leq y \leq 1)$. *Phys. Rev. B* **2005**, *72*, doi: 10.1103/PhysRevB.72.064401.

43. Belik, A.A.; Iikubo, S.; Kodama, K.; Igawa, N.; Shamoto, S.; Niitaka, S.; Azuma, M.; Shimakawa, Y.; Takano, M.; Izumi, F.; *et al.* Neutron powder diffraction study on the crystal and magnetic structures of $BiCoO_3$. *Chem. Mater.* **2006**, *18*, 798–803.

44. Loureiro, S.M.; Felser, C.; Huang, Q.; Cava, R.J. Refinement of the crystal structures of strontium cobalt oxychlorides by neutron powder diffraction. *Chem. Mater.* **2000**, *12*, 3181.

45. Shpanchenko, R.V.; Rozova, M.G.; Abakumov, A.M.; Ardashnikova, E.I.; Kovba, M.L.; Putilin, S.N.; Antipov, E.V.; Lebedev, O.I.; Tendeloo, G.V. Inducing superconductivity and structural transformations by fluorination of reduced YBCO. *Phys. C* **1997**, *280*, 272–280.

46. Berry, F.J.; Ren, X.; Hea, R.; Slater, P.; Thomas, M.F. Fluorination of perovskite-related $SrFeO_{3-\delta}$. *Solid State Commun.* **2005**, *134*, 621–624.

47. Tsujimoto, Y.; Yamaura, K.; Hayashi, N.; Kodama, K.; Igawa, N.; Matsushita, Y.; Katsuya, Y.; Shirako, Y.; Akaogi, M.; Takayama-Muromachi, E. Topotactic synthesis and crystal structure of a highly fluorinated Ruddlesden–Popper-type Iron oxide, $Sr_3Fe_2O_{5+x}F_{2-x}$ $(x \approx 0.44)$. *Chem. Mater.* **2011**, *23*, 3652–3658.

48. Hancock, C.A.; Herranz, T.; Marco, J.F.; Berry, F.J.; Slater, P.R. Low temperature fluorination of $Sr_3Fe_2O_{7-\delta}$ with polyvinylidine fluoride: An X-ray powder diffraction and Mössbauer spectroscopy study. *J. Solid State Chem.* **2012**, *186*, 195–203.

Article

Optimization of Fluorine Plasma Treatment for Interface Improvement on HfO$_2$/In$_{0.53}$Ga$_{0.47}$As MOSFETs

Yen-Ting Chen *, Yanzhen Wang, Fei Xue, Fei Zhou and Jack C. Lee

Microelectronics Research Center, Department of Electrical and Computer Engineering,
The University of Texas at Austin, TX 78758, USA; E-Mails: yanzhen@physics.utexas.edu (Y.W.);
xuefei.ee@gmail.com (F.X.); essenonvidare@gmail.com (F.Z.); jacklee@mail.utexas.edu (J.C.L.)

* Author to whom correspondence should be addressed; E-Mail: ytchen@mail.utexas.edu;
Tel.: +1-512-471-1627; Fax: +1-512-471-5625.

Abstract: This paper reports significant improvements in the electrical performance of In$_{0.53}$Ga$_{0.47}$As metal-oxide-semiconductor field-effect transistors (MOSFET) by a post-gate CF$_4$/O$_2$ plasma treatment. The optimum condition of CF$_4$/O$_2$ plasma treatment has been systematically studied and found to be 30 W for 3–5 min. Approximately 5× reduction in interface trap density from 2.8×10^{12} to 4.9×10^{11} cm^{-2}eV^{-1} has been demonstrated with fluorine (F) incorporation. Subthreshold swing has been improved from 127 to 109 mV/dec. Effective channel mobility has been enhanced from 826 to 1,144 cm^2/Vs.

Keywords: InGaAs; HfO$_2$; fluorine plasma treatment; high-k dielectrics

1. Introduction

In$_{0.53}$Ga$_{0.47}$As based-III-V compounds have attracted a great deal of attention for their advantages in high electron mobility over their Si-based counterparts. However, poor interface quality between In$_{0.53}$Ga$_{0.47}$As and high dielectric constant (high-k) gate dielectrics has imposed an enormous challenge for implementing inversion-type enhancement mode metal-oxide-semiconductor field-effect transistors (MOSFETs). Proper surface pre-treatment and insertion of interface passivation layer [1–3] have generally employed to achieve improved interface quality. Those approaches usually performed prior to high-k deposition, however, interface state traps created during the high-k deposition need to be passivated by a post-oxide treatment.

It can be expected that fluorine (F) will be an effective passivation agent for $In_{0.53}Ga_{0.47}As$ because F has high binding energy with In (5.25 eV), Ga (5.99 eV), and As (4.26 eV), respectively [4]. F incorporation has been demonstrated on Si, Ge, and $In_{0.53}Ga_{0.47}As$ substrates. It has been found that F can passivate high-k bulk traps and interface defects at high-k/substrates (Si, Ge and $In_{0.53}Ga_{0.47}As$) interface [5–9]. Although previous reports showed that the insertion of a thin interface passivation layer could improve interface quality [10], those layers usually have relative lower k value [11]. This may hinder equivalent oxide thickness (EOT) scaling and as a result, hardly meet the requirement for the sub 22 nm nodes.

In this paper, we systematically studied the effects of CF_4/O_2 plasma power wattage and treatment time on $HfO_2/In_{0.53}Ga_{0.47}As$ gate stack. The condition of CF_4/O_2 plasma has been optimized, which significantly improves the effective channel mobility (μ_{eff}), transconductance (G_m), drive current (I_d), and subthreshold swing (SS). With F incorporation, we have successfully developed excellent interface quality of HfO_2 directly on $In_{0.53}Ga_{0.47}As$ without using interface passivation layer. Fluorinated samples exhibit low interface trap density (D_{it}) of 4.9×10^{11} cm^{-2}eV^{-1}, which is the lowest value compared to prior reported $HfO_2/In_{0.53}Ga_{0.47}As$ gate stacks.

2. Experimental Section

Figure 1 shows the device structure and the illustration of F incorporation. The wafers used in our study were molecular beam epitaxy grown by a vender. P-type (Zn-doped, 3×10^{18}/cm^3) InP wafers were the starting substrates. P-type (Be-doped, 5×10^{16}/cm^3) $In_{0.52}Al_{0.48}As$ of 100 nm thick was grown as a buffer layer, followed by a 300 nm p-type $In_{0.53}Ga_{0.47}As$ layer (Be-doped, 5×10^{16}/cm^3), which was used as the channel layer. The native oxides were removed with 1% diluted HF solution, followed by 20% $(NH_4)_2S$ solution for sulfur passivation. To protect gate stack from the source and drain (S/D) activation annealing, the gate-last process was adopted: A 10-nm-thick atomic-layer-deposited (ALD) Al_2O_3 was deposited at a substrate temperature of 200 °C as an encapsulation layer. S/D regions were selectively implanted with a Si dose of 2×10^{14}/cm^2 at 35 keV. The S/D activation annealing was performed in nitrogen ambient at 700 °C/10 s. The encapsulation layer was then removed using buffered oxide etch solution. A 5 nm-thick ALD HfO_2 film was deposited after the same surface preparation (HF and $(NH_4)_2S$). Some samples were treated *ex situ* with CF_4 plasma with varied RF wattages and treatment times. A mixed flow of CF_4 and O_2 gas (ratio ~10:1) was introduced into the chamber with pressure of 100 mTorr. The purpose of O_2 flow was to avoid carbon contamination. Control samples without CF_4/O_2 plasma treatment were also fabricated as references. Post-deposition annealing was then performed for all the samples at 500 °C for 60 s in a nitrogen ambient. Subsequently, a 200 nm TaN was sputtered and patterned as gate electrode. AuGe/Ni/Au alloy was deposited by E-beam evaporation and a liftoff process to form S/D Ohmic contacts; backside contact was made by E-beam evaporation of Cr/Au, followed by annealing at 400 °C for 30 s in nitrogen ambient.

Figure 1. The device cross-sectional structure of $HfO_2/In_{0.53}Ga_{0.47}As$ gate stack. Samples were treated in a mixed flow of CF_4 and O_2 gas (ratio ~10:1) with varied RF power and treatment time.
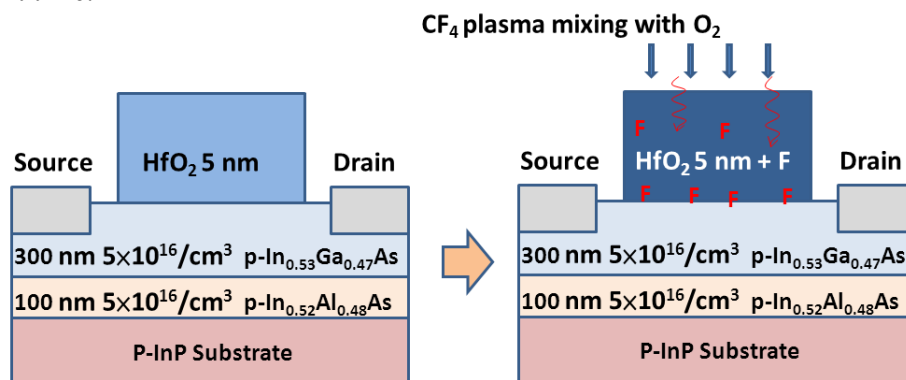
Figures 2 and 3 show the X-ray photoelectron spectroscopy (XPS) spectra of Hf $4f$ and F $1s$ for the $HfO_2/In_{0.53}Ga_{0.47}As$ gate stack with and without CF_4/O_2 plasma treatment. All the scanned binding energy was calibrated by the C $1s$ signal at 284.5 eV.

Figure 2. X-ray photoelectron spectroscopy (XPS) analysis of the Hf $4f$ electronic spectra for the samples with and without fluorine (F) incorporation.
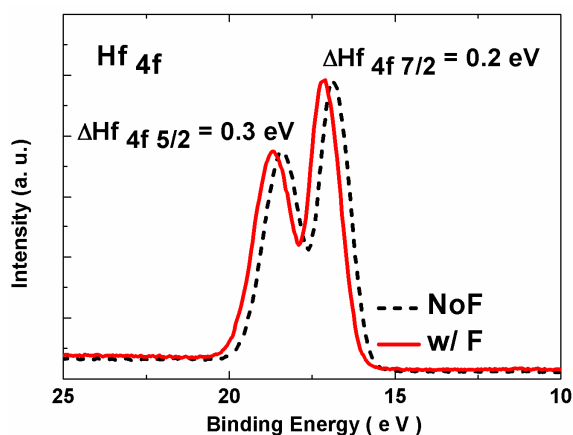
Figure 3. XPS analysis of the F $1s$ electronic spectra for the control sample and fluorinated sample.
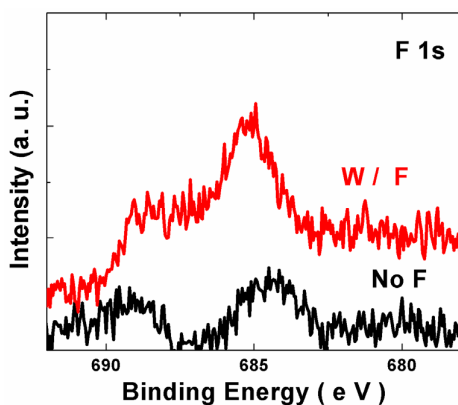
Compared to the control sample, the fluorinated sample has an increased binding energy by 0.2 eV and 0.3 eV for the Hf $4f_{7/2}$ and Hf $4f_{5/2}$ signal, respectively. This suggests that parts of the oxygen vacancies were terminated by the incorporated F atoms to form stronger Hf-F bonds with higher binding energy. In Figure 3, the peak signal located at ~685 eV corresponds to the F bonds in the bulk HfO_2, indicating that F was incorporated into the HfO_2 after CF_4/O_2 plasma treatment.

In order to search the F distribution in the $HfO_2/In_{0.53}Ga_{0.47}As$ gate stack, the secondary ion mass spectrometry (SIMS) technique was examined, as shown in Figure 4. A considerable amount of F was incorporated into the HfO_2 gate stacks with CF_4/O_2 plasma treatment while the oxygen concentration remained similar. Due to sudden structural transition at the $HfO_2/In_{0.53}Ga_{0.47}As$ interface, the density of defective bonds at the interface is much higher than that in the HfO_2 bulk. F tends to pile up at the $HfO_2/In_{0.53}Ga_{0.47}As$ interface passivating interface traps, resulting in a better interface quality (discussed later in this paper).

**Figure 4.** Secondary ion mass spectrometry (SIMS) profile of elements in the $HfO_2/In_{0.53}Ga_{0.47}As$ gate stack with and without CF_4/O_2 plasma treatment. The CF_4/O_2 plasma condition is 30 W for 3 min.
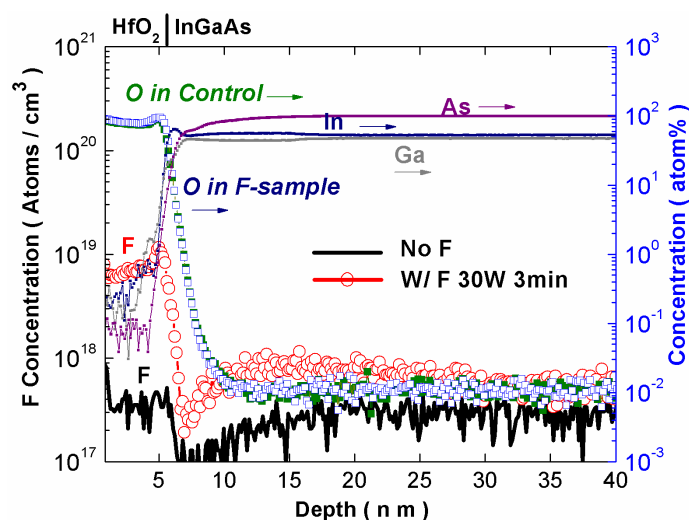
The composition and stoichiometry of HfO_2 were determined by XPS analysis (data not shown). For the control sample, HfO_2 was in good stoichiometry (Hf:O = 1:2) and it became oxygen-rich ($HfO_{2.25}$) after CF_4/O_2 plasma treatment. One possibility of improvements could be due to the oxygen vacancies passivation during the plasma treatment. The effect of O_2 plasma treatment is under investigation.

One concern of doping F into gate oxide is that dielectric constant of the gate oxide would decrease with heavy F incorporation. From XPS, the F concentration in our fluorinated HfO_2 is estimated to be 2.7 at.%, which is lower than that used in the low-k technology [12]. Therefore, the dielectric constant of HfO_2 remains similar (~17) after F incorporation, as shown in Figure 5. The inset of Figure 5 compares the gate leakage current of samples with and without F incorporation. The gate leakage current is slightly reduced with F incorporation.

Figure 5. Equivalent oxide thickness (EOT) *versus* physical thickness for the samples with and without F incorporation. Inset: the gate leakage current comparison of samples with and without F incorporation.
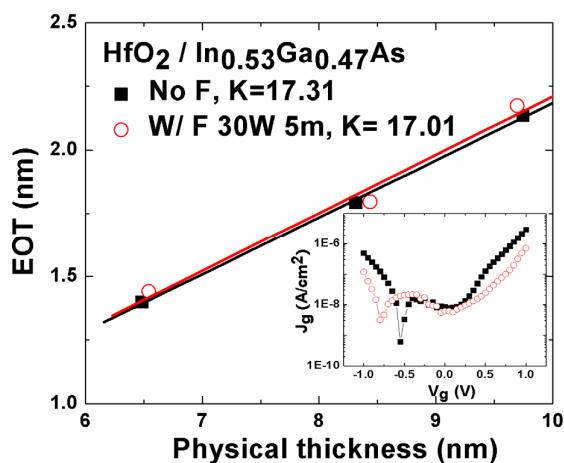
One objective of this work is to investigate the optimum condition of CF_4/O_2 plasma. The RF power and the plasma treatment time are two critical factors that affect the electrical characteristics significantly. Insufficient plasma treatment might not improve the gate dielectric quality, whereas excessive plasma treatment possibly causes plasma damage and corrodes the improvement. To study the effects of RF power on HfO_2 gate dielectrics, some samples were treated in CF_4/O_2 plasma for 3 min at different RF power in the range from 20 to 40 W. It was found that the samples treated by the power of 30 W improved most in terms of G_m, I_d and SS. With the fixed RF power of 30 W, we continued to study the effect of CF_4/O_2 plasma treatment time. Some samples were treated in CF_4/O_2 plasma at different treatment times ranging from 1 to 7 min with a fixed RF power of 30 W. It was found that 5 min plasma treatment further improved SS.

3. Results and Discussion

3.1. Optimization of CF_4/O_2 Plasma

The maximum G_m and I_d as a function of different RF power (CF_4/O_2 plasma treatment time: 3 min) are shown in Figure 6 (W/L = 600/20 μm, at V_d = 50 mV and 0.5 V). The maximum G_m and I_d of the control sample are 3.1 mS/mm and 1.3 mA/mm (V_d = 50 mV), and 20.3 mS/mm and 12 mA/mm (V_d = 0.5 V), respectively. With F plasma treatment of 30W, the maximum G_m and I_d reach 3.7 mS/mm and 1.7 mA/mm (V_d = 50 mV), and 26 mS/mm and 16.2 mA/mm (V_d = 0.5 V), respectively. However, the maximum G_m and I_d roll back with power larger than 30 W indicative of possible plasma damage. SS data with different RF power are shown in Figure 7. $In_{0.53}Ga_{0.47}As$ MOSFETs have similar EOT (~1.4 nm, data not shown) with different RF power treatment. With F incorporation, SS has been improved from 127 to 118.1 mV/dec (as shown in the inset of Figure 7), which suggests that the interface quality has been improved. For the RF power of 40W, SS increases to 127.5 mV/dec, indicating that excessive CF_4/O_2 plasma treatment degrades the interface quality.

Figure 6. Maximum G_m and I_d as a function of CF_4/O_2 plasma RF power (W/L = 600 µm/20 µm at V_d = 50 mV and 0.5 V). CF_4/O_2 plasma treatment time: 3 min.
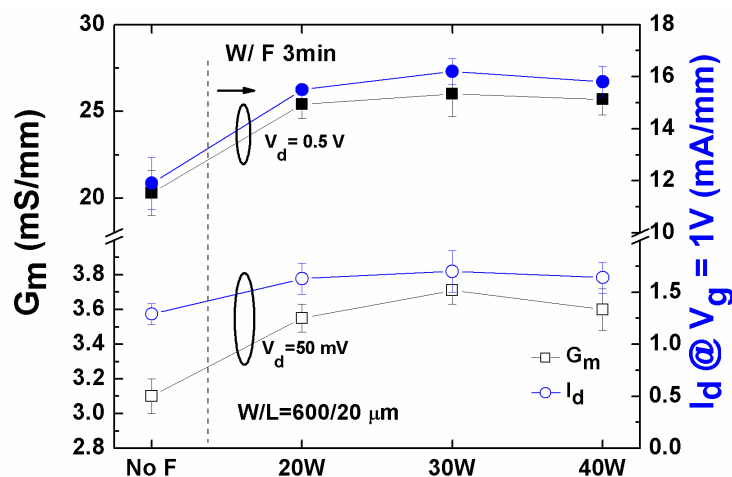

Figure 7. Subthreshold swing (SS) as a function of CF_4/O_2 plasma RF power. CF_4/O_2 plasma treatment time: 3 min. Inset: I_d-V_g comparison of the control sample and the sample with CF_4/O_2 plasma treatment for 30 W/3 min.
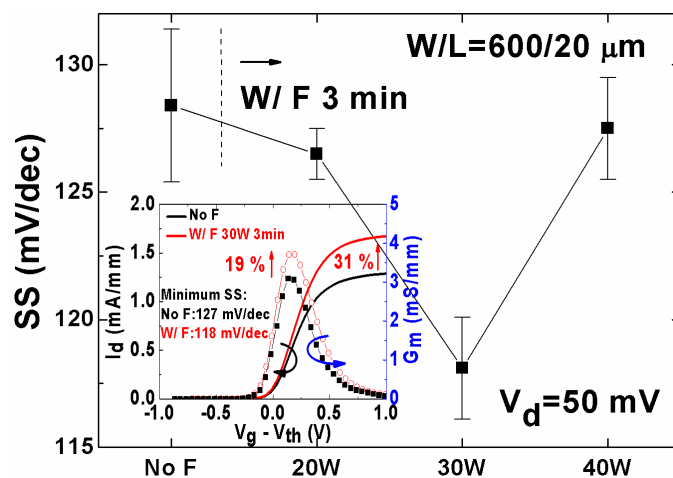

Figure 8 compares the maximum G_m and I_d as a function of plasma treatment times ranging from 1 to 7 min with a fixed RF power of 30W (W/L = 600 µm/20 µm at V_d = 50 mV and 0.5 V). 3 min plasma treatment reaches the peak values of the maximum G_m and I_d, whereas 5 min plasma treatment achieves the lowest SS value (Figure 9). The inset of Figure 8 compares the I_d-V_g curves (in log-linear scale) of the control sample and the sample with F treatment 30 W/5 min. A steeper SS slope is clearly observed.

Figure 8. Maximum G_m and I_d as a function of CF_4/O_2 plasma treatment time (W/L = 600 µm/20 µm at V_d = 50 mV and 0.5 V). RF power: 30 W.
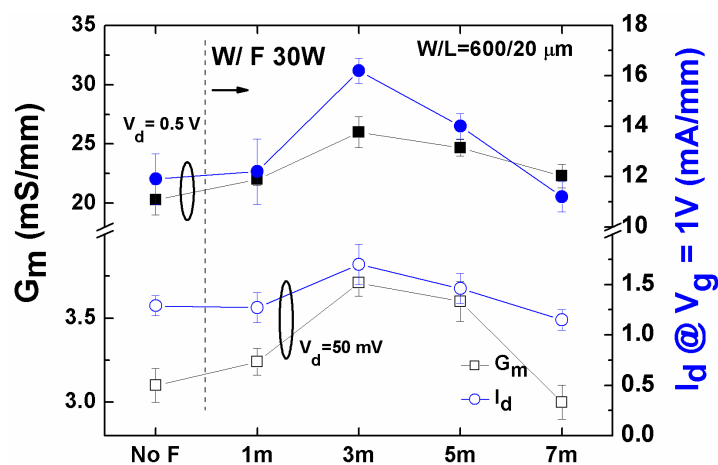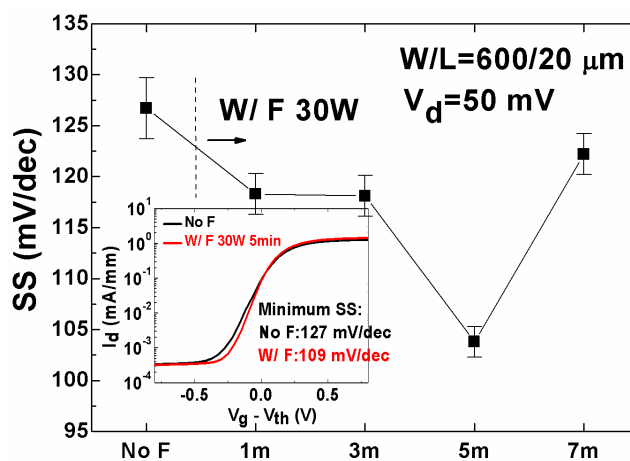

Figure 9. SS as a function of CF_4/O_2 plasma treatment time. RF power: 30 W. Inset: I_d-V_g comparison of the control sample and the sample with CF_4 plasma treatment for 30 W/5 min.

Effective channel mobility (μ_{eff}) of $In_{0.53}Ga_{0.47}As$ MOSFETs with different plasma treatment times are plotted in Figure 10. The peak μ_{eff} of 30 W/3 min reaches 1,144 cm^2/Vs, which is 38% improvement compared to the control samples (826 cm^2/Vs). The improvements in the I_d, G_m, SS and μ_{eff} are believed to be due to the improved interface quality by an appropriate amount of CF_4/O_2 plasma post-HfO_2 treatment.

Figure 10. Effective channel mobility *versus* inversion charge density as a function of CF_4/O_2 plasma treatment time. RF power: 30 W.
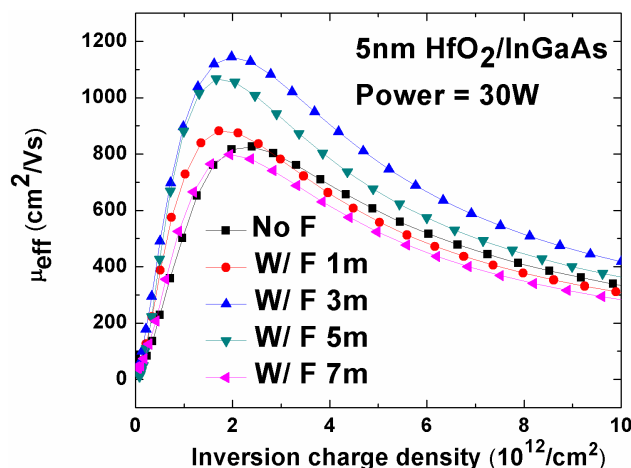
We noticed that the plasma damage occurred if excessive plasma (either plasma wattage or treatment time) was applied. The plasma damage could come from disordering, surface roughening, and fluorine contamination [13]. The disordering layer contains dangling bonds and broken bonds, which would scatter the electrons underneath (in the channel) and lower the electron mobility. Severe disordering would lead to surface roughness, which results in more dangling bonds and broken bonds. If the F concentration is too high (>5 at.%, [12]), the dielectric constant of HfO_2 decreases, resulting in lowering drive current.

3.2. Electrical Characterization of the Interface Trap Density

Charge pumping measurements were conducted to accurately evaluate the interface quality of the control and fluorinated MOSFETs. The charge pumping characterization was performed by sweeping the base level voltage (V_{base}, −2.3 V to 1 V in a step of 50 mV) of the trapezoidal gate pulse (with a constant-amplitude, 1 V) at 200 KHz. The S/D terminals were grounded. The region of the bandgap probed was from electron emission energy level to hole emission energy level, which was around the midgap. The charge pumping current (I_{cp}) is plotted as a function of V_{base} for equal trapezoidal pulse rise time (t_R) and fall time (t_F), as shown in Figure 11. t_R and t_F are varied from 100 to 800 ns. Lower I_{cp} for the fluorinated sample is indicative of reduced D_{it}. The mean D_{it} value can be extracted according to the following equation [14,15],

$$\frac{I_{cp}}{f} = 2qD_{it}AkT\left\{\ln\sqrt{t_Rt_F} + \ln\left(\frac{|V_{fb}-V_t|}{|\Delta V_g|}V_{th}n_i\sqrt{\sigma_n\sigma_p}\right)\right\}$$

where *q* is the electronic charge, *A* is the transistor gate area (2.08×10^{-4} cm^2 in our devices), *k* is the Boltzmann constant, V_{fb} is the flat band voltage, V_t is the threshold voltage, ΔV_g is the gate pulse amplitude, V_{th} is the thermal velocity of the carriers, n_i is the surface concentration of minority carriers, and σ_n and σ_p are the capture cross sections of electrons and holes, respectively. The mean D_{it} values were extracted from the slope of I_{cp}/f *versus* $\ln[(t_R \times t_F)^{1/2}]$, as shown in Figure 12. It has been found that the mean D_{it} value was reduced ~5× from 2.8×10^{12} to 4.9×10^{11} $cm^{-2}eV^{-1}$ after F plasma

treatment. F atoms possibly passivate dangling bonds and oxygen vacancies in the $HfO_2/In_{0.53}Ga_{0.47}As$ interface and thereby reduce D_{it} value.

Figure 11. Charge pumping measurement with rise/fall time dependence. Samples with F incorporation show much smaller I_{cp}. V_{base}: −2.3 V to 1 V in a step of 50 mV and the pulse amplitude is 1 V.
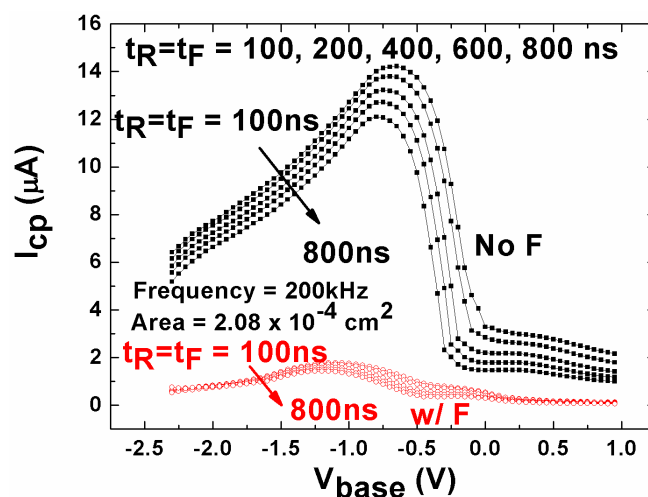

Figure 12. Q_{cp} ($=I_{cp}/f$) *vs.* $\ln[(t_R \times t_F)^{1/2}]$. The mean D_{it} value is extracted by linear fitting according to References [14,15]. Samples with F incorporation show less D_{it} value of $4.9 \times 10^{11}/eVcm^2$.

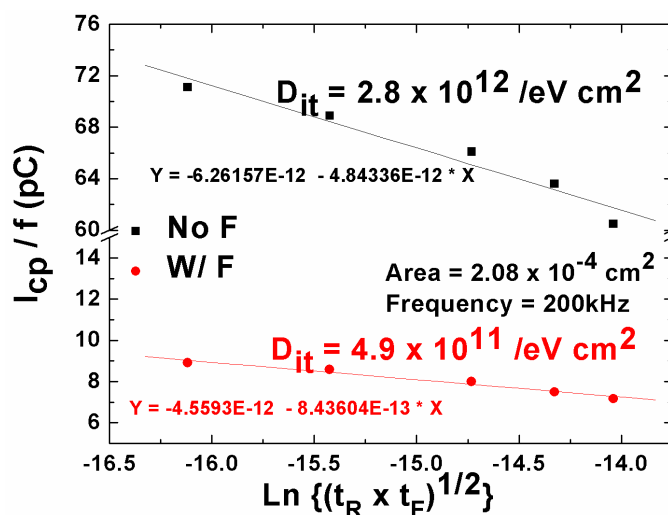Table 1 compares the device performance and interfacial properties of $In_{0.53}Ga_{0.47}As$ MOSFETs reported in this paper and other high-k/$In_{0.53}Ga_{0.47}As$ gate stacks in recent publications. The D_{it} value reported in this paper is the lowest value compared to prior reported $HfO_2/In_{0.53}Ga_{0.47}As$ gate stacks.

Table 1. Comparison of the electrical and interfacial properties of this work with some recently reported paper.

High k	Passivation method	Channel material	L_G	EOT or thickness of high-k	D_{it} ($cm^{-2}eV^{-1}$)	SS (mV/dec)	Ref.
Al_2O_3 *	-	$In_{0.53}Ga_{0.47}As$	-	4.2 nm	5×10^{11}	-	[16]
Al_2O_3	-	$In_{0.53}Ga_{0.47}As$	-	10 nm of Al_2O_3	2.5×10^{11}	-	[17]
Al_2O_3	-	$In_{0.53}Ga_{0.47}As$	1.5 μm	8 nm of Al_2O_3	1×10^{12}	>200	[18]
Al_2O_3	-	$In_{0.53}Ga_{0.47}As$	0.5 μm	30 nm of Al_2O_3	1.4×10^{12}	240	[19]
HfO_2 *	-	$In_{0.53}Ga_{0.47}As$	-	2.1 nm	1×10^{12}	-	[16]
HfO_2 *	-	$In_{0.53}Ga_{0.47}As$	-	7.8 nm of HfO_2	2×10^{12}	-	[20]
HfO_2 *	Al-doped	$In_{0.53}Ga_{0.47}As$	-	8–9 nm of HfO_2	6×10^{12}	-	[21]
HfO_2 *	PH_3	$In_{0.53}Ga_{0.47}As$	4 μm	1.7 nm	8.6×10^{11}	103	[22]
HfAlO	SiH_4+NH_3	$In_{0.53}Ga_{0.47}As$	2–10 μm	3.8 nm	6.5×10^{11}	155–210	[2]
ZrO_2	$LaAlO_3$	$In_{0.53}Ga_{0.47}As$	5 μm	1.63 nm	7.5×10^{11}	116	[23]
HfO_2	CF_4/O_2 post treatment	$In_{0.53}Ga_{0.47}As$	5–20 μm	1.4 nm	4.9×10^{11}	109	This work
HfO_2	Control			1.35 nm	2.8×10^{12}	127	This work

* Capacitor structure.

4. Conclusions

The effects of post-oxide CF_4/O_2 treatment on $HfO_2/In_{0.53}Ga_{0.47}As$ gate stack have been systematically investigated. The condition for the CF_4/O_2 plasma is optimized to be 30 W for 3–5 min. The gate stack interface quality has been notably improved by F incorporation. The mean D_{it} value has been reduced ~5× from 2.8×10^{12} to 4.9×10^{11} $cm^{-2}eV^{-1}$. As a result, enhanced electrical performances have been presented: steeper SS from 127 to 109 mV/dec, enhanced μ_{eff} from 826 to 1,144 cm^2/Vs, and improved G_m and I_d from 3.1 to 3.7 mS/mm and from 1.3 to 1.7 mA/mm, respectively (at $V_d = 50$ mV, 20 μm channel length). These results suggest that the post-HfO_2 F treatment could be a key technique to implement high performance III-V MOSFETs for the sub 22 nm nodes.

References

1. Shahrjerdi, D.; Tutuc, E.; Banerjee, S.K. Impact of surface chemical treatment on capacitance-voltage characteristics of GaAs metal-oxide-semiconductor capacitors with Al_2O_3 gate dielectric. *Appl. Phys. Lett.* **2007**, *91*, 063501.
2. Chin, H.-C.; Liu, X.; Gong, X.; Yeo, Y.-C. Silane and ammonia surface passivation technology for high-mobility $In_{0.53}Ga_{0.47}As$ MOSFETs. *Trans. Electron. Devices* **2010**, *57*, 973–979.
3. Chen, Y.-T.; Zhao, H.; Yum, J.H.; Wang, Y.; Lee, J.C. Metal-oxide-semiconductor field-effect-transistors on indium phosphide using HfO_2 and silicon passivation layer with equivalent oxide thickness of 18 Å. *Appl. Phys. Lett.* **2009**, *94*, 213505.
4. CRC. *Handbook of Physics and Chemistry*, 84th, ed.; CRC: Boca Raton, FL, USA, 2003.

5. Wu, W.-C.; Lai, C.-S.; Lee, S.-C.; Ma, M.-W.; Chao, T.-S.; Wang, J.-C.; Hsu, C.-W.; Chou, P.-C.; Chen, J.-H.; Kao, K.-H.; *et al*. Fluorinated HfO_2 Gate Dielectrics Engineering for CMOS by Pre- and Post-CF_4 Plasma Passivation. In *Proceedings of IEEE International Electron Devices Meeting*, San Francisco, CA, USA, 15–17 December 2008; pp. 1–4.

6. Seo, K.; Sreenivasan, R.; McIntyre, P.C.; Saraswat, K.C. Improvement in high-k (HfO_2/SiO_2) reliability by incorporation of fluorine. *IEEE Electron. Device Lett.* **2006**, *27*, 821–823.

7. Xie, R.; He, W.; Yu, M.; Zhu, C. Effects of fluorine incorporation and forming gas annealing on high-k gated germanium metal-oxide-semiconductor with GeO_2 surface passivation. *Appl. Phys. Lett.* **2008**, *93*, 073504.

8. Chin, H.-C.; Gong, X.; Wang, L.; Yeo, Y.-C. Fluorine incorporation in HfAlO gate dielectric for defect passivation and effect on electrical characteristics of $In_{0.53}Ga_{0.47}As$ n-MOSFETs. *Electrochem. Solid State Lett.* **2010**, *13*, H440–H442.

9. Chen, Y.-T.; Zhao, H.; Yum, J.H.; Wang, Y.; Xue, F.; Zhou, F.; Lee, J.C. Improved electrical characteristics of $TaN/Al_2O_3/In_{0.53}Ga_{0.47}As$ metal-oxide-semiconductor field-effect transistors by fluorine incorporation. *Appl. Phys. Lett.* **2009**, *95*, 013501.

10. Zhao, H.; Chen, Y.; Yum, J.H.; Wang, Y.; Lee, J.C. HfO_2-based $In_{0.53}Ga_{0.47}As$ MOSFETs (EOT ≈ 10Å) Using Various Interfacial Dielectric Layers. In *Proceedings of IEEE 67th Device Research Conference*, University Park, PA, USA, 22–24 June 2009; pp. 89–90.

11. Zhao, H.; Yum, J.H.; Chen, Y.-T.; Lee, J.C. $In_{0.53}Ga_{0.47}As$ n-metal-oxide-semiconductor field effect transistors with atomic layer deposited Al_2O_3, HfO_2, and $LaAlO_3$ gate dielectrics. *J. Vac. Sci. Technol. B* **2009**, *27*, 2024–2027.

12. Lee, S.; Park, J.-W. Effect of fluorine on dielectric properties of SiOF films. *J. Appl. Phys.* **1996**, *80,* 5260–5263.

13. Tatsumi, T.; Fukuda, S.; Kadomura, S. Etch rate acceleration of SiO_2 during wet treatment after gate etching. *Jpn. J. Appl. Phys*. **1993**, *32*, 6114–6118.

14. Groeseneken, G.; Maes, H.E.; Beltran, N.; Dekeersmaecker, R.F. A reliable approach to charge-pumping measurements in MOS transistors. *IEEE Trans. Electron. Devices* **1984**, *31*, 42–53.

15. Xie, R.; Phung, T.H.; He, W.; Sun, Z.; Yu, M.; Cheng, Z.; Zhu, C. High Mobility High-k/Ge pMOSFETs with 1 nm EOT—New Concept on Interface Engineering and Interface Characterization. In *Proceedings of 2008 IEEE International Electron Devices Meeting (IEDM)*, San Francisco, CA, USA, 15–17 December 2008; pp. 393–396.

16. Zhao, H.; Huang, J.; Chen, Y.-T.; Yum, J.H.; Wang, Y.; Xue, F.; Zhou, F.; Lee, J.C. Effects of gate-first and gate-last process on interface quality of $In_{0.53}Ga_{0.47}As$ metal-oxide-semiconductor capacitors using atomic-layer-deposited Al_2O_3 and HfO_2 oxides. *Appl. Phys. Lett.* **2009**, *95*, 253501.

17. Chiu, H.C.; Tung, L.T.; Chang, Y.H.; Lee, Y.J.; Chang, C.C.; Kwo, J.; Hong, M. Achieving a low interfacial density of states in atomic layer deposited Al_2O_3 on $In_{0.53}Ga_{0.47}As$. *Appl. Phys. Lett.* **2008**, *93*, 202903.

18. Lin, D.; Brammertz, G.; Sioncke, S.; Fleischmann, C.; Delabie, A.; Martens, K.; Bender, H.; Conard, T.; Tseng, W.H.; Lin, J.C.; *et al*. Enabling the high-performance InGaAs/Ge CMOS: A common gate stack solution. In *Proceedings of 2009 IEEE International Electron Devices Meeting (IEDM)*, Baltimore, MD, USA, 7–9 December 2009; pp. 1–4.

19. Xuan, Y.; Wu, Y.; Shen, T.; Yang, T.; Ye, P. High Performance Submicron Inversion-Type Enhancement-Mode InGaAs MOSFETs with ALD Al_2O_3, HfO_2 and HfAlO as Gate Dielectrics. In *Proceedings of 2007 IEEE International Electron Devices Meeting (IEDM)*, Washington, DC, USA, 10–12 December 2007; pp. 637–640.

20. Chang, Y.C.; Huang, M.L.; Lee, K.Y.; Lee, Y.J.; Lin, T.D.; Hong, M.; Kwo, J.; Lay, T.S.; Liao, C.C.; Cheng, K.Y. Atomic-layer-deposited HfO_2 on $In_{0.53}Ga_{0.47}As$: Passivation and energy-band parameters. *Appl. Phys. Lett.* **2008**, *92*, 072901.

21. Hwang, Y.; Chobpattana, V.; Zhang, J.Y.; LeBeau, J.M.; Engel-Herbert, R.; Stemmer, S. Al-doped $HfO_2/In_{0.53}Ga_{0.47}As$ metal-oxide-semiconductor capacitors. *Appl. Phys. Lett.* **2011**, *98*, 142901.

22. Lin, J.; Lee, S.; Oh, H.-J.; Yang, W.; Lo, G.Q.; Kwong, D.L.; Chi, D.Z. Plasma PH_3-Passivated High Mobility Inversion InGaAs MOSFET Fabricated with Self-Aligned Gate-First Process and HfO_2/TaN Gates Stack. In *Proceedings of 2008 IEEE International Electron Devices Meeting (IEDM)*, San Francisco, CA, USA, 15–17 December 2008; pp. 401–404.

23. Huang, J.; Goel, N.; Zhao, H.; Kang, C.Y.; Min, K.S.; Bersuker, G.; Oktyabrsky, S.; Gaspe, C.K.; Santos, M.B.; Majhi, P.; *et al*. InGaAs MOSFET Performance and Reliability Improvement by Simultaneous Reduction of Oxide and Interface Charge in ALD $(La)AlOx/ZrO_2$ Gate Stack. In *Proceedings of 2009 IEEE International Electron Devices Meeting (IEDM)*, Baltimore, MD, USA, 7–9 December 2009; pp. 335–338.

Review

Nucleic Acid Based Fluorinated Derivatives: New Tools for Biomedical Applications

Christel Dolain [1], Amit Patwa [1,2], Guilhem Godeau [1,2] and Philippe Barthélémy [1,2,]*

[1] Université de Bordeaux, Bordeaux F-33076, France; E-Mails: c.dolain@iecb.u-bordeaux.fr (C.D.); guilhem.godeau@unice.fr (G.G.)

[2] INSERM U869, Bordeaux F-33076, France; E-Mail: amit.patwa@inserm.fr (A.P.)

* Author to whom correspondence should be addressed; E-Mail: philippe.barthelemy@inserm.fr; Tel.: +33-0-5-57-57-48-53; Fax: +33-0-5-57-57-10-15.

Abstract: Nucleic acid-based fluorinated derivatives, e.g., nucleosides or oligonucleotides connected to highly fluorinated chains or labeled with one or more fluorine atoms, have been investigated recently due to their high potential for biomedical applications. This review deals with recent works on nucleoside and oligonucleotide fluorocarbon amphiphiles as well as with properties and applications of fluorine-labeled oligonucleotide analogues.

**Keywords:** fluorocarbon; amphiphile; lipids; nucleoside; oligonucleotides

1. Introduction

The nucleic acid architectures stabilized by base-pairing and aryl $\pi-\pi$ stacking interactions provides to scientists one of the most sophisticated supramolecular models. Since the determination of the structure of double-stranded DNA (dsDNA) by Watson, Crick, Wilkins and Franklin [1–3], artificial bio-inspired molecules featuring nucleic acid units have become a very powerful strategy to construct supramolecular systems [4–6]. Of particular interest is the design of hybrid amphiphilic nucleolipids featuring a bi-functionality based on the combination of nucleic acids and lipids [7–15]. Interestingly, different bottom-up approaches involving nucleolipids have been used for the construction of nanostructures for different applications, including materials [16–18] and biomedical devices [19–21]. In parallel to nucleolipid derivatives, the combination of nucleobase units with fluorocarbon

hydrophobic and lipophobic moieties to create novel materials, for diagnostics or in medical applications, is still in its infancy. It has been extensively reported that highly fluorinated derivatives possess unique properties, including chemical and biological inertness, strong hydro- and lipophobia. Interestingly, fluorocarbon colloids used for biomedical applications feature high gas solubility, low lipid and water solubility, and outstanding surface characteristics [22].

Hence, material and biomedical sciences could take advantage of the new properties coming from the combination of nucleic acids and fluorocarbon synthetic units for new applications. The availability of chemically modified nucleotides and fluorocarbon synthons and/or reagents, means that Nucleic Acids Fluorocarbon Amphiphiles (NAFAs) could be used in numerous fields of research including engineering, biology and medicine (Figure 1). Recently, the use of nucleoside-based fluorocarbon derivatives has been mainly motivated by three fundamental objectives: (i) construct novel supramolecular materials and/or devices; (ii) develop new drug delivery systems; and (iii) find new therapeutic molecules.

Figure 1. Nucleic Acids Fluorocarbon Amphiphiles (NAFAs), including Fluorocarbon Nucleoside and OligoNucleotide amphiphiles (FNs and FONs, respectively): building blocks for soft materials and biomedical applications.
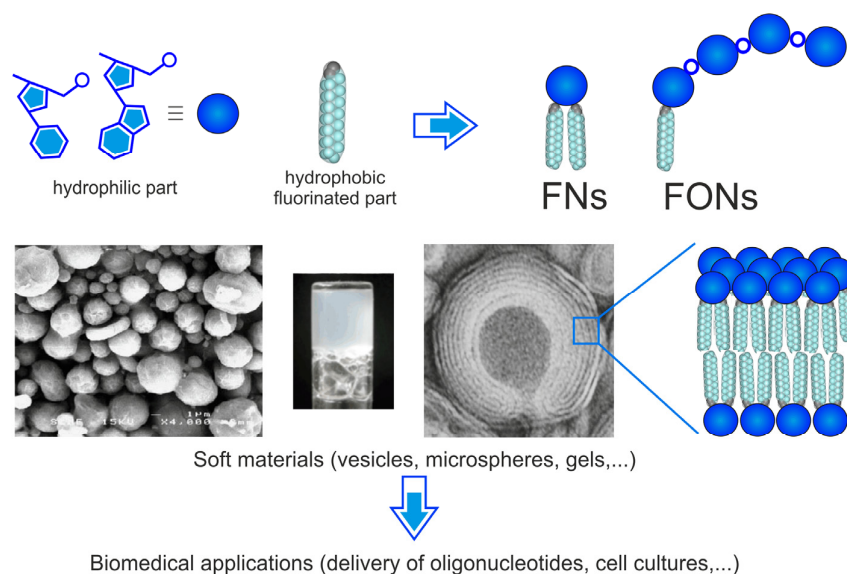
This short, non-exhaustive review intends to illustrate the role that highly fluorinated amphiphiles may play in chemistry, biology and material science. It consists primarily of an account of the authors' own efforts and experience in the field, hence will be limited to some specific aspects of this chemistry. It also intends to outline the potential applications of fluorinated nucleolipids, ranging from chemistry to biomedical research.

First, we will focus on the recent progress achieved in the fields of fluorocarbon and nucleoside amphiphiles. This first section includes hybrid molecules bearing both a nucleic acid and fluorocarbon chains: namely the Fluorocarbon Nucleoside amphiphiles (FNs). Second, we will present several Fluorocarbon OligoNucleotide amphiphiles (FONs) and fluorinated oligonucleotide analogues.

2. Fluorocarbon Nucleoside Amphiphiles (FNs)

2.1. Fluorocarbon Amphiphiles

Due to their unique properties, fluorocarbon chains represent a useful building block for the construction of supramolecular systems. Perfluoroalkyl chains have a larger cross section and are more rigid than their hydrogenated counterparts. They are considerably more hydrophobic and are lipophobic as well. As a result, when dispersed in water, fluorinated amphiphiles exhibit an enhanced capacity to self-assemble into highly stable and well-defined assemblies such as films, membranes, micelles, vesicles and other stable supramolecular systems [23,24]. The self-assembling behavior of a variety of synthesized single and double chain neutral, zwitterionicor anionic fluorinated phospholipids [25–28], glycolipid [29,30], glycophospholipids, glycopeptides [31,32] was already explored (Figure 2) [33], to evaluate the impact of the fluorinated chains on the properties of the resulting aggregates. It enhances stability, low permeability to both hydrophilic and lipophilic material and reduces interaction with biological media. These fluorinated amphiphiles possess a considerable potential for the delivery of materials such as drugs, prodrugs, markers, contrast agents and nucleic acids. Recently, new perfluorinated dimerizable polycationic amphiphiles were designed by Vierling *et al.* to evaluate the ability of the monomer to condense DNA and of the dimer to form stable nanoparticles capable of efficient cell transfection [34]. Although formulation of small-sized cationic monomolecular DNA nanoparticles (<40 nm) with the dimerizable perfluorinated succeeded, spermine-based amphiphiles proved to be poor non-specific transfection agents in vitro. Improvements are still in progress [35,36].

Figure 2. Examples of fluorocarbon amphiphiles; (**a**) sugar-based fluorocarbon amphiphile [30]; (**b**) fluorinated amphiphilic building block used for the synthesis of glycopeptide conjugates [32]; and (**c**) perfluorinated dimerizable polycationic amphiphile [34].
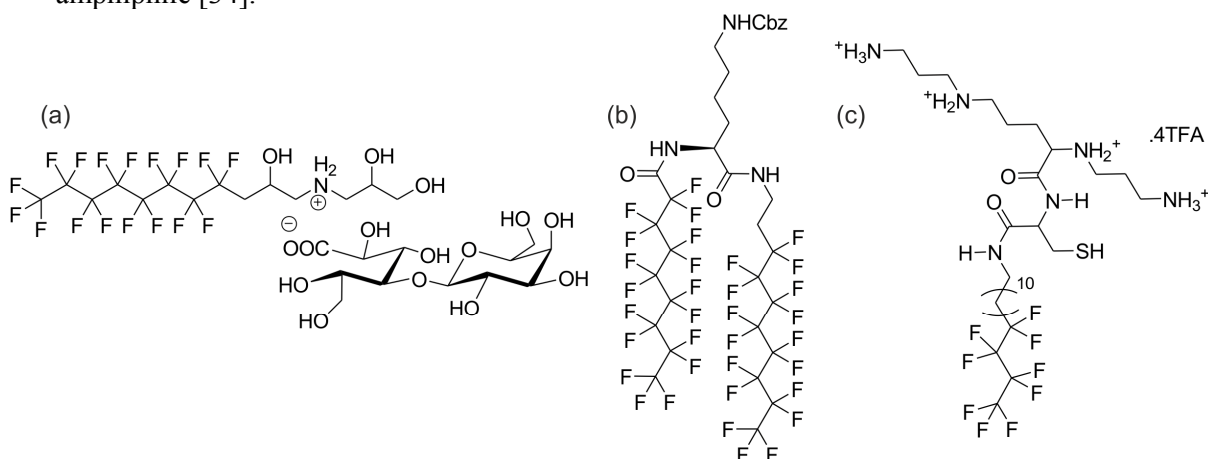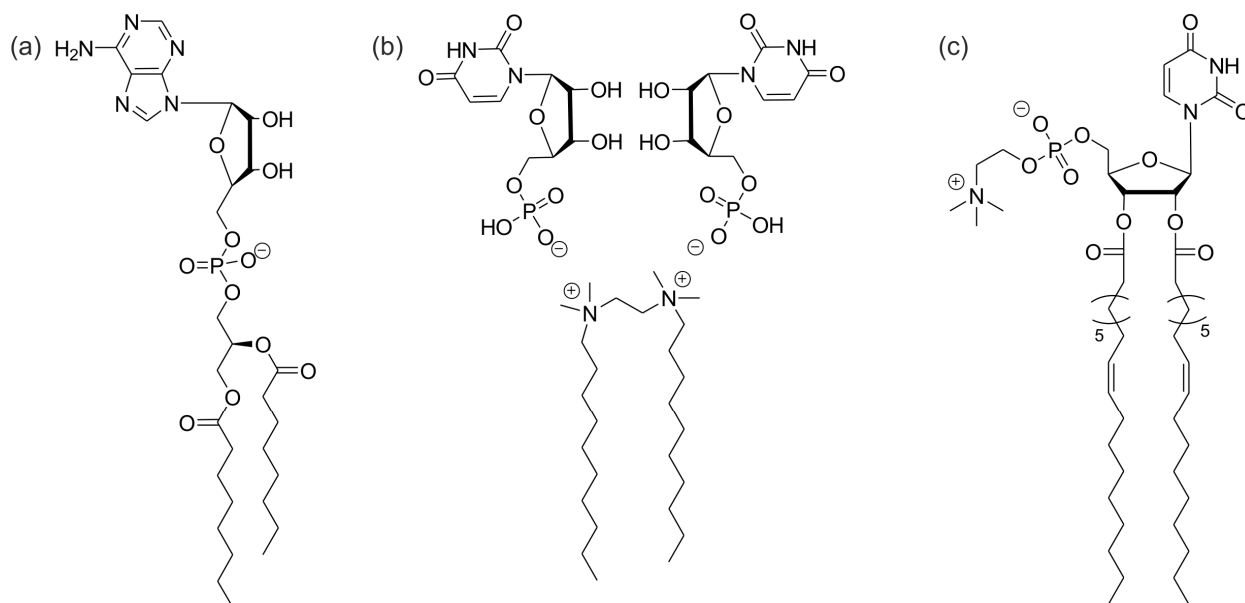

2.2. Nucleoside Amphiphiles

Nucleoside-based lipids commonly named nucleolipids [7] are hybrid molecules composed of a nucleobase, a nucleoside, a nucleotide or an oligonucleotide (either DNA or RNA), and a lipophilic moiety, which might be either simply a single- or double-chained alkyl moiety. Several improved

nucleolipids have been reported hereafter (Figure 3) [37–47]. Most nucleolipids have a polar head group at the 5' position and hydrophobic groups at both the 2' and 3' positions, patterned after natural glycerol phospholipids, which are key components of the cellular membrane. Nucleolipids were designed to interact with nucleic acids through hydrogen bonding, π–π stacking, and nucleobase recognition, as well as electrostatic interactions and the hydrophobic effect. Several cationic [12,48–51] and anionic [52,53] nucleolipids were first investigated as potential agents for the delivery of nucleic acids into cells. Indeed their self-assembled structures into lipoplexes mimic cellular membranes and their cationic properties attract both anionic oligonucleotides and negatively charged cellular membranes. New versions comprising neutral, zwitterionic, and anionic nucleolipids are currently evaluated.

Figure 3. Examples of nucleoside amphiphiles; (**a**) diC$_8$PA [37]; (**b**) a gemini nucleotide [39]; and (**c**) a zwitterionic nucleolipid.


2.3. Hybrid Fluorocarbon Nucleoside Amphiphiles

The combination of the self-assembly potential of nucleoside amphiphiles with the hydrophobic character of highly fluorinated chains is of high relevance to prepare new self-assembled structures with tunable physico-chemical properties and functions. To assess whether fluorinated chains can enhance the scope of supramolecular assemblies formed by hybrid fluorocarbon nucleoside amphiphiles, different molecules were synthesized (Figure 4).

The fluorocarbon amphiphile **1** is based on a uridine backbone modified by a phosphocholine moiety at the 5' position, and two *2H,2H,3H,3H*-perfluoroundecanoyl side chains at the 2' and 3' positions. One of the goals of the study was to characterize the properties of such new compounds and to compare those results with that observed for the analogous hydrocarbon nucleoamphiphiles. In aqueous solution, fluorocarbon nucleoamphiphiles were surprisingly able to form large vesicular assemblies and unexpected lamellar phases below their T_m, contrary to hydrocarbon analogs that self-assemble into helical structures below their T_m and bilayers above it [54]. These highly hydrophobic fluorocarbon amphiphiles exhibited interesting hybrid microspherical supramolecular

assemblies in the presence of thorium that were characterized by Scanning Electron Microscopy (SEM) [55].

> **Figure 4.** Chemical structures of compounds **1-3**, and corresponding electronic microscopy images of DiF$_{17}$UPC/Th^{4+} microspheres (SEM image from [55]), and supramolecular assemblies formed by GNFs **2** and **3** in water (TEM images from [58]).
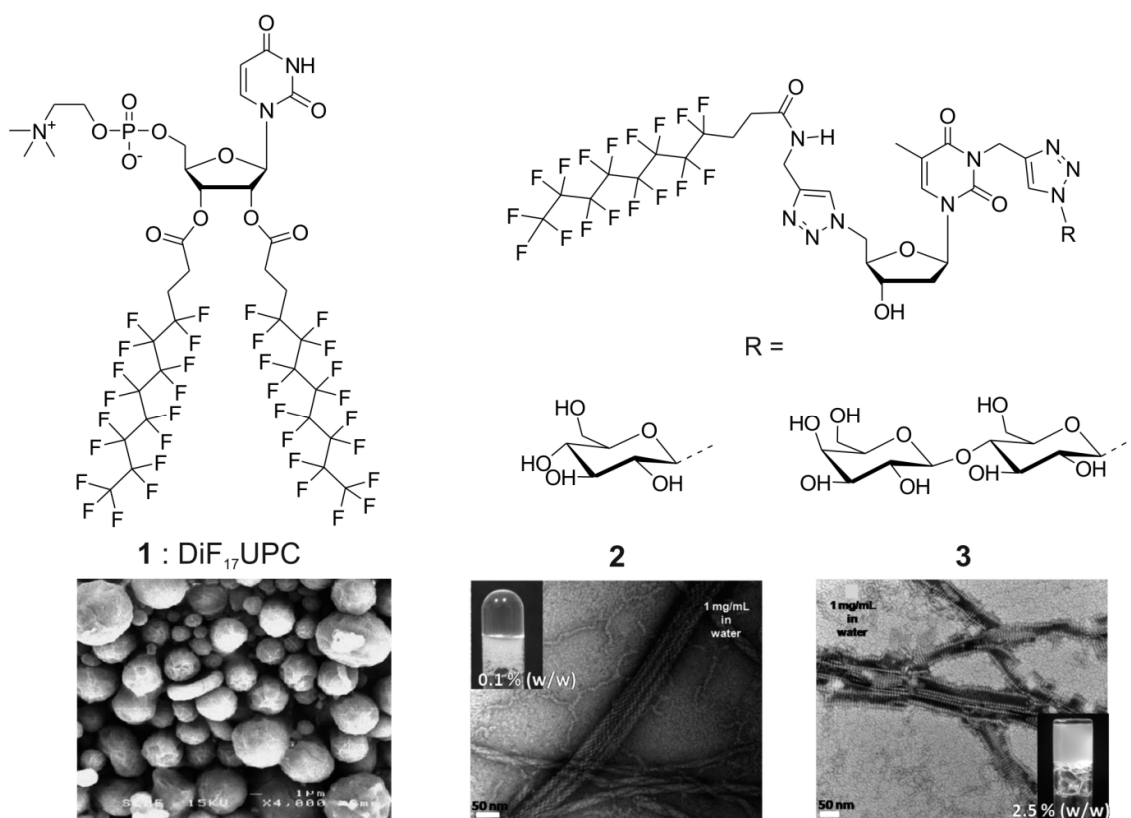
Recently, two glycosyl-nucleoside fluorinated amphiphiles (GNFs) were designed to construct new supramolecular hydrogels. Molecules **2** and **3** feature both sugar moieties attached to a thymidine base and a *2H,2H,3H,3H*-perfluoroundecanoyl side chain at the 5' position, linked via triazole bridges resulting from "click" chemistry. The self-assembly and gelation properties of such molecules were investigated. Similarly to their hydrocarbon analogs [56,57] GNFs stabilize hydrogels at low concentrations (0.1% w/w for compound **2**). GNFs gelators displayed supramolecular networks of varying morphologies, such as nanofibers and helical springs, which are correlated to the presence of fluorocarbon chains. Moreover, fluorocarbon amphiphile GNF **2** proved to be not toxic for human cells (Huh7) whereas hydrocarbon analogue becomes toxic above 100 µM, demonstrating the greater potential of such fluorocarbon nucleoside amphiphiles for biomedical applications [58].

3. Fluorocarbon OligoNucleotide Amphiphiles (FONs) and Fluorinated Oligonucleotide Analogues

In the previous section, several examples of nucleoside-based fluorinated amphiphiles have been discussed for gel stabilization. In this section we will discuss on Fluorocarbon OligoNucleotide amphiphiles (FONs). The fluorine atom is likely a mimic of either a hydroxyl group (in terms of

electronegativity) [59–62] or a hydrogen atom (in terms of steric factor). In this context, we will also provide an overview on properties and applications of oligonucleotides carrying fluorine modifications at different positions.

3.1. Fluorocarbon OligoNucleotide Amphiphiles (FONs)

Recently our group has reported on the synthesis and biological properties of FONs [63]. In previous studies, our group already reported on the synthesis and cellular uptake studies of lipid-oligonucleotide conjugates (LONs) [64,65]. The main purpose of attaching a fluorocarbon chain to a polyanionic oligonucleotide (ONs) was to study how cellular uptake or internalization of ONs are influenced by the nature of the hydrophobic moieties. To address this issue, Godeau *et al.* have synthesized two FONs featuring C_8F_{17} and C_6F_{13} chains using 1,3-dipolar Huisgen's reaction [66] via a "*post synthetic*" modification approach. Three different human cell lines were incubated with either FONs or LONs or unconjugated ONs for comparative study of cellular internalization (Figure 5). Moreover, internalization kinetics of FONs, LONs and unconjugated ONs with Huh7 cells were also evaluated. Keeping in mind the hydrophobic and lipophilic properties of fluorocarbon chains, it can be hypothesized that FONs self-assemble outside the cell to form nano aggregates. It is likely that these nanoobjects would be uptaken by the cell via an endocytosis pathway. It is worth mentioning here that to the best of our knowledge, there is no earlier report on oligonucleotide amphiphiles featuring perfluorinated chains.

Figure 5. Conjugation of fluorocarbon chain to the oligonucleotide (FONs) allows the delivery of highly polyanionic oligonucleotides into human cells.
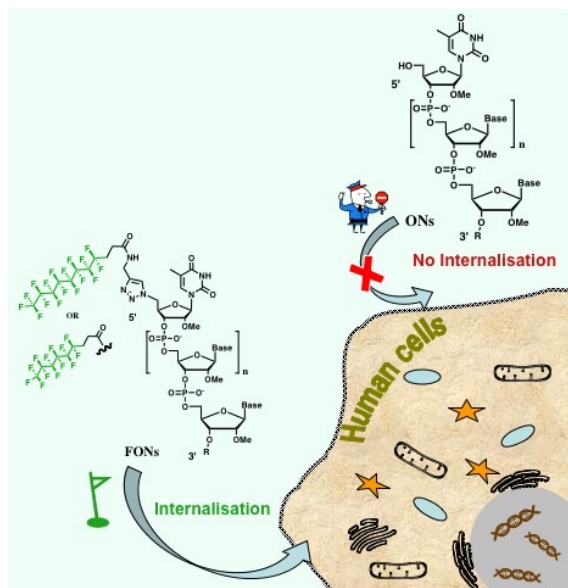

3.2. Application of Fluorinated Oligonucleotide Analogues

Various groups have been interested in the synthesis and application of fluorinated oligonucleotide analogues. There are different possible sites for the modification of an oligonucleotide with one or more fluorine atoms for various biological and therapeutical applications. Fluorine atoms have a strong

influence on both the electronic and the conformational properties of the nucleic acids' furanose ring. The 2'-position in the ribose moiety of RNA is prime target for chemical modifications. Extensive research work is going on towards the study of structural properties, biological applications and delivery strategies of oligonucleotides-incorporated with 2'-deoxy-2'fluoronucleotide in combination with other structural modifications [67–84]. Oligonucleotides containing 2'-deoxy-2'fluoronucleosides have been synthesized for regiospecific cleavage of RNA by RNase H [67]. Incorporation of 2'-deoxy-2'-fluoronucleotide into oligonucleotides induces substantial enhancement in their binding affinities to RNA targets [68]. Damha *et al.* have shown that fluorine-induced sugar pucker in 2'-deoxy-2'fluoro-β-D-ribonucleicacid (2'-F RNA; C3'-*endo*) and 2'-deoxy-2'fluoro-β-D-arabinonucleicacid (2'-F ANA; C2'/O4'-*endo*) can improve the activity of siRNA (Figure 6) and enhance its serum stability. They have also provided the evidences for an important role of a pseudohydrogen bond between the $F^{2'}$ and H^8 of the nucleobase for 2'-F ANA:RNA duplex stability [72–84].

Figure 6. Structure and sugar puckering equilibrium for (**a**) 2'-deoxy-2'-fluororibonucleic acid (2'-F RNA); C3'-endo is the most stable conformation for 2'-F RNA. (**b**) 2'-deoxy-2'-fluoroarabonucleic acid (2'-F ANA); C2'-endo is the most stable conformation for 2'-F ANA.
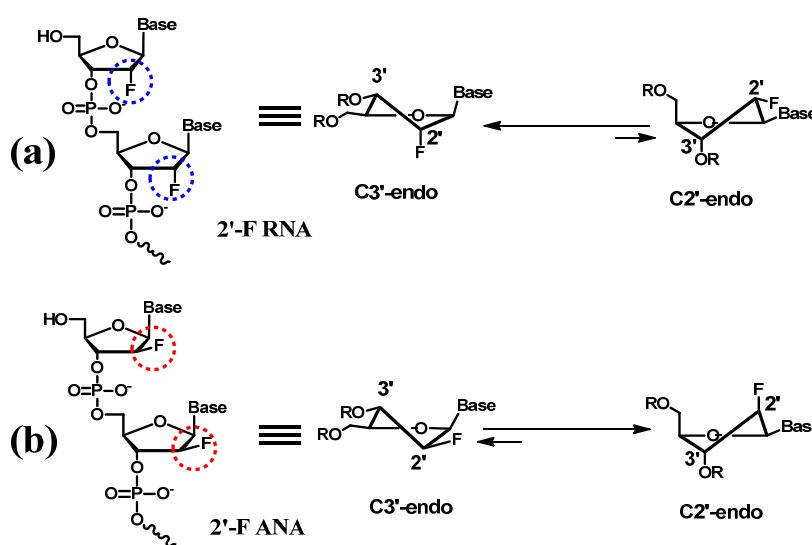

On the other side, very interesting and novel studies have been carried out by Erande *et al.* using 3'-deoxy-3'ribofluoro/xylofluoro uridine incorporated oligonucleotides (2'-5'-strand) [85]. They have shown the effect of incorporation of one or more unit of 3'-deoxy-3'-fluoronucleosides (having either locked or frozen S-type/Ntype sugar conformations) on the stability of *iso*DNA:RNA duplexes. For the first time, evidences were given that the DNA strand prefers S-type geometry in stable *iso*DNA:RNA duplexes (Figure 7) [85].

Figure 7. Structure and sugar puckering equilibrium for (**a**) 3'-deoxy-3'-ribofluorouridine. (**b**) 3'-deoxy-3'-xylofluorouridine.S-type (C2'-endo) conformation (preferred by 3'-deoxy-3'-ribofluorouridine) stabilized *iso*DNA:RNA duplexed while N-type (C3'-endo) conformation (preferred by 3'-deoxy-3'-xylofluorouridine) destabilized *iso*DNA:RNA duplexes.
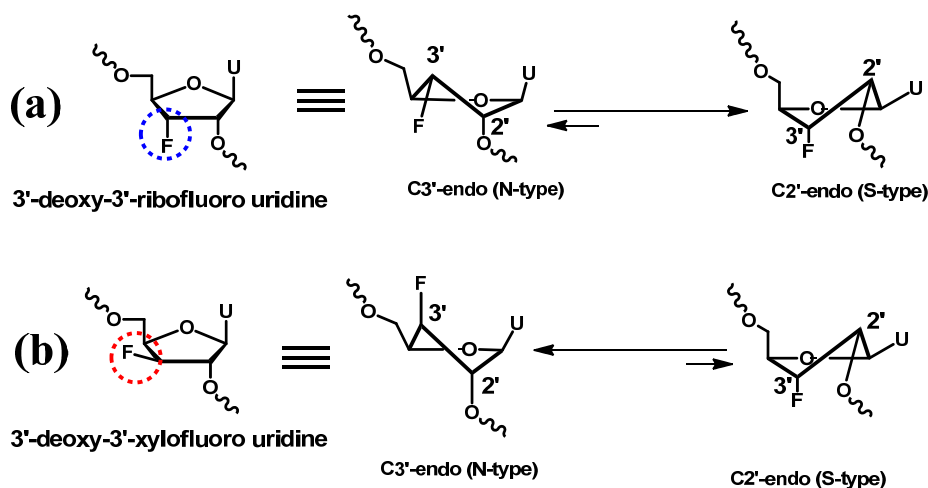
To investigate the forces (hydrogen bonding, base stacking and solvation) which are responsible for stability of the secondary structure of nucleic acids, Engels *et al.* have synthesized novel nucleic acid analogues in which nucleobases are replaced by their steric mimics, containing one or more fluorine atom. They have utilized fluorobenzene and fluorobenzimidazole derivatives (Figure 8) [86,87]. They have discussed how C–F···H–C hydrogen bonds affect the stability of the secondary structure of nucleic acids in details.

Figure 8. Monomer building blocks for the incorporation of fluorine derivative into RNA oligonucleotides by solid-phase synthesis.
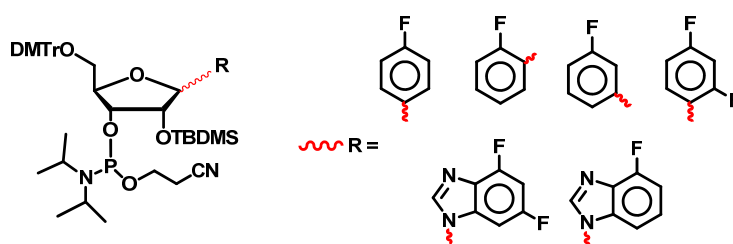
Owing to the favorable NMR properties of fluorine atom (^{19}F), fluorinated oligonucleotide derivatives provide a sensitive probe for structural study of nucleic acids in the solution state and their interactions with other biological moieties [71,88–95]. Barhate et *al.* have synthesized nucleosides with perfluorinated *tert*-butyl group and successfully incorporated it into the oligonucleotide at different positions and demonstrated as a sensitive ^{19}F NMR probe of nucleic acid conformation [95]. Oligonucleotides, labeled with radioactive isotopes, are new imaging tools to study gene expression at the nucleic acid and protein levels. Due to its positron-emission properties, fluorine-18 (radioactive isotope of fluorine) is widely used for oligonucleotide labeling for *in vivo* PET (Positron Emission Tomography) imaging. Dollé *et al.* [96–100]. have developed an original method for labeling

oligonucleotides with ^{18}F in different positions. Several other research groups have also synthesized ^{18}F labeled oligonucleotide analogues for imaging studies with PET [101–103].

4. Conclusions

The nucleic acids fluorocarbon amphiphiles belong to a new class of hybrid bioinspired molecules, which is clearly connected to soft materials, nanosciences and biomedical technology. It is a promising and exciting time for NAFAs and the emerging devices developed so far clearly open up interesting routes for the design and development of nanodevices, therapeutic strategies and biotechnological tools.The potential innovations using these fluorocarbon molecules are numerous in terms of chemical architectures, physicochemical and biological properties. This short survey highlights the interest to combine nucleic acids with fluorocarbons for developing soft and complex matters. The history of this field is still at the beginning and we can imagine that remarkable achievements will be realized in the future.

Acknowledgments

Conflict of Interest

The authors declare no conflict of interest.

References

1. Watson, J.D. A structure for deoxyribose nucleic acid. *Nature* **1953**, *171*, 737–738.
2. Franklin, R.E. Molecular configuration in sodium thymonucleate. *Nature* **1953**, *171*, 740–741
3. Wilkins, M.H.F. Molecular structure of deoxypentose nucleic acids. *Nature* **1953**, *171*, 738–740.
4. Sessler, J.L.; Lawrence, C.M.; Jayawickramarajah, J.G.M. Molecular recognition via base-pairing. *Chem. Soc. Rev.* **2007**, *36*, 314–325.
5. Whitesides, G.M.; Mathias, J.P.; Seto, C.T. Molecular self-assembly and nanochemistry: A chemical strategy for the synthesis of nanostructures. *Science* **1991**, *254*, 1312–1319.
6. Bowden, N.; Terfort, A.; Carbeck, J.; Whitesides, G.M. Self-assembly of mesoscale objects into ordered two-dimensional arrays. *Science* **1997**, *276*, 233–235.
7. Rosemeyer, H. Nucleolipids: Natural occurrence, synthesis, molecular recognition, and supramolecular assemblies as potential precursors of life and bioorganic materials. *Chem. Biodivers.* **2005**, *2*, 977–1062.
8. Gissot, A.; Camplo, M.; Grinstaff, M.W.; Barthélémy, P. Nucleoside, nucleotide and oligonucleotide based amphiphiles: A successful marriage of nucleic acids with lipids. *Org. Biomol. Chem.* **2008**, *6*, 1324–1333.
9. Ahlers, M.; Ringsdorf, H.; Rosemeyer, H.; Seela, F. Orientation, recognition, and photoreaction of nucleolipids in model membranes. *Colloid Polym. Sci.* **1990**, *268*, 132–142.

10. Huang, J.; Li, C.; Liang, Y. FT-SERS studies on molecular recognition capabilities of monolayers of novel nucleolipid amphiphiles. *Langmuir* **2000**, *16*, 3937–3940.

11. Lebeau, L.; Olland, S.; Oudet, P., Mioskowski, C. Rational design and synthesis of phospholipids for the two-dimensional crystallization of DNA gyrase, a key element in chromosome organization. *Chem. Phys. Lipid* **1992**, *62*, 93–103.

12. Barthélémy, P.; Lee, S.J.; Grinstaff, M. Supramolecular assemblies with DNA. *Pure Appl. Chem.* **2005**, *77*, 2133–2148.

13. Berti, D.; Franchi, L.; Baglioni, P.; Luisi, P.L. Molecular recognition in monolayers. Complementary base pairing in dioleoylphosphatidyl derivatives of adenosine, uridine, and cytidine. *Langmuir* **1997**, *13*, 3438–3444.

14. Baglioni, P.; Berti, D. Self assembly in micelles combining stacking and H-bonding. *Curr. Opin. Colloid Interface Sci.* **2003**, *8*, 55–61.

15. Fortini, M.; Berti, D.; Baglioni, P.; Ninham, B.W. Specific anion effects on the aggregation properties of anionic nucleolipids. *Curr. Opin. Colloid Interface Sci.* **2004**, *9*, 168–172.

16. Mulet, X.; Kaasgaard, T.; Conn, C.E.; Waddington, L.J.; Kennedy, D.F.; Weerawardena, A.; Drummond, C.J. Nanostructured nonionic thymidine nucleolipid self-assembly materials. *Langmuir* **2010**, *26*, 18415–18423.

17. Murgia, S.; Lampis, S.; Angius, R.; Berti, D.; Monduzzi, M. Orientation and specific interactions of nucleotides and nucleolipids inside monoolein-based liquid crystals. *J. Phys. Chem. B* **2009**, *113*, 9205–9215.

18. Godeau, G.; Barthélémy, P. Glycosyl-nucleoside lipids as low-molecular-weight gelators. *Langmuir* **2009**, *25*, 8447–8450.

19. Khiati, S.; Luvino, D.; Oumzil, K.; Chauffert, B.; Camplo, M.; Barthélémy, P. Nucleoside–lipid-based nanoparticles for cisplatin delivery. *ACS Nano* **2011**, *5*, 8649–8655.

20. Hong, C.I.; Nechaev, A.; Kirisits, A.J.; Vig, R.; West, C.R.; Manouilov, K.K.; Chu, C.K. Synthesis and biological activity of anti-HIV nucleoside conjugates of ether and thioether phospholipids. *J. Med. Chem.* **1996**, *39*, 1771–1777.

21. Ambike, A.; Rosilio, V.; Stella, B.; Lepétre-Mouelhi, S.; Couvreur, P. Interaction of self-assembled squalenoyl gemcitabine nanoparticles with phospholipid−cholesterol monolayers mimicking a biomembrane. *Langmuir* **2011**, *27*, 4891–4899.

22. Riess, J.G. Highly fluorinated amphiphilic molecules and self-assemblies with biomedical potential. *Curr. Opin. Colloid Interface Sci.* **2009**, *14*, 294–304.

23. Krafft, M.P. Controlling phospholipid self-assembly and film properties using highly fluorinated components—Fluorinated monolayers, vesicles, emulsions and microbubbles. *Biochimie* **2012**, *94*, 11–25.

24. Krafft, M.P.; Riess, J.G. Highly fluorinated amphiphiles and colloidal systems, and their applications in the biomedical field. A contribution. *Biochimie* **1998**, *80*, 489–514.

25. Riess, J.G.; Krafft, M.P. Fluorinated phosphocholine-based amphiphiles as components of fluorocarbon emulsions and fluorinated vesicles. *Chem. Phys. Lipids* **1995**, *75*, 1–14.

26. Held, P.; Lach, F.; Lebeau, L.; Mioskowski, C. Synthesis and preliminary evaluation of a new class of fluorinated amphiphiles designed for in-plane immobilisation of biological macromolecules. *Tetrahedron Lett.* **1997**, *38*, 1937–1940.

27. Lebeau, L.; Lach, F.; Vénien-Bryan, C.; Renault, A.; Dietrich, J.; Jahn, T.; Palmgren, M.G.; Kühlbrandt, W.; Mioskowski, C. Two-dimensional crystallization of a membrane protein on a detergent-resistant lipid monolayer. *J. Mol. Biol.* **2001**, *308*, 639–647.

28. Courty, S.; Lebeau, L.; Martel, L.; Lenné, P.-F.; Balavoine, F.; Dischert, W.; Konovalov, O.; Mioskowski, C.; Legrand, J.-F.; Vénien-Bryan, C. Two-dimensional crystallization of a histidine-tagged protein on monolayers of fluidity-enhanced Ni^{2+}-chelating lipids. *Langmuir* **2002**, *18*, 9502–9512.

29. Clary, L.; Gadras, C.; Greiner, J.; Rolland, J.-P.; Santaella, C.; Vierling, P.; Gulik, A. Phase behavior of fluorocarbon and hydrocarbon double-chain hydroxylated and galactosylated amphiphiles and bolaamphiphiles. Long-term shelf-stability of their liposomes. *Chem. Phys. Lipids* **1999**, *99*, 125–137.

30. Pasc-Banu, A.; Blanzat, M.; Belloni, M.; Perez, E.; Mingotaud, C.; Rico-Lattes, I.; Labrot, T.; Oda, R. Spontaneous vesicles of single-chain sugar-based fluorocarbon surfactants. *J. Fluor. Chem.* **2005**, *126*, 33–38.

31. Roytman, R.; Adler-Abramovich, L.; Ajish, K.S.; Kuan, T.-C.; Lin, C.-C.; Gazit, E.; Brik, A. Exploring the self-assembly of glycopeptides using a diphenylalanine scaffold. *Org. Biomol. Chem.* **2011**, *9*, 5755–5761.

32. Platen, T.; Schüler, T.; Tremel, W.; Hoffmann-Röder, A. Synthesis and antibody bonding of higly fluorinated amphiphilic MUC1 glycopeptide antigens. *Eur. J. Org. Chem.* **2011**, 3878–3887.

33. Riess, J.G. Fluorinated vesicles. *J. Drug Target.* **1994**, *2*, 455–468.

34. Fabio, K.; Di Giorgio, C.; Vierling, P. New perfluorinated polycationic dimerizable detergents for the formulation of monomolecular DNA nanoparticles and their *in vitro* transfection efficiency. *Biochim. Biophys. Acta* **2005**, *1724*, 203–214.

35. Klein, E.; Leborgne, C.; Ciobanu, M.; Klein, J.; Frisch, B.; Pons, F.; Zuber, G.; Scherman, D.; Kichler, A.; Lebeau, L. Nucleic acid transfer with hemifluorinated polycationic lipids. *Biomaterials* **2010**, *31*, 4781–4788.

36. Klein, E.; Ciobanu, M.; Klein, J.; MacHi, V.; Leborgne, C.; Vandamme, T.; Frisch, B.; Pons, F.; Kichler, A.; Zuber, G.; Lebeau, L. "HFP" fluorinated cationic lipids for enhanced lipoplex stability and gene delivery. *Bioconjug. Chem.* **2010**, *21*, 360–371.

37. Berti, D.; Montis, C.; Baglioni, P. Self-assembly of designer biosurfactants. *Soft Matter* **2011**, *7*, 7150–7158.

38. Wang, Y.; Moreau, L.; Barthélémy, P.; El Maataoui, M.; Grinstaff, M.W. Supramolecular assemblies of nucleoside phosphocholine amphiphiles. *J. Am. Chem. Soc.* **2004**, *126*, 7533–7539.

39. Desbat, B.; Manet, S.; Aimé, C.; Labrot, T.; Oda, R. Aggregation behaviors of gemini nucleotide at the air–water interface and in solutions induced by adenine–uracil interaction. *J. Colloid Interface Sci.* **2005**, *283*, 555–564.

40. Pincet, F.; Perez, E.; Bryant, G.; Lebeau, L.; Mioskowski, C. Long-range attraction between nucleosides with short-range specificity: Direct measurements. *Phys. Rev. Lett.* **1994**, *73*, 2780–2783.

41. Pincet, F.; Perez, E.; Lebeau, L.; Mioskowski, C. Long range H-bond specific interactions between nucleosides. *J. Chem. Soc. Faraday Trans.* **1995**, *91*, 4329–4330.

42. Pincet, F.; Perez, E.; Bryant, G.; Lebeau, L.; Mioskowski, C. Specific forces between DNA bases. *Mod. Phys. Lett. B* **1996**, *10*, 81–90.

43. Pincet, F.; Rawicz, W.; Perez, E.; Lebeau, L.; Mioskowski, C.; Evans, E. Electrostatic nanotitration of weak biochemical bonds. *Phys. Rev. Lett.* **1997**, *79*, 1949–1952.

44. Pincet, F.; Lebeau, L.; Cribier, S. Short-range specific forces are able to induce hemifusion. *Eur. Biophys. J.* **2001**, *30*, 91–97.

45. Perez, E.; Pincet, F.; Goldmann, M.; Mioskowski, C.; Lebeau, L. Translational order in liquid-expanded lipid monolayers functionalized with nucleosides. *Eur. Phys. J. B* **1998**, *6*, 1–4.

46. Tareste, D.; Pincet, F.; Perez, E.; Rickling, S.; Mioskowski, C.; Lebeau, L. Energy of hydrogen bonds probed by the adhesion of functionalized lipid layers. *Biophys. J.* **2002**, *83*, 3675–3681.

47. Tareste, D.; Pincet, F.; Lebeau, L.; Perez, É. Hydrophobic forces and hydrogen bonds in the adhesion between retinoid-coated surfaces. *Langmuir* **2007**, *23*, 3225–3229.

48. Yang, H.W.; Yi, J.W.; Bang, E.-K.; Jeon, E.M.; Kim, B.H. Cationic nucleolipids as efficient siRNA carriers. *Org. Biomol. Chem.* **2011**, *9*, 291–296.

49. Ceballos, C.; Khiati, S.; Prata, C.A.; Zhang, X.X.; Giorgio, S.; Marsal, P.; Grinstaff, M.W.; Barthélémy, P.; Camplo, M. Cationic nucleoside lipids derived from universal bases: A rational approach for siRNA transfection. *Bioconjug. Chem.* **2010**, *21*, 1062–1069.

50. Moreau, L.; Barthélémy, P.; Li, Y.; Luo, D.; Prata, C.A.H.; Grinstaff, M.W. Nucleoside Phosphocholine Amphiphile for *in vitro* DNA transfection. *Mol. BioSyst.* **2005**, *1*, 260–264.

51. Chabaud, P.; Camplo, M.; Payet, D.; Serin, G.; Moreau, L.; Barthélémy, P.; Grinstaff, M.W. Cationic nucleoside lipids for gene delivery. *Bioconjug. Chem.* **2006**, *17*, 466–472.

52. Céballos, C.; Khiati, S.; Barthélémy, P.; Camplo, M. Acyclic anionic nucleolipids for DNA delivery. *J. Nanosci. Lett.* **2012**, *2*, 20.

53. Khiati, S.; Pierre, N.; Andriamanarivo, S.; Grinstaff, M.W.; Arazam, N.; Nallet, F.; Navailles, L.; Barthélémy, P. Anionic nucleotide-lipids for *in vitro* DNA transfection. *Bioconjug. Chem.* **2009**, *20*, 1765–1772.

54. Moreau, L.; Barthélémy, P.; El Maataoui, M.; Grinstaff, M.W. Supramolecular assemblies of nucleoside phosphocholine amphiphiles. *J. Am. Chem. Soc.* **2004**, *126*, 7533–7539.

55. Moreau, L.; Campins, N.; Grinstaff, M.W.; Barthélémy, P. A fluorocarbon nucleoamphiphile for the construction of actinide loaded microspheres. *Tetrahedron Lett.* **2006**, *47*, 7117–7120.

56. Godeau, G.; Barthélémy, P. Glycosyl-nucleoside lipids as low-molecular-weight gelators. *Langmuir* **2009**, *25*, 8447–8450.

57. Godeau, G.; Bernard, L.; Staedel, C.; Barthélémy, P. Glycosyl-nucleoside-lipid based supramolecular assembly as a nanostructured material with nucleic acid delivery capabilities. *Chem. Commun.* **2009**, *34*, 5127–5129.

58. Godeau, G.; Brun, C.; Arnion, H.; Staedel, C.; Barthélémy, P. Glycosyl-nucleoside fluorinated amphiphiles as compoents of nanostructured hydrogels. *Tetrahedron Lett.* **2010**, *51*, 1012–1015.

59. Studer, A.; Hadida, S.; Ferritto, R.; Kim, S.-Y.; Jeger, P.; Wipf, P.; Curran, D.P. Fluorous synthesis: A fluorous-phase strategy for improving separation efficiency in organic synthesis. *Science* **1997**, *275*, 823–826.

60. Pongdee, R.; Liu, H.-W. Elucidation of enzyme mechanisms using fluorinated substrate analogues. *Bioorg. Chem.* **2004**, *32*, 393–437.

61. Müller, K.; Faeh, C.; Diederich, F. Fluorine in pharmaceuticals: Looking beyond intuition. *Science* **2007**, *317*, 1881–1886.

62. Curran, D.P. Chemistry: Fluorous tags unstick messy chemical biology problems. *Science* **2008**, *321*, 1645–1646.

63. Godeau, G.; Arnion, H.; Brun, C.; Staedel, C.; Barthélémy, P. Fluorocarbon oligonucleotide conjugates for nucleic acids delivery. *Med. Chem. Commun.* **2010**, *1*, 76–78.

64. Patwa, A.; Gissot, A.; Bestel, I.; Barthélémy, P. Hybrid lipid oligonucleotide conjugates: Synthesis, self-assemblies and biomedical applications. *Chem. Soc. Rev.* **2011**, *40*, 5844–5854.

65. Godeau, G.; Staedel, C.; Barthélémy, P. Lipid-conjugated oligonucleotides via "click chemistry" efficiently inhibit hepatitis C virus translation. *J. Med. Chem.* **2008**, *51*, 4374–4376.

66. Huisgen, R. *1,3-Dipolar Cycloaddition Chemistry*; Wiley: New York, NY, USA, 1984; Volume 1, pp. 1–176.

67. Schmidt, S.; Niemann, A.; Krynetskaya, N.F.; Oretskaya, T.S.; Metelev, V.G.; Suchomlinov, V.V.; Shabarova, Z.A.; Cech, D. The use of oligonucleotide probes containing 2'-deoxy-2'-fluoronucleosides for regiospecific cleavage of RNA by RNase H from Escherichia coli. *Biochim. Biophys. Acta* **1992**, *1130*, 41–46.

68. Kawasaki, A.M.; Casper, M.D.; Freier, S.M.; Lesnik, E.A.; Zounes, M.C.; Cummins, L.L.; Gonzalez, C.; Dan Cook, P. Uniformly modified 2′-deoxy-2′-fluoro phosphorothioate oligonucleotides as nuclease-resistant antisense compounds with high affinity and specificity for RNA targets. *J. Med. Chem.* **1993**, *36*, 831–841.

69. Kois, P.; Tocik, Z.; Spassova, M.; Ren, W.-Y.; Rosenberg, I.; Soler, J.F.; Watanabe, K.A. Synthesis and some properties of modified oligonucleotides. 2. oligonucleotides containing 2'-deoxy-2'-fluoro-β-D-arabinofuranosyl pyrimidine nucleosides. *Nucleosides Nucleotides* **1993**, *12*, 1093–1109.

70. Rosenberg, I.; Soler, J.F.; Tocik, Z.; Ren, W.-Y.; Ciszewski, L.A.; Kois, P.; Pankiewicz, K.W.; Spassova, M.; Watanabe, K.A. Synthesis of oligodeoxynucleotides containing the C-nucleoside and 2'- deoxy-2'-fluoro-ara-nucleoside moieties by the H-phosphonate method. *Nucleosides Nucleotides* **1993**, *12*, 381–401.

71. Reif, B.; Wittmann, V.; Schwalbe, H.; Griesinger, C.; Wörner, K.; Jahn-Hofmann, K.; Engels, J.W.; Bermel, W. 132. Structural comparison of oligoribonucleotides and their 2′-deoxy-2′-fluoro analogs by heteronuclear NMR spectroscopy. *Helv. Chim. Acta* **1997**, *80*, 1952–1971.

72. Damha, M.J.; Wilds, C.J.; Noronha, A.; Brukner, I.; Borkow, G.; Arion, D.; Parniak, M.A. Hybrids of RNA and arabinonucleic acids (ANA and 2'F-ANA) are substrates of ribonuclease H. *J. Am. Chem. Soc.* **1998**, *120*, 12976–12977.

73. Wilds, C.J.; Damha, M.J. Duplex recognition by oligonucleotides containing 2'-deoxy-2'-fluoro-D-arabinose and 2'-deoxy-2'-fluoro-D-ribose. Intermolecular 2'-OH-phosphate contacts *versus* sugar puckering in the stabilization of triple-helical complexes. *Bioconjugate Chem.* **1999**, *10*, 299–305.

74. Wilds, C.J.; Damha, M.J. 2'-Deoxy-2'-fluoro-β-D-arabinonucleosides and oligonucleotides (2'F-ANA): Synthesis and physicochemical studies. *Nucleic Acids Res.* **2000**, *28*, 3625–3635.

75. Damha, M.J.; Noronha, A.M.; Wilds, C.J.; Trempe, J.-F.; Denisov, A.; Pon, R.T.; Gehring, K. Properties of arabinonucleic acids (ANA & 20′F-ANA): Implications for the design of antisense therapeutics that invoke RNase H cleavage of RNA. *Nucleosides Nucleotides Nucleic Acids* **2001**, *20*, 429–440.

76. Denisov, A.Yu.; Noronha, A.M.; Wilds, C.J.; Trempe, J.-F.; Pon, R.T.; Gehring, K.; Damha, M.J. Solution structure of an arabinonucleic acid (ANA)/RNA duplex in a chimeric hairpin: Comparison with 2′-fluoro-ANA/RNA and DNA/RNA hybrids. *Nucleic Acids Res.* **2001**, *29*, 4284–4293.

77. Lok, C.-N.; Viazovkina, E.; Min, K.-L.; Nagy, E.; Wilds, C.J.; Damha, M.J.; Parniak, M.A. Potent gene-specific inhibitory properties of mixed-backbone antisense oligonucleotides comprised of 2′-deoxy-2′-fluoro-D-arabinose and 2′-deoxyribose nucleotides. *Biochemistry* **2002**, *41*, 3457–3467.

78. Doi, Y.; Katafuchi, A.; Fujiwara, Y.; Hitomi, K.; Tainer, J.A.; Ide, H.; Iwai, S. Synthesis and characterization of oligonucleotides containing 2′-fluorinated thymidine glycol as inhibitors of the endonuclease III reaction. *Nucleic Acids Res.* **2006**, *34*, 1540–1551.

79. Dowler, T.; Bergeron, D.; Tedeschi, A.-L.; Paquet, L.; Ferrari, N.; Damha, M.J. Improvements in siRNA properties mediated by 2′-deoxy-2′-fluoro-β-D-arabinonucleic acid (FANA). *Nucleic Acids Res.* **2006**, *34*, 1669–1675.

80. Watts, J.K.; Choubdar, N.; Sadalapure, K.; Robert, F.; Wahba, A.S.; Pelletier, J.; Pinto, B.M.; Damha, M.J. 2′-Fluoro-4′-thioarabino-modified oligonucleotides: Conformational switches linked to siRNA activity. *Nucleic Acids Res.* **2007**, *35*, 1441–1451.

81. Peng, C.G.; Damha, M.J. Polymerase-directed synthesis of 2′-deoxy-2′-fluoro-β-D-arabinonucleic acids. *J. Am. Chem. Soc.* **2007**, *129*, 5310–5311.

82. Peng, C.G.; Damha, M.J. G-quadruplex induced stabilization by 2′-deoxy-2′-fluoro-d-arabinonucleic acids (2′F-ANA). *Nucleic Acids Res.* **2007**, *35*, 4977–4988.

83. Watts, J.K.; Martín-Pintado, N.; Gómez-Pinto, I.; Schwartzentruber, J.; Portella, G.; Orozco, M.; González, C.; Damha, M.J. Differential stability of 2′F-ANA•RNA and ANA•RNA hybrid duplexes: Roles of structure, pseudohydrogen bonding, hydration, ion uptake and flexibility. *Nucleic Acids Res.* **2010**, *38*, 2498–2511.

84. Deleavey, G.F.; Watts, J.K.; Alain, T.; Robert, F.; Kalota, A.; Aishwarya, V.; Pelletier, J.; Gewirtz, A.M.; Sonenberg, N.; Damha, M.J. Synergistic effects between analogs of DNA and RNA improve the potency of siRNA-mediated gene silencing. *Nucleic Acids Res.* **2010**, *38*, 4547–4557.

85. Erande, N.; Gunjal, A.D.; Fernandes, M.; Kumar, V.A. Probing the furanose conformation in the 2'-5' strand of i*so*DNA:RNA duplexes by freezing the nucleoside conformations. *Chem. Commun.* **2011**, *47*, 4007–4009.

86. Parsch, J.; Engels, J.W. Synthesis of fluorobenzene and benzimidazole nucleic-acid analogues and their influence on stability of RNA duplexes. *Helv. Chim. Acta* **2000**, *83*, 1791–1808.

87. Parsch, J.; Engels, J.W. C–F···H–C hydrogen bonds in ribonucleic acids. *J. Am. Chem. Soc.* **2002**, *124*, 5664–5672.

88. Rastinejad, F.; Evilia, C.; Lu, P. Studies of nucleic acids and their protein interactions by ^{19}F NMR. *Methods Enzymol.* **1995**, *261*, 560–575.

89. Rastinejad, F.; Lu, P. Bacteriophage T7 RNA polymerase. ^{19}F-nuclear magnetic resonance observations at 5-fluorouracil-substituted promoter DNA and RNA transcript. *J. Mol. Biol.* **1993**, *232*, 105–122.

90. Chu, W.-C.; Feiz, V.; Derrick, W.B.; Horowitz, J. Fluorine-19 nuclear magnetic resonance as a probe of the solution structure of mutants of 5-Fluorouracil-substituted Escherichia coli valine *t*RNA. *J. Mol. Biol.* **1992**, *227*, 1164–1172.

91. Chu, W.-C.; Horowitz, J. Fluorine-19 NMR studies of the thermal unfolding of 5-fluorouracil-substituted Escherichia coli valine transfer RNA. *FEBS Lett.* **1991**, *295*, 159–162.

92. Parisot, D.; Malet-Martino, M.C.; Martino, R.; Crasnier, P. [19]F nuclear magnetic resonance analysis of 5-fluorouracil metabolism in four differently pigmented strains of Nectria haematococca. *Appl. Environ. Microbil.* **1991**, *57*, 3605–3612.

93. Tanabe, K.; Sugiura, M.; Nishimoto, S.-I. Monitoring of duplex and triplex formation by ^{19}F NMR using oligodeoxynucleotides possessing 5-fluorodeoxyuridine unit as ^{19}F signal transmitter. *Bioorg. Med. Chem.* **2010**, *18*, 6690–6694.

94. Danielson, M.A.; Falke, J.J. Use of 19F NMR to probe protein structure and conformational changes. *Annu. Rev. Biophys. Biomol. Struct.* **1996**, *25*, 163–195.

95. Barhate, N.B.; Barhate, R.N.; Cekan, P.; Drobny, G.; Sigurdsson, S.Th. A nonafluoro nucleoside as a sensitive ^{19}F NMR probe of nucleic acid conformation. *Org. Lett.* **2008**, *10*, 2745–2747.

96. Dollé, F.; Hinnen, F.; Vaufrey, F.; Tavitian, B.; Crouzel, C. A general method for labeling oligodeoxynucleotides with ^{18}F for *in vivo* PET imaging. *J. Label. Compd. Radiopharm.* **1997**, *39*, 319–330.

97. Tavitian, B.; Terrazzino, S.; Kühnast, B.; Marzabal, S.; Stettler, O.; Dollé, F.; Deverre, J.-R.; Jobert, A.; Hinnen, F.; Bendriem, B.; *et al*. *In vivo* imaging of oligonucleotides with positron emission tomography. *Nat. Med.* **1998**, *4*, 467–470.

98. Kuhnast, B.; Dollé, F.; Vaufrey, F.; Hinnen, F.; Crouzel, C.; Tavitian, B. Fluorine-18 labeling of oligonucleotides bearing chemically-modified ribose-phosphate backbones. *J. Label. Compd. Radiopharm.* **2000**, *43*, 837–848.

99. Kuhnast, B.; Hinnen, F.; Boisgard, R.; Tavitian, B.; Dollé, F. Fluorine-18 labelling of oligonucleotides: Prosthetic labelling at the 5′-end using the N-(4-[18F]fluorobenzyl)-2-bromoacetamide reagent. *J. Label. Compd. Radiopharm.* **2003**, *46*, 1093–1103.

100. Viel, T.; Kuhnast, B.; Hinnen, F.; Boisgard, R.; Tavitian, B.; Dollé, F. Fluorine-18 labelling of small interfering RNAs (siRNAs) for PET imaging. *J. Label. Compd. Radiopharm.* **2007**, *50*, 1159–1168.

101. Hedberg, E.; Långström, B. 18F-labelling of oligonucleotides using succinimido 4-[18F]fluorobenzoate. *Acta Chem. Scand.* **1998**, *52*, 1034–1039.

102. Pan, D.; Gambhir, S.S.; Toyokuni, T.; Iyer, M.R.; Acharya, N.; Phelps, M.E.; Barrio, J.R. Rapid synthesis of a 5'-fluorinated oligodeoxy-nucleotide: A model antisense probe for use in imaging with positron emission tomography (PET). *Bioorg. Med. Chem. Lett.* **1998**, *8*, 1317–1320.

103. Mercier, F.; Paris, J.; Kaisin, G.; Thonon, D.; Flagothier, J.; Teller, N.; Lemaire, C.; Luxen, A. General method for labeling siRNA by click chemistry with fluorine-18 for the purpose of PET imaging. *Bioconjug. Chem.* **2011**, *22*, 108–114.

Review

Silicon-[18F]Fluorine Radiochemistry: Basics, Applications and Challenges

Carmen Wängler [1],*, Alexey Kostikov [2], Jun Zhu [2], Joshua Chin [2], Björn Wängler [3] and Ralf Schirrmacher [2],*

[1] Department of Nuclear Medicine, University Hospital Munich, Ludwig-Maximilians University Munich, Marchioninistr. 15, 81377 Munich, Germany

[2] McConnell Brain Imaging Centre, McGill University, 3801 University Street, H3A 2B4 Montreal QC, Canada; E-Mails: alexey.kostikov@mail.mcgill.ca (A.K.); jun.zhu@mail.mcgill.ca (J.Z.); joshua.chin@mail.mcgill.ca (J.C.)

[3] Department of Molecular Imaging and Radiochemistry, University Hospital Mannheim, Institute for Clinical Radiology and Nuclear Medicine, Ruprecht Karls-University Heidelberg, Theodor-Kutzer-Ufer 1–3, 68167 Mannheim, Germany; E-Mail: Bjoern.Waengler@medma.uni-heidelberg.de

* Author to whom correspondence should be addressed; E-Mails: Carmen.Waengler@med.lmu.de (C.W.); Tel.: +49-89-7095-7543 (C.W.); Ralf.Schirrmacher@mcgill.ca (R.S.); Tel.: +1-514-398-8527 (R.S.)

Abstract: Silicon-[18F]fluorine (Si-18F) radiochemistry has recently emerged alongside other unconventional approaches such as aluminum-18F and boron-18F based labeling strategies, reshaping the landscape of modern 18F-radiochemistry. All these novel methodologies are driven by the demand for more convenient 18F-labeling procedures to further disseminate one of the most sophisticated imaging technologies, Positron Emission Tomography (PET). The PET methodology requires special radionuclides such as 18F (one of the most prominent examples) to be introduced into bioactive molecules. Si-18F radiochemistry contributed greatly towards the development of new radiopharmaceuticals for PET imaging. Herein, we describe the radiochemical basics of Si-18F bond formation, the application of Si-18F tracers for PET imaging, and additionally, the inherent chemical intricacies of this methodology.

---

1. Introduction: Fluorine-18, an Important Nuclide for PET Imaging

PET can be considered as one of the major advances in modern imaging technologies [1]. The method itself relies on the use of positron-emitting radionuclides which decay by positron emission (β^+ emission). These PET radionuclides are proton rich, unstable and lose energy by the conversion of a proton into a neutron, an electron neutrino and a positron (β^+).

Figure 1. A β^+ emitting radionuclide (e.g., fluorine-18) is attached to a biomolecule. After the β^+ particle is emitted, it travels within the tissue, depending on its β^+ energy. After coming to rest, the β^+ forms a hydrogen atom-like system (with a positron instead of a proton center) with an electron from the surrounding environment and finally disintegrates under emission of two diametrically opposed gamma rays of 511 keV. These photons can be detected in "coincidence" (meaning at the same time within a certain time frame) and used for reconstruction of a 3D image of the radioactive decay and thus tracer accumulation.
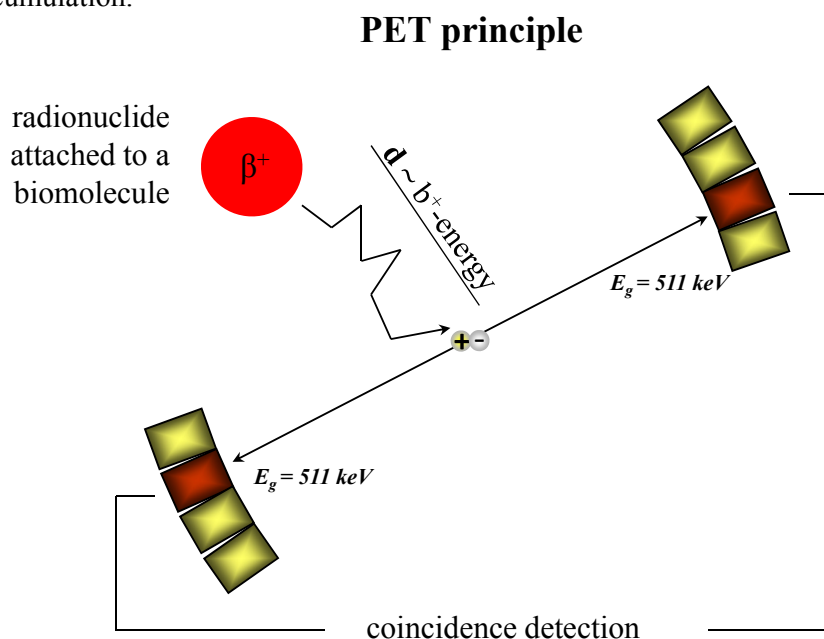
A positron is the antimatter counterpart of an electron and it can annihilate with an electron of the environment under full conversion of the positron-electron masses into energy. The conversion energy which is equivalent to 2 electron masses (a positron weighs the same as an electron) is 1,022 keV. As a result of the conservation of energy and momentum at annihilation, two gamma rays of 511 keV are emitted in an angle of 180° which are capable of penetrating most materials, including living tissue (Figure 1). These can be detected simultaneously by two radioactivity detectors outside of the object/subject within a certain time window. A PET camera consists of a multitude of such detectors (usually bismuth germanium oxide (BGO) crystal detectors) arranged in a circular shape stretching

over many layers and a subject (e.g., a human) can be placed inside that cavity. A computer system hooked up to these detectors registers coincidence detection of two gamma rays between two independent detectors at a time. In the end, after processing many of those events and subsequent data reconstructions, a 3D image of the object is obtained. The PET technique has been proven very useful in the detection of cancer, cardiovascular disease, metabolic disorders and for imaging of certain structures in the human brain as receptors or proteins which are associated with known afflictions, such as Parkinson's and Alzheimer's disease. One of the most useful radionuclides for PET imaging is ^{18}F. With a half-life of 109 min and low positron energy of 640 keV, ^{18}F can yield PET images of high resolution when PET scanners of the newest generation are used. In order to take advantage of the favorable physical characteristics of ^{18}F, methods have to be found to stably introduce ^{18}F into any useful molecule serving a biological purpose such as binding to a specific brain receptor or accumulating in tumor tissue. Until recently, ^{18}F was only incorporated into organic compounds by electrophilic or nucleophilic reactions resulting in the formation of a carbon-^{18}F bond [2–4]. The problem is that both electrophilic (e.g., using [^{18}F]F$_2$) and nucleophilic (using [^{18}F]F$^-$) reactions are not 100% specific and other radioactive products besides those intended are formed. This necessitates usually an extensive purification of the ^{18}F-tracer molecule by means of High Performance Liquid Chromatography (HPLC) and subsequent solid phase cartridge extraction, the former being a rather time consuming and costly process. Furthermore, the synthesis of ^{18}F-tracers for PET imaging requires a fully equipped radiochemistry unit, including a cyclotron in a reasonable distance which produces the ^{18}F by bombarding H$_2$^{18}O enriched water with protons, initiating a nuclear reaction converting the ^{18}O atom into a ^{18}F atom (^{18}O(p,n)^{18}F). However, this is only the first step in a long chain of procedures and reactions finally yielding the ^{18}F-labeled radiotracer. The actual radiochemistry is the most involved process and there is a demand for easier and less skill-demanding methods to introduce ^{18}F into organic compounds to disseminate the usage of PET in medicine and life science. A breakthrough would be the finding of labeling procedures which closely resemble the kit-like production of SPECT (Single Photon Emission Computed Tomography) radiopharmaceuticals. SPECT imaging remains the dominating imaging modality in nuclear medicine for diagnostic purposes, as the synthesis of the SPECT tracers is easy and requires only minimal technical skills and equipment. Although PET has many advantages over SPECT, it still suffers from its complicated infrastructural requirements and its difficulties to produce the required imaging agents. The main aim of modern ^{18}F-radiochemistry should therefore focus on more reliable and standardized synthetic methods to introduce ^{18}F into biomolecules like peptides and proteins, as these are increasingly screened as promising PET imaging agents. One-step labeling procedures of these complex compounds would be preferable and the purification of the final imaging agent should be possible without HPLC. The advent of novel ^{18}F-labeling methods has just begun. The introduction of Si-^{18}F [5–7], B-^{18}F [5,6] and Al-^{18}F [8–12] radiochemistry has set the foundation for the development of novel radiotracers and has the potential to reshape the landscape of ^{18}F-radiochemistry if some hurdles can be overcome in time. This review article deals primarily with Si-^{18}F radiochemistry and the interested reader is advised to further consult various excellent review articles on ^{18}F-radiochemistry [13–18] and original publications about B-^{18}F and Al-^{18}F chemistry.

2. Basics of Silicon-[18]F Radiochemistry

Up until recently, only sporadic attempts to bind ^{18}F to a different atom other than carbon have been reported in the literature. One reason might be that for many years, mainly small radiolabeled compounds were in the focus of ^{18}F labeling chemistry for PET imaging. Those small compounds are most of the time not amenable to heteroatomic modifications because of their sensitive nature and their very specific structure-related target binding. Only a few years ago, radiochemists started to use ^{18}F to label even complex molecules, such as peptides and proteins. Even today, the ^{18}F labeling of these compounds of high molecular weight is challenging, and requires elaborate pathways to introduce the radionuclide. Direct labeling approaches for peptides based on C-^{18}F bond formation are rare and not universally applicable. Thus, so-called prosthetic labeling sythons, already bearing the ^{18}F atom (attached to a carbon), have to be employed which is even more important in the case of proteins, bearing a multitude of different functional groups. It seems that C-^{18}F radiochemistry has reached its limits and alternative strategies have to be found to advance the field further in terms of convenience, applicability and reliability. The use of Si-F bond formation in radiochemistry dates back to 1958 [19] and a few more papers on that subject have been published before the first *in vivo* application was reported [20–22].

At first glance, the use of silicon for binding ^{18}F appears not to be a promising choice. Despite the fact that the bond energy of the Si-F bond is *ca.* 90 kJ higher than that of the C-F bond (570 kJ·mol^{-1} *vs.* 480 kJ·mol^{-1}), the kinetic stability of the Si-F bond against hydrolysis is very low due to strong bond polarization. This is an apparent obstacle for the use of Si-^{18}F bearing compounds as potential tracer probes for PET, since under physiological conditions present in the blood, the Si-^{18}F bond would undergo immediate hydrolysis, resulting in the detachment of the ^{18}F from the biomolecule. This was proved to be true in 1985 by Rosenthal and co-workers [23], who labeled a simple compound like chlorotrimethylsilane with anionic [18]F$^-$ in good radiochemical yields of 65% in one step. The resulting [^{18}F]fluorotrimethylsilane is a volatile compound which was shown to be quickly taken up in the bloodstream when inhaled by rats. It quickly turned out that the *in vivo* stability of the Si-^{18}F bond was rather low and the corresponding silanole was more or less formed immediately, resulting in the predominant uptake of [18]F$^-$ into the bones, forming fluoroapatite. Even back in 1985, the authors already suggested the use of bulkier substituents on the Si atom to shield the Si-F bond from hydrolysis. Interestingly, Gatley described a purification method for [18]F$^-$ using [^{18}F]fluorotrimethylsilane, exploiting the easy hydrolysis of the Si-^{18}F bond in nearly anhydrous acetonitrile to form highly nucleophilic [18]F$^-$ a few years later [24]. This is the first example in the literature where highly nucleophilic [18]F$^-$ was prepared without azeotropic water removal, which was then used in the synthesis of [^{18}F]2-fluoro-2-deoxy-D-glucose (FDG), the most prominent ^{18}F-radiotracer to date [25]. The need of bulky substituents at the Si atom was reiterated later by Walsh *et al.* [26]. They suggested the use of alkoxy silanes as potential precursor compounds for the ^{18}F-labeling with aqueous HF, actually a reaction already well known to organic chemists for the deprotection of silylated alcohols. The key to prevent fast hydrolysis is the introduction of sterically hindered substituents, a fact which was discovered and proven to be valid almost simultaneously by Blower and co-workers [27] and Schirrmacher and Jurkschat in 2006 [28]. Alkoxysilanes as well as hydroxylsilanes and chlorosilanes readily react with [18]F$^-$ in excellent to quantitative yields.

Some compounds displayed a reasonably high stability towards hydrolysis in neutral and acidic media, but underwent fast hydrolysis under even slightly basic conditions. On closer examination, the requirement for a Si-^{18}F compound to be useful *in vivo* is not to be stable over a wide range of pH values, but rather at the very slightly basic conditions of pH 7.4 as encountered *in vivo*. The aim should therefore be to achieve a hydrolytic stability of the Si-^{18}F bond under physiological conditions rather than over a wide pH range. The first two structurally simple model compounds which were injected into animals to investigate the *in vivo* stability were characterized by bulky substituents such as aryl and *tert*-butyl groups attached to the Si atom (**16** and **17**, Figure 5B). The Si-^{18}F compound bearing two aryl and one *tert*-butyl group, although stable for many hours under neutral or acidic conditions, displayed a rapid loss of the ^{18}F label *in vivo*. This has been proven by a strong radioactivity signal from the bones. After replacing one of the two aryl groups with a *tert*-butyl group, the resulting triorganofluorosilane **16**, labeled with ^{18}F, showed a remarkable *in vivo* stability and served as a lead structure to develop this labeling chemistry further for more practical applications. However, it was noticed early that chlorosilanes do not work as building blocks for the ^{18}F-labeling of more complex molecules as a result of their tendency to hydrolyze rapidly. The bioconjugation of chlorosilane synthons to peptides or proteins would fail simply because the chemical processing of any conjugation product entails HPLC and other aqueous workup, inevitably leading to the formation of the corresponding silanole. However, even silanols can serve as ^{18}F-labeling precursors. This has been elegantly demonstrated by Ametamey and co-workers in 2008 and this attractive labeling concept is discussed in depth alongside other appealing leaving groups attached to Si [29]. Historically, before OH, H and alkoxy groups were employed as leaving groups for ^{18}F-labeling, two different labeling strategies for silicon-bearing synthons were developed, both of which are still in heavy use. Perrin's group was the first to describe radioactive tetrafluorosiliconates "ate" salts, being elegantly obtained from their triethoxysilane precursors [5]. Almost parallel to these findings, Schirrmacher and Jurkschat observed that non-radioactive fluorine can be effectively replaced by radioactive [18]F$^-$ in a simple and convenient isotopic exchange [30].

3. [^{18}F]Tetrafluorosiliconates "Ate" Salts

Perrin and co-workers from TRIUMF convincingly demonstrated that biotinylated (aminopropyl)triethoxysilane (**1**) reacts quantitatively with aqueous [18]F$^-$ directly from the target water (target water is [18]O enriched water containing ^{18}F-anions) (Figure 2) [5]. In order to target the required stoichiometric silicon to fluoride ratio of 1:4, the experimental labeling setup required the addition of a non-radioactive fluoride source and their experimental conditions are characterized by very low solvent amounts. In a typical labeling experiment, 16 MBq of [18]F$^-$ in 5 μL buffer together with 3.3–4.4 equivalents of [19]F$^-$ were used for radiolabeling. This solution was then added to **1** in 5 μL of DMF, MeOH, MeCN, DMSO or water. The group is currently devoted to transfer their seminal findings to true no-carrier-added conditions. This is the first convincing example of nucleophilic [18]F$^-$ aqueous radiochemistry, giving a stable product in high radiochemical yields. Perrin's group is also working extensively on the field of boron-^{18}F chemistry which they have impressively advanced over the last few years.

Figure 2. Radioactive ^{18}F-labeling of **1** yielding the [^{18}F]tetrafluorosiliconate "ate" salt **2** in quantitative yields in aqueous buffered solution.
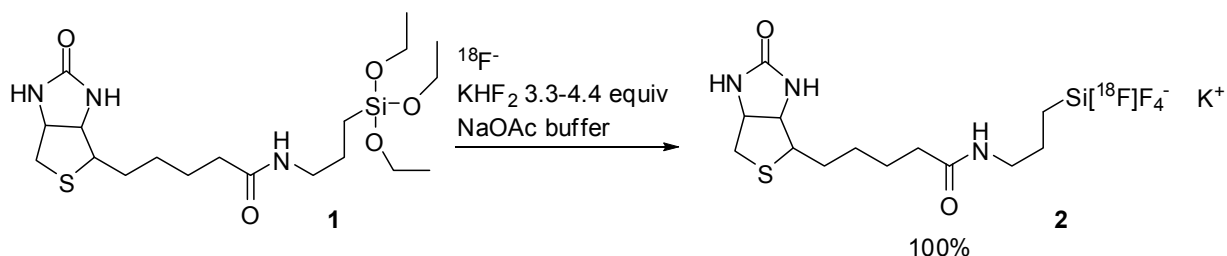
4. Silicon-Fluoride-Acceptors (SiFAs): An introduction

Isotopic exchange reactions in ^{18}F-radiochemistry have been deemed an inherently inferior way of labeling and considered only as a last resort if other labeling strategies fail. The reason behind this is the intention to maximize the specific activity of the compound (that is the proportion of radioactive to ^{18}F-labeled plus ^{19}F-bearing compound). Usually, in conventional C-^{18}F radiochemistry, when activated fluoroarenes are subjected to isotopic exchange reactions, specific activities in the low kBq/μmol range are accomplishable, most of the time not high enough to enable an *in vivo* application. Specific activity is an important issue, since the *in vivo* target of PET tracers are most often receptors or enzymes, which are present in low amounts only. If the specific activity is too low, the receptors are occupied with non-radioactive ligands leading to a loss of the signal resulting from specific binding, and potentially leading to pharmacologic effects. Normally, the amount of labeling precursor needed for isotopic exchange reactions is in the mmol range (a few mg). Unfortunately, the ^{19}F-labeled molecule cannot be chemically distinguished from the ^{18}F-labeled compound, meaning that both compounds are inseparable. This impediment in classical ^{18}F-C chemistry turns into an advantage in the case of ^{19}F for ^{18}F exchange at the Si atom. In conventional labeling chemistry, the labeling precursor, being chemically different from the labeled product, has to be removed from the reaction mixture prior to the *in vivo* application. In isotopic exchange reactions however, labeling precursor and labeled compound are identical, which eliminates the need for purification. If a sufficient specific activity can be achieved with isotopic exchange, the overall labeling procedure would be far more convenient, reducing the synthetic effort.

It was found that the fluorosilane *t*Bu$_2$PhSiF (**16**) could be labeled by isotopic exchange in high radiochemical yields and high specific activities of up to 230 GBq/μmol, using as little as 1 μg of the ^{19}F-fluorosilane in acetonitrile. The purification was exceptionally easy, since the only components in the labeling mixture that had to be removed were un-reacted [18]F$^-$ (less than 5%), Kryptofix 2.2.2 (a cryptand forming a complex with potassium, the counterion of [18]F$^-$, yielding a highly reactive "naked" [18]F$^-$ anion in dipolar aprotic solvents) and K$_2$CO$_3$. This could be easily achieved by simply purifying the [^{18}F]fluorosilane using a C18 solid phase cartridge. All other components of the labeling reaction mixture pass through the cartridge and are therefore separated from the ^{18}F-product. This surprisingly efficient isotopic exchange reaction was termed SiFA for Silicon-Fluoride-Acceptor. A great variety of SiFA compounds have been synthesized to date (Figure 3), and successfully labeled with [18]F. In the current wave of click chemistry, Tietze and Schmuck recently reported on the synthesis of SiFA azide (**12**) as a new building block for PET imaging using Click Chemistry [31].

Figure 3. Structures of small molecule SiFA building blocks.
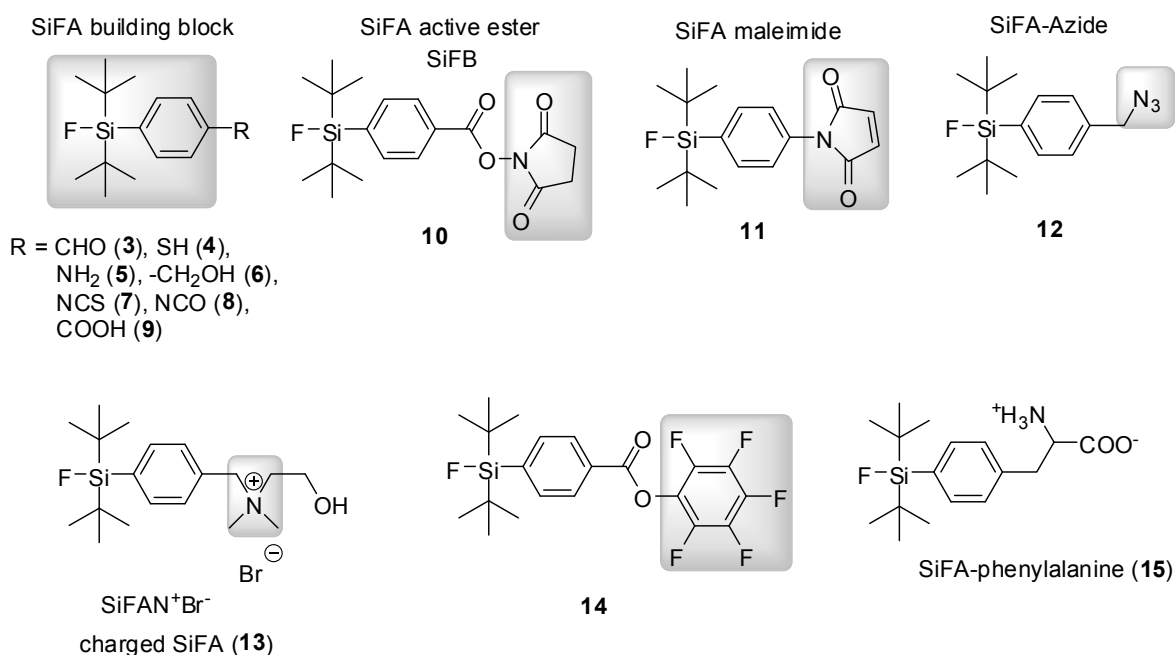
SiFA compound **3**, bearing an aldehyde functionality, displayed a remarkably high rate of isotopic exchange even when high radioactivity amounts of $^{18}F^-$ were used. Up to 3 GBq of $^{18}F^-$ reacted with just 1 µg (3.75 nmol) of **3** within 10 min at room temperature and yielded the [^{18}F]fluorosilane in 97% radiochemical yield (RCY). The calculated specific activity is between 225 and 640 GBq/µmol.

Under regular basic labeling conditions, the active esters could initially not be labeled with $^{18}F^-$ as a result of their tendency to hydrolyze quickly. Very recently, Kostikov and co-workers found a way to circumvent this problem by adding oxalic acid to the labeling cocktail [32]. The N-succinimidyl-3-(di-*tert*-butyl[^{18}F]fluorosilyl) benzoate ([^{18}F]SiFB), an active ester in the style of the most frequently-used ^{18}F-active ester [^{18}F]SFB, was obtained in high radiochemical yields and used for protein labeling (*cf.* Section 9). To shed some light on the mechanism and unanticipated efficiency of the isotopic exchange, Density Functional Theory (DFT) calculations were performed on three model fluorosilanes in the gas phase as well as in acetonitrile as a solvent.

The Gibbs free energies calculated in the gas phase and acetonitrile were −50 to −40 kcal/mol and +5 to 10 kcal/mol in acetonitrile, respectively. The fluoride ion in acetonitrile exhibits a drastically reduced basicity which accounts for the large difference in Gibbs energies in the gas and solution phases. The formation of the pentacoordinate siliconate is therefore less favored and results in a very fast isotopic exchange, as observed experimentally. In a follow-up study from 2011, it was shown that the activation energy (AE) of the isotopic exchange in acetonitrile is 15.7 kcal/mol [32]. This data was acquired from an Arrhenius plot of ln k against 1/T within a temperature range of −20 °C to 0 °C. Comparing these 15.7 kcal/mol to the AE of the simple carbon-^{18}F formation (e.g., the synthesis of 2-[^{18}F]fluoroethyl tosylate), which was just 1.3 kcal/mol higher, it became apparent that the 4 times larger pre-exponential factor of the isotopic exchange is responsible for the faster rate constant. Even at very low temperatures, the isotopic exchange was very fast and yielded the radioactive SiFA in high yields.

5. The synthesis of SiFAs

Jurkschat and his group developed the vast majority of the already described SiFA compounds, with the exception of a most recently described SiFA building block bearing a positive charge. Since the Si-F bond is very stable, the synthesis and purification of all fluorosilanes is straightforward and very convenient. The synthesis of most triorganofluorosilanes follows the scheme below (Figure 4).

Figure 4. Syntheses of various small SiFA building blocks intended for bioconjugation.

R = SH, NH$_2$, CH$_2$OH

PG=protecting groups such as: tBuMe$_2$Si, Me$_3$Si
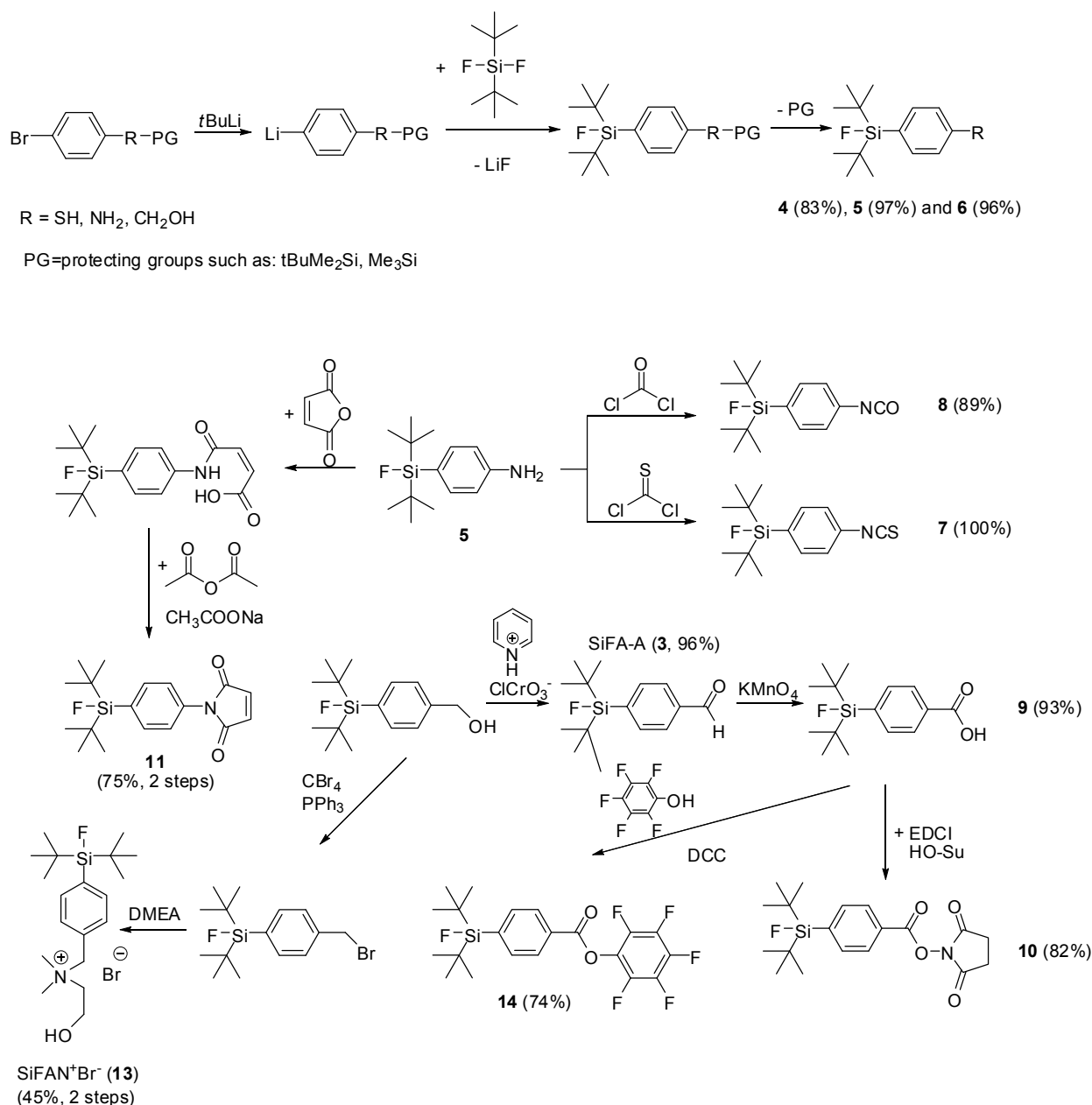
First, silyl-protected functionalized *p*-bromobenzenes are reacted with *tert*-butyllithium and subsequently di-*tert*-butyldifluorosilane at −78 °C. The product tri-organofluorosilanes (**4–6**) are obtained after final silyl-protecting group removal, releasing the respective functional group that can

be further derivatized or used for bioconjugation reactions. In addition to relatively stable -SH, -NH$_2$, -COOH and -CH$_2$OH groups in *para* position to the Si atom, compounds comprising sensitive and highly reactive functional groups such as -CHO, -NCO, -NCS and even active esters (succinimidyl- as well as pentafluorophenyl esters) could also be synthesized following the outlined synthetic procedures.

6. SiFAs and Their High Lipophilicity

Despite the ease of the isotopic exchange and its specificity, the SiFA chemistry exhibits a very unfortunate characteristic: its inherent, structure-related lipohilicity. Why is lipophilicity an issue? The ultimate utilization of the SiFA chemistry will be in the field of diagnostic radiotracer development for PET. This means that the new SiFA-based tracer probes will be administered intravenously to an animal or even to a human being for the purpose of acquiring *in vivo* information about certain diseases related to the specific binding of the tracer. However, if the lipophilicity of the injected compound is too high, the administered tracer will most probably end up in the liver, accumulating there and being no longer available for binding to its intended binding site. Compounds exhibiting a very high lipophilicity show such a rapid first pass effect. The liver basically siphons these compounds out of the blood stream obviating a proper binding to the target.

In terms of brain imaging, a certain degree of lipophilicity is required for passive transport across the blood-brain barrier, as only lipophilic, lipid soluble compounds pass through that protective membrane. However, if a compound is too lipophilic (logD > 4), a passive diffusion across the blood brain-barrier is less likely and the compound is trapped in the lipid layer.

The first small model SiFA compounds (Figure 5) all exhibited a very high lipophilicity, as displayed by the 1-octanol:buffer$_{pH7.4}$ partition coefficient (logD) of >4, basically as a result of the hydrophobic *tert*-butyl groups. None of these compounds are water soluble, but dissolve readily in organic solvents. Most of the time, compounds for PET imaging are used in nanomolar quantities. In this concentration range, the solubility product plays only a minor role, and so compounds usually insoluble in water can nevertheless be used for *in vivo* applications. When SiFA compound [^{18}F]**17** was administered to a rat, dynamic PET data were acquired over 1h. The liver uptake was initially high and the radioactivity uptake in bones became predominant over time, suggesting the hydrolysis of the Si-^{18}F bond. As already pointed out, just one *tert*-butyl group is not sufficiently bulky to protect the Si-^{18}F bond from hydrolysis. These results were independently corroborated by Ametamey and co-workers and are discussed in detail later. However, when the *bis-tert*-butyl SiFA [^{18}F]**16** was administered to rats, the compound did not lose its radiolabel *in vivo* (no bone uptake) and was primarily metabolized in the liver and excreted via the colon. The lipophilicity introduced by the SiFA moiety was later shown to be responsible for a SiFA-peptide conjugate to accumulate almost exclusively in the liver and not bind to its tumor target (*cf.* Section 8). One can certainly conclude that the high lipophilicity of the SiFA moiety is the biggest hurdle in the clinical setting. Efforts are currently underway to overcome this obstacle by reducing the high lipophilicity of the SiFA building blocks by introducing charges and hydrophilic moieties. Kostikov *et al.* in 2011 synthesized the first positively-charged SiFA compound, termed SiFAN$^+$Br$^-$, as a lead compound for a new generation of SiFA building blocks with reduced lipophilicity [32]. The compound could be labeled in high

radiochemical yields of up to 90% by isotopic exchange and specific activities of 20 GBq/µmol could be achieved.

> **Figure 5.** (**A**) Isotopic exchange mechanism resulting in a pentacoordinated silicon intermediate. The back-reaction yielding the original ^{19}F-SiFA compound is statistically not favored. (**B**) Density Functional Theory calculations on three model SiFAs result in a Gibbs free energy of −50 to −40 kcal/mol in gas phase and +5 to 10 kcal/mol in acetonitrile.
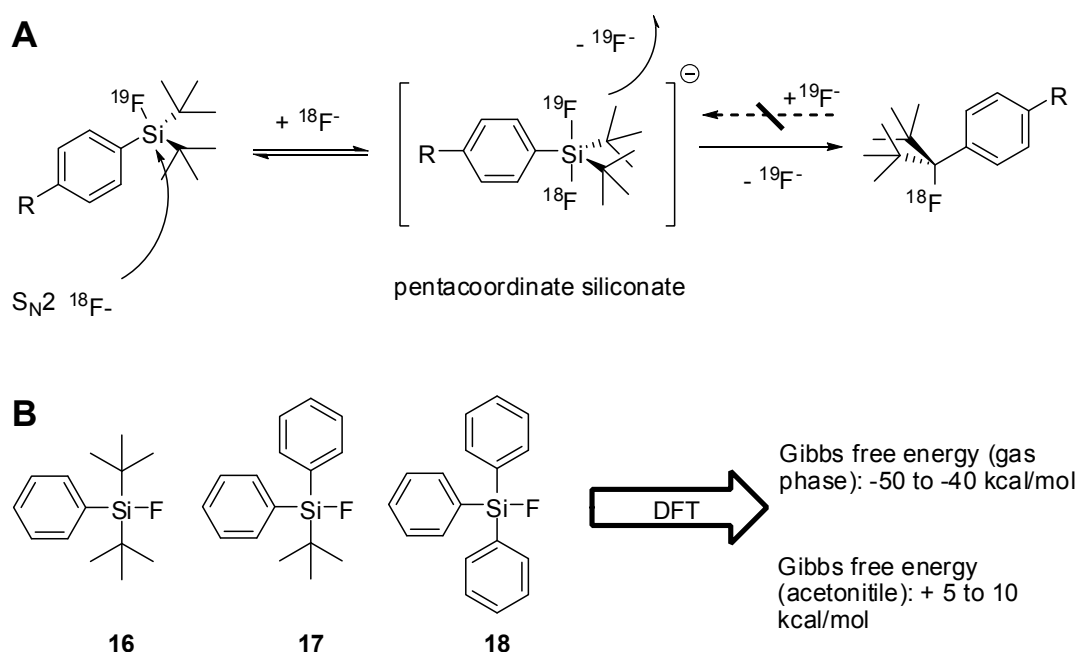

These first results of adding a positive charge to the SiFA molecule are encouraging. In the following sections, we will discuss practical examples of silicon-^{18}F chemistry used for peptide as well as protein labeling. At the end, we will present the first few small molecules modified with a silicon ^{18}F motif intended for PET imaging. Before these approaches are elucidated further, another silicon ^{18}F labeling strategy has to be highlighted, which was developed in parallel to the SiFA chemistry.

7. Silicon Building Blocks Containing H, OH and Alkoxy Moieties as Leaving Groups

In 2008, a group of researchers around Klar and Ametamey published their pioneering work on silicon-based building blocks for the one-step ^{18}F-radiolabeling of peptides (*cf.* Section 8). This innovative labeling approach, based on the exchange of leaving groups such as alkoxyl moieties, OH and H by [18]F⁻ under slightly acidic conditions, ultimately arrived at the same silicon-^{18}F building block structures as described by Schirrmacher and Jurkschat in 2006. It was confirmed that the steric hindrance as exerted by *iso*-propyl or *tert*-butyl groups is crucial for the compounds' hydrolytic stability. A very important finding was that the linker group used for further bioconjugation does not necessarily need to be an aryl group. Allyl linkers were proven to be hydrolytically stable as well, which significantly expands the potential structural variation of the silicon building blocks. Before

labeling larger organic compounds such as peptides, some silicon-based building blocks modified with hydrogen, methyl, *iso*-propyl, *tert*-butyl, aryl and various *n*-alkyl moieties were successfully labeled with $^{18}F^-$ (Figure 6). Some of the investigated compounds could be labeled in very high RCYs. It became apparent that in case of H as a leaving group, the addition of acid did not significantly influence the formation of the Si-^{18}F bond and was therefore regarded as the most promising strategy for further investigations. Using alkoxyl moieties or OH leaving groups requires the presence of protons to amplify the leaving group's exchange tendency via oxygen protonation. This can be difficult to achieve, since the $^{18}F^-$, in the form of its potassium-Kryptofix2.2.2 complex salt, is highly basic and before protonating the leaving group, the protons neutralize the K_2CO_3 (in the form of a $[K^+/Kryptofix]_2/CO_3^{2-}$ salt, also present in the labeling cocktail). This labeling strategy requires elevated labeling temperatures ranging from 30 °C up to 90 °C, which is in stark contrast to the SiFA labeling procedure (isotopic exchange) that works at room temperature or below. In particular, the hydrolytically stabilizing *tert*-butyl group-bearing building blocks require higher reaction temperatures, most probably as a result of steric effects.

Figure 6. Radioactive labeling of silicon building blocks bearing different leaving groups (LG = alkoxyl moiety, OH, H), sterically demanding residues (R = *iso*-propyl, *tert*-butyl) and linker structures (Linker).
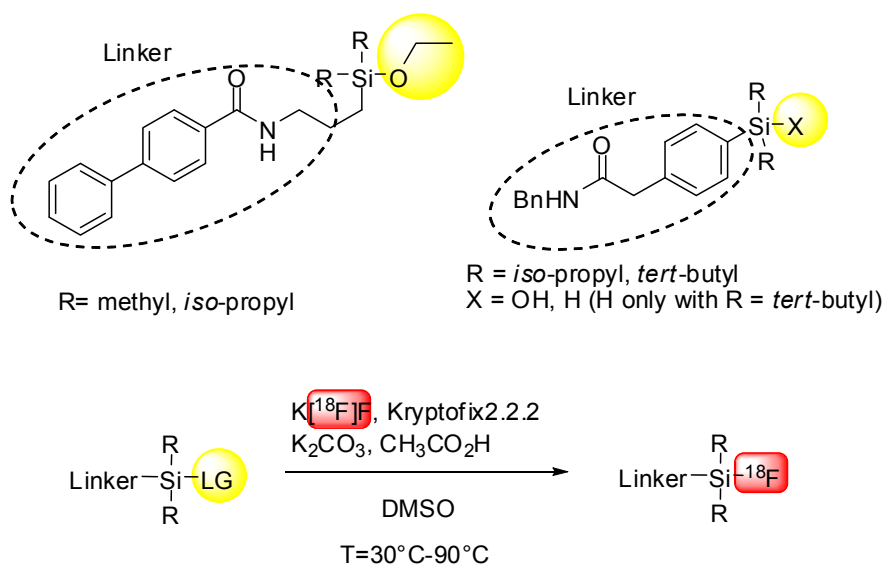

The hydrolytic stability of a large variety of different silicon building blocks was investigated in detail by Ametamey and co-workers [33]. Macroscopic amounts of the organofluorosilanes (15 compounds were tested) showed variable stability toward hydrolysis in a mixture of acetonitrile and buffer at pH 7. Although these conditions do not exactly resemble physiological conditions (pH 7.4 and no co-solvent), the trend of hydrolytic susceptibility discovered experimentally should not be influenced by this difference in pH and the fact that acetonitrile is present as co-solvent. However, the actual hydrolytic half-lives might be different and potentially shorter under true physiological conditions, especially when using very small amounts of ^{18}F-silicon building blocks. It would be

interesting to compare the data from the hydrolysis experiments conducted by the investigators using macroscopic amounts of fluorosilanes with the ^{18}F-labeled analogs under true nca conditions.

It could clearly be demonstrated that *iso*-propyl groups, when combined with a di-methyl substituted aryl system, result in a comparable hydrolytic stability of the Si-^{18}F bond as two *tert*-butyl groups and an un-substituted aryl system. Figure 7 is an excerpt of the original published table of compounds, highlighting the substituents substantially impacting on hydrolytic stability. Interestingly, the substitution on the phenyl residue as one of three substituents connected to the silicon atom plays an important role for the hydrolytic stability, hinting at the possibility of electronic effects in addition to steric effects.

Figure 7. (**A**) Silicon building blocks with very low hydrolytic stability. Compound **21**, bearing two *iso*-butyl groups exhibits a relatively high stability towards hydrolysis. (**B**) Silicon building blocks with highest hydrolytic stability. **C**: Influence of the substituent on the phenyl moiety on hydrolytic stability. (*****$t_{1/2}$: hydrolytic half-life).
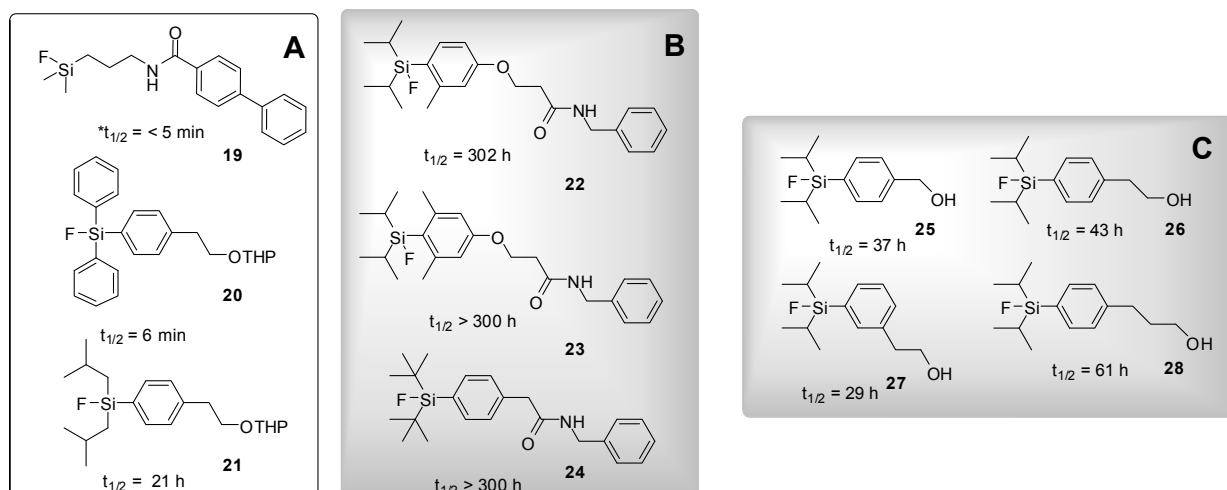

Column A (Figure **7**) corroborates the results on hydrolytic stability found by Schirrmacher *et al*. in 2006 [28]. Attaching three aryl substituents to Si results in a very low hydrolytic stability. Although the aryl moiety is considered to be a bulky substituent, water molecules seem to easily attack the Si atom in an S_N2 kind of way. Replacing two of the three aryl residues by *iso*-butyl-groups stabilizes the Si-F bond significantly. The silicon building blocks displayed in column B show the highest stability towards hydrolysis. The *tert*-butyl groups undoubtedly impart the highest amount of hydrolytic stability which corroborates the findings made for the SiFA compounds. In order to be on par with two *tert*-butyl groups, two *iso*-propyl groups have to be accompanied by an aryl residue having a higher grade of substitution. As shown under B, two methyl groups *ortho* to the Si atom combined with two *iso*-propyl residues result in a comparable hydrolytic stability. The substitution pattern of the aryl group also seems to have a profound influence on the hydrolytic stability of the Si-^{18}F bond. Column C reveals that a longer alkyl chain positioned *para* to the silicon atom leads to a higher stability, most probably due to increasing hyperconjugation and an increasing +I effect. The electron releasing effect of the alkyl chain stabilizes the highly polarized Si-F bond, affecting primarily the *ortho* and *para* position. In contrast, the 2-hydroxy ethyl chain in the *meta* position (compound **27**) does not exhibit

this stabilizing effect which is reflected by its shorter hydrolytic half-life in comparison to the *para* substituted compound (**26**). The likely mechanism of hydrolysis and final loss of fluoride is shown in Figure 8.

Ametamey and co-workers furthermore found some DFT function on the basis of the already characterized 2-(phenylazo)phenyl-allyldifluorosilane which structurally resembles the situation in fluorosilanes. The most fitting functional to describe the bond length of the Si-F bond of their model compounds was found to be the TPSS/RI/TZVP(P) functional. Besides the Si-F bond length, angles, partial charges as well as ligand exchange energies for the hydrolysis reaction were determined on that basis [33].

Figure 8. S_N2 mechanism of Si-F bond hydrolysis with the common pentacoordinate transition state (*ii*) as described in the literature. According to Ametamey and co-workers, water is a spectator in this mechanism.

nucleophilic attack of water
at the silicon atom (*i*)

pentacoordinate transition state (*ii*)

hydrolyzed
compound (*iii*)
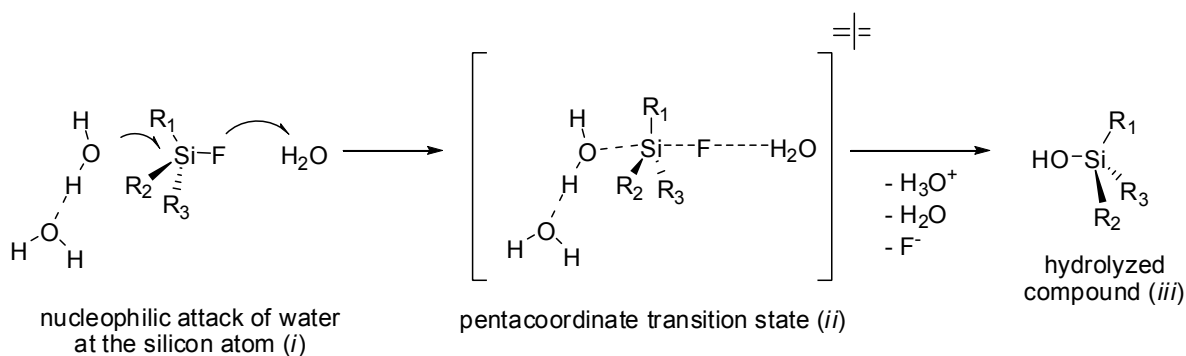
A model for the hydrolysis of Si-F compounds was derived from these data in combination with the experimentally acquired hydrolysis data from the aforementioned 15 model compounds. For the most stable compounds **22**, **23** and **24**, the bond lengths of the intermediate *ii* were 1.831, 1.817 and 1.827 Å respectively. After careful consideration of the obtained data, a linear relationship between the Si-F bond length difference between structure *ii* and *iii* and the corresponding half-lives were found to be reliable predictors of stability. However, the model was constructed on the simplified assumption that the hydrolytic half-lives are most probably impacted by kinetic and/or equilibrium effects, depending on the steric hindrance imparted by the organic rests attached to the Si atom. The radioactive labeling of the corresponding alkoxyl- and H-derivatized silanes demonstrated that steric hindrance impedes an easy access of the $^{18}F^-$ ion and reduces radiochemical yields. Even at 90 °C, the labeling precursor of **23**, bearing an H atom as leaving group, could only be labeled in 48% radiochemical yield. In all investigated cases, where either the H- or alkoxyl-derivatized silanes were used as precursors, an amount of 5 mg was used, which is a substantial amount that has to be separated by preparative HPLC after the reaction if the ^{18}F-labeled fluorosilane is required in pure form. The labeling experiments were extended to peptides which will be discussed in Section 8.

8. Peptides

Peptides, having an intermediate size between small molecules and proteins, normally show a relatively high stability towards even harsh labeling conditions, making a one-step labeling feasible.

However, the many different unprotected functional groups of the amino acid side chains can possibly hamper a selective one-step ^{18}F-introduction by nucleophilic substitution. Therefore, ^{18}F-labeling reactions of peptides normally imply multistep syntheses consisting of the production of a secondary labeling precursor bearing the F-18 label, which has then to be reacted with the peptide. Although the synthesis of several secondary labeling precursors has been improved in recent years, yielding the labeled peptides in high yields and relatively short reaction times, the multi-step syntheses of ^{18}F-labeled peptides using these synthons still require long preparation times—which is unfavorable, considering the short half-life of [18]F—as well as complex and costly in terms of technical equipment [34–36].

An alternative to the conventional secondary labeling precursor approach is the recently developed technique to introduce ^{18}F by reaction with Al^{3+} and the subsequent complication of the system formed by NOTA and NO2A derivatives or the ^{18}F-labeling of the preformed Al-NOXA complex [8,11,12,37] This method allows for a one-step and straightforward introduction of ^{18}F-fluoride, even into complex peptidic compounds at elevated temperatures of 100–110°C within 15 min, and will probably attract increasing attention within the next years. A modification of this technique involving the use of a NO2A chelator derivatized with a maleimide functionality also allowed for protein ^{18}F-labeling in a two-step labeling reaction applying *i*) the fast complication of Al-^{18}F by the chelator and *ii*) the efficient conjugation of the formed complex to the studied antibody fragment [12].

Another alternative to the use of conventional C-^{18}F secondary labeling precursors is the SiFA-technique for introduction of ^{18}F into peptides. There, the ^{19}F against ^{18}F isotopic exchange reaction on the SiFA moiety proved to be applicable for the one-step introduction of ^{18}F even into complex molecules such as peptides. The isotopic exchange is thereby so efficient that it takes place even at room temperature and within short reaction times, as demonstrated on the example of the clinically relevant peptide Tyr[3]-octreotate (TATE). The labeled compound **29** (Figure 9) was obtained in high radiochemical yields (RCYs) of 55–65% after purification and within 25 min overall synthesis time [28]. Important advantages of this procedure are the mild labeling conditions applied which result in the formation of only one radiolabeled product, making an HPLC purification dispensable.

However, in the first attempts of peptide labeling using this strategy, the achieved specific activities (SAs) of the labeled peptides were rather low (between 3–5 GBq/μmol) even when testing different reaction conditions. This resulted in the development of a two-step labeling approach in order to achieve higher specific activities which consisted of *i*) the ^{18}F-radiolabeling of SiFA-derivatized aldehyde (**3**) under mild conditions in high RCYs of up to 97% and high SAs of 225–680 GBq/μmol and *ii*) the subsequent chemo- and regioselective conjugation of the obtained aldehyde to different aminooxy-functionalized peptides [30]. The second step also proceeded efficiently and gave the products in short overall synthesis times of 40 min, comparably high specific activities and overall RCYs of 50–55% after HPLC purification. Using this experimental setup, Tyr[3]-octreotate, cRGD and BZH3, which have gained widespread interest in clinical imaging of different malignant diseases, could be radiolabeled with [18]F (Figure 9). Furthermore, this approach has the advantage of being applicable to the ^{18}F-labeling of various aminooxy-derivatized peptides.

Figure 9. Structures of ^{18}F-SiFA-TATE (**29**), ^{18}F-SiFA-cRGD (**30**) and ^{18}F-SiFA-BZH3 (**31**).

[18]F-SiFA-TATE, **29**

[18]F-SiFA-cRGD, **30**

[18]F-SiFA-BZH3, **31**
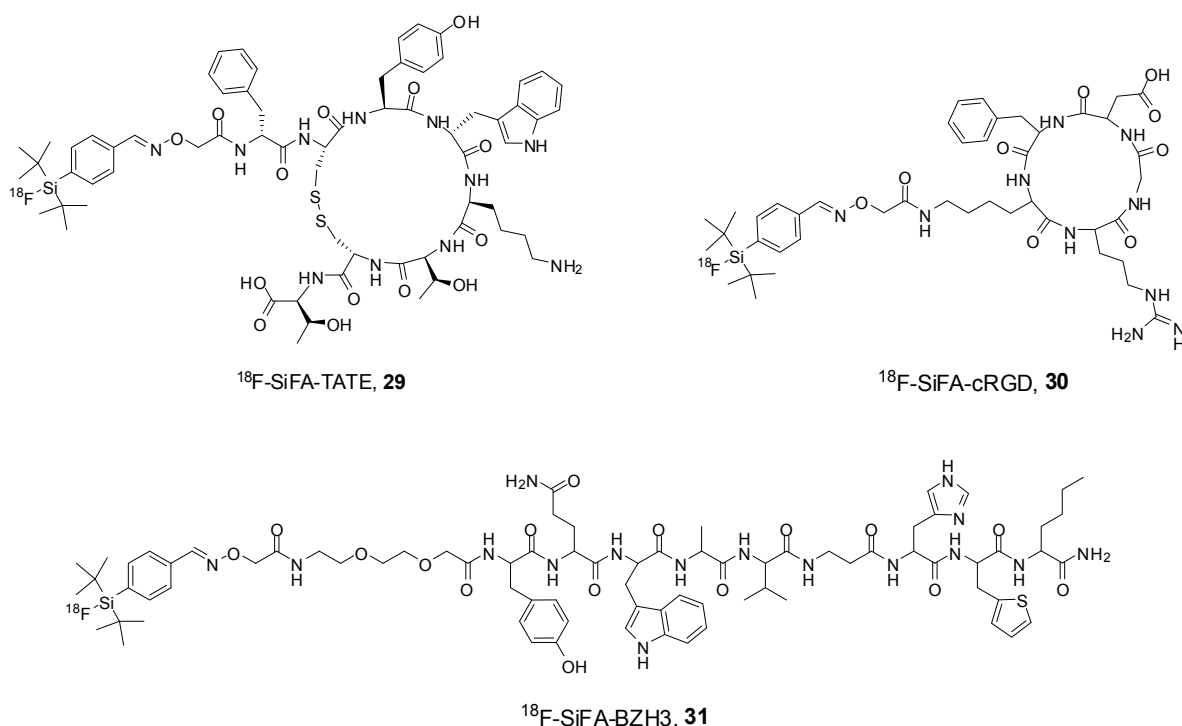
In order to circumvent a two-step labeling reaction requiring a final HPLC purification which reduces the convenience and lengthens the preparation time (despite the fast reaction kinetics of the SiFA approach), optimized labeling conditions were developed. These allow for an efficient reaction at room temperature yielding the product within 30 min in high RCYs of 38% after purification and specific activities between 29 and 56 GBq/μmol, which is sufficient for receptor imaging *in vivo*. The key to these favorable results is the use of very small nanomolar amounts of the respective ^{19}F-labeling precursors (10 to 25 nmol) [38].

In order to allow for a more modular synthesis of SiFA-peptides, enabling not only a terminal but also an intra-sequential introduction of the SiFA building block, a SiFA-containing amino acid derivative (**15**) was developed and shown to be useful for the intra-sequential SiFA-derivatization as demonstrated on the standard Fmoc-based SPPS of three model Tyr[3]-octreotate derivatives [39].

In later studies, when comparing the substitution pattern on the silicon atom with regard to radiolabeling efficiency and hydrolytic stability, an investigation was mounted to see if silicon moieties containing substituents sterically, not as demanding as *tert*-butyl groups, could be used—in order to achieve a high incorporation rate of ^{18}F into the silicon building block by substitution of H-, OH- and alkoxy-residues [29,33,40,41] Although it was found that, in general, the silicon moieties comprising smaller substituents on the silicon atom exhibited a higher isotopic exchange efficiency than the corresponding bulky *tert*-butyl-containing ones [29,33], it was also shown that the hydrolytic stability of the *tert*-butyl substituted building blocks was by far the highest [29,40]. This effect of limited hydrolytic stability was also observed in the case of the corresponding model peptides [29, 41] and bombesin derivatives [40] modified with isopropyl-containing silicon building blocks. With regard to ^{18}F-labeling, relatively high amounts of precursor (e.g., alkoxyl-silanes) had to be used. Belentova

and co-workers needed 6 mg (11 μmol) of a small model peptide derivatized with an alkoxyl-silane moiety (Figure 10) [41]. Of course, the use of such high amounts of precursor peptides necessitates a final HPLC purification of the ^{18}F-labeled peptide.

Figure 10. Course of labeling reactions described by Balentova *et al*.
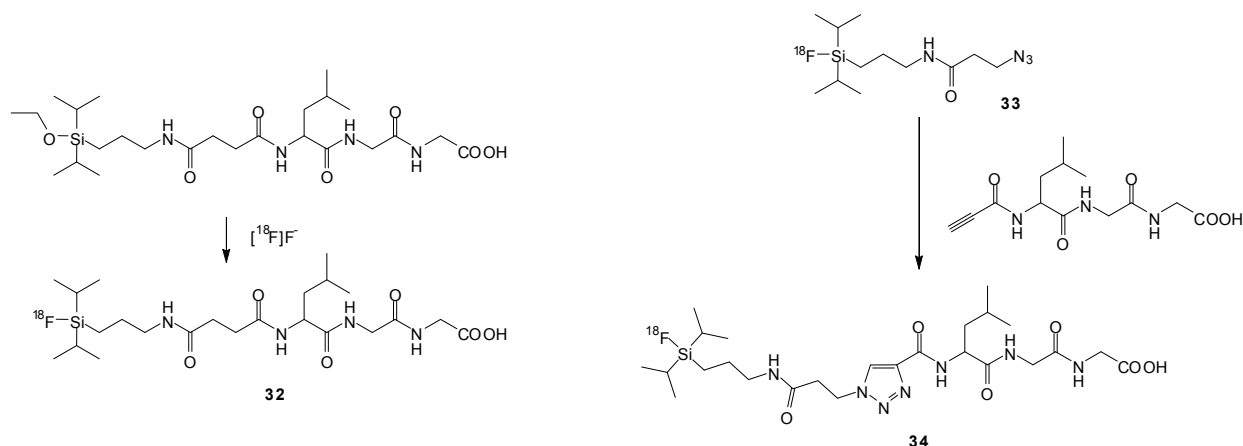
Of crucial importance are, not only the used labeling conditions, achievable RCYs and specific activities, but also the *in vivo* behavior of the ^{18}F-labeled peptides that were obtained. In a study carried out by Höhne *et al*. [40], a ^{18}F-silyl-bombesin derivative (**35**, Figure 11), exhibiting a most favorable *in vitro* binding affinity to the GRP receptor (IC$_{50}$ = 22.9 nM), was evaluated *in vivo* in a PC-3 tumor-bearing mouse model. In this study, the ^{18}F-labeled bombesin derivative unfavorably showed a low and unspecific *in vivo* tumor uptake of only 0.6 %ID/g at 1 h p.i., despite its high affinity to the target receptor. This effect can most probably be attributed to the high lipophilicity of the tracer caused by the stable but bulky and unfortunately highly hydrophobic silicon-containing moiety, resulting in the observed high accumulation in liver, gallbladder and intestine.

Figure 11. Structure of the ^{18}F-silyl-bombesin derivative **35** used for *in vivo* biodistribution studies in tumor-bearing mice.
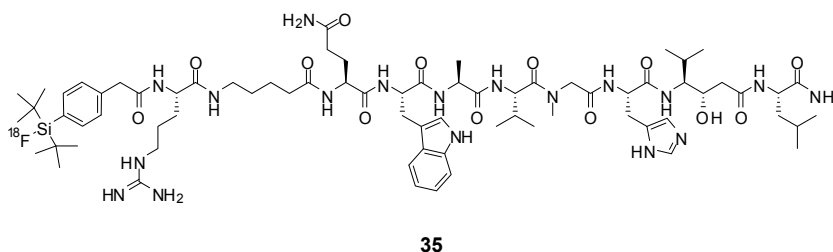
Thus, attempts were made to compensate the high lipophilicity of the organo-silicon moiety by introducing hydrophilic substituents into the peptide sequence in order to achieve a more favorable *in vivo* biodistribution of SiFA-derivatized peptides [38]. In order to increase the hydrophilicity of peptidic compounds, PEG and carbohydrate building blocks have been used before [42–44]. Thus, Tyr^3-octreotate derivatives were synthesized, comprising a SiFA moiety and a carbohydrate and/or a PEG moiety. The resulting peptide derivatives **36** and **37** (Figure 12) were radiolabeled, their

lipophilicity and *in vitro* binding affinities towards the Somatostatin receptors were determined, and their *in vivo* biodistribution characteristics determined and compared to the non-modified SiFA-Tyr[3]-octreotate **29** (Figure 12). The derivatization of the Tyr[3]-octreotate with hydrophilic building blocks showed only a minor influence on the binding affinities to the target receptors, resulting in potent target receptor binders while at the same time compensating, at least to some extent, the high lipophilicity of the organo-silicon moiety (log P_{OW}**36** = 1.23, log P_{OW}**37** = 0.96 *vs.* log P_{OW}**29** = 1.59). This positive effect was also reflected in the successful visualization of the tumor *in vivo* in an AR42J tumor-bearing mouse model by **37**, whereas the non-modified ^{18}F-SiFA-peptide **29** showed only a very low and unspecific accumulation in the tumor tissue due to its high lipophilicity [38].

Figure 12. Structures of ^{18}F-SiFA-TATE (**29**), ^{18}F-SiFA-Glc-TATE (**36**) and ^{18}F-SiFA-Glc-PEG-TATE (**37**).
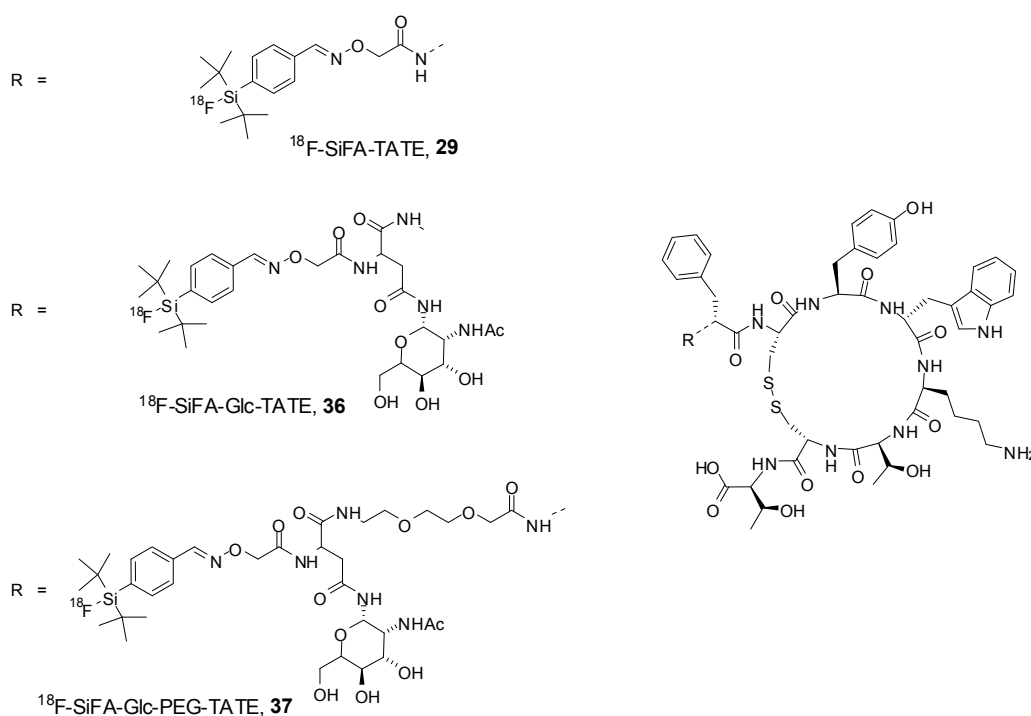
Thus, although many improvements have been made in the radiolabeling of peptides with ^{18}F using silicon building blocks carrying bulky substituents, some efforts still have to be undertaken to optimize the *in vivo* biodistribution properties of the resulting ^{18}F-silicon-derivatized peptides.

9. Protein Labeling

The successful labeling of proteins with the radionuclide ^{18}F has always been challenging. Unlike peptides, which are structurally manageable, proteins contain a vast number of side chain functionalities which cannot be masked by protecting groups to enable a direct one-step ^{18}F labeling strategy. Hence, the labeling of proteins requires prosthetic groups, small molecules which are ^{18}F-labeled prior to the actual protein labeling. These molecules bear functional groups, such as active esters, which react readily with nucleophilic groups in the protein via acylation. [^{18}F]SFB is currently

the most common protein labeling agent. Besides active esters, Click Chemistry has also been employed, especially the maleimide-thiol click reaction. Of all Si-^{18}F approaches, so far only the SiFA ^{19}F by ^{18}F-exchange chemistry has been used to develop small silicon-containing prosthetic groups for protein labeling. The first attempt to synthesize a SiFA-based active ester was made by Jurkschat and co-workers in 2009. The non-radioactive labeling precursors were obtained according to Figure 13 but could not be labeled with ^{18}F by isotopic exchange under basic labeling conditions. The active ester moiety was simply hydrolyzed during the isotopic exchange and no SiFA active ester could be isolated. Using a different strategy, rat serum albumin (RSA), a 64 kDa protein isolated from rat serum, was labeled with two different SiFA synthons, a maleimide-^{18}F-SiFA ([^{18}F]**11**) and a thiol-^{18}F-SiFA ([^{18}F]**4**) (Figure 13). In order to use the maleimide-SiFA, the protein was derivatized with 2-iminithiolane to provide additional thiol groups to react with the maleimide group of the SiFA synthon (Figure 13). In case of thiol-SiFA used for protein labeling, the protein was modified, complementary with sulfosuccinimidyl-4-(N-maleimidomethyl)cyclohexane-1-carboxylate sodium salt (sulfo-SMCC). Both SiFA prosthetic groups [^{18}F]**11** and [^{18}F]**4** readily reacted with the modified RSA via Click Chemistry and provided the ^{18}F-labeled proteins in good yields. This method is very convenient, since the number of derivatization sites introduced at the protein modification step (maleimide or thiol introduction) can be easily determined by Ellman's assay.

Figure 13. Kit-like labeling of RSA using two different SiFA sythons: A) sulfo-SMCC modified RSA reacts with thiol-SiFA (**[^{18}F]4**); B) 2-iminothiolane modified RSA reacts with maleimide-SiFA (**[^{18}F]11**).
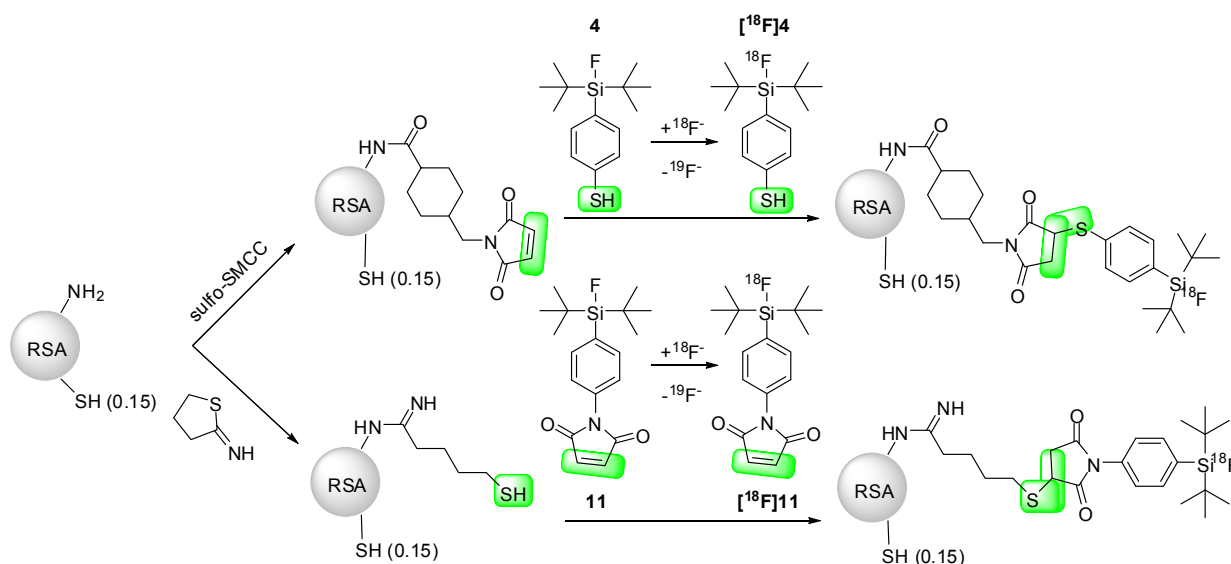
The labeled RSA was used in small animal PET imaging, visualizing the blood pool. However, one adverse feature of this strategy, despite being one of the most convenient procedures described so far, is that the proteins have to be modified before the actual labeling occurs. This requires certain special knowledge from the user and could be deemed as being less comfortable. To resolve this inconvenience, Schirrmacher and co-workers endeavored to mimic a well-known concept in bio-conjugation—the use of isothiocyanates for the modification and labeling of proteins. The goal of

their study was to develop a radioactive counterpart to fluorescein isothiocyanate which is the most commonly applied fluorescent labeling agent for lysine containing proteins. Following that idea, SiFA isothiocyanate (SiFA-NCS or SiFA-ITC) was synthesized and ^{18}F-labeled at room temperature via isotopic exchange [45]. The amount of SiFA used was very low (10–12 nmol) and the radiochemical yields were surprisingly high, keeping in mind that the isothiocyanate moiety is very labile. After 10 min reaction time, 95% of the introduced ^{18}F$^-$ was incorporated into the SiFA-NCS. The ^{18}F-SiFA-NCS reacts with primary amino functions of lysine residues. Three different proteins, varying in molecular weight (66–144 kDa), were labeled in radiochemical yields between 30–80%, depending on the SiFA/protein ratio. RSA was again chosen to serve as an *in vivo* blood pool imaging agent for PET. One shortcoming of this SiFA synthon is its inherent tendency towards hydrolysis and therefore associated challenging storage. The compound has to be meticulously stored under protecting gas and any exposure to humidity has to be avoided. Nevertheless, the use of isothiocyanates omits the necessity of modifying the protein but rather depends on lysine residues in the protein.

Figure 14. Radioactive labeling of RSA and other proteins (not shown) using (**A**) [^{18}F]SiFA-isothiocyante ([^{18}F]SiFA-ITC, **[^{18}F]7**), (**B**) [^{18}F]SiFB and (**C**) the non-silicon containing most frequently applied protein labeling synthon [^{18}F]SFB. (**D**) The PET images show the biodistribution of [^{18}F]SFB (a and a') and [^{18}F]SiFB (b and b') labeled RSA in rats (coronal plane sum images t = 5–60 min). The biodistribution was identical, validating the usefulness of [^{18}F]SiFB as an alternative labeling agent for proteins.
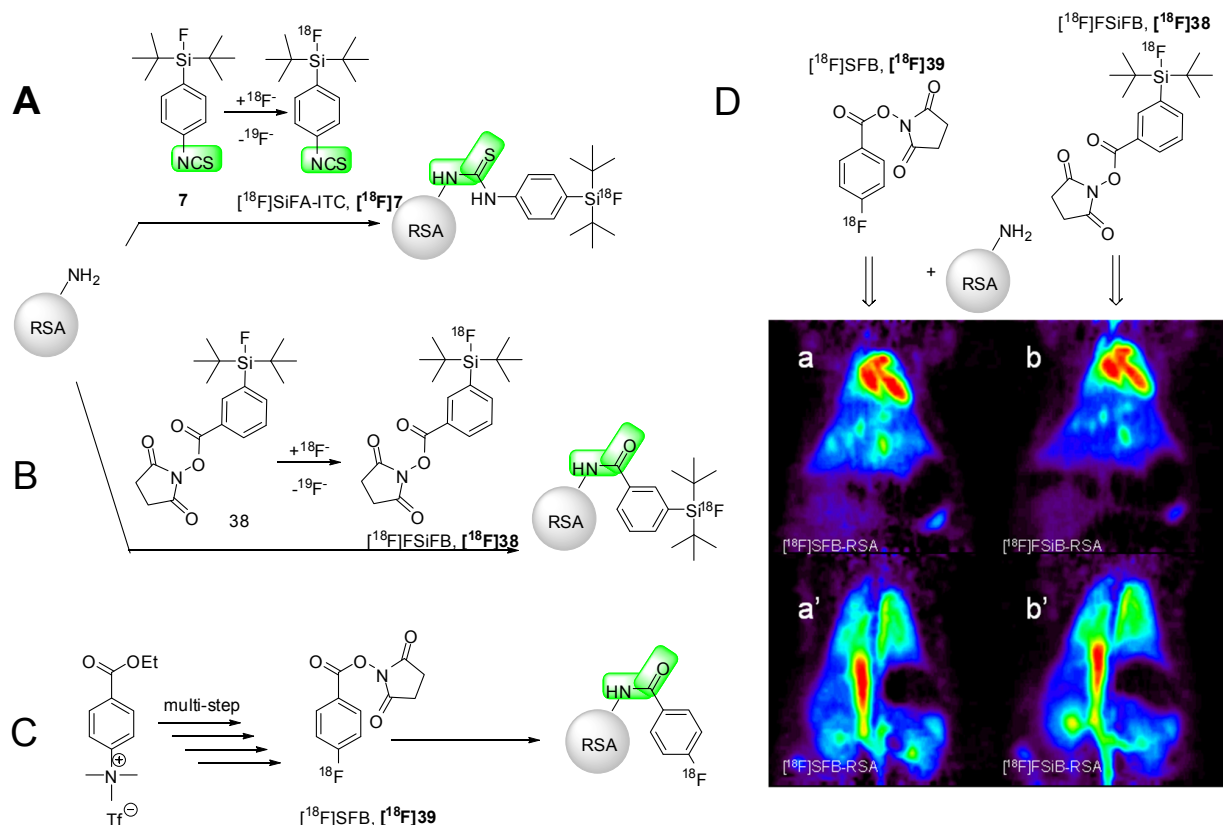
As already mentioned, by far the most common ^{18}F-labeling agent for proteins is [^{18}F]SFB. In contrast to ^{18}F-labeled SiFA active esters, the preparation of non-radioactive SiFA active esters has never posed a problem. The Si-F bond is stable under a great variety of reaction conditions and an active ester moiety, such as a succinimidyl ester, can be introduced without problems. The challenge, however, is to undertake the isotopic exchange reaction without disintegration of the highly reactive active ester moiety. The SiFA labeling so far described uses a highly basic labeling cocktail containing large amounts of carbonate ions in addition to [18]F[-]. Although not being an exceptionally good nucleophile under aqueous conditions, [18]F[-], in the presence of carbonate dissolved with Kryptofix2.2.2 to complexate the counter ion in dipolar aprotic solvents, is remarkably reactive. Under common labeling conditions, the [^{18}F]SiFA active esters could not be detected, either on radio-TLC, or on HPLC, but only the hydrolyzed products. Very recently, Kostikov and co-workers devised a modified composition of the ^{18}F-labeling solution. Strictly speaking, the isotopic exchange reaction on SiFAs does not mechanistically require a basic labeling environment. Thus, their hypothesis was that the basic ^{18}F-containing reaction mixture in acetonitrile can be simply neutralized by addition of a suitable acid. Indeed, the addition of oxalic acid to the labeling cocktail proved to be highly efficient and the isotopic exchange using SiFB (Figure 14B) proceeded without hydrolysis of the active ester moiety. [^{18}F]SiFB is very similar to the already mentioned SiFA active esters (*cf.* Figure 3). For stability reasons, the ester moiety was placed *meta* to the silicon atom, instead of *para*. The amount of oxalic acid added proved to be crucial. In all experiments, the less basic potassium oxalate had been used instead of carbonate and it was found that a ratio of oxalate/oxalic acid of 2:1 yielded the highest isotopic exchange yields. The reduction in complexity of synthesis and purification of [^{18}F]SiFB in comparison to [^{18}F]SFB was enormous. Depending on the [^{18}F]SiFB synthesis, if either a full batch of [18]F[-] or just an aliquot of [18]F[-] was used, 25–50 min of reaction time could be saved. No HPLC purification had to be performed. The synthesis merely requires a reaction vial and a solid phase extraction cartridge. The subsequent protein labeling was as efficient as that using [^{18}F]SFB. [^{18}F]SiFB, and [^{18}F]SFB labeled RSA were injected into healthy rats. The biodistribution of both proteins was identical (Figure 14D) which conclusively demonstrated the applicability of [^{18}F]SiFB as a labeling synthon for proteins.

## 10. Small Molecules

Although several examples of ^{18}F-radiolabeled peptides and proteins using the organo-silicon building block strategy for ^{18}F-introduction can be found, small biologically-active molecules have rarely been labeled using this approach. This can be attributed to the high lipophilicity exerted by the bulky hydrophobic substituents on the silicon core used to achieve a high *in vivo* stability of the Si-^{18}F-bond. This high lipophilicity can result in a dramatically altered *in vivo* biodistribution of the labeled substances, especially in the case of small molecules. Thus, examples for small molecules containing organo-silicon building blocks for the introduction of ^{18}F are rare, but some approaches have been described recently [46–48].

One example is the preparation of ^{18}F-labeled silicon-based nitromidazoles (Figure 15) that were designed as possible alternatives to the clinically relevant tracer [^{18}F]FMISO and intended for hypoxia-imaging [46]. The radiosynthesis of these compounds—bearing methyl, *iso*-propyl-,

phenyl- and naphthyl-moieties in order to stabilize the Si-^{18}F-bond—started from the corresponding alkoxy-silanes and gave good ^{18}F-incorporation yields at elevated temperatures of 75 °C for 20 min, but a final HPLC purification of the tracers was necessary.

Figure 15. Structures of [18]F- silicon-based nitromidazoles **40–43** intended for hypoxia-imaging.

40:	R = methyl
41:	R = *iso*propyl
42:	R = phenyl
43:	R = naphthyl
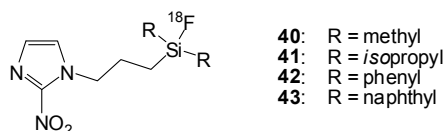
Stability studies confirmed the expected stability characteristics of the different ^{18}F-fluorinated compounds: a very low stability of **40** ($t_{1/2} < 5$'), a low stability of **42** ($t_{1/2} = 5$') and **41** ($t_{1/2} = 15$') and an at least moderate stability of **43** ($t_{1/2} = 130$'). Interestingly, and despite its short half-life, more favorable results could be obtained in the *in vivo* experiments in tumor-bearing animals with hypoxic tumor areas using **40** compared to **43**. In the case of **40**, hypoxic tumor areas could at least be visualized, despite a very high background activity, as confirmed by [^{18}F]FDG landmarking experiments, whereas in the case of **43**, only an unspecific uptake into the lungs was observed which was attributed to an accumulation of the tracer in the pulmonary capillaries. Thus, an optimization of the *in vivo* properties of the compounds regarding stability and biodistribution profile remains necessary.

Recently, attempts were made to radiolabel nucleosides and nucleotides using the silicon-^{18}F-labeling strategy [47]. In order to synthesize the labeling precursors, silicon building blocks, comprising azide and alkyne functionalities were synthesized, introduced into thymidine, derivatized accordingly via copper-catalyzed 1,3-dipolar cycloaddition, and subsequently radiolabeled with ^{18}F by an H against ^{18}F exchange reaction (Figure 16 shows the structures of the ^{18}F-labeled products).

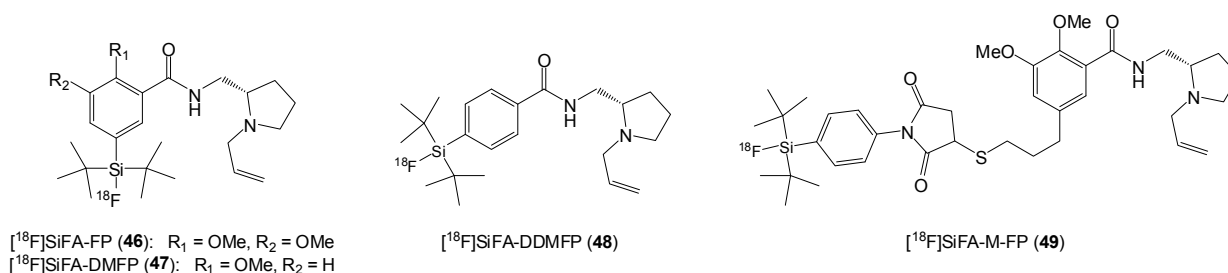**Figure 16.** Structures of the ^{18}F-labeled thymidine derivatives **44** and **45**.
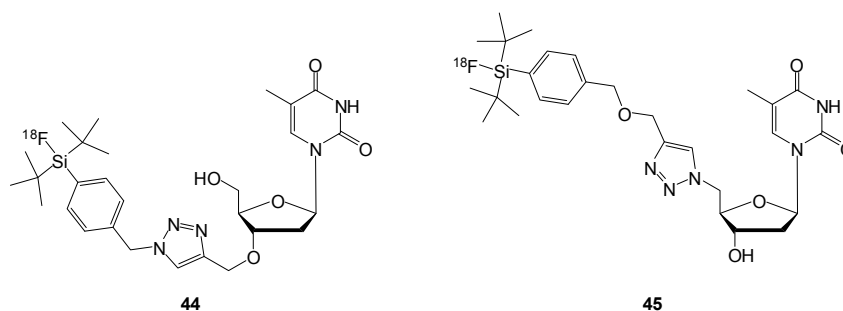
Starting from these mono-nucleosides, also model di-nucleotides and a model decameric oligodeoxynucleotide containing all four bases, were synthesized and the labeling conditions were optimized. As the H against ^{18}F-exchange reaction on the silicon core proceeds less efficiently than the isotopic exchange reaction, elevated temperatures were required to introduce the ^{18}F-label. Nevertheless, all substances—nucleosides, di-nucleotides and the decameric oligodeoxynucleotide— were compatible with the applied reaction temperatures of 60 °C, 165 °C and 100 °C, respectively,

neither affecting the phosphodiester linkage nor the purine bases. However, up to now, no *in vivo* data are available that would provide information about the biodistribution characteristics of such lipophilic nucleosides and nucleotides.

Another class of SiFA-building-block-containing small molecules described recently was that of organo-silicon-derivatized D$_2$-receptor ligands (Figure 17), derived from the clinically-relevant compounds [^{18}F]FP ([^{18}F]fallypride) and [^{18}F]DMFP ([^{18}F]desmethoxyfallypride) [48].

Figure 17. Structures of the ^{18}F-SiFA D$_2$-receptor ligands **46–49**.

[^{18}F]SiFA-FP (**46**): R$_1$ = OMe, R$_2$ = OMe
[^{18}F]SiFA-DMFP (**47**): R$_1$ = OMe, R$_2$ = H

[^{18}F]SiFA-DDMFP (**48**)

[^{18}F]SiFA-M-FP (**49**)

The synthesized ^{19}F-precursors were evaluated regarding their D$_2$-receptor affinities *in vitro*, showing less influence of the bulky SiFA-system on the receptor affinities than anticipated: SiFA-M-FP, SiFA-DMFP, SiFA-FP and SiFA-DDMFP showed K_i values of 4.2 nM, 13.6 nM, 33.0 nM and 62.7 nM, respectively, being in a comparable range to FP and DMFP that showed K_i values of 0.1 nM and 0.6 nM in the same assay. As anticipated, the derivative with a short linker and thus some distance between the binding motive and the SiFA moiety (**49**) showed the highest affinity to the target receptor. However, this compound gave only poor results in ^{18}F-labeling experiments, due to its limited stability. In contrast, the other derivatives **46–48** showed very favorable results in the labeling experiments, as high RCYs and SAs were synthesized within very short preparation times and showed high plasma stabilities. Again, the *in vivo* biodistribution properties remain to be determined.

11. Conclusions

The recent advent of silicon-^{18}F chemistry has already impressively demonstrated that novel labeling techniques in radiopharmaceutical sciences invigorate not only basic research, but also the development of clinically-oriented applications. The enumeration of different approaches towards new imaging agents on the basis of silicon-^{18}F bond formation presented in this overview is hopefully a prelude to a new generation of imaging agents for PET. The advancements in the field over a short period of time already improved the labeling of peptides and proteins. Small compounds still pose problems, especially with regard to the inherently high lipophilicity of all described organo-silicon building blocks so far. This issue becomes more pronounced with compounds of low molecular weight, because the effect of the organo-silicon building blocks on the compounds' overall lipophilicity weighs heavier. It cannot be concluded yet whether Si-^{18}F radiochemistry will be fully accepted by the radiopharmaceutical community. This holds true not only for silicon, but also for all of the other highly-innovative labeling approaches, including aluminum- as well as boron-^{18}F chemistry introduced most recently. As PET becomes more and more the most prominent *in vivo* imaging

modality, novel radiochemistry approaches will always be needed as a driving force to further advance all disciplines reliant on radiochemistry.

Conflict of Interest

The authors declare no conflict of interest.

References

1. Wahl, R.L.; Buchanan, J.W. *Principles and Practice of Positron Emission Tomography*; Lippincott Williams & Wilkins: Philadelphia, USA, 2002.
2. Cai, L.S.; Lu, S.Y.; Pike, V.W. Chemistry with [18F]fluoride ion. *Eur. J. Org. Chem.* **2008**, 2853–2873.
3. Schubiger, P.A.; Lehmann, L.; Friebe, M. *Chemistry—The Driving Force in Molecular Imaging*; Springer: Berlin Heidelberg, Germay, 2007; Volume 97, pp. 1291–1297.
4. Wester, H.J. *Munich Molecular Imaging Series*; Scintomics: Fürstenfeldbruck, Germany, 2010; Volume 1, pp. 5–74.
5. Ting, R.; Adam, M.J.; Ruth, T.J.; Perrin, D.M. Arylfluoroborates and alkylfluorosilicates as potential PET imaging agents: High-yielding aqueous biomolecular F-18-labeling. *J. Am. Chem. Soc.* **2005**, *127*, 13094–13095.
6. Ting, R.; Harwig, C.; auf dem Keller, U.; McCormick, S.; Austin, P.; Overall, C.M.; Adam, M.J.; Ruth, T.J.; Perrin, D.M. Toward [18F]-labeled aryltrifluoroborate radiotracers: *In vivo* Positron Emission Tomography imaging of stable aryltrifluoroborate clearance in mice. *J. Am. Chem. Soc.* **2008**, *130*, 12045–12055.
7. Keller, U.A.D.; Bellac, C.L.; Li, Y.; Lou, Y.M.; Lange, P.F.; Ting, R.; Harwig, C.; Kappelhoff, R.; Dedhar, S.; Adam, M.J.; Ruth, T.J.; Benard, F.; Perrin, D.M.; Overall, C.M. Novel matrix metalloproteinase inhibitor [18F]marimastat-aryltrifluoroborate as a probe for i*n vivo* Positron Emission Tomography imaging in cancer. *Cancer Res.* **2010**, *70*, 7562–7569.
8. McBride, W.J.; D'Souza, C.A.; Sharkey, R.M.; Karacay, H.; Rossi, E.A.; Chang, C.H.; Goldenberg, D.M. Improved 18F labeling of peptides with a fluoride-aluminum-chelate complex. *Bioconjugate Chem.* **2010**, *21*, 1331–1340.
9. McBride, W.J.; Sharkey, R.M.; Karacay, H.; D'Souza, C.A.; Rossi, E.A.; Laverman, P.; Chang, C.H.; Boerman, O.C.; Goldenberg, D.M. A novel method of 18F radiolabeling for PET. *J. Nucl. Med.* **2009**, *50*, 991–998.
10. Laverman, P.; McBride, W.J.; Sharkey, R.M.; Eek, A.; Joosten, L.; Oyen, W.J.G.; Goldenberg, D.M.; Boerman, O.C. A novel facile method of labeling octreotide with 18F-fluorine. *J. Nucl. Med.* **2010**, *51*, 454–461.
11. McBride, W.J.; D'Souza, C.A.; Karacay, H.; Sharkey, R.M.; Goldenberg, D.M. New lyophilized kit for rapid radiofluorination of peptides. *Bioconjugate Chem.* **2012**, *23*, 538-547.
12. McBride, W.J.; D'Souza, C.A.; Sharkey, R.M.; Goldenberg, D.M. The radiolabeling of proteins by the [18F]AlF method. *Appl. Radiat. Isotopes* **2012**, *70*, 200–204.

13. Mu, L.; Schubiger, A.P.; Ametamey, S.M. [18F]Fluorosilicon- and [18F]Fluoroboron-based biomolecules for PET imaging. *Curr. Radiophar.* **2010**, *3*, 224–242.

14. Ametamey, S.M.; Honer, M.; Schubiger, P.A. Molecular imaging with PET. *Chem. Rev.* **2008**, *108*, 1501–1516.

15. Schirrmacher, R.; Wangler, C.; Schirrmacher, E. Recent developments and trends in 18F-radiochemistry: Syntheses and applications. *Mini-Rev. Org. Chem.* **2007**, *4*, 317–329.

16. Smith, G.E.; Sladen, H.L.; Biagini, S.C.G.; Blower, P.J. Inorganic approaches for radiolabelling biomolecules with fluorine-18 for imaging with Positron Emission Tomography. *Dalton Trans* **2011**, *40*, 6196–6205.

17. Miller, P.W.; Long, N.J.; Vilar, R.; Gee, A.D. Synthesis of C-11, F-18, O-15, and N-13 radiolabels for Positron Emission Tomography. *Angew Chem. Int. Ed.* **2008**, *47*, 8998–9033.

18. Mamat, C.; Ramenda, T.; Wuest, F.R. Recent applications of click chemistry for the synthesis of radiotracers for molecular imaging. *Mini-Rev. Org. Chem.* **2009**, *6*, 21–34.

19. Gens, T.A.; Wethington, J.A.; Brosi, A.R. The exchange of F-18 between metallic fluorides and silicon tetrafluoride. *J. Phys. Chem.-Us* **1959**, *62*, 1593–1593.

20. Poole, R.T.; Winfield, J.M. Radiotracers in fluorine chemistry. 4. F-18 exchange between labeled alkylfluorosilanes and fluorides, or fluoride methoxides, of Tungsten(Vi), Molybdenum(Vi), Tellurium(Vi), and Iodine(V). *J. Chem. Soc. Dalton* **1976**, 1557–1560.

21. Winfield, J.M. Preparation and use of 18-fluorine labeled inorganic-compounds. *J. Fluorine Chem.* **1980**, *16*, 1–17.

22. Sanyal, D.K.; Winfield, J.M. Radiotracers in fluorine chemistry. 8. F-18 exchange-reactions involving Uranium(VI) or Uranium(V) fluorides—Evidence for surface complexation and comparisons with ligand-exchange reactions. *J. Fluorine Chem.* **1984**, *24*, 75–92.

23. Rosenthal, M.S.; Bosch, A.L.; Nickles, R.J.; Gatley, S.J. Synthesis and some characteristics of no-carrier added [18F]fluorotrimethylsilane. *Int. J. Appl. Radiat. Isotop.* **1985**, *36*, 318–319.

24. Gatley, S.J. Rapid production and trapping of [18F] Fluorotrimethylsilane, and its use in nucleophilic fluorine-18 labeling without an aqueous evaporation step. *Appl. Radiat. Isotope.* **1989**, *40*, 541–544.

25. Hamacher, K.; Coenen, H.H.; Stocklin, G. Efficient stereospecific synthesis of no-carrier-added 2-[18F]-Fluoro-2-deoxy-D-glucose using aminopolyether supported nucleophilic-substitution. *J. Nucl. Med.* **1986**, *27*, 235–238.

26. Walsh, J.C.; Fleming, L.M.; Satyamurthy, N.; Barrio, J.R.; Phelps, M.E.; Gambhir, S.S.; Toyokuni, T. Application of silicon-fluoride chemistry for the development of amine-reactive F-18-labeling agents for biomolecules. *J. Nucl. Med* **2000**, *41*, 249p-249p.

27. Choudhry, U.; Martin, K.E.; Biagini, S.; Blower, P.J. Alkoxysilane groups for instant labeling of biomolecules with 18F. *Nucl. Med. Commun.* **2006**, *27*.

28. Schirrmacher, R.; Bradtmöller, G.; Schirrmacher, E.; Thews, O.; Tillmanns, J.; Siessmeier, T.; Buchholz, H.G.; Bartenstein, P.; Wängler, B.; Niemeyer, C.M.; Jurkschat, K. 18F-labeling of peptides by means of an organosilicon-based fluoride acceptor. *Angew Chem. Int. Ed.* **2006**, *45*, 6047–6050.

29. Mu, L.J.; Hohne, A.; Schubiger, R.A.; Ametamey, S.M.; Graham, K.; Cyr, J.E.; Dinkelborg, L.; Stellfeld, T.; Srinivasan, A.; Voigtmann, U.; Klar, U. Silicon-based building blocks for one-step ^{18}F-radiolabeling of peptides for PET imaging. *Angew Chem. Int. Ed.* **2008**, *47*, 4922–4925.

30. Schirrmacher, E.; Wangler, B.; Cypryk, M.; Bradtmoller, G.; Schafer, M.; Eisenhut, M.; Jurkschat, K.; Schirrmacher, R. Synthesis of p-(Di-tert-butyl[18]f]fluorosilyl)benzaldehyde ([^{18}F]SiFA-A) with high specific activity by isotopic exchange: A convenient Labeling synthon for the ^{18}F-labeling of n-amino-oxy derivatized peptides. *Bioconjugate Chem.* **2007**, *18*, 2085–2089.

31. Tietze, L.F.; Schmuck, K. SiFA azide: A new building block for PET imaging using click chemistry. *Synlett* **2011**, 1697–1700.

32. Kostikov, A.P.; Iovkova, L.; Chin, J.; Schirrmacher, E.; Wangler, B.; Wangler, C.; Jurkschat, K.; Cosa, G.; Schirrmacher, R. *N*-(4-(di-tert-butyl[(18)F]fluorosilyl)benzyl)-2-hydroxy-N, *N*-dimethylethylammonium bromide ([^{18}F]SiFAN+Br−): A novel lead compound for the development of hydrophilic SiFA-based prosthetic groups for (18)F-labeling. *J. Fluorine Chem.* **2011**, *132*, 27–34.

33. Hohne, A.; Yu, L.; Mu, L.J.; Reiher, M.; Voigtmann, U.; Klar, U.; Graham, K.; Schubiger, P.A.; Ametamey, S.M. Organofluorosilanes as model compounds for ^{18}F-labeled Silicon-based PET tracers and their hydrolytic stability: Experimental data and theoretical calculations (PET = Positron Emission Tomography). *Chem. Eur. J.* **2009**, *15*, 3736–3743.

34. Kiesewetter, D.O.; Jacobson, O.; Lang, L.X.; Chen, X.Y. Automated radiochemical synthesis of [^{18}F]FBEM: A thiol reactive synthon for radiofluorination of peptides and proteins. *Appl. Radiat. Isotopes* **2011**, *69*, 410–414.

35. Speranza, A.; Ortosecco, G.; Castaldi, E.; Nardelli, A.; Pace, L.; Salvatore, M. Fully automated synthesis procedure of 4-[^{18}F]fluorobenzaldehyde by commercial synthesizer: Amino-oxi peptide labelling prosthetic group. *Appl. Radiat. Isotopes* **2009**, *67*, 1664–1669.

36. Thonon, D.; Goblet, D.; Goukens, E.; Kaisin, G.; Paris, J.; Aerts, J.; Lignon, S.; Franci, X.; Hustinx, R.; Luxen, A. Fully automated preparation and conjugation of *N*-succinimidyl 4-[^{18}F]fluorobenzoate ([^{18}F]SFB) with RGD peptide using a GE FASTlab (TM) synthesizer. *Mol. Imaging Biol.* **2011**, *13*, 1088–1095.

37. D'Souza, C.A.; McBride, W.J.; Sharkey, R.M.; Todaro, L.J.; Goldenberg, D.M. High-yielding aqueous ^{18}F-labeling of peptides via Al[18]F chelation. *Bioconjugate Chem.* **2011**, *22*, 1793–1803.

38. Wängler, C.; Waser, B.; Alke, A.; Iovkova, L.; Buchholz, H.G.; Niedermoser, S.; Jurkschat, K.; Fottner, C.; Bartenstein, P.; Schirrmacher, R.; Reubi, J.C.; Wester, H.J.; Wängler, B. One-step ^{18}F-labeling of carbohydrate-conjugated octreotate-derivatives containing a Silicon-Fluoride-Acceptor (SiFA): In vitro and in vivo evaluation as tumor imaging agents for Positron Emission Tomography (PET). *Bioconjugate Chem.* **2010**, *21*, 2289–2296.

39. Iovkova, L.; Konning, D.; Wangler, B.; Schirrmacher, R.; Schoof, S.; Arndt, H.D.; Jurkschat, K. SiFA-modified phenylalanine: A key compound for the efficient synthesis of ^{18}F-labelled peptides. *Eur. J. Inorg. Chem.* **2011**, 2238–2246.

40. Höhne, A.; Mu, L.; Honer, M.; Schubiger, P.A.; Ametamey, S.M.; Graham, K.; Stellfeld, T.; Borkowski, S.; Berndorff, D.; Klar, U.; Voigtmann, U.; Cyr, J.E.; Friebe, M.; Dinkelborg, L.; Srinivasan, A. Synthesis, ^{18}F-labeling, and *in vitro* and *in vivo* studies of bombesin peptides modified with silicon-based building blocks. *Bioconjugate Chem.* **2008**, *19*, 1871–1879.

41. Balentova, E.; Collet, C.; Lamande-Langle, S.; Chretien, F.; Thonon, D.; Aerts, J.; Lemaire, C.; Luxen, A.; Chapleur, Y. Synthesis and hydrolytic stability of novel 3-[[^{18}F]fluoroethoxybis (1-methylethyl)silyl]propanamine-based prosthetic groups. *J. Fluorine Chem.* **2011**, *132*, 250–257.

42. Schottelius, M.; Rau, F.; Reubi, J.C.; Schwaiger, M.; Wester, H.A. Modulation of pharmacokinetics of radioiodinated sugar-conjugated somatostatin analogues by variation of peptide net charge and carbohydration chemistry. *Bioconjugate Chem.* **2005**, *16*, 429–437.

43. Schottelius, M.; Wester, H.J.; Reubi, J.C.; Senekowitsch-Schmidtke, R.; Schwaiger, M. Improvement of pharmacokinetics of radioiodinated Tyr[3]-octreotide by conjugation with carbohydrates. *Bioconjugate Chem.* **2002**, *13*, 1021–1030.

44. Antunes, P.; Ginj, M.; Walter, M.A.; Chen, J.H.; Reubi, J.C.; Maecke, H.R. Influence of different spacers on the biological profile of a DOTA-somatostatin analogue. *Bioconjugate Chem.* **2007**, *18*, 84–92.

45. Rosa-Neto, P.; Wängler, B.; Iovkova, L.; Boening, G.; Reader, A.; Jurkschat, K.; Schirrmacher, E. [^{18}F]SiFA-isothiocyanate: A new highly effective radioactive labeling agent for lysine-containing proteins. *Chembiochem* **2009**, *10*, 1321–1324.

46. Bohn, P.; Deyine, A.; Azzouz, R.; Bailly, L.; Fiol-Petit, C.; Bischoff, L.; Fruit, C.; Marsais, F.; Vera, P. Design of silicon-based misonidazole analogues and ^{18}F-radiolabelling. *Nucl. Med. Biol.* **2009**, *36*, 895–905.

47. Schulz, J.; Vimont, D.; Bordenave, T.; James, D.; Escudier, J.M.; Allard, M.; Szlosek-Pinaud, M.; Fouquet, E. Silicon-based chemistry: An original and efficient one-step approach to [^{18}F]-nucleosides and [^{18}F]-oligonucleotides for PET imaging. *Chem. Eur. J.* **2011**, *17*, 3096–3100.

48. Iovkova-Berends, L.; Wangler, C.; Zoller, T.; Hofner, G.; Wanner, K. T.; Rensch, C.; Bartenstein, P.; Kostikov, A.; Schirrmacher, R.; Jurkschat, K.; Wangler, B. *t*-Bu$_2$SiF-derivatized D$_2$-receptor ligands: The first SiFA-containing small molecule radiotracers for target-specific PET-imaging. *Molecules* **2011**, *16*, 7458–7479.

Article

Application of Liquid-Phase Direct Fluorination: Novel Synthetic Methods for a Polyfluorinated Coating Material and a Monomer of a Perfluorinated Polymer Electrolyte Membrane

Takashi Okazoe [1],*, Daisuke Shirakawa [2] and Koichi Murata [1]

[1] Research Center, Asahi Glass Co., Ltd., 1150 Hazawa-cho, Kanagawa-ku, Yokohama 221-8755, Japan; E-Mail: koichi-murata3@agc.com

[2] Asahi Glass Co., Ltd., 1-5-1 Marunouchi, Chiyoda-ku, Tokyo 100-8405, Japan; E-Mail: daisuke-sirakawa@agc.com

* Author to whom correspondence should be addressed; E-Mail: takashi-okazoe@agc.com; Tel.: +81-45-374-7324; Fax: +81-45-374-8848.

Abstract: A new polyfluorinated anti-staining coating material $CF_3O(CF_2CF_2O)_xCF_2\text{-}CONHCH_2CH_2CH_2Si(OCH_3)_3$ has been developed by utilizing the PERFECT method, which employs a liquid-phase direct fluorination reaction with elemental fluorine as a key step. Direct fluorination of a partially-fluorinated ester, which was prepared from a non-fluorinated poly(ethylene glycol) and a perfluorinated acyl fluoride, followed by methanolysis, gave the perfluorinated corresponding compound, which was led to the coating material for surface treating agents, and the methyl ester of the starting perfluorinated acyl fluoride. Application to the synthesis of a new perfluorinated bifunctional sulfonate monomer $CF_2{=}CFOCF_2CF_2CF_2OCF(CF_2SO_2F)_2$ for polymer electrolyte membranes (PEMs) of fuel cells was also developed.

Keywords: direct fluorination; anti-staining coating; surface treating; polymer electrolyte membrane; fuel cell

1. Introduction

Nowadays, organofluorine compounds are essential materials, especially in recent IT, electronics, and medical applications [1]. For example, the low surface energy of an organofluorine compound leads to water repellent and oil repellent properties, so that it is utilized as surface treating agents for water-and-oil repellent film. Therefore, it is expected that an anti-staining coating material for glass, for example, for automobiles or displays (a liquid crystal display, a CRT display, a projection display, a plasma display, an EL display or the like), could be achieved by an organofluorine compound. One such compound **1** may be a candidate [2,3].

$$CF_3(CF_2)_7(CH_2)_2SiX_3 \qquad [X = OCH_3, NCO] \qquad \text{Compound } \mathbf{1}$$
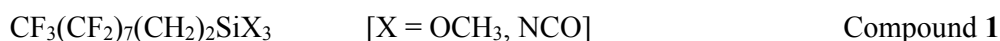
When the compound **1** is applied to the surface of a substrate, the hydrolyzable groups are hydrolyzed by hydroxyl groups of the substrate or moisture on the substrate to form silanol groups. Once the silanol groups are bonded to the substrate, perfluoroalkyl groups will be oriented on the atmosphere side, so that the coating film made of the compound **1** exhibits water repellency [4].

However, as perfluoroalkyl groups are highly crystalline and stiff, the coating film made of the compound **1** does not have enough efficiency for the removal of oil-and-fat stains. To solve the problem, a compound having a perfluoropolyether group **2** was reported [5].

$$CF_3CF_2CF_2O-(CF_2CF_2CF_2O)_n-CF_2CF_2(CH_2)_3Si(OCH_3)_3 \qquad \text{Compound } \mathbf{2}$$

The perfluoropolyether (PFPE) group has a flexible structure, because stiff perfluoroalkyl groups are separated by oxygen atoms and C-O-C bonding have high mobility, so that the coating film made of the compound **2** is excellent in its efficiency in removing oil-and-fat stains, and also has water and oil repellency.

However, the mobility of the PFPE groups in **2** cannot be regarded as sufficient, and the efficiency for removal of oil-and-fat stains is not enough, because the ratio of oxygen atoms to carbon atoms in the PFPE groups is still small. From the viewpoint of molecular design, $-(CF_2CF_2O)-$ as a repeating unit is ideal. However, there has not been a synthetic method for creating such a molecule, while it is possible to utilize the industrial intermediate of fluorinated oil to synthesize **2**.

An organofluorine compound also shows chemical and thermal stability, derived from the nature of a C-F bond. Although highly polarized, the C-F bond gains stability from the resultant electrostatic attraction between C and F atoms [6]. Thus, because of their high thermal and chemical stability and conductivity, perfluorinated sulfonic acid ionomers are often used in polymer electrolyte membranes (PEMs) of fuel cells [7],. Their performance is, however, still not enough.

To achieve much higher conductivity, it is necessary to increase the number of sulfonyl groups per unit. On the other hand, PEMs should have a certain mechanical strength to assemble membrane electrode assemblies. In the event that conventional monosulfonated monomers are increasingly used to raise this number, the copolymer obtained will have many branches, and the mechanical strength of the PEM from the copolymer decreases. A bifunctional monomer is expected to overcome this dilemma. However, there has not been a feasible synthetic method to realize such a molecule.

On the other hand, we have reported an entirely new synthetic method for perfluorinated molecules, the PERFECT (PERFluorination of an Esterified Compound then Thermolysis) process [8], which

makes it possible to create new fluorinated compounds because it utilizes organic synthesis in hydrocarbon molecules. For example, a nonfluorinated primary alcohol can be converted to the corresponding perfluorinated acyl fluoride (Scheme 1). PFPE lubricants for hard disk drive (HDD) [9] Afluid®, PFPE surfactants [10] and perfluoroalkanesulfonyl fluorides for ion-exchange membranes [11] have all been synthesized by employing the PERFECT process. Thus, it was considered to be possible to synthesize the molecules mentioned above by utilizing this process.

Scheme 1. The PERFECT process.
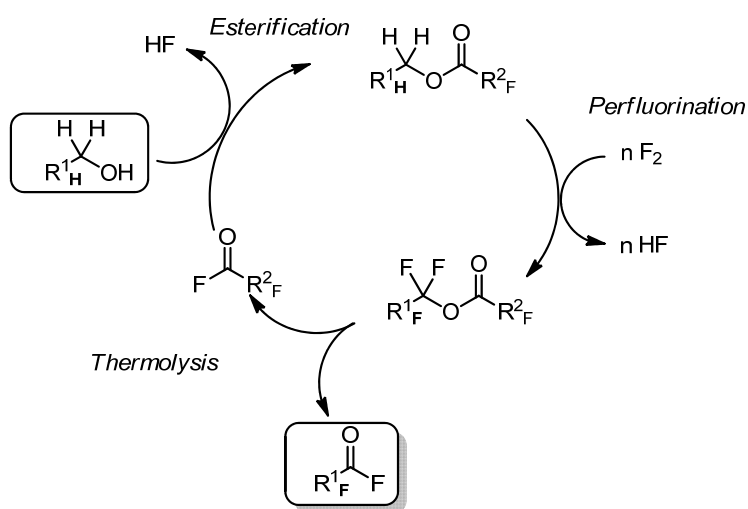
Here, we report the synthesis of a PFPE derivative, which possesses $-(CF_2CF_2O)-$ as a repeating unit, that is, $CF_3O(CF_2CF_2O)_xCF_2CONHCH_2CH_2CH_2Si(OCH_3)_3$ (**3**), and the synthesis of a perfluorobis(alkanesulfonyl) monomer $CF_2=CFOCF_2CF_2CF_2OCF(CF_2SO_2F)_2$ (**4**). The evaluation of the former on water and oil repellency and anti-staining property is also mentioned.

As for the PFPE derivative **3**, poly(ethylene glycol) monomethyl ether (**5**) is employed as a starting material in Scheme 1. The target, perfluorobis(alkanesulfonyl) monomer **4**, is considered to be synthesized by utilizing the PERFECT process according to the retrosynthesis shown in Scheme 2.

Scheme 2. Retrosynthetic analysis of perfluorobis(alkanesulfonyl) monomer.
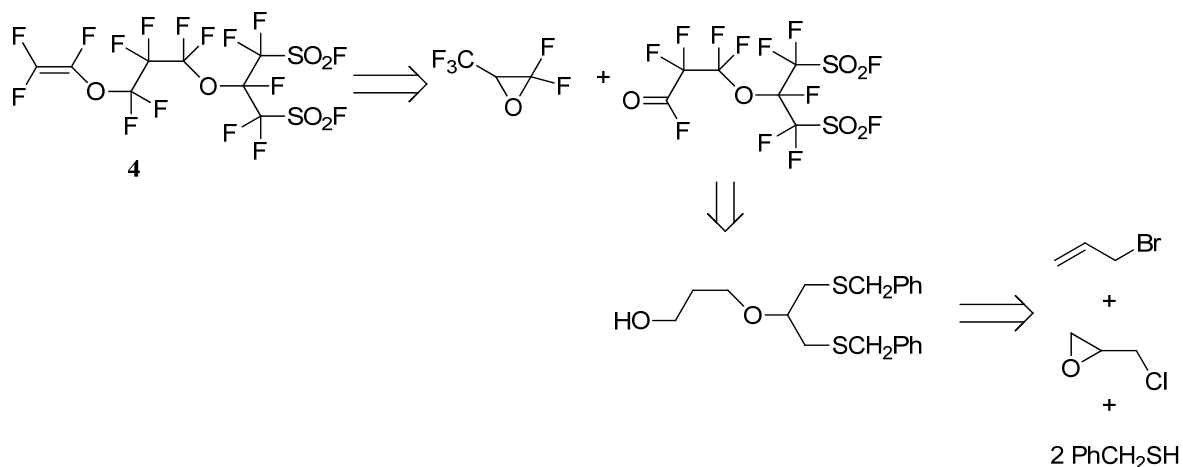
2. Experimental Section

2.1. General

All boiling points were not corrected. IR spectra were recorded on a Nicolet Impact 410 spectrometer. NMR spectra were obtained on a JEOL AL-300 or EX-400 (tetramethylsilane as internal standard for ^{1}H and ^{13}C, and trichlorofluoromethane for ^{19}F). High resolution mass spectra were obtained on a JEOL SX-102A coupled to a HP 5890 with a 60 m capillary column, J&W DB1301.

Average molecular weight (Mn) number and average molecular weight (Mw) weight were measured by gel permeation chromatography (GPC). A solvent mixture of R225 (Dichloropentafluoropropane, ASAHIKLIN® AK-225G, available from Asahi Glass Co., Ltd.) and hexafluoroisopropyl alcohol (HFIP) (AK-225G/HFIP=99/1 volume ratio) was used as a mobile phase. As the column for analysis, one having two PL-gel MIXED-E (Polymer Laboratories Ltd.) connected in series was used. As a detector, an evaporation light scattering detector (ELSD, Shimazu Co.) was used, and GPC was measured at a column temperature of 37 °C at a mobile phase flow rate of 1.0 mL/min.

As standard samples for measuring the molecular weight, five types of perfluoropolyethers having molecular weight distributions (Mw/Mn) of less than 1.1 and different molecular weights between 1,300 and 10,000.

Elemental fluorine was generated by Fluorodec^{TM} 30, Fluoro Gas (UK). *Elemental fluorine is a highly toxic and corrosive gas, and may cause an explosion on contact with organic compounds in the vapor-phase. Extreme care must be taken when handling! Hydrogen fluoride (bp. 19.5 °C), which evolved in both the liquid and vapor phases during the reaction, are also highly corrosive and cause severe burns on skin contact. Care must be taken! Prior to use, all hydrocarbon greases must be removed and apparatus gradually passivated with elemental fluorine.*

1,1,2-trichlorotrifluoroethane (R113: CCl_2FCClF_2) was used as a solvent in the fluorination reaction on a small scale. Although the use of R113 is regulated, we give experimental examples with it for convenience, because it is still much more cheaply available (Aldrich) than other solvents. *Care must be taken in order to avoid environment emission!*

Poly(ethylene glycol) monomethyl ether (**5**, Uniox M-400: $CH_3O–(CH_2CH_2O)_n–H$ average Mn 400. NOF Co.) was employed as the starting alcohol for the PFPE derivative **3**. Other reagents were obtained from Kanto Chemicals (Japan). Commercially obtained materials were used as received unless otherwise noted. All reactions sensitive to oxygen and/or moisture were conducted under nitrogen atmosphere with magnetic stirring. For large scale column chromatography, a Biotage Flash 150M pre-packed column (KP-Sil silica, 15 cm ID × 30 cm long) was used.

2.2. Typical Procedure for the Anti-staining Coating Material

2.2.1. Synthesis of the Anti-staining Coating Material (Scheme 3)

$CH_3O\text{-}(CH_2CH_2O)_nC(O)\text{-}CF(CF_3)OCF_2CF(CF_3)OCF_2CF_2CF_3$ (**7**)
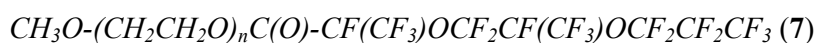
Prior to use, all glass flasks were oven dried at 120 °C. A mixture of **5** (25.0 g, 62.5 mmol), R225 (20.0 g, 98.5 mmol), NaF (1.20 g, 28.6 mmol) and pyridine (1.60 g, 20.2 mmol) was vigorously stirred

in a flask at under 10 °C. Subsequently, perfluoro(2,5-dimethyl-3,6-dioxanonanoyl) fluoride (**6**, 46.6 g, 93.5 mmol) was added to the flask over a period of 3.0 h while maintaining the internal temperature to be no higher than 5 °C. After completion of the addition, the mixture was stirred at 50 °C for 12 h and at room temperature for 24 h. The crude liquid was filtered under reduced pressure and dried for 12 h in a vacuum drier at 50 °C. The crude liquid was then dissolved in R225 (100 mL) and washed three times with a saturated sodium hydrogen carbonate aqueous solution (1,000 mL). To the organic phase, magnesium sulfate (1.0 g) was added, followed by stirring for 12 h, and removed by filtration under pressure. From the recovered liquid, R225 was evaporated to obtain **7** (56.1 g, 62.0 mmol, 99.0%, average value of n: 7.3) which was liquid at room temperature; ^{1}H-NMR (300.4 MHz, CDCl$_3$) δ (ppm): 3.50 (m, 3H, CH$_3$), 3.60–3.80 (m, 2H, OCH$_2$), 4.50–4.65 (m, 2H, *CH$_2$*CH$_2$OCO); ^{19}F-NMR (282.7 MHz, CDCl$_3$) δ (ppm): −79.5 (3F, CF$_3$), −80.0 (5F, CF$_2$*CF$_2$*CF$_3$), −82.5 to −85.0 (5F, OCF$_2$, CF$_3$), −129.2 (2F, *CF$_2$*CF$_2$CF$_3$), −131.5 (1F, OCOCF), −144.5 (1F, CFO).

CF$_3$O-(CF$_2$CF$_2$O)$_n$C(O)-CF(CF$_3$)OCF$_2$CF(CF$_3$)OCF$_2$CF$_2$CF$_3$ (**8**)

Prior to use, all hydrocarbon greases must be removed and the apparatus must be gradually passivated with elemental fluorine. Into a 3,000 mL hastelloy autoclave, R113 (1,560 g, 8.32 mol) was stirred at 25 °C. At a gas outlet of the autoclave, a condenser held at 20 °C, a NaF pellet-packed layer and a condenser held at −20 °C were connected in series. Further, a liquid-returning line was installed to return a liquid condensed by the condenser held at −20 °C to the autoclave.

Nitrogen gas was supplied for 1.0 h into the autoclave, and then fluorine gas, diluted to 10% by nitrogen gas, (hereafter referred to as 10% fluorine in nitrogen) was supplied for one hour at a flow rate of 24.8 L/h. Then, a solution of **7** (27.5 g, 31.3 mmol), dissolved in R113 (1,350 g, 7.20 mol), was injected over a period of 30 h into the autoclave, while supplying 10% fluorine in nitrogen at the same flow rate. Then, R113 (12 mL) was injected at 40 °C into the autoclave, while supplying 10% fluorine in nitrogen at the same flow rate. Then, 1% benzene in R113 (6 mL) was injected. Further, 10% fluorine in nitrogen was supplied for 1.0 h and then, nitrogen gas was supplied for 1.0 h. Then, the solvent was removed by vacuum drying at 60 °C for 6.0 h to obtain liquid **8** (45.4 g, 29.6 mmol, 94.6%). From the results of the NMR analysis of the compound, it was confirmed that 99.9% of the total number of hydrogen atoms in **7** were substituted by fluorine atoms, that is, **8** was the main component (average value of n: 7.1); ^{19}F-NMR (282.7 MHz, R113, internal standard for quantitative determination: hexafluorobenzene) δ (ppm) : −54.9 (3F, CF$_3$O), −79.5 (3F, CF$_3$), −80.0 (5F, CF$_2$*CF$_2$*CF$_3$), −82.5 to −85.0 (5F, OCF$_2$, CF$_3$), −87.5 (2F, OCF$_2$), −89.7 (2F, *CF$_3$*OCF$_2$), −91.5 (2F, CF$_2$OCO*CF*), −129.2 (2F, *CF$_2$*CF$_2$*CF$_3$*), −131.5 (1F, *CF$_2$*OCOCF), −144.5 (1F, CFO).

CF$_3$O-(CF$_2$CF$_2$O)$_{n-1}$CF$_2$COOCH$_3$ (**9**)

In a 300 mL egg-plant type PTFE flask, methanol (40.0 g, 1.25 mmol), NaF (5.60 g, 133 mmol) and R225 (50.0 g, 246 mmol) were stirred in nitrogen. Compound **8** (43.5g, 28.3mmol) was added, followed by vigorous stirring while bubbling nitrogen at room temperature for 8 h. The excess methanol and CH$_3$OC(O)-CF(CF$_3$)OCF$_2$CF(CF$_3$)OCF$_2$CF$_2$CF$_3$ that formed were distilled off by a vacuum pump installed at the condenser tube. After 24 h, liquid **9** (26.8 g, 25.5 mmol, 90.3%) was obtained. ^{1}H-NMR (300.4 MHz, R-113, internal standard for quantitative determination: nitrobenzene)

δ (ppm): 3.88 (m, 3H, CF$_2$COOCH$_3$); ^{19}F-NMR (282.7 MHz, R113, internal standard for quantitative determination: hexafluorobenzene) δ (ppm) : −54.9 (3F, CF$_3$O), −77.4 (2F, CF$_2$COOCH$_3$), −87.5 (2F, OCF$_2$), −89.7 (2F, *CF$_3$*OCF$_2$).

The molecular weight (Mn) of obtained **9** was 1718, and the molecular weight distribution was 1.11.

CF$_3$O(CF$_2$CF$_2$O)$_{n-1}$CF$_2$CONHCH$_2$CH$_2$CH$_2$Si(OCH$_3$)$_3$ (**3**)

In a 100 mL round-bottomed flask, a mixture of **9** (33.1 g, 31.6 mmol) and 3-trimethoxysilylpropylamine (**10**, 5.80 g, 32.3 mmol) were stirred at room temperature for 2 h. Then, unreacted **10** and by-product methanol were distilled off under reduced pressure to obtain **3** (32.3 g, 27.0 mmol) which was liquid at room temperature. From the results of the NMR analysis of the compound, it was confirmed that 98.0 mol% of -CF$_2$C(O)OCH$_3$ in **9** was converted to –CF$_2$C(O)NHCH$_2$CH$_2$CH$_2$Si(OCH$_3$)$_3$.

^{1}H-NMR (300.4 MHz, R113) δ (ppm) : 0.51 (m, 2H, CH$_2$Si), 1.60 (m, 2H, *CH$_2$*CH$_2$*CH$_2$*), 3.41 (2H, CF$_2$CONHCH$_2$), 3.67 (m, 3H, OCH$_3$), 7.20 (m, 1H, NH); ^{19}F-NMR (282.65 MHz, R113) δ (ppm) : −54.9 (3F, CF$_3$O), −77.4 (2F, CF$_2$COOCH$_3$), −87.5 (2F, OCF$_2$), −89.7 (2F, *CF$_3$* OCF$_2$).

The molecular weight (Mn) of **3** was 1072, and the molecular weight distribution was 1.33.

2.2.2. Evaluation of Anti-staining Performance

After synthesis, **3** was carried out to assess anti-staining performance compared with a conventional anti-staining material C$_6$F$_{13}$C$_2$H$_4$Si(OCH$_3$)$_3$ (**1a**). Both **3** and **1a** were applied on glass by dip coating in a dilute solution, as described below.

Glass substrate was cleaned in acetone with ultrasound for 10 minutes and dried at 60 °C for 10 min. It was dipped in a 0.05% solution of the material at room temperature for 10 min. ASAHIKLIN$^{®}$ AC6000 (C$_6$F$_{13}$C$_2$H$_5$, available from Asahi Glass Co., Ltd.) was used as a dilute solvent. Finally, the glass was cured at room temperature under a relative humidity between 40% and 60% for 24 h. After coating, contact angle, friction coefficient and the abrasion resistance were evaluated.

An abrasion test on the surface of a coating film of an article with a flannel cloth was carried out according to Japanese Industrial Standards JIS L0849 under conditions of a load of 1 kg and abrasion times of 1,000 reciprocations. The water contact angle was measured after various intervals to obtain the relationship with abrasion cycles.

2.3. Typical Procedure for the Synthesis of the Perfluorobis(alkanesulfonyl) Monomer (Scheme 4)

2.3.1. 1,3-Bis(phenylmethylthio)propan-2-ol (**11**)

α-toluenethiol (507 g, 4.08 mol) was added dropwise for 1 h to a stirred solution of NaOH (163.3 g, 4.08 mol) in methanol (2 L) under 10 °C. Epichlorohydrin (189 g, 2.04 mol) was further added dropwise for 1 h. The mixture was stirred for 3.5 h at 20 °C and poured into 5 L of water. The mixture was separated and the aqueous phase was extracted with methyl *tert*-butyl ether (MTBE, 3 × 1,000 mL). The combined organic phase was washed with saturated aqueous NH$_4$Cl (3 × 200 mL), dried over MgSO$_4$ and filtered, and the solvent was evaporated to afford 604 g

(1.98 mol, 97%) of **11**; ^{1}H NMR (300.4 MHz, CDCl$_3$) δ (ppm): 2.47 (dd, *J* = 7.5, 13.9 Hz, 2H), 2.58 (dd, *J* = 4.7, 13.9 Hz, 2H), 2.75 (d, *J* = 3.2 Hz, 1H), 3.63~3.73 (m, 1H), 3.68 (s, 4H), 7.18~7.33 (m, 10H); IR (neat): 3445.8, 3060.2, 3026.9, 2913.4, 1493.6, 1452.8, 1239.7, 1071.2, 1028.2, 767.6, 700.5 cm^{-1}.

The obtained crude **11** was used for the next step without carrying out purification.

2.3.2. 2-Allyloxy-1,3-Bis(phenylmethylthio)propane (**12**)

To a stirred suspension of 60% NaH (84.6 g, 2.12 mol) in anhydrous THF (2L) under 5 °C was added a solution of **11** (604 g, 1.98 mol) in anhydrous THF (400 mL) dropwise for 40 min. After stirring under 5 °C for one hour, allyl bromide (252 g, 2.08 mol) was further added dropwise for 45 min. The mixture was stirred for 19 h at 20 °C, and poured into water (5 L). The mixture was separated and the aqueous phase was extracted with MTBE (3 × 1000 mL). The combined organic phase was washed with saturated aqueous NH$_4$Cl (3 × 200 mL), dried over MgSO$_4$ and filtered, and the solvent was evaporated. The large scale column chromatography on silica gel using a Biotage Flash 150M pre-packed column (KP-Sil silica, 15 cm ID × 30 cm long) with hexane-ethyl acetate (7:1) as the eluent provided 643 g (1.86 mol, 94%) of **12**; ^{1}H NMR (300.4 MHz, CDCl$_3$) δ (ppm): 2.59 (dd, *J* = 5.8, 13.7 Hz, 2H), 2.64 (dd, *J* = 5.8, 13.7 Hz, 2H), 3.47 (qui, *J* = 5.8 Hz, 1H), 3.70 (s, 4H), 3.95 (dm, *J* = 5.8 Hz, 2H), 5.14 (dm, *J* = 10.3 Hz, 1H), 5.23 (dm, *J* = 17.1 Hz, 1H), 5.87 (ddt, *J* = 10.3, 17.1, 5.8 Hz, 1H), 7.18~7.34 (m, 10H); ^{13}C NMR (75.45 MHz, CDCl$_3$) δ (ppm): 34.45, 36.98, 70.81, 78.38, 116.98, 126.95, 128.39, 128.91, 134.79, 138.31; IR (neat): 3061.0, 3027.3, 2918.3, 1493.7, 1452.9, 1071.6, 923.1, 767.4, 700.5 cm^{-1}.

2.3.3. 4-Oxa-8-Phenyl-5-(Phenylmethylthiomethyl)-7-Thiaoctan-1-ol (**13**)

To 1.01 M solution of borane-THF complex in THF (1,880 mL, 1.90 mol) under 10 °C was added cyclohexene (312 g, 3.80 mol) dropwise for 1.5 h. After stirring under 5 °C for 3 h, **12** (643 g, 1.98 mol) was further added dropwise for 1 h. The mixture was stirred for 17 h at 10 °C. To the mixture was added a solution of NaOH (84.3 g, 2.11 mol) in water (700 mL) dropwise under 10 °C for 45 min. The mixture was stirred for 15 min at the same temperature, and 30% H$_2$O$_2$ (700 mL, 8.12 mol) was further added dropwise for 3.5 h. The temperature was maintained under 20 °C. The mixture was poured to a solution of K$_2$CO$_3$ (3 kg) in water (3 L), separated, and the aqueous phase was extracted with MTBE (3 × 800 mL). The combined organic phase was dried over MgSO$_4$, filtered and freed of solvent *in vacuo*. The large scale column chromatography on silica gel using a Biotage Flash 150M pre-packed column (KP-Sil silica, 15 cm ID × 30 cm long) with hexane-ethyl acetate (3:1) as the eluent produced **13** (569 g, 1.57 mol, 84%) and recovered **12** (46.0 g, 0.13 mol, 7%).

13: ^{1}H NMR (300.4 MHz, CDCl$_3$) δ (ppm): 1.75 (qui, *J* = 5.7 Hz, 2H), 2.46 (t, *J* = 5.7 Hz, 1H), 2.56 (dd, *J* = 6.2, 13.7 Hz, 2H), 2.62 (dd, *J* = 5.8, 13.7 Hz, 2H), 3.34 (qui, *J* = 5.8 Hz, 1H), 3.55 (t, *J* = 5.8 Hz, 2H), 3.69 (s, 4H), 3.74 (q, *J* = 5.4 Hz, 2H), 7.20~7.35 (m, 10H); ^{13}C NMR (75.45 MHz, CDCl$_3$) δ (ppm): 32.09, 34.63, 36.87, 60.95, 68.32, 78.55, 127.04, 128.45, 128.87, 138.14; IR (neat): 3439.8, 3026.9, 2917.3, 2870.8, 1493.7, 1452.9, 1239.7, 1088.5, 1072.0, 768.9, 701.2 cm^{-1}.

2.3.4. 4-Oxa-8-Phenyl-5-(Phenylmethylthiomethyl)-7-Thiaoctyl
Perfluoro(2,5-Dimethyl-3,6-Dioxanonanoate) (**14**)

To a stirred solution of **13** (596 g, 1.57 mol) and triethylamine (175 g, 1.73 mol) in dichloromethane (2.5 L) under 5 °C was added **6** (822 g, 1.65 mol) dropwise for 2 h. The mixture was stirred for 3 h at 20 °C. The mixture was washed with saturated aqueous $NaHCO_3$ (2 × 800 mL), 2 *N*-HCl (2 × 900 mL) and saturated aqueous NH_4Cl (500 mL). The organic phase was dried over $MgSO_4$, filtered, and freed of solvent *in vacuo* to afford **14** (1,323 g, 1.57 mol, >98%); ^{1}H NMR (300.4 MHz, $CDCl_3$)δ (ppm): 1.91 (qui, *J* = 6.1 Hz, 2H), 2.55 (dd, *J* = 6.1, 13.5 Hz, 1H), 2.61 (dd, *J* = 5.8, 13.5 Hz, 2H), 3.31 (qui, *J* = 6.0 Hz, 1H), 3.44 (t, *J* = 6.0 Hz, 2H), 3.68 (s, 4H), 4.49 (m, 2H), 7.20~7.35 (m, 10H); ^{19}F NMR (282.7 MHz, $CDCl_3$) δ (ppm): −78.98~−85.55 (m, 4F), −80.48 (m, 3F), −81.82 (q, *J* = 7.0 Hz, 3F), −82.65 (m, 3F), −130.06 (s, 2F), −131.93 (dm, *J* = 21.1 Hz, 1F), −145.65 (m, 1F); IR (neat): 3029.3, 2916.5, 1782.6, 1240.7, 1148.4, 1037.2, 993.5, 701.2 cm^{-1}.

The obtained crude **14** was used for the next step without carrying out purification.

2.3.5. 6-Fluorosulfonyl-5-(Fluorosulfonylmethyl)-4-Oxahexyl
Perfluoro(2,5-Dimethyl-3,6-Dioxanonanoate) (**16**)

A flask-equipped dry ice condenser was charged with **14** (642 g, 764 mmol), acetic acid (1,350 mL) and water (150 mL). Chlorine was bubbled in the stirred mixture at a flow rate of 600 mL/min for 2.5 h and 75 mL/min for 3.5 h at 20 °C. The mixture was cooled by water so that the reaction temperature did not exceed 30 °C. After bubbling, the mixture was purged with nitrogen, and water was added (1.5 L). The mixture was extracted with MTBE (3 × 500 mL). The combined organic phase was washed with water (500 mL), dried over $MgSO_4$, filtered, and the solvent was evaporated to afford 800 g of crude 6-Chlorosulfonyl-5-(chlorosulfonylmethyl)-4-oxahexyl perfluoro(2,5-dimethyl-3,6-dioxanonanoate) (**15**); ^{1}H NMR (300.4 MHz, $CDCl_3$) δ (ppm): 2.05 (m, 2H), 3.79 (t, *J* = 5.8 Hz, 2H), 4.11 (d, *J* = 6.0 Hz, 4H), 4.43~4.58 (m, 2H), 4.64 (m, 1H); ^{19}F NMR (282.7 MHz, $CDCl_3$) δ (ppm): −78.97~−85.64 (m, 4F), −80.48 (m, 3F), −81.82 (m, 3F), −82.63 (m, 3F), −130.06 (s, 2F), −132.01 (dm, *J* = 20.0 Hz, 1F), −145.65 (m, 1F).

A flask was charged with **15**, KHF_2 (239 g, 3.06 mol), acetnitrile (1.5 L) and water (1.5 L). The mixture was stirred at 20 °C for 24 h, and organic phase was separated from aqueous phase. The aqueous phase was extracted with MTBE (200 mL). The combined organic phase was washed with water (2 × 200 mL), dried over $MgSO_4$, filtered, and freed of solvent *in vacuo*. The residue separated into two layers and the upper one (mainly α-chlorotoluene) was removed. A crude mixture (373 g), including **16**, was obtained. The large scale column chromatography on silica gel using a Biotage Flash 150M pre-packed column (KP-Sil silica, 15 cm ID × 30 cm long) with hexane-ethyl acetate (3:1) as the eluent furnished **16** (269 g, 354 mmol, 46% from **14**), which was directly used for the next liquid phase fluorination reaction; ^{1}H NMR (300.4 MHz, $CDCl_3$) δ (ppm): 2.06 (qui, *J* = 6.0 Hz, 2H), 3.77 (t, *J* = 5.9 Hz, 2H), 3.79 (dd, *J* = 3.2, 5.7 Hz, 4H), 4.42~4.58 (m, 3H); ^{19}F NMR (282.7 MHz, $CDCl_3$) δ (ppm): 61.56 (s, 2F), −79.01~−85.62 (m, 4F), −80.51 (m, 3F), −81.86 (m, 3F), −82.69 (m, 3F), −130.09 (s, 2F), −132.03 (dm, *J* = 18.8 Hz, 1F), −145.65 (m, 1F); IR (neat): 3003.9, 2953.8, 1781.6, 1420.6, 1239.5, 1149.8, 1038.7, 993.8, 804.2, 744.8 cm^{-1}.

2.3.6. Perfluoro[6-Fluorosulfonyl-5-(Fluorosulfonylmethyl)-4-Oxahexanoyl] Fluoride (**18**)

In a 3 L autoclave made of stainless steel, equipped with a condenser maintained at 25 °C, an NaF pellet packed layer and a condenser maintained at −10 °C in series at its gas outlet, as well as a liquid returning line in order to return the condensed liquid from the condenser maintained at −10 °C, **6** (4,520 g) was stirred at 25 °C. Nitrogen was blown into the system for 1 hr, and then 20% F_2/N_2 for 0.5 h at a flow rate of 93.4 L/h. While blowing 20% F_2/N_2 at the same rate, the internal pressure of the reactor was raised to 0.1 MPa, and a solution of **16** (404 g, 532 mmol) in R113 (1,640 mL) was injected over a period of 31.5 h. After the injection, 20% F_2/N_2 was further blown at the same rate for 8 h. The reactor was cooled to room temperature and purged with nitrogen. The removal of the solvent afforded the crude mixture (643 g), including the perfluorinated ester **17**; ^{19}F NMR (282.7 MHz, CDCl$_3$) δ (ppm): 46.59 (2F), −78.62 ~ −80.46 (4F), −82.15 (8F), −84.23 ~ −87.36 (5F), −104.54 (4F), −128.40 (2F), −130.16 (2F), −132.26 (1F), −133.78 (1F), −145.96 (1F).

A flask was charged 623 g of the mixture above and KF (3.16 g, 54.3 mmol). The mixture was heated at 90 °C for 1.5 h. The distillation *in vacuo* provided **18** (99.5 g, 216 mmol, 36% from **16**); bp 77 ~ 78 °C/40 mmHg ; ^{19}F NMR (282.7 MHz, CDCl$_3$) δ (ppm): 46.65 (s, 2F), 25.29 (tt, J = 4.6, 9.2 Hz, 1F), −81.37 (d, J =13.7 Hz, 2F), −104.60 (m, 4F), −120.53 (m, 2F), −133.72 (t, J =19.8 Hz, 1F).

2.3.7. Perfluoro[9-Fluorosulfonyl-8-(Fluorosulfonylmethyl)-2-Methyl-3,7-Dioxanonanoyl] Fluoride (**19**)

18 (82.7 g, 180 mmol), CsF (2.33 g, 15.3 mmol) and monoglyme (18.0 g) were charged into a 200 mL vacuumed autoclave. The mixture was stirred and hexafluoropropene oxide (HFPO, 33.0 g, 199 mmol) was introduced at 5 °C. Internal pressure was raised to 1.4 atm. The mixture was further stirred for 1 h. The distillation *in vacuo* provided **19** (38.9 g, 62.0 mmol) and recovered **18** (35.9 g, 78.0 mmol) (conversion = 57%, yield of **19**: 60%); bp 79~80 °C/5 mmHg ; ^{19}F NMR (282.7 MHz, CDCl$_3$) δ (ppm): 46.65 (s, 2F), 26.66 (q, J = 4.6 Hz, 1F), −78.95 (ddt, J = 18.3, 149.5, 7.6 Hz, 1F), −79.32 (m, 2F), −82.08 (s, 3F), −86.35 (dm, J =149.5 Hz, 1F), −104.46 (m, 4F), −128.20 (s, 2F), −130.87 (d, J = 16.8 Hz, 1F), −133.73 (m, 1F).

2.3.8. Perfluoro[2-(Fluorosulfonylmethyl)-3,7-Dioxa-8-Nonene]Sulfonyl Fluoride (**4**)

To a suspension of KHCO$_3$ (6.03 g, 60.2 mmol) in monoglyme (59 mL) was added **19** (35.6 g, 52.6 mmol) dropwise for 30 min at 4 °C. The mixture was stirred for 30 min and freed of solvent *in vacuo* at 95 °C for 8 days and 120 °C for 2 days. Crude potassium perfluoro[9-fluorosulfonyl-8-(fluorosulfonylmethyl)-2-methyl-3,7-dioxanonanoate] (21.1 g, 29.7 mmol) was obtained. The potassium salt was heated to 200 °C under reduced pressure (3 mmHg). Gas generated was corrected in a liquid nitrogen trap. Condensed liquid in the trap was washed with water (10 mL) to afford **4** (8.35 g, 13 mmol, 25%); ^{19}F NMR (282.7 MHz, CDCl$_3$) δ (ppm): 46.62 (s, 2F), −79.45 (m, 2F), −85.56 (m, 2F), −103.14 ~ −105.38 (m, 4F), −113.27 (dd, J = 65.6, 82.4 Hz, 1F), −121.66 (ddt, J = 82.4, 112.9, 6.1 Hz, 1F), −128.27 (s, 2F), −133.65 (m, 1F), −135.67 (ddt, J = 65.6, 112.9, 6.1 Hz, 1F); IR (neat): 1839.4, 1777.6, 1468.6, 1340.6, 1286.4, 1213.6, 1167.1, 999.0, 812.2 cm^{-1}; HRMS (CI) m/z (M-F$^+$, $C_8F_{15}O_6S_2^+$) calculated 540.8897, found 540.8898.

3. Results and Discussion

3.1. Synthesis and Evaluation of the Anti-staining Coating Material

3.1.1. Synthesis of a PFPE which Possesses $-(CF_2CF_2O)-$ as a Repeating Unit (Scheme 3)

It has so far been quite limited to synthesize a perfluorinated poly(ethylene glycol) structure. It has only been achieved by liquid-phase direct fluorination. Lagow *et al.* reported this synthesis by utilizing liquid-phase direct fluorination with elemental fluorine [12]. However, the method cannot be applied directly to the synthesis of PFPE derivative **3**, because **3** has a non-fluorinated functionalized group in one end. The synthesis of PFPEs starting from diols and tetrafluoroethylene was also effective [13]. However, it seemed to be difficult to apply it to the mono-functionalized PFPE derivative **3**.

Scheme 3. Synthesis of PFPE derivative **3**.

R_F: $CF_3CF_2CF_2OCF(CF_3)CF_2OCF(CF_3)-$
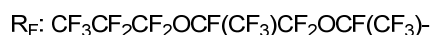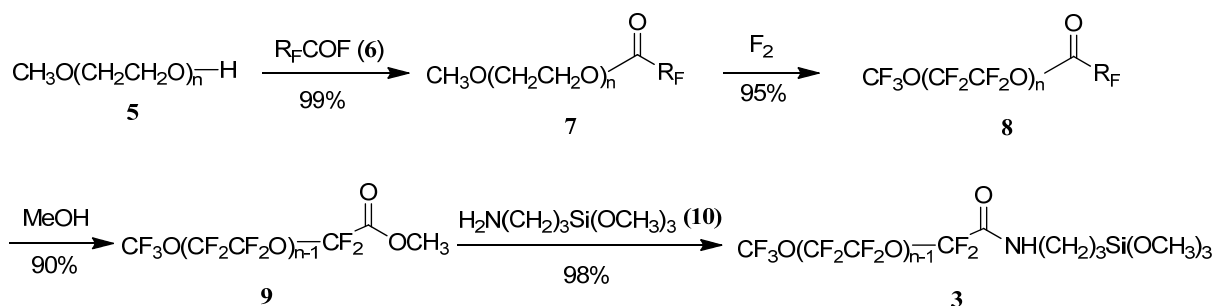
On the other hand, the PERFECT method enables it by employing a partially-fluorinated compound as the substrate, synthesized from a non-fluorinated alcohol [9]. According to the typical PERFECT procedure [8], firstly, poly(ethylene glycol) monomethyl ether (**5**) was reacted with a perfluoroacyl fluoride **6** to obtain partially-fluorinated ester **7**. Next, perfluorination was achieved by liquid-phase direct fluorination with elemental fluorine to give the perfluorinated ester **8**. Injection of a diluted solution of benzene after substrate addition was effective for complete perfluorination, because benzene reacts with elemental fluorine to generate many fresh fluorine radicals. Instead of the thermal elimination in the typical PERFECT procedure, methanol was added to perfluorinated ester **8** to provide the desired methyl ester **9** of the PFPE and the methyl ester of the starting perfluoroacyl fluoride **6**, which was removed from the mixture by distillation. Finally, **9** was treated with **10** to afford the desired **3**. The overall yield from the starting material **5** was 83%.

Thus, the target PFPE derivative **3** for an anti-staining coating material was successfully synthesized by employing the PERFECT process as a key step.

3.1.2. Evaluation of Water and Oil Repellency

Water and n-hexadecane contact angles and friction coefficient are summarized in Table 1. As can be seen in Table 1, **3** showed higher water and oil (n-hexadecane) contact angles and lower friction

coefficient than the conventional anti-staining material **1a**. This is because **3** has more fluorine contents in a molecule and a higher degree of molecular mobility, due more to an ether bond than **1a**. Higher hydrophobic and oleophobic properties will give a better anti-staining performance. Moreover, a lower friction coefficient predicts that **3** will have both better stay-clean and easy-to-clean characteristics.

Table 1. Contact angle and friction coefficient of coating glass.

Material	Water (deg.)	n-Hexadecane (deg.)	friction coefficient
3	108	71	0.159
1a	105	65	0.184

3.1.3. Abrasion Resistance Test

The effect of the abrasion resistance is also a key parameter when considering the use of **3** coating on surfaces subjected to physical wear. An abrasion test of the treated surface is a method commonly used to predict the effective life of the surface modification. The results are shown in Figure 1. As can be seen from Figure 1, there was a significant difference in the resistance to abrasion as measured by water contact angle. After 200 cycles the conventional **1a** material had a drastic reduction in water contact angle, while **3** maintained high contact angle even after 1,000 cycles. It is considered that both longer molecular chain and lower friction coefficient of **3** contribute to this higher abrasion property.

Figure 1. Abrasion Resistance Test.
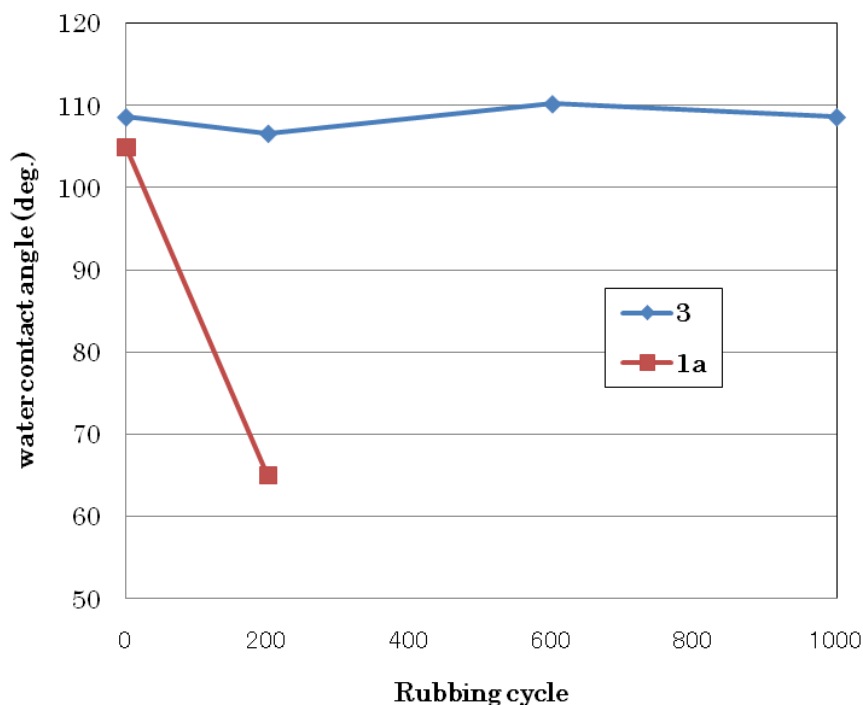
3.2. Synthesis of Perfluorobis(alkanesulfonyl) Monomer (Scheme 4)

To date, the method to prepare perfluorobis(sulfonyl) compounds has been very limited. Forohar and DesMarteau reported fluorobis(fluorosulfonyl)acetyl fluoride, $(FSO_2)_2CFCOF$ [14]. The yield of

this compound, however, was low, and it easily decarbonylated in the presence of fluoride ions. Instead of employing this method, we adopted a totally different approach, which includes the PERFECT process as a key step. It enabled us to build the perfluorinated backbone structure with two fluorosulfonyl groups and one fluorocarbonyl group from a non-fluorinated sulfonyl compound prepared by organic synthesis. Then, the introduction of a polymerizable trifluorovinyloxy group was carried out using hexafluoropropene oxide. Our method seemed not to have the problem described above, since the fluorocarbonyl group reacts with hexafluoropropene oxide prior to decarbonylation. The synthetic path to **4** is shown in Scheme 4.

Scheme 4. Synthesis of perfluorobis(alkanesulfonyl) monomer **4**.

R_F: CF$_3$CF$_2$CF$_2$OCF(CF$_3$)CF$_2$OCF(CF$_3$)-
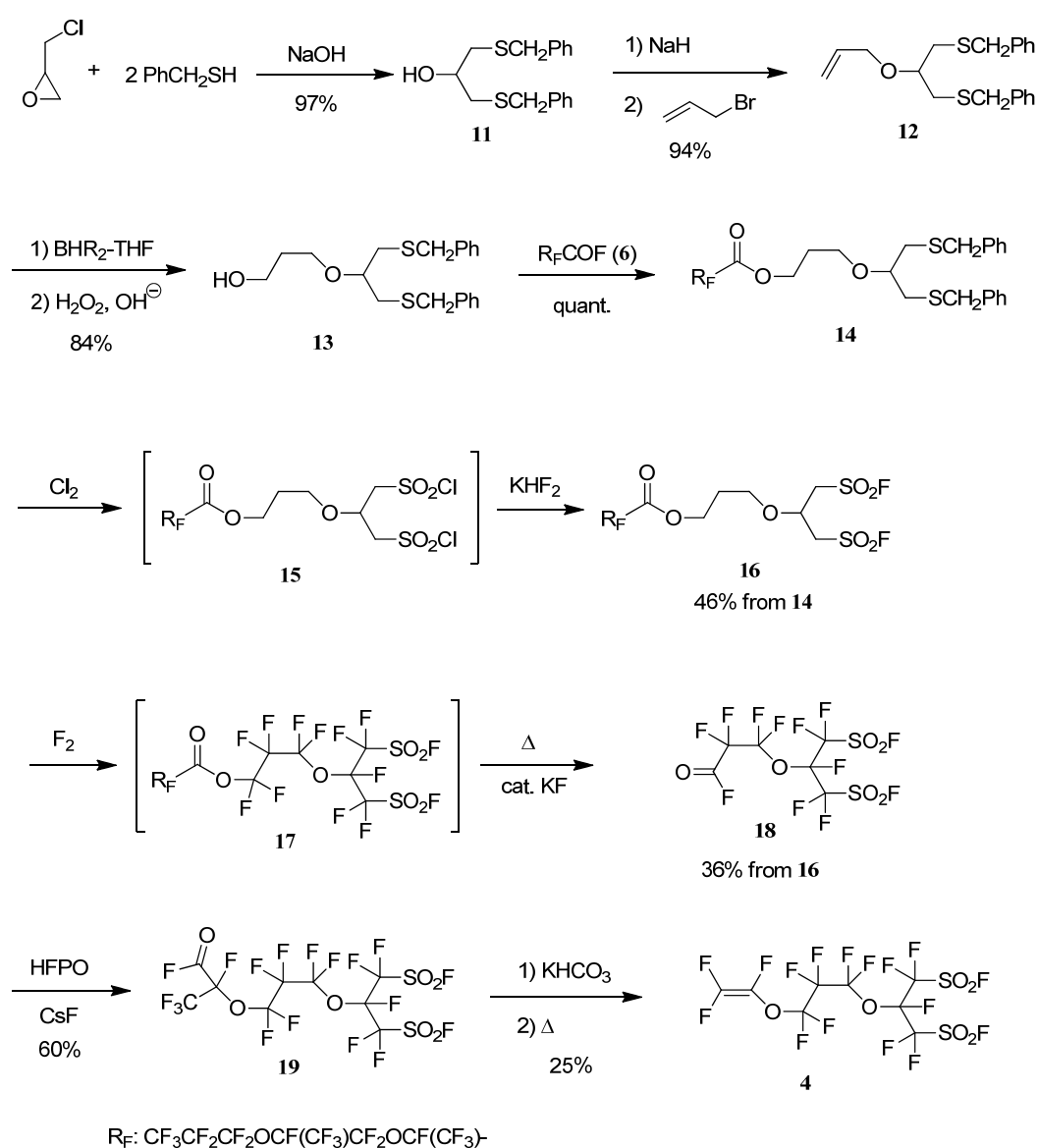
Compound **11** was prepared by a nucleophilic attack of α-toluenethiol to epichlorohydrin [15]. Allylation of the hydroxy group (allyl bromide-NaH-THF, 0 °C, 1 h, then 25 °C, 20 h) produced **12** [16]. Hydroboration-oxidation was performed to the double bond of **12** (1. dicyclohexylborane-THF,

0 °C, 19 h; 2. NaOH aq. then 30% H_2O_2) to furnish **13**. When the borane/THF complex was used as the hydroboration reagent, the unwanted secondary alcohol (2°-ol) was formed with the desired **13** (**13**: 2°-ol = 69:31). Using the more sterically hindered dicyclohexylborane as the borane reagent essentially eliminated 2°-ol [17]. The compound **13** was condensed with perfluoro-2,5-dimethyl-3,6-dioxanonanoyl fluoride (**6**) (triethylamine-dichloromethane, 0 °C, 1 h, then 25 °C, 3 h) to afford the ester **14**. Oxidation of **14** by chlorine (acetic acid-water, 25 °C, 16 h) [18], followed by treatment with KHF_2 (acetonitrile-water, 25 °C, 24 h) provided the sulfonyl fluoride **16** [19]. The PERFECT process was applied to **16** (1. 20% F_2/N_2-trichlorotrifluoroethane, 20 °C, 1.5 h; 2. KF, 90 °C, 1.5 h) to furnish **18** [8]. The reaction of **18** with hexafluoropropene oxide (CsF-diglyme, 0 °C, 1 h) proceeded to obtain **19**, which was decarbonylated (1. $KHCO_3$-glyme, 0 °C, 0.5 h; 2. 120 °C, 3 h, then 200 °C, 1 h) to afford the desired **4** [20].

The overall yield of **4** was as low as 2%, the net result of several low yield steps. The single lowest yield was the fluorination step. C-S bond disconnection occurred as in the case of the fluorination of other C-S bond containing substrates [11]. The typical yields of the fluorination of the substrates with one C-S bond have been 60–70%. The substrate **16**, however, has two C-S bonds so that there is a high chance of the disconnection compared with substrates with one C-S bond. The introduction of sulfur into fluorinated molecules should be reconsidered.

The yields of the steps after the fluorination were also low. They could be improved after optimizing the reaction conditions.

4. Conclusions

Applying the PERFECT process, a perfluoropoly(ethylene glycol) derivative has been synthesized, and proved to be a surface treating agent, which is excellent in water-and-oil repellency and efficiency for the removal of oil-and-fat stains. An industrial application to stain-proof glass is now being studied. Furthermore, the monomer having two sulfonyl groups has been synthesized by utilizing the PERFECT process. Polymerization with it and application to PEMs of fuel cells are items to be studied. The polymer made from the monomer is expected to show good performance and enhanced durability when used for PEMs of electropower systems.

Thus, the PERFECT process provides the synthetic method of entirely new functional fluorinated molecules for leading-edge industries.

References

1. For a recent review of organofluorine compounds in materials industries, see: Okazoe, T. Overview on the history of organofluorine chemistry from the viewpoint of material industry. *Proc. Jpn. Acad. Ser. B* **2009**, *85*, 276–289.
2. Asai, M.; Uehara, H.; Ogawa, N.; Kamiya, K. Glass-Water Repellent Agent Composition and Method for Manufacturing Water-Repellent Glass. JP Patent 2002-145645, May 22, 2002.
3. Fujita, H.; Nagai, K.; Sakagami, T.; Kai, Y.; Nakamura, I. Production of Water Repellent Glass for Automobile. JP Patent 9-286639, 4 November 1997.

4. Ogawa, K.; Mino, N.; Soga, S. Stainproof Adsorbent Film and Its Production. JP Patent No. 2,981,043, 22 November 1999.

5. Ohata, K.; Okubo, T.; Mitsuida, A.; Tomikawa, N.; Watanabe, J. Method for Forming Stainproof Layer. JP Patent No. 4174867, 5 November 2008.

6. O'Hagan, D. Understanding organofluorine chemistry. An introduction to the C-F bond. *Chem. Soc. Rev.* **2008**, *37*, 308–319.

7. Kinoshita, K.; Cairns, E.J. Fuel cells. In *Kirk-Othmer Encyclopedia of Chemical Technology*, 4th ed.; Howe-Grant, M., Ed.; John Wiley & Sons: New York, NY, USA, 1994; Volume 11, pp. 1098–1121.

8. Okazoe, T.; Watanabe, K.; Itoh, M.; Shirakawa, D.; Tatematsu, S. A new route to perfluorinated vinyl ether monomers: Synthesis of perfluoro(alkoxyalkanoyl) fluorides from non-fluorinated compounds. *J. Fluor. Chem.* **2001**, *112*, 109–116.

9. Shirakawa, D.; Ohnishi, K. A study on design and analysis of new lubricant for near contact recording. *IEEE Trans. Magn.* **2010**, *44*, 3710–3713.

10. Takagi, H.; Matsuoka, Y.; Higuchi, S.; Funaki, H.; Seki, R.; Oharu, K.; Kamiya, H. APFO Alternative Potentiality for Perfluoropolyether Surfactants Derived from AGC's "PERFECT" Process. In *Proceedings of the 1st International Workshop "Fluorinated Surfactants: New Developments"*, Idstein, Germany, 26–28 June 2008; Europa Fachhochschule Fresenius: Idstein, Germany; PA3.

11. Okazoe, T.; Murotani, E.; Watanabe, K.; Itoh, M.; Shirakawa, D.; Kawahara, K.; Kaneko, I.; Tatematsu, S. An entirely new methodology for synthesizing perfluorinated compounds: Synthesis of perfluoroalkanesulfonyl fluorides from non-fluorinated compounds. *J. Fluor. Chem.* **2004**, *125*, 1695–1701.

12. Lagow, R.J. Reactions of fluorine in the presence of solvents. In *Methoden Organic Chemistry (Houben-Weyl)*, 4th ed.; Baasner, B., Hagemann, H., Tatlow, J.C., Eds.; Georg Thieme Verlag: Stuttgart, Germany, 1999; Volume E10a, pp. 194–200.

13. Howell, J.L.; Shtarov, A.B.; Thrasher, J.S.; Waterfeld, A.; Murata, K.; Friesen, C.M.; Pérez, E.W. Synthesis of new linear perfluoroalkyl polyethers starting from diols and tetrafluoroethylene. *Lubr. Sci.* **2011**, *23*, 61–80.

14. Forohar, F.; DesMarteau, D.D. Synthesis and reactions of the β-sultone of perfluorovinylsulfonyl fluoride. *J. Fluor. Chem.* **1994**, *66*, 101–104.

15. Corey, E.J.; Erickson, B.W.; Noyori, R. A new synthesis of α, β-unsaturated aldehydes using 1,3-bis(methylthio)allyllithium. *J. Am. Chem. Soc.* **1971**, *93*, 1724–1729.

16. Barlow, C.G.; Ollmann, R.R.; Zinn-Warner, A.S.; Nairne, R.J.D.; Beck, A.L.; Mott, A. Image Toners for Silver Halide Photographic Films. U.S. Patent 5,922,527, 13 July 1999.

17. Zweifel, G.; Ayyangar, N.R.; Brown, H.C. Hydroboration. XVII. An examination of several representative dialkylboranes as selective hydroborating agents. *J. Am. Chem. Soc.* **1963**, *85*, 2072–2075.

18. Langler, R.F. A facile synthesis of sulfonyl chlorides. *Can. J. Chem.* **1976**, *54*, 498–499.

19. Gramstad, T.; Haszeldine, R.N. Perfluoroalkyl derivatives of sulphur. Part IV. Perfluoroalkanesulphonic acids. *J. Chem. Soc.* **1956**, 173–180.

20. Yamabe, M.; Matsuo, M.; Miyake, H. Fluoropolymers and fluoroelastomers. In *Maclomolecular Design of Polymeric Materials*; Hatada, K., Kitayama, T., Vogl, O., Eds.; Plastics Engineering Series 40; Marcel Dekker: New York, NY, USA, 1997; pp. 429–446.

Review

An Environmentally Friendly Class of Fluoropolyether: α,ω-Dialkoxyfluoropolyethers

Menghua Wu [1], Walter Navarrini [1,2,*], Gianfranco Spataro [3], Francesco Venturini [1] and Maurizio Sansotera [1]

[1] Dipartimento di Chimica, Politecnico di Milano,7, via Mancinelli, I-20131 Milano, Italy;
E-Mails: menghua.wu@mail.polimi.it (M.W.); francesco.venturini@chem.polimi.it (F.V.);
maurizio.sansotera@polimi.it (M.S.)

[2] Consorzio INSTM, Via G. Giusti 9, I-50121, Firenze, Italy

[3] C.R.S. Solvay Secialty Polymer, viale Lombardia 20, I-20021 Bollate (MI), Italy;
E-Mail: gianfranco.spataro@solvay.com

* Author to whom correspondence should be addressed; E-Mail: walter.navarrini@polimi.it;
Tel.: +39-02-2399-3029; Fax: +39-02-2399-3180.

Abstract: The α,ω-dialkoxyfluoropolyethers (DA-FPEs) characterized by the structure $R_HO(CF_2CF_2O)_n(CF_2O)_mR_H$ have been developed as a new class of environmentally friendly hydrofluoroethers (HFEs) suitable as solvents, long-term refrigerants, cleaning fluids, and heat transfer fluids. Synthetic methodologies for DA-FPEs described here consist of radical-initiated oxypolymerization of olefin, peroxy-elimination reaction in peroxidic perfluoropolyethers (P-PFPEs) and further chemical modification of α,ω-diacylfluoride PFPE. The physical properties of selected α,ω-dimethoxyfluoropolyethers (DM-FPEs) have been evaluated and compared with analogous hydrofluoropolyethers (HFPEs) having $-OCF_2H$ as end-groups. Atmospheric implications and global warming potentials (GWPs) of selected DA-FPEs are also considered.

Keywords: α,ω-dimethoxyfluoropolyethers; hydrofluoropolyethers; physical properties

1. Introduction

α,ω-Dialkoxyfluoropolyethers (DA-FPEs) are partially fluorinated polyethers not containing chlorine atoms. Hence, they do not contribute to ozone depletion [1].

$$R_HO(CF_2CF_2O)_n(CF_2O)_mR_H \qquad R_H = CH_3, C_2H_5, CH_2=CHCH_3 \qquad (1)$$
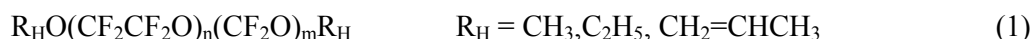
The incorporation of two alkoxy-groups provides reactive sites, which limit their atmospheric lifetime [1–3]; therefore, when compared with perfluoropolyethers (PFPEs), they have a lower environmental impact in terms of global warming potential (GWP) [1]. Furthermore, perfluorinated ether units from polymeric backbones also makes them well characterized by typical properties of PFPEs, like high thermal and chemical stability, no acute toxicity and excellent heat exchange properties [4]. Lastly, due to the presence of the above-mentioned alkoxy-groups as ending groups, they show good solvent properties with several organic liquids, such as ketones and alcohols [5]. All these appealing properties of DA-FPEs make them excellent candidates as CFC, perfluocarbons and halons substitutes in a number of applications, like foaming and fire extinguishing agents, cleaning agents for sophisticated electronic devices and heat transfer fluids [6–8].

2. Syntheses of α,ω-Dialkoxyfluoropolyethers

The synthesis of DA-FPEs described here involves a combination of a few innovative and conventional synthetic technologies. The whole process includes the following steps: (1) The oxidative polymerization of perfluoroolefinic monomers into peroxidic perfluoropolyethers (P-PFPEs) as a precursor; (2) the subsequent reduction of P-PFPEs to produce diacyl fluorides perfluoropolyether (DAF-PFPE); (3) and the further chemical modification of α,ω-diacyl functional groups of DAF-PFPE to yield the final products α,ω-dialkoxyfluoropolyethers.

2.1. Oxypolymerization of Perfluoroolefin

Oxidative polymerization of perfluoroolefinc monomers like tetrafluoroethylene (TFE) by molecular oxygen into P-PFPEs (**A**) described in Figure 1, is a well-known reaction [9].

Figure 1. Oxidative polymerization of tetrafluoroethylene.

$$\text{F}_2\text{C}\!=\!\!\text{CF}_2 + \text{O}_2 \xrightarrow[< -40^\circ\text{C, Solvent}]{\text{F}_2, \text{CF}_3\text{OF or UV light}} \text{TO}\!\!\left(\text{CF}_2\text{CF}_2\text{O}\right)_{\!p}\!\!\left(\text{CF}_2\text{O}\right)_{\!r}\!\!\left(\text{O}\right)_{\!q}\!\!\text{T'}$$

T,T' = CF₃, C(O)F (major), CF₂C(O)F (minor).

(A)
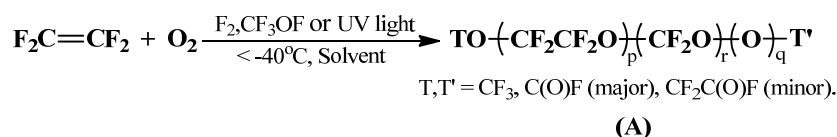
The forming peroxidic polymer has the following general structure: TO-(CF₂CF₂O)ₚ-(CF₂O)ᵣ-(O)_q-T', comprising fluoroether repeating units (-CF₂CF₂O- and -CF₂O-), interspersed peroxy units (-CF₂CF₂OO- and -CF₂OO-) and perfluorinated alkyl groups, acyl fluoride or fluoroformate as chain end-groups (T, T'). Practically, this oxypolymerization can be activated either by high energy UV light or by employing elemental fluorine or perfluoroalkyl hypofluorites, especially CF₃OF, as chemical initiators [9]. The peroxidic polymer is the result of a complex free radical oxidation reaction dominated by the chemistry of perfluoro oxyradicals [10]. The composition and the reaction yields of

forming PFPE polymers depend on irradiation condition, TFE concentration, fluid dynamics of the system and other classical physical parameters like temperature and pressure. Commonly, the average molecular weight of formed P-PFPEs (A) is more than 10^4 amu [11]. Carbonyl fluoride and tetrafluoroethylene oxide are the main by-products.
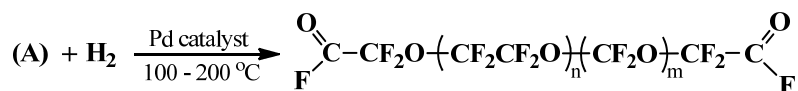
2.2. Deperoxidation of P-PFPEs

α,ω-Diacyl PFPE can be obtained by thermal treatment or chemical reduction of peroxide bonds present in the above mentioned peroxidic precursor. Under the appropriate thermal treatment, homolysis of fragile peroxide bonds in P-PFPEs (A) produces PFPE alkoxy radicals; subsequently, the cleavage of the bond in ß-position to the oxygen-centered radicals leads to the formation of reactive carbon-centered PFPE radicals [12,13]. The fast cage-combination reaction of these radicals takes place and leads to a PFPE material in which acyl fluoride and fluoroformyl moieties are nearly 50% of the end groups (Figure 2). Generally, above 150 °C those fluoroformate groups can also be converted into acyl fluorides. After the thermal treatment of the peroxidic PFPE, the reduced PFPE products can be distinguished into two fractions: The major one includes PFPE with monoacid end-groups, while the minor one comprises completely neutral (perfluoroalkyl end-groups) and diacyl fluoride PFPEs.

Figure 2. Deperoxidation of P-PFPEs by thermal treatment.

$$(A) \xrightarrow[150\text{-}200\ ^{\circ}C]{\text{Heat}} T-CF_2O\left(CF_2CF_2O\right)_n\left(CF_2O\right)_mCF_2-T'$$

$$T,T' = CF_3, C(O)F.$$
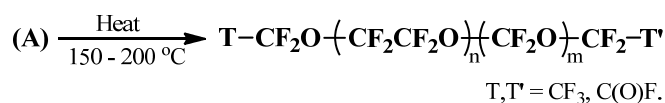
P-PFPEs (**A**) can also be converted directly to diacyl fluoride PFPEs, $F(O)CCF_2O(CF_2CF_2)_n(CF_2O)_mCF_2C(O)F$, by chemically induced reduction of the peroxide unites with better yield compared with thermal treatment (Figure 3). The chemical reduction is performed with reducing agents, such as hydrogen iodide or with molecular hydrogen in the presence of a noble metal catalyst (e.g., Palladium) [14].

Figure 3. Deperoxidation of P-PFPEs by chemical reduction.

$$(A) + H_2 \xrightarrow[100\text{-}200\ ^{\circ}C]{\text{Pd catalyst}} \overset{O}{\underset{F}{\diagdown}}C-CF_2O\left(CF_2CF_2O\right)_n\left(CF_2O\right)_mCF_2-C\overset{O}{\underset{F}{\diagup}}$$

2.3. Preparation of DA-FPEs by DAF-PFPE Alkylation

Finally, hydrofluoropolyethers DA-FPEs are prepared through the reaction of diacyl fluoride PFPEs (DAF-PFPEs) with electrophiles in the presence of a source of fluorine ions, generally, metal fluorides. This process actually comprises two steps (Figure 4): Firstly, in aprotic polar solvent, DAF-PFPEs react with fluoride ions released from metal fluorides to form metal perfluoroalkoxides $M^+{}^-OCF_2RFCF_2O^-M^+$ as intermediates; secondly, metal perfluoroalkoxide is alkylated by a suitable alkylating agent $X-R_H$ leading to the introduction of alkoxy groups at the end of the perfluoropolyether chain.

Figure 4. General two step reaction for synthesis DA-FPEs.

$R_H = CH_3, C_2H_5, CH_2=CHCH_2;$
$R_F = -(CF_2CF_2O)_n(CF_2O)_m-;$
X: leaving group
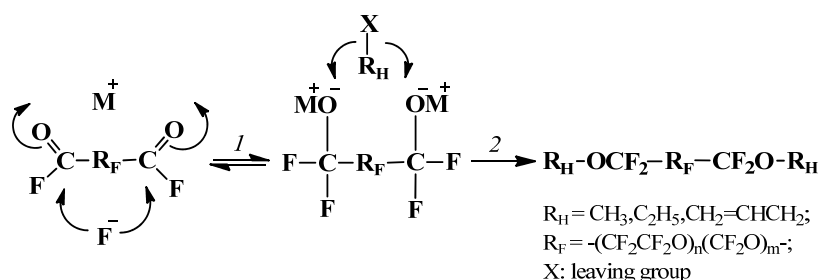
Metal perfluoroalkoxides are known as compounds characterized by low nucleophilicity [15] and they decompose into acylfluorides and metal fluorides, generally around room temperature. In order to increase the stability and the nucleophilic strength of these species, polar aprotic solvents (e.g., diglyme, tetraglyme) are generally required. The stability of these species depends on the nature of metal fluoride [16], temperature, and the solvent [17]. Metal perfluoroalkoxides are also important industrial intermediates in the synthesis of hypofluorites like CF_3CF_2OF [18] and fluorinated vinylethers [19,20]. Completely anhydrous reaction conditions are required, because in presence of water the hydrolysis of acyl fluoride groups generates hydrofluoric acid, HF, which can be absorbed by the solid metal fluoride giving MHF_2 [16]. Because of the low nucleophilicity of perfluoroalkoxides, strong alkylating agents with high electrophilicity are needed to effectively react with metal perfluoroalkoxides and form DA-FPEs.

2.3.1. Alkylation of PFPE Dialkoxides

In the past years, there have been many disclosures reported on finding effective alkylating agents suitable for perfluoroalkoxides. Dialkylsulfate was one of the first specific reagents used [21], because of its strong alkylating ability. In fact, it has been used to alkylate almost every nucleophile [22,23], but the alkylating temperature of dialkylsulfate needs to be lower than 20 °C and undesired viscose gels can be formed at this temperature and remarkably reduce the alkylation rate and yield. Moreover, dialkyl sulfates are highly toxic and their carcinogenic activity makes them inapplicable for large-scale industrial production.

Figure 5. Alkyl ester of the polysulphonic PFPE.

T,T' = CF_2H, CF_3, C_2F_5, CF_2Cl.
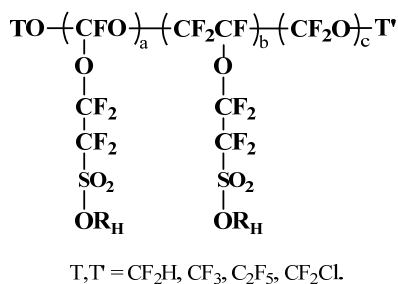
Dialkyl sulfites and the alkyl ester of polysulphonic PFPE (Figure 5) were also proposed and applied as alkylating agents in reactions with acylfluorides to synthesize hydrofluoroethers (HFE) [6,24]. Compared with dialkyl sulfate, dialkyl sulphite and the alkyl ester of polysulphonic PFPE are

considered non-carcinogenic, and their alkylating temperature over 100 °C avoids the formation of undesired gels. However, the molar yield of the product resulting from the use of these two alkylating agents is low (below 20%), in addition, the preparation of alkyl ester polysulphonic PFPE is particularly difficult.

Fluorovinyl alkyl ethers, $(CF_3)_2C=CFO-R_H$, were also considered as one of the most effient but expensive class of alkylating agent for metal perfluoroalkoxides [25]. A high molar yield of HFEs was achieved by using heptafluoro-*iso*-butenyl methyl ether [26] in the reaction with metal perfluoroalkoxides, shown in Figure 6(a). A nonvolatile conjugated base $(CF_3)C=CO^-FK^+$ was formed as by-product after the reaction that can be hydrolyzed into its carboxylic acid $(CF_3)_2CHC(O)OH$. Lastly, the carboxylic acid was decarboxylated with an aqueous base to form hexafluoropropane as another valuable product; this reaction is shown in Figure 6(b). Fluorovinyl alkyl ethers are commercially available products and they can also be prepared following the synthetic route described in Figure 6(c): The reaction between perfluoro-*iso*-butene (1) and a proper alcohol produces an octafluoro-*iso*-butyl alkyl ether (2) and by its subsequent dehydrofluorination the alkylating agent (3) and HF are synthesized.

Figure 6. (**a**) Reaction between DAF-PFPEs and fluorovinyl alkyl ethers; (**b**) Byproduct converted into hexafluoropropane; (**c**) Synthetic route for alkylating agent -fluorovinyl alkyl ethers.
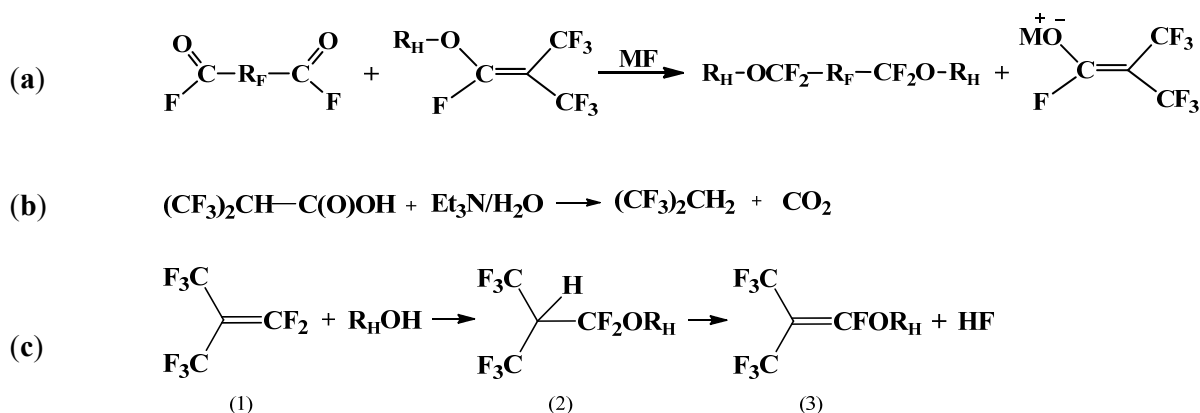
Newly developed alkylating agents which have strong a alkylating ability and less toxicity have been emerging in the past years, but these kinds of alkylating methods have an unavoidable common drawback: A stoichiometric amount of metal fluoride is usually needed to provide metal perfluoroalkoxides, and large amounts of partially reacted solid metal fluoride is left over after the reaction.

2.3.2. Catalytic Alkylation of Perfluoro(mono)acyl Fluorides and DAF-PFPE

A classical example of catalytic alkylation is the alkylation of perfluoroacyl fluorides performed by employing SbF_5 as acid catalyst in anhydrous medium that reacts with alkyl fluoride to produce HFE (Figure 7). The first step in this pathway is the reaction of SbF_5 with alkyl fluoride forming high valence metal SbF_6^-. The extra F ion from SbF_6^- attacks the carbonyl group of acyl fluorides forming

alkoxides. Subsequently, the nucleophilic addition to *in situ* generated alkoxides produces the PFPE with alkoxy-group endings. In this reaction, work-up with a large amount of partially reacted metal fluoride is avoided; however, the drawback of this method is that the active acid catalyst may promote undesired isomerization or decomposition reactions and consequently deliver low or erratic yields [27].

Figure 7. Alkylation of acylfluorides with SbF_5 as acid catalyst.
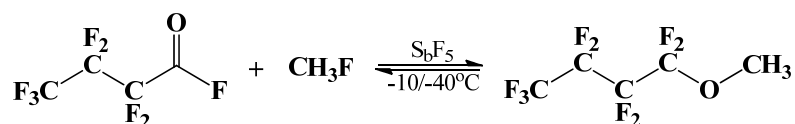
DA-PFPEs can be also successfully obtained via a novel synthetic route that consists in the reaction of DAF-PFPEs with alkyl fluoroformate (Figure 8) in the presence of a source of fluorine ions, generally metal fluoride (MF); the reaction can be regarded as catalytic alkylation of *in situ* generated PFPE dialkoxides.

Figure 8. Reaction between DAF-PFPEs and alkyl fluoroformate with metal fluoride as source fluorine ions.
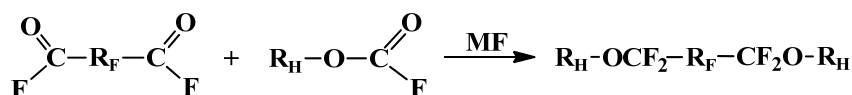
Table 1. Preparation of selected DA-PFFEs through perfluoropolyether acylfluorides alkylation.

Acylfluoride	Fluoroformate	HFE	Conv.%	Sel.%
z-DAF [a]	$CH_3OC(O)F$	CH_3O-(Z-PFPE)-OCH_3	90	100
z-DAF [a]	$CH_3CH_2OC(O)F$	CH_3CH_2O-(Z-PFPE)-OCH_2CH_3	96	100
z-DAF [a]	CH_2=$CHCH_2O(O)F$	CH_2=$CHCH_2O$-(Z-PFPE)-OCH_2CH=CH_2	90	100

[a] linear DAF-PFPE: $FC(O)CF_2O$-$(CF_2CF_2O)_n(CF_2O)_m$-$CF_2C(O)F$ (AMW 620 amu).

This fluoride-catalyzed fluoroformates alkylating reaction gives DA-PFPEs in good yield and CO_2 is the only by-product. Due to the big differences of boiling points among alkyl fluoroformates, DAF-PFPE and DA-PFPEs, un-reacted alkylating reagents can be easily restored through a standard distillation. Alkyl fluoroformate can be methyl, ethyl as well as allyl fluoroformates. The great variety of fluoroformate alkylating reagents improves the utility of this straightforward alkylating reaction. Examples of several successfully employed fluoroformates, which reacted with high boiling point linear DAF-PFPE with good selectivity and yield are reported in Table 1 [28,29].

This catalytic alkoxides alkylation followed two supposed pathways (Figure 9): (a) A nucleophilic addition of the perfluoroalkoxide to alkyl fluoroformate directly forming the DA-FPE and CO_2; or (b) through the carbonate intermediate, $R_FCFOC(O)OR_H$, followed by a second nucleophilic substitution to generate the corresponding products [28]. According to both pathways, the rearrangement of the fluoroformate group can release fluorides and replenish the perfluoro-alkyloxy-anions formation by reacting with a new acylfluoride. Therefore, alkyl fluoroformates can be applied not only as alkylating agents but also as an alternative fluorine ion source for the alkoxide formation.

Figure 9. Reaction mechanism for the synthesis of DM-FPEs. For clarity, here using R_f-C(O)F to represent DAF-PFPEs.
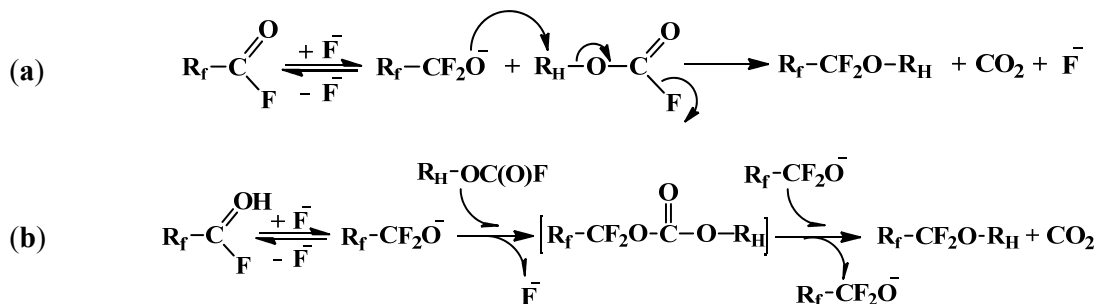
The alkyl fluoroformates are not commercially available and their synthesis comprises the reaction of carbonyl difluoride with alcohols at a low temperature in the presence of anhydrous sodium fluoride. The main by-products of their synthesis are alkyl carbonate, $R_HOC(O)OR_H$, and hydrogen fluoride. Alkyl carbonate is formed by further reaction of the forming methyl fluoroformate with alcohol. Hydrogen fluoride can be rapidly scavenged by sodium fluoride [30].

3. Chemical Physical Properties of α,ω-Dialkoxyperfluoropolyethers

One of the most representative classes of DA-FPEs is that of α,ω-dimethoxyfluoropolyethers (DM-FPEs) with the structure $CH_3O(CF_2CF_2O)_n(CF_2O)_mCH_3$ (where the indices *n* and *m* define the random distribution of the related moieties content). In Table 2, the structures and molecular weights of four DM-FPEs samples are reported. The chemical structure is also identified by two digit numbers (*i.e.*, 01, 02, 03 and 13): The first digit indicates the number of –CF$_2$O– units and the second digit indicates the number of –CF$_2$CF$_2$O– units in the molecule.

Table 2. Structure, molecular weight (MW) and purity of DM-FPEs samples.

Sample	Structure	MS	Purity (%, by GC)
DM01	$CH_3OCF_2CF_2OCH_3$	162	99.8
DM02	$CH_3OCF_2CF_2OCF_2CF_2OCH_3$	278	99.9
DM03	$CH_3OCF_2CF_2OCF_2CF_2OCF_2CF_2OCH_3$	394	99.0
DM13	$CH_3OCF_2CF_2OCF_2OCF_2CF_2OCF_2CF_2OCH_3$	460	96.8

3.1. Boiling Point

The boiling points (*b.p.*) of DM-FPEs are reported in Figure 10 as a function of the number of backbone chain atoms (*N*), *i.e.*, carbon plus oxygen atoms. They increase regularly with *N*. In Figure 10, DM-FPEs boiling points are also compared with those of α,ω-dihydrofluoroethers (HFEs) [31] and perfluoropolyethers (PFPEs) [32].

Figure 10. Boiling points as a function of the number of chain atoms, *N*, for DM-FPEs (×), HFEs (□) and PFPEs (○).
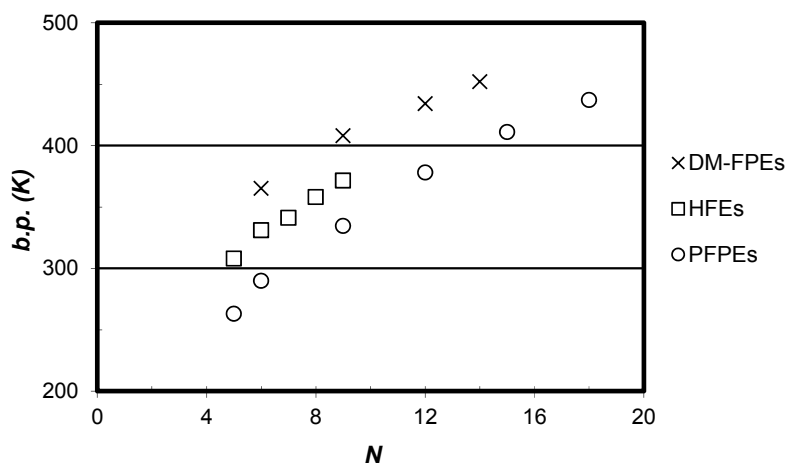
The highest boiling points are those of DM-FPEs, the intermediates are HFEs and the lowest ones are PFPEs. The above-mentioned result reflects the typical low intermolecular interactions of perfluorinated compounds. Partially fluorinated ethers, like HFEs and DM-FPEs, display higher boiling temperatures and this is indicative of greater intermolecular polar interactions [11].

Considering three similar fluoromethylethers, CF_3OCF_3 (b.p. 214 K; μ = 0.49 D), CF_2HOCF_3 (b.p. 238 K, μ = 1.18 D) and CH_3OCF_3 (b.p. 250 K, μ = 2.56 D), the boiling points and the dipole moments have analogous tendencies [33]. The progressive substitution of fluorine atoms with hydrogen in the methoxy end caps leads to a stronger dipole and consequently, to an increase of the boiling point, as shown in Figure 10. The boiling point differences between PFPEs and HFEs and between PFPEs and DM-FPEs are not constant but decrease continuously with the chain length. Since the attractive forces are due to polar terminal groups, their relative intensity decreases as *N* increases and, as a result, the boiling points of HFEs, DM-FPEs and PFPE tend to an asymptote at higher *N* values.

3.2. Density

A comparison of the specific volume (V_{sp}) at 298 K of DM-FPEs, HFEs and PFPEs series is shown in Figure 11. The DM-FPEs sequence shows the highest specific volume and the PFPEs the lowest at identical number of chain atoms, *N*. The V_{sp} of PFPEs is almost constant and independent of *N*. The specific volumes of DM-FPEs and HFEs decrease continuously to a plateau that approximately coincides with the constant V_{sp} of PFPEs. This behavior can also be explained on the basis of the differences between terminal groups. Moving from $-CF_3$ to $-CF_2H$ and to $-CH_3$, the molecular weight of the groups diminishes; on the contrary, the variation of volume is less noticeable because the Van der Waals radii of fluorine and hydrogen are similar [34]: 0.147 and 0.12 nm, respectively. Consequently, the difference in specific volume between the three series is mainly due to the variation of molecular weight, explaining the tendencies of V_{sp} observed in Figure 11. Furthermore, as the weight fraction of the chain ends decreases with *N*, it is logical that the specific volume of HFEs and DM-FPEs tends to the V_{sp} values of PFPEs when the chain is sufficiently long.

Figure 11. Specific volume at 298 K as a function of the number of chain atoms, *N*, for DM-FPEs (×), HFEs(□) and PFPEs (○).
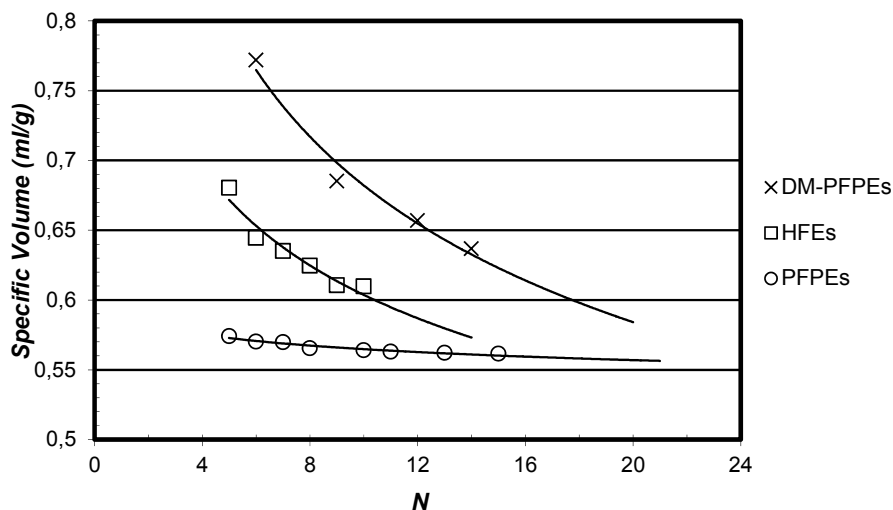
3.3. Vapor Pressure and Vaporization Enthalpy

The vapor pressure data, plotted as Clausius-Clapeyron equation in Figure 12, show a deviation from linearity at low temperatures, which is common for many oligomeric substances. Vaporization enthalpies (ΔHv) are also derived from the Clausius-Clapeyron plot in the range of temperatures in which the function is linear.

The ΔH_v data of DM-FPEs, reported as a function of number of chain atoms, *N*, are compared with those of HFEs and PFPEs in Figure 13. These data indicate the highest values for DM-FPEs, intermediate for HFEs and the lowest for PFPEs. As the effect of the polar terminal groups ($-OCF_2H$ and $-OCH_3$) diminishes with the length of the chain, ΔH_v also decreases and tends to the values of PFPEs when *N* is above 15 [4].

Figure 12. Clausius–Clapeyron plot for DM-FPEs: DM01 (×), DM02 (□), DM03 (○) and DM13 (Δ). (See also Table 2 for detailed composition of these DM-FPEs samples.)
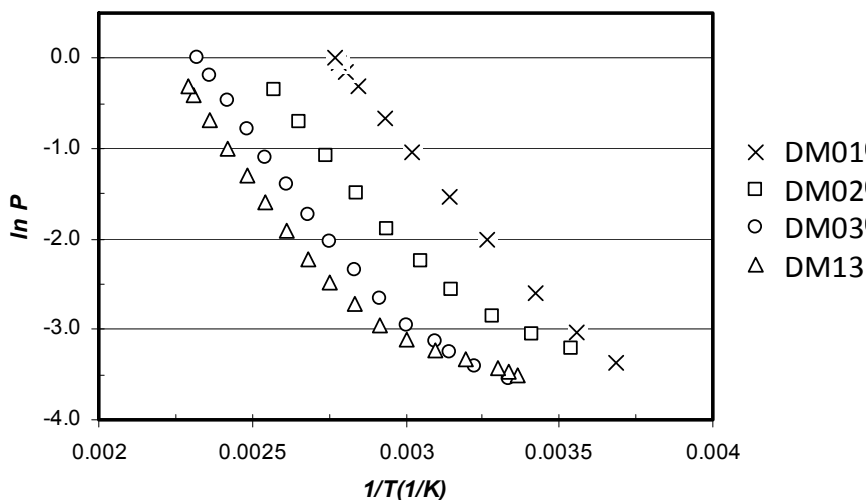
Figure 13. Vaporization enthalpy, ΔH_v, as a function of the number of chain atoms, N, for DM-FPEs ($\times$), HFEs ($\square$) and PFPEs ($\circ$).
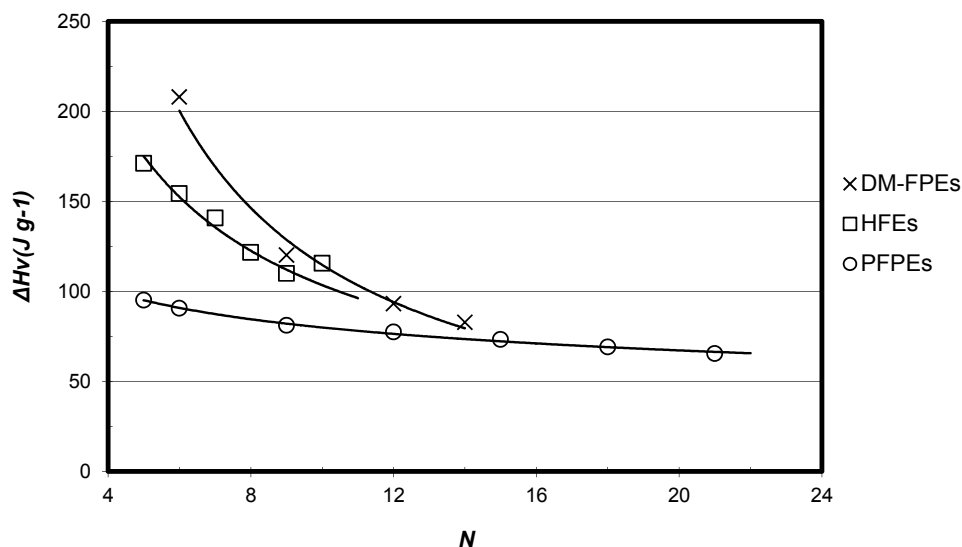
3.4. Refractive Index

The refractive indices of the series DM-FPEs and HFEs plotted as a function of the number of chain atoms, N, indicate two opposed behaviors (Figure 14). In particular the refractive index n increases for DM-FPEs and decreases for HFEs. In both cases, increasing the chain length, the refractive indices tend to a plateau value, close to the characteristic refractive index of linear PFPEs (1.290–1.295) [11]. The tendencies of DM-FPEs and HFEs refractive indices are mainly due to the terminal groups that contribute to n in an opposite way. As reported in the literature, the group influence of –OCH_3 is higher than that of –OCF_3, while that of –OCF_2H is lower [35].

Figure 14. Refractive index (n) at 293 K as a function of the number of chain atoms, N, for DM-FPEs ($\times$) and HFEs ($\square$), and the range of refractive index of linear PFPEs.
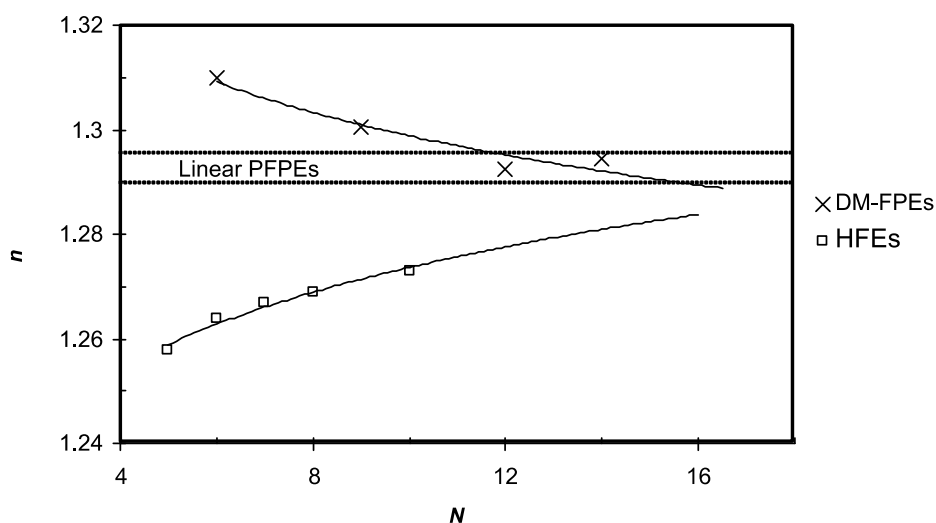
4. Atmospheric Chemistry of DA-FPEs

The absence of chlorine atoms in HFEs makes them possess a negligible ozone depleting potential (ODP), but the presence of C-F and C-O bonds may absorb in the terrestrial infrared radiation region (800–1200 cm^{-1}), and could play a significant role as a greenhouse gas. Therefore, considerable attention has been paid in recent years to perform both experimental and theoretical studies on atmospheric chemistry of HFEs. However, surprisingly, only relatively little information about DA-FPEs has been reported [36,37]. Since the only available data on DA-FPEs compounds are related to DM-FPEs with structure $CH_3O(CF_2CF_2O)_nCH_3$ that only contain the $-(CF_2CF_2O)-$ units, the discussion has been focused prevalently on the atmospheric chemistry of these compounds.

4.1. Atmospheric Lifetimes and Decomposition Mechanism of α,ω-Dialkoxyperfluoropolyethers

In 2004, the first understanding of the atmospheric chemistry for DM-FPEs was achieved by studying the kinetics and mechanism of $CH_3O(CF_2CF_2O)_nCH_3$ ($n = 1$–3) oxidation which is initiated by Cl atoms and OH radicals in the atmosphere; the impact of their degradation products on the climate were also discussed [1]. Like most organic compounds, the primary tropospheric degradation of $CH_3O(CF_2CF_2O)_nCH_3$ is mainly dominated by the attack of OH radicals [38]. Understanding of reaction kinetics is essential for the evaluation of the atmospheric lifetime of these molecules. In addition to the reaction with hydroxyl radicals (OH), organic compounds can also be removed from the atmosphere via photolysis, wet deposition, and reaction with NO_3 radicals, Cl atoms, and O_3 [38–40]. For saturated compounds such as $CH_3O(CF_2CF_2O)_nCH_3$, reactions with NO_3 radicals and O_3 are typically too slow to be of importance [1]. The average concentration of Cl atoms in the troposphere is orders of magnitude less than that of OH radicals [41]. Reaction with Cl atoms will be a less significant atmospheric loss mechanism. Since ethers do not absorb at UV wavelengths > 200 nm, photolytic sink will be not be an important degradation pathway [42] either. Highly fluorinated molecules, such as $CH_3O(CF_2CF_2O)_nCH_3$, are hydrophobic and wet deposition is unlikely to be of importance. In conclusion, the atmospheric lifetime of $CH_3O(CF_2CF_2O)_nCH_3$ is determined by its reaction with OH.

Smog chambers equipped with FTIR spectrometers were used to study the Cl atom and OH radical initiated oxidation of $CH_3O(CF_2CF_2O)_nCH_3$ in 720 Torr of air at 296.3 K. Relative rate methods were used to measure $k(Cl+CH_3O(CF_2CF_2O)_nCH_3)) = 3.7$ (± 0.7) $\times 10^{-13}$ and $k(OH+CH_3O(CF_2CF_2O)_nCH_3)$ $= 2.9$ (± 0.5) $\times 10^{-14}$ cm^3 $molecule^{-1} \cdot s^{-1}$. The relative rate method is widely used to measure the reactivity of OH radicals with organic compounds [43]. The hydrogen abstraction reaction from the terminal groups has been assumed, according to established literature data, as the rate-determining step for the decomposition of the entire molecule [44]. It is well known that $-CF_2CF_2-$ units are unreactive toward Cl and OH radicals. Thus, the reactivity of $CH_3O(CF_2CF_2O)_nCH_3$ is confined to the C–H bonds on either end-groups of the molecule. Indeed, appropriate studies showed that the reactivity of the methyl group did not change noticeably by increasing the number n of $-(CF_2CF_2O)-$ units from 1 to 3 [45]. Nevertheless, the average concentration of Cl atoms in the troposphere is orders of magnitude less than that of OH radicals [41]. Thus, knowing the $k(OH+CH_3O(CF_2CF_2O)_nCH_3)_s$ rate constant, the DM-FPEs atmospheric lifetime has been evaluated to be two years [1].

Tuazon *et al.* claimed that in air the oxidation of HFEs with difluoromethoxy ending groups, OCF_2H, like $HCF_2OCF_2OCF_2CF_2OCF_2H$, $HCF_2OCF_2CF_2OCF_2H$, and $HCF_2OCF_2OCF_2H$, gives $C(O)F_2$ as the only carbon-containing product [46]. For DM-PFEs which end with methoxy-groups, fluoroformates $CH_3O(CF_2CF_2O)_nC(O)H$ were recognized as the only oxidation decomposition products with a 100% yield; the formed fluoroformates can be further oxidized to di-formates $H(O)CO(CF_2CF_2O)_nC(O)H$ [1]. Concerning the impacts of fluoroformates on the climate, since fluorinated esters are known to be easily hydrolyzed [46,47], it is usually assumed that they can be easily removed though wet deposition; therefore Andersen *et al.* [1] deduced that formate $CH_3O(CF_2CF_2O)_nC(O)H$ is not expected to be persistent or pose any significant environmental hazard. However, Bravo *et al.* [48] assumed that the highly fluorinated nature of fluoroformates may decrease their solubility in water and could contribute a significant indirect GWP. Up to now, due to the lack of experimental data like gas-to-water equilibrium and solubility test of fluoroformates, it is still unclear how rapidly fluoroformates will be removed via uptake and hydrolysis in rain/cloud/seawater [49]. Further experimental examinations are needed for the determination of the atmospheric implication of fluoroformats.

4.2. Global Warming Potential

In 1995, Pinnock *et al.* outlined a method to determine the instantaneous forcings (IF) from the IR absorption spectra such as those reported in Figure 14. As the values of GWP can be estimated on the basis of the IF, in Table 3 GWP relative to carbon dioxide of DM-FPEs at 100 year time horizons has been reported, and the comparison with other greenhouse gases, such as CF_3Cl (CFC-11), CF_2HOCF_3 (HFE125), CH_3OCF_3 (HFE143a) and other HFEs, is reported in Table 3.

Table 3. Atmospheric lifetimes and global warming potential (GWP relative to carbon dioxide) of DM-FPEs, CFC and HFE.

	IF ($W \cdot m^{-2} \cdot ppb^{-1}$)	Lifetime (y)	GWP 100 years Time horizon	Reference
$CFCl_3$ (CFC11)	0.25	45	4750	IPCC/TEAP
CF_2HOCF_3 (HFE125)	0.44	136	14900	IPCC/TEAP
CH_3OCF_3 (HFE143a)	0.27	4.3	756	IPCC/TEAP
$C_4F_9OCH_3$ (HFE-7100)	0.31	5	390	[50]
HCF_2OCF_2H	0.40	11.3	3699	[8,9]
$HCF_2OCF_2OCF_2H$	0.66	12.1	2700	[50]
$HCF_2OCF_2CF_2OCF_2H$	0.87	6.2	1500	[50]
$HCF_2OCF_2OCF_2CF_2OCF_2H$	1.37	6.3	1840	[8,9]
CH_3OCH_3	0.020	0.015	0.3	[41,42]
DM01	0.32	2	230	[1]
DM02	0.61	2	270	[1]
DM03	0.83	2	250	[1]

Figure 15. Infrared spectra of $CH_3OCF_2CF_2OCH_3$ (**A**), $CH_3O(CF_2CF_2O)_2CH_3$ (**B**), and $CH_3O(CF_2CF_2O)_3CH_3$ (**C**).
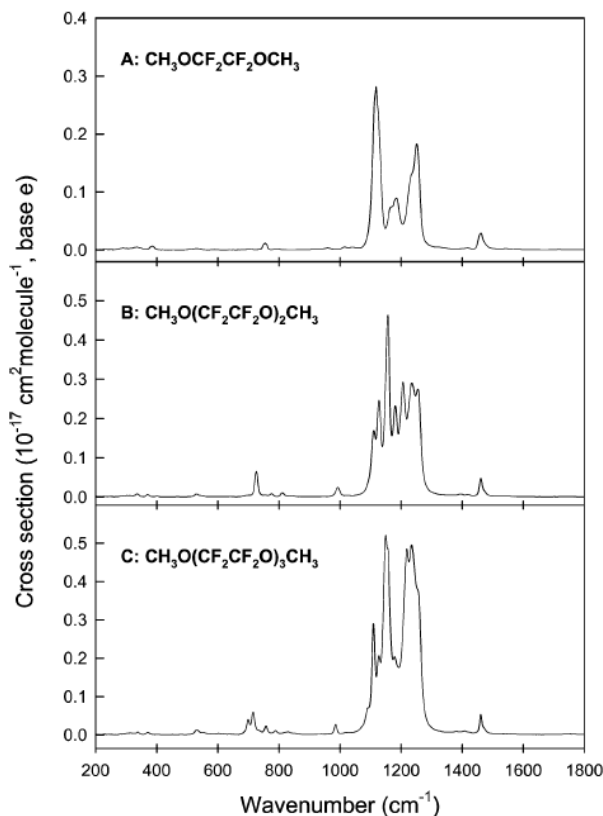
It is evident from Table 3 that DM-FPEs have relatively high instantaneous forcing (IF) but much lower GWPs, if compared with CFC11 and HFE compounds. In addition, the higher the number of $-(CF_2CF_2O)-$ units, the higher the absorption in the 800–1200 cm^{-1} range, that is responsible for the high IF. Thus the reason of the mitigation of DM-FPEs GWP is mostly due to their short atmospheric lifetimes and the emission of DM-FPEs into the atmosphere should not contribute significantly to the climate change.

On the basis of the data of DM-FPEs which contain only $-(CF_2CF_2O)-$ units and the studies on series of HFPE with $-CF_2H$ end-groups [51], it seems reasonable to expect that the reactivity of C–H bonds is independent from the number of $-CF_2O-$ units in the DM-FPE molecule. However, there are no available kinetic data for DM-FPEs with structure $CH_3O(CF_2CF_2O)_n(CF_2O)_mCH_3$ to confirm this assumption.

In addition, DM-FPE commercial products are mixtures of homologous copolymers with similar lengths but different unites, *i.e.*, different *n* and *m*; further experimental studies are most likely necessary for a better understanding of the effects of the $(CF_2CF_2O)_n/(CF_2O)_m$ ratio on atmospheric chemistry of DM-FPEs.

Acknowledgements

References

1. Andersen, M.P.S.; Hurley, M.D.; Wallington, T.J.; Blandini, F.N.; Jensen, R.; Librando, V.; Hjorth, J.; Marchionni, G.; Avataneo, M.; Visca, M.; *et al.* Atmospheric chemistry of $CH_3O(CF_2CF_2O)_nCH_3$ (n = 1–3): Kinetics and mechanism of oxidation initiated by Cl atoms and OH radicals, IR spectra, and global warming potentials. *Phys. Chem. A* **2004**, *108*, 1964–1972.

2. WMO (World Meteorological Organization). Scientific Assessment of Ozone Depletion: 2002, Global Ozone Research and Monitoring Project; Report No. 47, Geneva, Switzerland, 2003.

3. Wallington, T.J.; Schneider, W.F.; Sehested, J.; Bilde, M.; Platz, J.; Nielsen, O.J.; Molina, M.J. Atmospheric chemistry of HFE-7100 ($C_4F_9OCH_3$): Kinetics of its reaction with OH radicals, UV spectra and kinetic data for $C_4F_9OCH_2$• and $C_4F_9OCH_2O_2$• radicals, and the atmospheric fate of $C_4F_9OCH_2O$• radicals. *J. Phys. Chem. A* **1997**, *101*, 8264–8274.

4. Marchionni, G.; Avataneo, M.; de Patto, U.; Maccone, P.; Pezzin, G. Physical properties of four alpha-omega-dimethoxyfluoropolyethers. *J. Fluor. Chem.* **2005**, *126*, 465–473.

5. Marchionni, G.; de Patto, U.; Avataneo, M. Liquid-liquid extraction of polar organic substances from their aqueous solutions with fluorinated extracting liquids. European Patent Application, EP 1346757 A, 24 September 2003.

6. Marchionni, G.; Visca, M. Perfluoropolyethers (PFPEs) having at least an alkylether end group and respective preparation process. *European Patent Application.* EP 1275678, 23 April 2003.

7. Marchionni, G.; Petricci, S.; Guarda, P.A.; Spataro, G.; Pezzin, G. The comparison of thermal stability of some hydrofluoroethers and hydrofluoropolyethers. *J. Fluor. Chem.* **2004**, *125*, 1081–1086.

8. Marchionni, G.; Maccone, P.; Pezzin, G. Thermodynamic and other physical properties of several hydrofluoro-compounds. *J. Fluor. Chem.* **2002**, *118*, 149–155.

9. Malavasi, M.; Sianesi, D. Novelties and prospects in the synthesis of perfluoropolyethers by oxidative polymerization of fluoroolefins. *J. Fluor. Chem.* **1999**, *95*, 19–25.

10. Guarda, P.A.; Barchiesi, E.; Fontana, G.; Petricci, S.; Pianca, M.; marchionni, G. Peroxidic perfluoropolyether from tetrafluoroethylene oxidation: Micro structural analysis by NMR spectroscopy and mechanistic considerations. *J. Fluor. Chem.* **2005**, *126*, 141–153.

11. Sianesi, D.; Marchionni, G.; de Pasquale, R.J. Perfluoropolyethers (PFPEs) from perfluoroolefin photooxidation: Fomblin® and Galden® fluids. In *Organofluorine Chemistry Principles and Commercial Applications*; Bank, R.E., Smart, R.E., Tatlow, J.C., Eds.; Plenum Publishing Corporation: New York, NY, USA, 1994; pp. 431–457.

12. Sansotera, M.; Navarrini, W.; Gola, M.; Bianchi, L.C.; Wormald, P.; Famulari, A.; Avataneo, M. Peroxidic perfluoropolyether for the covalent binding of perfluoropolyether chains on carbon black surface. *J. Fluor. Chem.* **2011**, *132*, 1254–1261.

13. Navarrini, W.; Venturini, F.; Sansotera, M.; Ursini, M.; Metrangolo, P.; Resnati, G.; Galimberti, E.; Barchiesi, E.; Dardani, P. The use of perfluoroalkyl hypofluorites for an efficient synthesis of perfluorinated ethers characterized by low Ostwald coefficient. *J. Fluor. Chem.* **2008**, *129*, 680–685.

14. Sianesi, D.; Caporiccio, G. Sulphonic derivatives having the structure of polyoxapoly fluoroalkanes. U.S. Patent, 3,847,978, 23 December 1974.

15. Prakash, G.K.S.; Hu, J.; Olah, G.A. Alkylation of in situ generated fluorinated alkoxides: Novel synthesis of partially fluorinated ethers. *Arkivoc SD-369C* **2003**, 104–119.

16. Evans, F.W.; Litt, M.H.; Weidler-Kubanee, A.M.; Avonda, F.P. Formation of adducts between fluorinated ketones and metal fluorides. *J. Org. Chem.* **1968**, *33*, 1837–1839.

17. Parker, A.J. The effects of solvation on the properties of anions in dipolar aprotic solvents. *Q. Rev. Chem. Soc.* **1962**, *16*, 163–187.

18. Lerman, O.; Rozen, S. Novel method for introduction of the perfluoroethoxy group using elemental fluorine. Synthesis and chemistry of fluoroxypentafluoroethane. *J. Org. Chem.* **1980**, *45*, 4122–4125.

19. Navarrini, W.; Tortelli, V.; Russo, A.; Corti, S. Organic hypofluorites and their new role in industrial fluorine chemistry. *J. Fluor. Chem.* **1999**, *95*, 27–39.

20. Feiring, E.A.; Wonchoba, R.E.; Rozen, S. Synthesis of partially fluorinated monomers and polymers for ion-exchange resins. *J. Fluor. Chem.* **1999**, *93*, 93–101

21. Croix, L.S.; Szur, A.J. Ether compounds as inhalant anesthetics. U.S. Patent, 3,962,460, 8 June 1976.

22. Paquette, L.A. *Encyclopedia of Reagents for Organic Synthesis*; John Wiley & Sons: Hoboken, NJ, USA, 1995; pp. 2132–2135.

23. Suter, C.M. *The Organic Chemistry of Sulfur*; Wiley & Sons: Hoboken, NJ, USA, 1944; pp. 48–74.

24. Marchionni, G.; Mario, V. PFPEs having at least an alkylether end group and respective preparation process. U.S. Patent, 7,488,852, 10 February 2009.

25. Lamanna, W.M.; Flynn, R.M.; Vitcak, D.R.; Qiu, Z.-M. Catalytic process for making hydrofluoroethers. PCT WO 9947480, 23 September 1999.

26. Behr, F.E.; Cheburkov, Y. Process for preparing hydrofluoroethers. U.S. Patent, 6,023,002, 8 February 2000.

27. Lamanna, W.M.; Flynn, R.M.; Vitcak, D.R.; Qiu, Z.-M. Catalytic process for making hydrofluoroethers. U.S. Patent, 6,046,368, 4 April 2000.

28. Galimberti, M.; Fontana, G.; Resnati, G.; Navarrini, W. New catalytic alkylation of in situ generated perfluoro-alkyloxy-anions and perfluoro-carbanions. *J. Fluor. Chem.* **2005**, *126*, 1578–1586.

29. Navarrini, W.; Galimberti, M.; Fontana, G. Process for preparing hydrofluoroethers. European patent application EP 1462434A, 16 March 2004.

30. Klauke, E. Braden, R. Fluoroformates. GB 1216639, 23 December 1970.

31. Marchionni, G.; Bassi, M.; Fontana, G.; Maccone, P. Ajroldi, J. Some physical chemical properties of alpha-omega dihydroperfluoropolyethers. *J. Fluor. Chem.* **1999**, *98*, 41–54.

32. Marchionni, G.; Ajroldi, G.; Righetti, M.C.; Pezzin, G. Molecular interactions in perfluorinated and hydrogenated compounds: Linear paraffins and ethers. *Macromolecules* **1993**, *26*, 1751–1757.

33. Marchionni, G.; Avataneo, M.; de Patto, U.; Maccone, P.; Pezzin, G. Physical properties of four alpha-omega dimethoxyfluoropolyethers. *J. Fluor. Chem.* **2005**, *126*, 465–473.

34. Bondi, A. Van der waals volumes and radii. *J. Phys. Chem.* **1964**, *68*, 441–451.

35. Le, T.D.; Weers, J.G. Group contribution-additivity and quantum mechanical models for predicting the molar refractions, indexes of refraction, and boiling points of fluorochemicals. *J. Phys. Chem.* **1995**, *99*, 13909–13916.

36. Blowers, P.; Moline, D.M.; Tetrault, K.F.; Wheeler, R.R.; Tuchawena, S.L. Prediction of radiative forcing values for hydrofluoroethers using density functional theory methods. *J. Geophys. Res.* **2007**, *112*, doi: 10.1029/2006JD008098.

37. Blowers, P.; Moline, D.M.; Tetrault, K.F.; Wheeler, R.R.; Tuchawena, S.L. Global warming potentials of hydrofluoroethers. *Environ. Sci. Technol.* **2008**, *42*, 1301–1307.

38. Blanco, M.B.; Teruel, M.A. Atmospheric degradation of fluoroesters (FESs): Gas-phase reactivity study towards OH radicals at 298 K. *Atmos. Environ.* **2007**, *41*, 7330–7338.

39. Blanco, M.B.; Bejan, I.; Barnes, I.; Wiesen, P.; Teruel, M.A. Kinetics of the reactions of chlorine atoms with selected fluoroacetates at atmospheric pressure and 298 K. *Chem. Phys. Lett.* **2008**, *453*, 18–23.

40. Hudlicky, M. *Chemistry of Organic Fluorine Compounds*, 2nd ed.; Ellis Horwood: Chichester, UK, 1976; pp. 255–257.

41. Finlayson-Pitts, B.J.; Pitts, J.N., Jr. *Atmospheric Chemistry: Fundamentals and Experimental Techniques*; John Wiley and Sons: New York, NY, USA, 1986.

42. Calvert, J.G.; Pitts, J.N., Jr. *Photochemistry*; John Wiley: New York, NY, USA, 1966.

43. Atkinson, R.; Baulch, D.L.; Cox, R.A.; Crowley, J.N.; Hampson, R.F.; Hynes, R.G.; Jenkin, M.E.; Rossi, M.J.; Troe, J.; Wallington, T.J. Evaluated kinetic and photochemical data for atmospheric chemistry: Volume IV—Gas phase reactions of organic halogen species. *Atmos. Chem. Phys.* **2008**, *8*, 4141–4496.

44. AFEAS Workshop. *Kinetics and Mechanisms for the Reaction of Halogenated Organic Compounds in the Troposphere*; AFEAS Workshop: Dublin, Ireland, 1993.

45. Pinnock, S.; Hurley, M.D.; Shine, K.P.; Wallington, T.J.; Smyth, T.J. Radiative forcing of climate by hydrochloroflurocarbons and hydrofluorocarbons. *J. Geophys. Res. Atmos.* **1995**, *100*, 23227–23238.

46. Bunyard, W.C.; Kadla, J.F.; de Simone, M.S. Viscosity effects on the thermal decomposition of bis(perfluoro-2-N-propoxypropionyl) peroxide in dense carbon dioxide and fluorinated solvents. *J. Am. Chem.* **2001**, *123*, 7199–7206.

47. Sansotera, M.; Bianchi, C.L.; Lecardi, G.; Marchionni, G.; Metrangolo, P. Resnati, G.; Navarrini, W. Highly hydrophobic carbon black obtained by covalent linkage of perfluorocarbon and perfluoropolyether chains on the carbon surface. *Chem. Mater.* **2009**, *21*, 4498–4504.

48. Bravo, I.; Diaz-de-mera, Y.; Aranda, A.; Moreno, E.; Nutt, D.R.; Marston, G. Radiative efficiencies for fluorinated esters: Indirect global warming potentials of hydrofluoroethers. *Phys. Chem. Chem. Phys.* **2011**, *13*, 17185–17193.

49. Javadiando, S.M.; Nielsen, J.; Wallington, J.T.; Hurley, D.A.; Owens, G.J. Atmospheric chemistry of n-butanol: kinetics, mechanisms, and products of Cl atom and OH radical initiated oxidation in the presence and absence of NO(x). *Environ. Sci. Technol.* 2007, *41*, 7389–7395.

Appl. Sci. **2012**, *2*

50. IPCC. *Climate Change 2001: The Scientific Basis*; IPCC: Geneva, Switzerland, 2001.

51. Wallington, T.J.; Hurley, M.D.; Nielsen, O.J. The radiative efficiency of $HCF_2OCF_2OCF_2CF_2OCF_2H$ (Galden[®] PFPEs) revisited. *Int. J. Chem. Kinet.* **2008**, *40*, 819–825.

Article

Synthesis of Some New Fluorinated Hexahydroquinoline and Acridinedione Derivatives in Trifluoroethanol

Cosmas O. Okoro *, Mumiye A. Ogunwale and Tasneem Siddiquee

Department of Chemistry, Tennessee State University, Nashville, TN 37209, USA;
E-Mails: mumiye828@yahoo.com (M.A.O.); tsiddiqu@tnstate.edu (T.S.)

* Author to whom correspondence should be addressed; E-Mail: cokoro@tnstate.edu;
Tel.: +1-615-963-5325; Fax: +1-615-963-5326.

Abstract: This article describes one-pot synthesis of new fluorinated hexahydroquinoline derivatives via unsymmetric Hantzsch reaction involving 5-trifluoromethyl-1,3-cyclohexanedione, aldehydes, acetoacetate ester, and ammonium acetate in trifluoroethanol (TFE). The reaction is simple and rapid with high yield.

Keywords: unsymmetric Hantzsch reaction; dihydropyridine; trifluoromethyl; hexahydroquinoline; acridinedione; trifluoroethanol

1. Introduction

Substituted 1,4-dihydropyridines (1,4-DHPs) are analogs of nicotine adenine dinucleotide dehydrogenase (NADH) coenzymes and are an important class of drugs [1]. In recent years, attention has been paid to the synthesis of 1, 4-dihydropiridines due to their significant biological activities [2]. They are well known as calcium channel modulators and have emerged as an important class of drugs for the treatment of cardiovascular diseases [3]. In particular, dihydropyridine drugs, such as nifedipine, nicardipine, amlodipine are effective cardiovascular agents for the treatment of hypertension [4]. Due to their ability to block the L-type calcium channel, DHPs, such as felodipines have been characterized as potentiators of several mutant cystic fibrosis transmembrane conductance regulator (CFTR) channels [5]. In addition, dihydropyridine unit has been used as a hydride source for reductive amination [6].

Examples of 1,4-Dihydropyridine drugs.

Felodipine   Amlodipine   Azelnidipine
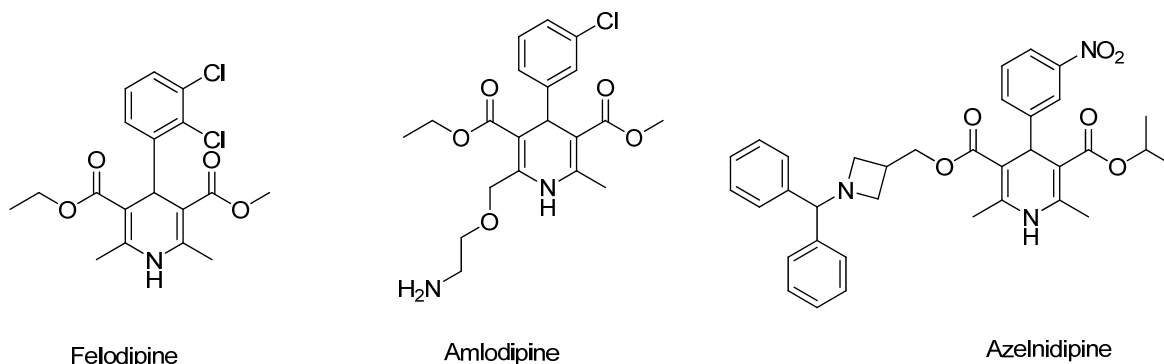
Heterocyclic ring system, such as acridinedione is generally considered to be among the most prevalent ring systems in medicinal chemistry [7]. They are known to be potent frameshift mutagens in virus and bacteria [8]. Acridinediones have also been reported as antimalarial agents [9].

Organic compounds bearing trifluoromethyl group have attracted considerable attention due to their role in organic, medicinal, and heterocyclic synthesis. In particular, the incorporation of fluorine atom has been used by medicinal chemists to tailor the physical and metabolic profiles of drug candidates [10]. For instance, addition of fluorine in the place of hydrogen has been known to enhance binding interactions, improve metabolic stability, increase CNS penetration, and eliminates ancillary ion channel activity by attenuating amine basicity [11]. The electronic effect of fluorine via induction is enormous and this change could have a major effect on the binding potential of the small molecules.

Polycyclic compounds, particularly heterocycles are important in medicinal chemistry because their rigid structures permit selective interaction with proteins and other receptors. The literature has few reports of dihydropyridines containing the highly electronegative and lipophilic trifluoromethyl group. Thus, the synthesis of trifluoromethylated heterocyclic compounds has drawn much attention in recent years. In continuation of our efforts towards the synthesis of fluorinated heterocycles of biological importance, we turned our attention to the synthesis of fluorinated hexahydroquinoline derivatives in trifluoroethanol (Scheme 1), as potential calcium channel modulators. We chose 2,2,2-trifluoroethanol because the solvent appears to have low nucleophilicity, strong hydrogen bond donating ability and high polarity [12]. It is also cheap and relatively nontoxic.

Scheme 1. Synthesis of fluorinated hexahydroquinoline from 5-trifluoromethyi-1,3-cyclohehexanedione, aldehydes, β- ketoesters and ammonium acetate.
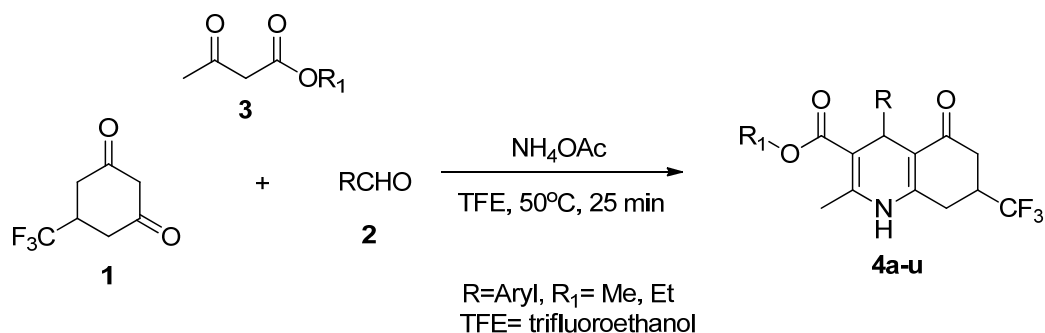
2. General

Apart from 5-trifluoromethyl-1,3-cyclohexanedione that was discovered by our group [13], the reagents and solvents in the appropriate grades were purchased and used without further purification. Melting points were done on Mel-temp LL and were uncorrected. IR spectra were recorded on a Perkin Elmer Spectrum One FT spectrometer. ^{1}H and ^{13}C were recorded in CDCl$_3$ on Oxford NMR (300 MHz) instrument using TMS as internal standard. The elemental analysis was carried out on Perkin Elmer 2400 Elemental Analysis (C-H-N). The single crystal X-ray diffraction of **4d** was performed on the Rigaku XtaLAB Mini.

General Procedure for synthesis of compounds 4a–u: 5-(trifluoromethyl)-1,3-cyclohexanedione (1 mmol), acetoacetate ester (1 mmol) aldehyde (1 mmol), ammonium acetate (1 mmol) were dissolved in 2 mL of TFE and stirred at 50 °C. The reaction progress was monitored by TLC and TFE was removed at the end of the reaction by distillation. The crude product was purified by recrystallization from ethanol with a few drops of water to afford pure fluorinated hexahydroquinoline derivatives.

General Procedure for synthesis of compounds 5a–b: A mixture of 5-(trifluoromethyl)-1,3-cyclohexanedione (2 mmol), aldehyde (1 mmol), ammonium acetate (1 mmol), were dissolved in 2 mL of TFE and stirred at 50 °C for 50 min. The progress of the reaction was monitored by TLC. The crude product was purified by recrystallization from ethanol to afford pure fluorinated acridinedione **5a-b**.

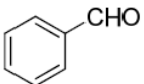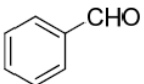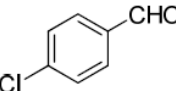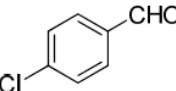The spectroscopic data of selected compounds are shown below.
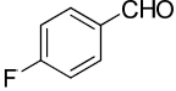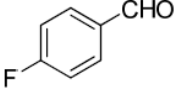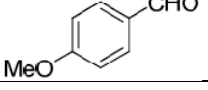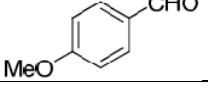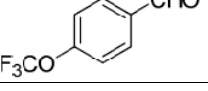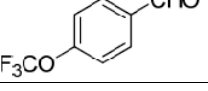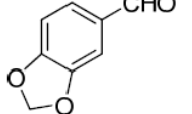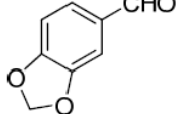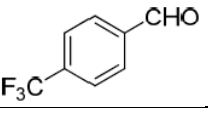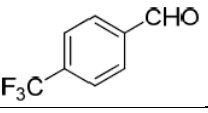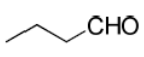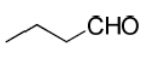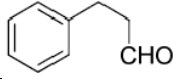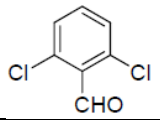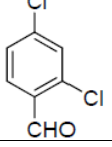
4-(4-chlorophenyl)-2-methyl-5-oxo-7-trifluoromethyl-1,4,5,6,7,8-hexahydroquinoline-3-carboxylic acid ethyl ester (4d): mp = 258–259 °C, ^{1}H NMR 300 MHz, CDCl$_3$: δ = 1.28 (t, J = 7.2 Hz, 3H), 1.65 (s, 3H), 2.55–2.80 (m, 1H), 4.05 (q, J = 7.2, 2H), 5.01 (s, 1H), 6.60 (s, 1H, NH), 6.77 (d, J = 8.4 Hz, 2H), 7.28 (d, J = 8.4 Hz, 2H), ^{13}C NMR (300 MHz CDCl$_3$): δ = 14.2, 19.1, 19.6, 25.9, 32.8, 41.4, 61.7, 102.3, 112.0, 128.7, 130.5, 131.2, 137.5, 142.2, 150.7, 167.7, 198.8; IR (KBr, cm^{-1}) 3287, 3209, 3088, 2950, 1708, 1610; MS m/z: 75 (5%), 303 (100%), 413 (M$^+$, 55%); Anal. Calc for C$_{20}$H$_{19}$ClF$_3$NO$_3$: C, 58.05; H, 4.63; N, 3.38%. Found: C, 57.02; H, 4.60; N, 3.40%.

9-(4-fluorophenyl)-3,6-bis(trifluoromethyl)-3,4,6,7,9,10-hexahydroacridine-1,8(2H,5H)-dione (5a): mp > 300 (decomposes), ^{1}H NMR 300 MHz, CDCl$_3$): δ = 1.36–2.81 (m, 8H, cyclohexyl-Hs), 2.81 (m, 4H), 2.99 (m, 2H, CH next to CF$_3$), 4.82 (s, 1H, CH), 7.10–7.21 (m, J = 8.0, 4H, Ar-H), 8.53 (s, 1H, NH); ^{13}C NMR (300 MHz CDCl$_3$): δ = 19.8, 25.8, 33.0, 111.9, 115.2, 130.7, 137.5, 140.0, 149.3, 160, 198.9; IR(Nujol, cm^{-1}): 3436 (NH), 1653 (O=C–C=C–NH). MS m/z: 75(5%), 353 (100%), 447(M$^+$, 50%). Calc for C$_{21}$H$_{16}$F$_7$NO$_2$: C, 56.38; H, 3.61; N, 3.13%. Found: C, 56.35; H, 3.66; N, 3.15%.

3. Results and Discussion

In an initial endeavor, we carried out the asymmetric Hantzsch reaction by condensing equimolar amount of 5-trifluoromethyl-1,3-cyclohexanedione, methylacetoacetate, unsubstituted benzaldehyde and ammonium acetate at 50 °C in trifluoroethanol. The reaction reached completion in 25 min (monitor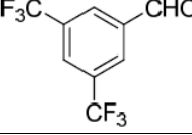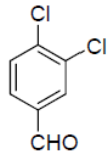ed by tlc) with 98% yield. Next, we extended the reactions using substituted aromatic aldehyde. The reactions were complete in 25 min as before with excellent yield regardless of the nature of the substituents on the aromatic ring. However when the reaction was carried out using butyraldehyde, the reaction was over in 50 min albeit in lower yields (entries 15, 16, Table 1)

Table 1. List of Compounds Synthesized and their percent yields.

Entry [a]	R	R₁	Product	Yield (%) [b]
1	(benzaldehyde, CHO)	Me	4a	98
2		Et	4b	92
3	(4-Cl-benzaldehyde, Cl, CHO)	Me	4c	91
4		Et	4d	90
5	(4-F-benzaldehyde, F, CHO)	Me	4e	90
6		Et	4f	89
7	(4-MeO-benzaldehyde, MeO, CHO)	Me	4g	95
8		Et	4h	96
9	(4-F₃CO-benzaldehyde, F₃CO, CHO)	Me	4i	97
10		Et	4j	93
11	(benzodioxole-CHO, O, O)	Me	4k	99
12		Et	4l	91
13	(4-F₃C-benzaldehyde, F₃C, CHO)	Me	4m	97
14		Et	4n	84
15	(butanal, CHO)	Me	4o	79
16		Et	4p	72
17	(3-phenylpropanal, CHO)	Me	4q	90
18	(3,5-bis(CF₃)benzaldehyde, F₃C, CHO, CF₃)	Me	4r	90
19	(3,4-dichlorobenzaldehyde, Cl, Cl, CHO)	Et	4s	97
20	(2,6-dichlorobenzaldehyde, Cl, Cl, CHO)	Et	4t	98
21	(2,4-dichlorobenzaldehyde, Cl, Cl, CHO)	Et	4u	97

[a] All reactions proceeded to completion

[b] Yield after recrystallization

Upon completion of the synthesis of fluorinated hexahydroquinoline derivatives, we explored the synthesis of hexahydroacridinedione under similar conditions (Scheme 2 below). The reaction of two equivalents of 5-trifluoromethyl-1,3-cyclohexanedione with one equivalent each of aromatic aldehyde and ammonium acetate proceeded with good yield to give 5a and 5b, as shown in Scheme 2.

Scheme 2. Synthesis of fluorinated hexahydroacridinedione from 5-trifluoromethyi-1,3-cyclohehexanedione, aldehydes, and ammonium acetate.
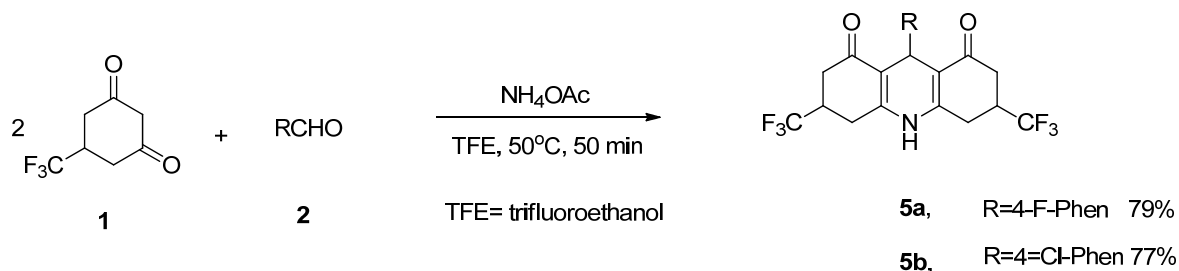
The Infra-red spectra of all the products showed intense signals for carbonyl (1740–1690 cm^{-1}) and NH (3500–3300 cm^{-1}) functional groups. The detailed results are given in Table 1. The structure of **4d** was established by single crystal X-ray analysis (Figure 1) [12] and IR, NMR, and elemental analysis. The crystal data has been deposited in the Cambridge Crystallographic Data Center as supplementary publication number, CCDC 843861. This is the first report of such synthesis using 5-trifluoromethyl-1,3-cyclohexanedione, rather than dimedone.

Figure 1. ORTEP diagram of the single-crystal X-ray structure of 4d [14].
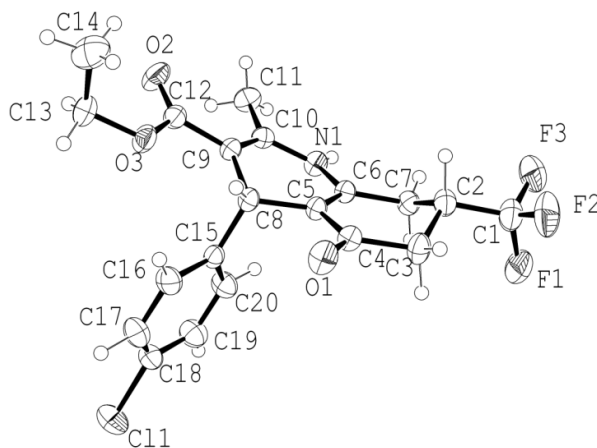
4. Conclusions

In summary, we have described the synthesis of some new trifluoromethylated hexahydroquinoline and acridinedione derivatives via Hantzsch route using 5-trifluoromethyl-1,3-cyclohexanedione as a CF$_3$-building block. The reaction conditions are mild, yields are high; reaction time is short; product isolation and purification are easy; and the overall process is cost effective and easy to handle. All the products are new and represent synthetically useful compounds for further elaboration. The

biological evaluation of these compounds will be investigated in the future and will be published in specialized journals.

Acknowledgments

Conflict of Interest.

There is no Conflict of Interest

References and Notes

1. Zhang, X.-L.; Sheng, S.-R.; Liu, X.-L.; Liu, X.-L. Solvent-free liquid-phase synthesis of polyhydroquinoline derivatives under microwave irradiation. ARKIVOC **2007**, pp. 79–86.
2. Kumar, A.; Awatar Maurya, R. Synthesis of polyhydroquinoline derivatives through unsymmetric Hantzsch reaction using organocatalysts. *Tetrahedron* **2007**, *63*, 1946–1952.
3. Heydari, A.; Khaksar, S.; Tajbakhsh, M.; Reza Bijanzadeh, H. One-step synthesis of Hantzsch esters and polyhydroquinoline derivatives in fluoro alcohols. *J. Fluor. Chem.* **2009**, *130*, 609–614.
4. Kendre, D.B.; Toche, R.B.; Jahak, M.N. Michael addition of dimedone with α,β-unsaturated ketones: Synthesis of quinoline and chromene derivatives. *J. Heterocyclic Chem.* **2008**, *45*, 667–671.
5. Hadida, S.; Goor, F.V.; Grootenhuis, P.D.J CFTR Modulators for the treatment of cystic fibrosis. *Annu. Rep. Med. Chem.* **2010**, *45*, 157–173.
6. Itoh, T.; Nagata, K.; Miyazaki, M.; Ishikawo, H.; Kurihara, A.; Ohsawa, A. A selective reductive amination of aldehydes by the use of Hantzsch dihydropyridines as reductant. *Tetrahedron* **2004**, *60*, 6649–6655.
7. Natarajan, S.; Mathews, R. The crystal structure and conformational studies of acridinedione derivatives. *J. Chem Crystallogr.* **2011**, *41*, 678–683.
8. Sivaraman, J.; Subramanian, K.; Velmurugan, D.; Subramanian, E.; Seetharaman, J.; Shanmugasundaram, P.S. X-ray structure of 5-[2-chlorophenyl]-10-[4-methylphenyl]-1,2,5,8,9,10-hexahydro 4,6[3H,6H]acridinedione and its interaction with calf thymus DNA by spectroscopic methods. *J. Mol. Struct.* **1996**, *385*, 129–135.
9. Palani, K.; Ambalavanan, P.; Ponnuswamy, M.N.; Murugan, P.; Ramakrishnan, V.T. Crystal structures of two acridinedione derivatives. *Cryst. Res. Technol.* **2005**, *40*, 277–282.
10. Kwiatkowski, P.; Beeson, T.D.; Conrad, J.C.; MacMillan, D.W.C. Enantioselective organocatalytic α-fluorination of cyclic ketones. *J. Am. Chem. Soc.* **2011**, *133*, 1738–1741.
11. Fadeyi, O.O.; Lindsley, C.W. Rapid, general access to chiral β-fluoroamines and β,β-difluoroamines via organocatalysis. *Org. Lett.* **2009**, *11*, 943–946.
12. Fioroni, M.; Diaz, M.D.; Berger, S.; Burger, K. Solvation phenomena of a tetrapeptide in water/trifluoroethanol and water/ethanol mixtures: a diffusion NMR, intermolecular NOE, and molecular dynamics study. *J. Am. Chem. Soc.* **2002**, *124*, 7737–7744.

13. Fadeyi, O.O.; Okoro, C.O. Synthesis of 5-(trifluoromethyl)cyclohexane-1,3-dione and 3-amino-5-(trifluoromethyl)cyclohex-2-en-1-one. *Tetrahedron Lett.* **2008**, *49*, 4725–4727.

14. X-ray diffraction studies were performed at room temperature on a pale yellow crystal of **4d** of approximate $0.57 \times 0.52 \times 0.36$ mm dimensions. All measurements were made on a Rigaku Mercury375R/M CCD (XtaLAB mini) diffractometer using graphite monochromated Mo-Kα radiation. Cell constants and an orientation matrix for data collection corresponded to a primitive monoclinic cell (space group P21/n) with dimensions: a = 11.8544(10) Å, b = 13.9622(12) Å, c = 12.5692(11) Å and β = 110.300(8)°. *Data reduction*: of the 20341 reflections that were collected, 4477 were unique (R_{int} = 0.0212). Data were collected and processed using CrystalClear [a] (Rigaku). The linear absorption coefficient, μ, for Mo-Kα radiation is 2.435 cm^{-1}. An empirical absorption correction was applied which resulted in transmission factors ranging from 0.796 to 0.916. The data were corrected for Lorentz and polarization effects. *Structure Solution and Refinement*: The structure was solved by direct methods [b] and expanded using Fourier techniques. The non-hydrogen atoms were refined anisotropically. Hydrogen atoms were refined using the riding model. The final cycle of full-matrix least-squares refinement on F^2 was based on 4477 observed reflections and 269 variable parameters and converged (largest parameter shift was 0.12 times its esd) with unweighted and weighted agreement factors of: R1 = 0.0490 and wR2 = 0.1938. This was conducted using the program suiteWINGX [c].

(a) *CrystalClear:* Rigaku Corporation, 1999. CrystalClear Software User's Guide, Molecular Structure Corporation, ©2000. Pflugrath, J.W. *Acta Cryst.* **1999**, *D55*, 1718–1725.

(b) Sheldrick, G.M. SHELX-97, Program for the Solution and Refinement of Crystal Structures; University of Göttingen: Göttingen, Germany, 1997.

(c) Farrugia, L.J. WinGX suite for small-molecule single-crystal crystallography. *J. Appl. Cryst.* **1999**, *32*, 837–838.

Article

Further Successes of the Meisenheimer Model

Jon Baker * and Max Muir

Parallel Quantum Solutions, 2013 Green Acres Road, Suite A, Fayetteville, AR 72703, USA

* Author to whom correspondence should be addressed; E-Mail: baker@pqs-chem.com; Tel.: +479-521-5118; Fax: +877-863-5705.

Abstract: Our simple Meisenheimer model for predicting the principal site for nucleophilic substitution in aromatic perfluorocarbons is further tested on a series of recently published reactions in liquid ammonia primarily from Malykhin and coworkers. The model accurately predicts the experimental results for all of the reactions reported further confirming its general applicability.

Keywords: nucleophilic substitution; fluorine-containing hetero-aromatics; Meisenheimer model

1. Introduction

In earlier work we introduced a simple calculational model for predicting the primary substitution site for nucleophilic substitution involving the replacement of fluorine, initially in aromatic perfluorocarbons [1] and subsequently in fluorinated aromatic systems containing both ring heteroatoms (principally nitrogen, but also oxygen, phosphorus and sulphur) and non-fluorine substituents [2]. The model assumes the standard two-stage description of nucleophilic aromatic substitution involving the formation of a negatively charged intermediate, known as a Meisenheimer complex [3], which is the anionic equivalent of the Wheland intermediate in electrophilic substitution [4].
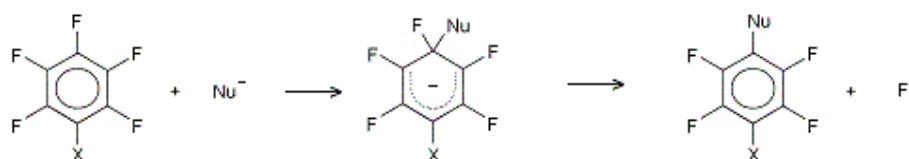
The negative charge in the Meisenheimer complex is delocalized into the aromatic π-system, which like the Wheland intermediate, can be considered as a resonance hybrid of multiple canonical forms.
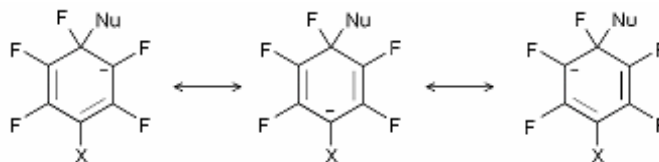
Specifically, the model involves calculating the energy of all possible Meisenheimer complexes at a standard level of *ab initio* theory (basic Hartree-Fock theory with the 6-31G* basis set [5]: HF/6-31G*), using the fluoride ion as a "typical" nucleophile, with the preferred site for nucleophilic substitution corresponding to the most stable (lowest energy) complex.

This simple model has been remarkably successful in predicting not only the primary site in aromatic nucleophilic substitution reactions, but also secondary sites. In our two previous papers on this topic [1,2] we have presented correct predictions for primary and secondary substitution sites for over 70 different nucleophilic substitution reactions. Currently we are aware of only one system (perfluorophthalazine) where our model fails to predict the correct primary substitution site (although there are certainly likely to be more). Although the model is only meant to be qualitative we note a recent attempt to use a very similar model quantitatively [6].

Our Meisenheimer model nominally involves a purely thermodynamic rationale, *i.e.*, the thermodynamically most stable Meisenheimer complex is the one most likely to form, and the substitution pattern follows directly from that. The underlying assumptions are, first, that the substitution reaction is indeed two-step, involving an at least meta-stable Meisenheimer complex as intermediate; second, that barrier heights—both from reactant to intermediate and intermediate to product—are either more or less identical in all cases, and can therefore be ignored, or reflect the thermodynamic stability in the Meisenheimer complex so that considering only the latter gives the correct substitution pattern; and third, that varying the reaction conditions, principally the solvent and the actual nucleophile itself, makes no difference to the preferred substitution site, *i.e.*, the mechanism is essentially the same for all nucleophiles in all solvents. Even for nucleophilic substitution reactions that are one-step, *i.e.*, do not involve a Meisenheimer intermediate, the model can still be successfully applied provided the Meisenheimer complex can reliably predict the relative energies in the respective transition states.

In the last few years liquid ammonia has become a very useful reagent for aminating aromatic fluorocarbons. It has proven to be a useful synthetic method as it is capable of substituting the amino group (-NH$_2$) for fluorine site-specifically in high yield. This use of liquid ammonia has been pioneered primarily by the Malykhin group at Novosibirsk State University in Russia. They have published a number of papers from 2007 onwards involving amination of polyfluorinated benzenes and pyridines [7,8], perfluorobiphenyl [7], perfluoronaphthalene [9] and tetrafluorophthalic acid [10]. Additionally, Page and coworkers have found that liquid ammonia aminates 1-nitro-2,4-difluorobenzene dominantly in the 2-position [11]. Collectively these papers present around 20 different nucleophilic substitution reactions (all aminations), the vast majority of which we have not looked at in our previous work. They represent a further series of reactions to test the Meisenheimer model.

2. Results and Discussion

For all of the calculations presented in this work we used the PQS program package from Parallel Quantum Solutions together with the associated graphical user interface, PQSMol [12,13].

Figure 1 depicts schematically the various amination reactions examined (as previously noted, the majority from the Malykhin group [7–10]). Since all of the reactions *are* aminations, we have made an important modification to our standard calculational approach: instead of using the fluoride ion as a generic attacking nucleophile we specifically use NH_2^-. The use of the actual nucleophile instead of the fluoride ion as a possible extension to the basic model was mentioned in our last paper [2], and it just seemed dogmatic to us to use fluorine when the substituting group was known to be NH_2 in every case.

Figure 1. Amination reactions in liquid ammonia.

Figure 1. *Cont.*

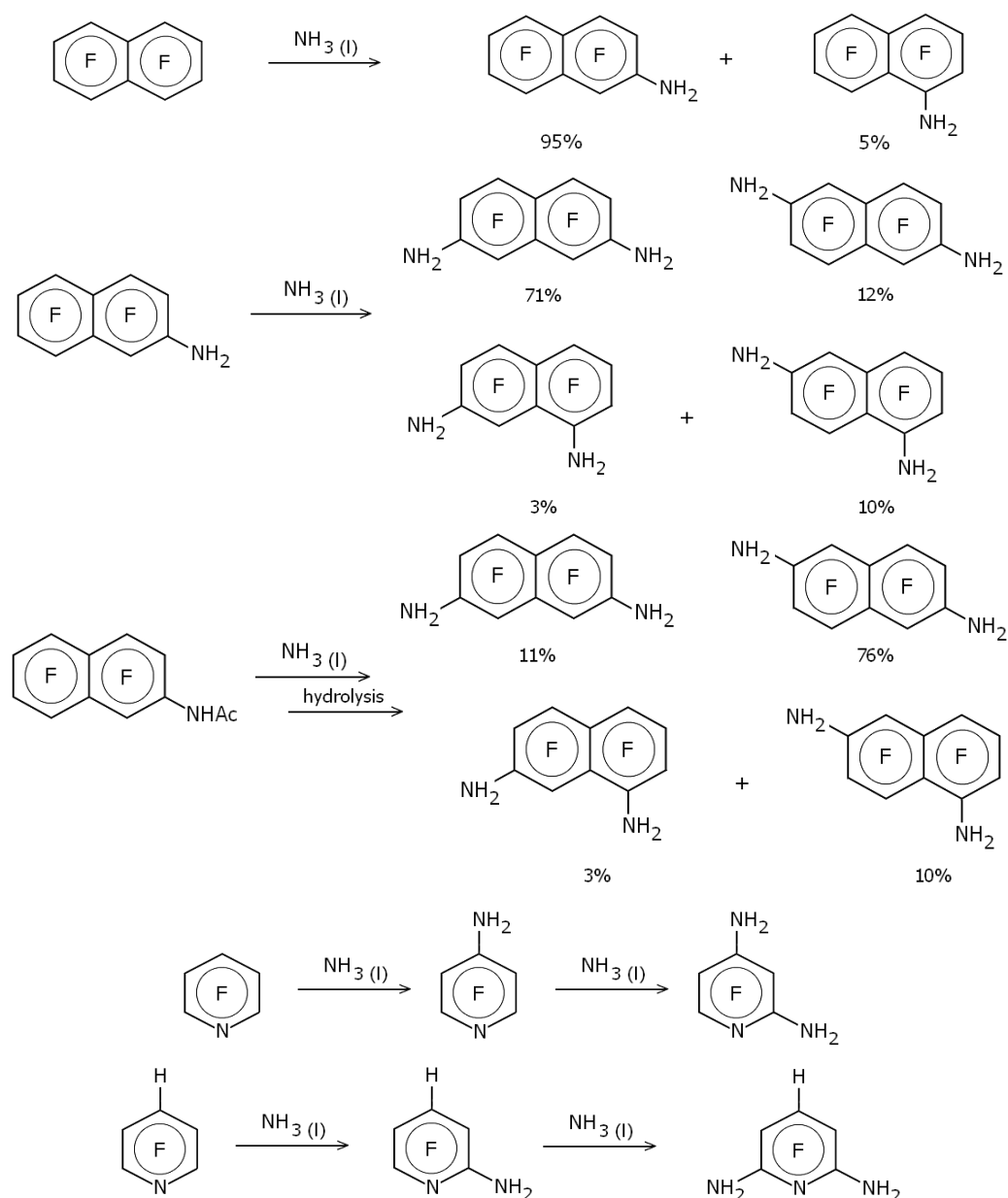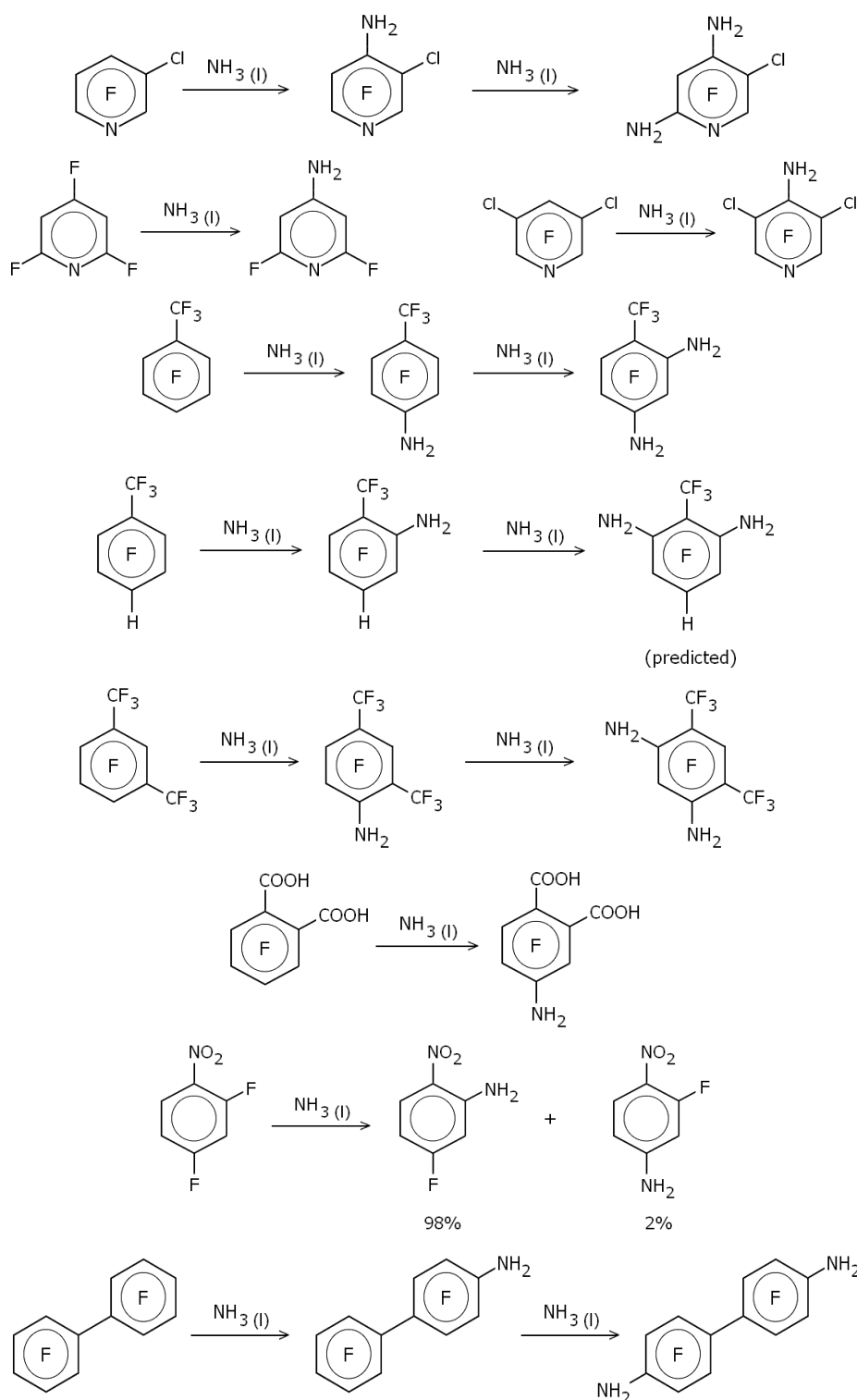The use of NH_2^- as the attacking nucleophile brings both advantages and disadvantages compared to F^-. One advantage of using the single-atom fluoride ion as a generic attacking nucleophile is that there are no additional conformational issues in the resulting Meisenheimer complex, greatly simplifying the calculations. On the other hand it is known that most substituents to an aromatic ring

direct para as far as replacement of fluorine is concerned, with any preferable ortho substitution nearly always resulting from direct interaction between the attacking nucleophile and the substituent, an interaction that cannot be modeled using fluorine. If we want to properly take into account interactions between an existing (already substituted) amino group and an attacking nucleophile, especially ortho to the existing amino substituent, then it seems pretty clear that the attacking nucleophile has to be represented more realistically, and so for these amination reactions we used NH_2^-.

The conformational issue is more problematic than might at first be thought. For example, consider toluene (Scheme 1a and b). This is known to have C_s symmetry and its vibrational spectrum can be fully analyzed under this point group [14]. Given C_s symmetry, there are two possible configurations of the methyl group—as shown in (a) and (b) —in which the symmetry plane is either perpendicular to, or in the plane of, the aromatic ring, respectively, bisecting a methyl HCH angle. The ground state geometry actually conforms to (a) with (b) being the transition state for methyl rotation. At room temperature the methyl group is essentially a free rotor with a 3-fold torsional potential.

The amino group is conformationally similar to the methyl group with one of the C-H bonds replaced by a lone pair, although the two N-H bonds in aniline are nowhere near as "bent" out of the plane of the aromatic ring as are the methyl C-H bonds in toluene. Aniline also has C_s symmetry in its ground state, with the lone pair occupying the position of the symmetry-unique C-H bond of the methyl group in toluene, *i.e.*, perpendicular to the benzene ring (Scheme 1c).

Scheme 1. Conformational preferences in toluene and aniline.

| (a) | (b) | (c) |
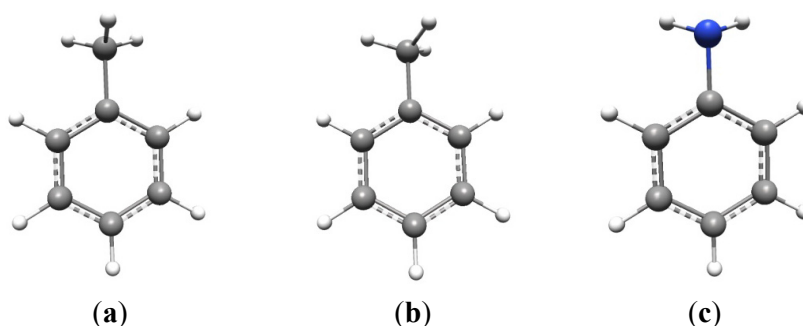
Now as soon as you add, e.g., a second methyl group to toluene, the conformational issues increase significantly. Not only do you have the conformation of the new methyl group to consider, but the local three-fold symmetry of the original methyl group no longer holds globally and the three methyl hydrogen atoms are no longer equivalent. More to the point for this work, the same thing applies of course to the amino group.

We have no desire to carry out an exhaustive conformational analysis each time we calculate the energy of a given Meisenheimer complex. We have found that the following tactics when constructing the initial starting geometry of a Meisenheimer complex increases the likelihood of optimizing to the global or a near-global minimum:

(1) Methyl or similar (e.g., perfluoromethyl) substituents are added to the aromatic ring such that one of the C-H bonds is perpendicular to the ring (as shown in Scheme 1a). Any directly adjacent methyl groups are added similarly, but rotated by 180°, *i.e.*, the perpendicular C-H bonds point above and below the plane of the ring, respectively.

(2) Amino (NH$_2$) groups are added in an equivalent way with the formal lone pair occupying the position of the perpendicular methyl C-H bond (Scheme 1c).

(3) When adding an attacking amino group to form the sp^3-hybridized carbon center in the Meisenheimer complex a local plane of symmetry is assumed which bisects the HNH angle and includes the C-F bond. The formal nitrogen lone pair points towards the center of the aromatic ring. (It is assumed that it is energetically unfavorable for the lone pair to eclipse the C-F bond).

One of the reactions studied by Malykhin and coworkers *was* included in our previous work [2], namely the amination of perfluoronaphthalene in liquid ammonia [9]. This was done with the standard Meisenheimer model in which the attacking nucleophile was the fluoride ion. Malykhin and coworkers found that single amination of perfluoronapthalene gave dominantly (~95%) the 2-substituted isomer; further amination of this (or direct diamination of perfluoronaphthalene) gave a mixture of the 2,7-, 2,6-, 1,7- (2,8-) and 1,6- (2,5-) isomers with the former dominating (~70%). Virtually all known nucleophilic di-substitution reactions involving perfluoronaphthalene result primarily (>75%) in the 2,6-isomer and the amination in liquid ammonia was claimed to be "the first example of the predominant substitution at position 7 in 2-substituted polyfluoronaphthalenes" [9].

These results were nicely reproduced with our standard Meisenheimer model and the first thing we are going to do here is to check that when the fluoride ion is replaced in our calculations by NH$_2^-$ we still reproduce the principal experimental results. Table 1 gives the relative energies (in kcal/mol) of each possible Meisenheimer complex, with the lowest energy complex–and hence the predicted most favorable site for nucleophilic substitution–taken as the energy zero. Results are shown both for NH$_2^-$ (this work) and F- (taken from reference [2]) as nucleophile.

Table 1. Relative Energies (kcal/mol) of the various Meisenheimer complexes for 2-amino-heptafluoronaphthalene.

Site	Fluoride [1]	Amino [2]
2,1-	4.0	4.8
2,3-	2.2	2.9
2,4-	1.5	3.6
2,5-	0.6	2.4
2,6-	1.3	0.9
2,7-	0.0	0.0
2,8-	1.9	3.7

[1] taken from [2]; [2] this work.

As can be seen, the results are similar, but not identical. Both sets of calculations correctly predict that 7-substitution is the most favorable with 5- and 6-substitution as the most likely secondary sites; however the energy ordering of the secondary sites is reversed. Neither set suggests that formation of the 1,7-isomer (the 2,8-) is particularly likely; however we have found that the most favorable substitution sites in 1-amino-heptafluoronapthalene (a by-product in the single amination reaction; see Figure 1) are positions 6 and 7, so this may well be a major source of the 1,6- and 1,7-isomers, especially for the direct di-amination reaction. Either way, the results shown in Table 1 certainly give us confidence in further predictions using NH$_2^-$ as nucleophile.

Appl. Sci. **2012**, *2*

Relative energies (in kcal/mol) of the various Meisenheimer complexes for the amination reactions shown in Figure 1 are given in Table 2. Comparison of the experimental results with the relative energies from Table 2 show that for every reaction depicted in Figure 1 the Meisenheimer model accurately predicts the primary substitution site. Furthermore, the large difference in relative energies between the lowest energy complex and the next lowest suggests that there is little secondary substitution in the majority of cases; again this is in full agreement with the experimental observations. For example, Malykhin and coworkers state that aminodefluorination of tetrafluorophthalic acid in anhydrous ammonia gives the 4-amino substituted isomer selectively and in high yield [10], while Page and coworkers found that amination of 1-nitro-2,4-difluorobenzene gave 98% of the 2-substituted isomer and 2% of the 4-substituted [11]. The relative energy differences between the two different Meisenheimer complexes in these two examples are 12.3 and 2.9 kcal/mol, respectively (see Table 2). Note that this is a clear case of ortho (not para) substitution to the nitro group which is correctly predicted by the Meisenheimer model.

Table 2. Relative energies (kcal/mol) of the various Meisenheimer complexes for the amination reactions shown in Figure 1.

System	E (relative)	Subst. site	System	E (relative)	Subst. site
2-acetylamidoheptafluoronaphthalene			**perfluorotoluene**		
1-NH$_2$	5.7		2-NH$_2$	6.9	
3-NH$_2$	5.2		3-NH$_2$	17.5	
4-NH$_2$	9.7		4-NH$_2$	0.0	p
5-NH$_2$	7.8				
6-NH$_2$	0.0	p	**4-aminoperfluorotoluene**		
7-NH$_2$	1.5	s	2-NH$_2$	0.0	p
8-NH$_2$	3.4		3-NH$_2$	12.5	
perfluoropyridine			**1-(CF$_3$)-2,3,5,6-tetrafluorobenzene**		
2-NH$_2$	9.9		2-NH$_2$	0.0	p
3-NH$_2$	23.6		3-NH$_2$	9.1	
4-NH$_2$	0.0	p			
			1-(CF$_3$)-2-amino-3,5,6-trifluorobenzene		
4-amino-2,3,5,6-tetrafluoropyridine			3-NH$_2$	10.5	
2-NH$_2$	0.0	p	5-NH$_2$	6.0	
3-NH$_2$	14.5		6-NH$_2$	0.0	p
2,3,5,6-tetrafluoropyridine			**1,3-di(CF$_3$)-2,4,5,6-tetrafluorobenzene**		
2-NH$_2$	0.0	p	2-NH$_2$	9.1	
3-NH$_2$	0.8		4-NH$_2$	0.0	p
			5-NH$_2$	26.0	
2-amino-3,5,6-trifluoropyridine					
3-NH$_2$	12.2		**1,3-di(CF$_3$)-4-amino-2,5,6-trifluorobenzene**		
5-NH$_2$	7.9		2-NH$_2$	8.9	
6-NH$_2$	0.0	p	5-NH$_2$	30.5	
			6-NH$_2$	0.0	p

Table 2. *Cont.*

System	E (relative)	Subst. site	System	E (relative)	Subst. site
3-chloro-2,4,5,6-tetrafluoropyridine					
2-NH$_2$	10.3		**tetrafluorophthalic acid**		
4-NH$_2$	0.0	p	3-NH$_2$	12.3	
5-NH$_2$	27.7		4-NH$_2$	0.0	p
6-NH$_2$	6.3				
			1-nitro-2,4-difluorobenzene		
3-chloro-4-amino-2,5,6-trifluoropyridine			2-NH$_2$	0.0	p
2-NH$_2$	3.1		4-NH$_2$	2.9	
5-NH$_2$	22.4				
6-NH$_2$	0.0	p	**perfluorobiphenyl**		
			2-NH$_2$	8.7	
2,4,6-trifluoropyridine			3-NH$_2$	16.5	
2-NH$_2$	3.2		4-NH$_2$	0.0	p
4-NH$_2$	0.0	p			
			4-aminoperfluorobiphenyl		
3,5-dichloro-2,4,6-trifluoropyridine			2-NH$_2$	11.4	
2-NH$_2$	6.2		3-NH$_2$	20.8	
4-NH$_2$	0.0	p	2'-NH$_2$	8.8	
			3'-NH$_2$	15.2	
			4'-NH$_2$	0.0	p

p–experimental primary (or sole) substitution site; s–experimental secondary substitution site.

One reaction for which we do predict significant secondary substitution (*i.e.*, more than a few percent) is for the amination of 2-acetylamidoheptafluoronaphthalene (Table 2). This was one of the reactions studied in reference [9] along with 2-aminoheptafluoronaphthalene (see Table 1). Experimentally amination of 2-acetylamidoheptafluoronaphthalene gives mainly the 6- and 7-substituted isomers in a 5:1 ratio (similar to the amination of 2-aminoheptafluoronaphthalene except that the ratio is reversed). Our calculations, in which the 6- and 7-substituted Meisenheimer complexes have the lowest energy, with the 7-substituted complex 1.5 kcal/mol higher in energy than the 6-substituted, fully concur with the experimental observations.

Note that no experimental data was reported for the amination of 1-trifluoromethyl-2-amino-3,5,6-trifluorobenzene and the depiction in Figure 1—substitution at position 6—is theoretical only, derived from the calculational results shown in Table 2. This is thus a prediction based on our model which is open to experimental confirmation.

3. Conclusions

Our simple Meisenheimer model for predicting which fluorine atom will be replaced by an attacking nucleophile in substituted aromatic perfluorocarbons has been further verified on a series of animation reactions in liquid ammonia specifically using NH$_2^-$ as the attacking nucleophile. For every reaction for which experimental data was available the model accurately predicts the primary substitution site. Based on our model, we predict that single amination of 1-trifluoromethyl-2-amino-

3,5,6-trifluorobenzene in liquid ammonia should produce almost exclusively 1-trifluoromethyl-2,6-diamino-3,5-difluorobenzene.

Acknowledgements

References

1. Muir, M.; Baker, J. A simple calculational model for predicting the site for nucleophilic substitution in aromatic perfluorocarbons. *J. Fluorine Chem.* **2005**, *126*, 727–738.
2. Baker, J.; Muir, M. The Meisenheimer model for predicting the principal site for nucleophilic substitution in aromatic perfluorocarbons—Generalization to include ring-nitrogen atoms and non-fluorine ring substituents. *Can. J. Chem.* **2010**, *88*, 588–597.
3. Meisenheimer, J. Ueber reactionen aromatischer nitro korper. *Justus Liebigs Ann. Chem.* **1902**, *323*, 205–246.
4. Wheland, G.W. A quantum mechanical investigation of the orientation of substituents in aromatic molecules. *J. Am. Chem. Soc.* **1942**, *64*, 900–909.
5. Harihan, P.C.; Pople, J.A. The influence of polarization functions on molecular orbital hydrogenation energies. *Theor. Chim. Acta* **1973**, *28*, 213–222.
6. Liljenberg, M.; Brinck, T.; Herschend, B.; Rein, T.; Rockwell, G.; Svensson, M. A pragmatic procedure for predicting regioselectivity in nucleophilic substitution of aromatic fluorides. *Tetrahedron Lett.* **2011**, *52*, 3150–3153.
7. Vaganova, T.A.; Kusov, S.Z.; Rodionov, V.I.; Shundrina, I.K.; Malykhin, E.V. Selective mono-and diamination of polyfluorinated benzenes and pyridines with liquid ammonia. *Russ. Chem. Bull. Int. Ed.* **2007**, *56*, 2239–2246.
8. Kusov, S.Z.; Rodionov, V.I.; Vaganova, T.A.; Shundrina, I.K.; Malykhin, E.V. Direct di- and triamination of polyfluoropyridines in anhydrous ammonia. *J. Fluorine Chem.* **2009**, *130*, 461–465.
9. Vaganova, T.A.; Kusov, S.Z.; Rodionov, V.I.; Shundrina, I.K.; Sal'nikov, G.E.; Mamatyuk, V.I.; Malykhin, E.V. Amination of octafluoronaphthalene in liquid ammonia. *J. Fluorine Chem.* **2008**, *129*, 253–260.
10. Vaganova, T.A.; Shundrina, I.K.; Kusov, S.Z.; Karpova, E.V.; Bagryanskaya, I.Y.; Malykhin, E.V. Synthesis and characterization of the first perfluoroaromatic polyimide of the AB-type. *J. Fluorine Chem.* **2012**, *135*, 129–136.
11. Pengju, J.; Atherton, J.H.; Page, M.I. The kinetics and mechanisms of aromatic nucleophilic substitution reactions in liquid ammonia. *J. Org. Chem.* **2011**, *76*, 3286–3295.
12. *PQS* version 4.0. Parallel Quantum Solutions, 2013 Green Acres Road, Suite A, Fayetteville, Arkansas 72703, USA. Available online: http://www.pqs-chem.com (accessed on 3 May 2012)
13. Baker, J.; Wolinski, K.; Malagoli, M.; Kinghorn, D.; Wolinski, P.; Magyarfalvi, G.; Saebo, S.; Janowski, T.; Pulay, P. Quantum chemistry in parallel with PQS. *J. Comput. Chem.* **2009**, *30*, 317–335.

Appl. Sci. **2012**, *2*

14. Baker, J. A scaled quantum mechanical reinvestigation of the vibrational spectrum of toluene. *J. Mol. Struct.: Theochem* **2008**, *865*, 49–52 and references therein.

Article

Fluorine Based Superhydrophobic Coatings

Jean-Denis Brassard [1,2,*], D.K. Sarkar [2,*] and Jean Perron [1]

[1] Anti-icing Materials International Laboratory (AMIL), Université du Québec à Chicoutimi, 555 Boulevard de l'Université, Chicoutimi, Québec G7H 2B1, Canada; E-Mail: jean_perron@uqac.ca

[2] Centre Universitaire de Recherche sur l'Aluminium (CURAL), Université du Québec à Chicoutimi, 555 Boulevard de l'Université, Chicoutimi, Québec G7H 2B1, Canada

* Authors to whom correspondence should be addressed; E-Mails: jean-denis.brassard@uqac.ca (J.D.B.); dsarkar@uqac.ca (D.K.S.); Tel.: +1-418-545-5011 (ext. 2543).

Abstract: Superhydrophobic coatings, inspired by nature, are an emerging technology. These water repellent coatings can be used as solutions for corrosion, biofouling and even water and air drag reduction applications. In this work, synthesis of monodispersive silica nanoparticles of ~120 nm diameter has been realized via Stöber process and further functionalized using fluoroalkylsilane (FAS-17) molecules to incorporate the fluorinated groups with the silica nanoparticles in an ethanolic solution. The synthesized fluorinated silica nanoparticles have been spin coated on flat aluminum alloy, silicon and glass substrates. Functionalization of silica nanoparticles with fluorinated groups has been confirmed by Fourier Transform Infrared spectroscopy (FTIR) by showing the presence of C-F and Si-O-Si bonds. The water contact angles and surface roughness increase with the number of spin-coated thin films layers. The critical size of ~119 nm renders aluminum surface superhydrophobic with three layers of coating using as-prepared nanoparticle suspended solution. On the other hand, seven layers are required for a 50 vol.% diluted solution to achieve superhydrophobicity. In both the cases, water contact angles were more than 150°, contact angle hysteresis was less than 2° having a critical roughness value of ~0.700 µm. The fluorinated silica nanoparticle coated surfaces are also transparent and can be used as paint additives to obtain transparent coatings.

1. Introduction

Superhydrophobic coatings are increasingly attractive to the industry and academia due to their unique self-cleaning properties as a result of their water repelling characteristics [1]. Fabrication of superhydrophobic coating is an inspiration from nature as water is seen to repel on many natural surfaces such as those of the lotus leaves, butterfly wings, water striders' legs, and so on [2–5]. This behavior of water drops rolling off their surfaces is due mainly to the presence of a combination of rough micro-nanostructure and low surface energy waxy materials on their surfaces. This concept has been well elaborated by Neinhuis *et al.* [4] on the surface of the lotus leaves which has been the classic example is the field of superhydrophobicity for researchers around the globe emphasizing the importance of the geometry and the chemistry of the surface. Inspired by this phenomenon, we have recently transformed aluminum surfaces, copper and silicon surfaces superhydrophobic by first creating surface roughness using methods such as chemical bath deposition, electrochemical methods and chemical etching methods and then modifying those surfaces by either passivating using low surface energy molecules such as stearic acid or fluoroalkyl-silane (FAS-17) or by coating with rf-sputtered Teflon thin films [6–11]. The multilayer deposition process of organic and inorganic materials [12,13] such as nanoparticles as rough hydrophobic material [14,15] are also techniques to obtain superhydrophobic surfaces.

In all these cases, the surfaces exhibited water roll-off properties providing water contact angle values greater than 150°, which is due to the air entrapment in the gaps of the rough structure produced in the first step, resulting in a composite structure of air and solid in combination with the presence of low surface energy components on the roughened surface which reduces the affinity of water to the surface. The effect of surface roughness on superhydrophobic properties has been elucidated by Wenzel and Cassie-Baxter in their mathematical models formulated in 1940s [16,17].

Superhydrophobic surfaces find tremendous importance in the technological world where they can be applied in domains such as anti-corrosion, anti-biofouling, electrowetting and even in drag reductions [7,18–23]. However, the most important challenge faced by industries is the feasibility of large-scaling in an effective and economical manner. Therefore, in this study, we present a simple sol-gel technique where silica nanoparticles are synthesized via a Stöber process. In order to eliminate a second step of passivation or coating to obtain low surface energy, these silica nanoparticles are functionalized in the suspension using FAS-17 molecules before coating on aluminum substrates. The functionalized fluorinated silica nanoparticles suspended in a solution are then deposited via a spin-coating technique on to the aluminum substrates to obtain superhydrophobic coatings demonstrating large-scale feasibility.

2. Experimental Section

The solutions containing fluorinated silica nanoparticles are prepared in the laboratory using standard Stöber process [24]. Initially, at a hotplate temperature of 50 °C, ethanol and ammonium hydroxide (NH$_4$OH) were mixed in a beaker using a magnetic stir bar. While stirring, a solution of tetraethoxysilane or TEOS (Si(OC$_2$H$_5$)$_4$) is added drop by drop in the mixed solution. The transparent mixed solution turns opaque confirming the formation of silica nanoparticles [25–27]. The synthesized silica nanoparticles are further funtionalized in an ethanolic fluoroalkylsilane or FAS17 (C$_{16}$H$_{19}$F$_{17}$O$_3$Si) solution. The AA-6061 aluminum alloy, silicon and sodalime glass substrates were coated with the fluorinated silica nanoparticles by spin-coating processes. The nanoparticle coated films were dried at 70 °C on a hotplate to allow the ethanol and excess water to evaporate from the films. Transform Infrared spectroscopy (IRRAS) was used to evaluate the atomic bonding in the films. IRRAS (Nicolet 6700 FT-IR) is equipped with a Mid-IR MCT-A N$_2$-cooled detector and a KBr beam splitter. The thin films were also analysed via a high-resolution field emission gun scanning electron microscope (FEGSEM: Hitachi SU-70) for morphological analysis. The wetting properties of the functionalized particles coated on multiple substrates were performed by measuring both static and dynamic contact angles (Krüss contact angle goniometer) at five positions on each substrate using a 5 μL deionized water drop. The static contact angle has been abbreviated as CA and dynamic contact angle or contact angle hysteresis has been abbreviated as CAH throughout the text. The CAH is the difference between the advancing and the receding angle. The CAH measurements were made at room temperature following a very standard and commonly used experimental procedure as reported in the literature [28–30]. In this method, a water drop of volume ~5 μL was suspended with the needle and brought in contact with the superhydrophobic surfaces using a computer controlled device as provided by Krüss GmbH. The contact CAH was measured by holding the water drop with a stationary needle in contact with the surface and moving the goniometer stage in one direction. The surface roughness of the films were measured using an optical profilometer (MicroXAM-100 HR 3D surface profilometer).

3. Results and Discussion

The molecular bonding of the fluorinated species as well as the silica bonds on surfaces coated with varying numbers of layers of the fluorine-functionalized silica nanoparticles were investigated with IRRAS spectral analyses. The Figure 1(A) shows the IRRAS spectra of the fluorinated silica nanoparticles spin coated aluminum substrates in one and nine layers. When one and nine layers are spin coated on the substrate, several peaks appear. The peak at 1,100 cm^{-1} is due to the asymmetric stretching vibration of Si-O-Si bonds in the silica nanoparticles in the thin films [31–34]. Another small peak appearing at around 800 cm^{-1} is associated with the bending mode of Si-O-Si bonds. Also, the peak at 480 cm^{-1} is associated with Si-O-Si bond for the rocking vibration [35]. This particular peak shows clearly an increase in intensity with an increase in the number of layers, proving an increase of the concentration of nanoparticles on the Al surface. Infrared analysis of the surface shows a peak around 945 cm^{-1} which is attributed to silicon hydroxide (Si-OH) bonds present on unfunctionnalized silica nanoparticles [6].

Other interesting peaks are those present in the FAS17 molecules. At the beginning of the molecules, hydro-carbon bonds are present. A reasonably broad peak around 900 cm^{-1} is assigned to the C-H bonds. Continuing on the molecules, fluoro-carbon bonds are present. The existence of C-F bonds in the form of CF, CF$_2$ or CF$_3$ are also located at 610, 730, 960 and 1,250 cm^{-1} [33,34,36,37]. The most important peak appears at 1,145 cm^{-1}. This particular peak represents a Si-O-C bond which confirms that the FAS17 molecule is clearly attached to silica nanoparticles. The presence of additional new peaks arising from the fluorinated functional groups present in the films confirms that the nanoparticles of silica are functionalized by fluorine from the FAS17 molecules. Figure 1(B) shows on the top a representation of a silica nanoparticle covered with a thin film of FAS17. On the bottom of the figure, a molecular representation of the fluorinated nanoparticles is presented with their corresponding wavenumbers.

Figure 1. (**A**) Transform Infrared spectroscopy (IRRAS) spectra of fluorinated silica nanoparticles coated aluminum surfaces as a function of the number of layers. (**B**) Schematic presentation of a silica nanoparticle functionalized with a thin layer of FAS17 (top) presented along with the corresponding wavenumbers on the IR spectra (bottom).
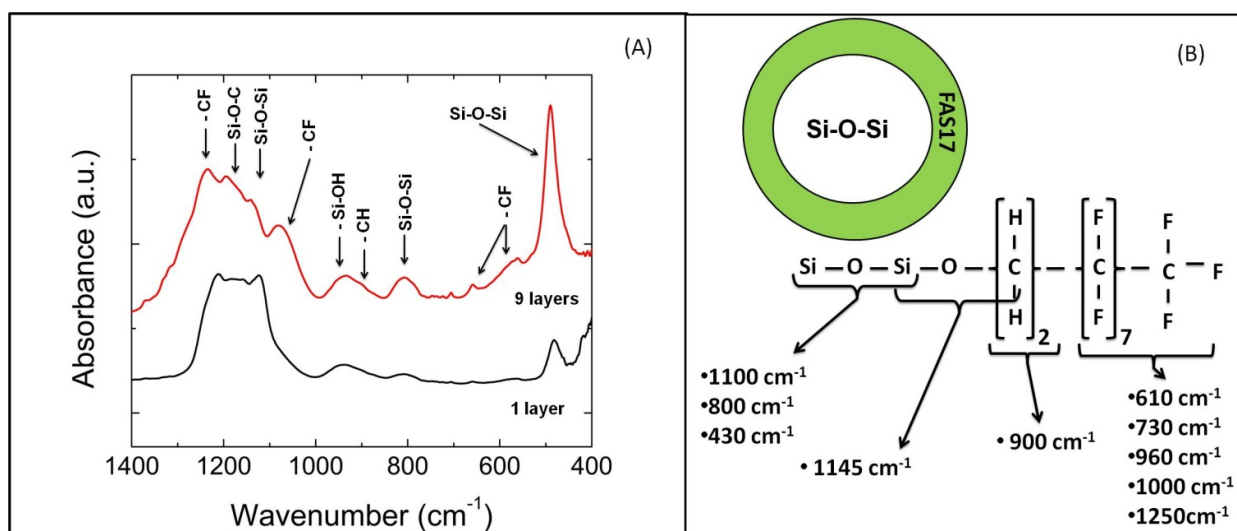
We have previously reported that that the size of silica nanoparticles can be easily controlled through the concentration of catalyst [6,24,38,39]. Figure 2 shows SEM images of spherically shaped fluorinated silica nanoparticles of diameter 119 ± 12 nm deposited in three layers on aluminum substrates. The inset of Figure 2(A) shows the image of a water drop placed on this aluminum substrate surface showing a very high water contact angle of ~152°. It is clear from these images that this surface is composed of several micrometer sized clusters of these spherical nanoparticles presenting randomly distributed holes and cracks by which the clusters are separated. It can also be seen from the higher magnification image in Figure 2(B) that these spherical fluorinated silica nanoparticles are also randomly stacked in steps of layers presenting different depths. Such an arrangement of randomly stacked spherical nanoparticles in clusters separated by cracks and holes provides the surface a rough micro-nanopattern. Nozawa *et al.* [38] obtained 110 ± 20 nm silica

nanoparticles using the Stöber process at a NH$_4$OH/TEOS molar ratio of 10, however, in our case, the size of the nanoparticles obtained under the same conditions are ~10 nm larger (119 ± 12 nm). The larger size in our case is attributed to the presence of an outer shell of fluorinated silane bonded around the silica nanospheres as a result of their functionalization using FAS-17 molecules as presented schematically in Figure 1(B).

Figure 2. (**A**) SEM images of fluorinated silica nanoparticles of 119 ± 12 nm diameter deposited on aluminum substrates in three layers by spin coating; Inset of Figure 2 (**A**) shows the image of a water drop placed on this surface exhibiting a very high water contact angle of ~152°, and (**B**) higher magnification image of (A).
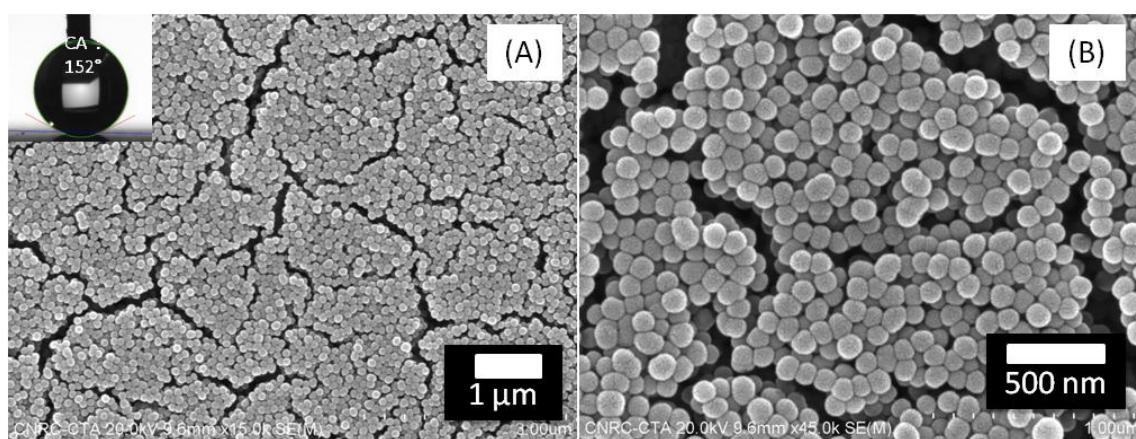

Water contact angle measurements were used to evaluate the wetting properties of the prepared surfaces. Increased contact angles are, partially, increased because of roughness, which increased air entrapment as stated by Cassie-Baxter equation. Figure 3 (A) shows the contact angles variation on the aluminum surfaces coated using the as-prepared fluorinated silica nanoparticles in the solution as well as the ones coated by diluting the same. In both cases, the water contact angle values were found to increase with the increase in the number of layers of the fluorinated silica nanoparticles deposited on the substrates until a critical number of layers was reached after which the water contact angle values remained similar on the surfaces coated using as-prepared solution. However, higher water contact angle values were obtained on surfaces coated using the as-prepared fluorinated silica nanoparticles solution. For example, on the aluminum surfaces coated with one layer of as-prepared solution, an increased water contact angle value of 137 ± 1° was obtained, making these surfaces hydrophobic since a clean aluminum surface provides a water contact angle of only ~70°. The surface was rendered superhydrophobic when the number of layers was increased to three providing a higher water contact angle value of 152 ± 1°. This increase in water contact value is attributed to the rough micro-nanomorphogical pattern obtained on these surfaces (Figure 2) as well as the presence of low surface energy fluorinated species present on these surfaces as confirmed by the IRRAS analyses (Figure 1(A)). This emphasizes the importance of the presence of both surface roughness as well as low surface energy, a phenomenon reported on lotus effect [4]. Further, the influence of surface roughness in leading to a large amount of air entrapment in the gaps of the rough structure to result in a composite structure of air and solid has been well elucidated by Cassie and Baxter [16]. With a further

increase in the number of layers to five, the water contact angle values slightly increased to ~153° and remained similar when coated with seven and nine layers. Therefore, three layers of coating may be considered as a critical parameter for obtaining superhydrophobic properties when the coating is made with the as-prepared solution. Similarly, an increasing tendency in water contact angle values was observed also in cases of coatings prepared with the dilute solution. However, the water contact angle reached lower values when the same number of layers was used as with the as-prepared solution. Such lower values may be attributed to the lower concentration of the fluorinated silica nanoparticles in the diluted solution, possibly resulting in morphologies with less surface roughness (Figure 3(B)). However, with the diluted solution, superhydrophobic properties were indeed obtained when the numbers of layers deposited on the surface was increased. For example, with only one layer coated with the dilute solution, the water contact angle increased to $128 \pm 2°$ (although this is lower than on the same coating using as-prepared solution). With three layers, the contact angle reached $135 \pm 3°$ which further increased to $144 \pm 1°$ on deposition of five layers. With seven and nine layers of coating, the contact angle values reached to a high of $150 \pm 1°$ and $151 \pm 1°$, respectively. These values show that a critical number of seven layers was required to attain superhydrophobicity when using dilute solution as compared to only three layers that was sufficient to obtain this property with the as-prepared solution of the fluorinated silica nanoparticles.

Although superhydrophobic properties could be obtained using both as-prepared and diluted solutions, the difference in the critical number of layers required in obtain these properties is attributed to the difference in the surface roughness obtained on the corresponding surfaces. Figure 3(B) shows the variation in the root mean square (rms) roughness measured on the surfaces prepared with varying numbers of layers coated using the two different solutions deposited on aluminum substrates. As an example, a three dimensional surface profile obtained during the rms measurements of aluminum surface prepared by coating three layers using as prepared solution has been presented in the inset of Figure 3(B). These graphs show that the contact angle and the roughness vary proportionally as it is clear that the water contact angle increases with increase in surface roughness until a critical roughness value is reached. Figure 3(C) shows a plot of water contact angle as a function of rms roughness on the coatings prepared using as prepared solution. We have previously reported a detailed mathematical model to show the relationship between the roughness and water contact angle in reference to Cassie model [6]. Huang *et al.* [40] have also shown similar behavior on their electrochemically deposited copper state surface. On the coatings prepared using the as-prepared solution, an rms value of 0.60 ± 0.10 µm on a one layer coating increased to 0.69 ± 0.01 µm when coated with three layers where superhydrophobic properties were obtained with a contact angle above 150°. With further increase in the number of layers to five, seven and nine, the rms roughness remained unchanged (~0.71 µm). The similar rms values on the coatings prepared with more than three layers shows that increasing the number of layers further does not cause any change in the surface roughness and therefore provides the same contact angle values on these surfaces. Therefore, an rms roughness of 0.69 ± 0.01 µm obtained with three layer coating is found to be a critical value in obtaining superhydrophobic properties. Similarly, in case of the coatings prepared using diluted solution, the rms values show that superhydrophobic properties were only reached when the rms values reached 0.70 ± 0.02 µm when coated with seven layers on the substrate providing a water contact angle value of $150 \pm 1°$. These values were lower on the surfaces coated using less layers, that is, 0.57 ± 0.10 µm,

0.61 ± 0.03 μm and 0.67 ± 0.03 μm, respectively on the surfaces coated with one, three and five layers, which provided water contact angles lower than 150°. With nine layers of coating, the rms value slightly increased to 0.72 ± 0.05 μm, maintaining superhydrophobic properties. Therefore, a critical rms roughness value of 0.69 ± 0.01 μm in case of as-prepared solution which is not very different from the rms values of 0.70 ± 0.02 μm in case of diluted solution is required for obtaining superhydrophobic properties, however, the presence of low surface energy fluorinated components is another key factor in obtaining these properties. In our case, the presence of a low surface energy fluorinated component is inherent as the silica nanoparticles are funtionalized with FAS-17 molecules prior to deposition on the substrate surfaces. The combination of the critical surface roughness of ~0.70 μm and presence of fluorinated species as confirmed by IRRAS analyses leads to the superhydrophobic properties with water roll-off properties.

Figure 3. (**A**) Water contact angle variation, and (**B**) rms roughness as a function of number of layers coated using as-prepared (black) and dilute solution (red); (**C**) relationship between water contact angle and rms roughness as obtained on the coatings prepared using as-prepared solution on aluminum substrates; and (**D**) water contact angle variation with number of layers coated using dilute solution on different substrates, namely, aluminum (black), silicon (100) (red) and sodalime glass (blue). Inset shows transparency of our superhydrophobic coatings on glass substrates.
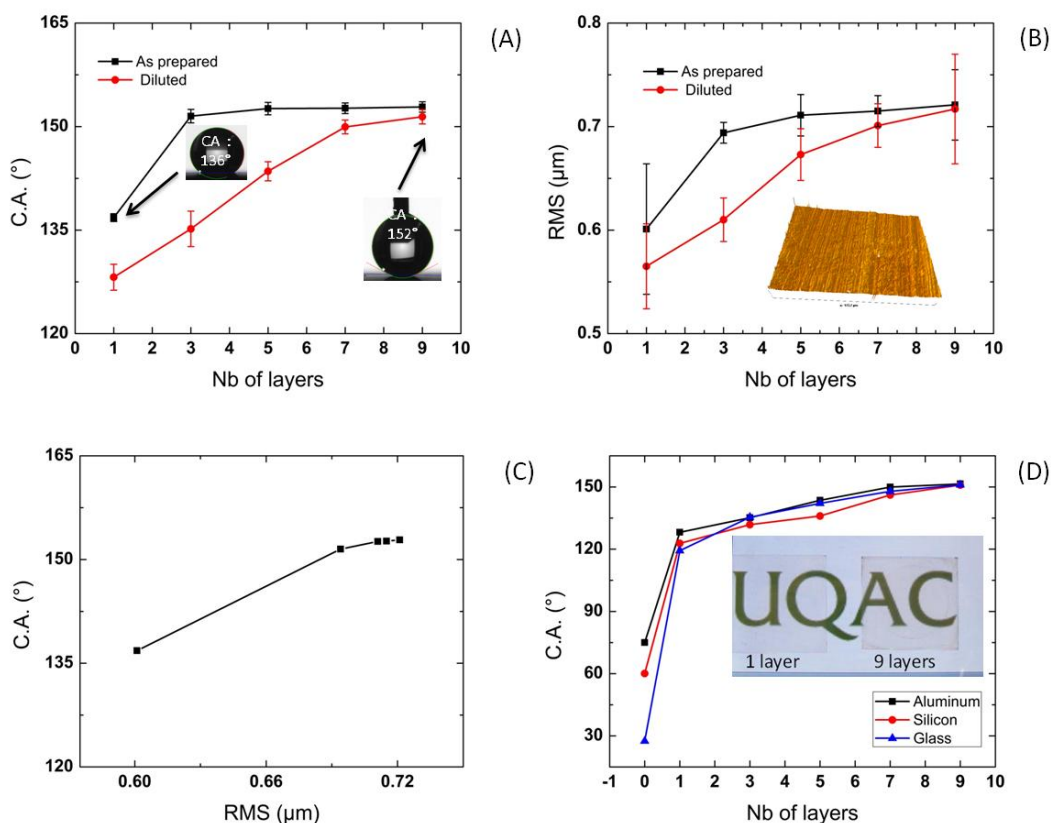
The uniformity of the coating has been verified on various substrates as shown in Figure 3(D). In addition to aluminum substrates, the feasibility of the coatings were also tested on silicon (100) and sodalime glass substrates. Figure 3 (D) shows the water contact angle behavior for all the three substrates coated with diluted solution of fluorinated silica nanoparticles. The water contact values obtained on as-received flat substrates of Si(100) and glass are ~60° and ~30°, respectively. In both cases, the water contact angle value increases with an increase in number of deposited layers. With just one layer of coating, the surface reaches the hydrophobic zone by providing water contact values greater than 90° in case of all the three substrates. Superhydrophobic properties are reached by increasing the number of deposited layers. The feasibility of obtaining superhydrophobicity on different substrate surfaces can have great potential in industrial use. As a potential for applications on glass windows or car wind-shields, we have provided images of glass substrates coated with one layer and nine layers of diluted solution in the inset of Figure 3(B). It is clear from these images that one layer or nine layers does not dramatically alter the transparency of the glass following coating visually, the only difference being that the one layer coating is hydrophobic while the nine layer coating is superhydrophobic. Such coatings also present promise for applications for aesthetic purposes when coated on opaque substrates.

Figure 4. Contact angle hysteresis (CAH) as a function of number of layers coated using as-prepared (black) and diluted solution (red). Inset image at the left shows high CAH of ~15° for one layer coating and right shows low CAH of 2° for nine layers coating.
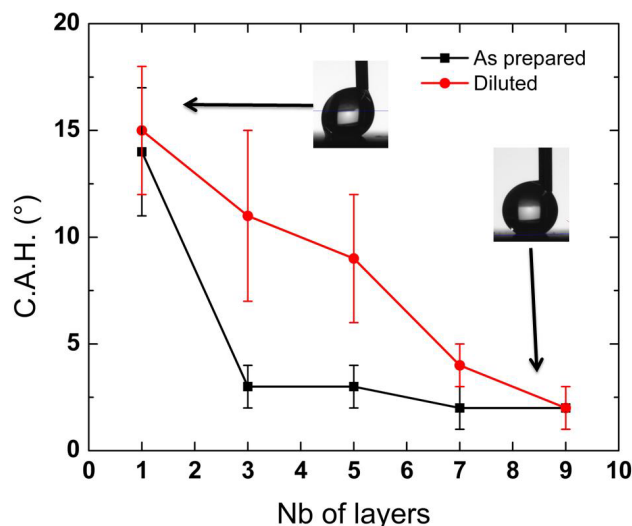
The combined effect of CA and CAH determine the self-cleaning properties [29]. A surface having CA more than 150° and CAH less than 5 degree shows self-cleaning properties. On the other hand, a surface showing CA more than 150° and CAH more than 10° does not show the self-cleaning properties [41]. In the view of claiming the self-cleaning properties of our superhydrophobic surfaces, we have performed both CA and CAH experiments. The CA results have been discussed in the previous section. In this section we describe the results of dynamic contact or CAH. Figure 4 shows the CAH data of the coatings prepared with fluorinated silica nanoparticles on flat aluminum substrates. One layer coating using both as-prepared as well as diluted solution provides CAH of

14 ± 3° and 15 ± 3°, respectively. The CAH reduced to 3 ± 1° with three layers coatings of as-prepared solution. However, in the three layer coatings using diluted solution, the CAH was 11 ± 4°. The CAH reduced to 2 ± 1° for the coatings obtained by seven layers using as-prepared solution. On the other hand, the seven layer coatings with the diluted solution provided a CAH of 4 ± 1°. Finally, for both the solutions with nine layers of coatings, the CAH reduced to 2 ± 1°. Therefore, the self-cleaning properties (coating having CA more than 150° and CAH less than 5°) can be obtained with three layer coatings using as-prepared solution. However, for diluted solution a coating with seven layers is required.

The mechanical properties of the superhydrophobic coatings are very important for their uses against surface erosion, friction as well as corrosion protection [42–44]. Keeping these important applications in mind, we will be investigating the mechanical properties of our superhydrophobic coatings in future.

4. Conclusions

Solutions of monodispersive spherical fluorinated silica nanoparticles of ~120 nm have been prepared by sol-gel processes and have been used to prepare thin films on flat aluminum, silicon and glass substrates by spin-coating processes. FAS-17 molecules are used for the fluorination of the silica nanoparticles. IRRAS spectra show the presence of C-F and Si-O bonds resulting from the functionalization of silica nanoparticles by FAS-17 molecules. An increase in the surface area of the C-F and Si-O peaks has been encountered in the spectra with an increase in the number of layers used for coating. The water contact angle values were found to increase with increasing numbers of layers until a critical number of layers: three in the case of as-prepared solution used for coating and seven in case of the diluted solution used for coating. As we have achieved the contact angle of more than 150° and CAH less than 2°, we consider our coatings possess self-cleaning properties. Water contact angle in relation to surface roughness measurements show both parameters are proportional as water contact angle increases with an increase in surface roughness. The roughness measurements also show that the rms values increase with the increase in the number of layers coated. When applied on other substrates, like silicon or glass, superhydrophobicity is obtained by tuning the number of layers of deposition. The transparency of the coating has been demonstrated on glass substrates, which shows the great potential of such coatings in industrial use on large scale, such as on windows and car windshields as well as for aesthetic purposes on opaque substrates. With its good optical properties, these fluorinated silica nanoparticles can be used as paint additives to obtain large-scale superhydrophobic coatings.

Acknowledgments

Appl. Sci. **2012**, *2*

Conflict of Interest

The authors declare no conflict of interest.

References

1. Liu, X.; Liang, Y.; Zhou, F.; Liu, W. Extreme wettability and tunable adhesion: Biomimicking beyond nature? *Soft Matter* **2012**, *8*, 2070–2086.
2. Gao, X.; Jiang, L. Water-repellent legs of water striders. *Nature* **2004**, *432*, doi: 10.1038/432036a.
3. Huang, J.; Wang, X.; Wang, Z.L. Controlled replication of butterfly wings for achieving tunable photonic properties. *Nano Lett.* **2006**, *6*, 2325–2331.
4. Neinhuis, C.; Barthlott, W. Characterization and distribution of water-repellent, self-cleaning plant surfaces. *Ann. Botan.* **1997**, *79*, 667–677.
5. Zheng, Y.; Gao, X.; Jiang, L. Directional adhesion of superhydrophobic butterfly wings. *Soft Matter* **2007**, *3*, 178–182.
6. Brassard, J.-D.; Sarkar, D.K.; Perron, J. Synthesis of monodisperse fluorinated silica nanoparticles and their superhydrophobic thin films. *ACS Appl. Mater. Interfaces* **2011**, *3*, 3583–3588.
7. Huang, Y.; Sarkar, D.K.; Chen, X.G. A one-step process to engineer superhydrophobic copper surfaces. *Mater. Lett.* **2010**, *64*, 2722–2724.
8. Safaee, A.; Sarkar, D.K.; Farzaneh, M. Superhydrophobic properties of silver-coated films on copper surface bye galvanic exchange reaction. *Appl. Surf. Sci.* **2008**, *254*, 2493–2498.
9. Saleema, N.; Sarkar, D.K.; Gallant, D.; Paynter, R.W.; Chen, X.G. Chemical nature of superhydrophobic aluminum alloy surfaces produced via a one-step process using fluoroalkyl-silane in a base medium. *ACS Appl. Mater. Interfaces* **2011**, *3*, 4775–4781.
10. Sarkar, D.K.; Farzaneh, M.; Paynter, R.W. Superhydrophobic properties of ultrathin rf-sputtered Teflon films coated etched aluminum surfaces. *Mater. Lett.* **2008**, *62*, 1226–1229.
11. Sarkar, D.K.; Saleema, N. One-step fabrication process of superhydrophobic green coatings. *Surf.Coat. Technol.* **2010**, *204*, 2483–2486.
12. Garcia, N.; Benito, E.; Tiemblo, P.; Hasan, M.M.B.; Synytska, A.; Stamm, M. Chemically guided topography in alkylsilane- and oligosiloxane-modified silica nanoparticle coatings: From very hydrophobic surfaces to "pearl" bouncing droplets. *Soft Matter* **2010**, *6*, 4768–4776.
13. Taurino, R.; Fabbri, E.; Messori, M.; Pilati, F.; Pospiech, D.; Synytska, A. Facile preparation of superhydrophobic coatings by sol-gel processes. *J. Colloid Interface Sci.* **2008**, *325*, 149–156.
14. Liu, H.; Szunerits, S.; Pisarek, M.; Xu, W.; Boukherroub, R. Preparation of superhydrophobic coatings on zinc, silicon, and steel by a solution-immersion technique. *ACS Appl. Mater. Interfaces* **2009**, *1*, 2086–2091.
15. Liu, H.; Szunerits, S.; Xu, W.; Boukherroub, R. Preparation of superhydrophobic coatings on zinc as effective corrosion barriers. *ACS Appl. Mater. Interfaces* **2009**, *1*, 1150–1153.
16. Cassie, A.B.D.; Baxter, S. Wettability of porous surfaces. *Trans. Faraday Soc.* **1944**, *40*, 546–551.
17. Wenzel, R.N. Resistance of solid surfaces to wetting by water. *Ind. Eng. Chem.* **1936**, *28*, 988–994.
18. Bushnell, D.M.; Moore, K.J. Drag reduction in nature. *Annu. Rev. Fluid Mech.* **1991**, *23*, 65–79.

19. Cao, L.; Jones, A.K.; Sikka, V.K.; Wu, J.; Gao, D. Anti-icing superhydrophobic coatings. *Langmuir* **2009**, *25*, 12444–12448.

20. Carlborg, C.F.; van der Wijngaart, W. Sustained superhydrophobic friction reduction at high liquid pressures and large flows. *Langmuir* **2010**, *27*, 487–493.

21. Carré, A.; Mittal, K.L. *Superhydrophobic Surfaces*; VSP: Leiden, The Netherlands, 2009.

22. Karmouch, R.; Ross, G.G. Superhydrophobic wind turbine blade surfaces obtained by a simple deposition of silica nanoparticles embedded in epoxy. *Appl. Surf. Sci.* **2010**, *257*, 665–669.

23. Verplanck, N.; Coffinier, Y.; Thomy, V.; Boukherroub, R. Wettability switching techniques on superhydrophobic surfaces. *Nanoscale Res. Lett.* **2007**, *2*, 577–596.

24. Stöber, W.; Fink, A.; Bohn, E. Controlled growth of monodisperse silica spheres in the micron size range. *J. Colloid Interface Sci.* **1968**, *26*, 62–69.

25. Chen, S.-L.; Dong, P.; Yang, G.-H.; Yang, J.-J. Kinetics of formation of monodisperse colloidal silica particles through the hydrolysis and condensation of tetraethylorthosilicate. *Ind. Eng. Chem. Res.* **1996**, *35*, 4487–4493.

26. Yang, H.; Pi, P.; Cai, Z.-Q.; Wen, X.; Wang, X.; Cheng, J.; Yang, Z.-R. Facile preparation of super-hydrophobic and super-oleophilic silica film on stainless steel mesh via sol-gel process. *Appl. Surf. Sci.* **2010**, *256*, 4095–4102.

27. Bravo, J.; Zhai, L.; Wu, Z.; Cohen, R.E.; Rubner, M.F. Transparent superhydrophobic films based on silica nanoparticles. *Langmuir* **2007**, *23*, 7293–7298.

28. Callies, M.; Chen, Y.; Marty, F.; Pépin, A.; Quéré, D. Microfabricated textured surfaces for super-hydrophobicity investigations. *Microelectron. Eng.* **2005**, *78–79*, 100–105.

29. Quéré, D. Non-sticking drops. *Reports on Progress in Physics* **2005**, *68*, 2495–2532.

30. Sarkar, D.K.; Farzaneh, M.; Paynter, R.W. Superhydrophobic properties of ultrathin rf-sputtered Teflon films coated etched aluminum surfaces. *Mater. Lett.* **2008**, *62*, 1226–1229.

31. Hozumi, A.; Takai, O. Preparation of ultra water-repellent films by microwave plasma-enhanced CVD. *Thin Solid Films* **1997**, *303*, 222–225.

32. Latthe, S.S.; Imai, H.; Ganesan, V.; Rao, A.V. Superhydrophobic silica films by sol-gel co-precursor method. *Appl. Surf. Sci.* **2009**, *256*, 217–222.

33. Teshima, K.; Sugimura, H.; Inoue, Y.; Takai, O. Gas barrier performance of surface-modified silica films with grafted organosilane molecules. *Langmuir* **2003**, *19*, 8331–8334.

34. Zhao, Y.; Li, M.; Lu, Q.; Shi, Z. Superhydrophobic polyimide films with a hierarchical topography: Combined replica molding and layer-by-layer assembly. *Langmuir* **2008**, *24*, 12651–12657.

35. Sarkar, D.K.; Brassard, D.; Khakani, M.A.E.; Ouellet, L. Dielectric properties of sol-gel derived high-k titanium silicate thin films. *Thin Solid Films* **2007**, *515*, 4788–4793.

36. Hozumi, A.; Takai, O. Effect of hydrolysis groups in fluoro-alkyl silanes on water repellency of transparent two-layer hard-coatings. *App. Surf. Sci.* **1996**, *103*, 431–441.

37. Latthe, S.S.; Imai, H.; Ganesan, V.; Rao, A.V. Superhydrophobic silica films by sol-gel co-precursor method. *Appl. Surf. Sci.* **2009**, *256*, 217–222.

38. Nozawa, K.; Gailhanou, H.; Raison, L.; Panizza, P.; Ushiki, H.; Sellier, E.; Delville, J.P.; Delville, M.H. Smart control of monodisperse stöber silica particles: Effect of reactant addition rate on growth process. *Langmuir* **2004**, *21*, 1516–1523.

39. Qu, A.L.; Wen, X.F.; Pi, P.H.; Cheng, J.; Yang, Z.R. Study on superhydrophobicity of composite silica film surface. *Wuji Cailiao Xuebao/J. Inorg. Mater.* **2008**, *23*, 373–378.
40. Huang, Y.; Sarkar, D.K.; Chen, X.G. Fabrication of superhydrophobic surfaces on aluminum alloy via electrodeposition of copper followed by electrochemical modification. *Nano Micro Lett.* **2011**, *3*, 160–165.
41. Dufour, R.; Harnois, M.; Coffinier, Y.; Thomy, V.; Boukherroub, R.; Senez, V. Engineering sticky superomniphobic surfaces on transparent and flexible PDMS substrate. *Langmuir* **2010**, *26*, 17242–17247.
42. Ke, Q.; Fu, W.; Jin, H.; Zhang, L.; Tang, T.; Zhang, J. Fabrication of mechanically robust superhydrophobic surfaces based on silica micro-nanoparticles and polydimethylsiloxane. *Surf. Coat. Technol.* **2011**, *205*, 4910–4914.
43. Lakshmi, R.V.; Bharathidasan, T.; Basu, B.J. Superhydrophobic sol–gel nanocomposite coatings with enhanced hardness. *Appl. Surf. Sci.* **2011**, *257*, 10421–10426.
44. Ou, J.; Liu, M.; Li, W.; Wang, F.; Xue, M.; Li, C. Corrosion behavior of superhydrophobic surfaces of Ti alloys in NaCl solutions. *Appl. Surf. Sci.* **2012**, *258*, 4724–4728.

Review

Overview of the Development of the Fluoropolymer Industry

Hongxiang Teng

Polymer Research Institute, Department of Chemical and Biological Sciences, Polytechnic Institute of New York University, 6 Metrotech Center, Brooklyn, NY 11201, USA; E-Mail: hoteng@poly.edu

Abstract: The present review briefly describes the development of the fluoropolymer industry in the past 70 years. Discussed are industrial fluoropolymers including polytetrafluoroethylene, polychlorotrifluoroethylene, polyvinylidenefluoride, polyvinylfluoride, ETFE, ECTFE, FEP, PFA, THV, Teflon AF and Cytop. Nafion is included as a special functional fluoropolymer material. These industrial fluoropolymers are introduced in the order of their discovery or time of first production, included are their chemical structures, thermal properties, mechanical properties, electrical and electronic properties, optical properties, chemical resistance, oxidative stabilities, weather stabilities, processabilities and their general applications. The main manufacturing companies for the different types of fluoropolymer products are also mentioned.

Keywords: fluorine chemistry; fluoropolymer; fluorine industry

List of Abbreviations

CTFE	chlorotrifluoroethylene
Cytop	homopolymer of PBVE
ECTFE	copolymer of ethylene and CTFE
ETFE	copolymer of ethylene and TFE
FEP	copolymer of fluorinated ethylene and propylene
HFP	hexafluoropropylene
Nafion	TFE and perfluoro-3,6-dioxa-4-methyl-7-octenesulfonic acid copolymer
PBVE	perfluoro-3-butenyl-vinyl ether
PCTFE	polychlorotrifluoroethylene
PDD	perfluoro-2,2-dimethyl-1,3-dioxole
PE	polyethylene
PFA	copolymer of TFE and PPVE

PPVE	perfluoropropylvinylether
PTFE	polytetrafluoroethylene
PVDF	polyvinylidenefluoride
PVF	polyvinylfluoride
Teflon AF	copolymer of TFE and PDD
TFE	tetrafluoroethylene
THV	poly(TFE-co-HFP-co-VDF)
VDF	vinylidene fluoride

1. Introduction

Fluoropolymers are the polymer materials containing fluorine atoms in their chemical structures. From general organic polymer concepts, there are two types of fluoropolymer materials, *i.e.* perfluoropolymers and partially fluorinated polymers. In the former case, all the hydrogen atoms in the analogous hydrocarbon polymer structures were replaced by fluorine atoms. In the latter case, there are both hydrogen and fluorine atoms in the polymer structures. The fluoropolymer industry discussed here is mainly concerned with the perfluoropolymers, although in some cases the partially fluorinated polymers are included. In the latter case, there are both hydrogen and fluorine atoms in the polymer structures, along with additional elements in selected cases, such as polyvinylidenefluoride (PVDF) and polychlorotrifluoroethylene (PCTFE).

Fluoropolymers possess excellent properties such as outstanding chemical resistance, weather stability, low surface energy, low coefficient of friction, and low dielectric constant. These properties come from the special electronic structure of the fluorine atom, the stable carbon-fluorine covalent bonding, and the unique intramolecular and intermolecular interactions between the fluorinated polymer segments and the main chains.

Due to their special chemical and physical properties, the fluoropolymers are widely applied in the chemical, electrical/electronic, construction, architectural, and automotive industries. The world consumption of fluoropolymers is growing tremendously. Worldwide sales of fluoropolymers in 2000 exceeded \$2.0 billion compared with \$1.5 billion in 1994. Even though the fluoropolymer industry was affected in the same way as other industries because of the economic downturn after 2008, there will be a turnaround along with the recovery of the world economy for fluoropolymer markets, especially in the motor vehicles, wire and cable, advanced batteries, fuel cells and photovoltaic modules.

This review discusses the development of the most popular industrial fluoropolymers along with their chemical structures, basic properties, and general applications. For additional details, previously published books and journals would be helpful for monomer activities, polymerization methods, processing methods, polymer properties, and the applications [1–8].

2. The Development of the Fluoropolymer Industry from 1930s ~ 1990s

1930s

The development of the fluoropolymer industry began with the discovery of the polytetrafluoroethylene (PTFE) by Dr. Plunkett at DuPont in 1938 [9]. The white powder found by

accident opened the magic door to one of the most important applied chemistry areas—the fluoropolymer industry—which greatly influenced the whole world in the following 70 years.

PTFE is a linear polymer of tetrafluoroethylene (TFE) (Figure 1). The preparation of PTFE is hazardous because of the chemical properties of TFE. Therefore, special production equipments and processing conditions are required [10,11].

Figure 1. The polymerization of TFE.

$$F_2C{=}CF_2 \xrightarrow{\text{Initiator}} {}^*{\left[CF_2{-}CF_2 \right]}_n{}^*$$
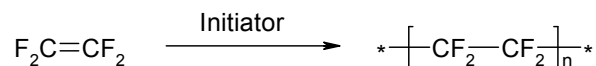
The chemical structure of PTFE is similar to that of polyethylene (PE), except that the hydrogen atoms are completely replaced by fluorine. Unlike the planer zigzag chain confirmation of PE, PTFE has a helical chain confirmation due to the larger fluorine volume. The rigid helical polymer chains can crystallize very easily and result in a high crystallinity (up to 98%). Because of the compact crystalline structure and the dense fluorine atoms, PTFE is the heaviest polymer material with a density of 2.1 g/cm^3. The rigid polymer chain structure also caused a high melting temperature (~320 °C) and a high melt viscosity for PTFE, which made it difficult to process PTFE with the traditional methods for polymer materials. For quite a long time after the discovery of PTFE, scientists kept working on the different approaches to process PTFE materials, and it can be processed into all kinds of shapes for almost every application area.

PTFE is available in granular, fine powder and water-based dispersion forms. The granular PTFE resin is produced by suspension polymerization in an aqueous medium with little or no dispersing agent. Granular PTFE resins are mainly used for molding (compression and isostatic) and ram extrusion. The fine PTFE powder is prepared by controlled emulsion polymerization, and the products are white, small sized particles. Fine PTFE powders can be processed into thin sections by paste extrusion or used as additives to increase wear resistance or frictional property of other materials. PTFE dispersions are prepared by the aqueous polymerization using more dispersing agent with agitation. Dispersions are used for coatings and film casting.

One of the most distinguishing properties of PTFE is its outstanding chemical resistance, except for some extreme conditions such as molten alkali metals or elemental fluorine. Basically, PTFE is not soluble in any organic solvents. PTFE exhibits high thermal stability without obvious degradation below 440 °C. PTFE materials can be continuously used below 260 °C. The combustion of PTFE can only continue in a nearly pure oxygen atmosphere, and it is widely used as an additive in other polymer materials as a flame suppressant. PTFE has an extremely low dielectric constant (2.0) due to the highly symmetric structure of the macromolecules.

The conventional PTFE has some limitations in its applications, such as poor weldability, low creep resistance, low radiation resistance, and high microvoid content. Therefore, research efforts were mainly trying to modify PTFE in different ways to overcome the shortcomings of the conventional PTFE. Modified PTFE significantly reduced melt viscosity by lowering the crystallinity through the incorporation of bulky comonomers into the polymer main chain. Modified PTFE has the advantages such as lower microvoid content and reduced permeation, better weldability and easier bonding

treatment, better sealing properties, excellent electrical insulation properties, smoother surface finishes and higher gloss.

Even after modification, PTFE materials still have low tensile strength, wear resistance and creep resistance compared to other engineering polymers. The properties of the PTFE products are strongly dependent on the processing procedure, such as polymer particle size, sintering temperature and processing pressure. Therefore, other fluoropolymers are still needed for some specific applications where PTFE is not completely suitable.

1940s

In the beginning, PTFE polymers found no use for any application due to its insolubility, high melting temperature and extremely high melt viscosity. During World War II people realized the importance of this new material. At the time, the Manhattan Project was carrying out the development of the atomic bomb. Practically, U-235 needs to be separated from U-238 using differential diffusion of UF_6. UF_6 is highly corrosive to most metals and it was difficult to purify this material. As a result, the Manhattan project was looking for new corrosion resistant materials to meet the novel needs of purifying UF_6. The then strange new material and its resistance to chemicals proved that PTFE could survive the extremely corrosive purification conditions. Therefore, PTFE got its first business order from the Manhattan project. After the war, PTFE was commercially available in 1947 with the trademark Teflon from DuPont to meet the growing market needs of the US and the world. The rate of market growth for PTFE has been 3%–5% per year for the past 30 years. In the late 1990s, annual consumption worldwide for PTFE was over 55,000 tons, which is almost doubled now. Some typical commercially available PTFE products are Teflon (DuPont), Polyflon (Daikin), Dyneon PTFE (Dyneon), and Fluon (Ashai Glass).

Noticeably, even now PTFE still remains the largest type of fluoropolymers with about 70% of the total fluoropolymer market worldwide.

1950s

In 1953, a new fluoropolymer, polychlorotrifluoroethylene (PCTFE) was commercialized by M. W. Kellog Company under the trade mark Kel-F. PCTFE is produced by the free radical polymerization of chlorotrifluoroethylene (CTFE) with a linear polymer chain structure (Figure 2).

Figure 2. The polymerization of CTFE.
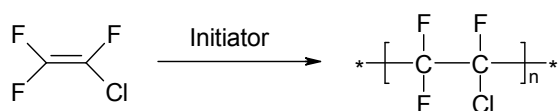
High molecular weight PCTFE can be prepared by polymerization in bulk, in solution, in suspension and in emulsion forms [12]. Compared to PTFE, only one fluorine atom was replaced by the chlorine in PCTFE. The introduction of chlorine atom in the polymer structure interrupted the crystallization ability of the polymer main chain, and resulted in lower crystallinity, lower melting temperature, better intermolecular interaction, and better mechanical properties of PCTFE compared to

PTFE. PCTFE showed higher hardness, higher tensile strength, higher resistance to creep, and less water vapor and gas permeability. One important advantage of PCTFE is its melt processability.

PCTFE is easily melt processed and the products are more transparent. PCTFE can be used continuously from −100 °C to 200 °C. Especially, its better cold-flow characteristics made it more competitive to PTFE materials. It showed similar flame retardancy and better radiation resistance compared to PTFE. The chemical resistance and electrical properties of PCTFE are not as good as those of PTFE, but still better than most polymer materials.

The price of PCTFE is higher than that of PTFE due to the expensive monomer as well as the small market size. Therefore, its main application is limited to use as a moisture barrier film in packaging and special engineering devices, where PTFE cannot meet the high performance requirements. Some examples are the aeronautical and space applications for cryogenic seals and gaskets. Low molecular weight PCTFE are used as oils, waxes and greases, inert sealants, lubricants for oxygen-handling equipment or corrosive media, plasticizers for thermoplastics and gyroscopic floatation fluids.

PCTFE was originally produced by M. W. Kellog and 3M under the trade name of Kel-F [13]. After 3M discontinued the production of PCTFE (1995) [14], Daikin purchased the manufacture rights to PCTFE and produced it under the trade name Neoflon. PCTFE resin is also produced by Honeywell as Aclar and by Arkema as Voltalef.

1960s

Considering the shortcoming of PTFE, researchers looked for new ideas to solve the existing problems. The copolymerization of TFE with other monomers offered many opportunities. The first TFE copolymer was FEP (fluorinated ethylene propylene), which was prepared by the random copolymerization of TFE and hexafluoropropylene (HFP). FEP was commercially introduced to the market in 1960 by DuPont.

The structure of FEP is similar to PTFE except that a trifluoromethyl group was introduced along the side of the polymer main chain (Figure 3). FEP is generally prepared by the copolymerization of TFE and HFP in an aqueous medium with a free radical initiator and a dispersing agent. The comonomer ratio and the polymerization conditions are carefully controlled to achieve the desired copolymer composition and molecular weight, which are closely related to the melt viscosity, the processability and the mechanical properties of the final products [15,16].

Figure 3. The preparation of FEP.
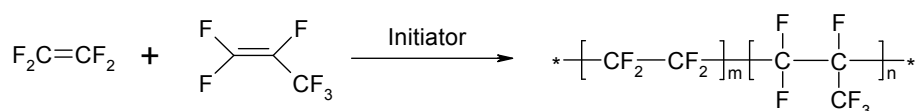
Generally, FEP contains about 5 mol% of HFP. The introduction of HFP units in the polymer main chain disrupted the crystallization ability of FEP copolymer compared with the homopolymer of TFE. The crystallinity of FEP is about 70%, and its melting temperature is in the range of 260–280 °C depending on the HFP content. It can be used continuously up to 200 °C. The molecular weight of FEP is much lower than that of PTFE and resulted in a much lower melt viscosity and better processability.

FEP can be processed by the conventional polymer processing techniques such as injection molding, extrusion and film casting. FEP has better impact strength, better wear resistance, and less permeability for organic solvents compared with PTFE. The disadvantage of FEP is the poorer resistance to thermal stress cracking. FEP exhibits similar chemical resistance, weather resistance, flame resistance, radiation resistance, and the electrical properties to PTFE. FEP is easier to surface modify to increase wettability and adhesive bonding.

FEP dispersions are generally used for coatings followed by the fuse treatment above the melting temperature of the polymer. The major applications of FEP are wire insulation, thermocouple wire insulation, chemical resistance liners for pipes and fittings, lined tanks for chemical storage, anti-stick applications, and sheet and film products for solar panels and solar collectors.

About 65% of overall worldwide consumption for FEP is for plenum cable insulation. The increasing use of local area network (LAN) cable led to a huge increase in the market of FEP. Some typical commercial FEP products are Teflon FEP from DuPont, Neoflon FEP from Daikin, and Dyneon FEP from Dyneon.

In 1961, DuPont introduced another fluoropolymer, polyvinylfluoride (PVF) (Figure 4) with the trademark Tedlar. Although only one hydrogen atom was replaced by a fluorine atom compared to the polyethylene, PVF showed more interesting properties than most fluoropolymers.

Figure 4. The polymerization of VF.
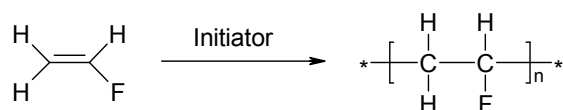
PVF is prepared by the polymerization of vinyl fluoride (VF) in an aqueous medium using a free radical initiator. A higher pressure is necessary due to the lower polymerization activity of VF compared to TFE.

The presence of the fluorine atom in PVF put it in between PE and PTFE in terms of crystallization. With a crystallinity of 40%, PVF has a melting temperature around 200 °C, and can be continuously used in the temperature range from -70 °C to 110 °C. The lower crystallinity of PVF compared to PTFE resulted in higher impact strength and better tensile strength. The relatively poor thermal stability of PVF makes PVF difficult to process traditionally. PVF film is manufactured using a plasticized melt extrusion method with plasticizers and stabilizers.

The main uses of PVF are in films and coatings applications, such as the premier surface finish for aluminum and steel home siding. The excellent resistances to weather and radiation have led to the wide application of PVF as glazing materials for solar energy collectors.

The formability of PVF is very important for lamination applications. It is critical that the laminate can stand bending during the roll forming process. PVF laminated steel finds application in industrial plants, warehouses, highway sound barriers and parking garages and provides long lasting aesthetics.

Currently, DuPont is still the main company for PVF production. With a recent expansion it plans to achieve $1 billion in sales by 2012.

Compared to VF, vinylidene fluoride (VDF) has one more fluorine atom on the same carbon in its chemical structure. The free radical polymerization of VDF resulted in a partially fluorinated,

semi-crystalline polymer PVDF (polyvinylidenefluoride) (Figure 5), which was introduced by Pennsalt (now Arkema) with the tradename Kynar in 1961.

Figure 5. The polymerization of VDF.
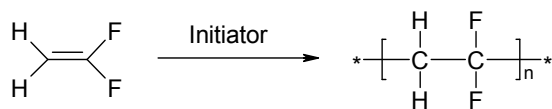
PVDF is generally prepared by two kinds of polymerization methods, the suspension method and the emulsion method. Suspension polymerization produces PVDF with high head-to-tail structure in the polymer chains, which results in higher crystallinity, higher melting temperature, and better mechanical properties at elevated temperatures [17,18].

PVDF is a polymer with several crystalline forms depending on the processing conditions. It has a melting temperature (~170 °C) significantly lower than that of the other fluoropolymers. The normal processing temperatures for PVDF are in the range 200–260 °C, and the continuous service temperature for PVDF is up to 150 °C. The crystallinity of PVDF increases significantly in the first week after processing and stabilizes after 4 weeks. This phenomenon increases crystallinity up to 65% and results in the intrinsic stress and the potential stress cracking.

PVDF has very good chemical resistance to a wide range of chemicals, but it is not as good as that of other fluoropolymers. For example, PVDF can be swollen by polar solvents such as ethyl acetate and acetone. It shows medium flame resistance properties. PVDF also shares many of the characteristics of other fluoropolymers, such as thermal and oxidative stability, as well as outstanding weatherability. PVDF has substantially greater strength, wear resistance, and creep resistance than PTFE and FEP. PVDF undergoes cross-linking when exposed to ionizing radiation, which leads to a modification of its mechanical properties.

PVDF has been used in the architectural coating industry, the wire and cable industry and the chemical industry for valves, pumps and bearings. Heat-shrinkable tubing made from PVDF is used in the electronics, aerospace, and aircraft industries. The alternative arrangement of fluorine and hydrogen atoms on the polymer main chain leads to an unusual polarity with a dramatic effect on dielectric properties. PVDF has a high dielectric constant (8 ~ 9) relative to the other fluoropolymers, and it also shows strong piezoelectricity. The promising developments include actuator materials, piezoelectric ceramics, piezoelectric composites and piezomicrosensors.

The commercial PVDF products include Kynar from Arkema, Solef from Solvay, and Neoflon PVDF from Daikin. Solvay increased PVDF production capacity by 50% in 2011 to serve the strong growing demand.

In the late 1960s, Nafion was discovered by Walther Grot of DuPont. Nafion is a fluoropolymer containing sulfonate groups onto a tetrafluoroethylene backbone (Figure 6) [19–27]. It is the first of a class of synthetic polymers with ionic properties which are called ionomers.

Figure 6. The preparation of Nafion.
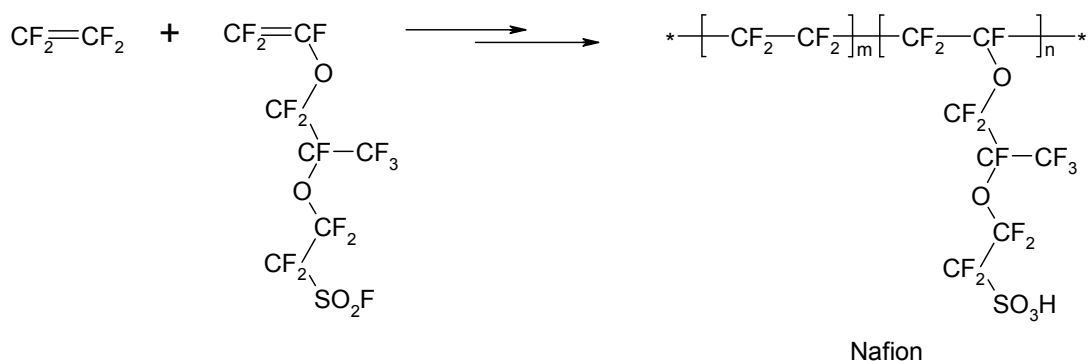
Nafion

Nafion is synthesized firstly by the copolymerization of TFE and a perfluoro(alkyl vinyl ether) with sulfonyl acid fluoride. The resulting polymer is extruded into films and treated with hot aqueous NaOH converting the sulfonyl fluoride groups ($-SO_2F$) into sulfonate groups ($-SO_3Na$). This form of Nafion, referred to as the neutral or salt form, is finally converted to the acid form containing the sulfonic acid ($-SO_3H$) groups. Nafion can be cast into thin films by heating in aqueous alcohol at 250 °C in an autoclave. By this process, Nafion can be used to generate composite films, coat electrodes, or repair damaged membranes.

The combination of the stable Teflon backbone with the acidic sulfonic groups gives Nafion many special characteristics. It is highly conductive to cations, making it suitable for many membrane applications. The Teflon backbone interlaced with the ionic sulfonate groups gives Nafion a high operating temperature, e.g. up to 190 °C. The combination of fluorinated backbone, sulfonic acid groups, and the stabilizing effect of the polymer matrix make Nafion a very strong acid, with pK_a of -6. Nafion's superior properties allowed for broad application. Nafion has found use in fuel cells, electrochemical devices, chlor-alkali production, metal-ion recovery, water electrolysis, plating, surface treatment of metals, batteries, sensors, Donnan dialysis cells, drug release, gas drying or humidifaction, and superacid catalysis for the production of fine chemicals (Gelbard, 2005). Nafion is also often cited for theoretical potential (*i.e.*, thus far untested) in a number of fields.

Although fuel cells have been used since the 1960s as power supplies for satellites, recently they have received renewed attention for their potential to efficiently produce clean energy from hydrogen. Nafion was found effective as a membrane for proton exchange membrane (PEM) fuel cells by permitting hydrogen ion transport while preventing electron conduction. Solid Polymer Electrolytes, which are made by connecting or depositing electrodes (usually noble metal) to both sides of the membrane, conduct the electrons through an energy requiring process and rejoin the hydrogen ions to react with oxygen and produce water. Fuel cells are expected to find strong use in the transportation industry.

Nafion is the first and still one of the most important functional fluoropolymer materials. The further development in the fuel cell industry and the automotive industry offered the prominent future for the interesting polymer systems.

1970s

After discovering that ethylene has good copolymerization properties with fluorinated monomers, many new fluoropolymers were developed to achieve more favorable application properties. The first fluoropolymer containing ethylene units was ECTFE, which was introduced to the market by the Italian company Ausimont in 1970. ECTFE is an alternating copolymer of ethylene and CTFE (Figure 7).

Figure 7. The preparation of ECTFE.

$$H_2C{=}CH_2 \;+\; \underset{F}{\overset{F}{>}}{=}\underset{Cl}{\overset{F}{<}} \;\xrightarrow{\text{Initiator}}\; *{-}[CH_2{-}CH_2]_m[\,\underset{F}{\overset{F}{C}}{-}\underset{Cl}{\overset{F}{C}}\,]_n{-}*$$
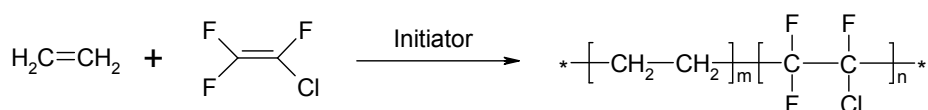
ECTFE is prepared by the copolymerization of ethylene and CTFE at relatively low temperatures (<10 °C) in an aqueous medium using a peroxide catalyst and a halogenated solvent chain transfer agent to regulate the molecular weight [28].

ECTFE polymer chains pack in an extended zigzag confirmation, which results in a crystallinity of 50%–60%. ECTFE has a melting temperature in the range of 220–245 °C depending on the polymerization methods. ECTFE can be used over a broad temperature range from −100 °C to 150°.
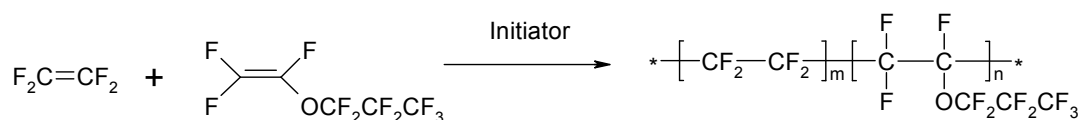
ECTFE can be processed by the standard processing methods for traditional thermoplastics in the range of 260–300 °C. It is readily converted into fibers, filaments, films, sheets, and wire and cable insulation. Noticeably, the molten ECTFE is corrosive and special corrosion-resistant steels are used for screw and barrel components.

As the copolymer with ethylene, ECTFE has moderate chemical resistance, flame resistance, and dielectric constant (2.6). While, it still has excellent radiation resistance, weathering resistance, and barrier properties, as well as good tensile, flexural and wear-related properties. The strength, wear resistance and creep resistance of ECTFE are significantly greater than that of PTFE and FEP. ECTFE film is the most abrasion resistant and highest tensile strength fluoropolymer film available.

The single largest use of ECTFE is the flame-resistant insulation for wire and cable applications, extensively used for aircraft, mass transit and automotive wiring. ECTFE also finds applications in chemical process equipments and components. ECTFE is used in aerospace applications, such as gaskets for liquid oxygen and other propellants, components for spacecraft and aircraft cabins, convoluted tubing, abrasion resistant braid and hose for expandable conduit for space suits.

At the end of 1999, Ausimont introduced a new family of ECTFE resins under the trademark Vatar, specifically designed to meet the requirements for plenum cable applications. ETCFE is currently manufactured by Solvay under the trademark Halar after acquiring Ausimont in 2002.

Figure 8. The preparation of PFA.

$$F_2C{=}CF_2 \;+\; \underset{F}{\overset{F}{>}}{=}\underset{OCF_2CF_2CF_3}{\overset{F}{<}} \;\xrightarrow{\text{Initiator}}\; *{-}[CF_2{-}CF_2]_m[\,\underset{F}{\overset{F}{C}}{-}\underset{OCF_2CF_2CF_3}{\overset{F}{C}}\,]_n{-}*$$

After the introduction of FEP, further research on TFE copolymers led to the development of PFA (Figure 8)—a copolymer of TFE and perfluoropropylvinylether (PPVE), which was introduced in 1972 by DuPont.

Generally, PFA is prepared by an aqueous dispersion process. The copolymerization must be controlled carefully to produce a uniform copolymer with the required molecular weight and polydispersity [29,30].

Due to the PPVE units in the polymer main chain, PFA has lower crystallinity compared to PTFE. Correspondingly, PFA has a lower melting temperature (305–310 °C), lower melt viscosity and better processability. This improvement for PTFE dramatically enlarged its market by lowering the processing cost and enriched the available product categories by the flexibility of thermoplastic processing.

PFA shows comparable mechanical properties as FEP below 200 °C, and performs comparable mechanical properties as PTFE above 200 °C. The thermal stability of PFA is almost the same as that of PTFE and better than that of FEP. PFA has the same chemical resistance, flame resistance and radiation resistance as PTFE. The electrical properties of PFA and PTFE are similar. Importantly, PFA thin films have better transparency compared to PTFE.

PFA can be processed by conventional melt techniques such as extrusion, injection molding and rotational molding. PFA powder can be used directly for extrusion or injection molding, and a PFA dispersion can be prepared for spray or dip-coating applications. Like PTFE, PFA can be filled with glass or carbon fibers, graphite or bronze powder to improve wear and creep properties.

The main applications of PFA are chemical resistance components for valves, pumps and pipes. PFA is also widely used in the semiconductor manufacturing industries for high purity and chemical resistant moldings.

The commercial PFA products are Teflon PFA from DuPont, Aflon PFA from Asahi Glass, Dyneon PFA from Dyneon, Neoflon PFA from Daikin, and Hyflon PFA from Solvay.

After ECTFE, the other fluoropolymer containing ethylene units—ETFE was commercialized in 1973 by DuPont. ETFE is comprised of alternating ethylene and TFE units in the polymer main chain (Figure 9).

Figure 9. The preparation of ETFE.
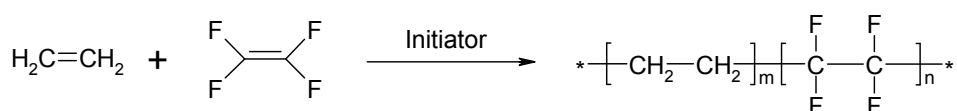
Due to the risk of explosive decomposition reaction, the copolymerization of ethylene and TFE must be conducted in special vessels at low pressure. Suspension polymerization is generally carried out in an inert chlorofluorocarbon solvent using fluorinated peroxides as initiator and methanol as a chain transfer agent [31,32].

The polymer chains in ETFE adopt an extended zigzag conformation and a close packing. The crystallinity of ETFE ranges from 40% to 60%, and it has a melting temperature of 225–300 °C depending on the comonomer ratio and the processing method.

ETFE possesses superior processability and improved mechanical properties compared to other TFE copolymers. ETFE can be processed by all thermoplastic processing methods such as injection molding, compression molding, blow molding, rotational molding, extrusion, and wire coating. ETFE has high tensile strength, high flexibility, excellent impact strength, moderate stiffness, good abrasion resistance and high cutting resistance. ETFE modified by glass fiber reinforcement is tougher and stiffer and has higher tensile strength than PTFE, PFA or FEP. ETFE has a broad operating temperature range from as low as −100 °C to 150 °C.

As a copolymer of ethylene and TFE, ETFE has medium chemical resistance and flame resistance. Its radiation resistance is high with the advantage of being cross-linked by high-energy radiation. The radiation cross-linked ETFE wire insulation can be continuously used at 200 °C.

The main application for ETFE is wire and cable insulation, accounting for 60% of its market. ETFE has good resistance to petroleum and fuel permeation, which resulted in a significant growth of ETFE as fuel tubing.

The commercial ETFE products include Tefzel from DuPont, Fluon from Asahi Glass, Halon ETFE from Solvay, Neoflon ETFE from Daikin, and Dyneon ETFE from Dyneon.

1980s

Before 1980s, all the industrial fluoropolymers were semicrystalline materials. Crystalline fluoropolymers have certain shortcomings such as low optical clarity, high creep and poor solubility, which limited their processability and the type of applications. In 1985, DuPont developed an amorphous perfluoropolymer—Teflon AF. Teflon AF is a copolymer of TFE and perfluoro-2,2-dimethyl-1,3-dioxole (PDD) (Figure 10). The copolymerization of PDD and TFE is carried out in aqueous media with a fluorinated surfactant and ammonium persulfate as an initiator [33,34]. The composition of the copolymers could be adjusted by the comonomer feeding ratios. Different grades of Teflon AF products were prepared for different applications. At the same time, Asahi Glass also introduced a new amorphous perfluoropolymer—Cytop. Cytop is a homopolymer obtained via the cyclo-polymerization of perfluoro-3-butenyl-vinyl ether (PBVE) (Figure 10) [35,36].

**Figure 10.** The preparation of Teflon AF and Cytop.
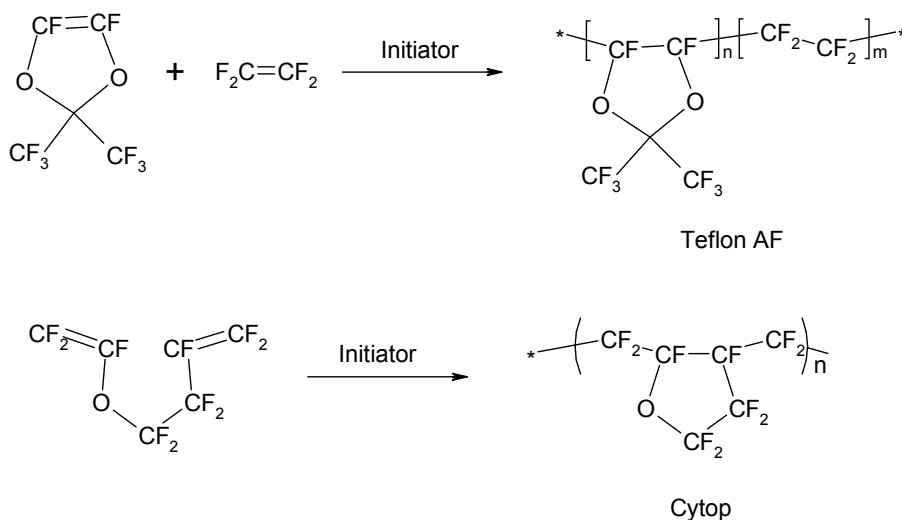
Teflon AF

Cytop

As amorphous perfluoropolymers, Teflon AF and Cytop share certain advantageous properties compared to the crystalline perfluoropolymers. Amorphous perfluoropolymers inherited the excellent chemical, thermal and electrical properties from the crystalline perfluoropolymers. At the same time, they also have high transparency, good solubility and better mechanical properties. The thin films formed from Teflon-AF and Cytop have excellent optical clarity and the lowest refractive index of all known organic materials, which makes them suitable for some special optical applications. They showed extremely high transparency over the UV, visible and near IR wavelengths. These amorphous perfluoropolymers also have the lowest dielectric constant (1.9) of all known polymers.

Amorphous perfluoropolymers can be melt-processed by all conventional processing techniques. At the same time, the good solubility in certain solvents offered them the versatile abilities in some special applications such as the ultrathin films or use with integrated circuits. For example, the spin coating of an amorphous perfluoropolymer solution is a useful processing technique for thin uniform coatings on flat substrates, and non-planar surfaces are usually coated using spraying or dip-coating methods. Amorphous fluoropolymers are used to make deep UV pellicles for electronic chip manufacturing processes. The low dielectric constant and low water absorption are great attributes for inter-layer dielectrics. The high optical transparency and very low refractive index of amorphous perfluoropolymers make them suitable for optical lenses and protective coatings. A new application for amorphous fluoropolymers is as core and cladding in optical fibers, for example the Lucina from Asahi Glass. Other interesting applications include photolithography uses for electronics, high-speed computer circuits and low dielectric constant insulators for high-performance electronic interconnects. While, the extremely high prices of amorphous perfluoropolymers restricted their use only to some special applications.

Recently, Solvay also introduced an amorphous perfluoropolymer Hyflon–AD, which is a family of copolymers from TFE and 2,2,4-trifluoro-5-trifluoromethoxy-1,3-dioxole (TTD) (Figure 11) [37].

Figure 11. The preparation of Hyflon AD.

Hyflon AD
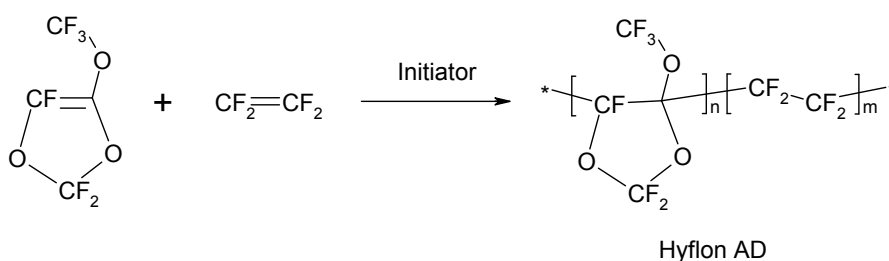
1990s

After the 1970s, little work was done on the traditional semicrystalline fluoropolymer materials, then in 1993 Hoechst invented THV by the copolymerization of TFE, HFP and VDF (Figure 12). Later, Hoechst granted 3M the rights for the production of THV by forming a joint venture—Dyneon in 1996. The new fluoropolymer is now known as Dyneon THV.

Figure 12. The preparation of THV.
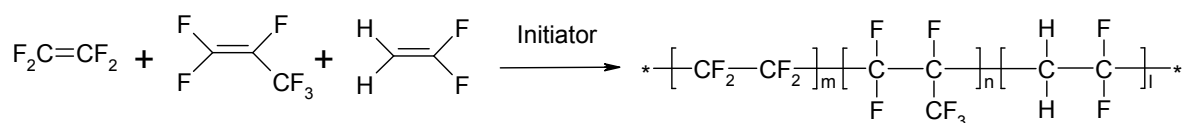
The preparation of THV is quite similar to the traditional procedures for PTFE, FEP and PVDF [38]. THV polymer is soluble in polar organic solvents and can easily form thin films by solution casting. The film obtained is transparent through UV, visible and near IR wavelengths. THV film also exhibited excellent adhesive ability to other polymers, making them easy to utilize in a very wide range of applications.

THV fluoropolymers are processed in the range of 230–250 °C by general polymer processing equipments. THV can be processed by extrusion, blow-molding and injection.

Most applications of THV are the multilayer constructions, where a thin layer of THV provides enhanced barrier properties to other layers. THV has excellent permeation resistance and chemical resistance to be used as fuel tubings due to its flexibility and the ease of processing. Similarly, THV is used for wire and cable insulation because of its flexibility and the flame resistance. THV can also serve as a flexible liner for chemical holding tanks.

The low processing temperatures, high clarity, high flexibility and excellent adhesive properties made THV very competitive compared to other fluoropolymers.

3. The Present and the Future of the Fluoropolymer Industry

The fluoropolymer industry has not come up with any really new product since the turn of the 21st century. The existing products can satisfy most of the requirements from their industrial applications. The current efforts are focusing on reducing production costs and expanding the application markets with continued globalization development (as with most other industries).

North America is still the most dominant market for fluoropolymers especially due to the significant demand in the U.S. by the wire and cable markets. The Asia-Pacific region is expected to be the fastest growing markets for fluoropolymers, with tremendous growth driven by Japan, China and India.

Typical applications of fluoropolymers are summarized in Table 1 for different industrial segments. FEP and PVDF are the fastest growing fluoropolymer products, especially in solar cell and fiber optic applications. PVDF is expected to grow enormously due to its increasing applications in lithium-ion batteries and architectural coatings. The growths in the chemical processing, cookware, bakeware, and medical markets are also important driving forces for the fluoropolymer industry.

The general properties were summarized in Table 2 for most fluoropolymers. Additional details about each fluoropolymer can be found in the references. In order to choose a suitable material for a specific application, it is necessary to thoroughly compare all the relevant properties and the total cost of the fluoropolymer candidate [39]. There could be several choices since the application properties of the fluoropolymers overlap in most cases. Therefore, any decision should consider the requirements, the cost, the benefit, and the competitive advantage of the final product.

Table 1. Typical applications of fluoropolymers for different industry segments.

Industries	Functions	Forms
Automotive	Mechanical property, thermal property, chemical property, and friction property.	O-rings, gaskets, valve stem seals, shaft seals, linings for fuel hoses, power steering, and transmission.
Chemical industry	Chemical resistance, mechanical property, thermal property, and weather stability.	Coatings for heat exchangers, pumps, diaphragms, impellers, tanks, reaction vessels, autoclaves, containers, flue duct expansion joints, heavy-wall solid pipe and fittings.
Electrical/electronic	Dielectric constant, flame resistance, and thermal stability.	Electrical insulation, flexible printed circuits, ultra-pure components for semiconductor manufacture.
Architectural and domestic	Weatherability, flame retardancy, friction property, thermal stability.	Water-repellent fabric, architectural fabric, non-stick coatings for cookware, and fiberglass composite for constructions.
Engineering	Mechanical property, thermal stability, chemical stability, weatherability, and surface energy.	Seats and plugs, bearings, non-stick surfaces, coatings for pipes, fittings, valve and pump parts, and gears.
Medical	Surface energy, biological stability, mechanical property, chemical resistance.	Cardiovascular grafts, ligament replacement, and heart patches.

Table 2. The summary of fluoropolymers with their general properties.

Fluoropolymer	Starting Year	Melting temperature (°C)	Tensile Modulus (MPa)	Break Elongation (%)	Dielectric Strength (kV/mm)	Appl. Temp (°C)	Main Applications
PTFE	1947	317–337	550	300-550	19.7	260	Chemical processing, wire and cable
PCTFE	1953	210-215	60-100	100-250	19.7	200	Barrier film, packaging and sealing
FEP	1960	260-282	345	~300	19.7	200	Cable insulation
PVF	1961	190-200	2000	90-250	12–14	110	Lamination, film and coating
PVDF	1961	155–192	1,040-2,070	50-250	63–67	150	Coating, wire, cable, electronic
ECTFE	1970	235–245	240	250-300	80	150	Flame resistant insulation
PFA	1972	302–310	276	~300	19.7	260	Chemical resistant components
ETFE	1973	254–279	827	150-300	14.6	150	Wire and cable insulation
THV	1996	145–155	82–207	500-600	48–62	93	Barrier film and insulation

Along with the development of the fluoropolymer industry, there are more concerns about the safety and environment effects of these materials. For example, people doubt that fluoropolymers may be contributing to the buildup of the fluorinated pollutants in the environment that could threaten the whole biological system on the earth. The pollutants of most concern include trifluoroacetic acid (TFA) and perfluorooctanoic acid (PFOA). Researchers stressed that there is no evidence that the amount of TFA from fluoropolymers is dangerous to people. However, because TFA lasts so long, it could build up to levels in the environment that may pose a problem for plants [40]. Several government agencies have reviewed the safety of fluoropolymer products, including the U.S. Consumer Product Safety Commission (CPSC), the U.S. Food and Drug Administration (FDA) and the U.S. Environmental Protection Agency (EPA). As a result, U.S. and international regulatory agencies—including the U.S. Food and Drug Administration and European Food Safety Authority—affirm the safety and reliability of fluoropolymers in their various uses, as long as the materials are used according to the industry guidance [41,42].

In summary, fluoropolymers have come a long way in the past 70 years. No doubt many new fluoropolymer materials will be developed and new applications will be found for old fluoropolymers. The importance of the fluoropolymer industry will not be destabilized before the emergence of new substitute materials.

Conflict of Interest

The author declares no conflict of interest.

References

1. Smart, B.E.; Feiring, A.E.; Krespan, C.G.; Yang, Z.-Y.; Hung, M.-H.; Resnick, P.R.; Dolbier, W.R., Jr.; Rong, X.X. New industrial fluoropolymer science and technology. *Macromol. Symposia* **1995**, *98*, 753–767.
2. Salamone, J.C. *Polymeric Materials Encyclopedia*; CRC Press: Boca Raton, FL, USA, 1996; Volume 4.
3. Scheirs, J. *Modern Fluoropolymers*; Wiley: Chichester, UK, 1997.
4. Hougham, G. *Fluoropolymers*; Kluwer Academic: New York, NY, USA, 1999.
5. Ebnesajjad, S. *Fluoroplastics*; Plastic Design Library: New York, NY, USA, 2002.
6. Ameduri, B.; Boutevin, B. *Well-Architectured Fluoropolymers*; Elsevier: Oxford, UK, 2004.
7. Drobny, J.G. *Technology of Fluoropolymers*, 2nd ed.; CRC Press: Boca Raton, FL, USA, 2008.
8. Fluoropolymers Division. Available online: http://www.fluoropolymers.org/index.htm (accessed on 20 January 2012).
9. Plunkett, R.J. The History of Polytetrafluoroethylene: Discovery and Development. In *High Performance Polymers: Their Origin and Development, Proceed. Symp.*; Seymour, R.B., Kirshenbaum, G.S., Eds.; Hist. High Performance Polymers at the ACS Meeting in New York, April 1986; Elsevier: New York, NY, USA, 1987.
10. Plunkett, R.J. Tetrafluoroethylene polymers. U.S. Patent 2,230,654, 1941.
11. Gangal, S.V. Polytetrafluoroethylene, homopolymers of tetrafluoroethylene. In *Encyclopedia of Polymer Science and Engineering*, 2nd ed.; John Wiley & Sons: New York, NY, USA, 1989.
12. Brasure, D.E.; Ebnesajjad, S. Vinyl fluoride polymers. In *Encyclopedia of Polymer Science and Engineering*, 2nd ed.; John Wiley & Sons: New York, NY, USA, 1989.
13. Dittman, A.L.; Wrightson, J.M. Manufacture of halocarbons. U.S. Patent 2,636,908, 1953.
14. Daikin's PCTFE equivalent to 3M's Kel-F®. Available online: http://www.daikin-america.com/faq/default.aspx (accessed on 20 April 2012).
15. Ebnesajjad, S. *Melt Processible Fluoroplastics: The Definitive User's Guide and Data Book*, Plastics Design Library, William Andrew Publishing; Elsevier: New York, NY, USA, 2002.
16. Gangal, S.V.; Brothers, P.D. Perfluorinated polymers, perfluorinated ethylene-propylene copolymers. In *Encyclopedia of Polymer Science and Technology*; Wiley Online Library; June 2010.
17. England, D.C.; Uschold, R.E.; Starkweather, H. Fluoropolymers: Their Development and Performance. In *Proceedings of the Robert A. Welch Foundation Conference on Chemical Research, XXVI*; Houston, TX, USA, 1982.

18. Sperati, C.A.; Starkweather, H.W., Jr. Fluorine-containing polymers II. Polytetrafluoroethylene. *Adv. Polym. Sci.* **1961**, *2*, 465–495.

19. Heitner-Wirguin, C. Recent advances in perfluorinated ionomer membranes. *J. Membrane Sci.* **1996**, *120*, 1–33.

20. Mauritz, K.A.; Moore, R.B. State of understanding of Nafion. *Chem. Rev.* **2004**, *104*, 4535–4585.

21. Connolly, D.J.; Longwood; Gresham, W.F. Fluorocarbon vinyl ether polymers. U.S. Patent 3,282,875, 1966.

22. Perma Pure LLC. Available online: http://www.permapure.com/tech-notes/key-concepts/nafion-physical-and-chemical-properties/ (accessed on 20 April 2012).

23. Kreuer, K.D.; Ise, M.; Fuchs, A.; Maier, J. Proton and water transport in nano-separated polymer membrane. *J. Phys. IV France* **2000**, *10*, 279–281.

24. Gierke, T.D.; Munn, G.E.; Wilson, F.C.J. The morphology in Nafion perfluorinated membrane products, as determined by wide- and small-angle X-ray studies. *J. Polym. Sci.: Polym. Phys.* **1981**, *19*, 1687–1704.

25. Schmidt-Rohr, K.; Chen, Q. Parallel cylindrical water nanochannels in Nafion fuel-cell membranes. *Nat. Mater.* **2008**, *7*, 75–83.

26. Gelbard, G. Organic Synthesis by Catalysis with Ion-Exchange Resins. *Ind. Eng. Chem. Res.* **2005**, *44*, 8468–8498.

27. Nafion, Wikipedia. Available online: http://en.wikipedia.org/wiki/Nafion (accessed on 20 April 2012).

28. Ford, T.A. Copolymers of vinylidene fluoride. U.S. Patent 2,468,054, 1949.

29. Bro, M.I. Polymerization of perfluorocarbon polymers. U.S. Patent 2,952,669, 1960.

30. Berry, K.L. Aqueous colloidal dispersions of polymers. U.S. Patent 2,559,752, 1951.

31. Carlson, D.P. Heat stable tetrafluoroethylene-perfluoro(alkyl vinyl ether) copolymers. U.S. Patent 4,599,386, 1986.

32. Ford, T.A.; Hanford, W.E. Polyvinylidene fluoride and process. U.S. Patent 2,435,537, 1948.

33. Resnick, P.R. Fluorinated dioxoles. U.S. Patent 3,865,845, 1975.

34. Resnick, P.R. Polymers of fluorinated dioxoles. U.S. Patent 3,978,030, 1976.

35. Nakamura, M.; Kaneko, I.; Oharu, K.; Kojima, G.; Matsuo, M.; Samejuma, S.; Kamba, M. Novel fluorine-containing cyclic polymer. U.S. Patent 4,897,457, 1990.

36. Nakamura, M.; Unoki, M.; Aosaki, K.; Yokotsuka, S. Cyclized perfluoropolymer (CPFP) a low k dielectric for microelectronics device. *IMC 1992 Proceedings*, Yokohama, Japan, June 1992; pp. 76–80.

37. Navarrini, W.; Tortelli, V.; Colaianna, P.; Abusleme, J. Inventors; Ausimont S.p.A., Assignee. Perfluorodioxoles, the preparation process thereof, and homopolymers and copolymers obtained therefrom. European Patent EP 0633257 B1, 1997.

38. Hull, D.E.; Johnson, B.V.; Rodricks, I.P.; Staley, J.B. *Modern Fluoroplastics*; Scheirs, J. Ed.; John Wiley and Sons: Chichester, UK, 1997; pp. 257–270.

39. Magdzinski, L. Select the right fluoropolymers for your plant. *Chem. Eng. Progr.* **2000**, 96(10) 21–30.

40. Vedantam, S. Accumulating Teflon chemical raises environmental concern. *Washington Post* **2001**, July 19.

41. SPI: the plastics industry trade association. Available online: http://www.fluoropolymer-facts.com/PFOA/content.cfm?ItemNumber=4137&navItemNumber=4040 (accessed on 20 April 2012).

42. *The Guide to Safe Handling of Fluoropolymers Resins*, 4th ed.; The Society of Plastic Industry, Inc.: Washington D.C., WA, USA, 2005.

Editorial

Special Feature *Organo-Fluorine Chemical Science*

Helmut Martin Hügel * and Neale Jackson

Health Innovations Research Institute & School of Applied Sciences, RMIT University, Melbourne, 3001 Australia

* Author to whom correspondence should be addressed; E-Mail: helmut.hugel@rmit.edu.au; Tel.: +61-3-9925-2626; Fax: +61-3-9925-3747.

1. Inventing the Fluorine Future

Fluorine is the 13th most abundant element and, with other fluorine containing functional groups, is a most effective element in biological substances, pharmaceuticals, agrochemicals, liquid crystals, dyes, polymers and a wide range of consumer products. This reflects its resistance to metabolic change due to the strength of the C-F bond providing biological stability and the application of its nonstick-interfacial physical characteristics. Its introduction often remains a synthetic challenge. The widespread use of organofluorines has increased the demand for the development of practical and simple reagents and experimental strategies for the incorporation of fluorine into all types of molecular structures and this was the reasoning behind this special feature on *Organo-Fluorine Chemical Science*.

The contributed articles belong to two broad groups: (i) preparation of fluorine materials, polymers; (ii) the synthesis/applications of organo-fluorine molecules.

2. Fluorine-Fatness—Due to Lack of Fitness

Theoretical [1] and experimental observations to explain the molecular origins of fluorocarbon hydrophobicity suggest that the hydrophobicity of a fluorocarbon, whether the interaction with water is as solute or as surface, is due to its "fatness". In solution, the extra work of cavity formation to accommodate a fluorocarbon, compared to a hydrocarbon, is not offset by enhanced energetic interactions with water. The enhanced hydrophobicity of fluorinated surfaces arises because fluorocarbons pack less densely on surfaces leading to poorer van der Waals interactions with water. The interaction of water with a hydrophobic solute/surface is primarily a function of van der Waals interactions and is substantially independent of electrostatic interactions. This independence is primarily due to the strong tendency of water at room temperature to maintain its hydrogen bonding network structure at an interface lacking hydrophilic sites.

3. Fluorine Materials and Polymers

For over a decade, a major synthetic target in fluorine material science has been the preparation of hydrophobic and superhydrophobic surfaces that are suitable for non-stick self-cleaning and anticorrosion applications. There is great interest in developing practical methods to generate such surfaces.

Jean-Denis Brassard and coworkers [2] in their paper on *Fluorine Based Superhydrophobic Coatings,* synthesized monodispersive silica nanoparticles of ~120 nm diameter via the Stöber process that were further functionalized using fluoroalkylsilane (FAS-17) molecules to incorporate the fluorinated groups with the silica nanoparticles in an ethanolic solution. The synthesized fluorinated silica nanoparticles were spin coated on flat aluminum alloy, silicon and glass substrates. The water contact angles and surface roughness increased with the number of spin-coated thin films layers. The critical size of ~119 nm rendered the aluminum surface superhydrophobic with three layers of coating using as-prepared nanoparticles suspended solution. On the other hand seven layers are required for a 50 vol.% diluted solution to achieve superhydrophobicity. In both the cases, water contact angles were more than 150°, and contact angle hysteresis was less than 2°. The authors considered that their coatings possessed self-cleaning properties. When applied on other substrates, like silicon or glass, superhydrophobicity is obtained by tuning the number of layers of deposition.

The α,ω-dialkoxyfluoropolyethers (DA-FPEs) prepared and characterized by Menghua Wu and coworkers [3] in their contribution: *An Environmentally Friendly Class of Fluoropolyether: α,ω-Dialkoxyfluoropolyethers* have been developed as a new class of environmentally friendly hydrofluoroethers (HFEs) with multiple uses; suitable as solvents, long-term refrigerants, cleaning fluids, and heat transfer fluids. Synthetic methodologies for DA-FPEs described here consist of radical-initiated oxypolymerization of olefin, peroxy-elimination reaction in peroxidic perfluoropolyethers (PFPE) and further chemical modification of α,ω-diacylfluoride PFPE. Physical properties of selected α,ω-dimethoxyfluoropolyethers have been evaluated and compared with analogous hydrofluoropolyethers having -OCF_2H as end-groups. The rationalization of the physical properties of these hybrid polymers is quite challenging. The highest boiling points are those of DM-FPEs, the intermediates are HFEs and the lowest ones are PFPEs. The above-mentioned result reflects the typical low intermolecular interactions of perfluorinated compounds. Partially fluorinated ethers, such as HFEs and DM-FPEs (α,ω-dimethoxyfluoropolyethers), display higher boiling temperatures and this is indicative of greater intermolecular polar interactions. Comparison of three similar fluoromethylethers, CF_3OCF_3 (b.p. 214 K; μ = 0.49 D), CF_2HOCF_3 (b.p. 238 K, μ = 1.18 D) and CH_3OCF_3 (b.p. 250 K, μ = 2.56 D) when contrasted to dimethyl ether, CH_3OCH_3 (b.p. 249K, μ = 1.30 D) the dipole moments really tell the story of the degree of polar interactions due to the presence of fluorine atoms. Interestingly, it is known that the presence of oxygen in PFPE impacts on chain flexibility but not on molecular polarity when compared with perfluoroalkyl analogues. Therefore, the glass transition temperature was found to decrease as the oxygen to carbon ratio was increased, maintaining a low cohesive energy density comparable with that of perfluoroalkanes. The progressive substitution of fluorine atoms with hydrogen in the methoxy end caps was found to lead to a stronger dipole and, consequently, to an increase of the boiling point. The boiling point differences between PFPEs and HFEs and between PFPEs and DM-FPEs are not constant but decrease continuously with

the chain length. Since the attractive forces are due to polar terminal groups, their relative intensity decreases as N increases and, as a result, the boiling points of HFEs, DM-FPEs and PFPE tend to an asymptote at higher N values. Atmospheric implications and global warming potentials of selected dialkoxyfluoropolyethers were also considered.

Srinivas Hanumansetty and coworkers [4] describe in their article: *Stain Resistance of Cotton Fabrics before and after Finishing with Admicellar Polymerization* that admicellar polymerization permitted the formation of durable finishes that exhibited high performance in stain resistance and stain repellency. The mild method of fabric modification by admicellar polymerization is its greatest advantage. However innovative protocols to implement admicellar polymerization are needed for its application on a commercial scale.

Takashi Okazoe and collaborators [5] in their contribution: *Application of Liquid-Phase Direct Fluorination: Novel Synthetic Methods for a Polyfluorinated Coating Material and a Monomer of a Perfluorinated Polymer Electrolyte Membrane* showcase the utilization of their PERFECT chemical fluorine synthesis procedure for the preparation of novel multifunctional polyfluorinated anti-staining material. Perfluorination with fluorine gas is hazardous, is it possible to engineer the PERFECT process into a flow system to make it greener chemistry?

In the manuscript: *Overview of the Development of the Fluoropolymer Industry*, Hongxiang Teng [6] presents his views on the subject that fluoropolymers are important specialty polymers for their high performance properties and also for the combination of these properties as described in the review. The introduction attributes the reasons to the chemistry of fluorine and replacement of typically all hydrogens by fluorine in these polymers. The author continues to relate properties to structure (the larger size of fluorine relative to hydrogen) and chemistry of fluorine (such as the strong bonds to carbon). These aspects of the chemistry of fluoropolymers create a unique range of "on cursory inspection" unrelated properties. Preparation of FEP (copolymer of fluorinated ethylene and propylene), is said to contain 5% hexafluoropropylene. However the critical aspect of the chemistry of this copolymerization is the reactivity ratios of the two monomers. A difficulty in preparing many of the tetrafluoroethylene copolymers is widely separated reactivity ratios, or in the case of ECTFE (copolymer of ethylene and CTFE), the cross-reaction rates must be large to form an alternating copolymer. The included tables are useful and provide an effective summary to position individual discussions. This review provides a brief summary of fluoropolymers in order of development or manufacturing time. The fluoropolymers provide an example of how the high performance PTFE has been modified using polymer chemistry to decrease absolute properties and increase diversity of properties by substitution of fluorines or copolymerization.

The paper on *Nanoimprint Resist Material Containing Ultraviolet Reactive Fluorine Surfactant for Defect Reduction in Lithographic Fabrication* by Satoshi Takei and Atsushi Sekiguchi [7] describe their development and optimization of using 4.5 wt% of the fluorine surfactant 4,4,5,5,6,6,7,7,8,8,9,9,10,10,11,11,1-heptadecafluoro-2-hydroxyundecyl acrylate as a template release component in their formulation of nanoimprint resist materials. The fluorine surfactant effectively contributed to providing a clean separation technology for mass-production using UV curing nanoimprint lithography.

The focus of Yen-Ting Chen and coworkers [8] in *Optimization of Fluorine Plasma Treatment for Interface Improvement on $HfO_2/In0_{.53}Ga0_{.47}As$ MOSFETs* was to optimize the effects of CF_4/O_2

plasma power wattage and treatment time on $HfO_2/In_{0.53}Ga_{0.47}As$ gate stack. This resulted in significant improvement of the effective channel mobility (μ_{eff}), transconductance (G_m), drive current (I_d), and sub-threshold swing (SS). With F incorporation, they have successfully developed excellent interface quality of HfO_2 directly on $In_{0.53}Ga_{0.47}As$ without using interface passivation layer. Fluorinated samples exhibit low interface trap density (Dit) of 4.9×10^{11} cm^{-2}eV^{-1}, which is the lowest value compared to prior reported $HfO_2/In_{0.53}Ga_{0.47}As$ gate stacks. Incidentally, Hou and coworkers [9] have reported a simple technique to synthesize highly crystalline InGaAs NWs by a novel two-step chemical vapor deposition (CVD) method with a high growth yield. The NWs exhibit impressive electrical performance with a I_{ON}/I_{OFF} ratio of ~10^5 and field-effect mobility of ~2,700 cm^2/(V·s) when configured in the back-gate NW field-effect transistors (FETs).

Yosuke Mizuno and Kentaro Nakamura [10] in their article *Enhancement of Brillouin Scattering Signal in Perfluorinated Graded-Index Polymer Optical Fibers* studied two methods to enhance the Brillouin Stokes signal in perfluorinated graded-index polymer optical fibers [PFGI-POFs]. The backscattered Brillouin light spectrum properties of [PFGI-POFs] with 62.5-μm core diameter were investigated. The Stokes power was extremely high compared to that of a PFGI-POF with 120-μm core, and the Brillouin threshold power for 5-m PFGI-POF was estimated to be 53.3 W. It was also shown that employing a PFGI-POF longer than ~50 m is not an effective way to enhance the Stokes signal. In addition, it was theoretically found that it is difficult to reduce the Brillouin threshold power of PFGI-POFs at 1.55-μm wavelength below that of long silica single-mode fibers even if their core diameter is sufficiently decreased to satisfy the single-mode condition. Finally, the Brillouin linewidth narrowing effect was confirmed. The authors conclude that these results will be a good guideline for developing practical Brillouin systems using PFGI-POFs, as well as for designing new PFGI-POF structures for Brillouin applications in future.

As urea and amide derivatives are ideal functional groups for the design of low molecular weight gelators, attributed to their rigidity, strength and ability to form highly directional hydrogen bonds, Anilkumar Raghavanpillai and Vincent Franco [11] in their article *Self-Assembled Fluorinated Organogelators for Surface Modification* prepared some novel alkyl- and perfluoroalkyl-containing urea and amides from amino acid derivatives and investigated their utilization as low molecular weight organogelators. Most of these compounds showed excellent gelation behavior in organic solvents at low concentrations. A few organogelators selected from the initial screening were used for surface modification of fibrous substrates to create hydrophobic and oleophobic composites. The hydrophobic and oleophobic behaviors of these composites were ascribed to a combination of increased surface roughness and the alkyl/fluorinated functionalities present in the gelator backbone. In general the urea-amide derivatives were better gelators than the corresponding bis- or tris-amide derivatives. Analogous urea-ester derivatives failed to gel in any organic solvents, indicating a combination of urea and amide functionalities, or multiple amide groups, are desirable to induce gelation. The nonwoven surfaces impregnated with perfluoroalkyl-containing organogelators showed excellent oleophobic behavior. Superior hydrophobic and oleophobic behavior exhibited by these composites were attributed to a combination of micro-structured surface morphology created by the xerogel and the presence of fluorocarbon/hydrocarbon functionalities in the gelator backbone.

Yoshihiro Tsujimoto, Kazunari Yamaura and Eiji Takayama-Muromachi [12] in their paper *Oxyfluoride Chemistry of Layered Perovskite Compounds* review recent progress and new challenges

in the area of oxyfluoride perovskite, especially layered systems including Ruddlesden-Popper (RP), Dion-Jacobson (DJ) and Aurivillius (AV) type perovskite families. Each of the fluorinating agents that have been reported so far, including F_2 gas, NH_4F, XeF_2, CuF_2 and PVDF and PTFE, exhibits a distinct fluorinating power and reaction pathway. Examples are given illustrating that the fluorine contents in the resultant material depend on the choice, not only of the fluorinating agent, but also the anion lattice of the precursors. Synthetic strategies are proposed to further extend RP type perovskite compounds, with particular reference to newly synthesized oxyfluorides, Sr_2CoO_3F and $Sr_3Fe_2O_{5+x}F_{2-x}$ ($x \sim 0.44$). In future it will be interesting to explore the applications of these extended fluorinated oxyfluoride Perovskite compounds.

4. Synthesis/Applications of Organo-Fluorine Molecules

Organofluorine compounds possess desirable physical properties that are utilized widely in pharmaceuticals, agrochemicals, polymers and as biomaterials. In the case of medicinal chemistry, fluorine functionalities including $-R_F$, -F, $-CF_3$ $-OCF_3$ impart valuable *drug like* physiological properties on molecules that improve receptor binding selectivity, increase lipophilicity and metabolic stability. The practical synthesis of organofluorine compounds is an important scientific endeavor.

Christel Dolain and coworkers contribution [13]: *Nucleic Acid Based Fluorinated Derivatives: New Tools for Biomedical Applications*, reviews recent developments in the preparation of nucleic acid-based fluorinated derivatives, e.g., nucleosides or oligonucleotides connected to fabricated by coupling highly fluorinated chains or labeled with either a nucleoside or an oligonucleotides-modified with one or more fluorine atoms, have been investigated recently due to their high potential for biomedical applications. The application of nucleoside-based fluorocarbon derivatives is focused on three broad objectives: (i) construction of novel supramolecular materials and/or devices; (ii) development of new drug delivery systems; and (iii) discovery of new therapeutic molecules. The authors' review recent research on highly fluorinated nucleic acids derivatives, in particular nucleoside and oligonucleotide fluorocarbon amphiphiles as well as those with properties and applications of fluorine-labeled fluorinated oligonucleotide analogues. The review succeeds in showcasing the future potential role that highly fluorinated amphiphiles could play in chemistry, biology and material science.

Synthesis of Some New Fluorinated Hexahydroquinoline and Acridinedione Derivatives in Trifluoroethanol is the article contribution by Cosmas Okoro, Mumiye Ogunwale and Tasneem Siddiquee [14] in which they describe a facile one-pot synthesis of new fluorinated hexahydroquinoline derivatives via an unsymmetric Hantzsch reaction utilizing 5-trifluoromethyl-1,3-cyclohexanedione, aldehydes, acetoacetate ester, and ammonium acetate in trifluoroethanol. The reaction is simple and rapid with high yield. The reaction was extended to the synthesis of hexahydroacridinedione under similar conditions. The biological activities of the products will be investigated.

Understanding/predicting chemical reactions relies on the ability to calculate (simply) the energy and thermodynamics involved in the transformations. Jon Baker and Max Muir's contributed paper [15]: *Further Successes of the Meisenheimer Model* illustrate that this concept is true. Their model involves calculating the energy of all possible Meisenheimer complexes at a standard level of *ab initio* theory using the fluoride ion as a "typical" nucleophile, the preferred site for nucleophilic

substitution then corresponds to the most stable (lowest energy) complex. This simple approach that predicted the principal site for 15 nucleophilic substitutions in aromatic perfluorocarbons has been extended and reliably tested by comparison to the series of recently published NH2 amination reactions of perfluoro-arenes in liquid ammonia by Malykhin and coworkers. The model accurately predicted the experimental results for all of the SNAr reactions therefore confirming the model's general utility. The authors conclude with the prediction that their model predicts that mono-amination of 1-trifluoromethyl-2-amino 3,5,6-trifluorobenzene in liquid ammonia should produce almost exclusively 1-trifluoromethyl-2,6-diamino-3,5-difluorobenzene.

Joseph Sloop [16] and coworkers present interesting organofluorine synthesis in their paper: *Novel Fluorinated Indanone, Tetralone and Naphthone Derivatives: Synthesis and Unique Structural Features.* They analyzed the uncommon product outcomes from the Claisen condensation coupled with the fluorinating reagent Selectfluor® with the above ketones.

The article entitled: *Computational Study on the Acid Catalyzed Reactions of Fluorine-Containing 2,4-Dialkoxy-3,4-dihydro-2H-pyrans with Aromatic Compounds* by Norio Ota [17] and coworkers illustrated that the predicted product outcomes from DFT calculations were consistent with the experimental data and mechanistic pathways to products when fluorinated dihydropyrans were reacted with aromatics.

Fluorine-18, widely used in clinical positron emission tomography (PET) imaging in biomedical science because its optimal physical decay properties (**t**$1/2$ = 110 min, $\mathbf{E_{\beta+,\,max}}$ = 0.6 MeV) facilitates multistep syntheses and PET images of high quality. Wångler and coworkers [18] in their review *Silicon-[^{18}F] Fluorine Radiochemistry: Basics, Applications and Challenges* describe the radiochemical science surrounding Si-^{18}F bond synthesis, the application of Si-^{18}F tracers for PET imaging and some of the remaining challenges regarding the optimization/balance of the *in vivo* physic-chemical properties of these radiochemicals in relation to their stability and biodistribution. The increased application of ^{18}F Fluoro-click-bioconjugation to the variety of bio-scaffolds employed, promises to be an effective strategy able to counter balance the high lipophilicity-hydrophilicity nature of the radiochemical carriers, thereby enhancing target visualization via PET with only minute retention of radioactivity in other tissues and organs.

One of the most significant classes of synthetic antibacterials are fluoro-quinolone antibiotics. The article: *A Study of Fluorinated β-Nitrostyrenes as Antimicrobial Agents* by King Lo *et al*. [19] examined the effect of the presence of fluorine functionalities in *β*-methyl-*β*-nitrostyrenes on their antimicrobial activity. The MIC values confirmed that fluorinated *β*-methyl-*β*-nitrostyrenes had the highest antimicrobial activity against Gram negative, Gram positive bacteria and the fungus *C. albicans*. However the correlations between MIC and K_D [logP] values were not straightforward. Similarly it was also difficult to correlate the position of fluorine substitution on the benzene ring or the effect of multiple fluorine substituents with antibacterial activity and logP values. Can aromatic ring fluorine/hydrogen exchange influence membrane permeability? Generally, aromatic F/H substitution tends to increase compound lipophilicity, in direct contrast to what was observed. Alternatively, the reason for the effectiveness of fluorine substitution on the aromatic ring may be connected with the high electronegativity of fluorine, although size factors could also be important. Perhaps the electronegativity of fluorine could affect binding affinity to the binding site of the bacteria, thus causing inhibition of the enzyme. Further investigations with other fluorine-substituted

compounds to determine the structural features required for the optimal anti-bacterial activity of *β*-methyl-*β*-nitrostyrene compounds, and where the activity occurs, are currently being carried out.

References

1. Dalvi, V.H.; Rossky, P.J. Molecular origins of fluorocarbon hydrophobicity. *PNAS* **2010**, *107*, 13603–13607.
2. Brassard, J.-D.; Sarkar, D.; Perron, J. Fluorine Based Superhydrophobic Coatings. *Appl. Sci.* **2012**, *2*, 453–464.
3. Wu, M.; Navarrini, W.; Spataro, G.; Venturini, F.; Sansotera, M. An Environmentally Friendly Class of Fluoropolyether: α,ω-Dialkoxyfluoropolyethers. *Appl. Sci.* **2012**, *2*, 351–367.
4. Hanumansetty, S.; Maity, J.; Foster, R.; O'Rear, E.A. Stain Resistance of Cotton Fabrics before and after Finishing with Admicellar Polymerization. *Appl. Sci.* **2012**, *2*, 192–205.
5. Okazoe, T.; Shirakawa, D.; Murata, K. Application of Liquid-Phase Direct Fluorination: Novel Synthetic Methods for a Polyfluorinated Coating Material and a Monomer of a Perfluorinated Polymer Electrolyte Membrane. *Appl. Sci.* **2012**, *2*, 327–341.
6. Teng, H. Overview of the Development of the Fluoropolymer Industry. *Appl. Sci.* **2012**, *2*, 496–512.
7. Takei, S.; Sekiguchi, A. Nanoimprint Resist Material Containing Ultraviolet Reactive Fluorine Surfactant for Defect Reduction in Lithographic Fabrication. *Appl. Sci.* **2012**, *2*, 24–34.
8. Chen, Y.-T.; Wang, Y.; Xue, F.; Zhou, F.; Lee, J.C. Optimization of Fluorine Plasma Treatment for Interface Improvement on $HfO_2/In_{0.53}Ga_{0.47}As$ MOSFETs. *Appl. Sci.* **2012**, *2*, 233–244.
9. Hou, J.J.; Han, N.; Wang, F.; Xiu, F.; Yip, S-P.; Hui, A.T.; Hung, T-F. Ho, J.C. Synthesis and characterizations of ternary in gas nanowires by a two-step growth method for high-performance electronic devices. *ACS Nano* **2012,** *6*, 3624–3630.
10. Mizuno, Y.; Nakamura, K. Enhancement of Brillouin Scattering Signal in Perfluorinated Graded-Index Polymer Optical Fibers. *Appl. Sci.* **2012**, *2*, 46–60.
11. Raghavanpillai, A.; Franco, V.A. Self-Assembled Fluorinated Organogelators for Surface Modification. *Appl. Sci.* **2012**, *2*, 175–191.
12. Tsujimoto, Y.; Yamaura, K.; Takayama-Muromachi, E. Oxyfluoride Chemistry of Layered Perovskite Compounds. *Appl. Sci.* **2012**, *2*, 206–219.
13. Dolain, C.; Patwa, A.; Godeau, G.; Barthélémy, P. Nucleic Acid Based Fluorinated Derivatives: New Tools for Biomedical Applications. *Appl. Sci.* **2012**, *2*, 245–259.
14. Okoro, C.O.; Ogunwale, M.A.; Siddiquee, T. Synthesis of Some New Fluorinated Hexahydroquinoline and Acridinedione Derivatives in Trifluoroethanol. *Appl. Sci.* **2012**, *2*, 368–374.

15. Baker, J.B.; Muir, M. Further Successes of the Meisenheimer Model. *Appl. Sci.* **2012**, *2*, 443–452.

16. Sloop, J.C.; Boyle, P.D.; Fountain, A.W.; Gomez, C.; Jackson, J.L.; Pearman, W.F.; Schmidt, R.D.; Weyand, J. Novel Fluorinated Indanone, Tetralone and Naphthone Derivatives: Synthesis and Unique Structural Features. *Appl. Sci.* **2012**, *2*, 61–99.

17. Ota, N.; Kamitori, Y.; Shirai, R.; Hatakenaka, M.; Okada, E. Computational Study on the Acid Catalyzed Reactions of Fluorine-Containing 2,4-Dialkoxy-3,4-dihydro-2*H*-pyrans with Aromatic Compounds. *Appl. Sci.* **2012**, *2*, 129–138.

18. Wångler, C.; Kostikov, A.; Zhu, J.; Chin, J.; Wångler, B.; Schirmacher, R. Silicon-[^{18}F]Fluorine Radiochemistry: Basics, Applications and Challenges. *Appl. Sci.* **2012**, *2*, 277–303.

19. Lo, K.; Cornell, H.; Nicoletti, G.; Jackson, N.; Hügel, H. A Study of Fluorinated β-Nitrostyrenes as Antimicrobial Agents. *Appl. Sci.* **2012**, *2*, 114–128.

applied sciences

Aims

Applied Sciences (ISSN 2076-3417) provides an advanced forum on all aspects of applied natural sciences. It publishes reviews, research papers and communications. Our aim is to encourage scientists to publish their experimental and theoretical results in as much detail as possible. There is no restriction on the length of the papers. The full experimental details must be provided so that the results can be reproduced. Electronic files and software regarding the full details of the calculation or experimental procedure, if unable to be published in a normal way, can be deposited as supplementary electronic material.

Please see the Scope of *Applied Sciences* at www.mdpi.com/journal/applsci/about.

Applied Sciences Indexing and Abstracting

Applied Sciences is covered by following indexing and abstracting databases:

- Chemical Abstracts (CAS)
- Directory of Open Access Journals (DOAJ)
- e-Helvetica (Swiss National Library Archive)
- Google Scholar
- Open-J-Gate
- Ulrich's™

The foundation for the Ulrich's Global Serials Intelligence services is the Ulrich's knowledgebase - the world's most authoritative source of bibliographic and publisher information for serials and the most comprehensive source of print and electronic serials data available.

MDPI journals are generally Medline indexed and available in PubMed where appropriate; we understand the importance of this. We submit our journals to be considered for retrospective Medline indexing as soon as they are eligible.

Applied Sciences is published by MDPI quarterly. If you would like to submit a paper, please first visit the Instructions for Authors website (www.mdpi.com/journal/applsci/instructions). Manuscripts should be submitted through the online manuscript submission and editorial system at www.mdpi.com/user/manuscripts/upload.

MDPI publishes several peer-reviewed, open access journals listed at www.mdpi.com. All MDPI journals maintain a rapid, yet rigorous, peer-review and editorial process.

Final Acknowledgements

I would like to thank the Guest Editor Helmut Martin Hügel of this special issue "Organo-Fluorine Chemical Science" for the excellent job. I would also like to thank the authors for so many relevant and high quality papers within the specific topic of this special issue, which together are an important contribution to studies on Organo-Fluorine.

Finally, I would like to use this opportunity to extend a general invitation to scholars whose expertise matches the interdisciplinary areas of Applied Sciences to submit their original research articles or reviews to our journal *Applied Sciences*. Further, we also welcome proposals from scholars interested in guest editing a special issue for our journal; please contact the Editorial Office at applsci@mdpi.com.

Sincerely,

Dr. Shu-Kun Lin
Publisher

This book contains the printed edition of the special issue on Organo-Fluorine Chemical Science that appeared in *Appl. Sci.* (http://www.mdpi.com/journal/applsci).

Applied Sciences (ISSN 2076-3417; CODEN: ASPCC7), an international scientific open access journal on all aspects of applied natural sciences, is published by MDPI online quarterly.